

JAYCOR

Research in Pulsed Power Plasma Physics

Final Report

Volume I
Sections One, Two, and Three

August 1996

Prepared by:

Steve Swanekamp
David Rose

Prepared for:

Naval Research Laboratory
4555 Overlook Avenue, SW
Washington, DC 20375-5000

Contract Number: N00014-93-C-2086

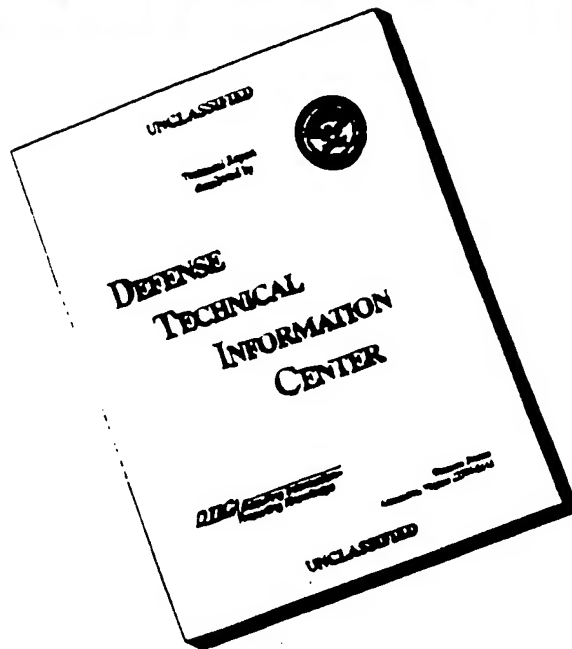
19970103 117

DEIC QUALITY INSPECTION

1410 Spring Hill Road • Suite 300 • McLean, Virginia 22102 • (703) 847-4000

**APPROVED FOR PUBLIC RELEASE
DISTRIBUTION UNLIMITED**

DISCLAIMER NOTICE



**THIS DOCUMENT IS BEST
QUALITY AVAILABLE. THE
COPY FURNISHED TO DTIC
CONTAINED A SIGNIFICANT
NUMBER OF PAGES WHICH DO
NOT REPRODUCE LEGIBLY.**

TABLE OF CONTENTS

VOLUME I

SECTION ONE OVERVIEW

SECTION TWO INTENSE ION BEAM GENERATION

- 2.1 Applied-B Ion Diode Development II-1
- 2.2 Pulser Development for the Active Plasma Source II-2

SECTION THREE INTENSE BEAM TRANSPORT

- 3.1 Transport of Intense Ion Beams in Gas III-1
- 3.2 Analysis of Ion Beam Transport Constraints III-1
- 3.3 Diagnostic Development III-2
- 3.4 Additional Beam Transport Work III-2
- 3.5 List of Papers III-2

VOLUME II

SECTION FOUR MICROSECOND CONDUCTION TIME PLASMA OPENING SWITCHES

- 4.1 Plasma source development IV-2
- 4.2 Microsecond POS operation IV-2
- 4.3 POS-Load Coupling IV-3
- 4.4 The ZFX Facility IV-3
- 4.5 List of papers IV-3

SECTION ONE

OVERVIEW

This final report covers work performed by JAYCOR under Contract N00014-93-C-2086 with the Pulsed-Power Branch of the Plasma Physics Division of the Naval Research Laboratory (NRL). The research was conducted on-site at NRL by JAYCOR personnel as part of NRL's research programs in support of light ion inertial confinement fusion for the Department of Energy, and advanced pulsed-power systems for Nuclear Weapons effects simulations (NWES) for the Defense Nuclear Agency (DNA), now the Defense Special Weapons Agency (DSWA). The tasks performed under this contract included work in several areas. The original statement of work included the following tasks:

- 1a. investigate and optimize POS operation in the 1 microsecond conduction time regime;
- 1b. study the use of other opening switch concepts for use in greater than 10 microsecond conduction time regime;
- 1c. investigate the coupling of a ten microsecond time opening switch to a one microsecond opening switch;
- 1d. investigate the optimization of coupling between the POS and a load;
- 1e. develop plasma sources for use in inductive energy store applications;
- 1f. develop and study techniques for the transport of light ion beams; and
- 1g. develop ion beam conditions appropriate for the various transport schemes (addressed in task 1f).

JAYCOR personnel provided skilled design and, in the case of small items, fabrication of experimental hardware used in various experiments performed during this contract period. During the course of this contract JAYCOR was directed by the COTR to discontinue work on tasks 1b and 1c. Significant progress was made on the remaining tasks in the statement of work. The results of that work are described in this report.

SECTION TWO

INTENSE ION BEAM GENERATION

During the contract period, research on intense ion beam generation was centered around the development of an applied-magnetic-field ion diode for the Gamble II generator at NRL. This section summarizes JAYCOR efforts in this area of research. Section 2.1 summarizes the results of several experimental runs during the development of the applied-B ion diode on Gamble II. These experiments used both active and passive plasma sources. Section 2.2 summarizes the development of the pulser for the active plasma source. In addition to the work reported here, development of other intense ion beam sources continued at NRL with active JAYCOR participation.

2.1 Applied-B Ion Diode Development

During the contract period, the applied-B extraction ion diode, built by Sandia National Laboratories and installed on Gamble II, was tested. An intensive effort to characterize the performance and optimization of this diode was carried out with JAYCOR participation. This Sandia designed diode uses two pairs of magnetic field coils, located beyond the anode and the cathode, to produce a radial magnetic field in the diode gap. Currents are varied independently to obtain the desired magnetic field configuration. This diode design was tested with both passive grooved anodes (epoxy-fills the grooves) and active anodes or "Exploding Metallic Foil Anode Plasma Sources" (EMFAPS). In the latter case, either an external power source (see Section 2.2) or energy diverted from a plasma-opening-switch drives current (> 10 kA) through a thin film foil in the anode surface at the start of the generator pulse. This current vaporizes the foil, leading to the formation of an anode plasma and therefore a ready supply of ions. A sputter-coating system was developed by JAYCOR personnel to prepare the anodes for use in the EMFAPS-driven applied-B diode. The performance of the sputter-coating system was improved several times by JAYCOR personnel during the contract period by careful and detailed redesign efforts.

The evolution of the anode plasma (including the breakdown of the foil) was studied in bench-top experiments using several diagnostics including photography, spectroscopy, electrical measurements, and interferometry. Improvements in the uniformity of the breakdown of the foil were observed when the epoxy substrate surface was roughened before coating. Redesign of the current contacts to the EMFAPS foil also demonstrated improved uniformity of the foil breakdown and made the anodes more robust and easier to field.

After a significant development effort (see attached reports), it was determined that the existing Sandia designed, 4-coil applied-B ion diode would not meet NRL's requirements for ion beam generation. A new 2-coil applied-B ion diode design was put forward, with active JAYCOR participation. This new applied-B diode is designed to better match the Gamble II generator specifications. At this time, construction of the new diode is under way. The new diode design will be fielded with both passive and EMFAPS anodes.

2.2 Pulser Development for the Active Plasma Source

As discussed in Section 2.1, the applied-B ion diode requires an active plasma source. A new external pulser circuit was developed by JAYCOR personnel to deliver 50-150 kA of current with a risetime of less than 10 ns and a pulse duration of approximately 20 ns. The pulser uses a three stage Marx generator followed by a water-loaded pulse forming line. The current is switched into multiple-cable feeds leading to the diode. The enclosed reports document the details of the design and testing of this pulser. A copy of this pulser has been supplied to Sandia National Laboratories for EMFAPS experiments on the SABRE generator.

2.3 List of Papers

- 2.3.1 "Extraction, applied-B ion diode development with externally-driven, active anode plasma source," J.M. Neri, D.D. Hinshelwood, J.R. Boller, R. Fisher, J. Greenly, W.A. Noonan, P.F. Ottinger, S.J. Stephanakis, and F.C. Young, in the Proceedings of the Tenth International Conference on High Power Particle Beams, (June 20-24, 1994, San Diego, Ca), p. 431.
- 2.3.2 "Analysis of applied-B diode runs 9 and 10," D. Hinshelwood, Pulsed Power Physics Technote 95-06 (1995).
- 2.3.3 "(Re) Analysis of applied-B diode run 8," D. Hinshelwood, Pulsed Power Physics Technote 95-04 (1995).
- 2.3.4 "Analysis of applied-B diode run 7," D. Hinshelwood, Pulsed Power Physics Technote 95-03 (1995).
- 2.3.5 "Analysis of applied-B diode run 6," D. Hinshelwood, Pulsed Power Physics Technote 95-02 (1995).
- 2.3.6 "Analysis of applied-B diode run 5," D. Hinshelwood, Pulsed Power Physics Technote 95-01 (1995).
- 2.3.7 "Analysis of applied-B diode run 8," D. Hinshelwood, Pulsed Power Physics Technote 94-16 (1994).
- 2.3.8 "Initial results with an EMFAPS on Gamble II," D. Hinshelwood, Pulsed Power Physics Technote 93-03 (1993).
- 2.3.9 "EMFAPS pulser development," D. Hinshelwood and R. Fisher, Pulsed Power Physics Technote 95-33 (1995).
- 2.3.10 "Initial pulser-driven EMFAPS results," D. Hinshelwood, R. Fisher, and J. Neri, Pulsed Power Physics Technote 93-19 (1993).
- 2.3.11 "Calibration of applied-B diode monitors," D. Hinshelwood, Pulsed Power Physics Technote 94-09 (1994).

EXTRACTION, APPLIED-B ION DIODE WITH EXTERNALLY-DRIVEN, ACTIVE ANODE PLASMA SOURCE

J. M. Neri, D. D. Hinshelwood,* J. R. Boller, R. Fisher,* J. Greenly,***

W. A. Noonan,** P. F. Ottinger, S. J. Stephanakis, and F. C. Young

Pulsed Power Physics Branch, Plasma Physics Division

Naval Research Laboratory, Washington, DC 20375-5346

Abstract

We report the first use of an external current source to drive an exploding foil anode plasma source. The source is fielded in an extraction, applied-B ion diode furnished by Sandia National Laboratories (SNL). An ion beam is produced with parameters approaching those required for ion beam transport research in support of the DOE ICF program. The time-resolved ion beam current density is measured using Rutherford scattering and a novel Faraday cup developed at Cornell University.

We are developing an extraction, applied-B ion diode, on the Gamble II generator at NRL, for ion-beam-transport research in support of the SNL ion-beam ICF effort. An ion beam with a voltage above 1 MV and a proton current above 200 kA is required. At present we are using diode hardware from the SNL SABRE generator. Development of this diode on Gamble II is a challenge because of the relatively low (~ 1 MV) voltage, high (~ 300 kA) ion current, and small (~ 60 cm²) anode area involved. These result in required enhancement factors 2-3 times greater than those in similar experiments on LION¹ at Cornell, SABRE² at SNL, and KALIF³ at KfK, Karlsruhe. The need for stable, low-impedance diode operation with early turn-on (to avoid insulator flashover) necessitates the use of an active anode plasma source. We are using a version of the Exploding Metallic Foil Anode Plasma Source (EMFAPS). First developed at Cornell,¹ this technology has been advanced significantly by work at KfK.^{4,5} This source comprises a thin metallic foil deposited on an insulating anode substrate. A plasma opening switch is used to divert the leading edge of the generator current through the foil, rapidly heating the foil and releasing desorbed gases. Subsequent breakdown of this gas layer results in a

uniform, largely protonic plasma conformal to the anode surface.

The relatively large jitter of the Gamble II Marx and intermediate water switch precludes reproducible current diversion with a plasma switch. Instead, we report here on the first use of an EMFAPS driven by an external pulser, triggered in our case by the water-switch output. A four-stage L-C inversion pulser is used to drive 30-40 kA through the foil with a 10-90 risetime of 20 ns. An array of 30, RG-223 cables connects the pulser to the foil through the Gamble II transit-time isolator. The total jitter, arising from the pulser and the Gamble II oil output switch, is about 15 ns, which is seen to be acceptable.

The EMFAPS anode and experimental arrangement used in bench tests are shown in Fig. 1a. The anode comprises an epoxy substrate cast between a stainless outer ring and a thin brass inner ring. First, copper current contacts are sputter-deposited over the epoxy-metal joints. Then, 400 to 1200-Å aluminum films are sputter-deposited over the entire anode face. These films are characterized by a thin-film monitor during deposition and by electrical resistance measurements afterwards. Typical film resistance is about four times the bulk value.

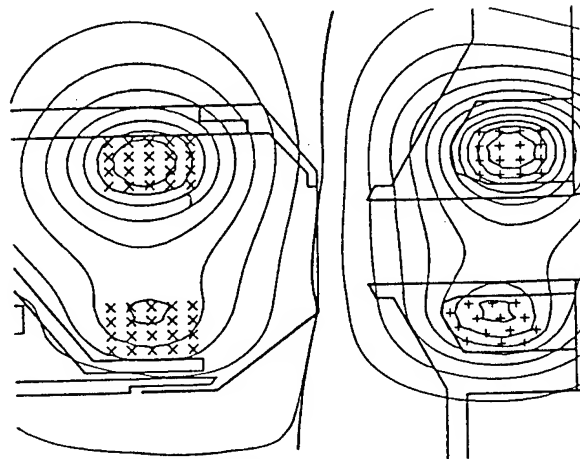
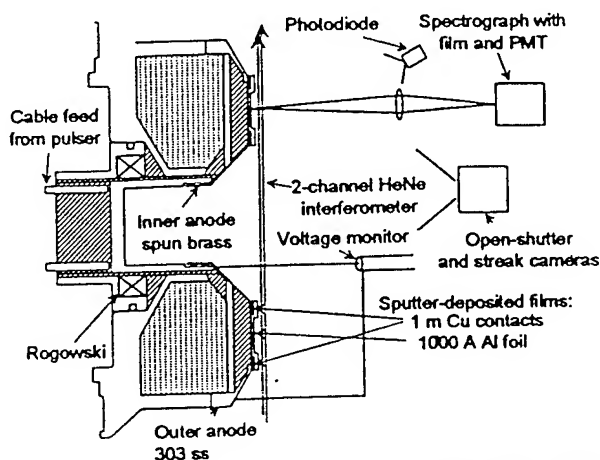


Fig. 1: The EMFAPS arrangement used in bench tests (left) and Gamble II experiments (right).

The foil voltage is measured by a probe with connections on the front side to eliminate inductive pickup. Electrical data from a 1200-Å foil are shown in Fig. 2a. The foil resistance breaks down after an energy input of about 1.5 J. Both this value, and the foil resistance, are consistent with breakdown occurring at melt. This is the expected behavior of an EMFAPS, since melting results in strong gas desorption.

Other diagnostics used to study the EMFAPS operation are shown in Fig. 1a. Open-shutter photographs show some arcing at the foil contacts that varies shot-to-shot, although streak photography indicates that these arcs tend to occur after the times of interest. A HeNe interferometer with heterodyne phase detection is used to measure the electron density. The observed density is

seen to be localized to within 1.5 mm of the cathode surface during the times of interest. Typical data are shown in Fig. 2b. The negative phase shift late in time indicates a large neutral component that may also be affecting the phase shift earlier in time. Two-color interferometry is planned for the future to allow resolution of both components.

The diode arrangement on Gamble II, along with a typical, calculated field geometry, is shown in Fig. 1b. This calculation, which includes the effects of magnetic field diffusion through the anode and cathode structures, is performed using the code ATHETA.⁶ We have recently measured $rA\theta$ directly, and found a discrepancy with the code predictions. The cathode coil flux into the diode gap is about 20% greater than predicted, which has

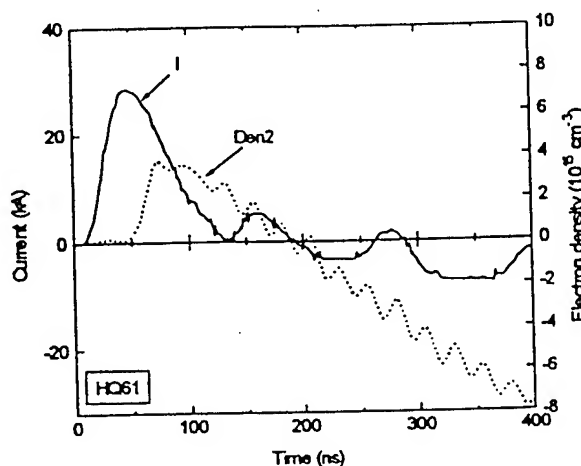
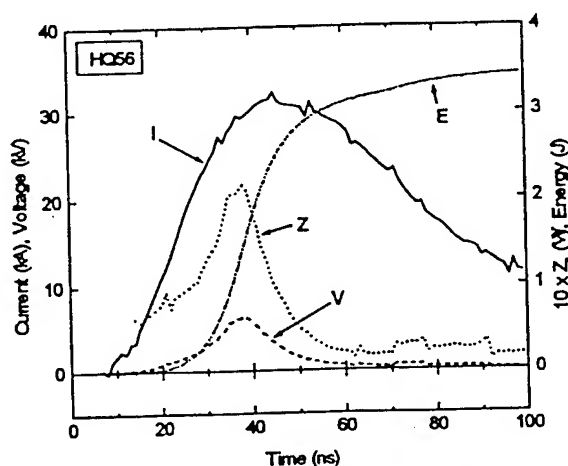


Fig. 2: Electrical (left) and electron density (right) data from EMFAPS bench experiments.

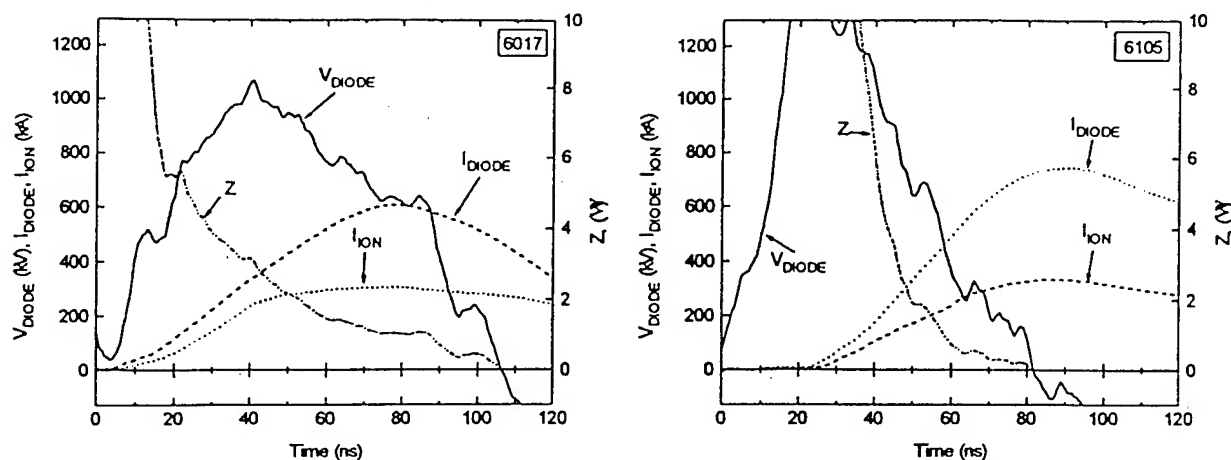


Figure 3: Electrical waveforms obtained with (left) and without (right) driving the EMFAPS on Gamble II shots.

the effect of pushing the separatrix back into the anode. We are studying this discrepancy further.

The ion beam is transported through 1-Torr air, which is separated from the diode vacuum by a 1.8- μ polycarbonate foil located behind the cathode tips.

Diode electrical data from our best shot to date is shown in Fig. 3a. This shot had the calculated field geometry shown in Fig. 1b, with the above caveat. The ion current begins early with reasonable efficiency. Later in time, the electron loss increases, loading down the generator and limiting the ion beam energy to 15 kJ. The effect of the EMFAPS is seen by comparing these data to those in Fig. 3b, from a similar shot taken without driving the foil current. Here the ion current begins much later although the diode actually shorts out earlier. The lower early-time impedance obtained with the EMFAPS will allow the diode to be operated at higher power in the future without insulator flashover.

Shots have been taken with different magnetic field configurations, pulser delays, foil thicknesses and foil resistivities. The anodes used on some shots had a 75- μ thick copper insert cast into the epoxy at a distance of 2 mm behind the anode surface. This insert is designed to conserve flux during the shot timescale, preventing the expanding,

diamagnetic electron cloud from pushing flux into the anode during the shot.

The pulser delay has been the most important parameter to date. In general, increasing the delay (up to at least 80 ns) hastens the diode current onset without affecting the time of impedance collapse. The need for such a long delay, and the large neutral component to the anode plasma mentioned previously, indicate that the pulser may not be driving the foil hard enough.

Little or no effect of foil thickness or resistivity, or the use of an anode insert, is seen. Changes in the field configuration on the order of 10 percent have shown little effect. Future experiments using a more optimum field configuration (i.e., Fig 1b) may show more sensitivity of diode performance to these variables.

The ion beam is diagnosed using shadowbox techniques and Rutherford scattering. The shadowbox data show a microdivergence on the order of 20 mrad, and some angular momentum. The latter is expected because of the separatrix location inside the anode that existed on these shots. The 90-degree Rutherford scattering yield from a thick aluminum target is compared in Fig. 4a with the signal predicted based on the ion current and voltage waveforms, the assumed total beam area, and the scattering geometry. The prediction has an uncertainty

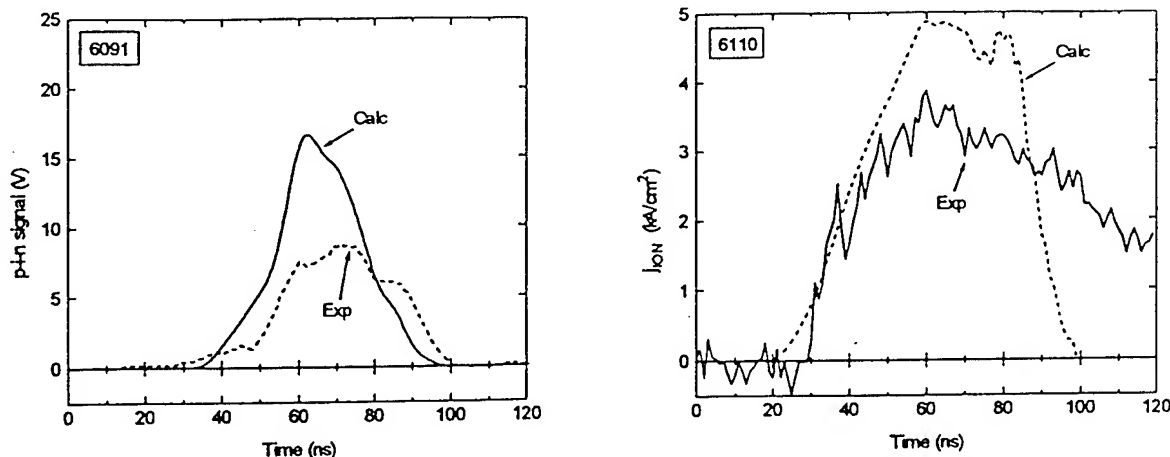


Figure 4: Observed and calculated signals from Rutherford scattering (left) and a large-aperture Faraday cup (right).

of about 20 percent. The signals are similar in shape although the observed signal is lower than predicted. In general, reasonable shape agreement is observed, including signals from shots where the detector was located far enough away to resolve differences in the ion voltage. Averaged over 9 shots, the integral of the observed signal is 65 percent of the integral of the predicted signal. This is evidence of a non-protonic component of the ion beam, since the p-i-n had a foil filter that would stop any heavier ions.

A large-aperture Faraday cup⁷ was used to diagnose the ion beam on one shot. This cup is unbiased and was located 1.5 cm behind the cathode foil, where the diode magnetic field provides good insulation of secondaries and co-moving electrons. The cup is terminated with a 0.05- Ω shunt to reduce the voltage produced. Calculated and observed signals are compared in Fig. 4b. The tail on the observed signal is not understood at present. The observed signal is about 70 percent of the predicted value, a value consistent with the Rutherford scattering data.

In order to obtain ion beam parameters adequate for transport experiments, the diode impedance late in time must be increased without sacrificing the early ion current onset. We plan to accomplish this by increasing the diode gap while driving the foil with more current. A Marx-waterline pulser, capable of

driving over 50 kA through the foil, has been constructed and will be used in future experiments. The aluminum anode foil will be replaced by hydrogen-loaded titanium in effort to boost the proton component of the beam.^{4,5} The use of a more optimum field geometry is also expected to improve the diode performance.

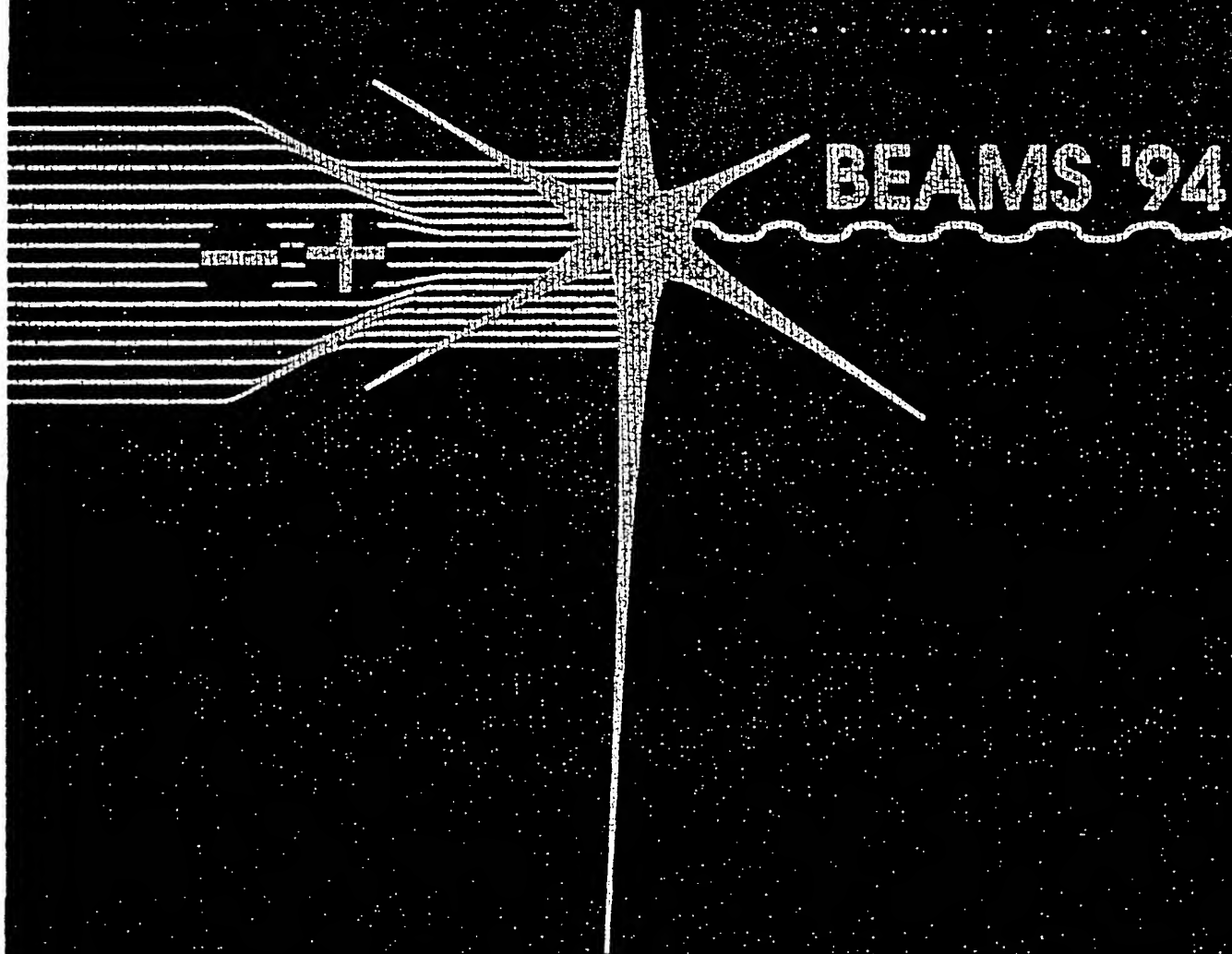
In conclusion, we have demonstrated operation of an EMFAPS driven by an external current source in an extraction applied-B diode. Future improvements to the diode are expected to produce an ion beam with parameters suitable for transport research.

It is a pleasure to acknowledge helpful discussions with Mike Cuneo and Kerry Lampa of SNL and Hans Bluhm and Peter Hoppe of KfK. This work was supported by the US DOE through Sandia National Laboratories.

- * JAYCOR, Vienna, VA
- ** NRC Research Associate
- *** Cornell University

1. G. D. Rondeau, Ph.D. thesis, Cornell Univ., NY (1989).
2. M. Cuneo, et al, Proc. 1993 Pulsed Power Conf., p. 423.
3. H. Bluhm, et al, Proc. IEEE, 80, 995 (1992).
4. H. Bluhm, et al, Proc. Beams 90, p. 927 (1990).
5. H. J. Bluhm, et al, IEEE Trans. Pl. Sci., 21, 560 (1993).
6. J. P. Quintenz and D. B. Seidel, Sandia internal rep. SAND84-1336 (1985).
7. J. Olson, Cornell University, personal communication.

10th
International
Conference
on High Power
Particle Beams



June 20-24, 1994
San Diego, CA

PULSED POWER PHYSICS TECHNOTE 95-06

TITLE: ANALYSIS OF APPLIED-B DIODE RUNS 9 AND 10

Author: D. Hinshelwood

Date: March 14, 1995

Abstract: This is one of a series of teknotes, composing a first cut at analysis of the reams of applied-B diode (MID) data we have acquired so far. The purpose here is to get the data out on the table and to identify the best shots, obvious trends, and any unexpected results.

The major difference between these and previous runs is that the diode is operating at lower impedance, with some shots exhibiting PFD-like behavior and all shots showing rapid current onset. Since this effect is seen on no-pulser shots as well, it is not solely due to the higher pulser current on this run.

This trend toward lower impedance is a continuation from runs 7 and 8. One possibility is that this trend is due to particulars of the anode foils. Data from this run gives further indication of the effect of the anode conditions on the diode impedance, and indicates that material does expand very quickly from the foils.

Another possibility is that the trend is due to changes in the fields. It is interesting to note that in going from runs 5 to 7 to 8 to 9 and 10, the separatrix was moved out from behind the anode, and the flux surfaces moved from slanting in at small radii, to straight. This would have the effect of decreasing the uniformity of insulation with radius.

One encouraging trend is that the beam angular momentum seems to vary with the fields in a predictable way, and is tunable.

As stated before, further study of the EMFAPS process, and field mapping, are imperative.

While further study with better diagnostics, etc., may show us the way to improve the diode, we should always keep Krasik's conundrum (CK) in mind: even if we understand the diode perfectly, what can we do, that we have not done already, to improve it? At this time, the answer to C_K is not obvious. However, we know that we can obtain good diode performance at high impedance under flashover conditions. Therefore, if all else fails, we can go to a parallel electron-diode, or maybe even a PFD, load to suppress flashover.

INTRODUCTION

This is one of a series of teknotes, composing a first cut at analysis of the reams of applied-B diode (MID) data we have acquired so far. The purpose here is to get the data out on the table and to identify the best shots, obvious trends, and any unexpected results. No attempt will be made to draw final conclusions yet. To date there have been ten MID runs. The first three runs used wax-filled-groove, hereafter referred to as passive, anodes. Run 4 was our only attempt with POS-driven, EMFAPS anodes. Run 5 was the first run using a pulser to drive the EMFAPS anodes. On run 6, EMFAPS anodes were used without the pulser. In this case the early electron loss current returning through the anode foil is used to form the anode plasma. These will be referred to as limiter-EMFAPS anodes, although a physical limiter was rarely used. Runs 7-10 used pulser-EMFAPS anodes. Results from runs 5, 6, 7, and 8 have already been presented in TN's 95-01, 95-02, 95-03, 94-16, and 95-04. This note is a further analysis of run 8, with some fresh observations.

MASTER SPREADSHEET

The enclosed spreadsheet lists all shots of this run other than short-circuit shots. This is part of an evolving master spreadsheet that will summarize all of our MID data. The first page gives the basic shot parameters. The column "voc2i" on the RAW sheet refers to the integral of VOC^2 . This quantity is now used to normalize energies. The column "e2(kJ)" refers to the integral of $VCOR \times IK2T$, and is a weighted measure of the current emitted from the inner cathode.

The second sheet presents some of the shot parameters in more useful form. (Obvious dud shots are not included on this sheet.) The second column gives the closest A-K gap, i.e., the distance between the cathode tips and the anode.

The values "e2/e", "e4/e", and "ei/e" are the ratios of the inner-cathode, outer cathode, and ion energies to the total energy (these add up to unity). The values "e19" and "ei19" give the total and ion energies, normalized to shot 6019 by assuming that the energies scale as voc2i. Shot 6019 had a typical open-circuit voltage for a 32 kV Marx charge.

OVERVIEW OF RUNS 9 AND 10

These runs comprised 30 shots, at 32-kV Marx charge. We had two problems with the anode field coils on these runs. An intermittent breakdown in the cable to one of the anode coils bedeviled us during run 9. This resulted in 3 shots with one of the anode fields missing and the other changed in amplitude (because of mutual coupling); these shots are worthless. On run ten, IIA caused the machine to prefire on 5 shots. Since the prefire occurred at the start of IIA, these are effectively field-free shots and they will be analyzed further in a later note. (This prefire problem is still not understood. It may be related to the existence of a high-resistance short to ground in both of the anode coils. If so, use of the new anode coil set kindly supplied by Mike Cuneo will solve the problem. In any

event, we will resolve this problem before the next run.) Three other shots were lost because of machine problems, leaving 19 'good' shots.

The outer vacuum hardware was modified for these runs to allow visual access to the anode (for future studies) and reduce the number of seals. After run 9, the anode stalk was cut down to increase the coil set gap by 2 mm. At present there is a ~1 mm uncertainty in some of the diode gap measurements, resulting from possible variations in flexing of the urethane insulator. I am fairly sure, though, that the nominal gap in run 9 was 0.5 mm smaller than that on run 8, and the nominal gap in run 10 was 1.5 mm larger than the run 8 gap. On several shots during these runs, different cathode tips were used to provide gaps different from the nominal values.

Before run 9, direct measurements of rA_θ were performed for the first time. These measurements showed that the field was different than predicted by ATHETA. This discrepancy is still being investigated. Because of this, the fields used at the beginning of both runs 9 and 10 were determined based on in situ measurements of rA_θ at the anode plane. The coil currents and timings were adjusted to place the separatrix at the anode plane. These runs, then, have the only shots so far where we know this to be the case. (Note: on all run 9 shots but 6224, and on 6283 of run 10, the IOA and IIA timings were reversed. This was taken into account during the measurements, but means that the coil settings cannot be compared by inspection with those on other shots.)

Six of the 7 useful shots on run 9 have the same field shape, henceforth referred to as the '6218 fields'. Again, this shape has the separatrix at the anode surface. The sixth shot, shot 6224, was taken with the 6017 fields used in two run-7, and most run-8, shots. Six of the 12 useful shots on run 10 were taken with the initial, shot-6276, fields. The shot-6276 fields also had the separatrix on the anode, but had stronger inner fields relative to those on shot 6218.

The foils differed from those in previous runs. For runs 7 and 8, the anodes were cast so as to produce a very smooth epoxy surface. During bench tests prior to run 9, we found that if the epoxy were lightly roughened (~600 grit) prior to coating, the foil breakdown had very uniform luminosity. On these runs, then, foils were coated on roughened anodes. This resulted in more resistive foils than in the past. The reason for this effect of surface roughness on breakdown luminosity is as yet unknown. John Greenly has suggested, and I tend to agree, that with a rough surface the foil may have many micro-regions of reduced thickness that form distributed breakdown sites. These would effectively cause the breakdown process to 'multichannel' in the same way that a sandblasted cathode is a uniform explosive-emitter.

A new pulser was used for these runs. The foil current was increased from about 35-40 kA in runs 7 and 8, to 50-55 kA here.

The usual electrical diagnostics were used on this run. Only two shots had useful shadowbox data, and no other beam diagnostics were used.

COMPARISON WITH RUNS 7 AND 8

Typical open-circuit voltage waveforms from these runs are compared in Fig. 1. Because of modifications to the oil switch after run 8, the duration of the prepulse is greatly reduced.

Shot 6224 was the only shot on these runs with the same fields as shots on previous runs. The impedance history for this shot, with '6017' fields, is compared with those from four run 8 shots in Fig. 2. Shot 6224 shows a rather rapid current onset considering the short delay. The subsequent behavior is not obviously different from the run 8 shots.

IMPEDANCE BEHAVIOR ON RUNS 9 AND 10

Impedance traces from the first three shots with 6218 fields are shown in Fig. 3. Note that in this and all following figures, the axis starts at 20 ns, rather than 40 ns as in most impedance-trace figures in previous teknotes. In general, both current onset and impedance collapse occurred much quicker on runs 9 and 10 than before. The traces in this figure show the expected behavior in that with higher fields and reduced delay (i.e., no pulser) the onset occurs later and the diode operates at higher impedance. Shot 6218 shows behavior suggestive of a PFD, where the diode turns on very quickly and operates relatively stably at a very low impedance.

Figure 4 shows data from shots with the same fields, and similar delays, but different gaps. Here the gaps were changed by using different cathode tips without changing the coil set separation. Again as might be expected, onset is delayed as the gap is increased. It appears that the diode operating impedance on these shots is independent of the gap, which is surprising. However, the wiggles on the impedance traces provide a 'noise' that may be obscuring a difference in behavior.

Shots with coil-set separations differing by 2 mm, but the same gap, are compared in Fig. 5. Here, the later onset on shot 6283 may be attributed to the shorter delay. This shot appears to short out earlier, but it is hard to tell.

More comparisons of shots with different gaps are shown in Fig. 6. All shots had 6276 fields. Decreasing the gap by 2 mm (shot 6277) results in a slightly faster onset and lower impedance, but the difference is barely out of the 'noise'. Increasing the inner gap only (shot 6278) shows no discernible effect. With a larger gap (shot 6281) onset is later and the diode operates at higher impedance, but this difference may also be due to the shorter delay.

The bottom line here is that changing the gap affects the impedance in the expected direction, but the magnitude of this effect is less than I would have guessed. Again, the 'noise' here may be obscuring things: because the diode operates at a relatively low impedance on these shots, a large fractional change in impedance may be hard to observe.

Figure 7 compares shots with 6218 and 6276 fields and the same gap. Again, these fields both had the separatrix on the anode, but the inner fields are relatively larger in the 6276 configuration. For shots with similar delays, any difference is again obscured by the noise.

The anode is seen to affect the impedance behavior as is seen in Figs. 8-10. Shot 6226 in Fig. 8 was taken with a standard, EMFAPS anode that was lightly coated with Aerodag. Such anodes were examined on a few bench shots, with the interferometric data pointing to a very high density at the anode surface. The one machine shot with an Aerodag anode is seen to be virtually a dead short.

Shots with EMFAPS and passive (wax-groove) anodes are compared in Figs. 9-10. Even without the pulser, the EMFAPS anodes are seen to produce a faster current onset. It is possible that this difference is not due to the anode structure, but to the anode width. The passive anodes used in these shots had a 1-cm delta-r, whereas the active area of the EMFAPS anodes was about 1.8 cm. We had planned to resolve this with a shot using a narrow, EMFAPS anode, but the oil switch breakdown at the end of the run prevented this.

While obviously not conclusive, the data in Figs. 8-10 are further indication the impedance behavior is significantly influenced by the EMFAPS anode.

Two no-pulser shots are compared in Fig. 11. Here, a 30 percent increase in one of the four fields on shot 6279 is seen to produce a marked change in impedance behavior. When shot 6279 flashes, it is operating at six times the impedance of shot 6280. Shot 6279 also operated at higher ion efficiency until the flash. On Gamble II, the impedance has been less sensitive to the applied field than this, although the behavior here is not atypical of MID experiments in general. Perhaps at these higher impedances, the diode is operating more like the 'typical' MID.

TYPICAL ELECTRICAL DATA

The photodiode signal on this run shows the same general agreement with the calculated trace, that was seen in other runs. On shots 6276-6283, the IK2 scope had a large noise pickup which obscured the signal, and so IK2 has been set to zero for these shots. Since the subsequent shots had a very low IK2, neglecting it for shots 6276-81 does not introduce a significant error.

Data from shot 6218 is shown in Fig. 12. This shot exhibits the general behavior seen in runs 7 and 8: the diode starts out at reasonable efficiency, but after about 30-40 ns, the electron loss increases greatly. Most EMFAPS shots in runs 9 and 10 are qualitatively similar.

The no-pulser shot 6290, in Fig. 13, operates at a high ion efficiency during the entire pulse, although the impedance still crashes. The data show a general (albeit faint) trend to

higher efficiency as the pulser delay is reduced. The ion efficiency is plotted against the pulser delay in Fig. 14.

In analyzing these runs sequentially, it is easy to forget data from earlier runs. Just for fun, let's look at a no-pulser shot from run 5 in Fig. 13a. Shot 5827 has a high ion impedance like shot 6290, but operates at a higher impedance, with a later onset and then much slower impedance collapse. This shot had (I think) a 1-mm-greater coil-set separation and a 1-mm-smaller gap than shot 6290. With no pulser and a similar gap, these shots differ only in the fields, the anode foil specifics, and the active anode area, which was a bit narrower (1.5 rather than 1.8 cm) on shot 5827.

Data from the best EMFAPS shot is shown in Fig. 15. This shot shows the same general features as shot 6218 but operates at higher ion efficiency until it flashes. Impedance traces for this and for shot 6017 are compared in Fig. 15a. The slower onset on shot 6282 can be attributed to the shorter pulser delay. As with most shots on this run, the subsequent impedance collapse is faster than on previous runs.

Data from one of the passive shots is shown in Fig. 16. The other two passive shots, which had earlier flashovers, have similar waveforms until the shots flash. With the passive anode, the current rises more slowly than on the EMFAPS shots. The diode operates at a more desirable impedance for transport experiments, but the resulting flashover limits the pulse.

ENERGY PARTITION

A glance at the spreadsheet shows that the energy partition varied widely on this run and so I have not compiled any averages. In general, the ion efficiency is lower than on previous runs. The passive shots are seen to have higher ion efficiencies.

BEAM DIAGNOSTICS

Only two shots produced shadowbox data on these runs (the shadowbox was fielded on several shots in run 9 but no damage was observed because of the low ion voltages). Targets from passive-anode shots 6293 and 6294 are shown in Figs. 17 and 18. Shot 6294 had the 6276 field shape, with the separatrix at the anode. Shot 6293 had a higher relative IOA, which would be expected to push the separatrix toward the cathode. Shot 6294 shows no average angular momentum as predicted, which is encouraging. However, note that the spots are displaced in different directions at different azimuthal locations. This is reminiscent of the odd results from two shots in run 8 and is not understood. Shot 6293 shows angular momentum of the opposite sign as the shots in previous runs. This, again, is as predicted, because on previous runs the separatrix is now believed to have been behind the anode.

Radial projections for these shots are shown in Fig. 19. As mentioned in the previous note, we have to be careful about interpreting such projections. It is interesting that

pushing out the outer anode field seems to make the beam expand. This might be expected assuming electrostatic focusing between the anode and the virtual cathode lying on one of the field lines.

A photograph of the anode damage is shown in Fig. 20. It's hard to see in the Xerox, but this anode has a ring of damage at the outside, with spokes going inward. (I leave their explanation to the theorists). Shots with more electron loss show more uniform damage, while shots with lower loss show damage only at the outside. This is reasonable: With the separatrix at the anode, the insulation will be weaker at the outer edge and more damage would be expected there. To the extent that damage is a threshold phenomenon, one would expect more apparent uniformity as the total loss increases.

SUMMARY

In this first cut at revisiting the MID data, I will attempt to answer four questions for each run:

(1) What are the key shots, in terms of performance, for each run?

Shot 6282 was the best EMFAPS shot. Shot 6290, a no-pulser shot, showed high efficiency during the entire pulse. Shot 6293 is a good example of a passive-anode shot. Shot 6218, while not impressive in terms of results, shows the interesting PFD-like behavior seen on some shots from other runs.

(2) Which field configurations should we concentrate on mapping out?

The profiles used on shots 6218, 6276, 6279, 6282, and 6293 account for all shots in these runs except for 6224, which used the 6017 fields. We might as well map out all five fields, then.

(3) What are the significant trends in the data?

The major difference between these and previous runs is that the diode is operating at lower impedance. Shots on this run have traces toward the left of the 'universal' family of impedance traces suggested in the previous note, with some shots exhibiting PFD-like behavior and all shots showing rapid current onset. Since this effect is seen on no-pulser shots as well, it is not solely due to the higher pulser current on this run.

This trend toward lower impedance is a continuation from runs 7 and 8. One possibility is that this trend is due to particulars of the anode foils. For example, there were shots in run 8 that showed unusually fast impedance collapse, with no other obvious cause. Also, the results with the Aerodag anode, and the comparisons of passive and EMFAPS anodes, indicate an influence of the anode characteristics on the diode impedance.

Another possibility is that the trend is due to changes in the fields, either in shape or magnitude. With different shapes, magnitudes cannot really be compared, and it is

impossible to estimate how V_{crit} changes as the fields change. Nonetheless, the fields on runs 9 and 10 were rather large compared to earlier runs. It is interesting to note that in going from runs 5 to 7 to 8 to 9 and 10, the separatrix was moved out from behind the anode, and the flux surfaces moved, from slanting in at small radii to straight. This would have the effect of decreasing the uniformity of insulation with radius.

One encouraging trend is that the beam angular momentum seems to vary with the fields in a predictable way, and is tunable.

(4) What are the most puzzling features to these data?

All along, we have been surprised that the pulser (or more properly, the lack of it) has not had a larger effect. Data from this run is even more surprising, where no-pulser shots also exhibit rapid impedance collapse. And while I hate to make too much of one shot, the Aerodag anode shot is unexpected. The dead short on shot 6226 implies that material from the foil breakdown has gotten well into the gap quite rapidly. These data, and the PFD-like shots, imply that material does expand very quickly from the foils.

CONCLUSIONS

I repeat from TN 95-04:

We are in the same trap as before: we cannot get early the early current onset necessary to prevent flashover without operation at an undesirably low impedance. As I said in the last note, the anode source is critical to resolving this problem. To begin with, we need to determine to what degree the effect of long pulser delay is related to the condition of the resulting anode plasma, and to what degree it is related to the presence of plasma or neutrals in the diode gap. Again, the SRL interferometer will be very useful here.

And, as before, another reason for source study is to obtain (and know that we have) reproducible source operation. By keeping the source constant from shot to shot, we will have an easier time investigating the effects of the magnetic field configuration. Finally, as usual, field mapping will be necessary to interpret fully the results of this run.

While further study with better diagnostics, etc., may show us the way to improve the diode, we should always keep Krasik's conundrum (C_K) in mind: even if we understand the diode perfectly, what can we do, that we have not done already, to improve it? In the last note, I speculated that driving the foil with a high current and short delay might be the answer. However, shots on this run with short, or no, delays, also showed rapid impedance collapse, so this approach cannot be the whole answer. At this time, the answer to C_K is not obvious. However, we know that we can obtain good diode performance at high impedance under flashover conditions. Therefore, if all else fails, we can go to a parallel electron-diode, or maybe even a PFD, load to suppress flashover.

shot	gap	tips	IIA	IOA	IIC	IOC	W-m	eff th	Ins	If	delay, r/z=10	voc2i	e1(ki)	e2(ki)	e(k)	Vpp	lipp	comnts
6215	11	4	2.22	2.55	1.35	3.6	500	50	Y									pulser prefire, don't know about fields, prob no IIA
6216	11	4	2.66	3.06	1.62	3.6	500	60	Y		0	12	3.929	5.64	3.7	22.07		no pulser (very late)
6217	11	4	2.66	3.06	1.62	3.6	500	40	Y		?	7	4.287	1.04	0.9	6.886		NOTE: on run 9 shots, and 6283, IIA, IOA timings reversed
6218	11	4	3.46	3.98	2.11	4.7	500	56	Y		47	6	3.891	6.89	1.5	15.96		
6219	11	0	3.46	3.98	2.11	4.7	500	60	Y		58	10	3.856	4.61	0.2	17.67		6-mm K tips
6220	11	2	3.46	3.98	2.11	4.7	500	50	Y		57	6	3.948	4.04	0.5	12.68		8-mm K tips
6221	11	6	3.46	3.98	2.11	4.7	500	?	?								prefire, 12-mm tips	
6222	11	6	3.46	3.98	2.11	4.7	500	57	Y								coil bd, bad fields	
6223	11	6	3.46	3.98	2.11	4.7	500	?	?								coil bd, maybe no fields	
6224	11	4	3.48	2.66	3.37	4.22	500	?	?		8	16	3.191	7.00	0.9	14.07		
6225	11	4	3.46	3.98	2.11	4.7	500	?	Y				0	0.00	0.0	0		aerodagged, coil bd, bad fields
6226	11	4	3.46	3.98	2.11	4.7	500	?	Y		56	0	4.407	0.02	0.3	0.73		aerodagged, dead short
6276	13	4	4.13	1.88	2.38	2.25	500	70	Y		51	14	3.467	7.86	0.0	15.15		
6277	13	6	4.13	1.88	2.38	2.25	500	80	Y		54	13	3.271	4.73	0.0	10.92		12-mm outer, 1-cm inner tips
6278	13	4	4.13	1.88	2.38	2.25	500	60	Y		54	16	3.095	6.77	0.0	14.34		inner tips 0 mm
6279	13	4	4.13	1.88	2.38	3	500	50	Y	0	0	63	2.298	4.61	0.0	5.608		inner tips 0 mm, no pulser, IOC high by mistake
6280	13	4	4.13	1.88	2.38	2.25	500	50	Y	0	0	24	3.655	7.29	0.0	16.98		inner tips 0 mm, no pulser
6281	13	0	4.13	1.88	2.38	2.25	500	65	Y		43	22	2.789	8.32	0.0	16.18		6-mm inner and outer tips
6282	13	4	4.13	3.76	2.38	4.5	500	73	Y		22	25	3.401	12.50	0.0	16.64		
6283	13	4	3.46	3.98	2.11	4.7	500	70	Y		34	15	4.109	4.96	0.0	8.938		
6284	13	4	3.48	2.66	3.37	4.22	500	100	Y								prefire at IIA, bad or no fields	
6285	13	4	?	?	0	0	500	50	Y								prefire on IIA	
6286	13	4	?	?	0	0	passv	NA	Y	NA	NA						prefire on IIA, major hardware damage	
6289	13	4	4.13	2.89	2.38	2.25	passv	NA	Y	NA	0	36	2.706	14.71	0.2	14.63		flash
6290	13	4	4.13	2.89	2.38	2.25	500	?	Y	0	0	21	3.734	12.35	0.2	18.19		no pulser
6291	13	4	?	?	0	0	passv	NA	Y	NA	NA						prefire on IIA	
6292	13	4	?	?	0	0	passv	NA	Y	NA	NA						prefire on IIA	
6293	13	4	2.48	1.73	1.43	1.35	passv	NA	Y	NA	0	34	2.961	12.07	0.3	20.87		flash
6294	13	4	4.13	1.88	2.38	2.25	passv	NA	Y	NA	0	34	2.162	8.55	0.1	10.94		flash
6295	13	4						NA	Y	NA	NA							oil switch punch through, prefire on IIA

shot	AK gp	W-m	IIA	IOA	IIc	IOC	ic/oc	ia/oc	oa/oc	delns	e(kj)	ei(kj)	ei/e	e2/e	e4/e	e19	e19	comnts
6216	7.00	500	2.66	3.06	1.62	3.60	0.45	0.74	0.85	0	22.1	5.6	0.26	0.17	0.58	5.6	21.8	no pulser (very late)
6217	7.00	500	2.66	3.06	1.62	3.60	0.45	0.74	0.85	?	6.9	1.0	0.15	0.13	0.72	0.9	6.2	NOTE: on run 9 shots, and 6283, IIA, IOA timings reversed
6218	7.00	500	3.46	3.98	2.11	4.70	0.45	0.74	0.85	55	16.0	6.9	0.43	0.10	0.47	6.9	15.9	
6219	11.00	500	3.46	3.98	2.11	4.70	0.45	0.74	0.85	68	17.7	4.6	0.26	0.01	0.73	4.6	17.8	6-mm K tips
6220	9.00	500	3.46	3.98	2.11	4.70	0.45	0.74	0.85	67	12.7	4.0	0.32	0.04	0.65	4.0	12.5	8-mm K tips
6224	7.00	500	3.48	2.66	3.37	4.22	0.80	0.82	0.63	9	14.1	7.0	0.50	0.06	0.44	8.5	17.1	
6226	7.00	500	3.46	3.98	2.11	4.70	0.45	0.74	0.85	66	0.7	0.0	0.02	0.38	0.60	0.0	0.6	aerodagged, dead short
6276	7.00	500	4.13	1.88	2.38	2.25	1.06	1.84	0.84	60	15.2	7.9	0.52	0.00	0.48	8.8	17.0	
6277	7.00	500	4.13	1.88	2.38	2.25	1.06	1.84	0.84	64	10.9	4.7	0.43	0.00	0.57	5.6	13.0	12-mm outer, 1-cm inner tips
6278	9.00	500	4.13	1.88	2.38	2.25	1.06	1.84	0.84	64	14.3	6.8	0.47	0.00	0.53	8.5	18.0	inner tips 0 mm
6279	9.00	500	4.13	1.88	2.38	3.00	0.79	1.38	0.63	0	5.6	4.6	0.82	0.00	0.18	7.8	9.5	inner tips 0 mm, no pulser, IOC high by mistake
6280	9.00	500	4.13	1.88	2.38	2.25	1.06	1.84	0.84	0	17.0	7.3	0.43	0.00	0.57	7.7	18.0	inner tips 0 mm, no pulser
6281	13.00	500	4.13	1.88	2.38	2.25	1.06	1.84	0.84	51	16.2	8.3	0.51	0.00	0.49	11.6	22.5	6-mm inner and outer tips
6282	9.00	500	4.13	3.76	2.38	4.50	0.53	0.92	0.84	26	16.6	12.5	0.75	0.00	0.25	14.3	19.0	
6283	9.00	500	3.46	3.98	2.11	4.70	0.45	0.74	0.85	40	8.9	5.0	0.55	0.00	0.45	4.7	8.4	
6289	9.00	passv	4.13	2.89	2.38	2.25	1.06	1.84	1.28	NA	14.6	14.7	1.01	0.01	-0.02	21.1	21.0	flash
6290	9.00	500	4.13	2.89	2.38	2.25	1.06	1.84	1.28	0	18.2	12.4	0.68	0.01	0.31	12.8	18.9	no pulser
6293	9.00	passv	2.48	1.73	1.43	1.35	1.06	1.84	1.28	NA	20.9	12.1	0.58	0.01	0.41	15.8	27.3	flash
6294	9.00	passv	4.13	1.88	2.38	2.25	1.06	1.84	0.84	NA	10.9	8.5	0.78	0.01	0.21	15.3	19.6	flash

Shot 6224

Fig 1

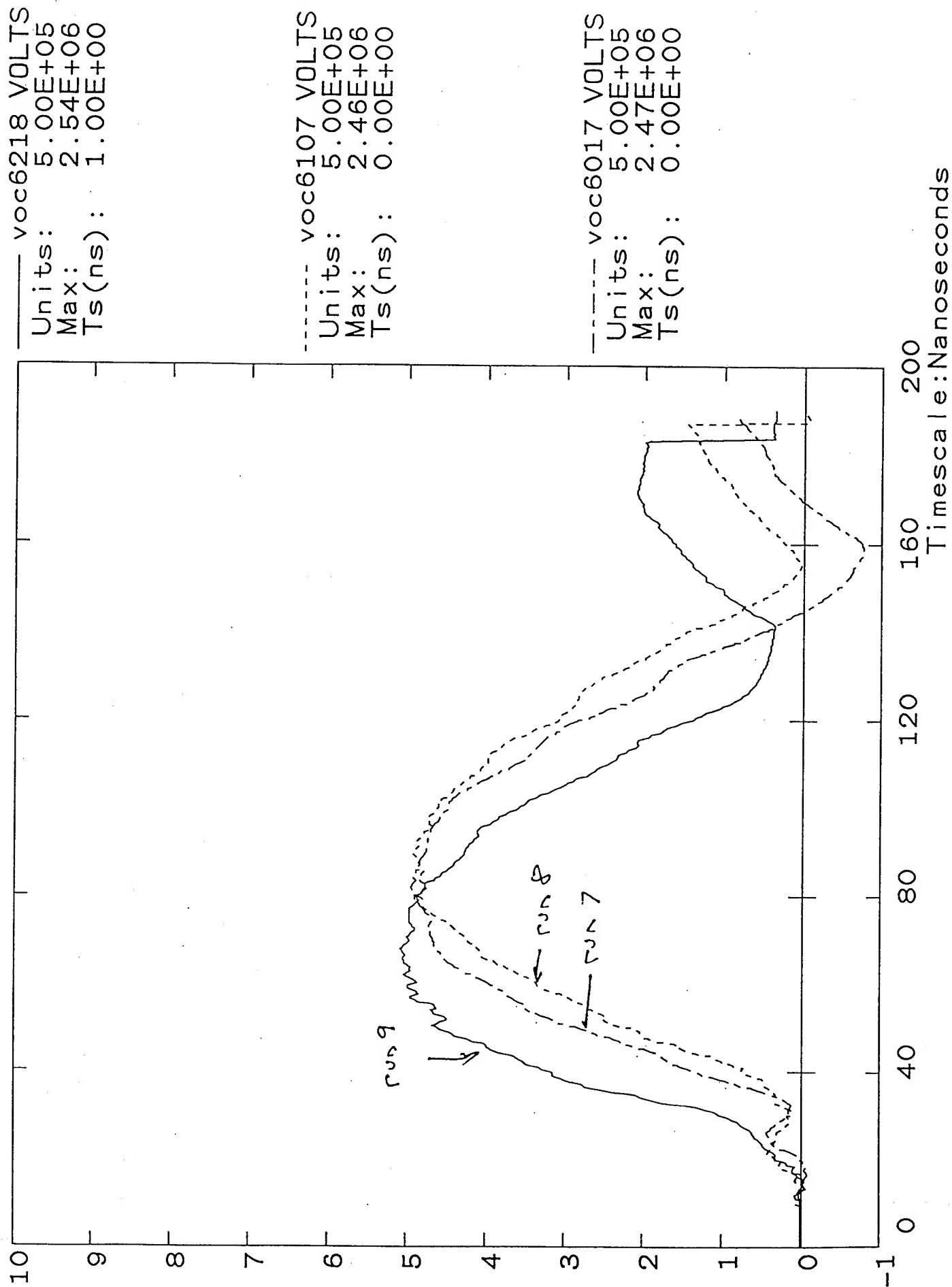
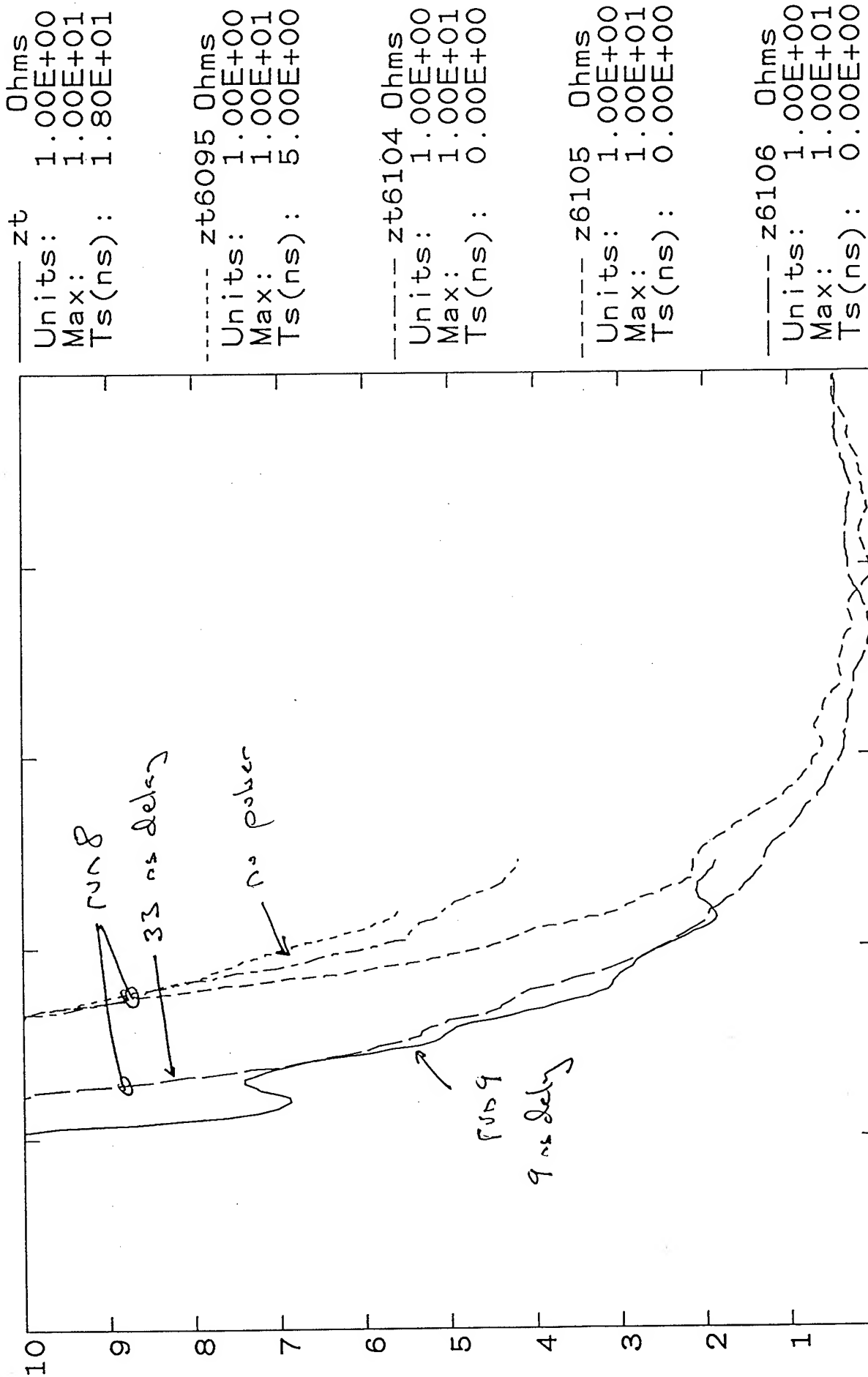


Fig 2

Shot 6224



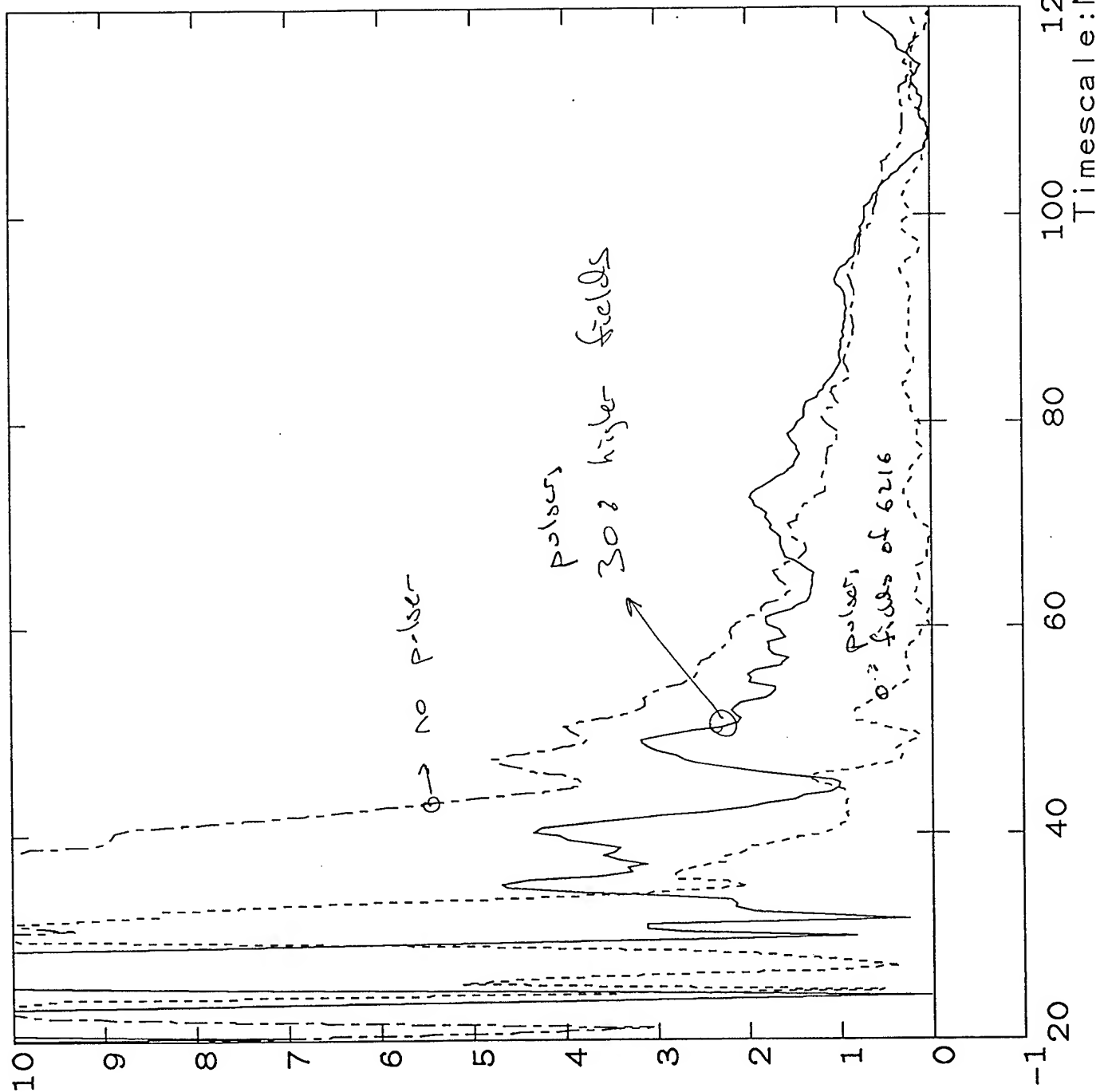
Shot 6224

Fig 3

----- z6218 Ohms
Units: 5.00E-01
Max: 1.00E+01
Ts(ns): 8.88E-07

----- z6217 Ohms
Units: 1.00E+00
Max: 1.00E+01
Ts(ns): 1.00E+00

----- z6216 Ohms
Units: 1.00E+00
Max: 1.00E+01
Ts(ns): 8.88E-07



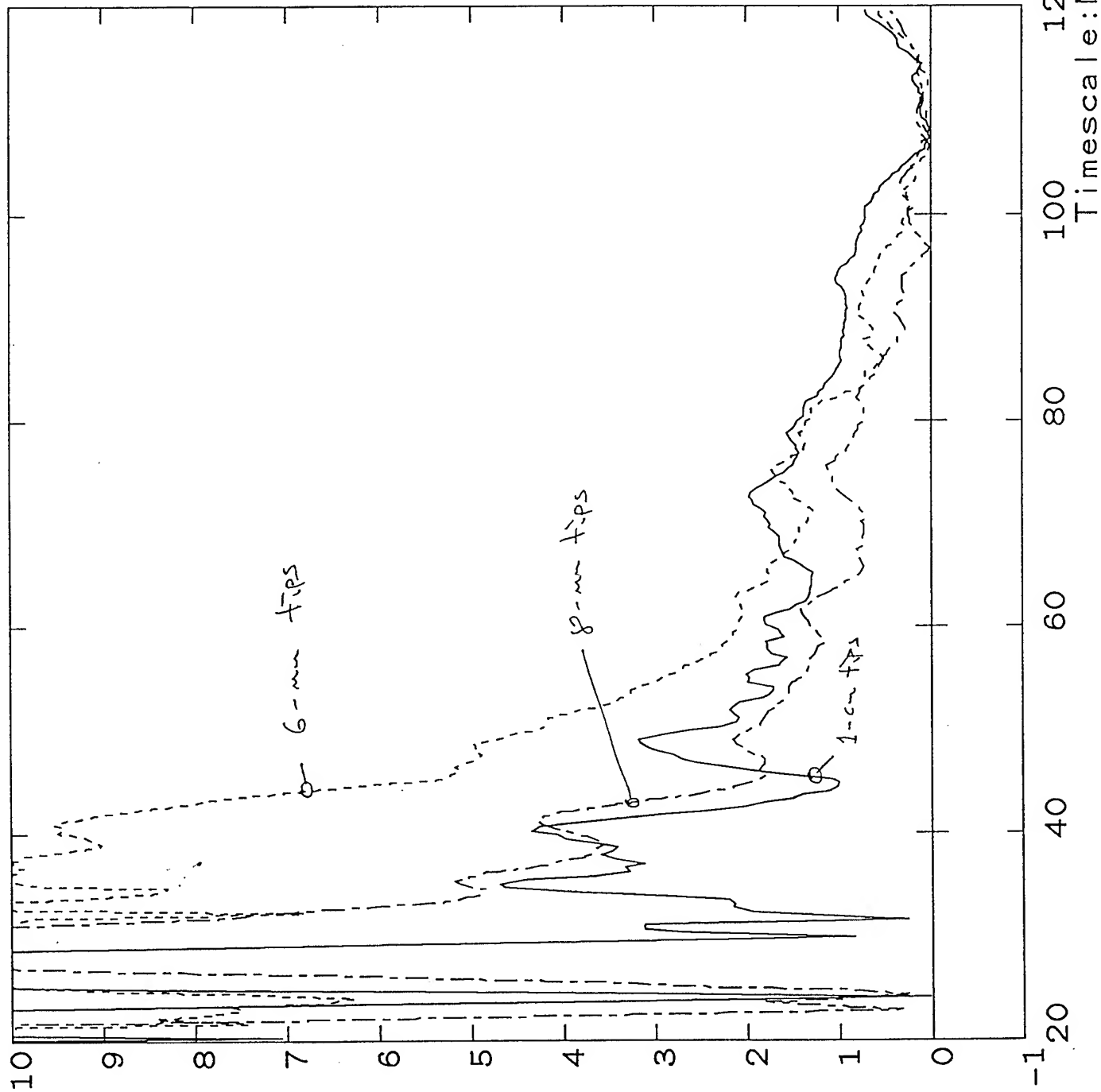
Shot 6224

Fig 4

____ z6218 Ohms
Units: 5.00E-01
Max: 1.00E+01
Ts(ns): 8.88E-07

----- z6219 Ohms
Units: 1.00E+00
Max: 1.00E+01
Ts(ns): 1.00E+00

----- z6220 Ohms
Units: 1.00E+00
Max: 1.00E+01
Ts(ns): 1.00E+00



Shot 6224

Fig 5

----- z6283 Ohms
Units: 1.00E+00
Max: 1.00E+01
Ts(ns): 0.00E+00

----- z6220 Ohms
Units: 1.00E+00
Max: 1.00E+01
Ts(ns): 1.00E+00

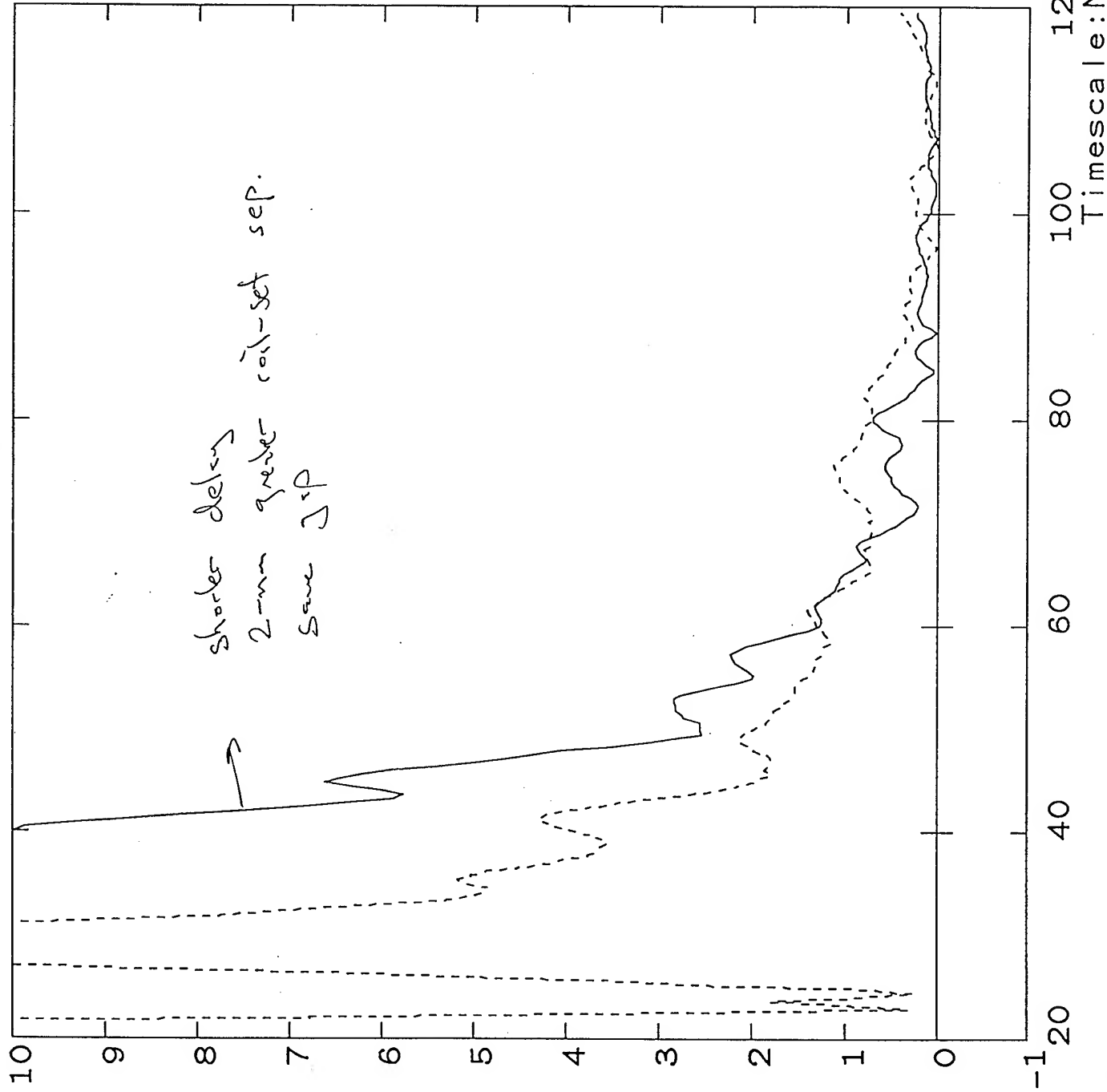


Fig 6

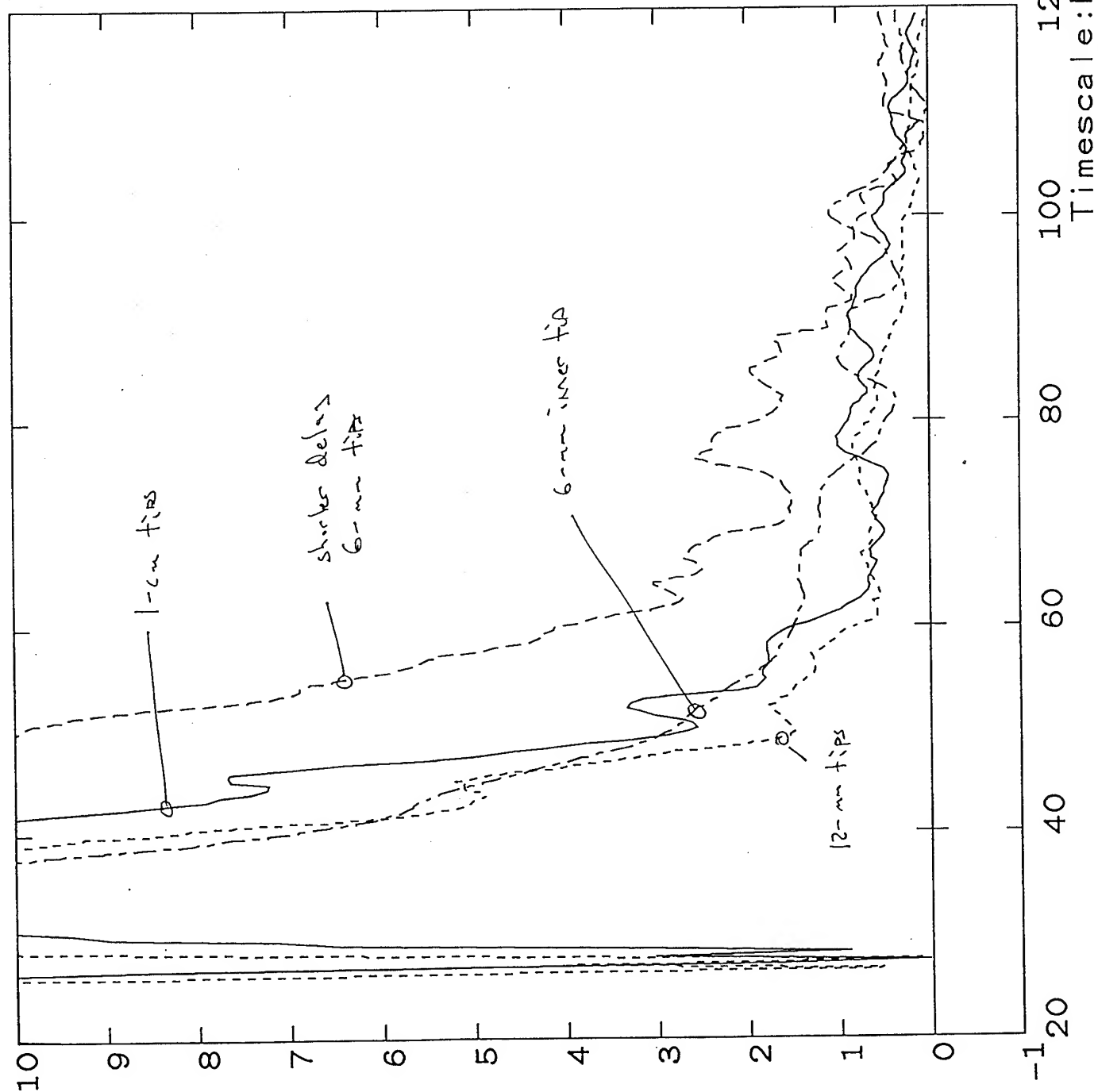
Shot 6276

Units: 1.00E+00
Max: 1.00E+01
Ts(ns): 0.00E+00

Units: 1.00E+00
Max: 1.00E+01
Ts(ns): 0.00E+00

Units: 1.00E+00
Max: 1.00E+01
Ts(ns): 0.00E+00

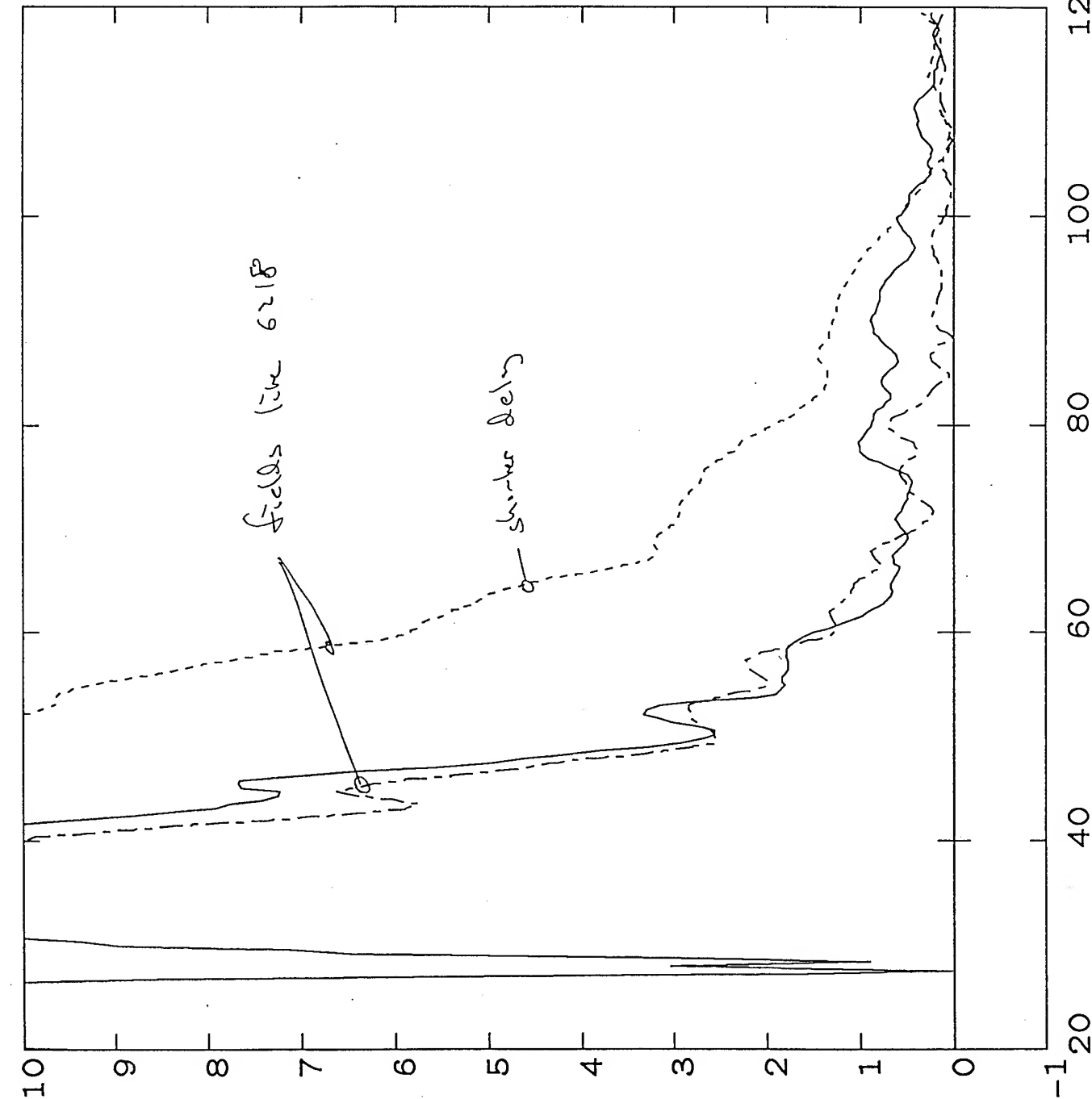
Units: 1.00E+00
Max: 1.00E+01
Ts(ns): 0.00E+00



Shot 6276

Fig 7

Units: 1.00E+00
Max: 1.00E+01
Ts(ns): 0.00E+00



Units: 1.00E+00
Max: 1.00E+01
Ts(ns): 0.00E+00

Units: 1.00E+00
Max: 1.00E+01
Ts(ns): 0.00E+00

Fig 8

Shot 6276

— z6218 Ohms
Units: 5.00E-01
Max: 1.00E+01
Ts(ns): 8.88E-07

----- z6226 Ohms
Units: 1.00E+00
Max: 1.00E+01
Ts(ns): 1.00E+00

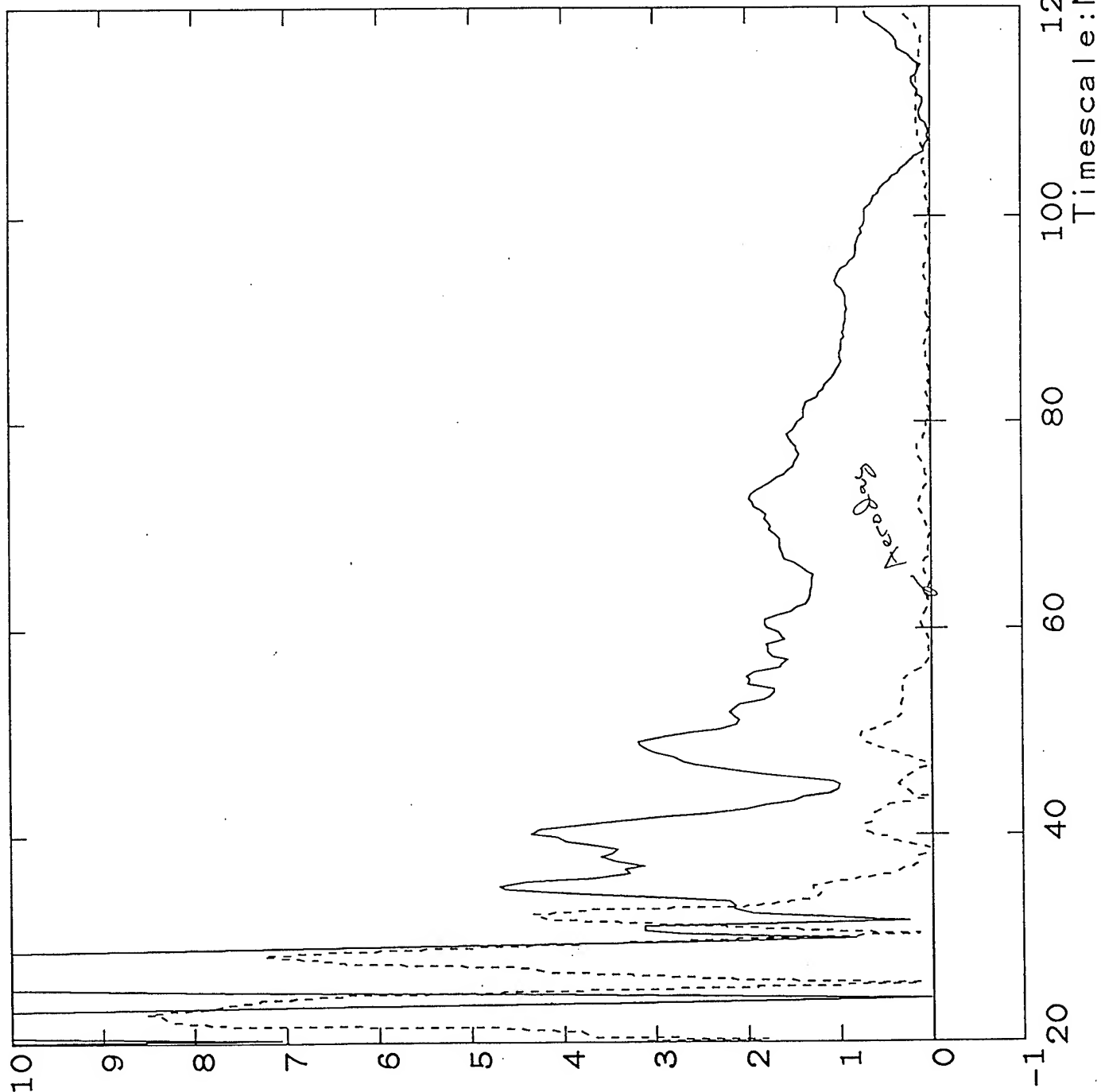
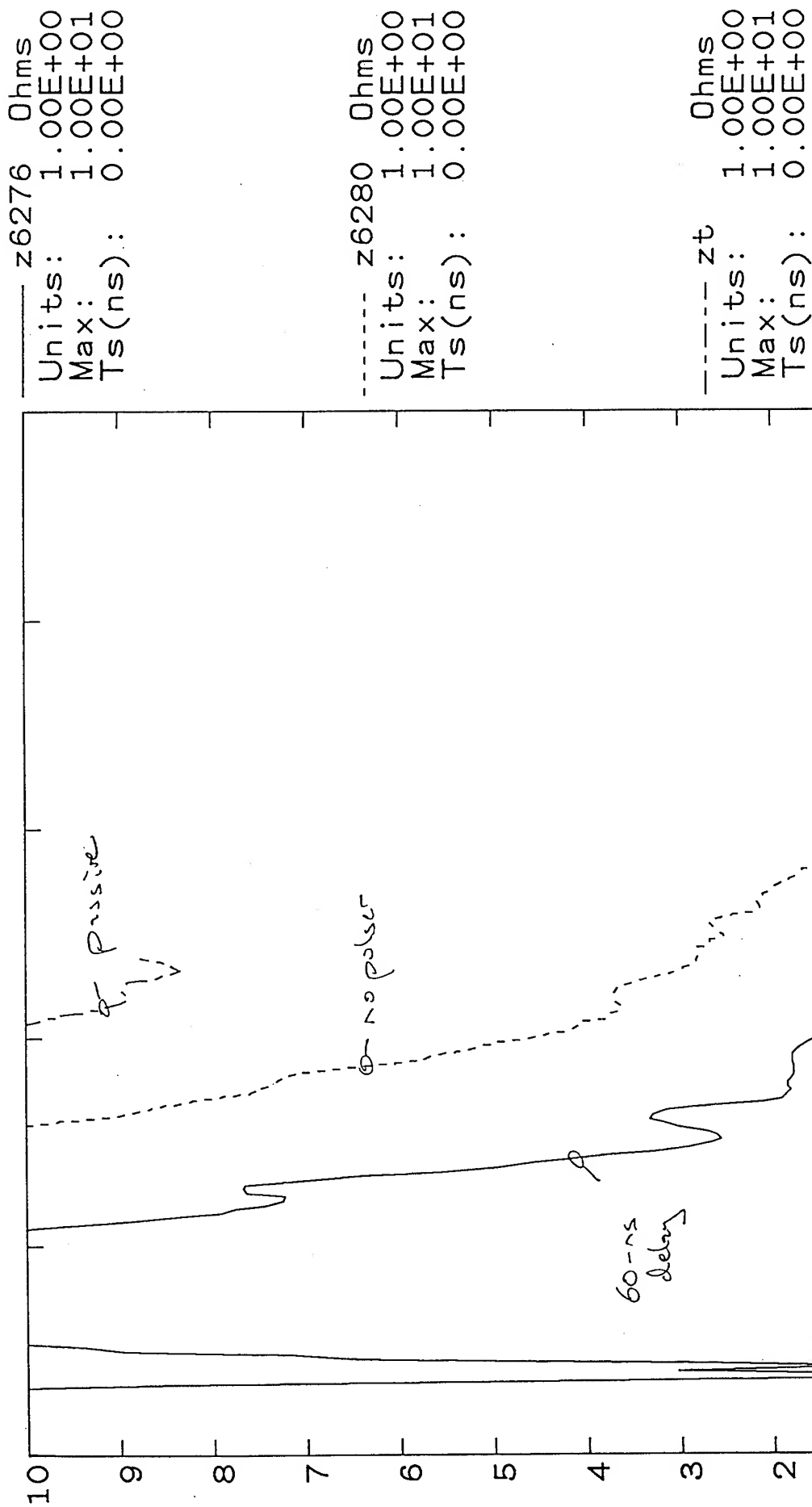


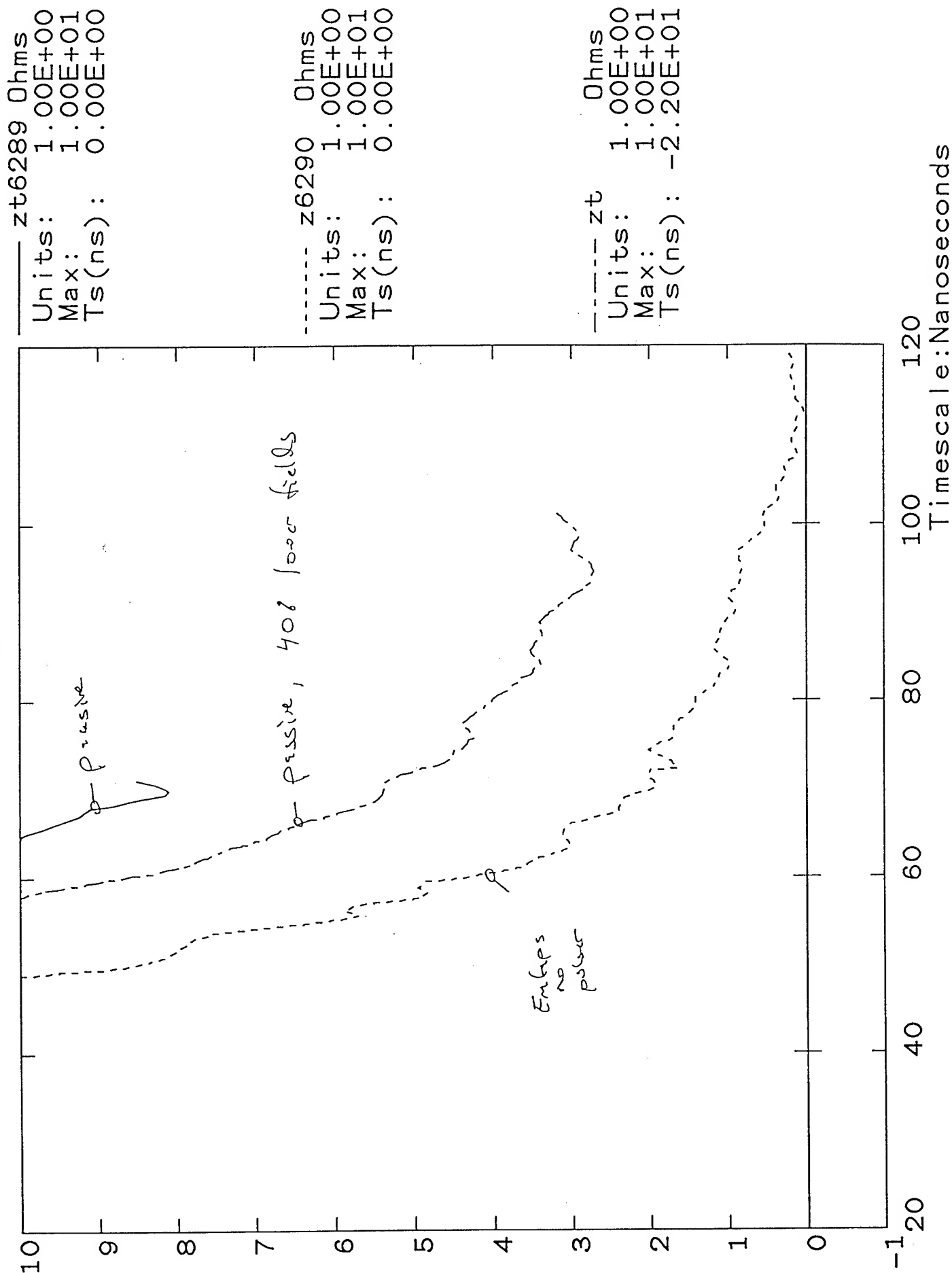
Fig 9

Shot 6294



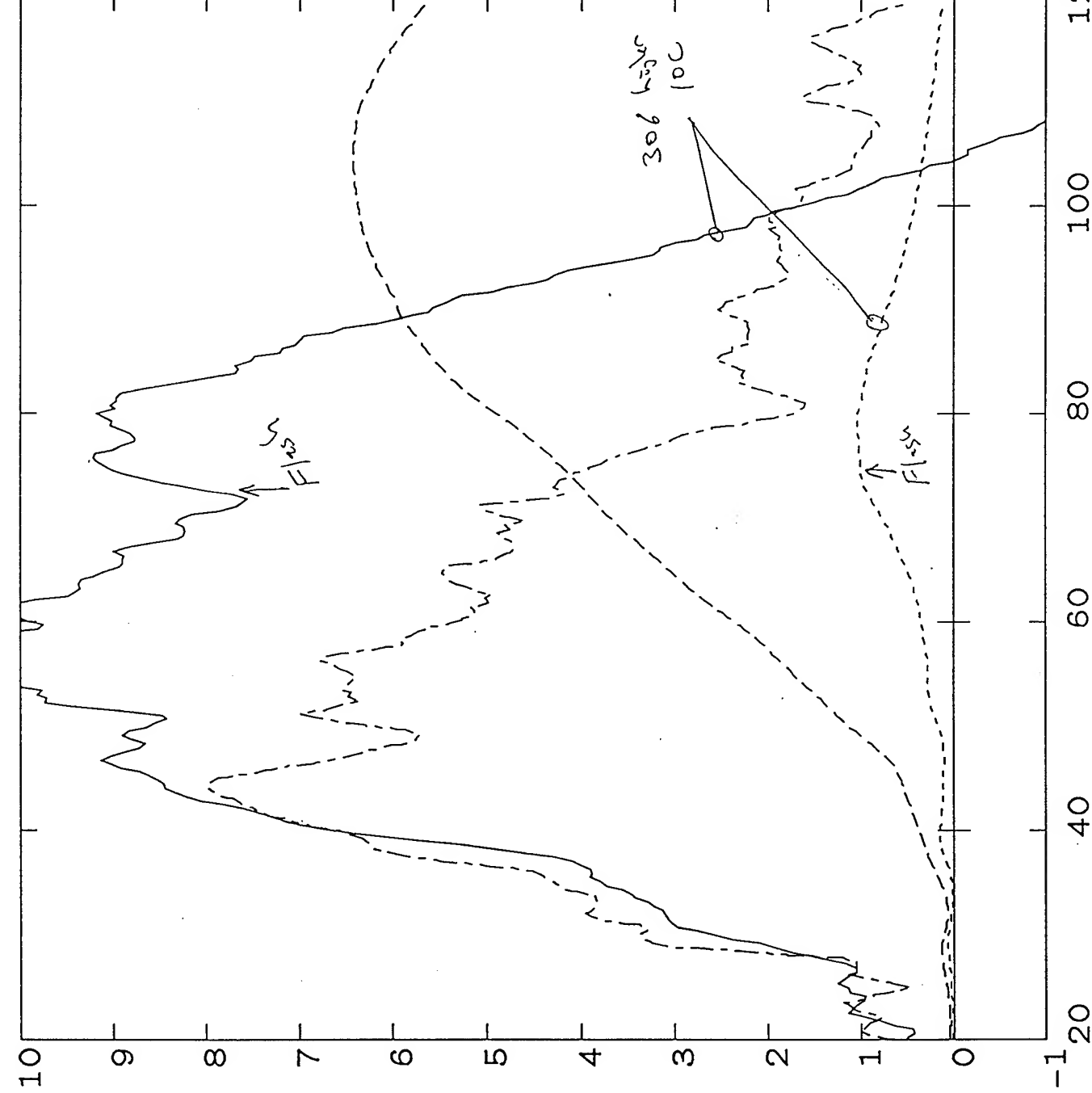
Shot 6293

Fig 10



Shot 6279

Fig 11



Timescale:Nanoseconds

Shot 623

Fig 12

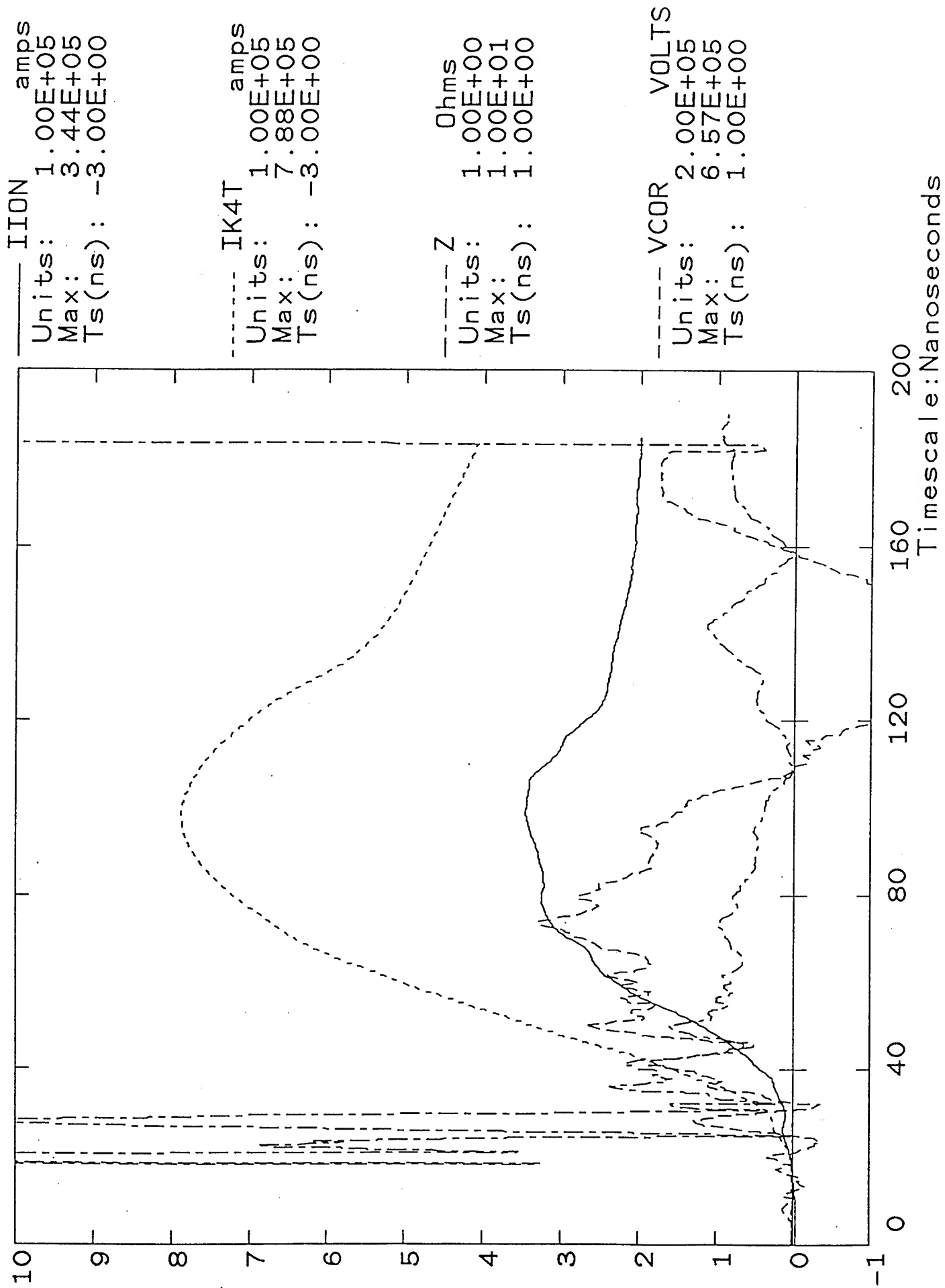
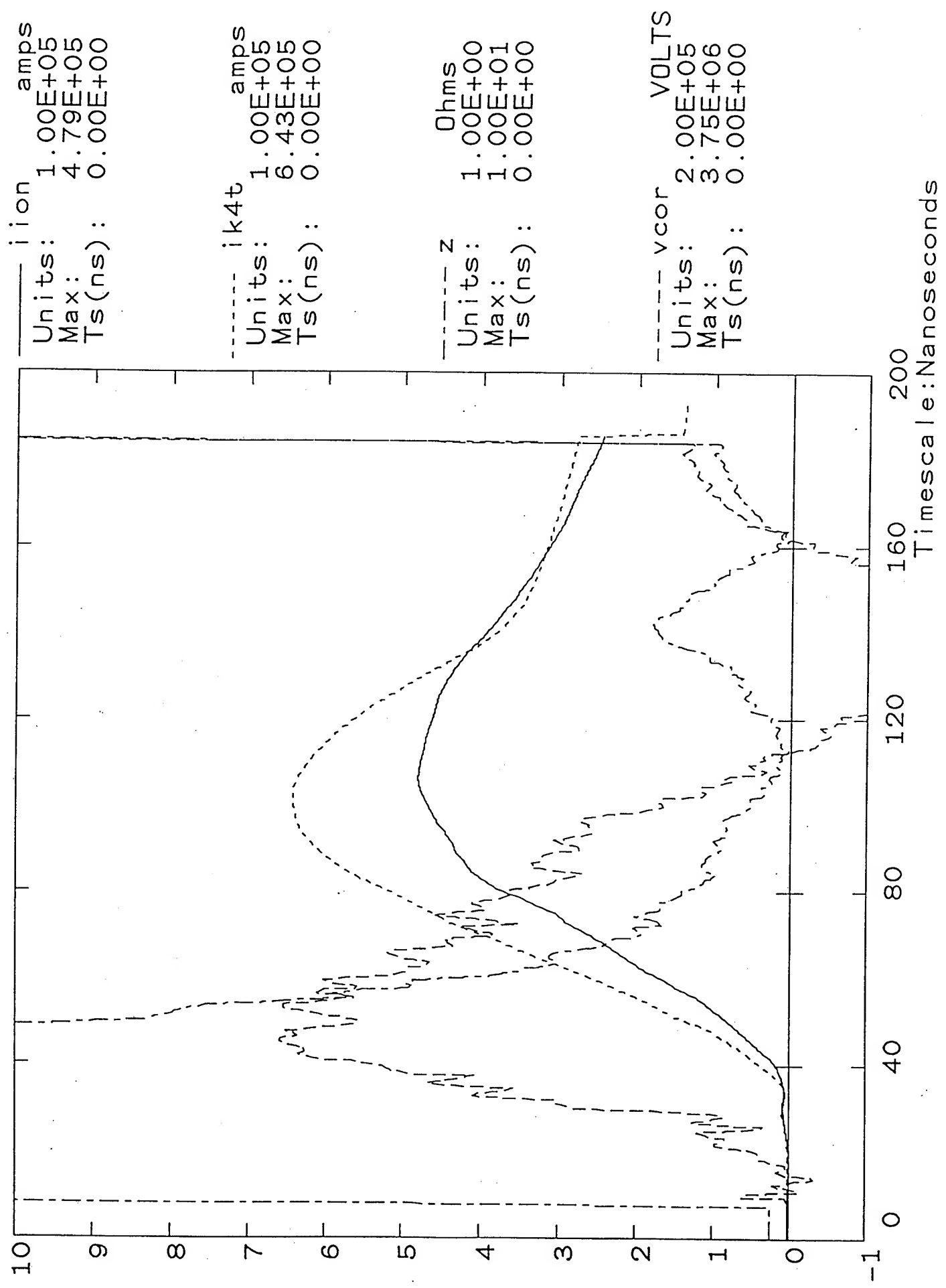
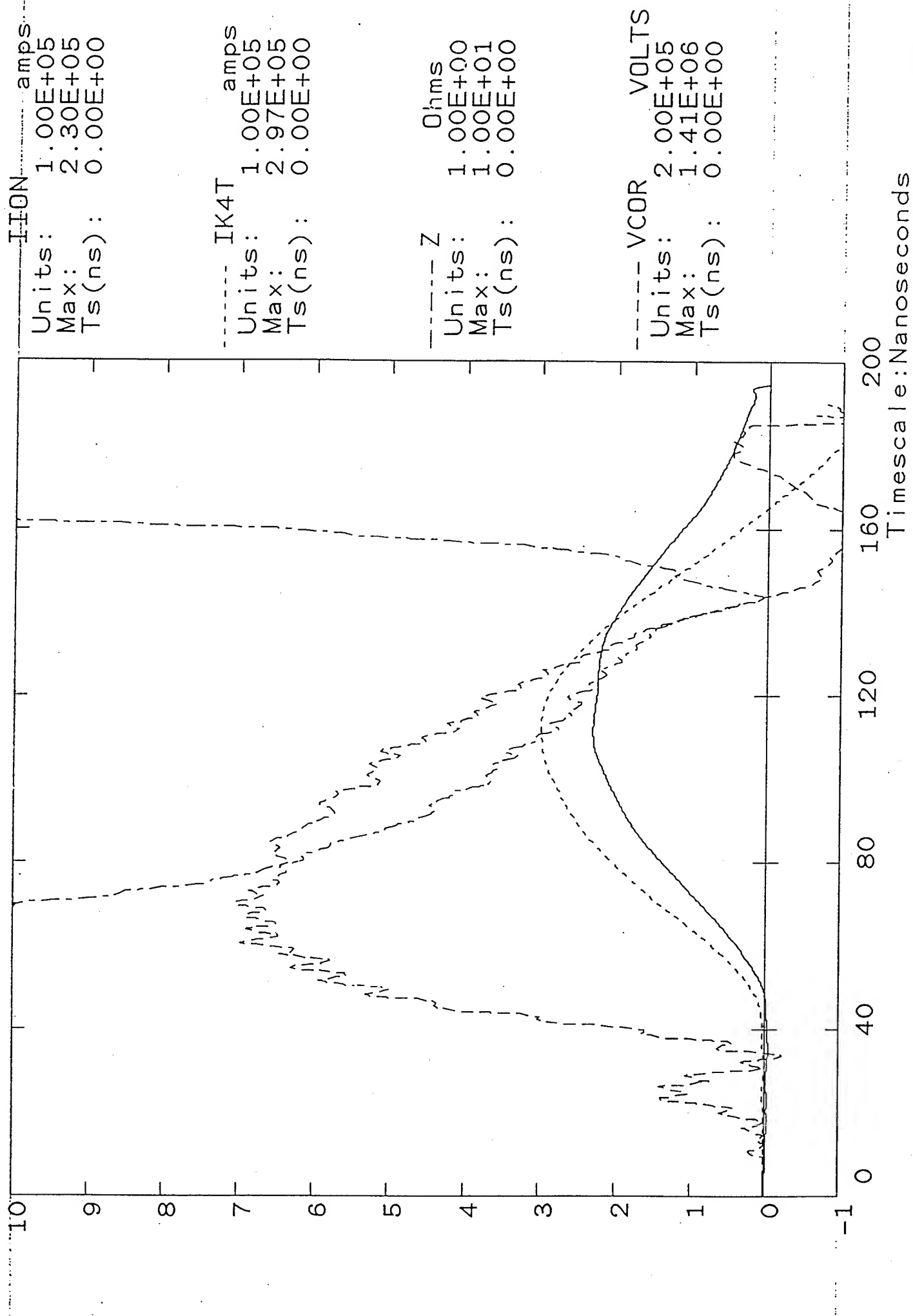


Fig 13

Shot 6290

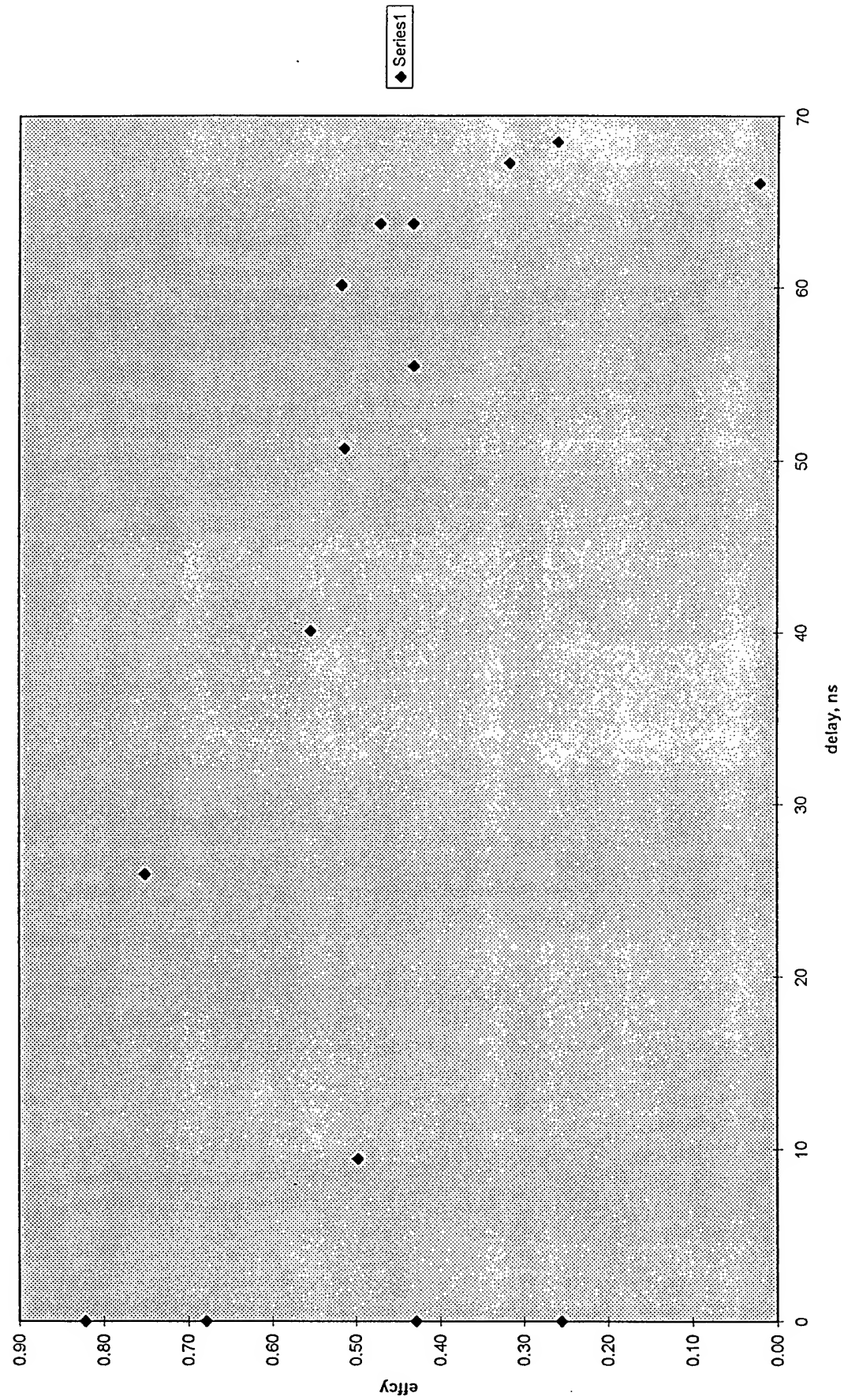




1 0 2 1 1

effcy Chart 2

ion efficiency



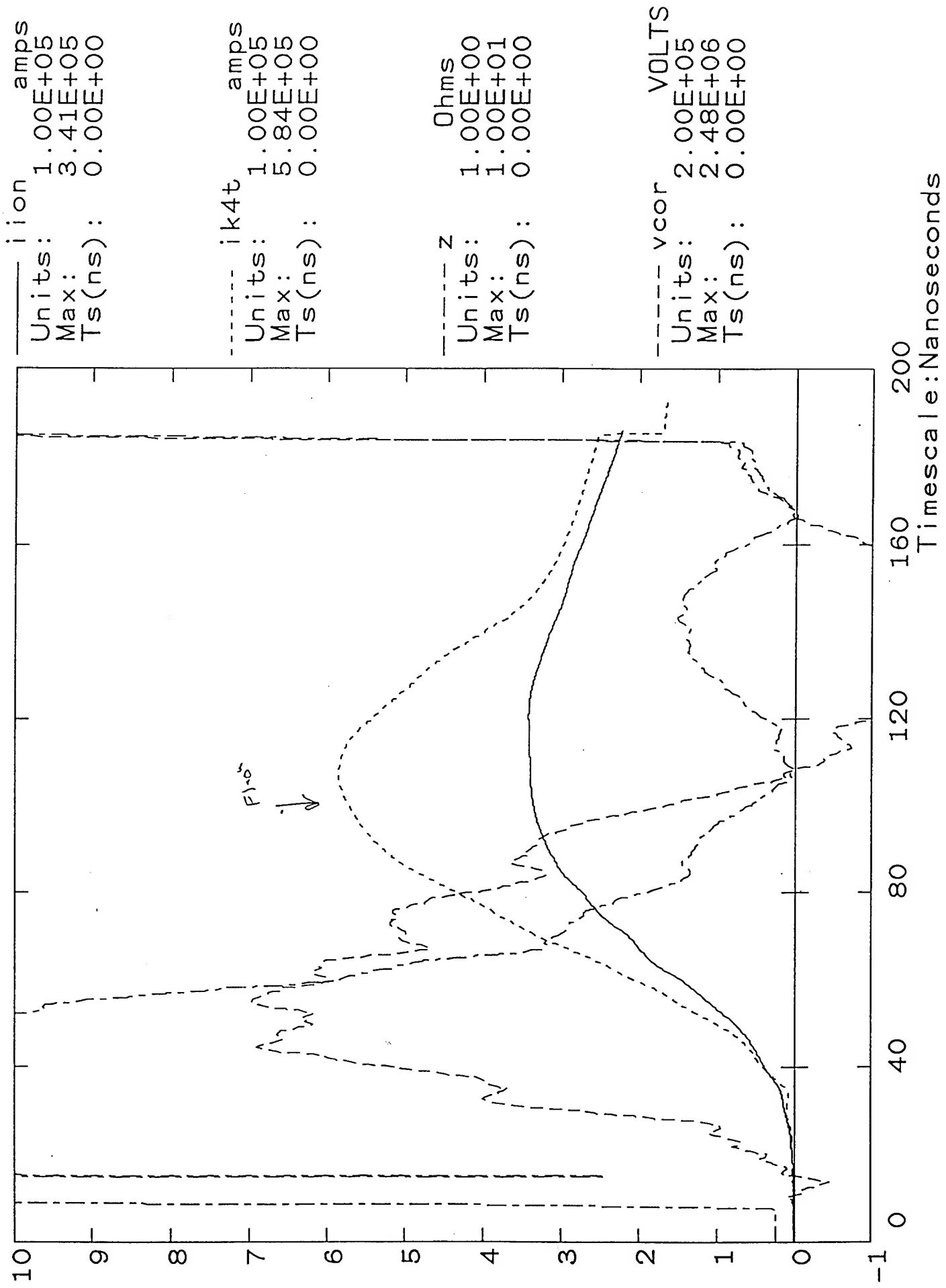
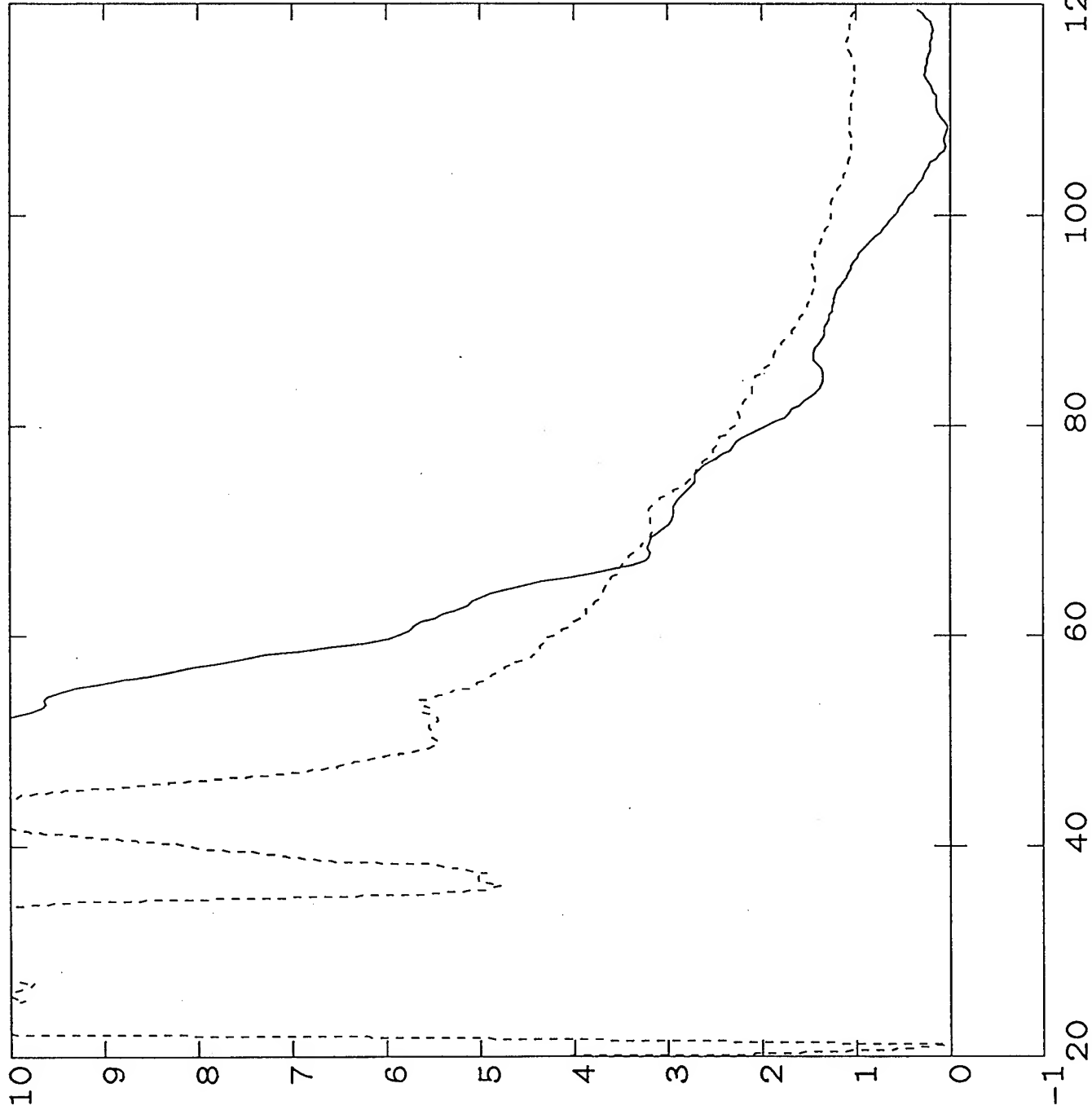


Fig 15a

Shot 6218

----- Z6282 Ohms
Units: 1.00E+00
Max: 1.00E+01
Ts(ns): 0.00E+00

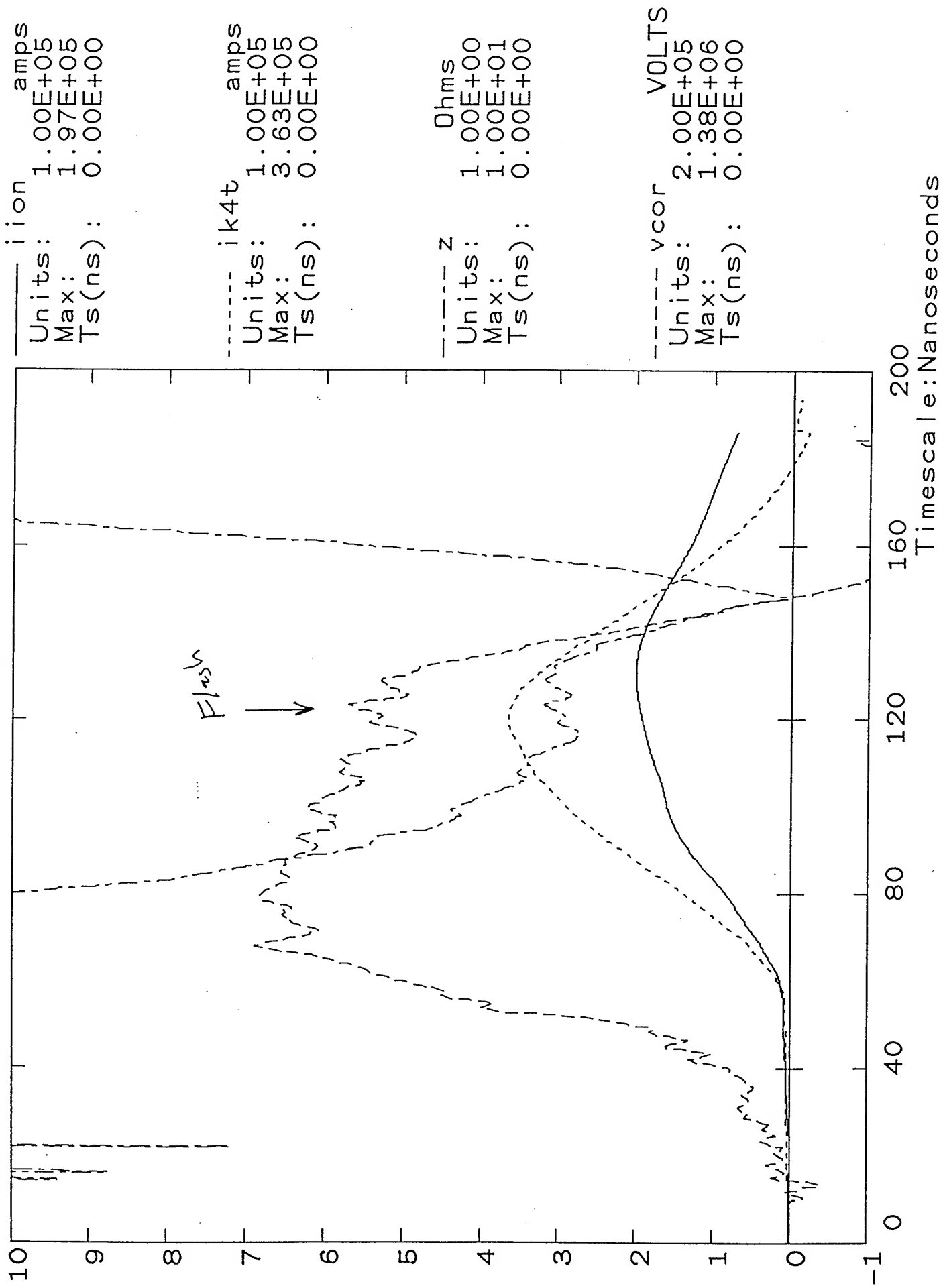
----- Z6017 Ohms
Units: 1.00E+00
Max: 1.00E+01
Ts(ns): 2.50E+00



Timescale: Nanoseconds

Shot 6293

Fig 18



~~60003~~
6293

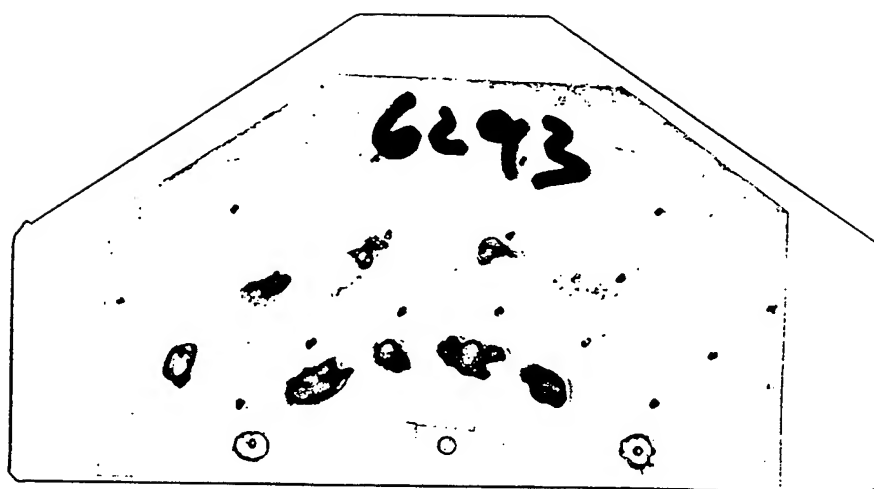


Fig 187

6294

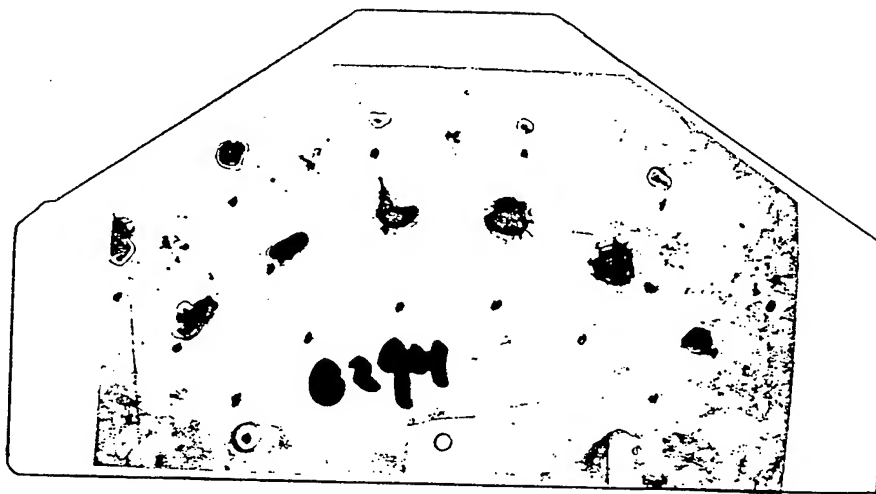


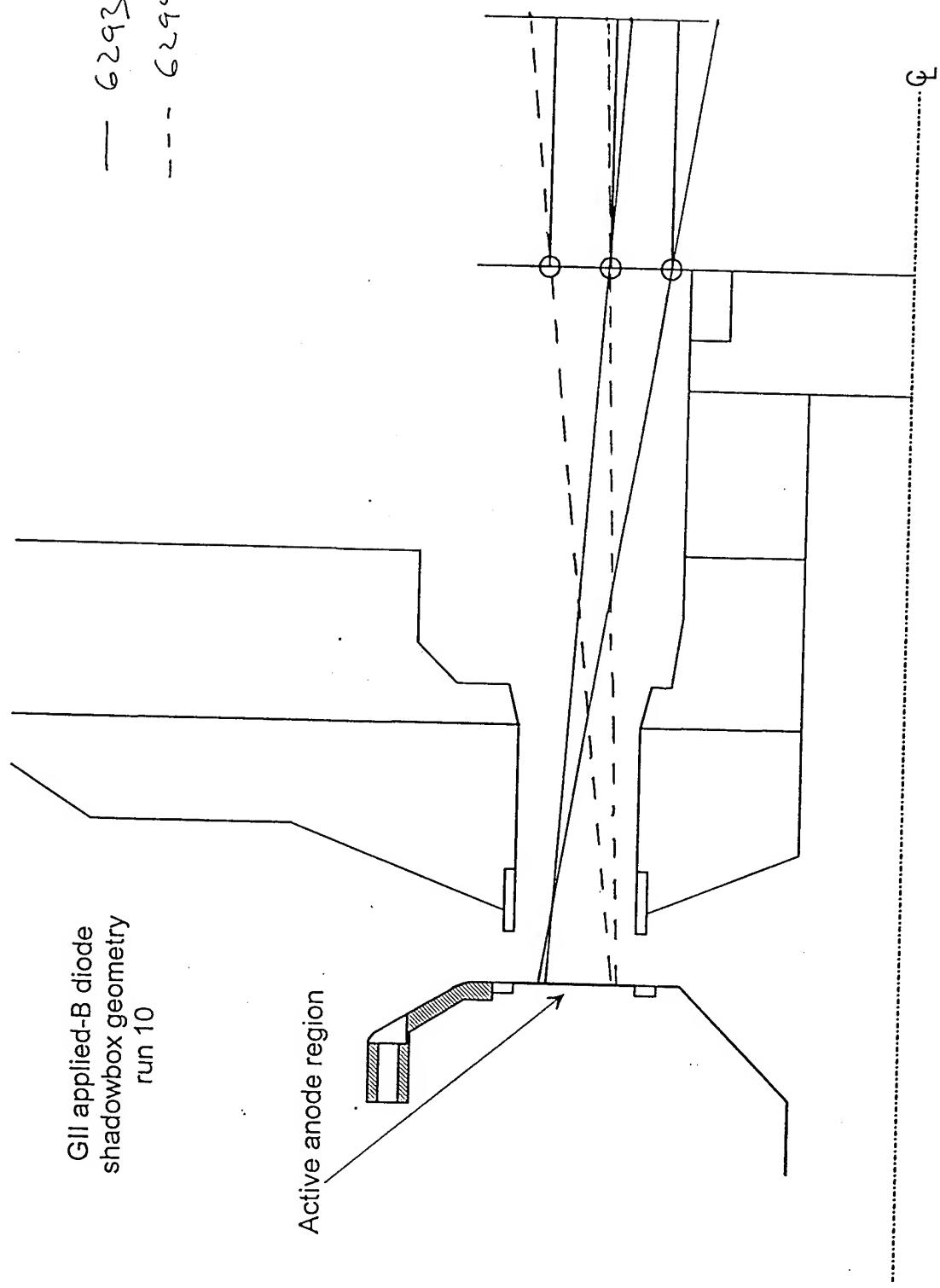
Fig 1A

Fig 109

GII applied-B diode
shadowbox geometry
run 10

— 6293
--- 6294

Active anode region



Shot 6220

(In this figure, damaged areas are dark)

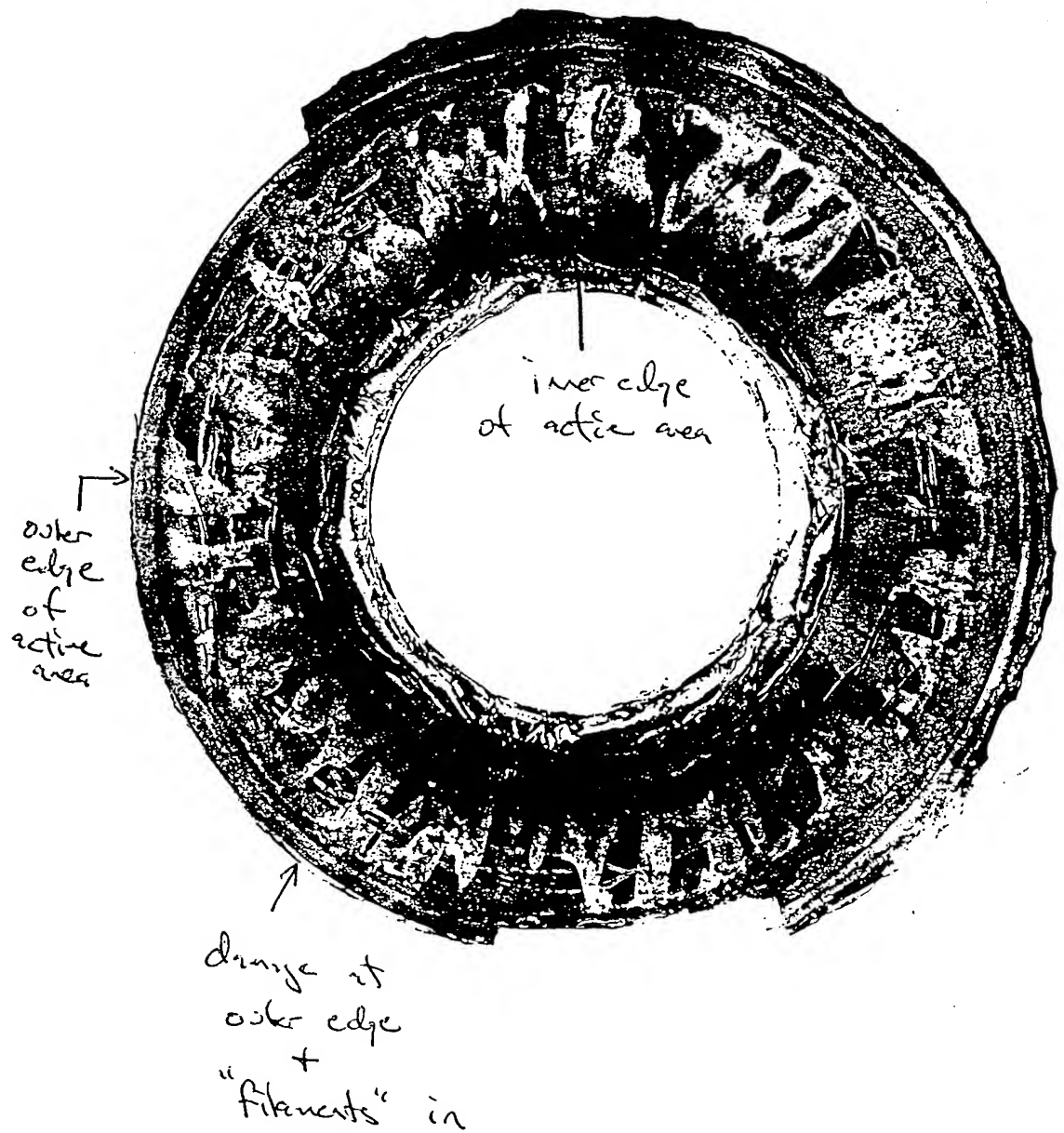


Fig 20

PULSED POWER PHYSICS TECHNOTE 95-04

TITLE: (RE) ANALYSIS OF APPLIED-B DIODE RUN 8

Author: D. Hinshelwood

Date: March 3, 1995

Abstract: This is one of a series of teknotes, composing a first cut at analysis of the reams of applied-B diode (MID) data we have acquired so far. The purpose here is to get the data out on the table and to identify the best shots, obvious trends, and any unexpected results.

Again, we see an effect of pulser delay on the impedance traces: with longer delays, the current onset begins earlier. A longer pulser delay was required on this run to obtain the same performance as on run 7. Some shots show premature impedance collapse. This may be related to a less-uniform foil breakdown (arising from some unknown reason).

The shots on this run had on the average higher ion efficiencies, but lower coupled energies, than shots on run 7. When comparing similar shots, e.g., 6103 and 6017, the results are in closer agreement.

The shadowbox data causes me to rethink earlier analysis - we may have to use ATHETA to interpret this diagnostic.

As on run 7, Rutherford scattering indicates that the beam has a proton fraction of at least, and probably significantly greater than, 50 percent. The average fraction for this run (see TN 94-19) is 77 percent.

We are in the same trap as before: we cannot get early the early current onset necessary to prevent flashover without operation at an undesirably low impedance. The anode source is critical to resolving this problem. To begin with, we need to determine to what degree the effect of long pulser delay is related to the condition of the resulting anode plasma, and to what degree it is related to the presence of plasma or neutrals in the diode gap.

Improved source measurements may show us a way to obtain a rapid current onset without an overly low impedance. Perhaps the key will be to drive the foil with a higher current but with a reduced delay.

INTRODUCTION

This is one of a series of teknotes, composing a first cut at analysis of the reams of applied-B diode (MID) data we have acquired so far. The purpose here is to get the data out on the table and to identify the best shots, obvious trends, and any unexpected results. No attempt will be made to draw final conclusions yet. To date there have been ten MID runs. The first three runs used wax-filled-groove, hereafter referred to as passive, anodes. Run 4 was our only attempt with POS-driven, EMFAPS anodes. Run 5 was the first run using a pulser to drive the EMFAPS anodes. On run 6, EMFAPS anodes were used without the pulser. In this case the early electron loss current returning through the anode foil is used to form the anode plasma. These will be referred to as limiter-EMFAPS anodes, although a physical limiter was rarely used. Runs 7-10 used pulser-EMFAPS anodes. Results from runs 5, 6, 7, and 8 have already been presented in TN's 95-01, 95-02, 95-03, and 94-16. This note is a further analysis of run 8, with some fresh observations.

MASTER SPREADSHEET

The enclosed spreadsheet lists all shots of this run other than short-circuit shots. This is part of an evolving master spreadsheet that will summarize all of our MID data. The first page gives the basic shot parameters. The column "voc2i" on the RAW sheet refers to the integral of VOC^2 . This quantity is now used to normalize energies. The column "e2(kJ)" refers to the integral of $VCOR \times IK2T$, and is a weighted measure of the current emitted from the inner cathode.

The second sheet presents some of the shot parameters in more useful form. (Obvious dud shots are not included on this sheet.) The second column gives the closest A-K gap, i.e., the distance between the cathode tips and the anode.

The values "e2/e", "e4/e", and "ei/e" are the ratios of the inner-cathode, outer cathode, and ion energies to the total energy (these add up to unity). The values "e19" and "ei19" give the total and ion energies, normalized to shot 6019 by assuming that the energies scale as voc2i. Shot 6019 had a typical open-circuit voltage for a 32 kV Marx charge, so the values in columns 17 and 18 might be expected if the shots were repeated at 32 kV. (A 26 kV Marx charge was used for this run.)

RUN EIGHT OVERVIEW

This run comprised 36 shots, at 32-kV Marx charge. As mentioned in TN 94-16, the early part of this run was plagued with Marx trouble which resulted in several prefires and a few shots where the machine came late relative to the applied fields. The prefires will be analyzed along with other, field-free shots, in a future note.

A smaller gap was used on the first few shots. Also, the IOA and IIA coils were switched with one another, as was the case on run 6, until shot 6090. Field mapping is required to

determine the resulting field on these shots. To some degree, the change in relative amplitude of IOA and IIA will be offset by the change in relative delay.

ATHETA calculations subsequent to run 7 indicated that on shots 6017 and 6019 (the nominal best shots of the run) the separatrix was behind the anode, especially at the inner edge. On this run, the coil currents were changed, based on ATHETA predictions, to give a more optimum field geometry with the separatrix closer to the anode surface. However, the results were deemed inferior to those on run 7, and we switched to the 6017 fields. These were used on 14 of the 20 good shots with the correct coil connections. The 'optimum' fields, by contrast, corresponded to roughly 15 percent higher values of IIA and IOA than the '6017' fields. In hindsight, based on all of the data examined so far, I would not expect a major change in diode performance to result from this level of field change. Therefore, I will lump together shots at these two field settings in the following analysis. This run, then, consists of 20 shots at similar fields, 5 shots with different, and as yet unknown, fields, and 4 shots with the unknown fields and a smaller gap.

The foils were cast and coated under conditions similar to those on run 7. As on run 7, these conditions resulted in thicker, apparently smoother, lower-resistance foils than those used in runs 5 and 6. The net effect of all of these changes is unknown at present. Photographs of the foil breakdowns taken on bench tests before the run suggest that foil breakdown may have been a bit less uniform on this run, but I can't quantify this.

The usual electrical diagnostics were used on this run, with the exception of the photodiode.

From shot 6091 on, the beam was diagnosed with the shadowbox and with Rutherford scattering. The scattering results have already been presented in TN 94-19 and will only be summarized here.

COMPARISON WITH RUNS 5, 6, AND 7

Typical open-circuit voltage waveforms from these 4 runs are compared in Fig. 1. These have been shifted to align the small prepulse that is always present. Waveforms from runs 5 (26 kV Marx, optimized oil switch), 6 (26 kV, un-optimized switch), and 7 (32 kV) have about the same timing. In contrast, on run 8 the prepulse has roughly doubled in duration to 20 ns. This, longer prepulse was also seen on neighboring experimental runs and Steve attributes it to further oil switch troubles that were fixed later.

On all runs, the time of current onset is seen to decrease as the pulser delay is increased. This relationship is quantified and compared among runs in Fig. 2. Current onset is defined here as the time when the impedance drops to $10\ \Omega$, as measured from the (extrapolated) start of the main pulse of the open-circuit voltage. Several shots are noted on the graph: Shots 6075-6078 had the 2-mm smaller gap and crossed field connections. In addition, the machine fired very late on shot 6077, when the fields had probably decreased. Shots 6082-6088 had crossed field connections but the normal gap. Shot

6098 had the correct field connections but a 1-mm smaller gap. Shot 6110 had unusual impedance behavior as will be discussed later.

These data exhibit considerable scatter, which may not be surprising considering that different field and foil conditions are lumped together. The data from run 7 lie significantly below (i.e., quicker current onsets) those from run 5. This was discussed in TN 95-03 and attributed to the different foil conditions. The standard-gap data from run 8 lie in between data from runs 5 and 7. The reversed-connection, standard-gap shots from run 8 lie at the top of the band of run 8 data, but their difference from the correct-connection shots is within the scatter and may not be significant. (Shot 6082 is way out of line, and I would guess that something was wrong with the foil discharge on that shot.) The 2-mm-smaller-gap shots on run 8 show significantly faster current onsets, but the 1-mm-smaller-gap shot 6098 does not.

Based on the foil conditions, I would have expected the data from runs 7 and 8 to overlay. In TN 95-03 I mentioned that there is some uncertainty (~ 1 -1.5 mm) in the gap on run 7. One possibility is that run 7 had a smaller gap than runs 5 and 8, and that the smaller gap, rather than a difference in foil behavior, accounts for the difference between runs 5, 7, and 8.

Figures 3-5 compare impedance traces from shots in run 8 with those from shots in run 7. Shots are compared based on current onset times rather than on pulser delay. No-pulser shots are compared in Fig. 3. Shot 5997 from run 7 did not have exactly the same field as those from run 8 but the fields were close enough that similar behavior would be expected. As on run 7, flashover occurred on many shots during this run. This shows that operation of the diode at 32 kV Marx charge is marginal at present. After flashover, the accuracy of the diode voltage monitor becomes suspect and for that reason, the impedance traces are truncated at that time. Figure 3 shows some shots whose behavior resembles shot 5997. Shot 6105, however, shows a much faster impedance collapse. This sort of behavior has not been seen on other runs: previous no-pulser shots exhibit a rather slowly-falling impedance. Other shots on this run with small pulser delays show a similar, rapid impedance collapse.

Run 8 shots with moderate pulser delays (about 60 ns) are compared with the same shot 5997 in Fig. 4. There are several shots from run 8, two of which are shown, that show impedance behavior similar to shot 5997. Again, however, there are some shots that have the same current onset time but much faster impedance collapse. Two of these shots had a wider anode area, with the outer diameter of the active region close to the diameter of the outer cathode tip; perhaps this contributed to the faster collapse.

Shots with longer delays are compared in Fig. 5. Several shots are seen to have impedance behavior similar to that of shot 6017. Among these are shots in both the '6017' and 'optimum' field configurations. As seen in Fig. 2, these shots had much longer delays than shot 6017. Shot 6098 in Fig. 5 had a 1-mm smaller gap, and appears to show a more rapid impedance collapse as might be expected.

Shot 6083 from this run, with the reversed anode field connection, is compared with shot 5915 from run 6 in Fig. 6. These shots had the same field shape but shot 6083 had over twice the field amplitude with only a slightly greater open-circuit voltage. Onset is earlier on shot 5915. Shot 6083 seems to show a faster impedance collapse, but the early truncation due to flashover prevents a definitive statement.

IMPEDANCE BEHAVIOR ON RUN 8

Representative shots from Figs. 3-5 are compared in Fig. 7. The variation in impedance behavior with delay time seen in these shots is similar to that seen in run 7, but at correspondingly longer delay times. One way to look at the run 8 data is to say that many shots exhibit behavior that qualitatively resembles that of run 7 shots, while a few shots show unusually rapid impedance collapse and/or unusually slow current onset.

Shot 6110 in Fig. 7 is such a shot, with an uncharacteristically late onset followed by a rapid collapse. It is interesting that the three shots with the fastest, 'anomalous' impedance collapse (6105, 6106, and 6110) had 200 W-min, rather than the usual 500 W-min foils. The two other shots in the run with thin foils, 6101 and 6102, had unusually rapid onsets (see Fig. 5: shot 6101 has a faster onset, but smaller delay, than shot 6103). This apparent dependence on foil thickness was not seen in run 7. For example, shots 6017 and 6019 in run 7 have virtually identical impedance traces but different foil thicknesses of 500 and 200 W-min, respectively.

Is the occasional, rapid impedance collapse a result of the longer prepulse during this run? Or is it related to some, as yet undetermined, nonuniform foil breakdown?

The shots with reversed connections and standard gap all had early flashovers, which precludes a careful comparison of impedance traces. Figures 9 and 10 show impedance traces from shots with reversed field connections and 2-mm-smaller gaps. Figure 9 shows examples of small-gap shots that exhibit similar impedance behavior to that of larger-gap shots at longer delays. Figure 10 shows two small-gap shots with very early onsets: one with a longer delay, and one where the machine came late, presumably after the applied fields had decreased.

IMPEDANCE RECONSIDERED(?)

In previous notes, I have pointed out apparent trends in impedance behavior within and between different runs. As the data has accumulated, however, so has the scatter, and I am beginning to doubt some of the earlier conclusions. Perhaps we should consider an alternate, simplified picture, as sketched in Fig. 11. This envisions a universal family of impedance curves. The curve for a given shot depends on the experimental details, but in general, lower fields, smaller gaps, thinner foils, and especially, longer delays, will push the shot to a leftward curve. Moving to this direction, the current onset begins earlier, and the diode operates at a lower impedance. Eventually, a stable, or even rising impedance

occurs, suggesting PFD operation. While potentially attractive, so far this mode of operation is always characterized by an impedance that is too low to be interesting. Occasionally, a shot will exhibit 'anomalous' impedance collapse, as indicated by the dashed line in the figure.

TYPICAL ELECTRICAL DATA

Electrical data from shot 6103, the nominal best shot of the run, are shown in Fig. 12. This shot had a normalized ion energy of 14 kJ. The energy was partitioned as 55% ions, 10% inner cathode current, and 35% outer cathode current. This shot exhibits the general features of many shots in run 7. These features are also typical of all shots during this run: Initially, ion current is produced with high efficiency (some shots in this run show even higher initial efficiency). Then, after about 40 ns, the ion current levels off while the electron current keeps rising. This additional electron current loads down the diode, reducing the voltage.

ENERGY PARTITION

As mentioned in TN 95-03, energy partition between ion, inner-cathode, and outer-cathode current is a useful metric. For the correct-field-connection shots of this run, the partition between ions, inner electrons, and outer electrons, has an average of (55:10:35), with an average normalized ion energy of 10.6 kJ. By comparison, the averages for runs 5, 6, and 7 were (63:6:30), (42:17:41), and (44:13:43), respectively. The average, normalized ion energies for runs 5, 6, and 7 are 14.6, 10.9, and 12.5 kJ.

The energy partition on this run shows no obvious dependence on any of the experimental conditions. Partitions on the small-gap and reversed-connection shots are not consistently different than the above average.

Relative to run 7, the average ion energy is lower on this run in spite of the higher ion efficiency because of less efficient energy coupling to the generator. The reduction in energy coupling on this run occurs because on the average, impedance collapse occurs a bit more rapidly than on run 7.

BEAM DIAGNOSTICS

A typical shadowbox pattern is shown in Fig. 13. The inferred radial trajectories for this shot are shown in Fig. 14. Most shots on this run yield similar radial trajectory plots. As in run 7, the beam is seen to be expanding both inward and outward. However, here orbit crossing is implied. I think what is happening, though, is that the simple ballistic projection backwards is invalid when angular momentum is present. With angular momentum, centrifugal effects can cause trajectories that are not a straight line in r-z space. Therefore, previous, radial analysis of shadowbox data may not be valid. To interpret these data accurately, it may be necessary to determine the applied fields, assume an emission location, and predict the trajectories using ATHETA.

A small but consistent difference is seen between shots on this run and shots on run 7 with the same fields and similar impedance behavior: on this run the trajectories show slightly more outward motion at the beam outer radius, and slightly more inward motion at the inside.

The inferred angular momentum on these shots is similar to that for shots on run 7 with the same fields. However, there is almost a factor of two shot-to-shot variation in angular displacement of the spots in the data here. This variation shows no correlation with impedance behavior.

To improve this diagnostic in the future, we should expand the hole-to-film distance and try to develop a time-resolved version.

Figure 15 shows a strange film, where the hole pattern appears to be offset. This was observed on two shots during the run; I am sure that the film was not mis-aligned. These data are very odd and just add to the confusion regarding this diagnostic.

Figures 16 and 17 show the film and inferred trajectories from a different arrangement that sheds more light on the current density distribution at the anode. Here, ion emission appears to be fairly uniform across the anode (the angular orientation of the film relative to the holes is not known exactly, so on Fig. 16 the film and hole patterns are arbitrarily aligned azimuthally and no information on angular trajectories can be obtained).

The pattern of electron damage on the anode is worth noting, to the extent that it is not simply dominated by late time, low-energy electrons. On most of these shots, the damage was centered radially, covering a roughly 1.5-cm radial band. On shots showing premature impedance collapse, the damage tended to be peaked at the outer edge of the anode.

Rutherford scattering results are described in TN 94-19.

SUMMARY

In this first cut at revisiting the MID data, I will attempt to answer four questions for each run:

(1) What are the key shots, in terms of performance, for each run?

Shot 6103 is a good example of one of the better shots from this run. Shot 6078, which had different fields and a smaller gap but similar behavior, is also interesting.

(2) Which field configurations should we concentrate on mapping out?

The profile for shot 6103 was also used on run 7. The new ones to map out are the profiles from shot 6108 (the 'optimum' fields) and shot 6078 (at two times - when the machine fired on 6078 and also 6077).

(3) What are the significant trends in the data?

Again, we see an effect of pulser delay, and perhaps an effect of foil thickness, on the impedance traces: with longer delays, (and thinner foils) the current onset begins earlier. A longer pulser delay was required here to obtain the same performance as in run 7. Some shots show premature impedance collapse. This may be related to the longer prepulse, or to a less-uniform foil breakdown (arising from some unknown reason). These shots tend to have anode damage peaked toward the outer edge.

The shots on this run had on the average higher ion efficiencies, but lower coupled energies, than shots on run 7. When comparing similar shots, e.g., 6103 and 6017, the results are in closer agreement.

The shadowbox data causes me to rethink earlier analysis - we may have to use ATHETA to interpret this diagnostic.

As on run 7, Rutherford scattering indicates that the beam has a proton fraction of at least, and probably significantly greater than, 50 percent. The average fraction for this run (see TN 94-19) is 77 percent.

(4) What are the most puzzling features to these data?

As on run 7, the most disturbing feature is the rather abrupt increase in electron loss that occurs midway into the pulse.

Also as on run 7, another puzzling feature is the divergent ion trajectories, with outer ions bending outward. This may be explicable by more careful analysis.

The difference in pulser delay needed to obtain similar behavior on runs 7 and 8 is not understood. It is possible that the gap on run 7 was less than that on run 8 (as mentioned in TN 95-03, there is an uncertainty about the gap on run 7).

CONCLUSIONS

We are in the same trap as before: we cannot get early the early current onset necessary to prevent flashover without operation at an undesirably low impedance. As I said in the last note, the anode source is critical to resolving this problem. To begin with, we need to determine to what degree the effect of long pulser delay is related to the condition of the resulting anode plasma, and to what degree it is related to the presence of plasma or neutrals in the diode gap. Again, the SRL interferometer will be very useful here.

And, as before, another reason for source study is to obtain (and know that we have) reproducible source operation. By keeping the source constant from shot to shot, we will have an easier time investigating the effects of the magnetic field configuration. Finally, as usual, field mapping will be necessary to interpret fully the results of this run.

Improved source measurements may show us a way to obtain a rapid current onset without an overly low impedance. Perhaps the key will be to drive the foil with a higher current but with a reduced delay.

shot	gap	tips	IAA	IOA	IIC	IOC	W-m	eff th	ins	lf	delay, r	z=10	voc2l	ei(k)	e2(k)	e(k)	Vpp	lpp	comnts
6075	9.5	4	3.13	4	3.37	4.22	?	?	?		44	9	2.87	4.6	1.4	11.0			5 mm gap, machine late
6076	9.5	4	3.13	4	3.37	4.22	500	155	?		60	0	3.55	5.1	1.3	13.2			5 mm gap
6077	9.5	4	3.13	4	3.37	4.22	?	?	?		50	0	2.88	5.2	1.0	8.5			5 mm gap, machine very late
6078	9.5	4	3.13	4	3.37	4.22	?	?	?		47	10	3.54	11.7	1.7	18.1			5 mm gap, machine late
6079	11.5	4	0	0	0	0	500	110	N										prefire
6080	11.5	4	0	0	0	0	?	?	?										prefire, did not record data
6081	11.5	4	0	0	0	0	?	?	?										prefire
6082	11.5	4	3.13	4	3.37	4.22	500	153	Y		43	50	1.29	2.9	0.1	4.2			flash
6083	11.5	4	3.13	4	3.37	4.22	500	224	Y		20	33	2.50	9.3	0.7	15.9			flash
6084	11.5	4	2.82	3.6	3.03	3.8	500	242	?		40	26	2.44	8.4	1.3	15.8			flash
6085	11.5	4	2.82	3.6	2.73	3.42	?	?	?										no pulser, shot not analyzed yet
6086	11.5	4	0	0	0	0	?	?	?										prefire
6087	11.5	4	2.82	3.6	2.73	3.42	500	220	?		56	25	2.41	6.8	1.1	12.6			flash
6088	11.5	4	2.66	3.48	3.37	4.22	500	210	Y		3	40	1.76	4.6	1.5	7.6			no pulser
6089	11.5	4	2.66	3.48	3.37	4.22	500	120	Y										no pulser, shot not analyzed yet
6090	11.5	4	4	3.13	3.37	4.22	500	212	N		48	24	2.03	7.5	1.4	13.9			flash
6091	11.5	4	3.6	2.82	3.03	3.8	500	165	N		16	27	2.55	7.6	1.2	12.8			flash
6092	11.5	4	3.42	2.67	3.03	3.8	500	200	Y		28	26	3.34	7.2	2.3	16.0			flash
6093	11.5	4	3.42	2.67	3.03	3.8	500	240	N		50	26	2.23	9.6	2.5	16.0			flash
6094	11.5	4	3.48	2.66	3.37	4.22	500	160	N		53	25	2.44	7.3	1.5	16.3			flash
6095	11.5	4	3.48	2.66	3.37	4.22	500	257	?		0	27	1.78	6.1	1.1	10.4			flash, no pulser
6096	11.5	4	3.48	2.66	3.37	4.22	500	85	?		51	25	2.02	7.9	1.8	14.2			flash
6097	11.5	4	3.3	3.07	3.15	4.3	500	250	N		64	20	2.24	7.7	3.6	15.9			flash
6098	10.5	4	3.48	2.66	3.37	4.22	500	225	N		67	15	3.31	7.0	1.0	11.1			6 mm gap
6099	11.5	4	3.48	2.66	3.37	4.22	500	130	Y		54	20	3.38	4.5	0.2	9.2			wider area
6100	11.5	4	3.48	2.66	3.37	4.22	500	275	N		49	20	3.30	8.9	2.9	17.1			wider area
6101	11.5	4	3.48	2.66	3.37	4.22	200	50	N		61	9	3.00	8.8	1.7	15.7			slightly wider
6102	11.5	4	3.48	2.66	3.37	4.22	200	20	Y		66	11	2.98	7.3	0.3	11.5			area here on
6103	11.5	4	3.48	2.66	3.37	4.22	500	216	N		69	15	2.55	8.9	1.7	16.1			
6104	11.5	4	3.48	2.66	3.37	4.22	500	137	N		0	29	3.32	8.5	2.8	17.5			no pulser, flash
6105	11.5	4	3.48	2.66	3.37	4.22	200	9	Y		0	28	3.78	4.8	0.7	9.2			no pulser
6106	11.5	4	3.48	2.66	3.37	4.22	200	37	Y		28	21	3.82	4.2	0.2	7.4			
6107	11.5	4	3.48	2.66	3.37	4.22	950	225	N			14	3.49	11.2	0.0	18.5			
6108	11.5	4	3.6	2.82	3.03	3.8	500	200	N		77	14	3.11	8.7	1.3	16.4			
6109	11.5	4	3.6	2.82	3.03	3.8	500	40	Y				3.70	13.2	4.9	26.8			prefire
6110	11.5	4	3.6	2.82	3.03	3.8	200	6	Y		88	21	2.94	6.2	0.5	9.6			

shot	AK gp	W-m	IIA	IOA	IIC	IOC	ic/oc	la/oc	oa/oc	delns	e(kj)	ei(kj)	e/e	e2/e	e4/e	ei19	e19	comnts
6075	5.50	?	3.13	4.00	3.37	4.22	0.80	0.74	0.95	52	11.0	4.6	0.42	0.13	0.45	6.2	14.9	5 mm gap, machine late
6076	5.50	500	3.13	4.00	3.37	4.22	0.80	0.74	0.95	71	13.2	5.1	0.39	0.10	0.52	5.6	14.4	5 mm gap
6077	5.50	?	3.13	4.00	3.37	4.22	0.80	0.74	0.95	59	8.5	5.2	0.61	0.12	0.27	7.0	11.4	5 mm gap, machine very late
6078	5.50	?	3.13	4.00	3.37	4.22	0.80	0.74	0.95	55	18.1	11.7	0.64	0.09	0.26	12.8	19.8	5 mm gap, machine late
6082	7.50	500	3.13	4.00	3.37	4.22	0.80	0.74	0.95	51	4.2	2.9	0.69	0.02	0.29	8.8	12.7	flash
6083	7.50	500	3.13	4.00	3.37	4.22	0.80	0.74	0.95	24	15.9	9.3	0.58	0.04	0.38	14.4	24.7	flash
6084	7.50	500	2.82	3.60	3.03	3.80	0.80	0.74	0.95	47	15.8	8.4	0.54	0.08	0.38	13.4	25.1	flash
6087	7.50	500	2.82	3.60	2.73	3.42	0.80	0.82	1.05	66	12.6	6.8	0.54	0.09	0.37	10.9	20.2	flash
6088	7.50	500	2.66	3.48	3.37	4.22	0.80	0.63	0.82	4	7.6	4.6	0.60	0.19	0.21	10.1	16.8	no pulser
6090	7.50	500	4.00	3.13	3.37	4.22	0.80	0.95	0.74	57	13.9	7.5	0.54	0.10	0.36	14.2	26.6	flash
6091	7.50	500	3.60	2.82	3.03	3.80	0.80	0.95	0.74	19	12.8	7.6	0.59	0.09	0.31	11.6	19.5	flash
6092	7.50	500	3.42	2.67	3.03	3.80	0.80	0.90	0.70	33	16.0	7.2	0.45	0.15	0.40	8.3	18.5	flash
6093	7.50	500	3.42	2.67	3.03	3.80	0.80	0.90	0.70	59	16.0	9.6	0.60	0.16	0.24	16.7	27.8	flash
6094	7.50	500	3.48	2.66	3.37	4.22	0.80	0.82	0.63	63	16.3	7.3	0.45	0.09	0.46	11.6	25.9	flash
6095	7.50	500	3.48	2.66	3.37	4.22	0.80	0.82	0.63	0	10.4	6.1	0.58	0.10	0.31	13.2	22.6	flash, no pulser
6096	7.50	500	3.48	2.66	3.37	4.22	0.80	0.82	0.63	60	14.2	7.9	0.56	0.13	0.31	15.2	27.2	flash
6097	7.50	500	3.30	3.07	3.15	4.30	0.73	0.77	0.71	76	15.9	7.7	0.48	0.22	0.29	13.3	27.6	flash
6098	6.50	500	3.48	2.66	3.37	4.22	0.80	0.82	0.63	79	11.1	7.0	0.64	0.09	0.28	8.3	13.0	6 mm gap
6099	7.50	500	3.48	2.66	3.37	4.22	0.80	0.82	0.63	64	9.2	4.5	0.49	0.02	0.49	5.2	10.6	wider area
6100	7.50	500	3.48	2.66	3.37	4.22	0.80	0.82	0.63	58	17.1	8.9	0.52	0.17	0.31	10.4	20.1	wider area
6101	7.50	200	3.48	2.66	3.37	4.22	0.80	0.82	0.63	72	15.7	8.8	0.56	0.11	0.33	11.3	20.3	slightly wider
6102	7.50	200	3.48	2.66	3.37	4.22	0.80	0.82	0.63	78	11.5	7.3	0.63	0.03	0.34	9.5	15.0	area here on
6103	7.50	500	3.48	2.66	3.37	4.22	0.80	0.82	0.63	81	16.1	8.9	0.55	0.10	0.35	13.5	24.5	
6104	7.50	500	3.48	2.66	3.37	4.22	0.80	0.82	0.63	0	17.5	8.5	0.48	0.16	0.35	9.9	20.4	no pulser, flash
6105	7.50	200	3.48	2.66	3.37	4.22	0.80	0.82	0.63	0	9.2	4.8	0.52	0.08	0.40	4.9	9.4	no pulser
6106	7.50	200	3.48	2.66	3.37	4.22	0.80	0.82	0.63	33	7.4	4.2	0.57	0.02	0.40	4.3	7.5	
6107	7.50	950	3.48	2.66	3.37	4.22	0.80	0.82	0.63	0	18.5	11.2	0.60	0.00	0.40	12.4	20.6	
6108	7.50	500	3.60	2.82	3.03	3.80	0.80	0.95	0.74	91	16.4	8.7	0.53	0.08	0.39	10.8	20.4	
6110	7.50	200	3.60	2.82	3.03	3.80	0.80	0.95	0.74	104	9.6	6.2	0.65	0.05	0.31	8.2	12.7	
AV8											13.7	7.5	0.55	0.10	0.35	10.6	19.5	AVERAGE FOR RUN 8 SHOTS 6090-6110

Fig 1

Shot 5915

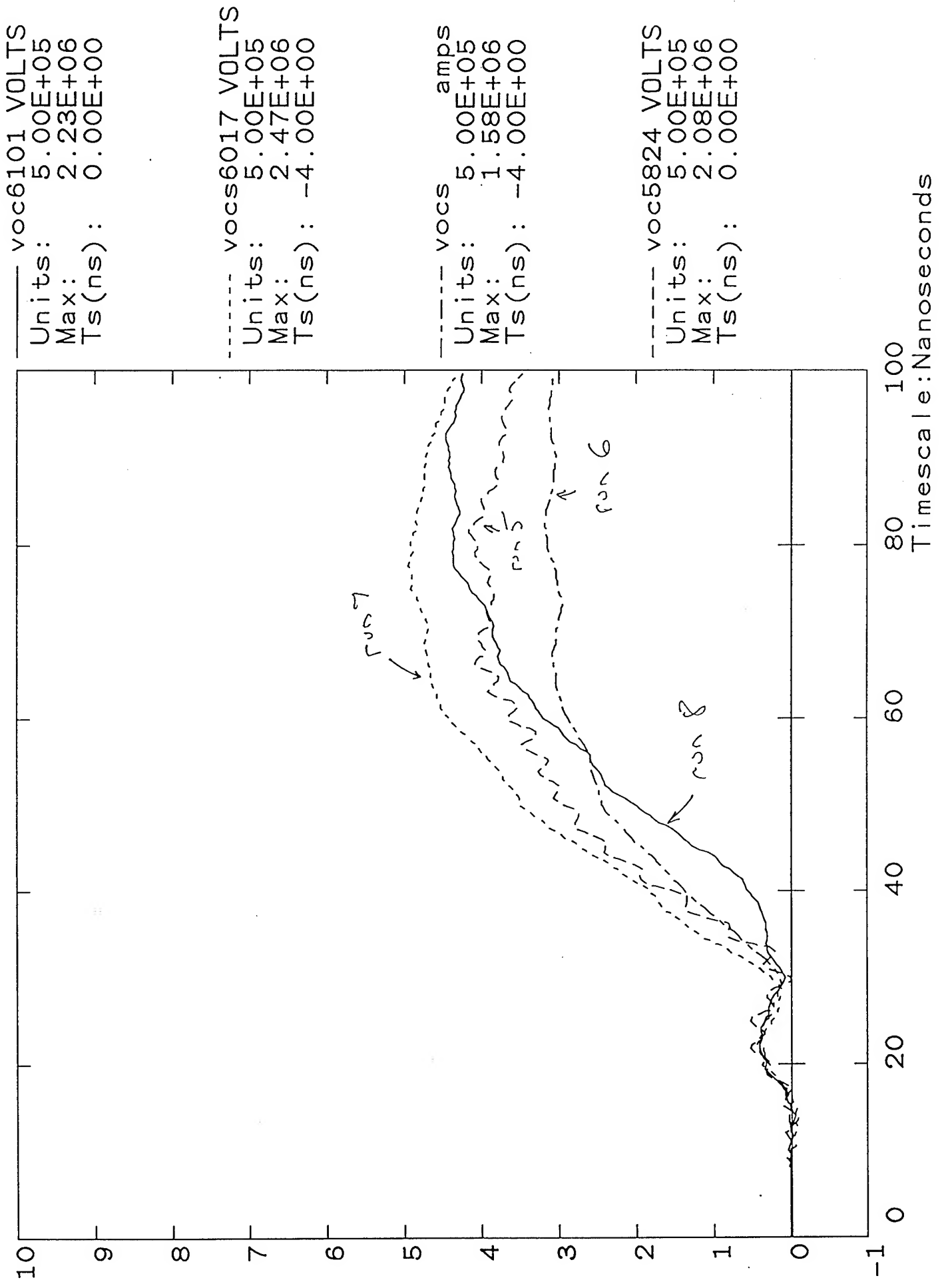


Fig 2

Delays Chart 1

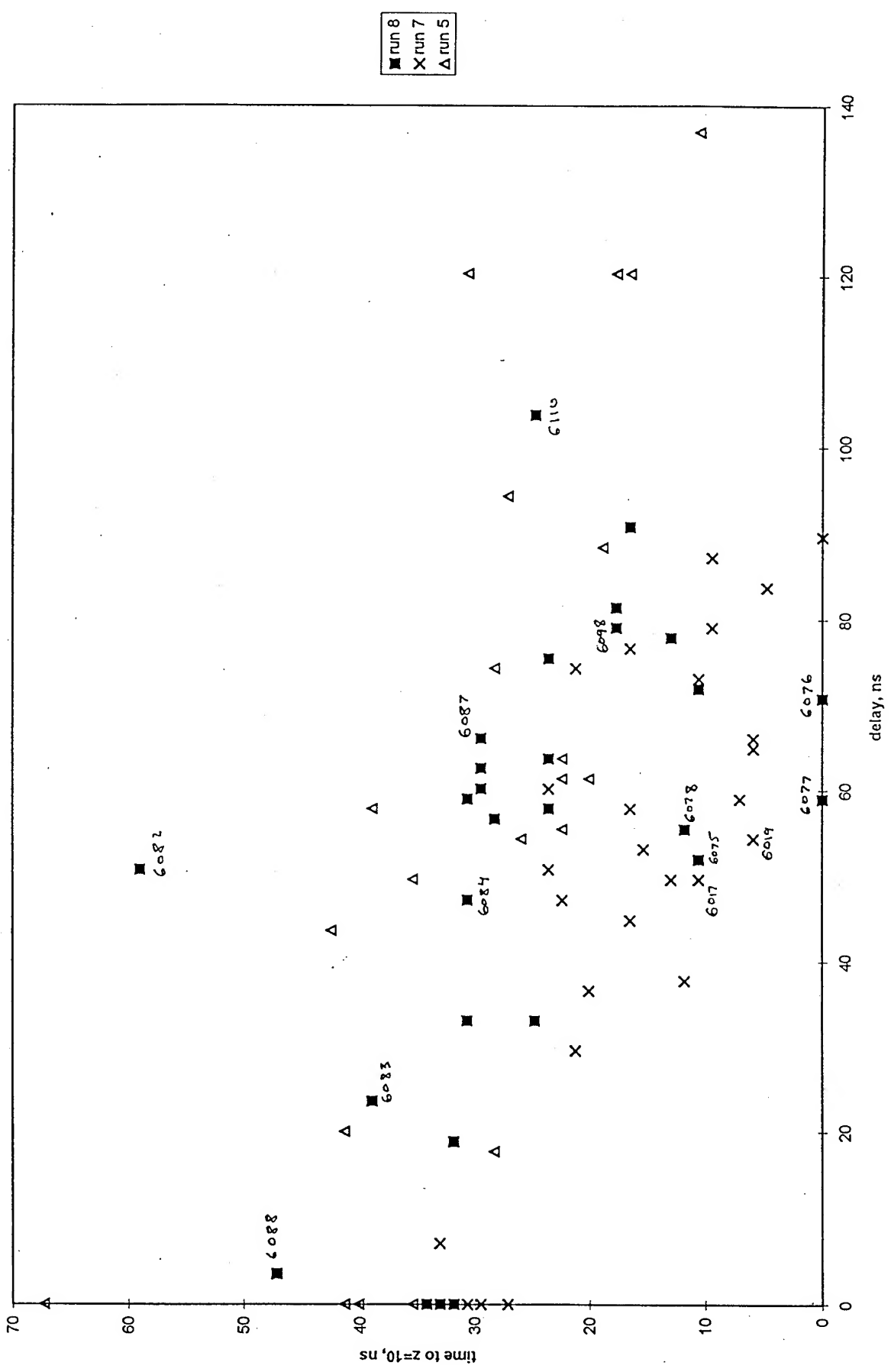


Fig 3

Shot 6104

zt5997 Ohms
Units: 1.00E+00
Max: 1.00E+01
Ts(ns): 5.00E+00

zt6095 Ohms
Units: 1.00E+00
Max: 1.00E+01
Ts(ns): 5.00E+00

zt Ohms
Units: 1.00E+00
Max: 1.00E+01
Ts(ns): 0.00E+00

z6105 Ohms
Units: 1.00E+00
Max: 1.00E+01
Ts(ns): 0.00E+00

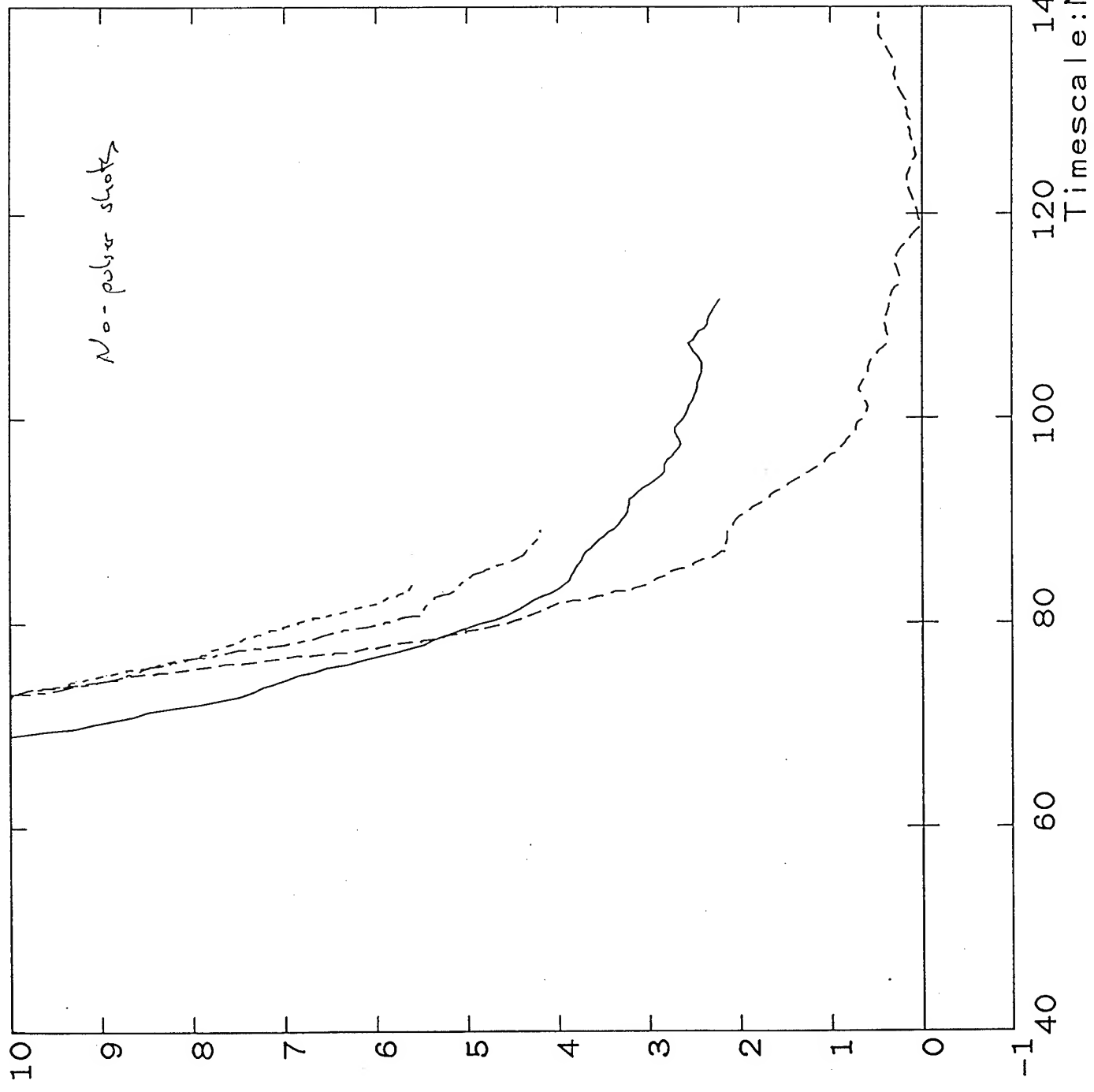
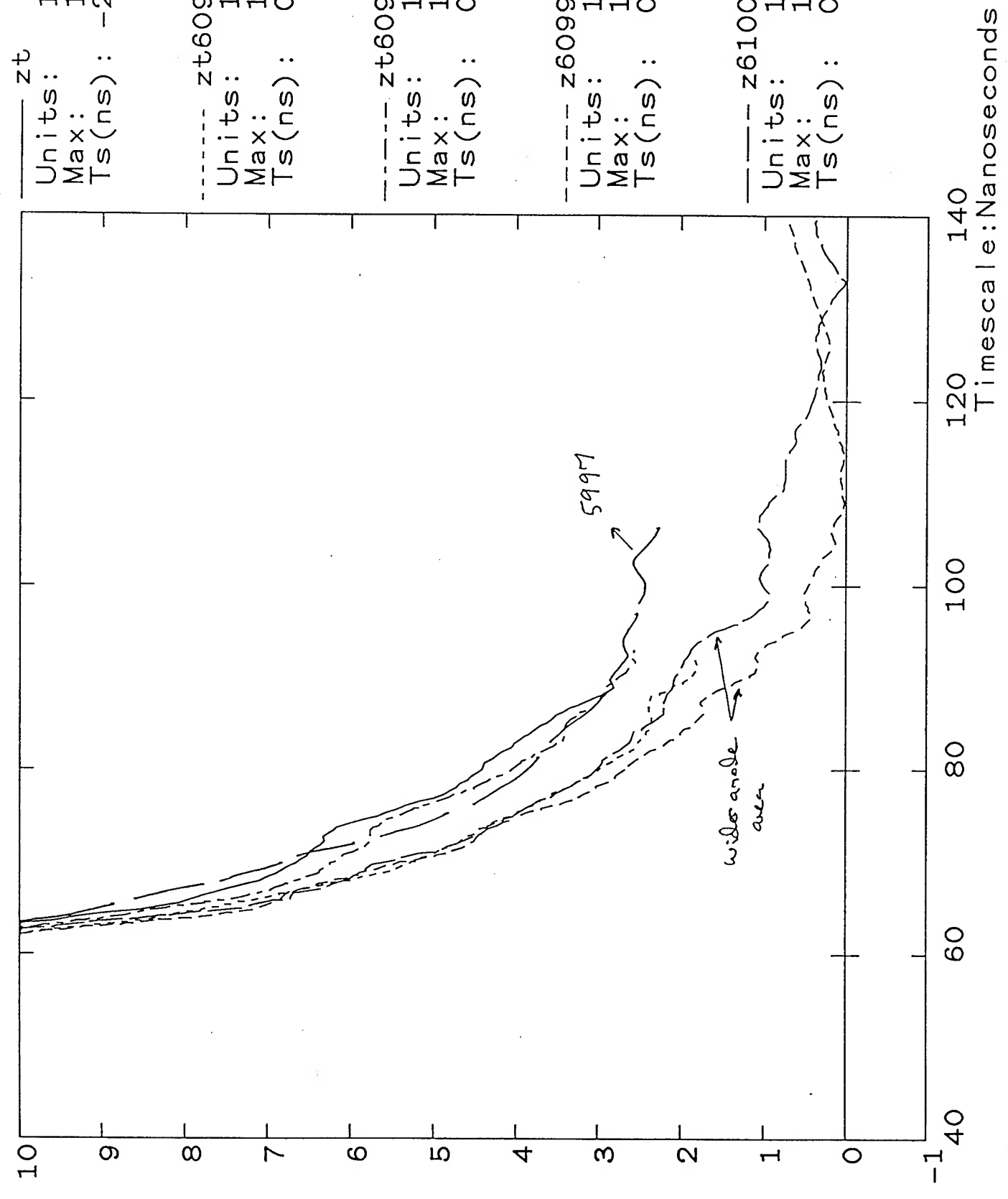


Figure 4

Shot 6093



ztb
Units: 1.00E+00
Max: 1.00E+01
Ts(ns): -2.00E+00

zt6094
Units: 1.00E+00
Max: 1.00E+01
Ts(ns): 0.00E+00

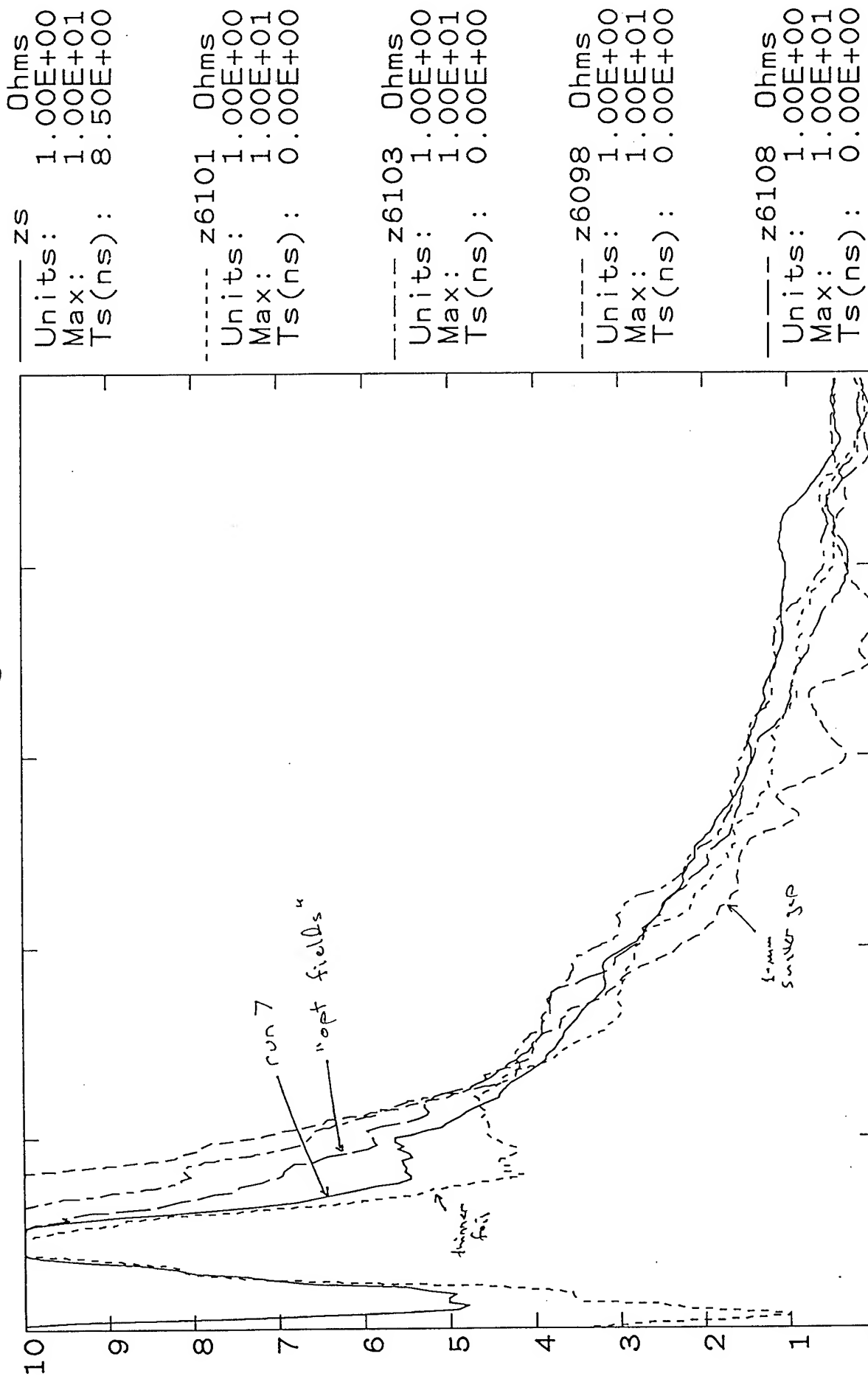
zt6096
Units: 1.00E+00
Max: 1.00E+01
Ts(ns): 0.00E+00

z6099
Units: 1.00E+00
Max: 1.00E+01
Ts(ns): 0.00E+00

z6100
Units: 1.00E+00
Max: 1.00E+01
Ts(ns): 0.00E+00

Shot 6017

Fig 5



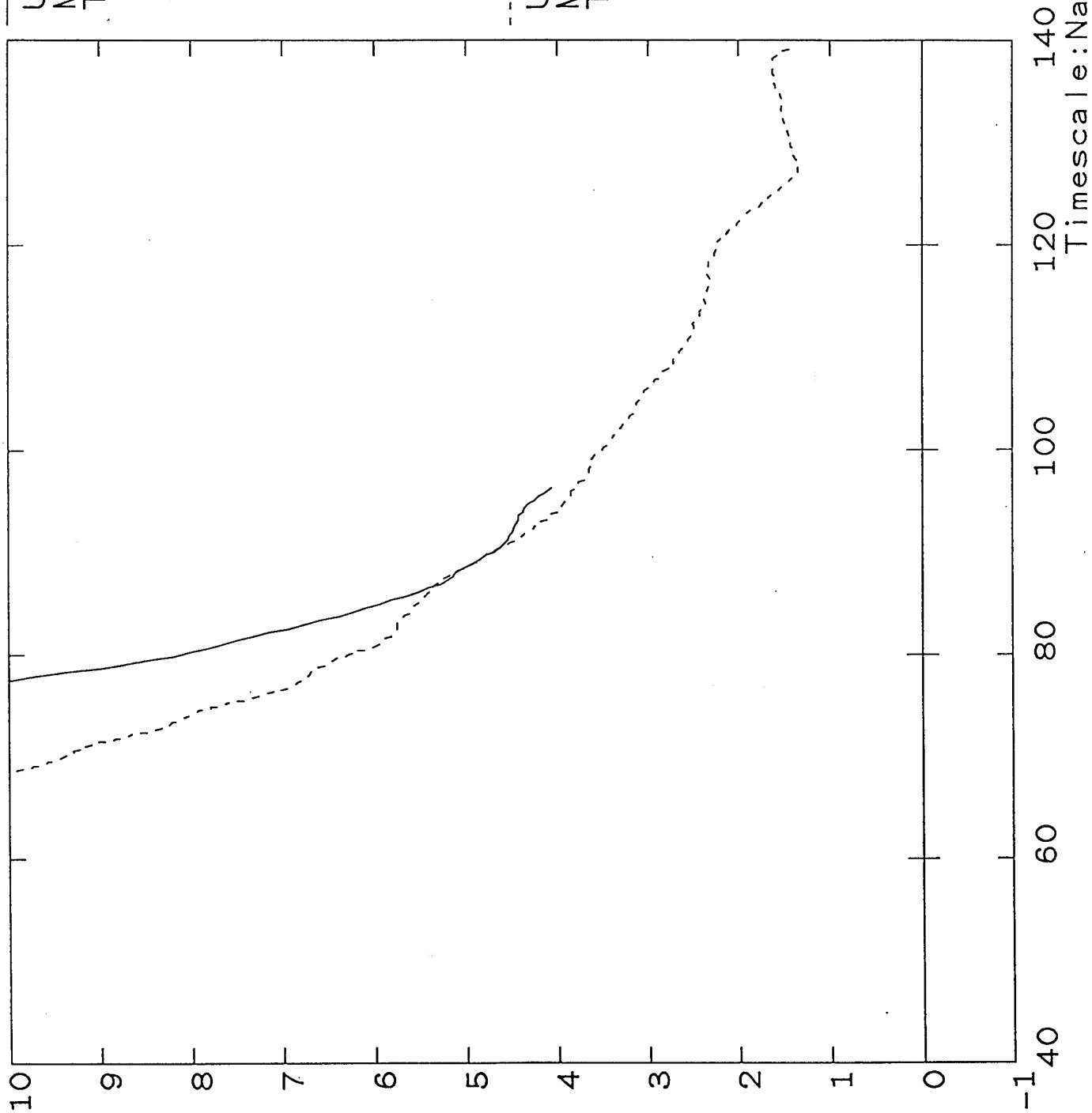
Timescale: Nanoseconds

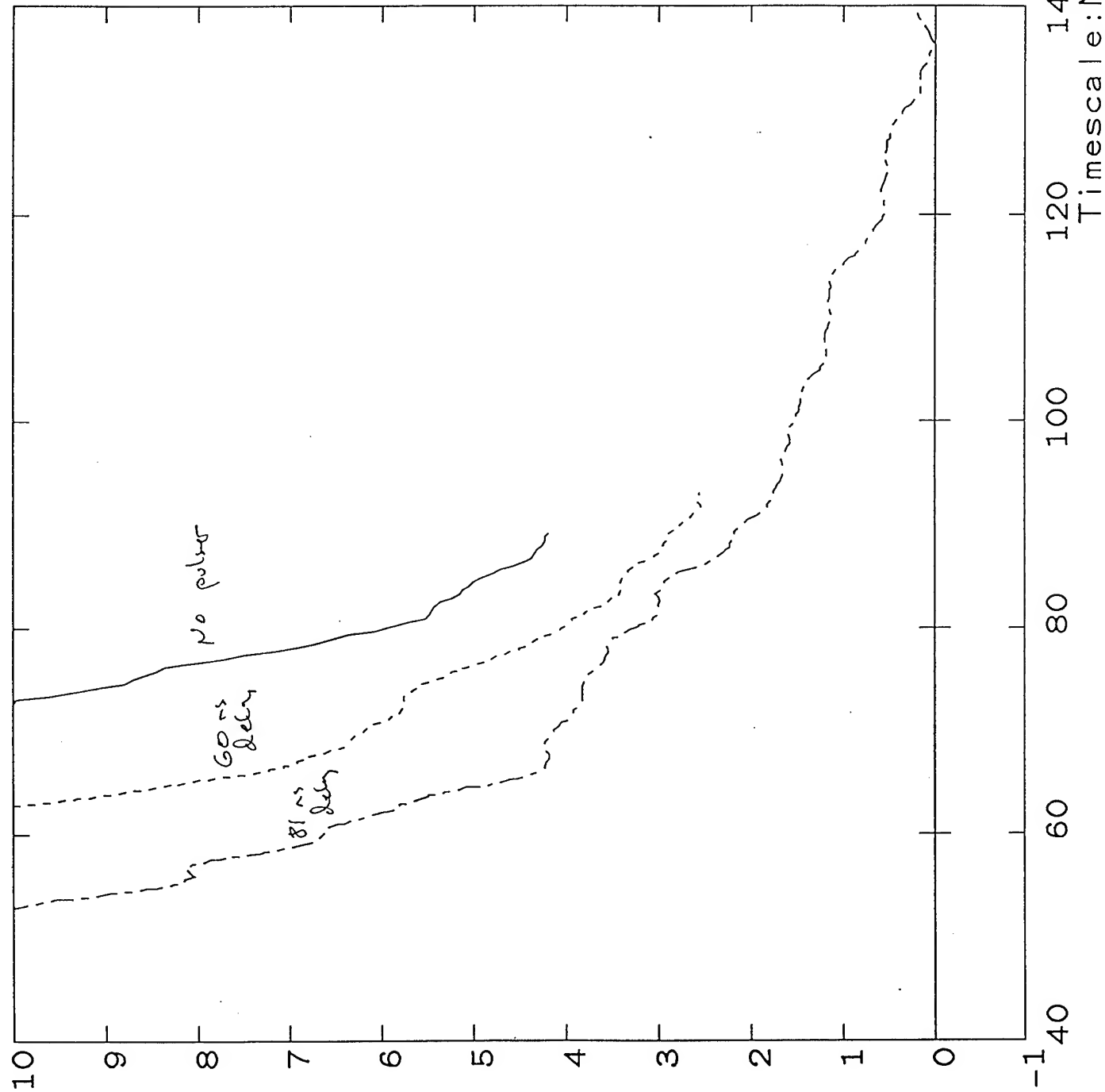
Fig 6

Shot 6083

Units: 1.00E+00
Max: 1.00E+01
Ts(ns): 0.00E+00

----- z5915 Ohms
Units: 1.00E+00
Max: 1.00E+01
Ts(ns): 2.00E+00





_____ zt6104 Ohms
Units: 1.00E+00
Max: 1.00E+01
Ts(ns): 0.00E+00

----- zt6096 Ohms
Units: 1.00E+00
Max: 1.00E+01
Ts(ns): 0.00E+00

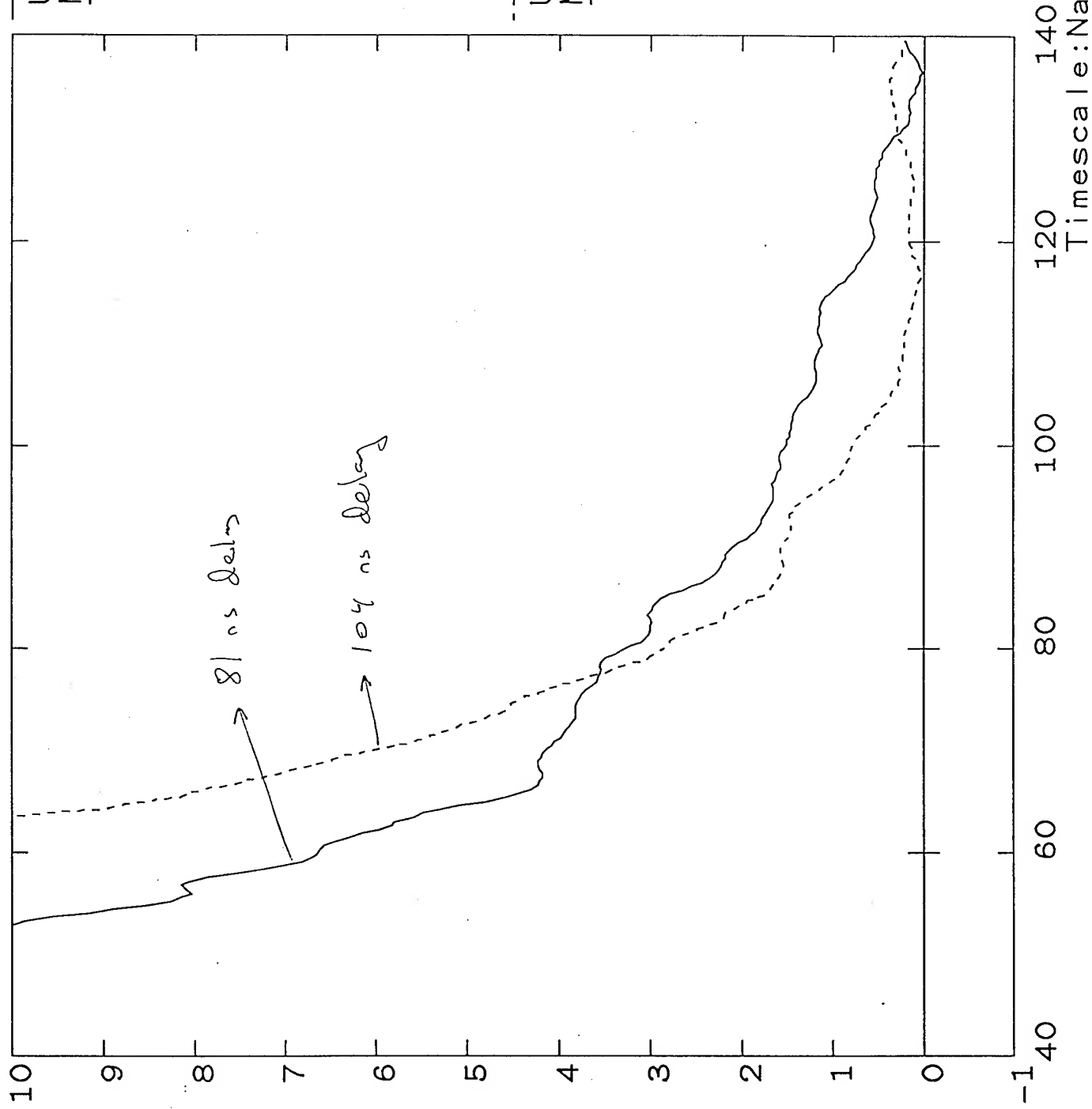
----- z6103 Ohms
Units: 1.00E+00
Max: 1.00E+01
Ts(ns): 0.00E+00

Fig 8

Shot 6077

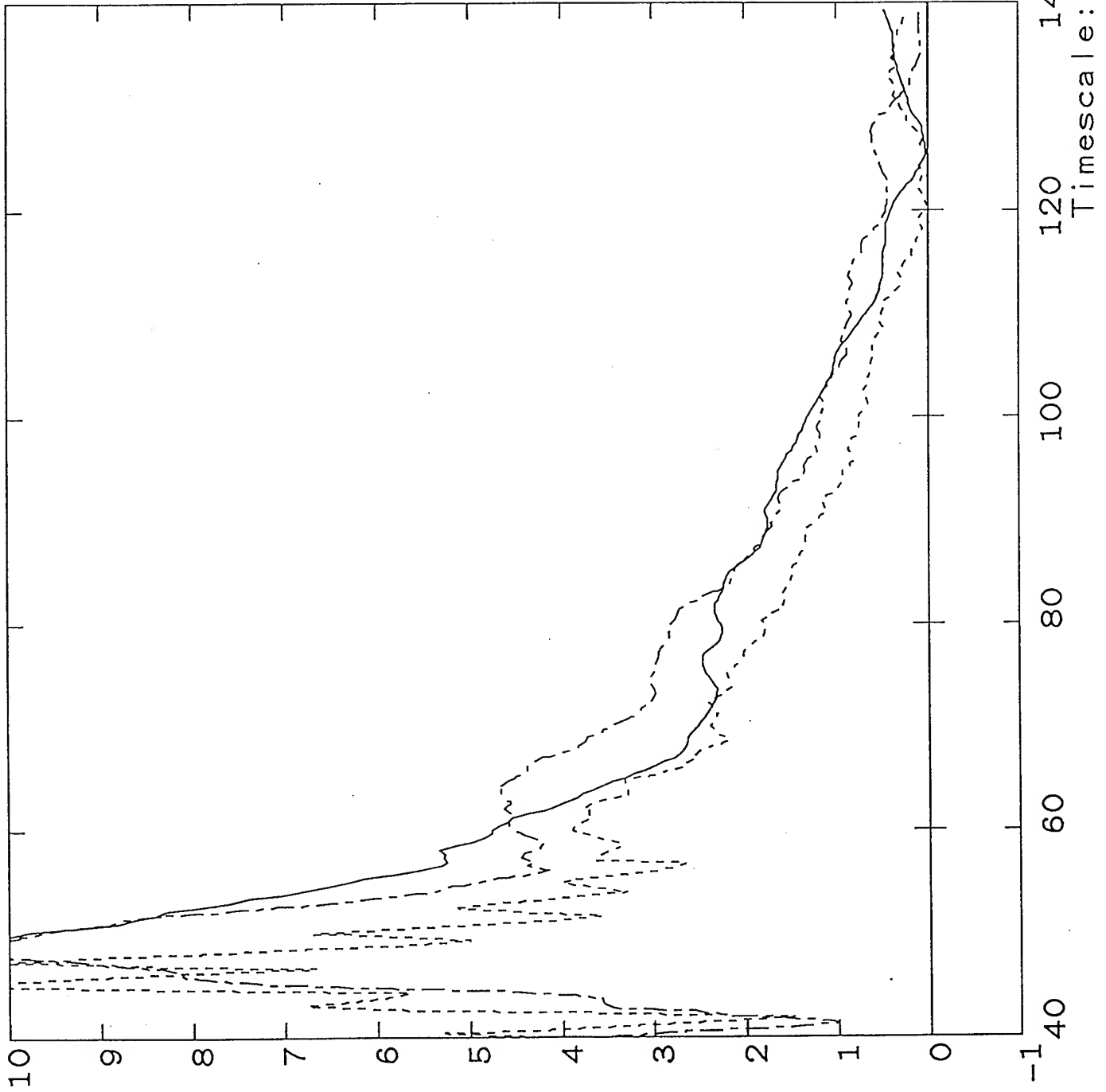
----- z6103 Ohms
Units: 1.00E+00
Max: 1.00E+01
Ts(ns): 0.00E+00

----- z6110 Ohms
Units: 1.00E+00
Max: 1.00E+01
Ts(ns): 0.00E+00



Shot 6075

Fig 9



____ zs6078 Ohms
Units: 1.00E+00
Max: 1.00E+01
Ts(ns): 4.00E+00

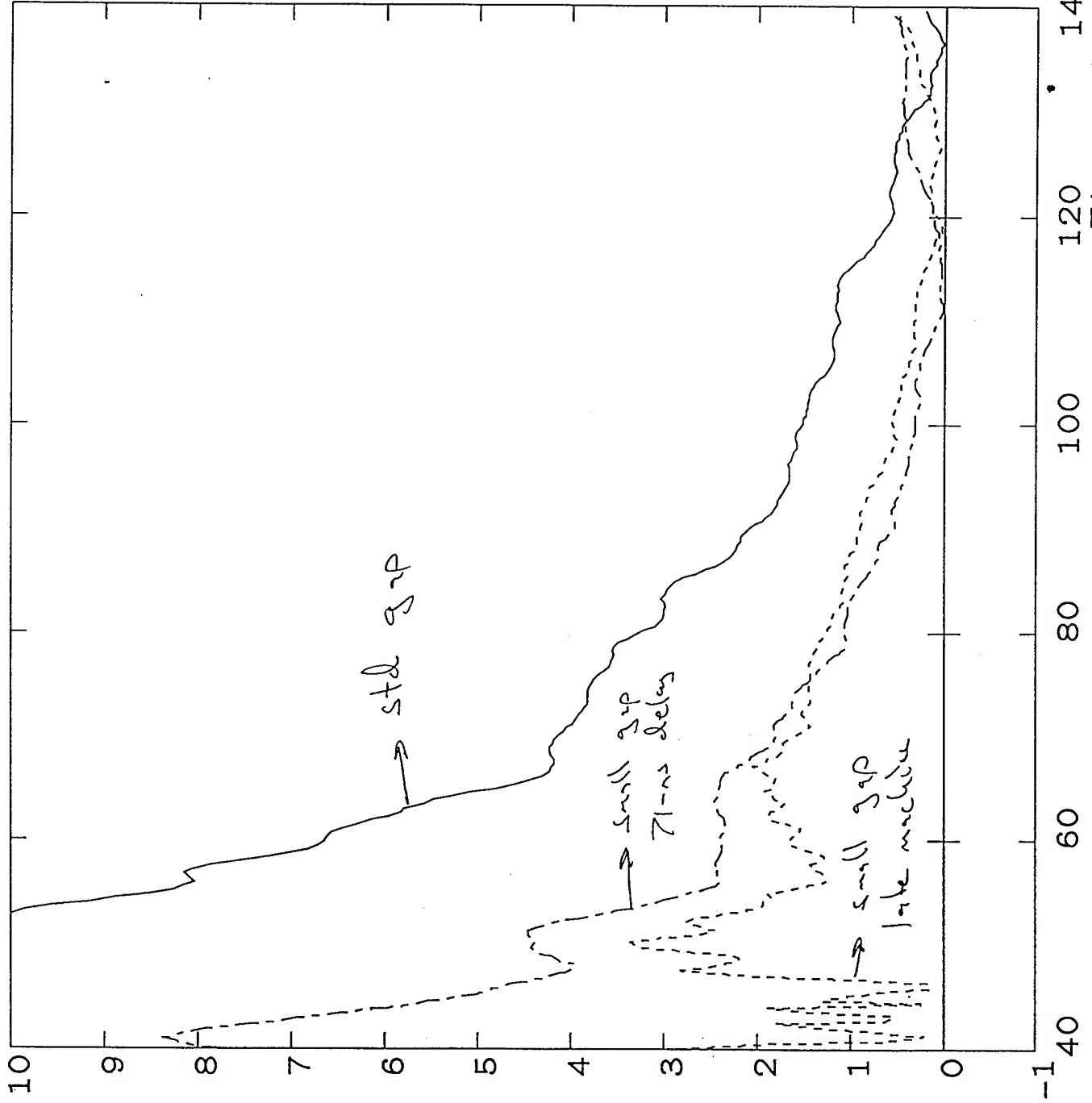
----- zs Ohms
Units: 1.00E+00
Max: 1.00E+01
Ts(ns): -5.00E+00

----- z6101 Ohms
Units: 1.00E+00
Max: 1.00E+01
Ts(ns): 0.00E+00

std corrections
7.5-ns JIP
72 ns delay

Shot 6077

Fig 10



----- z6103 Ohms
Units: 1.00E+00
Max: 1.00E+01
Ts(ns): 0.00E+00

----- z6076 Ohms
Units: 1.00E+00
Max: 1.00E+01
Ts(ns): 0.00E+00

----- zS Ohms
Units: 1.00E+00
Max: 1.00E+01
Ts(ns): -1.00E+01

Timescale: Nanoseconds

Fig 11
generic impedance traces

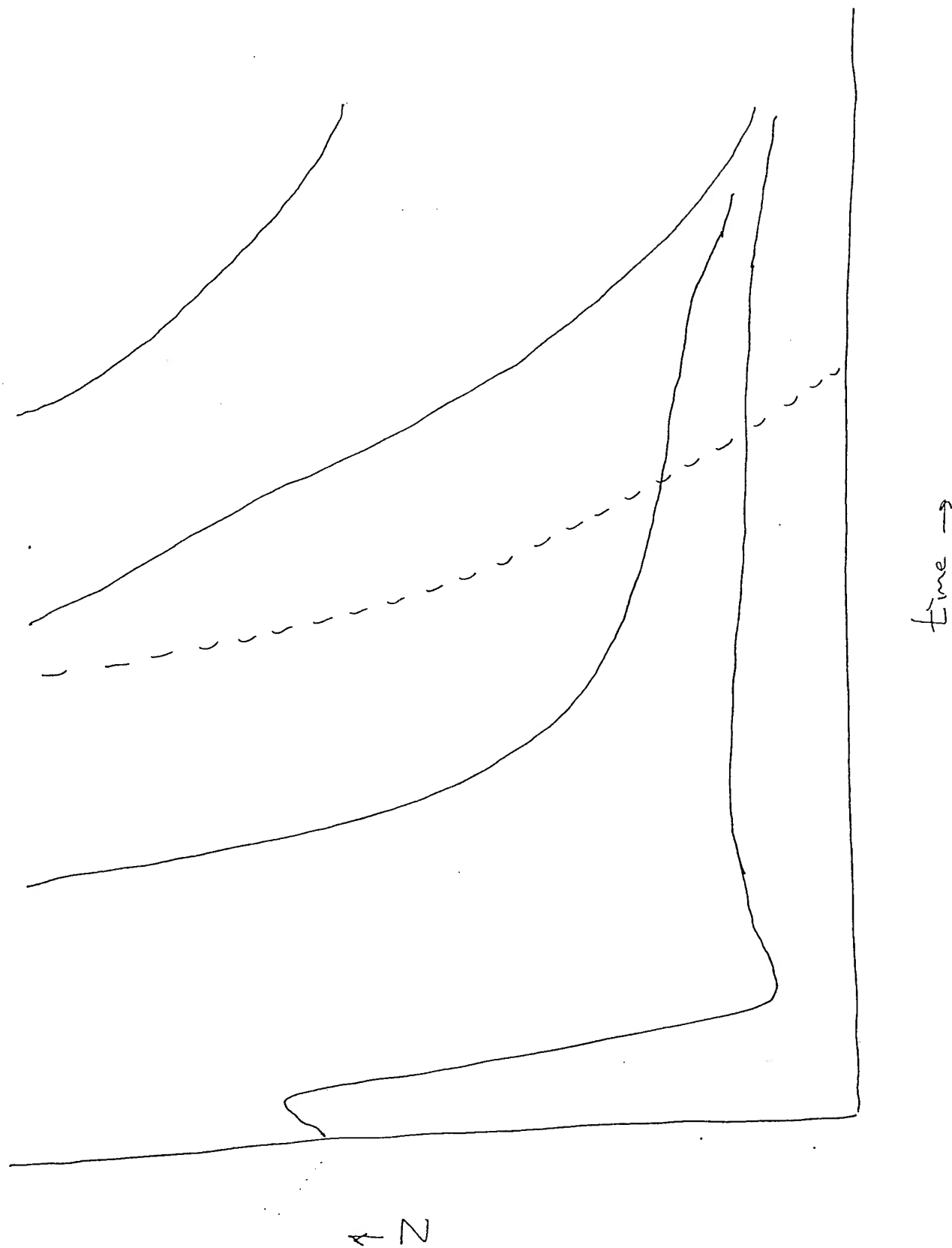
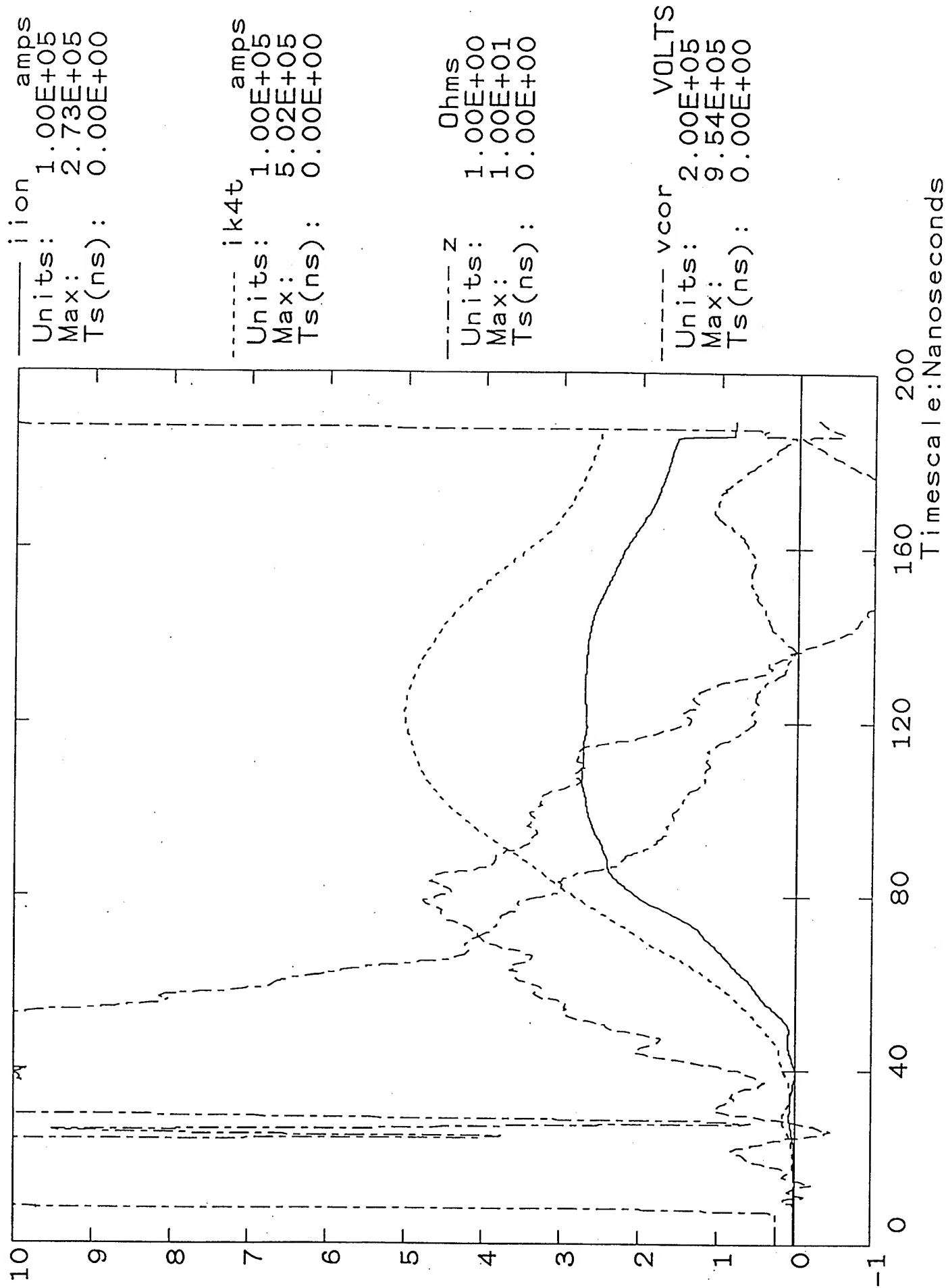


Fig 12

Shot 6103



EMFAPS run beginning 6/94

Beam diagnostics summary for shot 6101

Gas, pressure: 1.5 Acm

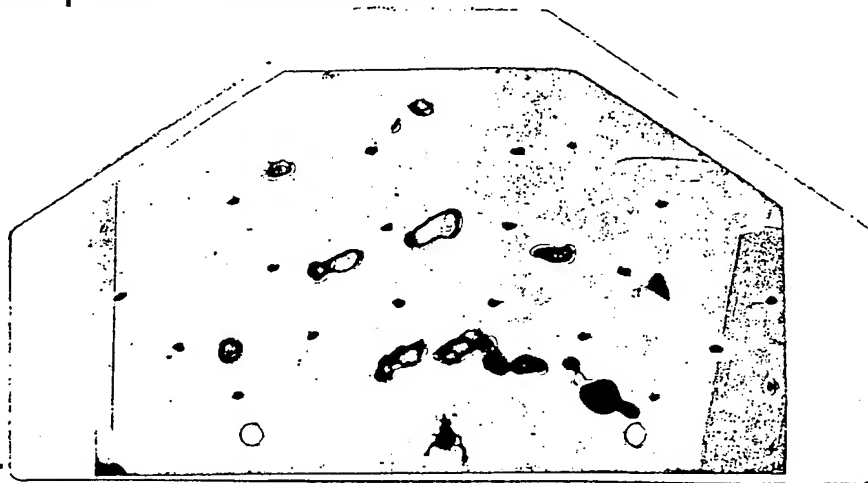
Rutherford scattering

Trace name	PW1			
PIN type	SrL			
Anode - sc foil dist	7			
Sc foil, tr or refl	thick Al			
Sc foil - PIN dist	18			
PIN filter	2.5 μ Ti			
Addl apertures	—			

Comments:

cleared PW before shot by swirling in ethanol, in addition to scrubbing

Witness plate/shadowbox:

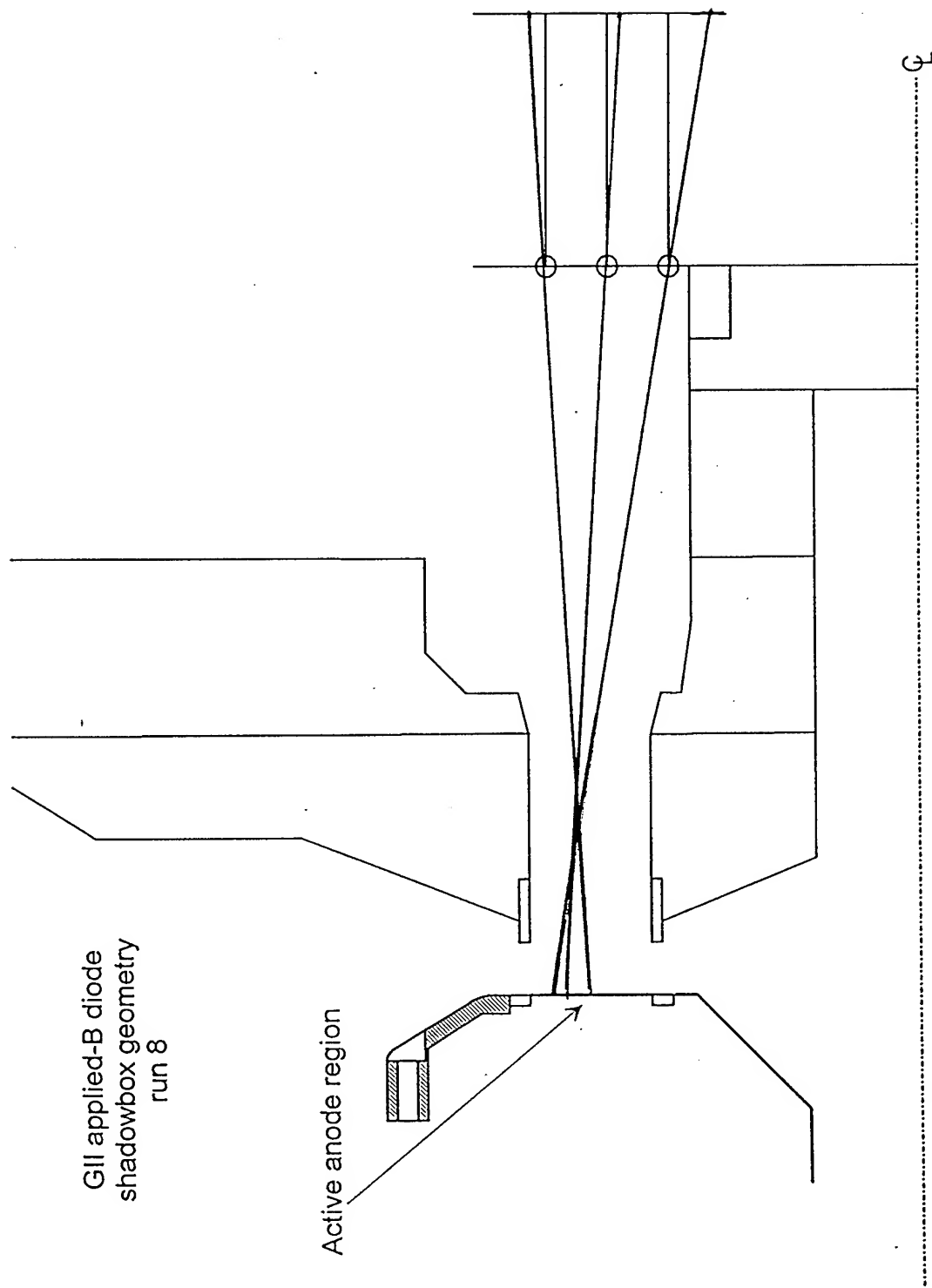


Other:

Fig 13

Fig 134

6101



EMFAPS run beginning 6/94

Beam diagnostics summary for shot 6108

Gas, pressure: 1 T air

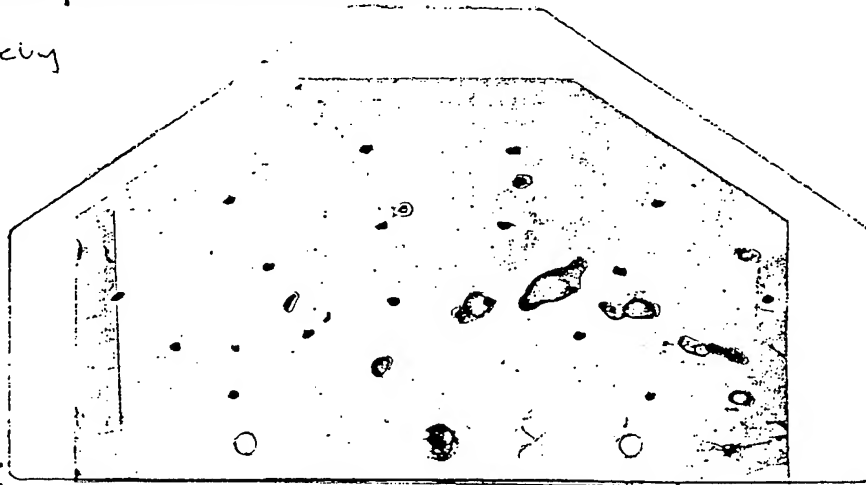
Rutherford scattering

Trace name	PIN1			
PIN type	SRL			
Anode - sc foil dist	7			
Sc foil, tr or refl	thick Al			
Sc foil - PIN dist	18			
PIN filter	2.5 μ Ti			
Addl apertures	/			

Comments:

Witness plate/shadowbox:

Film definitely
aligned



??

Other:

Size mode due to 6107

i.e., 1.5-2 μ m dr, centered in mode region,
irreg

EMFAPS run beginning 6/94

Beam diagnostics summary for shot 6098

Gas, pressure: LT air

Rutherford scattering None

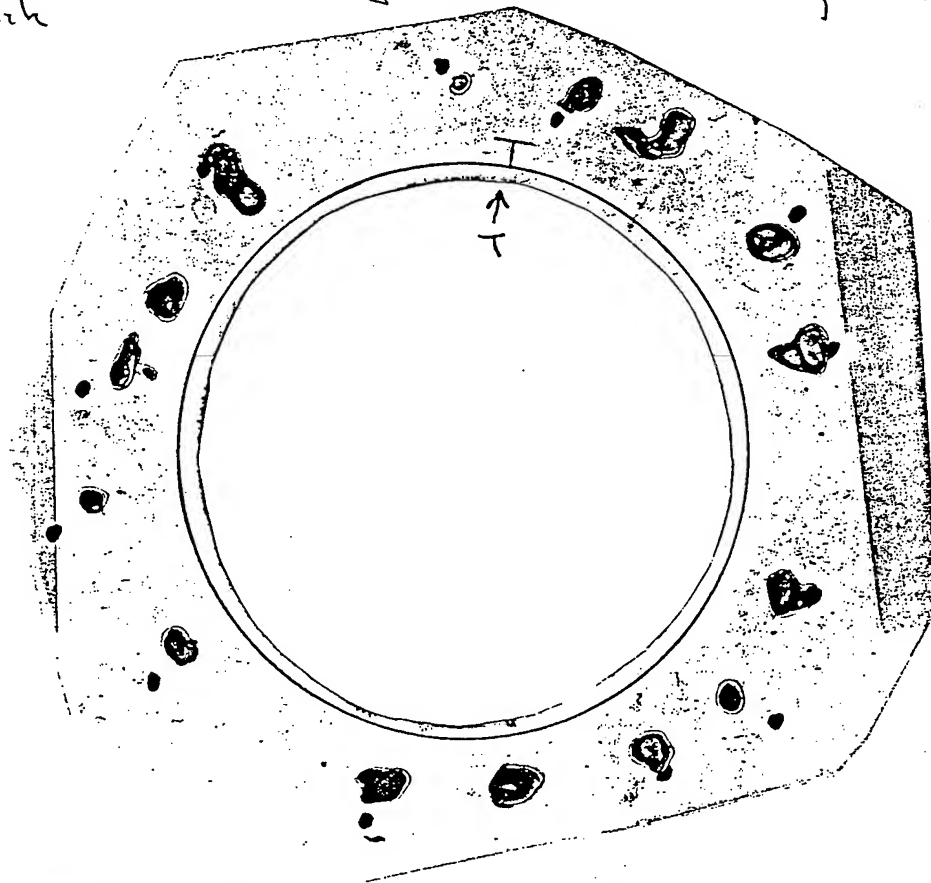
Trace name				
PIN type				
Anode - sc foil dist				
Sc foil, tr or refl				
Sc foil - PIN dist				
PIN filter				
Addl apertures				

Comments:

Witness plate/shadowbox:

use $\frac{1}{16}$ " ss plate at kinfol location. Drill
15 holes - at each sector, 3 on 4" diam,
1 on $+5\text{mm } \Delta r$, 1 at $-5\text{mm } \Delta r$. Locate viewgraph
paper on flat mounting surface normally used for
aperture plate

Other:

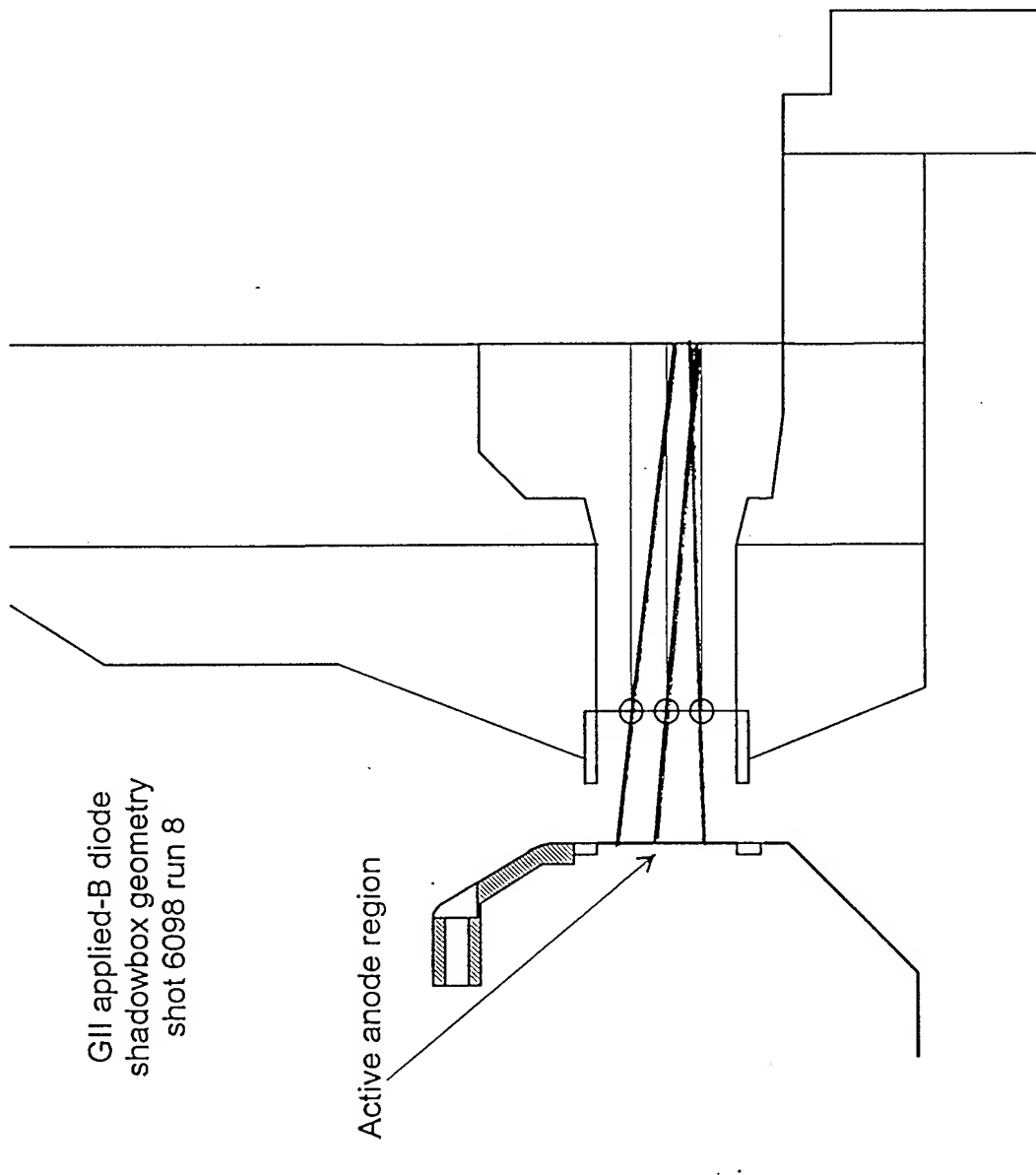


92 in.
orientation \pm
5-10°

Fig 18

GII applied-B diode
shadowbox geometry
shot 6098 run 8

Active anode region



9

PULSED POWER PHYSICS TECHNOTE 95-03

TITLE: ANALYSIS OF APPLIED-B DIODE RUN 7

Author: D. Hinshelwood

Date: February 15, 1995

Abstract: This is one of a series of teknotes, composing a first cut at analysis of the reams of applied-B diode (MID) data we have acquired so far. The purpose here is to get the data out on the table and to identify the best shots, obvious trends, and any unexpected results.

The impedance behavior shows a consistent dependence on pulser delay and foil thickness, as current onset begins earlier with thinner foils and longer delays. Current onset begins earlier, in general, than on shots in run 5, which had roughly comparable fields. This earlier onset leads to flatter impedance histories. Shots at the longest delays exhibit impedance behavior that is suggestive of a PFD. I speculate that this difference from run 5 results from the different foil and pulser conditions.

In spite of the improved impedance history, the shots on run 7 have lower normalized ion energies, because they operate at lower ion efficiencies. In this regard they are similar to the shots in run 6.

Little effect of the magnetic field shape or magnitude is seen, over the range of fields used in this run.

Rutherford scattering indicates that the beam has a proton fraction of at least, and probably significantly greater than, 50 percent.

Based on the results so far, I believe that we can control the trajectory and angular momentum of the ion beam by tuning the fields. Obtaining both the desired impedance behavior and high ion efficiency remains a problem. The anode source is critical to resolving this problem. In order for the generator to tolerate the higher impedance required for stable, reasonably efficient behavior, we need to have a rapid current onset. The trick will be to optimize the source, to provide the rapid onsets seen in this run, without the subsequent, low-impedance behavior seen here. After looking in more detail at the results of this run, I am more eager to study the source further on the bench.

INTRODUCTION

This is one of a series of teknotes, composing a first cut at analysis of the reams of applied-B diode (MID) data we have acquired so far. The purpose here is to get the data out on the table and to identify the best shots, obvious trends, and any unexpected results. No attempt will be made to draw final conclusions yet. To date there have been ten MID runs. The first three runs used wax-filled-groove, hereafter referred to as passive, anodes. Run 4 was our only attempt with POS-driven, EMFAPS anodes. Run 5 was the first run using a pulser to drive the EMFAPS anodes. On run 6, EMFAPS anodes were used without the pulser. In this case the early electron loss current returning through the anode foil is used to form the anode plasma. These will be referred to as limiter-EMFAPS anodes, although a physical limiter was rarely used. Runs 7-10 used pulser-EMFAPS anodes. Results from runs 5, 6, and 8 have already been presented in TN's 95-01, 95-02, and 94-16.

MASTER SPREADSHEET

The enclosed spreadsheet lists all shots of this run other than short-circuit shots. This is part of an evolving master spreadsheet that will summarize all of our MID data. The first page gives the basic shot parameters. The column "voc2i" on the RAW sheet refers to the integral of VOC^2 . This quantity is now used to normalize energies. The column "e2(kJ)" refers to the integral of $VCOR \times IK2T$, and is a weighted measure of the current emitted from the inner cathode.

The second sheet presents some of the shot parameters in more useful form. (Obvious dud shots are not included on this sheet.) The second column gives the closest A-K gap, i.e., the distance between the cathode tips and the anode.

The values " $e2/e$ " " $e4/e$ ", and " ei/e " are the ratios of the inner-cathode, outer cathode, and ion energies to the total energy (these add up to unity). The values " $e19$ " and " $ei19$ " give the total and ion energies, normalized to shot 6019 by assuming that the energies scale as voc2i. Shot 6019 had a typical open-circuit voltage for a 32 kV Marx charge, so the values in columns 17 and 18 might be expected if the shots were repeated at 32 kV. (A 26 kV Marx charge was used for this run.)

RUN SEVEN OVERVIEW

A Marx charge of 26 kV was used on the first ten shots of this run. After that, the Marx charge was increased to 32 kV. The standard Marx charge for other experiments is 36 kV. As in run 6, the oil-switch gap was not optimized for the 26 kV charge, so the open-circuit voltages on this run were similar to those in run 6 and lower than those in run 5.

This run comprised 33 shots. Three shots were taken without the applied magnetic fields and will be considered in a future note. The field shapes used in this run are compared in Fig. 1 with those used in run 5. (It is not immediately useful to compare this run with run

6 because of the uncertain field geometry in the latter.) Again, IIC, IOC, IIA, and IOA refer to the charging voltages on the capacitor banks used to drive the four coils. For almost all shots in these runs, the ratio IIC/IOC was kept constant. Therefore, the field shape has two degrees of freedom, and may be represented on a graph. In Fig. 1 the field shapes are parameterized by the ratios IIA/IOC and IOA/IOC. Both runs are seen to inhabit approximately the same region in field-parameter space. (The rightmost point on the run 7 graph represents three shots where the ratio IIC/IOC was increased by 50 percent and so cannot be compared directly with the other points.)

The conditions of this run differed in several ways from those on run 5. The coil-set separation was reduced by 3 mm. The change in coil-set distance makes comparison of fields difficult until mapping is performed. The use of shorter cathode tips resulted in a 1-mm decrease in the net gap. A more powerful pulser was used, increasing the foil current from 20-30 kA on run 5 to 35-40 kA on this run. A larger, nominal active anode area was also used. Photographs of the foil breakdown indicate that the anode radial width increased from 1.5 to 1.8 cm.

Thicker foils were used on this run, and they were coated under better vacuum conditions which resulted in lower foil resistivity. Also, a different epoxy anode casting technique was used, which gave foils that appeared smoother than those in run 5. The net effect of all of these changes is unknown at present.

On most of the shots in this run, the beam was diagnosed with either witness plates and the shadowbox, or with Rutherford scattering. The scattering results have already been presented in TN 94-19 and will only be summarized here.

COMPARISON WITH RUNS 5 AND 6

The 26-kV Marx charge shots in this run are compared with run 5 results in Figs 2-4. Shot 5985 in Fig. 2 had a very short pulser delay and may be considered to be a no-pulser shot. The impedance history is compared with those from no-pulser and short-delay shots from run 5. The traces have been offset in time to align the open-circuit voltages. In addition to the differences mentioned above, the shots from run 5 had higher open-circuit voltages and higher absolute fields than shot 5985. The field shapes are similar, with shot-to-shot variations in individual field ratios of 10-20 percent (see the spreadsheets for these shots). Because of all these differences, we can't make too much of this comparison. However, the general shapes of the impedance histories agree. The differences that are seen are consistent with the larger anode area and slightly smaller gap on this run.

Shot 5985 is compared with shot 5895 from run 6 in Fig. 2a. Again, we don't know the field shape in run 6 yet, but the two shots do show the same impedance behavior.

Figures 3 and 4 show impedance histories for roughly comparable shots with 50 and 90 ns pulser delays. As the delay increases, a qualitative difference in the impedance behavior emerges. In run 7, the impedance history shows a plateau, and on one shot at the longer

delay, the behavior begins to resemble that of a plasma-filled diode. I believe that the major difference between these two runs results from differences in operation of the anode source. For some reason, more plasma and/or neutrals are produced under the conditions of run 7.

TYPICAL ELECTRICAL DATA

Electrical data from shot 5992 are shown in Fig. 5. (See TN's 95-01 and 95-02 for more explanation of the terminology used here.) This shot had a normalized ion energy of 14 kJ. The energy was partitioned as 50% ions, 14% inner cathode current, and 36 % outer cathode current. Both the normalized ion energy and the energy partition are fairly representative of this run. While it does not have the highest energy, this shot is attractive because both the voltage and ion current are reasonably flat for almost 40 ns. If this shot could be repeated at 36 kV Marx charge, we would have almost 300 kA of ions at about 1 MV. These parameters are adequate for transport research. This shot, however, did have a late flashover. Shot 6010, with similar fields but a shorter delay, had an earlier flash. (Shot 6014, with the same fields but a longer delay, did not exhibit the level voltage seen on shot 5992.) Therefore, it may not be possible to repeat this shot at a higher Marx charge.

This shot exhibits several general features of shots on this run. Initially, the diode operates with high ion efficiency. Then, after about 40 ns, the ion current levels off while the electron current keeps rising. This additional electron current loads down the diode, reducing the voltage. Individual current traces are shown in Fig. 6. When the ion current levels off, a sharp increase in the inner cathode current is seen. Nonetheless, most of the electron loss seems to originate from the outer cathode.

Figure 7 shows a typical comparison of calculated and observed x-ray signals. Reasonable agreement is generally seen, but the calculated signal tends to peak later in time. This could mean that we are overestimating the electron current, or fewer electrons are striking metal late in time. On most shots, the individual IK3 loops agree within 20 percent. Good agreement between IK4T, IOUT, and ISHT is observed, indicating that negligible electron emission occurs outside the outer cathode.

Figure 8 shows impedance histories for four shots at 26-kV Marx charge. These shots have the same field configuration but different foil thicknesses and delays. The impedance scales as expected, as shots with thinner foils and longer delays show a faster onset. Traces for four more shots are shown in Fig. 9. Two of these shots had long delays, and the other two are believed to have had long delays (the scope signal was lost). As with the longer-delay shots in Fig. 8, these show a very rapid impedance fall, followed by a long plateau. This behavior may indicate a partial plasma/neutral fill. Figure 10 shows impedance traces for five shots at 36-kV Marx charge. These also had the same fields, with different foils and delays. The scaling seen in Fig. 8 is also seen here.

Shots with similar foils and delays but different fields are compared in Fig. 11. Shot 6020 had a 10 percent higher IIA and, more importantly, a 50 percent higher IOA. Similar impedance behavior is observed, although somewhat faster current onset is seen on the shot with the higher field. My first guess here is that, for the field shapes used in this run, the diode impedance behavior is not strongly affected by the field shape. I would tend to attribute the small difference between these two shots to irreproducibility.

Another pair of shots is compared in Fig. 12. These shots also had similar foils and delays but different fields. While all four fields differed on these shots, the major change is that on shot 6012 the inner fields were boosted relative to the outer fields. Again, similar impedance behavior is observed.

This run has only one pair of shots that differ only in field magnitude. Shots 6004 and 6015 had the same foils and delays, and almost the same field shapes. The field amplitude, however, was 50 percent higher on shot 6015. Impedance histories and x-ray signals for these shots are compared in Fig. 13. At the higher field, the current onset begins later but a longer pulse is obtained, although the difference is not dramatic. This suggests that the combination of a long pulser delay and high field might be interesting.

Two shots on this run were taken with a copper-tape insert located 2 mm behind the anode surface to oppose flux penetration into the anode on the shot timescale. The closest comparison involving these shots is shown in Fig. 14. The difference in impedance behavior can be attributed to the different delay used, and no strong effect of the excluder is seen. It may be that the 2-mm recess distance of the excluder is too large.

Impedance histories for five no-pulser shots are compared in Fig. 15. Shot 6006 had a similar field shape but lower amplitude than shot 5997. Also, on shot 6006 a thin shim disk was placed on axis as a kind of limiter. Shots 6003, 6005, and 6007 had a solid aluminum plug on axis, which might be expected to alter the field, and fields close to 6006, except for shot 6005 which had a reduced IOC. All of these shots have reasonably similar impedance behaviors, and no dramatic trend leaps out of these data. (The limiter would be expected to have little effect based on the results of run 6.) This is further sign of the relative independence of the impedance behavior on the field.

Electrical data from shot 6017 are shown in Fig. 16. This shot has been described as one of our best, and it does exhibit a high ion current, ion efficiency, and normalized ion energy. However, because of the voltage collapse, I am not sure that other shots, such as 5992, are not more interesting for transport research.

ENERGY PARTITION

Analysis of these runs is made difficult by the sheer volume of data: metrics are needed that allow the data to be compressed. The impedance history, which is no principle not affected by the open-circuit voltage waveform, is one such metric. Another is to use the energy partition between ion, inner-cathode, and outer-cathode current. Energy partition

has the advantage of giving information on the ion production, which the impedance does not. For this run as a whole, the partition between ions, inner electrons, and outer electrons, has an average of (44:13:43). By comparison, the averages for runs 5 and 6 were (63:6:30) and (42:17:41), respectively. The average, normalized ion energies for runs 5, 6, and 7 are 14.6, 10.9, and 12.5 kJ.

Runs 6 and 7 are seen to have some features in common. Both show better-looking impedance behavior than run 5, but lower ion efficiency and normalized energy. The difference is that the improved impedance behavior on run 7 results from an earlier onset, while that on run 6 results from a slower collapse.

The average partition from run 7 is almost the same as that from run 6. In a practical sense, however, this is somewhat misleading. The no-pulser shots on run 6 had a later current onset, which would make scaling the results to higher Marx charges very difficult.

There is a wide variation in the energy partition among the shots of run 7, and it is difficult to make much sense of it. There is not an obvious correlation with field shape, as shots 5992 and 6020 have the same partitions. Likewise, shots 6004 and 6015, with significantly different field amplitudes, show the same ion efficiency, and while lower inner-cathode current is seen with the higher field, the difference is within the noise. The three shots 6011-6013, with higher inner fields, do show reduced inner-cathode current, but again, the difference is barely significant. Shots 5986-5991, with long delays and PFD-like behavior, have an average partition of (37:14:49), again not significantly different than the run average.

BEAM DIAGNOSTICS

Either the shadowbox/witness-plate combination, or Rutherford scattering, were used on most shots of this run. The shadowbox geometry and extrapolated trajectories for shot 5992 are shown in Fig. 17, and the image itself is shown in Fig. 18. This is a typical image for this run.

The ion beam is seen to have angular momentum, with the separatrix lying behind (toward the Marx) the anode emission surface at all radii. The beam is radially diverging by about 80 mrad, and appears to be bending in slightly more than out. The image implies a microdivergence of about 30-50 mrad. The ion current density appears to be strongly peaked at inner radii, with little ion current originating from locations near the outer cathode tip.

It has been suggested that the electron loss we see could actually be ions hitting the cathode tips, or hitting the b-dot loops and causing them to fail. The shadowbox data leads me to doubt that significant ion current flow to the outer cathode tip occurred on this run. It is possible that flow to the inner tip did occur. Since electron loss is dominated by the outer tip on these shots, ion flow to the inner cathode tips, or to the b-dot loops, cannot explain this loss. Bryan has suggested that electrons emitted from the

outer cathode can neutralize the ion beam and mask the ion current, and maybe we should think more about this.

The image from shot 6020, which had a 50 percent higher IOA, is shown in Fig. 19. The image here shows similar radial behavior, with perhaps a bit more outward motion to the beam. However, ions emitted at outer radii have negligible angular momentum, indicating that the separatrix had moved out to the emission surface at outer radii on this shot. This is consistent with the field change, and is further evidence of our ability to tune the angular momentum.

Witness plates for this run also show a diverging ion beam, but as stated in the last note, I don't want to make much of them, since they are so imprecise.

Rutherford scattering results are described in TN 94-19 and are only summarized here in Fig. 20 (see the note for a description of the spreadsheet). The relevant columns here are labeled 'Al*1.1' and 'Ta*1.1'. These are the ratios of the observed to calculated scattering signals, and thus can be interpreted as the proton fraction in the beam, and average to 50 percent, excluding shots 6003-6007, which show much lower fractions. (In TN94-19 I attributed these low fractions to the lack of a pulser, but that is contradicted by shot 5997. I would now attribute the low apparent fraction on these shots to a difference in trajectories resulting from the different fields used.)

Calculation of the scattering yield requires a knowledge of the ion trajectories. This is particularly true for the scattering arrangement used here, where the scattered portion of the beam is limited by three circular apertures, as indicated in Fig 17. The numbers in the spreadsheet reflect an assumption that the ion current density is higher at inner radii, but not by as much as the shadowbox data indicate. The shadowbox data imply that fewer ions will pass through the apertures than were assumed in the calculation. Therefore, the actual fraction of protons in the beam is probably higher the values on the spreadsheet. (The scattering arrangement used in run 8 was less trajectory-sensitive.)

SUMMARY

In this first cut at revisiting the MID data, I will attempt to answer four questions for each run:

(1) What are the key shots, in terms of performance, for each run?

Shot 6017, with one of the highest normalized ion energies, and shot 5992, with relatively flat voltage and ion current, are good examples. Shot 5986 shows the most PFD-like behavior and is interesting for that reason.

(2) Which field configurations should we concentrate on mapping out?

The configurations on shots 5992, 6012, and 6020 bound those used on most shots.

(3) What are the significant trends in the data?

The impedance behavior shows a consistent dependence on pulser delay and foil thickness, as current onset begins earlier with thinner foils and longer delays. Current onset begins earlier, in general, than on shots in run 5, which had roughly comparable fields. This earlier onset leads to flatter impedance histories. Shots at the longest delays exhibit impedance behavior that is suggestive of a PFD. I speculate that this difference from run 5 results from the different foil and pulser conditions. The flatter impedance histories on this run lead to better average energy coupling to the generator. The average normalized energy is 29 kJ on this run, as compared with 23 kJ on run 5. The earlier current onset also allows operation at increased Marx charge.

In spite of the improved impedance history, the shots on run 7 have lower normalized ion energies, because they operate at lower ion efficiencies. In this regard they are similar to the shots in run 6.

Little effect of the magnetic field shape or magnitude is seen, over the range of fields used in this run.

As in run 6, the ion current density is peaked at the inside, and these ions are inward-bending. In this run, ions emitted from the outer radii bend outward. Since no shadowbox images were seen from ions emitted at the outer radii in run 6 (the images in general were weaker then, so this may be a threshold effect), I don't know what their trajectories were. Unlike on run 6, the beam is seen to have angular momentum, and this momentum can be tuned by adjusting the fields.

Rutherford scattering indicates that the beam has a proton fraction of at least, and probably significantly greater than, 50 percent.

(4) What are the most puzzling features to these data?

Certainly the most disturbing feature is the rather abrupt increase in electron loss that occurs midway into the pulse.

Another puzzling feature is the divergent ion trajectories, with outer ions bending outward.

We might expect to see more effect of the field shape and magnitude, but without knowing the fields (and V_{crits}), one can't say for sure.

CONCLUSIONS

Based on the results so far, I believe that we can control the trajectory and angular momentum of the ion beam by tuning the fields. Obtaining both the desired impedance behavior and high ion efficiency remains a problem. The anode source is critical to

resolving this problem. In order for the generator to tolerate the higher impedance required for stable, reasonably efficient behavior, we need to have a rapid current onset. The trick will be to optimize the source, to provide the rapid onsets seen in this run, without the subsequent, low-impedance behavior seen here.

After looking in more detail at the results of this run, I am more eager to study the source further on the bench. I had become doubtful about the utility of interferometry because of the high density gradients near the anode. However, the results of this run suggest that there may be plasma and/or neutrals out in the gap during the time of the shot. The SRL interferometer will be very useful in diagnosing this.

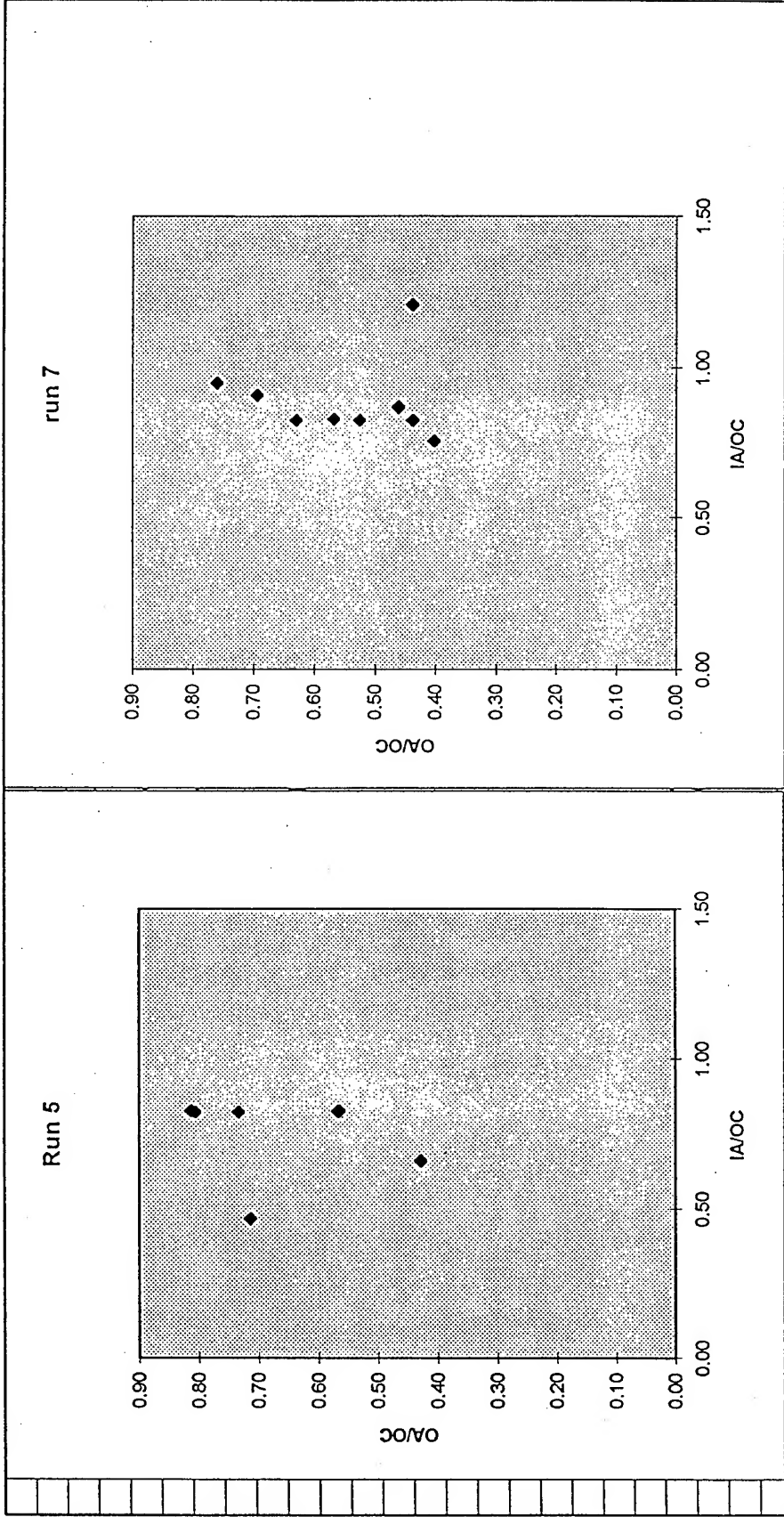
Another reason for source study is to obtain (and know that we have) reproducible source operation. By keeping the source constant from shot to shot, we will have an easier time investigating the effects of the magnetic field configuration.

Finally, as usual, field mapping will be necessary to interpret fully the results of this run.

shot	gap	tips	IIA	IOA	IIc	IOC	W-m	eff th	ins	lf	delay, tz=10	voc2l	el(ki)	e2(ki)	e(k)	Vpp	lipp	comnts
5982	11	4	0.00	0.00	0.00	0.00	500	100 N					7.0	0.7	13.7			first shot of run 7 no fields
5983	11	4	0.00	0.00	0.00	0.00	250	72 N					5.6	2.6	12.6			no fields
5984	11	4	1.82	1.46	1.52	1.92	250	24 N			43	20	1.862	7.4	1.3	13.9		
5985	11	4	1.82	1.46	1.52	1.92	1000	280 N			6	28	1.509	6.6	2.1	11.3		
5986	11	4	1.82	1.46	1.52	1.92	500	250 N			76	0	1.066	3.5	0.9	8.7		
5987	11	4	1.82	1.46	1.52	1.92	1000	500 N			74	8	1.445	2.3	1.5	10.7		some el dam on outer anode
5988	11	4	2.48	1.32	2.28	2.86	1000	240 N			?	8	1.261	3.1	1.5	10.8		lost HP signals
5989	11	4	2.98	1.58	2.74	3.43	1000	150 N			?	11	0.978	4.7	1.2	8.5		lost HP signals
5990	11	4	3.28	1.74	3.01	3.77	1000	313 N			65	14	1.72	5.1	1.6	12.3		
5991	11	4	2.83	1.50	2.74	3.43	1000	250 N			67	8	1.633	4.9	2.1	13.5		
5992	11	4	3.48	1.85	3.37	4.22	500	200 N			40	19	3.569	12.7	3.4	25.0		first shot at 32 kV late flash
5993	11	4	3.12	1.66	3.29	4.12	1000	360 N			51		3.598	8.5	5.5	25.2		
5994	11	4	3.28	1.74	3.45	4.33	500	160 N			62		3.545	11.5	2.8	27.8		
5995	11	4	3.28	1.74	3.45	4.33	500	205 N			71		3.835	7.8	2.9	26.2		
5996	11	4	3.28	1.74	3.45	4.33	500	150 N			38		3.685	10.1	3.8	27.5		
5997	11	4	3.28	1.74	3.45	4.33	500	213 N			0		3.403	5.7	3.9	23.5		flash, no pulser
5998	11	4	3.28	1.74	3.45	4.33	100	25 N			50		3.281	9.0	3.8	24.9		
6003	11	4	2.36	1.62	2.28	2.85	500	215 N			0		2.86	7.8	3.9	20.8		no pulser, plug on axis, maybe no B fields
6004	11	4	2.36	1.62	2.28	2.85	500	160 N			32		3.541	8.8	3.3	21.1		
6005	11	4	2.36	1.62	2.28	2.85	500	200 N			0		3.21	10.3	4.2	20.4		lt flash, no pulser plug on axis
6006	11	4	2.59	1.78	2.28	2.85	500	160 N			0		2.69	5.4	2.6	19.9		lt flash, no pulser shim on axis
6007	11	4	2.59	1.78	2.28	2.85	500	211 N			0		3.18	10.4	2.2	19.8		lt flash, no pulser plug on axis
6010	11	4	3.48	1.85	3.37	4.22	500	182 N			25		2.693	10.6	2.5	20.7		flash
6011	11	4	3.83	1.39	3.7	3.17	200	72 N			42		2.493	12.3	1.6	21.8		flash
6012	11	4	3.83	1.39	3.7	3.17	1000	261 Y			63		2.871	8.2	1.9	21.3		ins 5 mm back
6013	11	4	3.83	1.39	3.7	3.17	500	268 N			49		2.37	10.3	1.4	19.9		flash
6014	11	4	3.48	1.85	3.37	4.22	500	263 Y			56	5	3.403	10.1	1.5	19.3		
6015	11	4	3.48	2.22	3.37	4.22	500	213 N			31	17	3.612	11.4	1.5	26.1		may have been pulser prefire during charge
6016	11	4	3.48	2.22	3.37	4.22	500	232 Y			55	5	3.395	12.6	3.5	21.3		
6017	11	4	3.48	2.66	3.37	4.22	500	300 N			42	11	3.496	14.9	2.5	25.7		
6018	11	4	0	0	0	0	1000	488 N					3.508	9.9	5.3	31.9		no fields
6019	11	4	3.48	2.66	3.37	4.22	200	83 N			46	5	3.876	16.3	2.3	30.9		
6020	11	4	3.83	2.93	3.37	4.22	500	232 N		37	45	13	3.759	14.3	3.7	27.4		

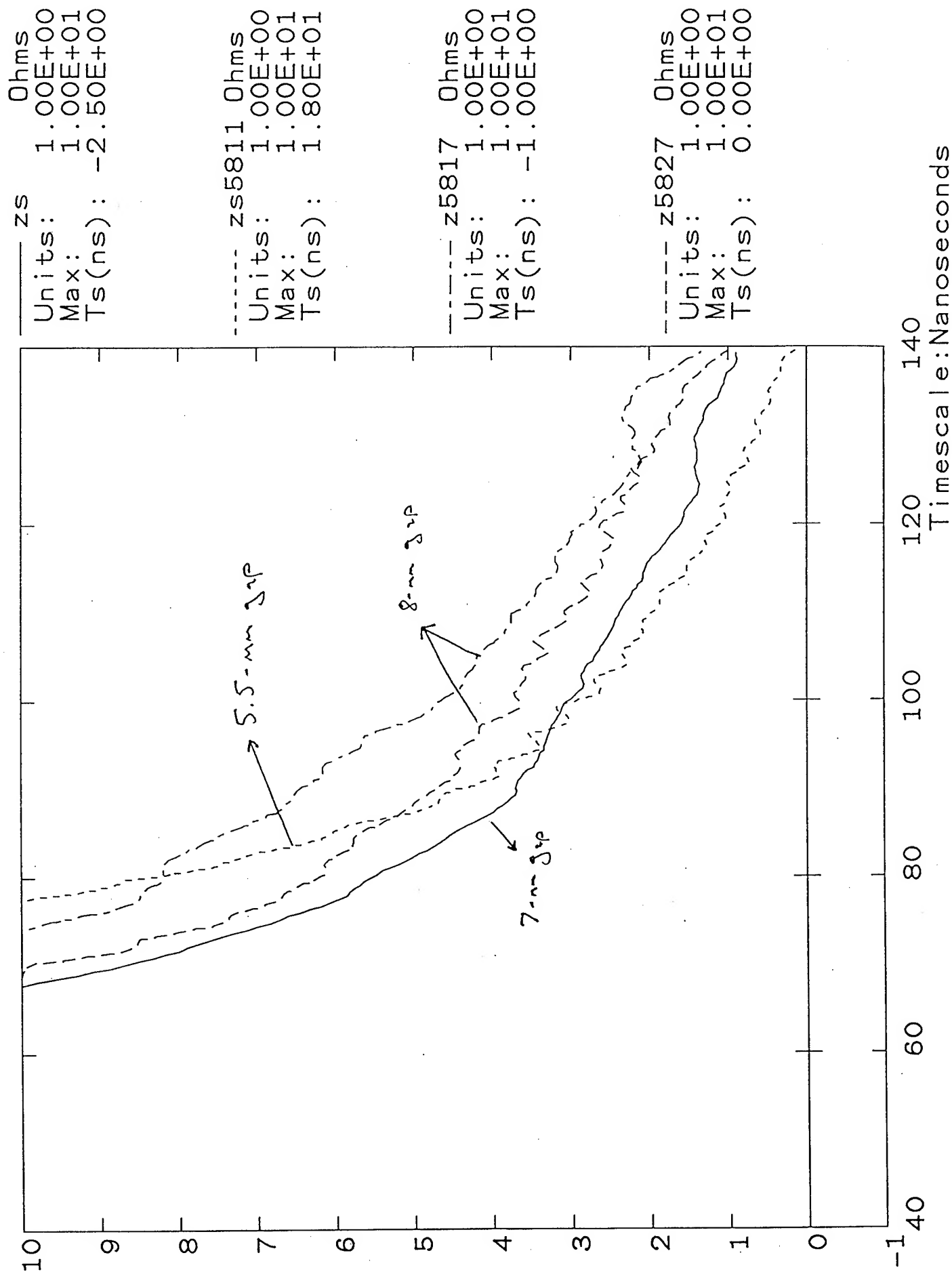
Fig 1

Fields



Shot 5985

Fig 2



Shot 5992

Fig 2a

____ Z5985 Ohms
Units: 1.00E+00
Max: 1.00E+01
Ts(ns): 2.50E+00

run 7

----- Z5895 Ohms
Units: 1.00E+00
Max: 1.00E+01
Ts(ns): 2.00E+00

run 6

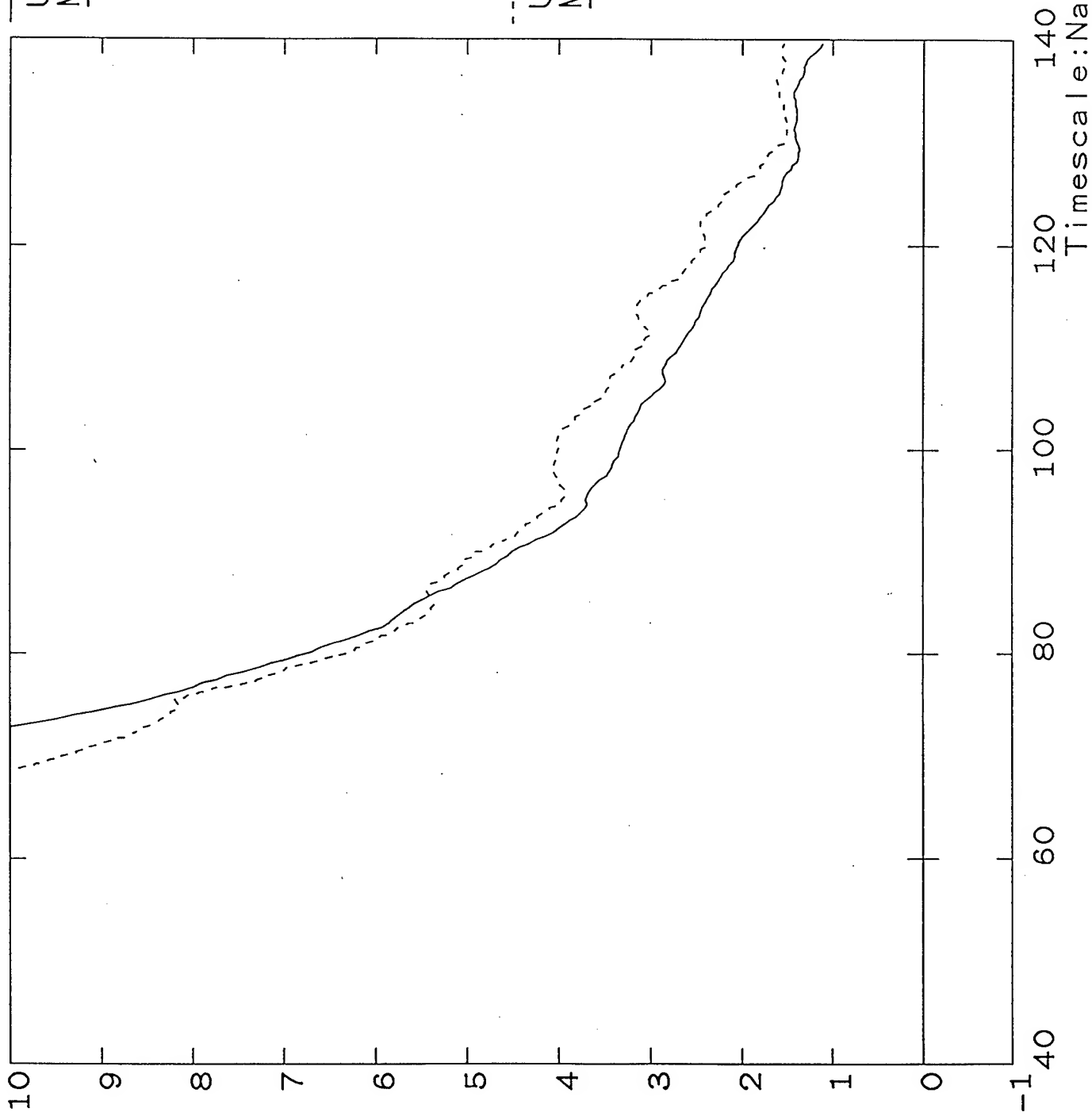
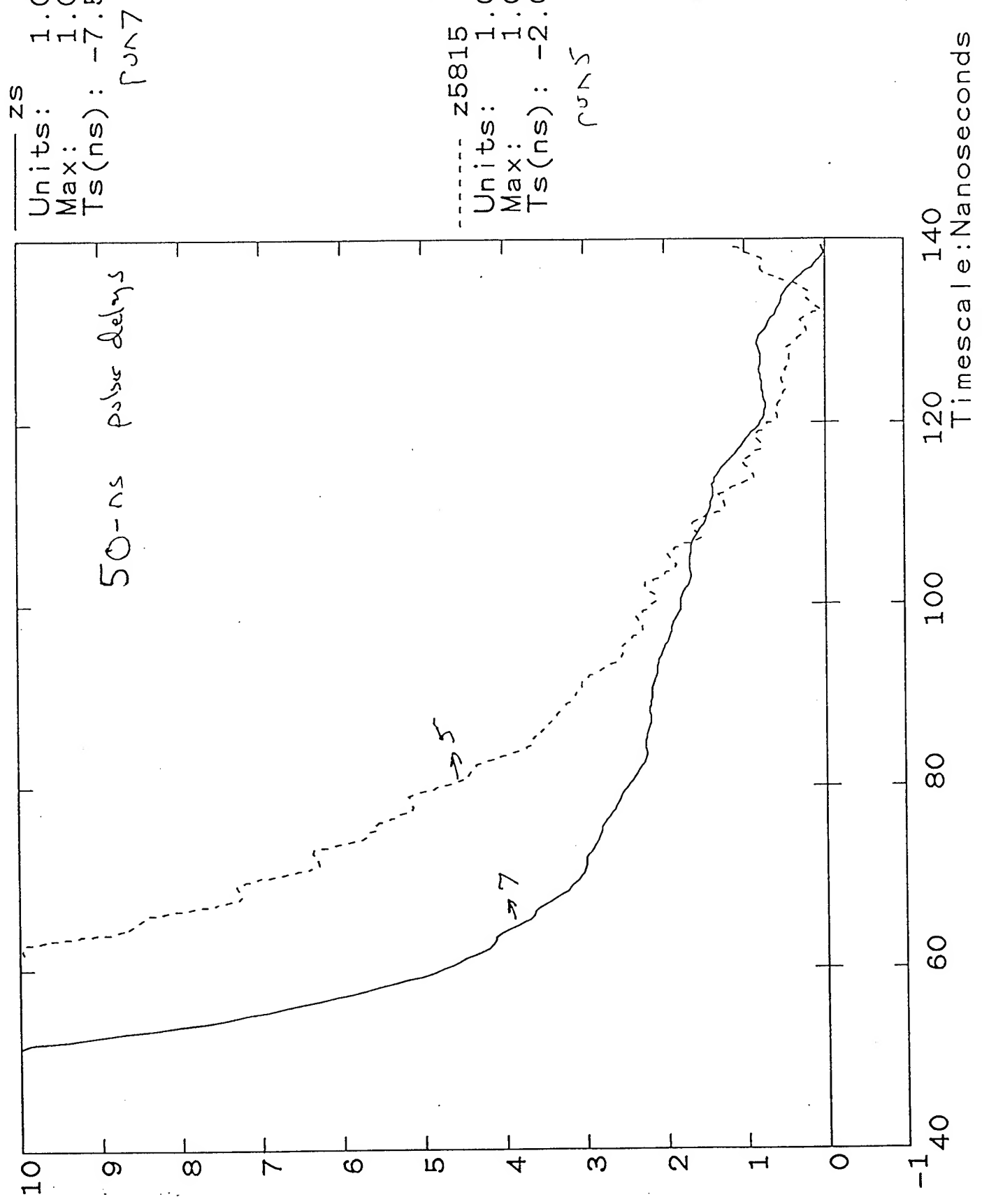


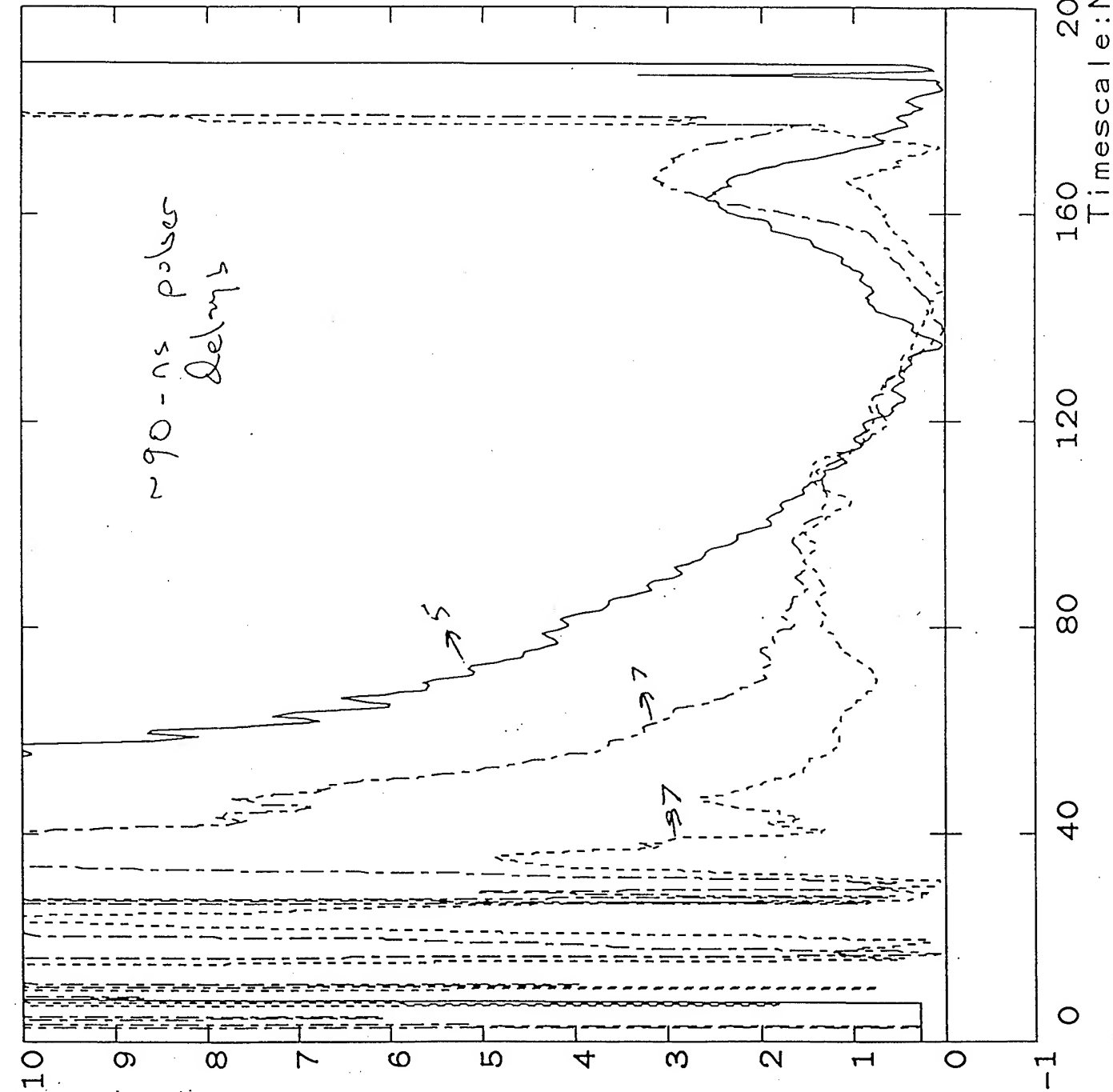
Fig 3

Shot 5984



Shot 5987

Fig 4



z5824 Ohms
Units: 1.00E+00
Max: 1.00E+01
Ts(ns): -1.00E+00
run 5

zs5986 Ohms
Units: 1.00E+00
Max: 1.00E+01
Ts(ns): -7.50E+00
run 7

zs Ohms
Units: 1.00E+00
Max: 1.00E+01
Ts(ns): -7.50E+00
run 7

Shot 5992

Fig 5

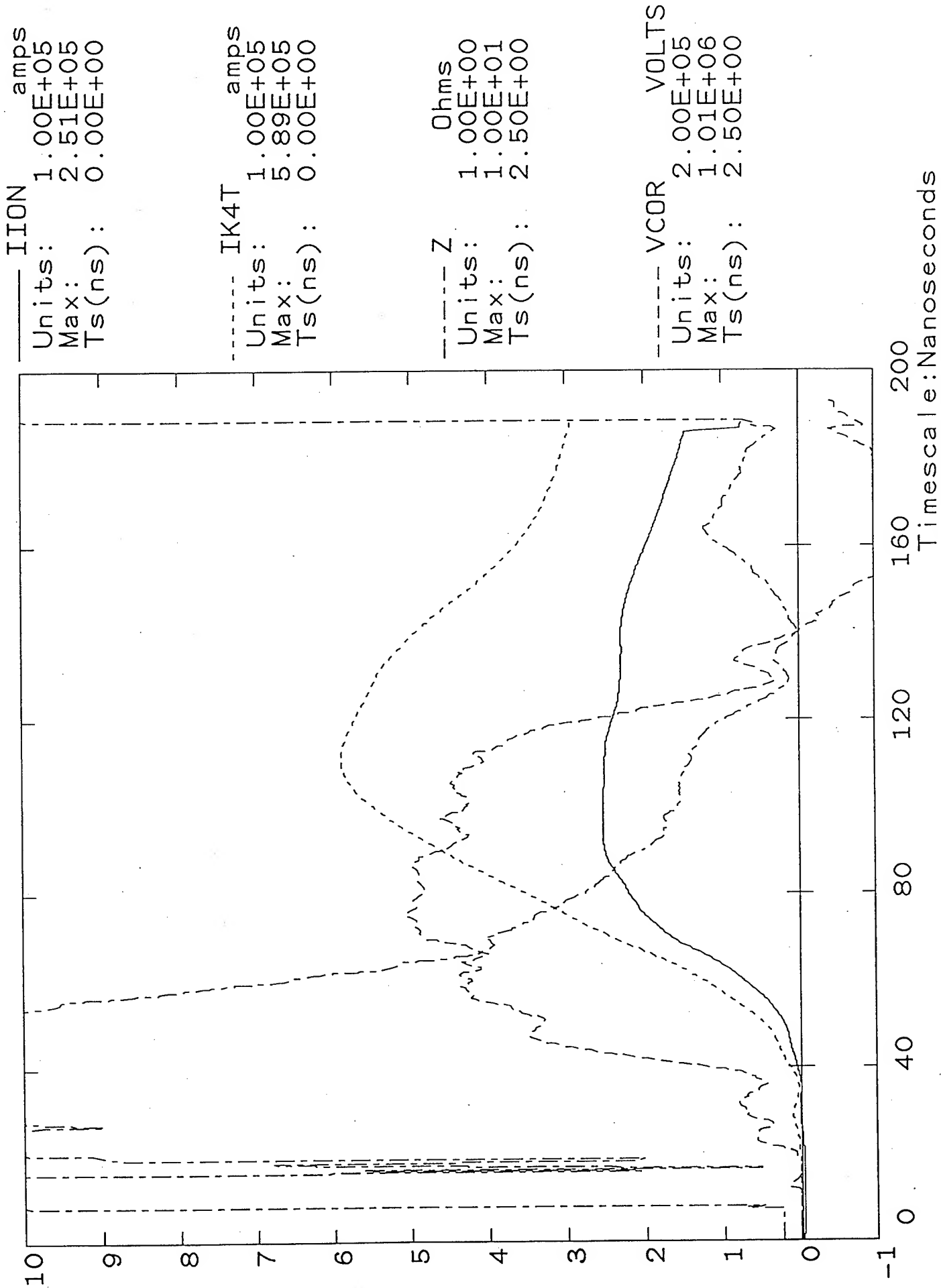


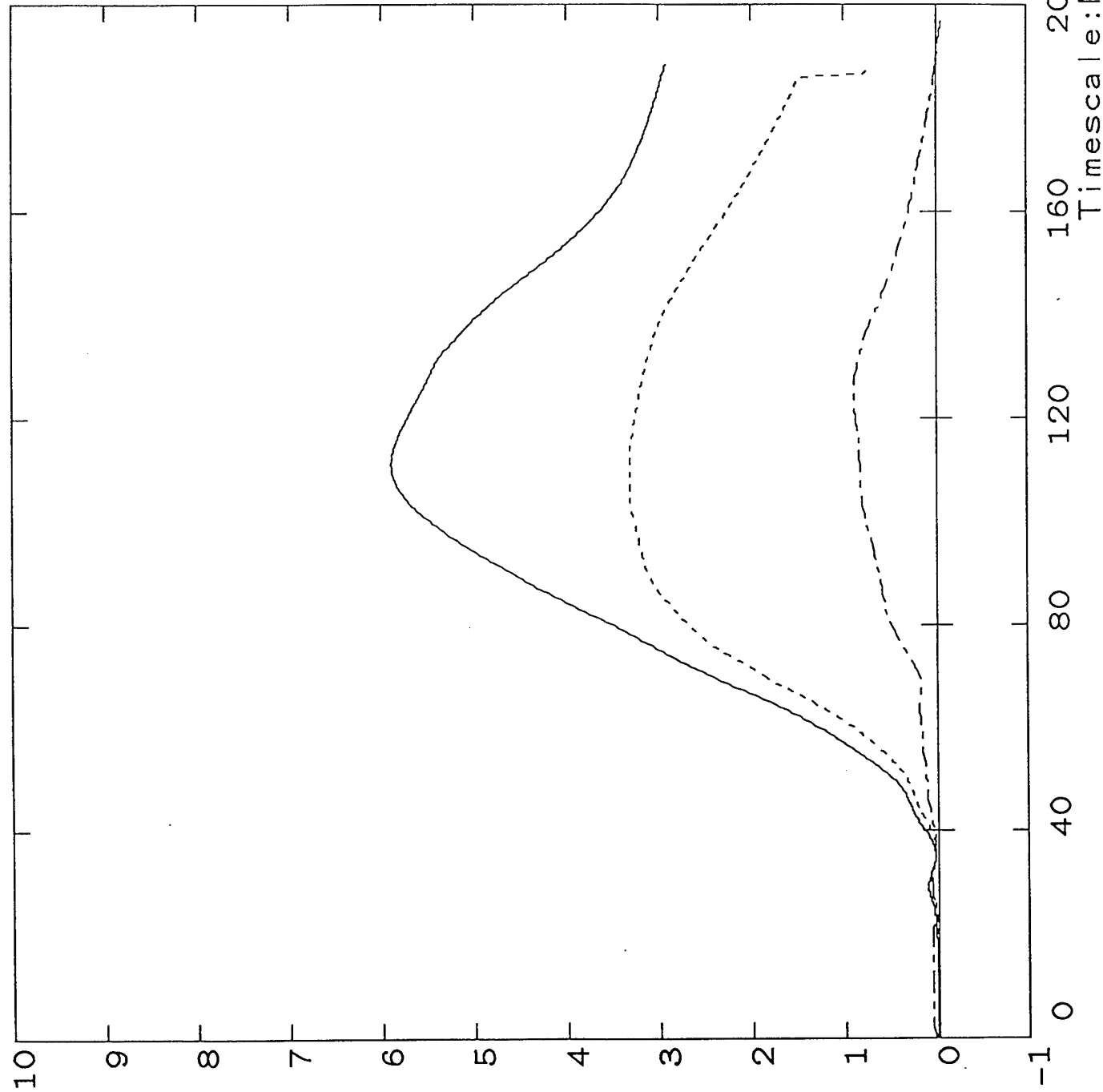
Fig 6

Shot 5992

ik4t amps
Units: 1.00E+05
Max: 5.89E+05
Ts(ns): 0.00E+00

ik3t amps
Units: 1.00E+05
Max: 3.31E+05
Ts(ns): 0.00E+00

ik2t amps
Units: 1.00E+05
Max: 8.79E+04
Ts(ns): -8.70E+00



Shot 6019

Fig 7

2

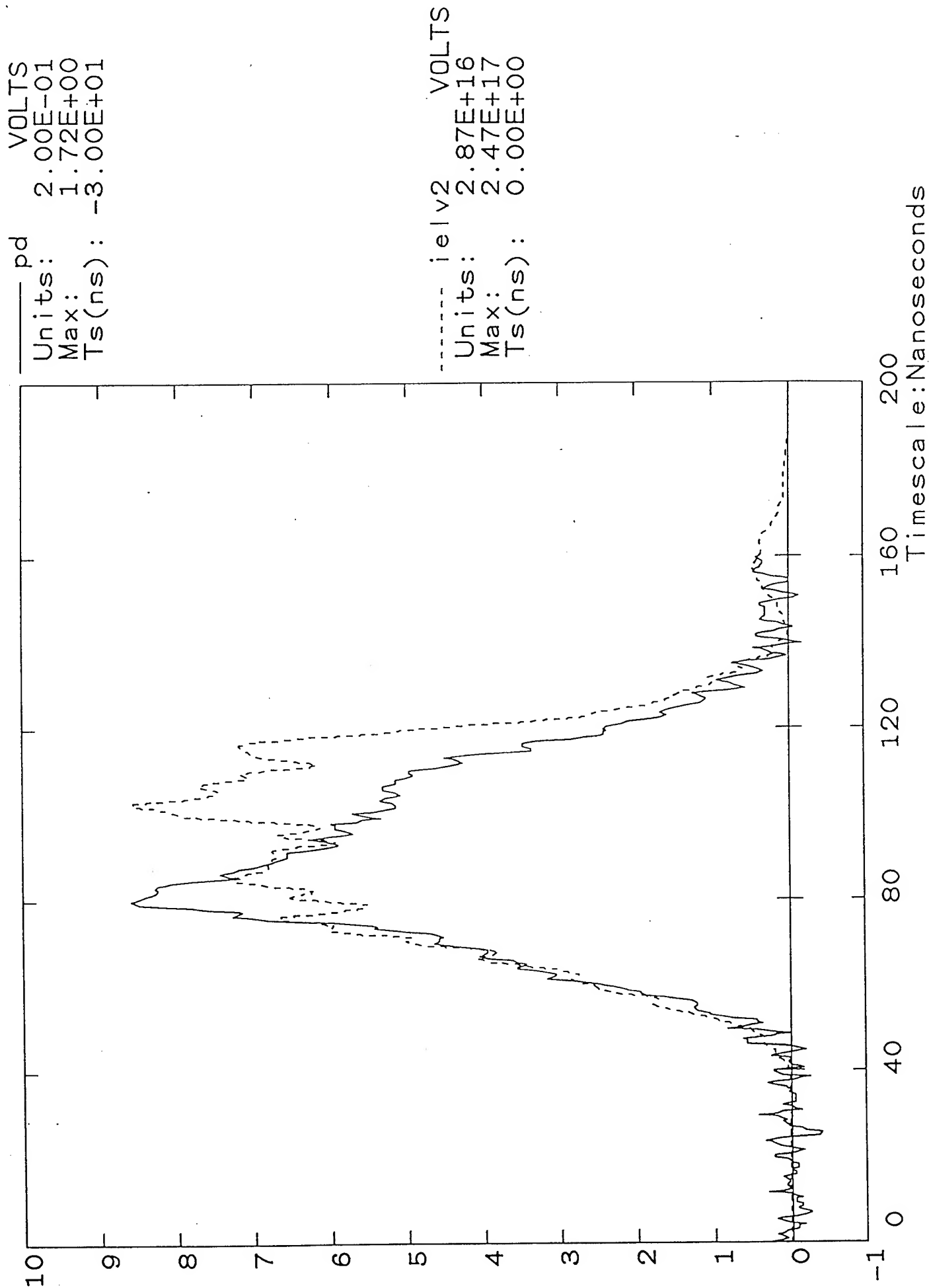


Fig 8

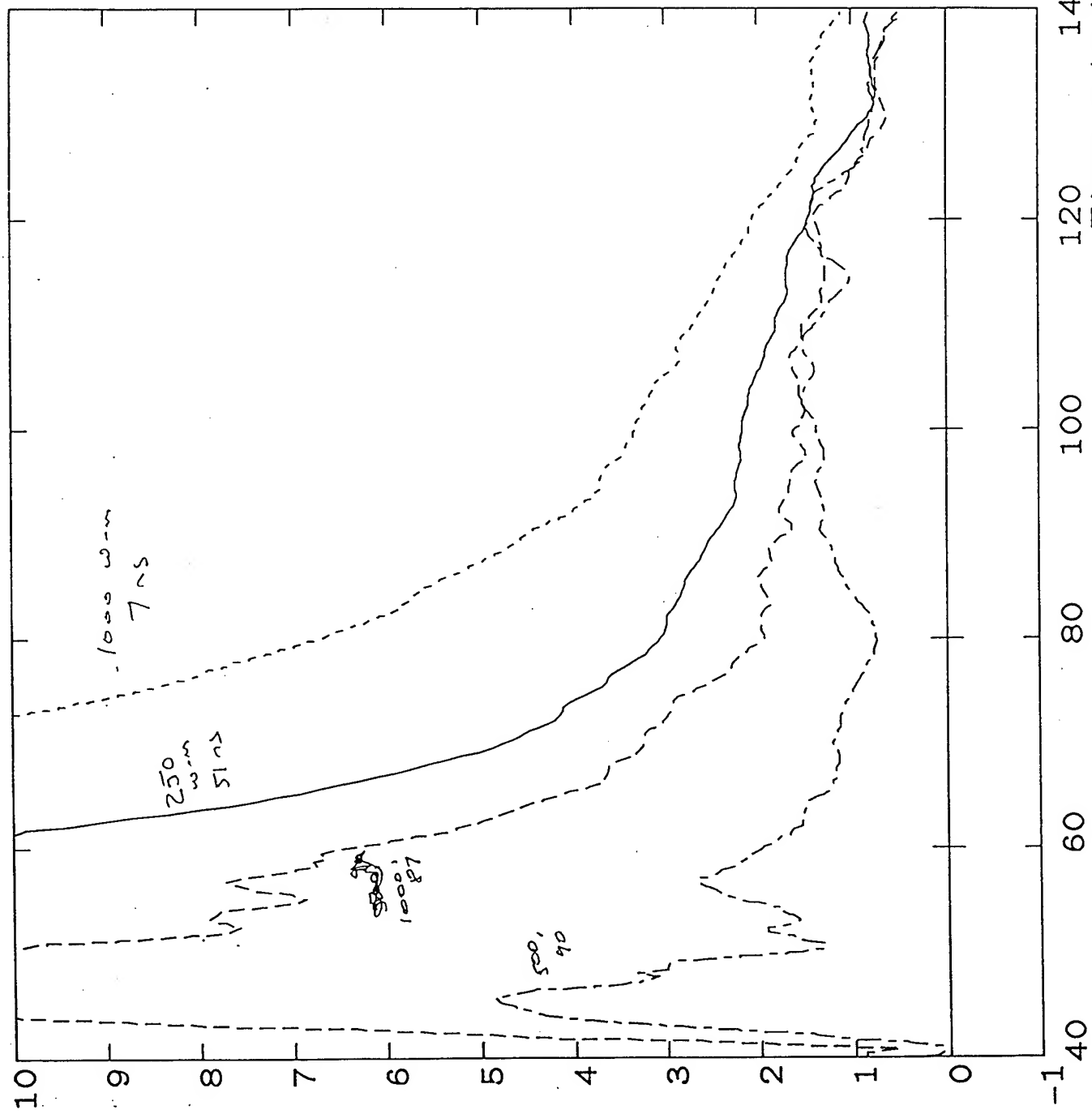
Shot 5985

z5984 Ohms
Units: 1.00E+00
Max: 1.00E+01
Ts(ns): 2.50E+00
should be shifted
~ 7 ns

z Ohms
Units: 1.00E+00
Max: 1.00E+01
Ts(ns): 2.50E+00

z5986 Ohms
Units: 1.00E+00
Max: 1.00E+01
Ts(ns): 2.50E+00

z5987 Ohms
Units: 1.00E+00
Max: 1.00E+01
Ts(ns): 2.50E+00



Timescale: Nanoseconds

Fig 9

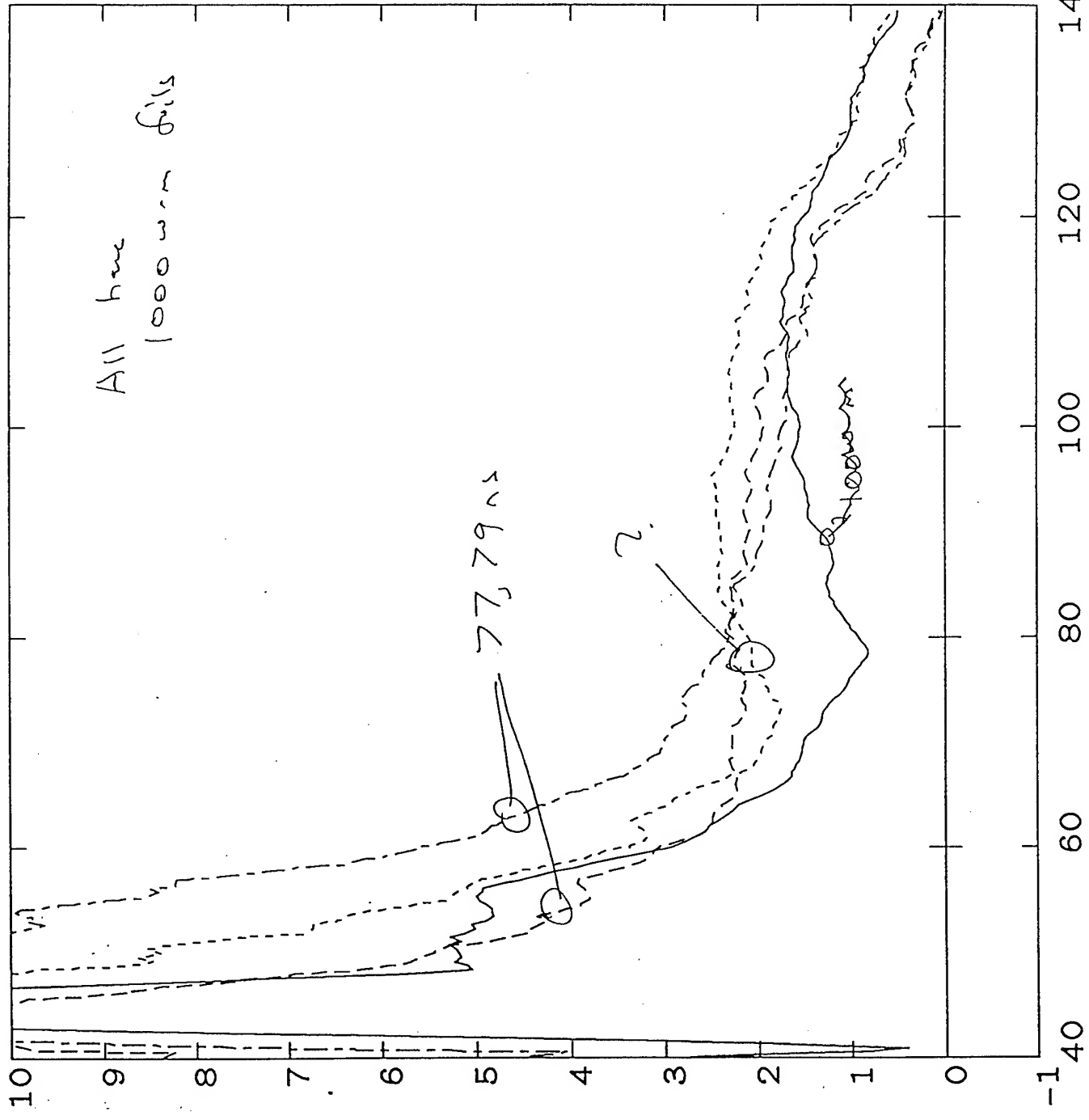
Shot 5991

z5988 Ohms
Units: 1.00E+00
Max: 1.00E+01
Ts(ns): 2.50E+00

z5989 Ohms
Units: 1.00E+00
Max: 1.00E+01
Ts(ns): 2.50E+00

z5990 Ohms
Units: 1.00E+00
Max: 1.00E+01
Ts(ns): 2.50E+00

z Ohms
Units: 1.00E+00
Max: 1.00E+01
Ts(ns): 2.50E+00



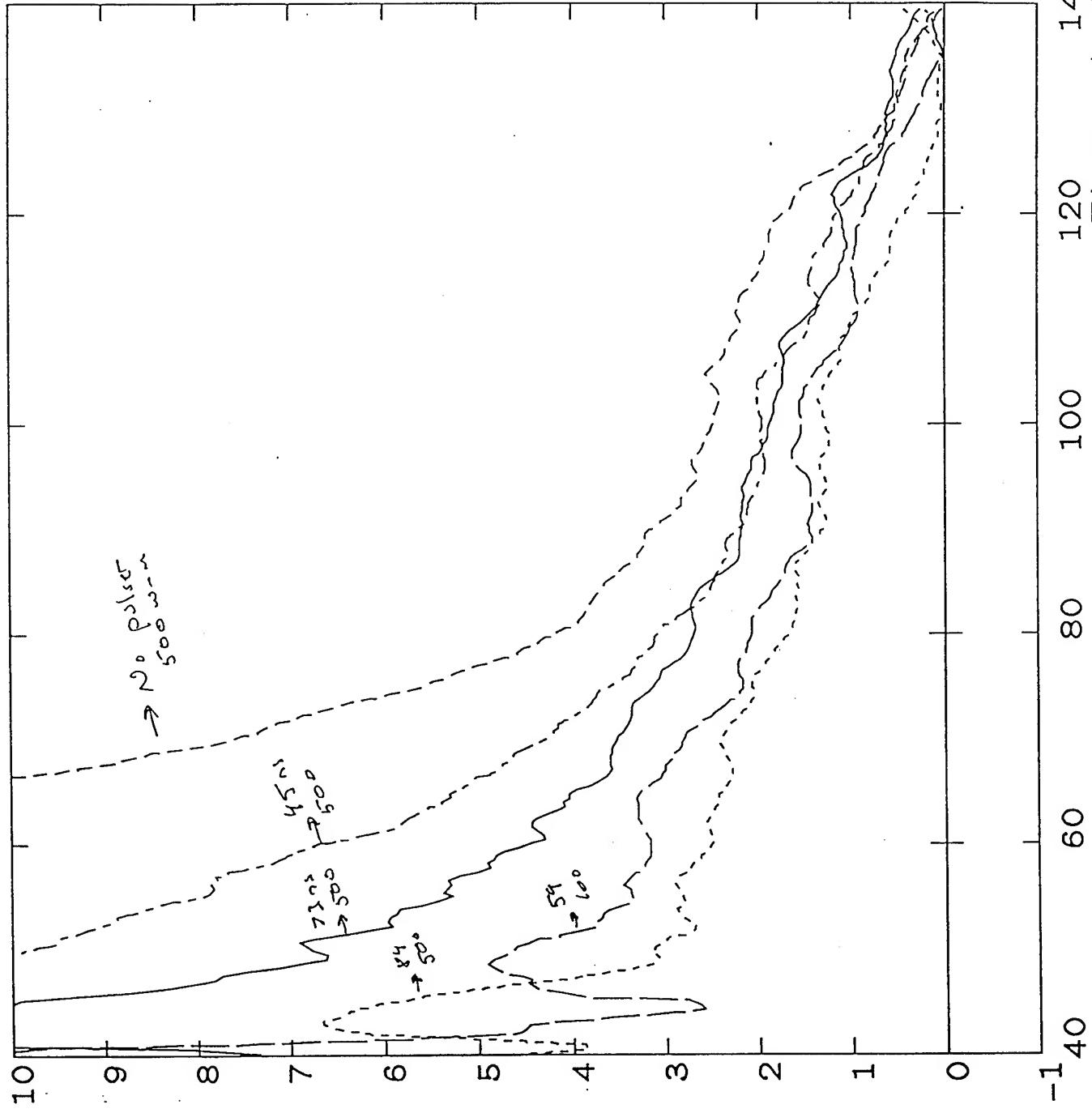
Timescale: Nanoseconds

104

Fig 10

Shot 5998

Units:	z5994	Ohms
Max:	1.00E+00	
Ts(ns):	2.50E+00	
----- z5995 Ohms		
Units:	1.00E+00	
Max:	1.00E+01	
Ts(ns):	2.50E+00	
----- z5996 Ohms		
Units:	1.00E+00	
Max:	1.00E+01	
Ts(ns):	2.50E+00	
----- z5997 Ohms		
Units:	1.00E+00	
Max:	1.00E+01	
Ts(ns):	2.50E+00	
----- z5 Ohms		
Units:	1.00E+00	
Max:	1.00E+01	
Ts(ns):	-4.50E+00	

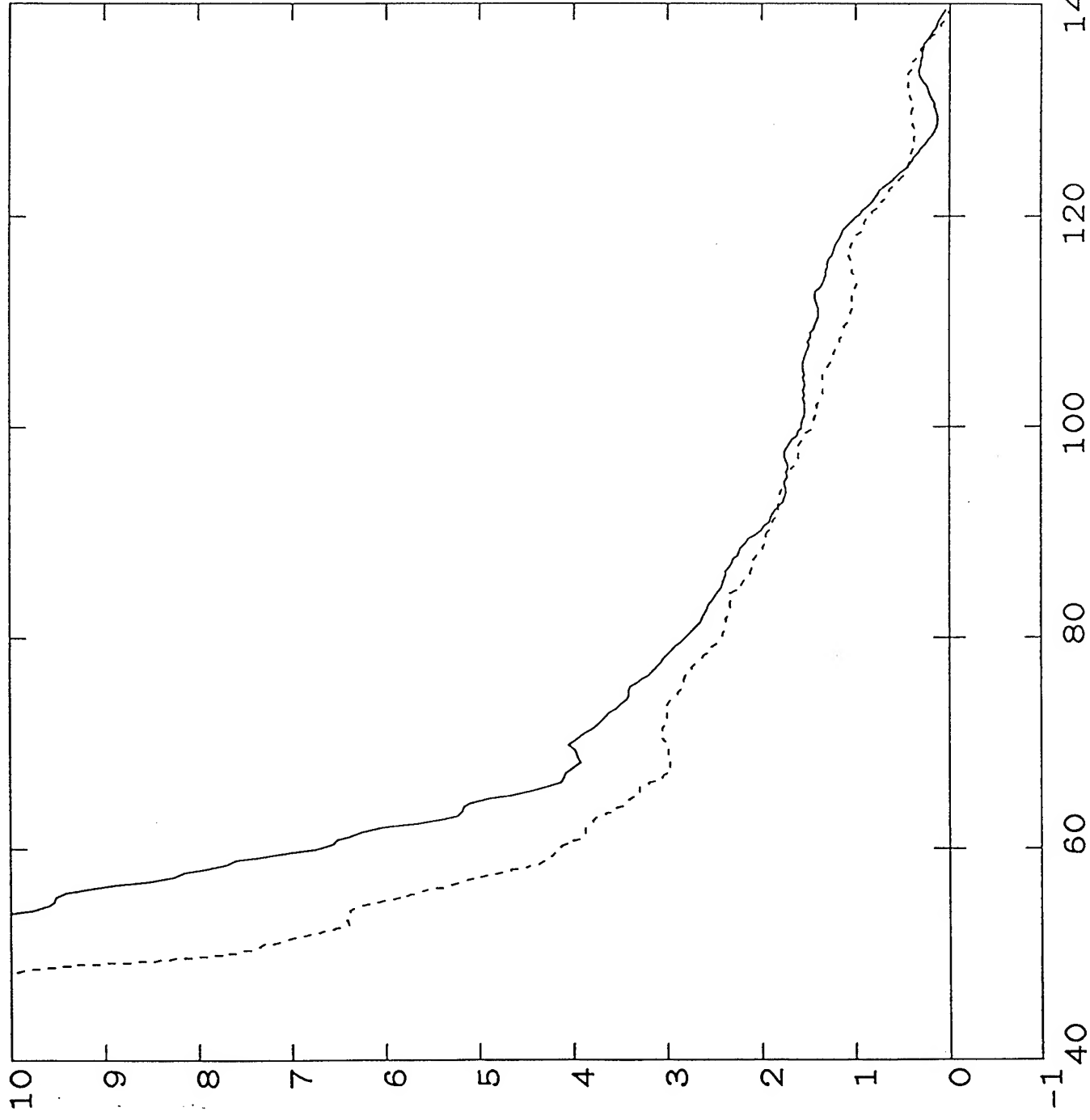


Timescale: Nanoseconds

Fig 11

Shot 5998

1800



z5992 Ohms
Units: 1.00E+00
Max: 1.00E+01
Ts(ns): 2.50E+00
47-ns delay
500 w-m

z6020 Ohms
Units: 1.00E+00
Max: 1.00E+01
Ts(ns): 2.50E+00
53-ns delay
500 w-m

Timescale: Nanoseconds

Shot 5992

Fig 12

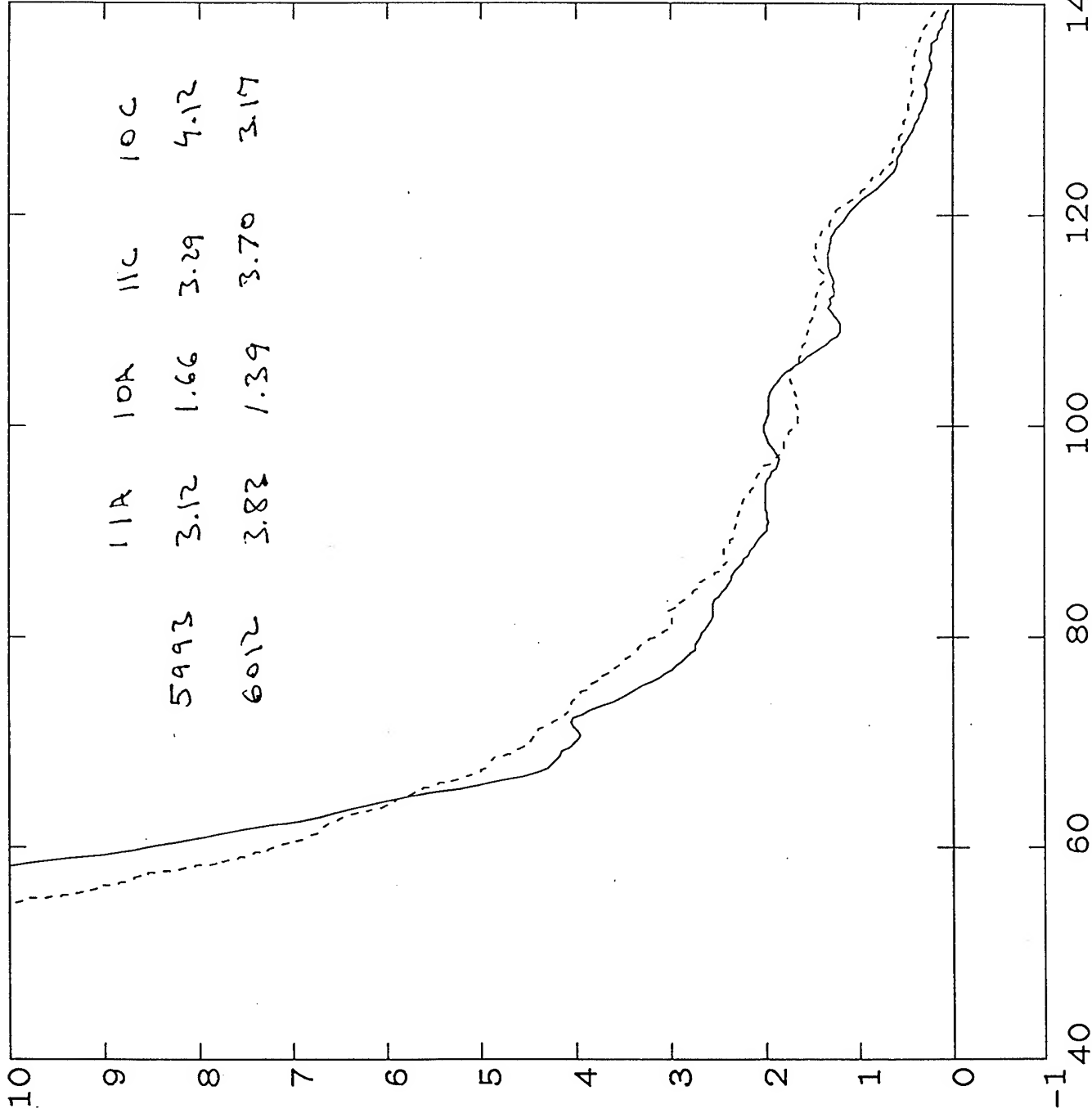
— Z5993 Ohms
Units: 1.00E+00
Max: 1.00E+01
Ts(ns): 2.50E+00

1000 ~ ~ ~
60 ns delay

----- Z6012 Ohms
Units: 1.00E+00
Max: 1.00E+01
Ts(ns): 2.50E+00

1000 ~ ~ ~

74 ns delay



Timescale: Nanoseconds

Fig 13

Shot 6003

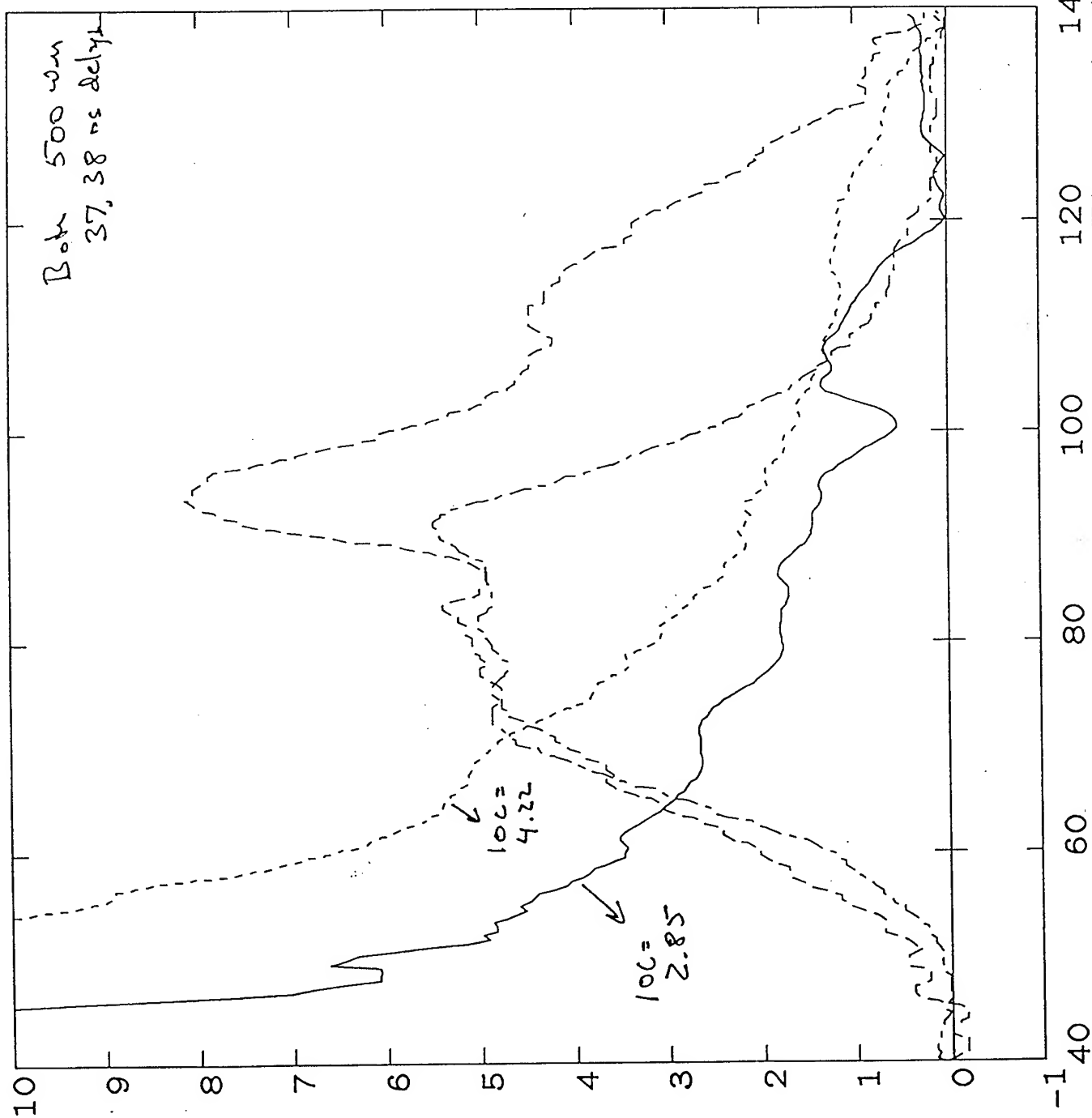
Both 500 m
37, 38 ns delay

----- z6004 Ohms
Units: 1.00E+00
Max: 1.00E+01
Ts(ns): 2.50E+00

----- z6015 Ohms
Units: 1.00E+00
Max: 1.00E+01
Ts(ns): 2.50E+00

----- pd6004 VOLTS
Units: 2.00E-01
Max: 1.10E+00
Ts(ns): -3.00E+01

----- pd6015 VOLTS
Units: 1.00E-01
Max: 8.12E-01
Ts(ns): -3.00E+01



Timescale: Nanoseconds

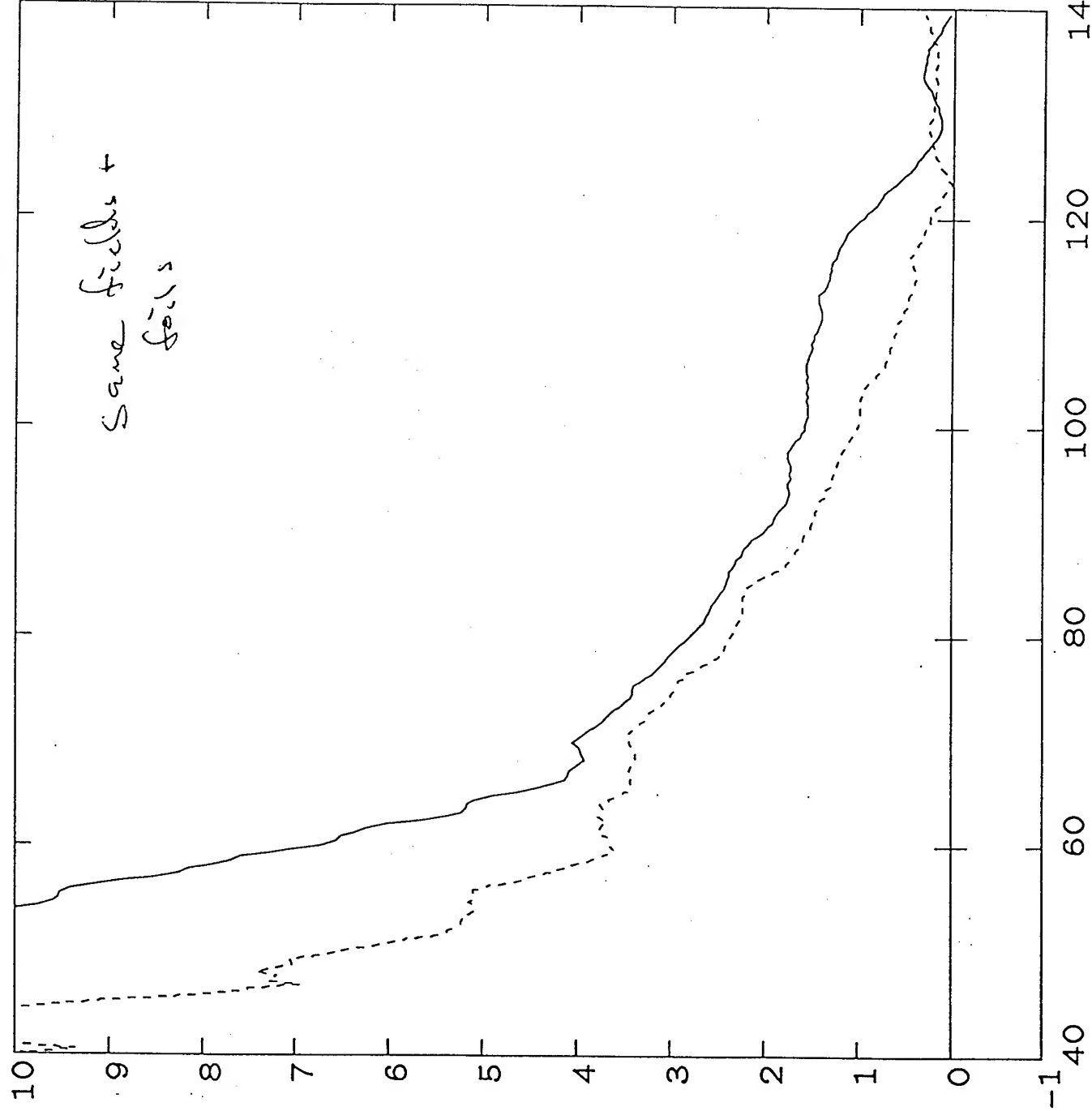
Shot 5998

Reg

Fig 14

10

Same fields +
fields



z5992 Ohms
Units: 1.00E+00
Max: 1.00E+01
Ts(ns): 2.50E+00

47 ns, no insert

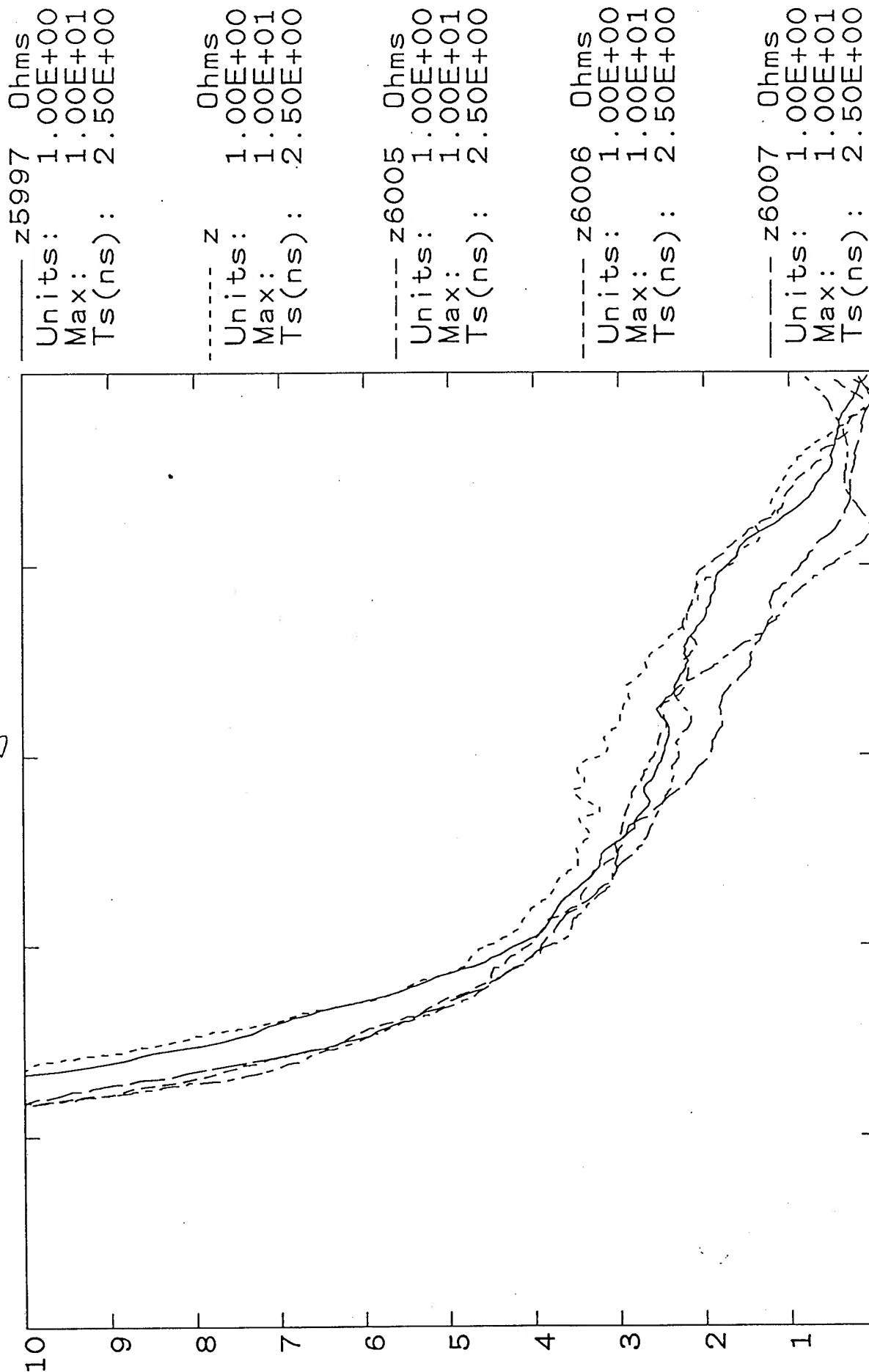
z6014 Ohms
Units: 1.00E+00
Max: 1.00E+01
Ts(ns): 2.50E+00

66 ns
insert

Timescale: Nanoseconds

Shot 6003

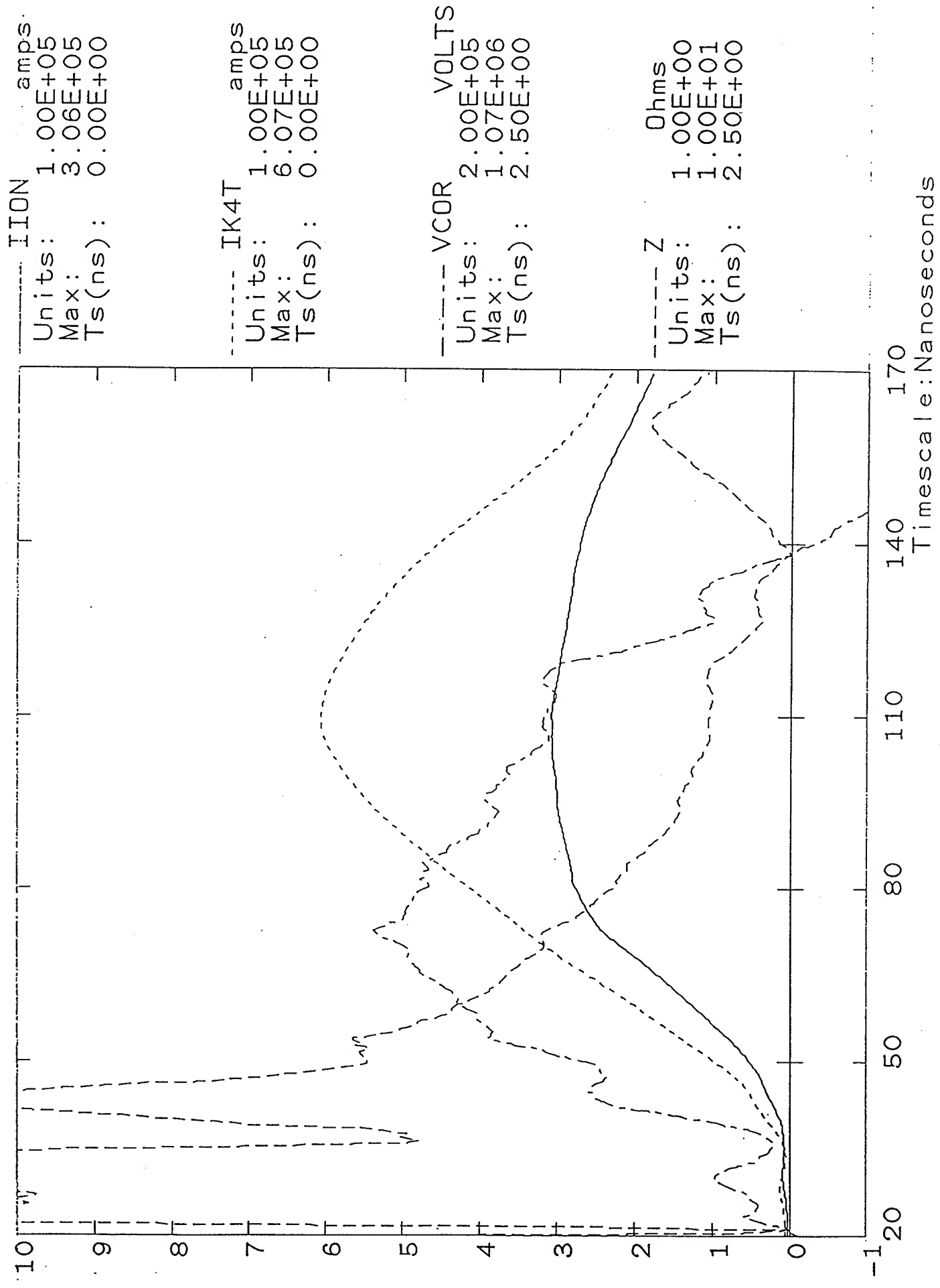
Fig 15



Timescale:Nanoseconds

Fig 18

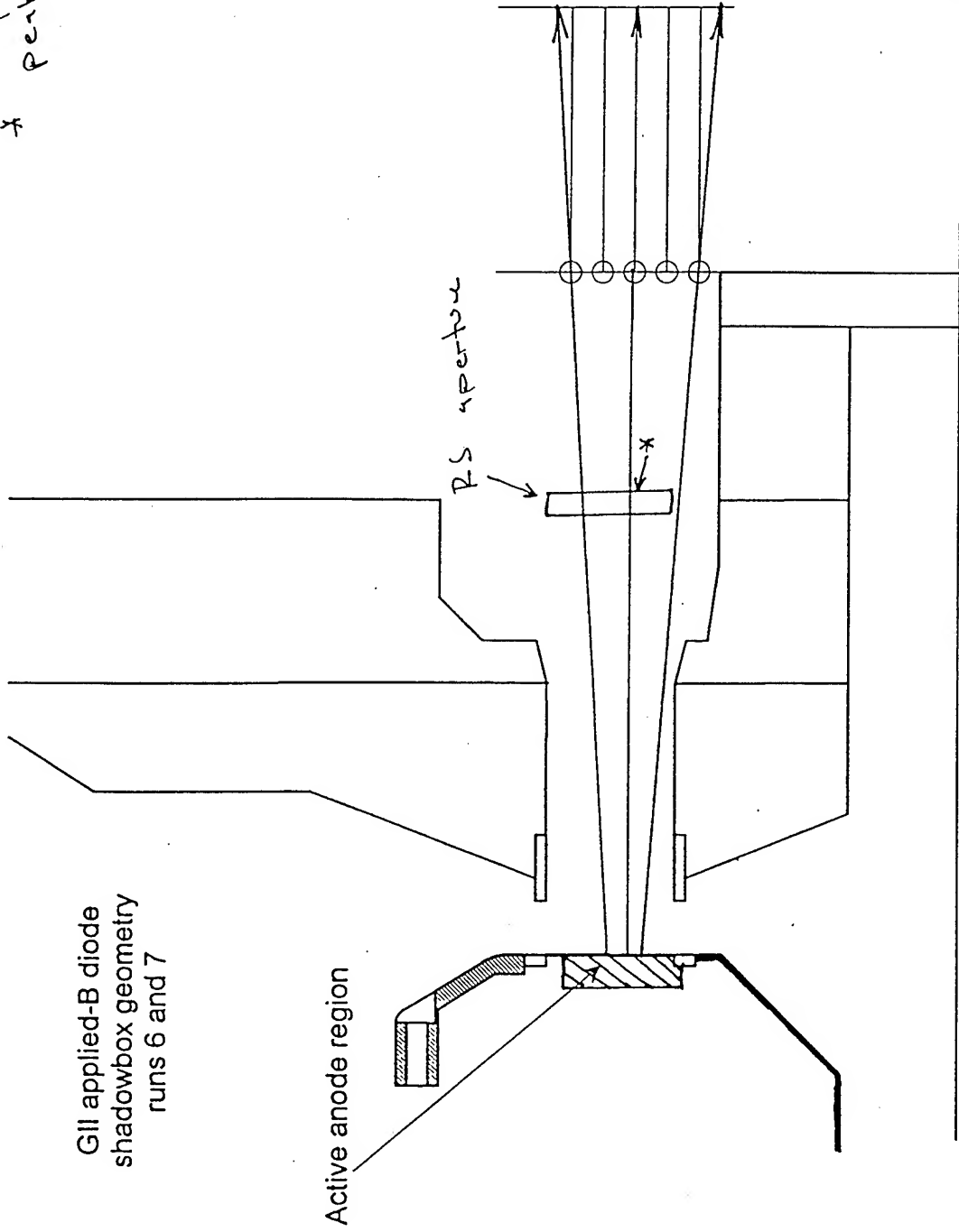
Shot 6017



shot 5992

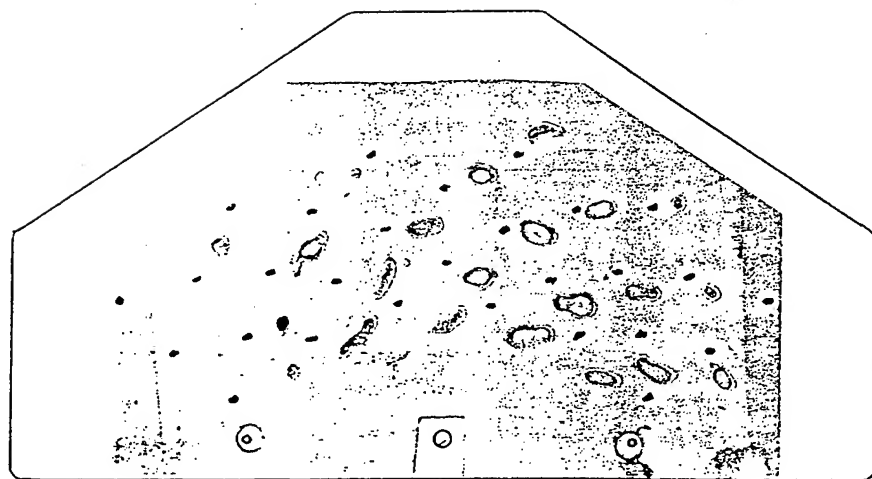
Fig 14

* approx rad of
pent divergence or
aperture plate



6

Fig 18



2695

6020

Fig 19

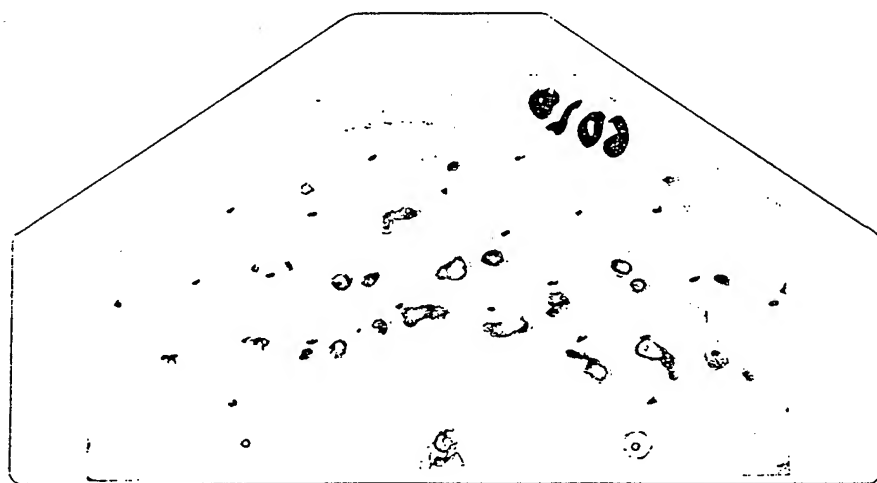


Fig 20

shot	comnts	fields	TFM	eff th	delay, ns	e(kJ)	RS	ratio AI	ratio Ta	AI*1.1	Ta*1.1	comnts
5992	lt flash	5992	950	200	47	12.7	1					saturated
5993		~5992	1800	360	60	8.5	2					weak sigs
5994		5994	950	160	73	11.5	2					weak sigs
5995		5994	950	205	84	7.8	2	0.17		0.19		cent ques
5996		5994	950	150	45	10.1	2	0.31		0.34		cent ques
5997	no pulser	5994	950	213	0	5.7	2	0.34		0.37		cent ques
5998		5994	180	25	59	9	2	0.31		0.34		
6003	flash, no pulser	5994	950	215	0	7.8	3	0.08	0.09	0.09	0.10	welrd shot
6004		55584, no plug	950	180	38	8.8	1					
6005	lt flash, no puls	~6004, plug	950	200	0	10.3	3	0.04	0.07	0.04	0.08	pin1 possibly
6006	lt flash, no puls	~6005, thn plug	950	160	0	5.4	3	0.09	0.07	0.10	0.08	out of
6007	lt flash, no puls	6006, plug	950	211	0	10.4	3	0.08	0.08	0.09	0.07	alignment
6010	flash	5992	950	182	30	10.6	3	0.63	1	0.69	1.10	on shots
6011	flash	6011	360	72	50	12.3	3	0.48	0.61	0.53	0.67	5998-6013
6012		6011	1800	261	74	8.3	3	0.38	0.31	0.42	0.34	
6013	flash	6011	950	268	58	10.3	3	0.44	0.5	0.48	0.55	
6091	flash	opt	950	165	19	7.6	4	0.74		0.81		
6092	flash	opt, K x .95	950	200	33	7.2	4	0.6		0.68		
6093	flash	opt, K x .95	950	240	59	9.6	4	0.63		0.69		tail (2nd hump)
6094	flash	6019	950	160	63	7.3	4	0.85		0.94		tail (2nd hump)
6095	flash, no pulser	6019	950	257	0	6.1	4	0.29		0.32		
6096	flash	6019	950	85	60	7.9	4	0.89		0.98		
6097	flash	sim 6019	950	250	78	7.7	4	0.59		0.65		
6098	8 mm gap	6019	950	225	79	7	N					no pin
6099	wider area	6019	950	130	64	4.5	4	0.29		0.32		
6100	wider area	6019	950	275	58	8.9	4	0.82		0.90		tail
6101	slightly wider	6019	320	50	72	8.8	4	2.6		2.86		
6102	area here on	6019	320	20	78	7.3	4	0.82		0.90		
6103		6019	950	216	81	8.9	4	0.47		0.52		tail (2nd hump)
6104	no pulser	6019					4	0.27		0.30		tail
6105	no pulser	6019	360	9	0	4.8	4	0.43		0.47		tail
6106		6019	360	37	33	4.2	4	0.17		0.19		
6107		6019	950	225	0	11.1	4					no HP
6108		6019			91	8.7	4	0.46		0.51		tail
6109		prefire					4					
6110		6019	300	6	104	8.2	4	1		1.10		tail

PULSED POWER PHYSICS TECHNOTE 95-02

TITLE: ANALYSIS OF APPLIED-B DIODE RUN 6

Author: D. Hinshelwood

Date: January 22, 1994

Abstract: This is one of a series of teknotes, composing a first cut at analysis of the reams of applied-B diode (MID) data we have acquired so far. The purpose here is to get the data out on the table and to identify the best shots, obvious trends, and any unexpected results.

As was seen in run 5, increasing the magnetic field delays both current onset and closure. Coupling of energy from the generator is relatively constant.

Increasing the anode area tends to reduce the diode impedance. Inspection of the spreadsheet indicates that the increase in area is associated with increased inner-cathode current more than outer-cathode current.

At least in one field configuration, the beam is inward-bending with small angular momentum. In this case the ion current density peaks at smaller radii.

The shots in this run show some global differences in behavior compared with those in run 5. Shots on this run show slightly better normalized total energies, higher inner-cathode energies, and lower ion efficiencies. This results in lower normalized ion energies than in run 5. I would guess that the differences on this run are due to the different field configurations, rather than the lack of a pulser.

Field mapping is necessary to interpret the results of this run. The fields, and the way in which they differed from those in run 5, can be compared with the higher inner-cathode currents observed here, as well as with the shadowbox data. While nothing from this run is striking in itself, these data here will (hopefully) form part of a clearer picture when all runs are analyzed.

INTRODUCTION

This is one of a series of teknotes, composing a first cut at analysis of the reams of applied-B diode (MID) data we have acquired so far. The purpose here is to get the data out on the table and to identify the best shots, obvious trends, and any unexpected results. No attempt will be made to draw final conclusions yet. To date there have been ten MID runs. The first three runs used wax-filled-groove, hereafter referred to as passive, anodes. Run 4 was our only attempt with POS-driven, EMFAPS anodes. Run 5 was the first run using a pulser to drive the EMFAPS anodes. On run 6, EMFAPS anodes were used without the pulser. In this case the early electron loss current returning through the anode foil is used to form the anode plasma. These will be referred to as limiter-EMFAPS anodes, although a physical limiter was rarely used. Runs 7-10 used pulser-EMFAPS anodes. Results from runs 5 and 8 have already been presented in TN's 95-01 and 94-16.

MASTER SPREADSHEET

The enclosed spreadsheet lists all shots of this run other than short-circuit shots. This is part of an evolving master spreadsheet that will summarize all of our MID data. The first page gives the basic shot parameters. This sheet has been altered slightly from that in TN 95-01. The column "voc2i" on the RAW sheet refers to the integral of VOC^2 . This quantity, rather than the square of the peak value of VOC, is now used to normalize energies. The column "e2(kJ)" refers to the integral of $VCOR \times IK2T$, and is a weighted measure of the current emitted from the inner cathode.

The second sheet presents some of the shot parameters in more useful form. (Obvious dud shots are not included on this sheet.) The second column gives the closest A-K gap, i.e., the distance between the cathode tips and the anode.

The values "e2/e", "e4/e", and "ei/e" are the ratios of the inner-cathode, outer cathode, and ion energies to the total energy (these add up to unity). The values "e19" and "ei19" give the total and ion energies, normalized to shot 6019 by assuming that the energies scale as voc2i. Shot 6019 had a typical open-circuit voltage for a 32 kV Marx charge, so the values in columns 14 and 15 might be expected if the shots were repeated at 32 kV. (A 26 kV Marx charge was used for this run.)

ELECTRICAL WAVEFORMS

See TN 95-01 for a description of these.

RUN FIVE OVERVIEW

A Marx charge of 26 kV was used on this run, as compared to 32 kV on recent runs, and 36 kV on other Gamble II experiments.

This run comprised 29 shots with two duds. The first shot, 5887, was taken using the 6-mm cathode tips of run 5. All other shots were taken using the standard, 4-mm tips. I am not completely sure that the value of the A-K gap is correct: there may be a 1-mm uncertainty here.

More variations in field shape were used on this run than on run 5. Also, we found out later that the IIA and IOA leads were reversed for the entire run. Normally, IOA is pulsed 35 μ s before IIA. On this run that order was reversed, therefore, these field shapes cannot be compared by inspection with those on run 5: Field mapping will be needed to establish how the fields on the two runs compared.

All shots on this run were taken without using the pulser, which removes any variation resulting from pulser delay or peak current. On the other hand, different anode foils were used here, as shown in column 8 of the first page. The foils were coated at 500-1400 W-min (corresponding to expected thicknesses of roughly 1000-3000 \AA), as compared with 200 W-min on run 5.

After shot 5897 the nominal anode active area was increased by widening the region between the copper contacts from 1.5 cm to 1.8 cm (changing the area from 47 to 57 cm^2). These numbers are only a guess: the copper contacts are estimated to be about 8 times thicker than the aluminum. They would not be expected to be heated significantly by the pulser current, and indeed, open-shutter pictures on bench tests usually show no light from the copper regions. However, the full machine electron current, returning through the outer copper contact, might heat and flash that region also.

In addition to the electrical measurements used on run 5, a scintillator-photodiode combination was used to record the diode x-rays. This was located about 3 meters from the diode and so offered no spatial resolution.

On some shots on this run, the beam was diagnosed with witness plates and a shadowbox. These were located in the 1-Torr-air region, at about 10 cm from the anode. The shadowbox patterns were recorded on the standard, view-graph film, which was located about 4 cm behind the 1.5-mm-diam shadowbox holes. Aluminum, brass, and acrylic witness plates were used.

ELECTRICAL DATA

Two open-circuit voltages from this run are compared with a typical VOC waveform from run 5 in Fig. 1. Because of the oil switch behavior on this run, rather low VOC waveforms were produced, which should be taken into consideration when examining voltage and current amplitudes on this run.

Figures. 1a-1c show electrical data from shot 5895. (See TN95-01 for descriptions of the traces.) This shot had one of the highest normalized ion energies and its waveforms are representative of most shots on this run. The relatively low ion efficiency here is typical,

as can be seen from page two of the spreadsheet. The average ion efficiency was 43 percent for this run as compared with 65 percent on run 5. As on run 5, there is good agreement between the shunt, door, and outer diode (IK4T) current waveforms, so that significant electron emission from outside the outer cathode did not occur. Figure 1b illustrates a possible problem with the IK3B signal (again, the IK3 loops are located on the inside of the outer cathode). On all shots in this run, that signal was lower, and started later, than the other two loop signals. On many shots the difference is more pronounced than it is in Fig 1b. I don't know the reason for this, but the result is that the IK3T (and hence, the ion) currents given here may be 5-10 percent low.

The x-ray signal is calculated by multiplying the diode electron current (IK4T minus IION) by VCOR². This is compared with the photodiode signal, after normalizing the amplitudes, in Fig 1c. Excellent general waveshape agreement is observed. This level of agreement is typical of the run. (We have to be a little careful with this comparison: The anode damage indicates that most of the electron flow to the anode impinges on the epoxy region. However, the x-ray signal could well be dominated by a small fraction of the electrons that strike the stainless. If this fraction varies with time, agreement might not be expected. In fact, I am a little surprised that the agreement is this good.) Note that the x-ray signal goes to zero only a little later than the corrected voltage does. This is encouraging, as it gives confidence in the veracity of VCOR until just before closure.

Another general feature of this run is that in contrast to run 5, finite electron emission from the inner cathode occurred. The average total electron beam energy from the inner cathode was about 16 percent, or almost a third of the total electron beam energy. This value is typical of shots 5819-22 on run 5, but not the other shots, where the average was more like 3 percent.

Because the ion efficiency did not show any significant systematic variation over the course of this run, shot-to-shot comparisons will be made in terms of the diode impedance.

Shots 5887 and 5888 are an interesting comparison. The shots had the same A-K gaps and field settings, but different coil-set separations. Both shots had early flashovers, so it is difficult to get too much from them, but they did exhibit virtually identical early-time behavior, as shown in Fig. 1d.

On three shots in this run, limiters were used in an attempt to capture some of the electron flow and direct it through the foil. The limiters were thin cylinders in the axial direction, attached to the inner anode, and sticking out about 5 mm. Impedances from five shots, including the three limiter shots, are compared in Fig. 2. All show very similar impedance behavior. These shots had the same cathode fields but anode fields that differed by 10-20 percent in amplitude and direction (i.e., IIA/IOA). Field mapping will show whether the insensitivity of the impedance to the anode fields or to the presence of the limiter on these shots is reasonable.

One of the five shots in Fig. 2 is compared in Fig. 3 with the two limiter-EMFAPS shots of run 5, and the shot of run 5 with a very short delay. Reasonable agreement is seen, especially with shot 5828 which was one of the better shots of that run. So far, the slightly different diode geometry, thicker anode foils, and different field shapes of this run are associated with lower ion efficiency and greater inner cathode currents, but similar impedance behavior, relative to run 5.

Shot 5895, the typical shot from Fig. 2, is shown again as the solid curve in Fig. 4. The impedance history for this shot is compared with that for three shots with higher magnetic fields. As was seen in run 5, with a higher field, the current onset and diode closure both begin later as the field is increased. Also shown in the figure are impedance traces from three shots, where onset and closure both begin earlier. Two of these shots were taken with a wider anode area and might be expected to yield a lower impedance. Shot 5892, however, had conditions identical to one of the shots in Fig. 2, and would not be expected to have a lower impedance.

Figure 5 shows impedance traces from three shots with the same fields but different foil thicknesses. As the foil thickness is increased, the current onset begins later but closure is not delayed.

The two shots in Figure 6 differ only by a slight variation in inner cathode field. Is the significant difference in the impedance history caused by the field difference, in contrast to the results in Figure 2?

In the above shots, with a few exceptions, the variations in impedance history with field, anode area, and foil thickness seem reasonable. However, Figure 7 casts doubt on the validity of these comparisons. Two pairs of shots are shown. Each pair was taken under the same conditions but shows a significant variation in impedance history. Shots 5905 and 5908 differ in onset and closure times. Shots 5907 and 5914 also show a significant difference in apparent closure rate. These results point to a lack of reproducibility, at least under the conditions of this run. Note from the spreadsheet that shots on the second half of the run, which appear to show less reproducible behavior, were taken with wider anode areas and thicker foils. Are either of these conditions responsible for the less-reproducible behavior?

More impedance comparisons are shown in Figures 8-10. Figure 8 shows four shots, with different fields, that have similar impedance behavior. Figure 9 shows shots with different fields that have similar onsets but different apparent closure times. Figure 10 shows shots with different apparent closure rates.

There are two reasons we want a flat impedance: to optimize coupling to the generator, and to produce a beam with relatively constant parameters. As to the former, it is probably more useful to examine the energy coupling directly (on the spreadsheet) than to look in detail at each wiggle on the impedance traces. The sheet shows (column "e19") a very reproducible normalized beam energy in spite of the differing impedance behavior on

these shots. Evidently, for the higher-impedance shots, the later closure balances the later onset.

BEAM DIAGNOSTICS

As indicated on the spreadsheet, a shadowbox and witness plates were fielded on six shots during this run. All of these shots had the same field shape. Typical data are shown and analyzed in Fig. 11. Exposures are not observed for all holes, indicating a non-uniform beam. The shadowbox data show that the beam is bending inward, with an angle that increases at smaller radii and averages to about 65 mR. The current density is also peaked at smaller radii. A microdivergence of about 25 mR is inferred. More importantly, the angular momentum is zero within the measurement resolution of 10-20 mR.

This diagnostic as it stands is a very useful source of qualitative data. However, the unknown response curve of the film makes quantitative interpretation difficult, and I would be careful about quoting the microdivergence numbers. Another complication is introduced by possible hole closure. At these current densities, the Cornell results show that the 1.5-mm diam holes used here are too small, and we may be only sampling the early part of the beam.

Witness plates for this shot are shown in Fig. 12. This diagnostic is relatively useless, but has results consistent with the shadowbox in showing an inward-bending beam. In a gross sense the damage has reasonable azimuthal uniformity.

SUMMARY

In this first cut at revisiting the MID data, I will attempt to answer four questions for each run:

(1) What are the key shots, in terms of performance, for each run?

Nothing particularly stands out. Shot 5889, a very high-impedance shot, had the highest normalized ion energy. Shot 5895, shown in Figs. 1a-1c, also had a high normalized ion energy, and fairly typical waveshapes. There are shots with greater or lesser flatness to the impedance histories, but in view of the observed irreproducibility of some shots, I don't want to make too much of these differences.

(2) Which field configurations should we concentrate on mapping out?

Many different configurations were used on this run. That from 5915 is important to compare with the shadowbox data. Shots 5895 and 5894, which showed the same impedance behavior but different IIA/IOA ratios, should be mapped out. Shot 5899, with the highest normalized ion energy, should also be mapped out.

(3) What are the significant trends in the data?

As was seen in run 5, increasing the magnetic field delays both current onset and closure. Some effect of foil thickness is seen, but it is not large compared with the observed reproducibility. No effect of the physical limiter is seen. In some cases, the impedance behavior is not strongly affected by the field shape. Coupling of energy from the generator is relatively constant.

Increasing the anode area tends to reduce the diode impedance. Inspection of the spreadsheet indicates that the increase in area is associated with increased inner-cathode current more than outer-cathode current.

→ (or ions hitting the inner cathode)

At least in one field configuration, the beam is inward-bending with small angular momentum. In this case the ion current density peaks at smaller radii.

The shots in this run show some global differences in behavior compared with those in run 5, as is best seen in the energy columns on the spreadsheet. Shots on this run show slightly better normalized total energies, higher inner-cathode energies, and lower ion efficiencies. This results in lower normalized ion energies than in run 5. (One set of shots in run 5, shots 5819-5822, including the no-pulser shot 5822, had results more similar to this run.) Since there were a few no-pulser shots on the last run, I would guess that the differences on this run are due to the different field configurations, rather than the lack of a pulser.

(4) What are the most puzzling features to these data?

The lack of reproducibility on some shots.

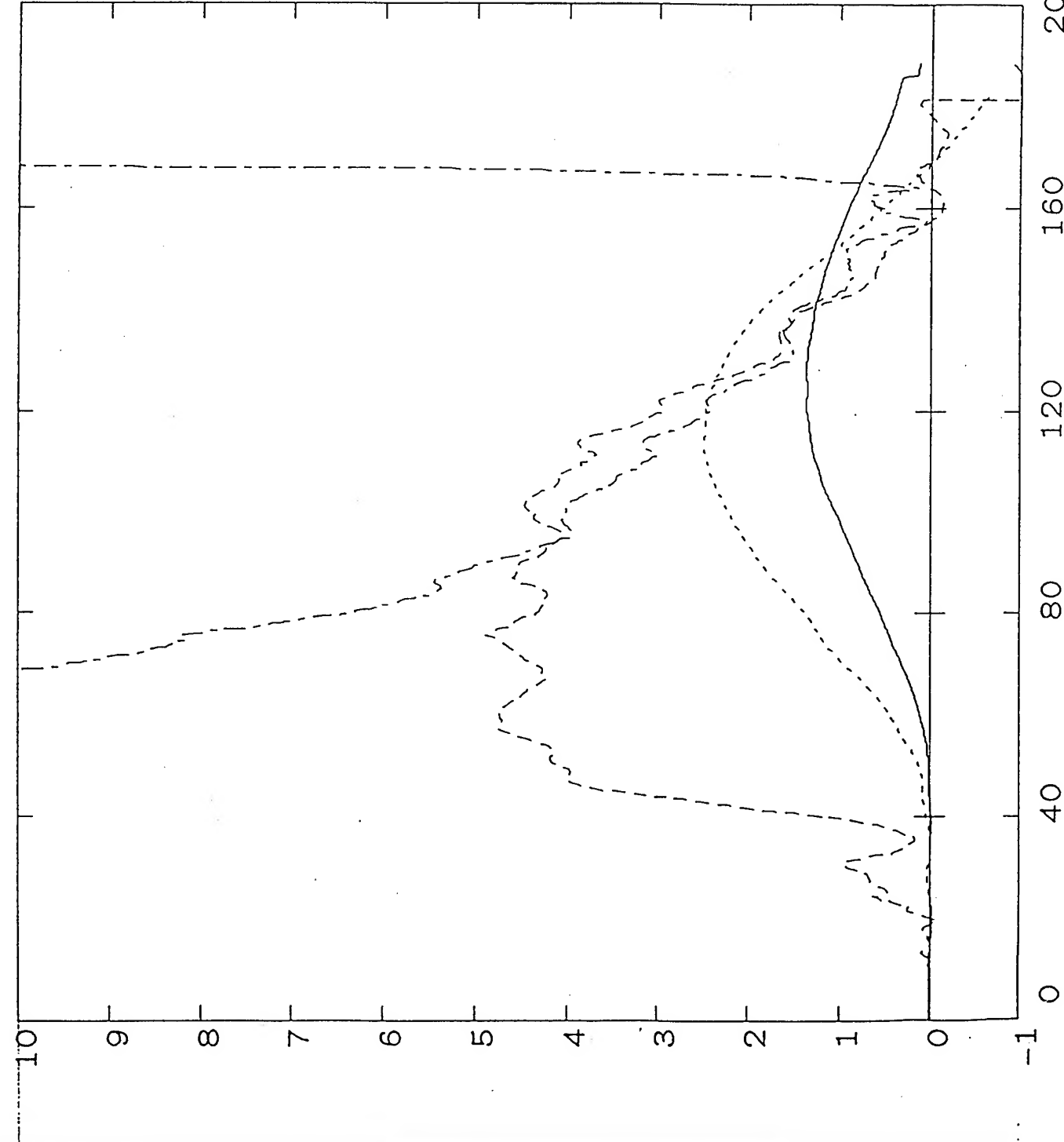
CONCLUSIONS

Field mapping is necessary to interpret the results of this run. The fields, and the way in which they differed from those in run 5, can be compared with the higher inner-cathode currents observed here, as well as with the shadowbox data. While nothing from this run is striking in itself, these data here will (hopefully) form part of a clearer picture when all runs are analyzed.

shot	gap	tips	IIA	IOA	IIC	IOC	W-m	eff th	ins	lf	delay, if z=10	voc2l	e1(kl)	e2(kl)	e(k)	Vpp	lpp	comnts
5887	13.5	6	1.19	1.82	2.04	2.55	500 NA	500 NA	N	0	0		2.2	0.0	4.3			flash NOTE: for 5887-5915, bank delays are 0,35,50,40,170
5888	11.5	4	1.19	1.82	2.04	2.55	500 NA	500 NA	N	0	0		1.8	0.0	4.5			flash
5889	11.5	4	1.07	1.64	1.84	2.50	500 NA	500 NA	N	0	0		1.04	4.3	0.0	6.2		very late flash
5890	11.5	4	0.95	1.46	1.63	2.04	500 NA	500 NA	N	0	0							no electrical data
5891	11.5	4	0.95	1.46	1.63	2.04	1000 NA	1000 NA	N	0	0		1.195	2.0	0.6	7.1		flash
5892	11.5	4	0.86	1.31	1.47	1.84?	NA	NA	N	0	0		2.119	7.2	1.7	14.7		
5893	11.5	4	0.95	1.44	1.47	1.84	500 NA	500 NA	N	0	0		1.547	4.1	1.2	10.4		
5894	11.5	4	0.86	1.31	1.47	1.84	500 NA	500 NA	N	0	0		1.554	5.1	1.1	11.4		brass limiter
5895	11.5	4	0.95	1.18	1.47	1.84	500 NA	500 NA	N	0	0		1.522	5.1	1.2	10.9		thinner brass limiter
5896	11.5	4	0.95	1.44	1.47	1.84	500 NA	500 NA	N	0	0		1.724	4.7	3.5	12.0		
5897	11.5	4	0.86	1.31	1.47	1.84	500 NA	500 NA	N	0	0		2.024	6.2	2.3	14.3		ss limiter
5898	11.5	4	0.95	1.44	1.47	1.84	500 NA	500 NA	N	0	0		1.751	4.9	2.3	12.4		increased active anode area to ~1.8 cm
5899	11.5	4	1.05	1.31	1.47	1.84	500 NA	500 NA	N	0	0		1.569	4.5	1.9	10.9		
5900	11.5	4	1.05	1.31	1.47	1.84	1000 NA	1000 NA	N	0	0		1.891	6.0	2.5	12.9		
5901	11.5	4	1.05	1.31	1.47	1.84	1400 NA	1400 NA	N	0	0		1.638	4.6	1.9	10.7		
5902	11.5	4	1.05	1.31	1.60	1.84	1000 NA	1000 NA	N	0	0		1.196	3.3	0.9	7.6		
5903	11.5	4	1.05	1.31	1.32	1.66	1000 NA	1000 NA	N	0	0		1.505	3.5	2.4	10.1		
5904	11.5	4	1.15	1.44	1.32	1.66	1000 NA	1000 NA	N	0	0		1.595	4.3	2.2	10.8		
5905	11.5	4	1.26	1.58	1.32	1.66	1000 NA	1000 NA	N	0	0		2.078	6.0	2.8	13.3		
5906	11.5	4	0.00	1.74	1.45	1.82	1000 NA	1000 NA	N	0	0		1.444	4.2	1.6	9.2		was IIA 0, or just no sig? shot like 5908 beam diags
5907	11.5	4	1.39	1.74	1.45	1.82	1000 NA	1000 NA	N	0	0		1.897	4.7	2.3	10.9		beam diags
5908	11.5	4	1.26	1.58	1.32	1.66	1000 NA	1000 NA	N	0	0		1.556	4.7	2.3	10.9		beam diags
5909	11.5	4	1.26	1.58	1.32	1.66	1000 NA	1000 NA	N	0	0		1.743	4.8	2.4	11.7		beam diags
5910	11.5	4	1.20	1.50	1.26	1.58	1000 NA	1000 NA	N	0	0		1.519	3.6	2.3	9.5		
5911	11.5	4	1.14	1.43	1.20	1.52	1000 NA	1000 NA	N	0	0		2.048	5.0	2.9	14.9		
5912	11.5	4	1.20	1.50	1.14	1.46	1000 NA	1000 NA	N	0	0		1.607	3.8	2.2	11.1		
5913	11.5	4	1.04	1.30	1.14	1.45	1000 NA	1000 NA	N	0	0		1.762	4.5	2.3	13.1		
5914	11.5	4	1.39	1.74	1.45	1.83	1000 NA	1000 NA	N	0	0		2.203	6.6	2.7	16.0		beam diags
5915	11.5	4	1.46	1.82	1.52	1.92	1000 NA	1000 NA	N	0	0		1.632	5.1	1.6	11.0		beam diags

Shot 5895

F_{ij} ~~10~~ / a



Timescale: Nanoseconds

----- IION ----- amps
Units: 1.00E+05
Max: 1.35E+05
Ts(ns): 0.00E+00

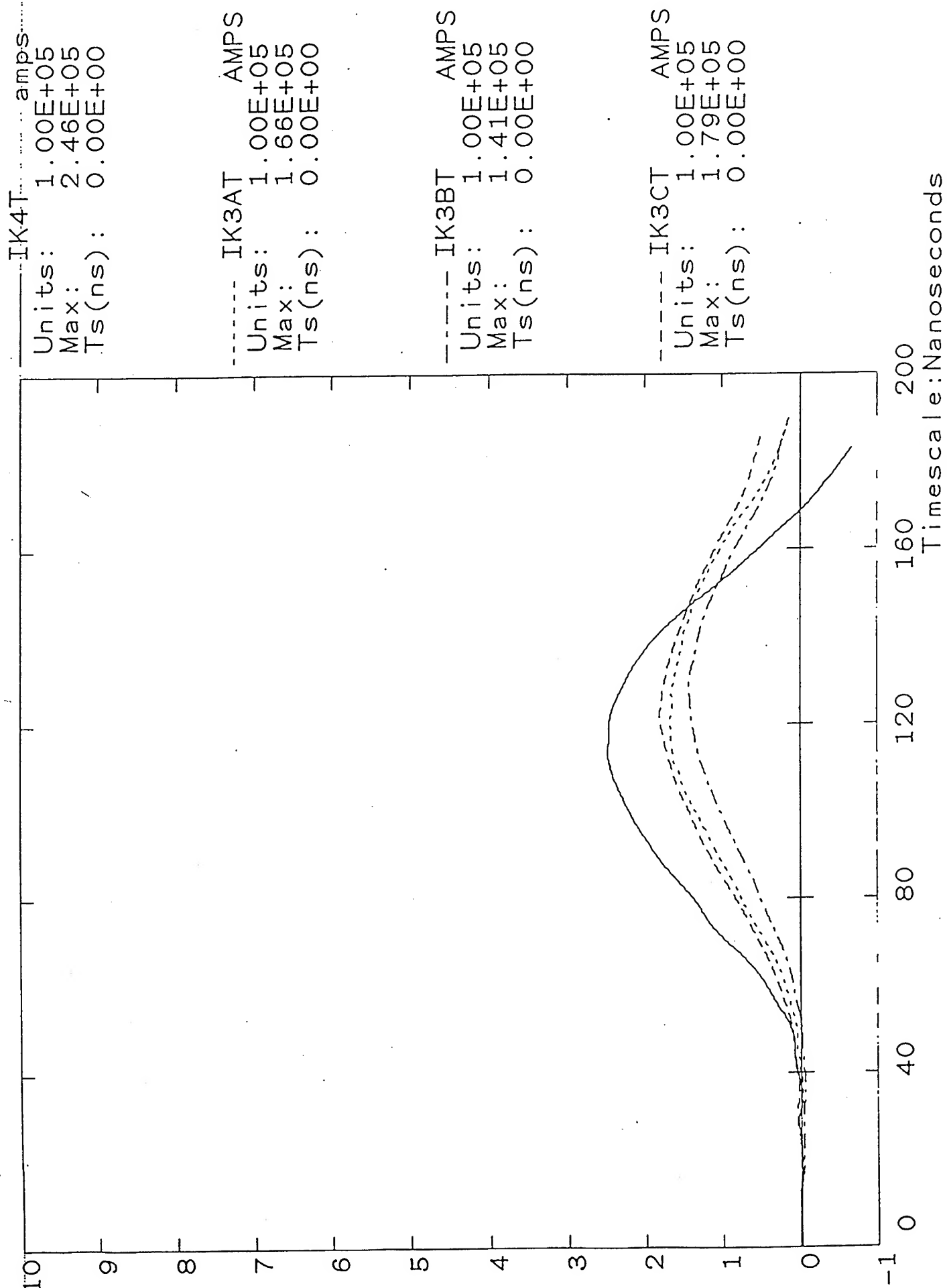
----- IK4T ----- amps
Units: 1.00E+05
Max: 2.46E+05
Ts(ns): 0.00E+00

----- Z ----- Ohms
Units: 1.00E+00
Max: 1.00E+01
Ts(ns): 2.00E+00

----- VCOR ----- VOLTS
Units: 2.00E+05
Max: 9.74E+05
Ts(ns): 2.00E+00

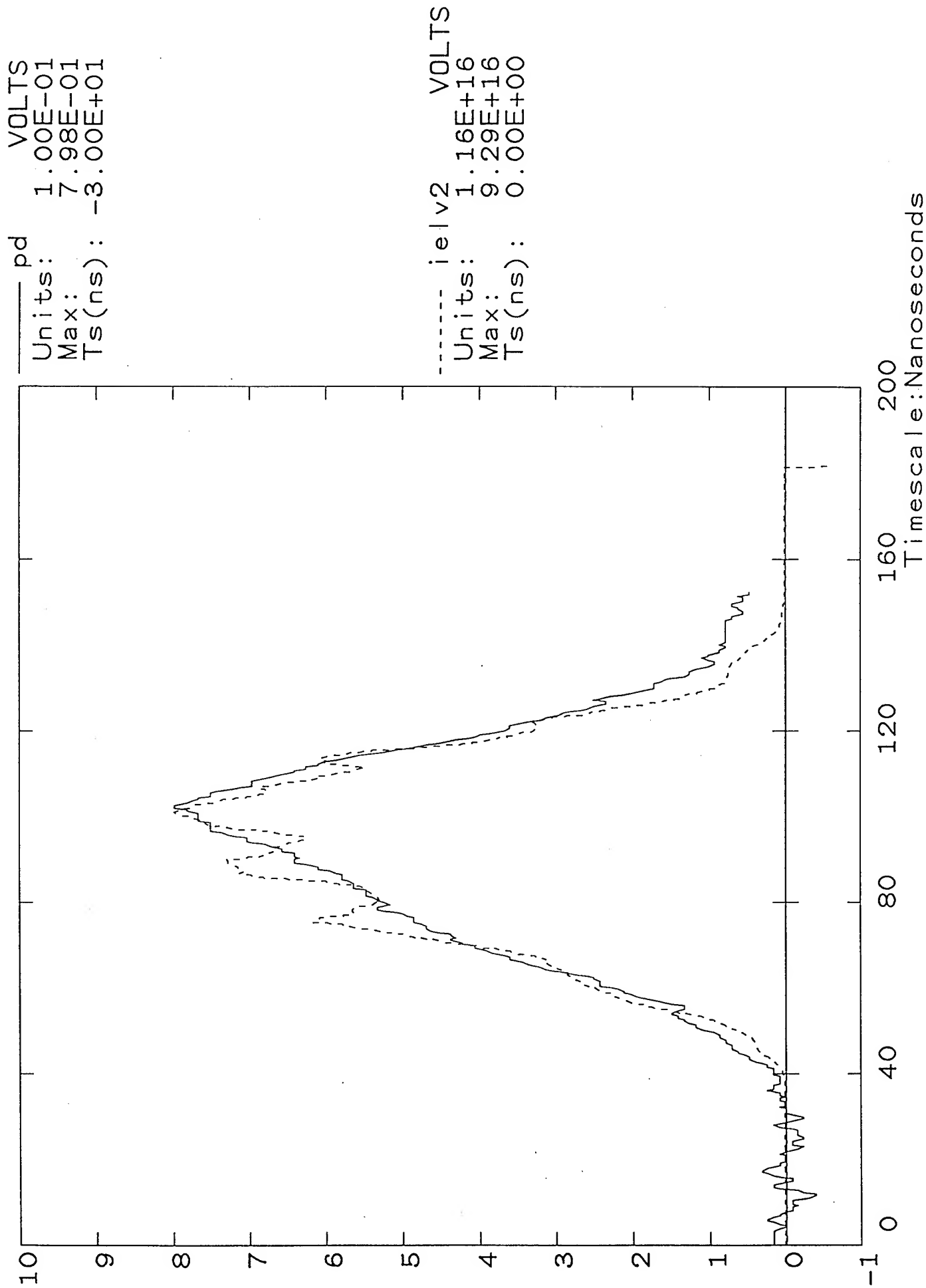
Shot 5895

Fig 16



Shot 5895

F310



Shot 5887

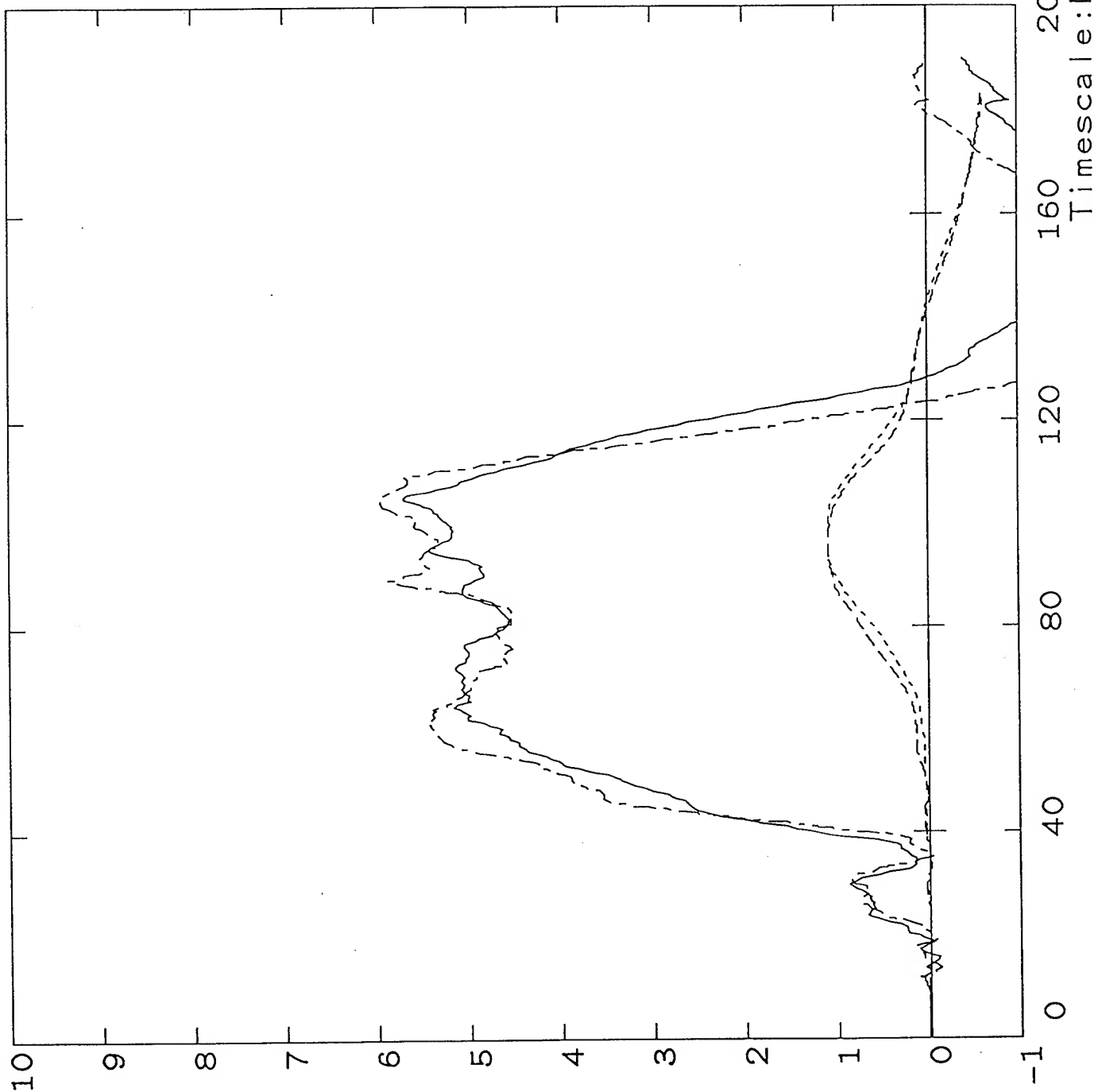
Fig 1d

----- vcor VOLTS
Units: 2.00E+05
Max: 1.14E+06
Ts(ns): 2.00E+00

----- ik4t amps
Units: 1.00E+05
Max: 1.07E+05
Ts(ns): 0.00E+00

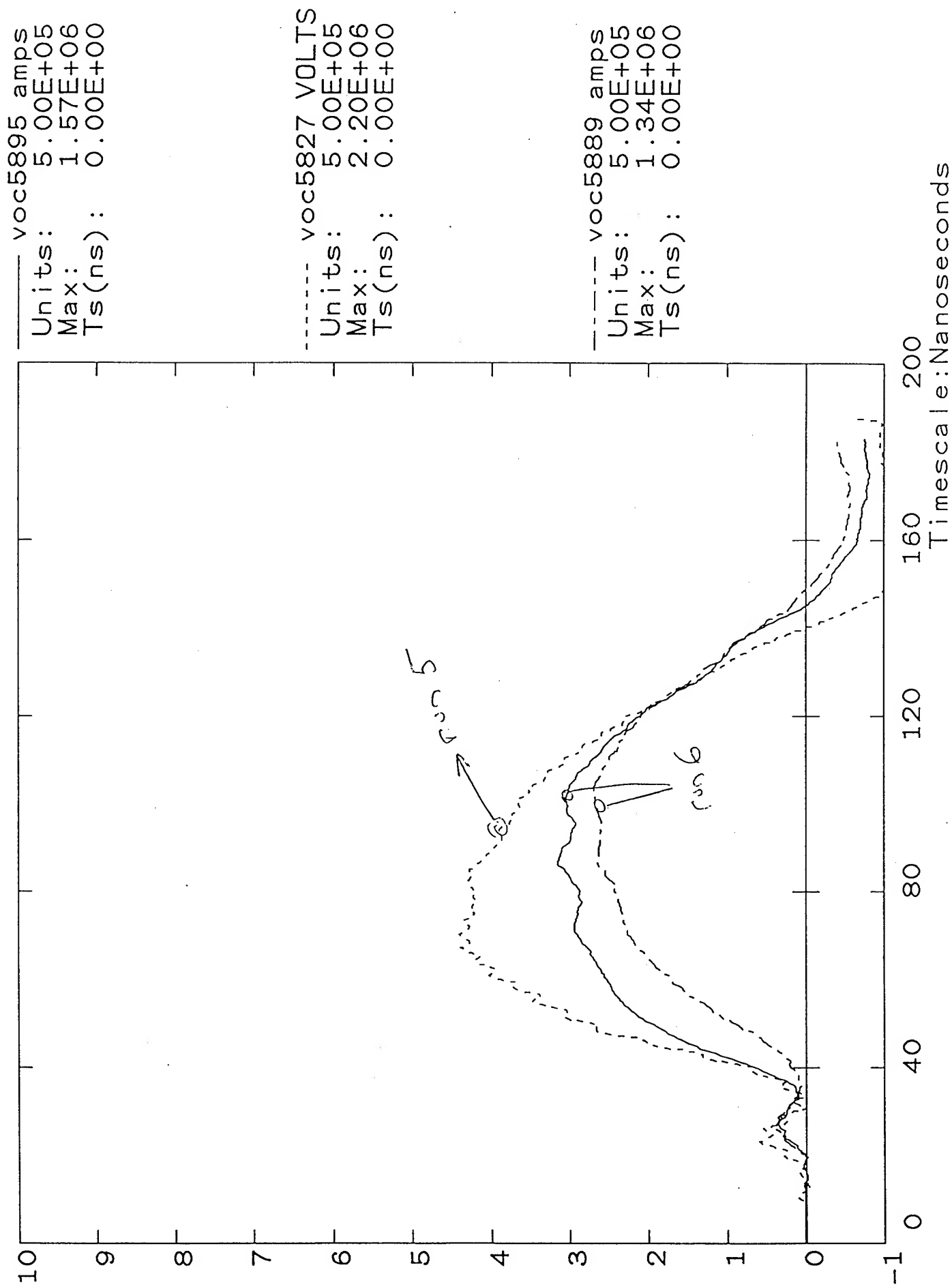
----- vcor5888 VOLTS
Units: 2.00E+05
Max: 1.19E+06
Ts(ns): 2.00E+00

----- ik4t5888 amps
Units: 1.00E+05
Max: 1.07E+05
Ts(ns): 0.00E+00



Shot 5893

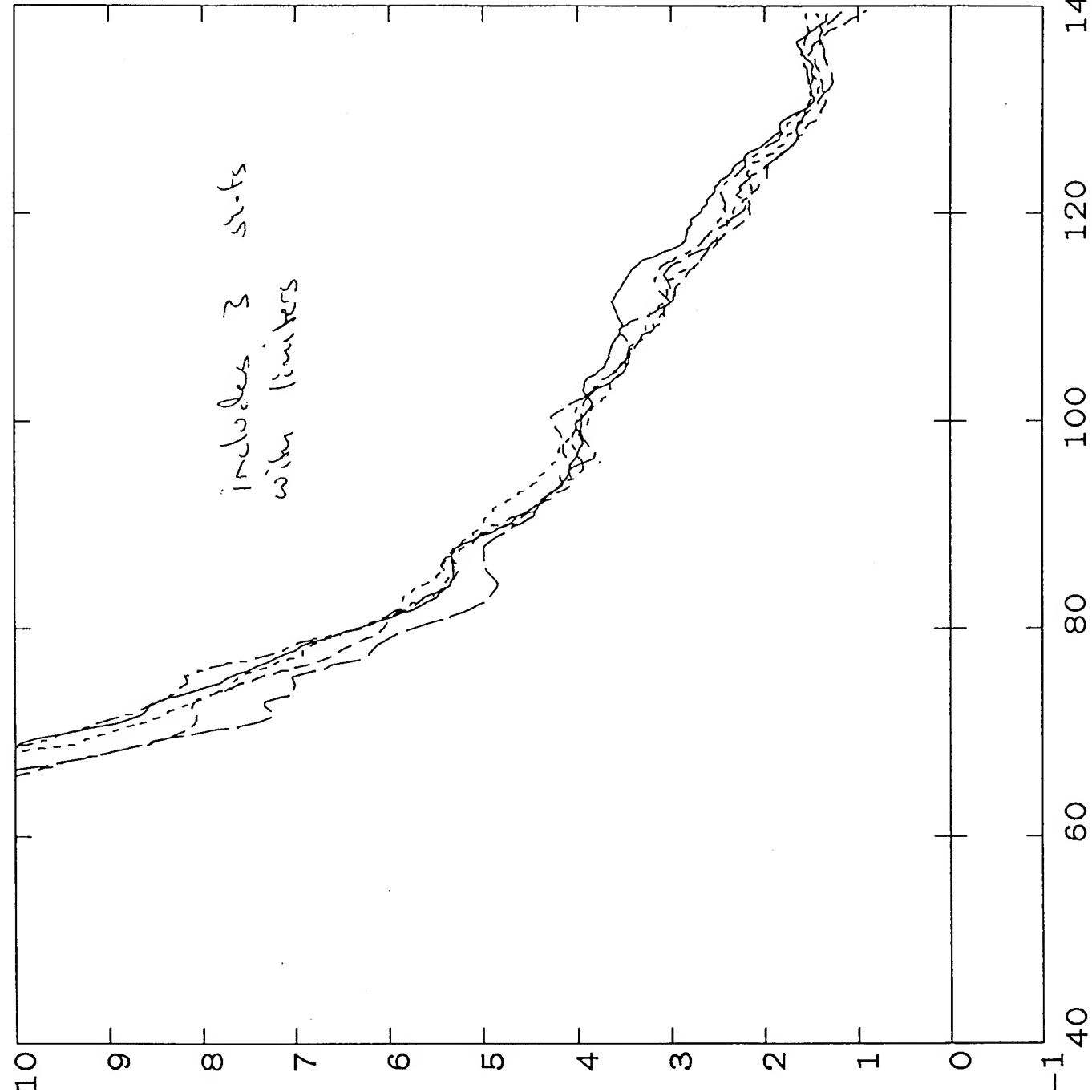
Fig 1



shot	AK gp	IIA	IOA	IIC	IOC	IC/OC	IA/OC	OA/OC	delns	e(k)	ei(k)	eI/e	e2/e	e19	ei19	e4/e	ZIPP	comnts
5887	7.50	1.19	1.82	2.04	2.55	0.80	0.47	0.71	0	4.3	2.2	0.52	0.00	####	####	0.48	####	flash NOTE: for 5887-5915, bank delays are 0.35,50,40,170
5888	7.50	1.19	1.82	2.04	2.55	0.80	0.47	0.71	0	4.5	1.8	0.40	0.00			0.60		flash
5889	7.50	1.07	1.64	1.84	2.50	0.74	0.43	0.66	0	6.2	4.3	0.69	0.01	23.25	16.0	0.30		very late flash
5891	7.50	0.95	1.46	1.63	2.04	0.80	0.47	0.72	0	7.1	2.0	0.28	0.09	23.15	6.5	0.63		flash
5892	7.50	0.86	1.31	1.47	1.84	0.80	0.47	0.71	0	14.7	7.2	0.49	0.12	26.84	13.1	0.39		
5893	7.50	0.95	1.44	1.47	1.84	0.80	0.52	0.78	0	10.4	4.1	0.39	0.11	26.18	10.2	0.50		
5894	7.50	0.86	1.31	1.47	1.84	0.80	0.47	0.71	0	11.4	5.1	0.45	0.10	28.36	12.9	0.45		brass limiter
5895	7.50	0.95	1.18	1.47	1.84	0.80	0.52	0.64	0	10.9	5.1	0.47	0.11	27.69	13.0	0.42		thinner brass limiter
5896	7.50	0.95	1.44	1.47	1.84	0.80	0.52	0.78	0	12.0	4.7	0.39	0.29	27.05	10.6	0.32		
5897	7.50	0.86	1.31	1.47	1.84	0.80	0.47	0.71	0	14.3	6.2	0.43	0.16	27.43	11.9	0.41		ss limiter
5898	7.50	0.95	1.44	1.47	1.84	0.80	0.52	0.78	0	12.4	4.9	0.40	0.18	27.57	11.0	0.42		increased active anode area to ~1.8 cm
5899	7.50	1.05	1.31	1.47	1.84	0.80	0.57	0.71	0	10.9	4.5	0.41	0.18	26.98	11.1	0.41		
5900	7.50	1.05	1.31	1.47	1.84	0.80	0.57	0.71	0	12.9	6.0	0.46	0.19	26.45	12.2	0.34		
5901	7.50	1.05	1.31	1.47	1.84	0.80	0.57	0.71	0	10.7	4.6	0.43	0.17	25.27	10.9	0.39		
5902	7.50	1.05	1.31	1.60	1.84	0.87	0.57	0.71	0	7.6	3.3	0.43	0.12	24.69	10.6	0.45		
5903	7.50	1.05	1.31	1.32	1.66	0.80	0.63	0.79	0	10.1	3.5	0.35	0.24	25.91	9.1	0.41		
5904	7.50	1.15	1.44	1.32	1.66	0.80	0.69	0.87	0	10.8	4.3	0.39	0.20	26.3	10.4	0.40		
5905	7.50	1.26	1.58	1.32	1.66	0.80	0.76	0.95	0	13.3	6.0	0.45	0.21	24.89	11.2	0.34		
5907	7.50	1.39	1.74	1.45	1.82	0.80	0.76	0.96	0	10.9	4.7	0.43	0.21	22.38	9.6	0.36		beam diags
5908	7.50	1.26	1.58	1.32	1.66	0.80	0.76	0.95	0	10.9	4.7	0.43	0.21	27.28	11.8	0.36		beam diags
5909	7.50	1.26	1.58	1.32	1.66	0.80	0.76	0.95	0	11.7	4.8	0.41	0.21	26.04	10.7	0.39		beam diags
5910	7.50	1.20	1.50	1.26	1.58	0.80	0.76	0.95	0	9.5	3.6	0.37	0.24	24.37	9.1	0.38		
5911	7.50	1.14	1.43	1.20	1.52	0.79	0.75	0.94	0	14.9	5.0	0.33	0.19	28.15	9.4	0.47		
5912	7.50	1.20	1.50	1.14	1.46	0.78	0.82	1.03	0	11.1	3.8	0.34	0.20	26.8	9.2	0.46		
5913	7.50	1.04	1.30	1.14	1.45	0.79	0.72	0.90	0	13.1	4.5	0.35	0.18	28.82	10.0	0.48		
5914	7.50	1.39	1.74	1.45	1.83	0.79	0.76	0.95	0	16.0	6.6	0.41	0.17	28.21	11.7	0.41		beam diags
5915	7.50	1.46	1.82	1.52	1.92	0.79	0.76	0.95	0	11.0	5.1	0.46	0.15	26.25	12.1	0.39		beam diags

F/L-2

Shot 5893



Timescale: Nanoseconds

Units: 1.00E+00
Max: 1.00E+01
Ts(ns): 2.00E+00

Units: 1.00E+00
Max: 1.00E+01
Ts(ns): 2.00E+00

Units: 1.00E+00
Max: 1.00E+01
Ts(ns): 2.00E+00

Units: 1.00E+00
Max: 1.00E+01
Ts(ns): 2.00E+00

Units: 1.00E+00
Max: 1.00E+01
Ts(ns): 2.00E+00

Fig 3

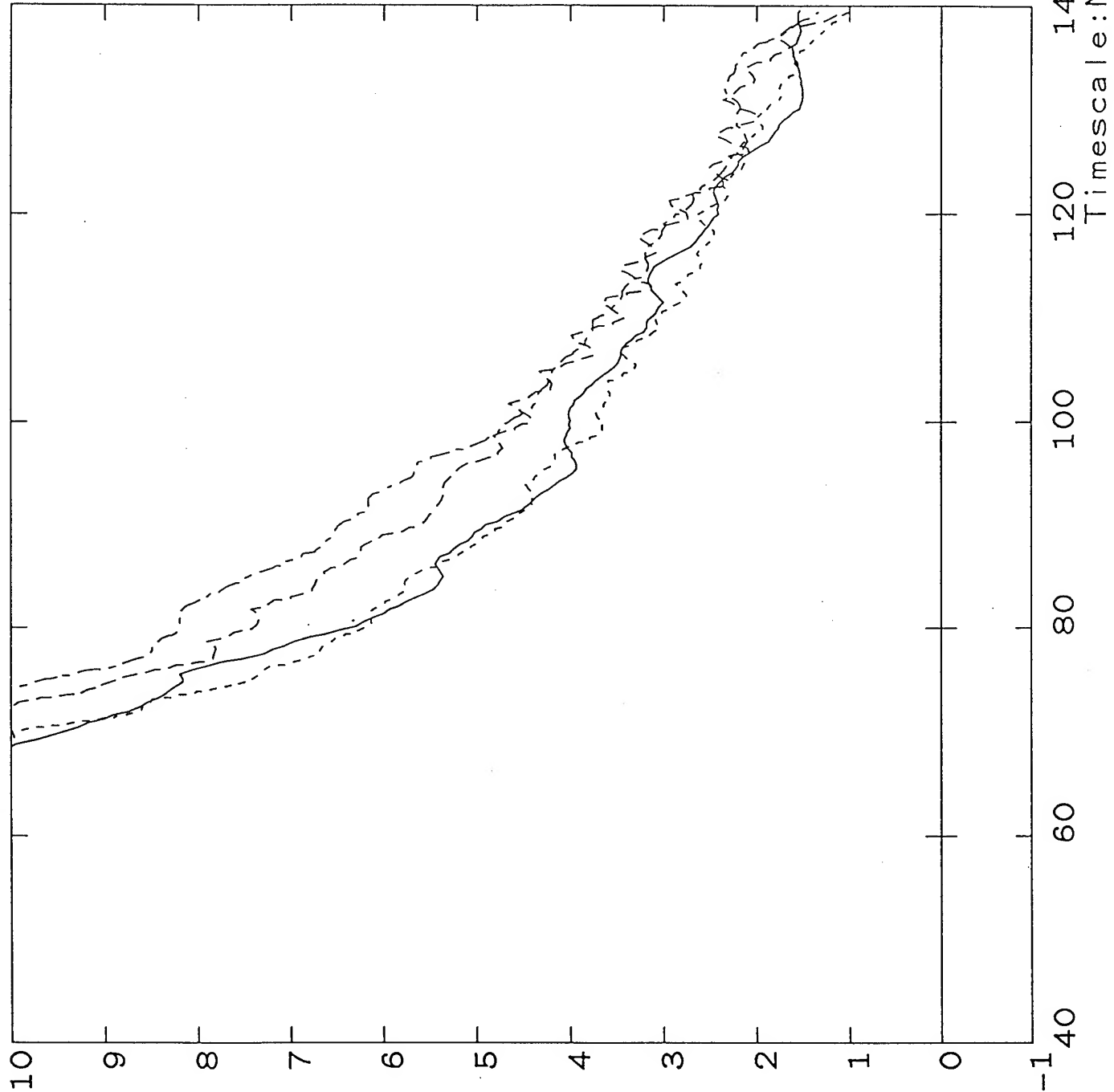
Shot 5893

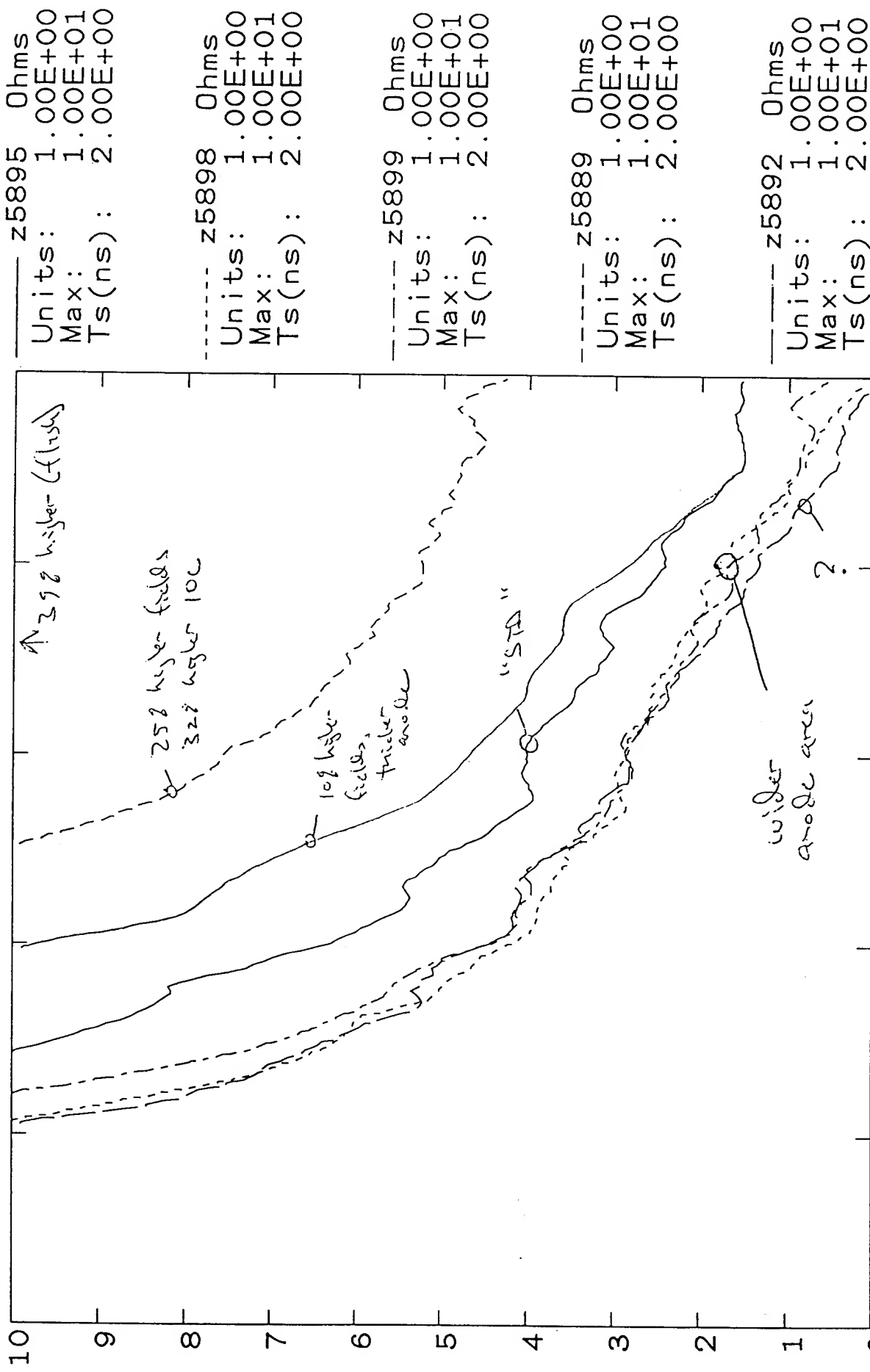
_____ z5895 Ohms
Units: 1.00E+00
Max: 1.00E+01
Ts(ns): 2.00E+00

----- z5827 Ohms
Units: 1.00E+00
Max: 1.00E+01
Ts(ns): 0.00E+00

----- z5817 Ohms
Units: 1.00E+00
Max: 1.00E+01
Ts(ns): -1.00E+00

----- z5822 Ohms
Units: 1.00E+00
Max: 1.00E+01
Ts(ns): 0.00E+00





Timescale: Nanoseconds

Fig 5

Shot 5911

----- z5899 Ohms
Units: 1.00E+00
Max: 1.00E+01
Ts(ns): 2.00E+00

----- z5900 Ohms
Units: 1.00E+00
Max: 1.00E+01
Ts(ns): 2.00E+00

----- z5901 Ohms
Units: 1.00E+00
Max: 1.00E+01
Ts(ns): 2.00E+00

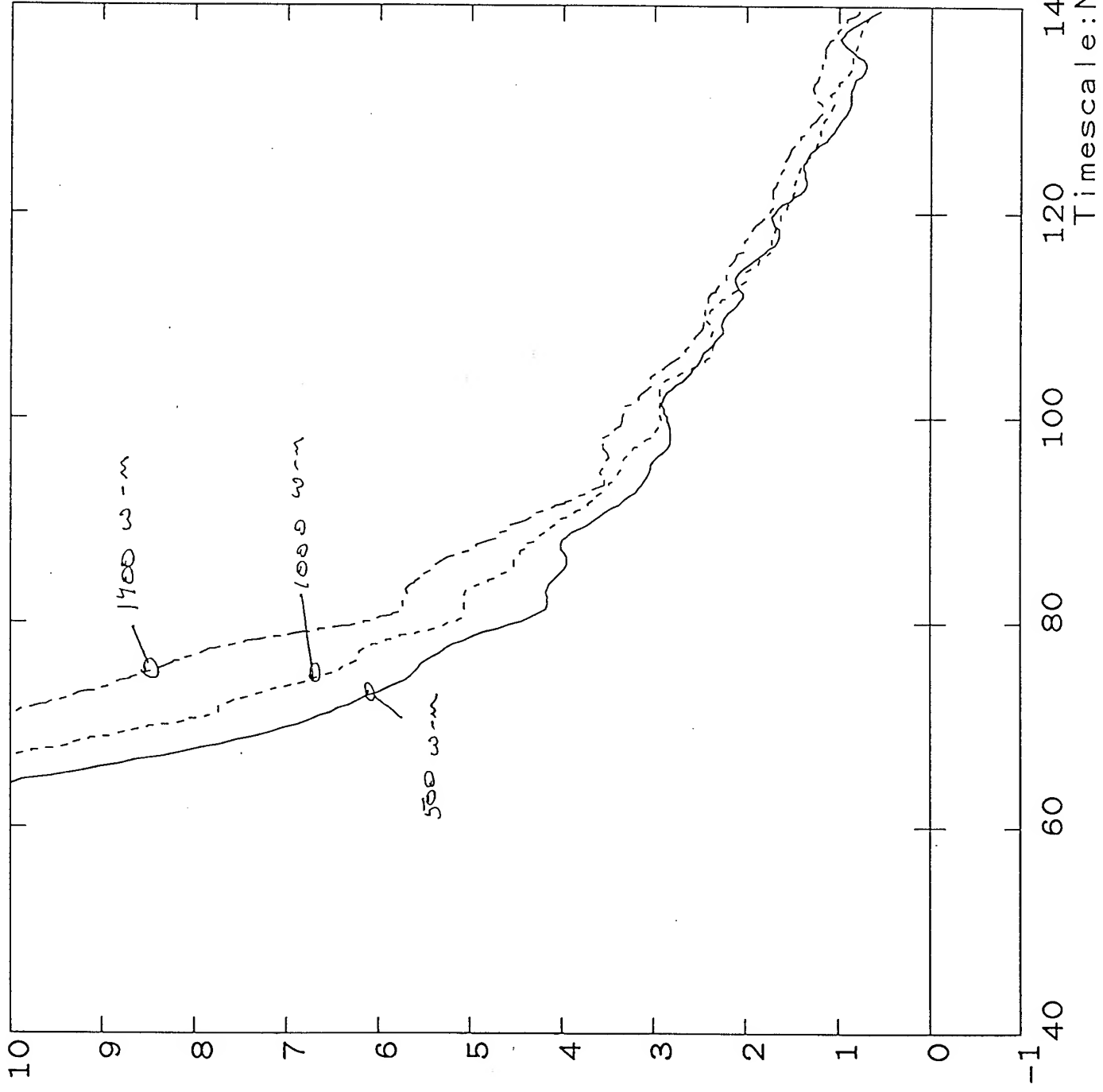
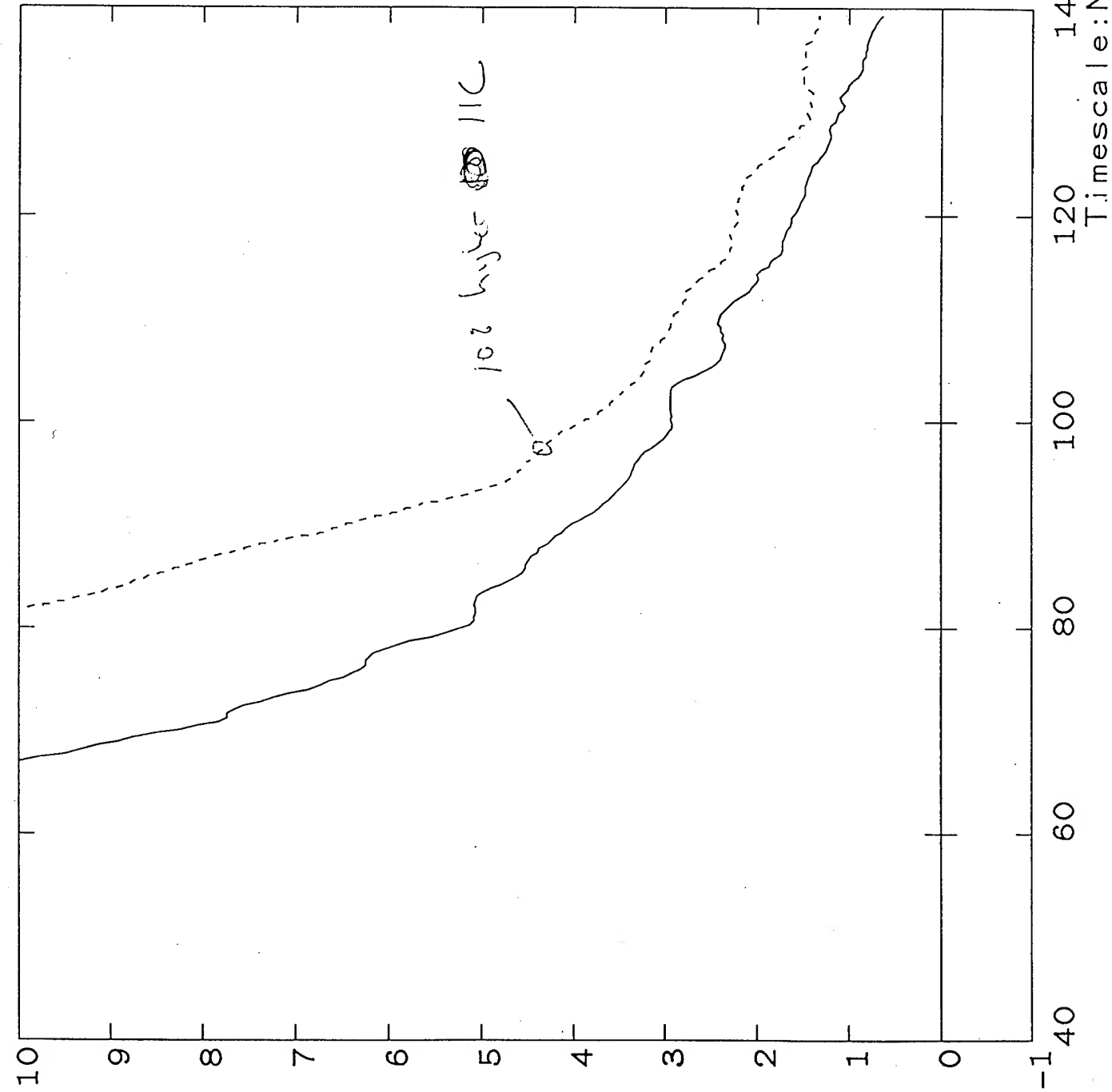


Fig 6

Shot 5893



z5900 Ohms
Units: 1.00E+00
Max: 1.00E+01
Ts(ns): 2.00E+00

z5902 Ohms
Units: 1.00E+00
Max: 1.00E+01
Ts(ns): 2.00E+00

FS7

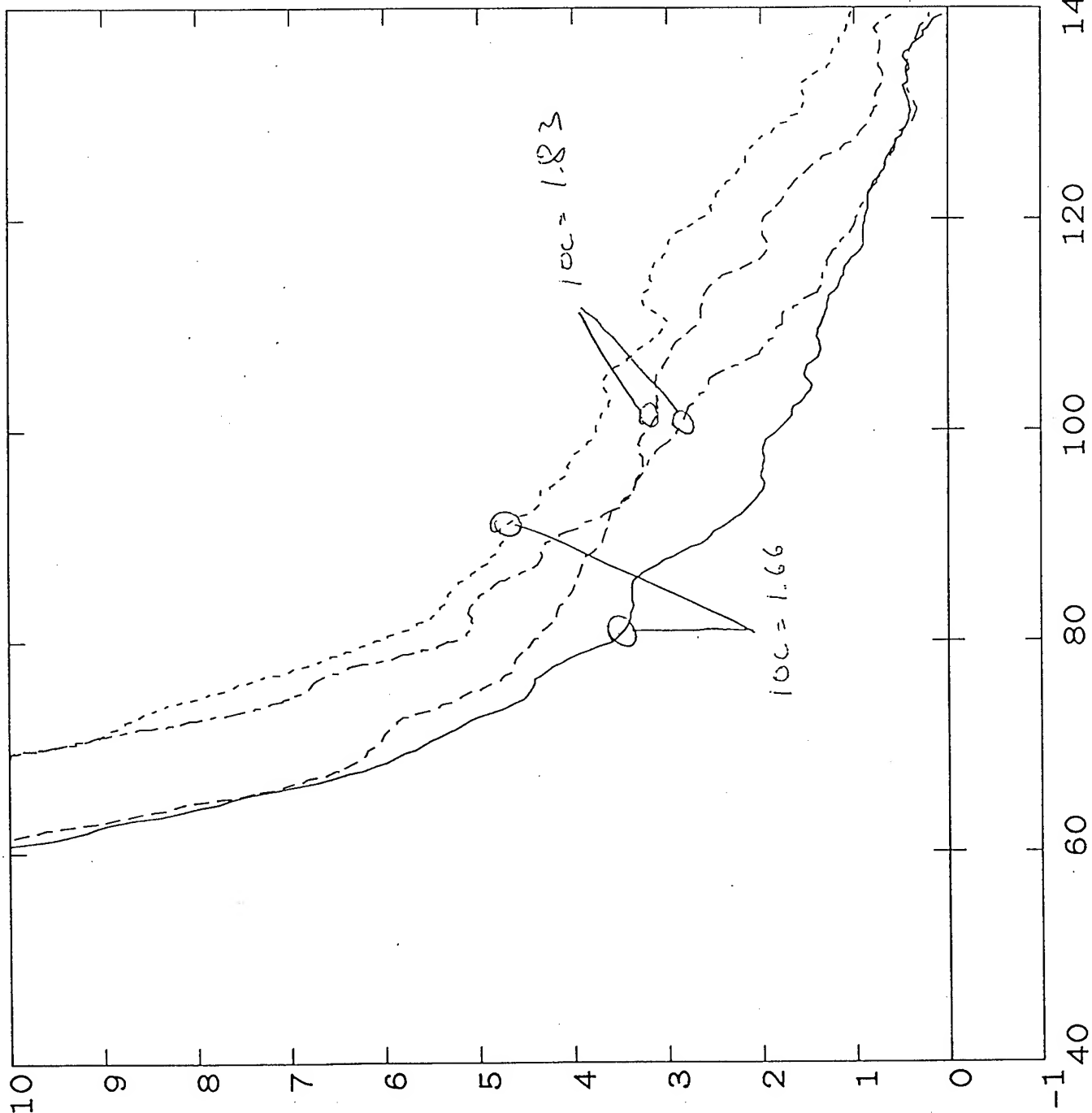
Shot 5911

z5905 Ohms
Units: 1.00E+00
Max: 1.00E+01
Ts(ns): 2.00E+00

z5908 Ohms
Units: 1.00E+00
Max: 1.00E+01
Ts(ns): 2.00E+00

z5907 Ohms
Units: 1.00E+00
Max: 1.00E+01
Ts(ns): 2.00E+00

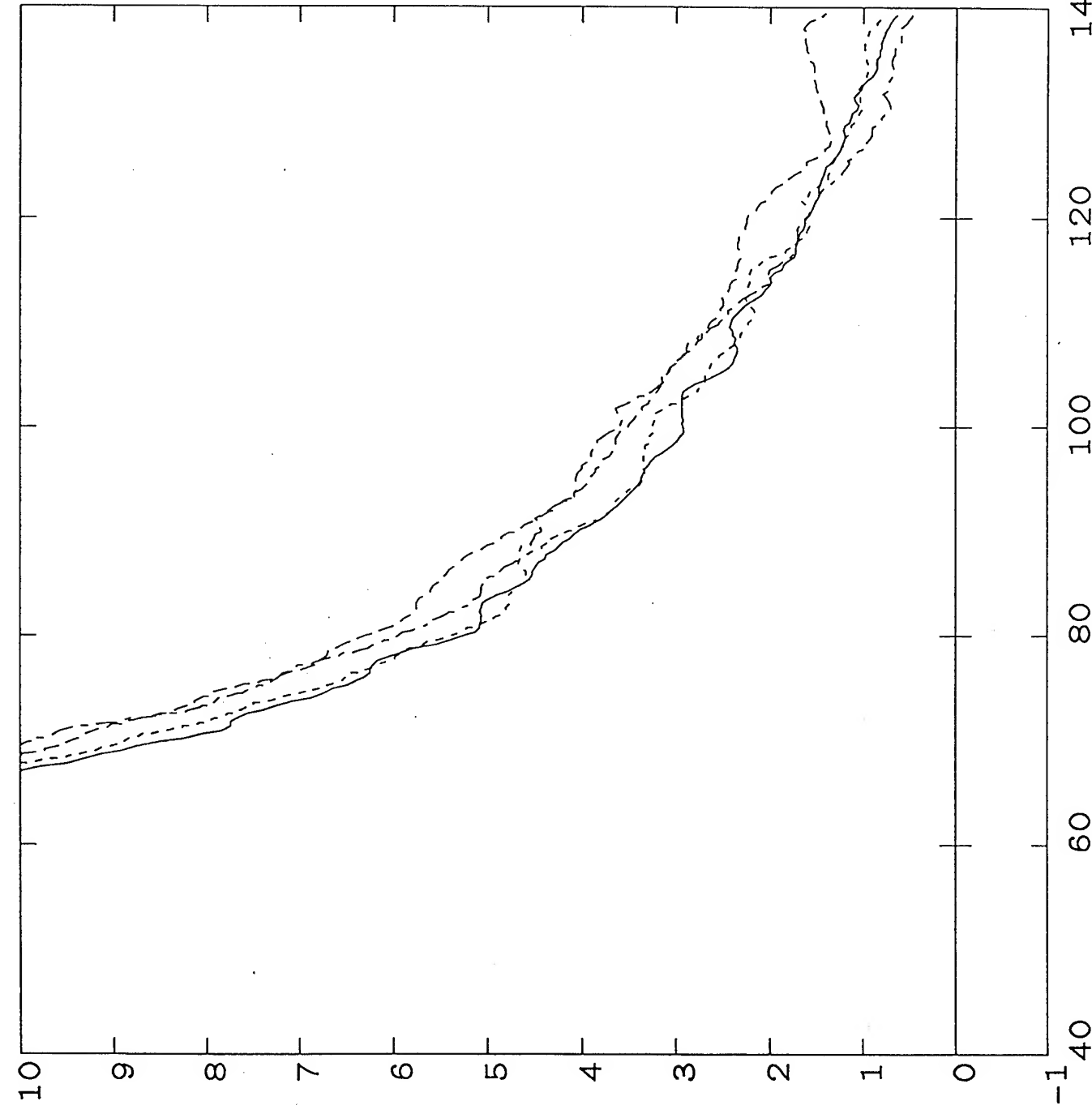
z5914 Ohms
Units: 1.00E+00
Max: 1.00E+01
Ts(ns): 2.00E+00



Timescale: Nanoseconds

F₃₈

Shot 5893



----- z5900 Ohms
Units: 1.00E+00
Max: 1.00E+01
Ts(ns): 2.00E+00

----- z5904 Ohms
Units: 1.00E+00
Max: 1.00E+01
Ts(ns): 2.00E+00

----- z5910 Ohms
Units: 1.00E+00
Max: 1.00E+01
Ts(ns): 2.00E+00

----- z5915 Ohms
Units: 1.00E+00
Max: 1.00E+01
Ts(ns): 2.00E+00

20% higher than 5910

Timescale: Nanoseconds

Fig 9

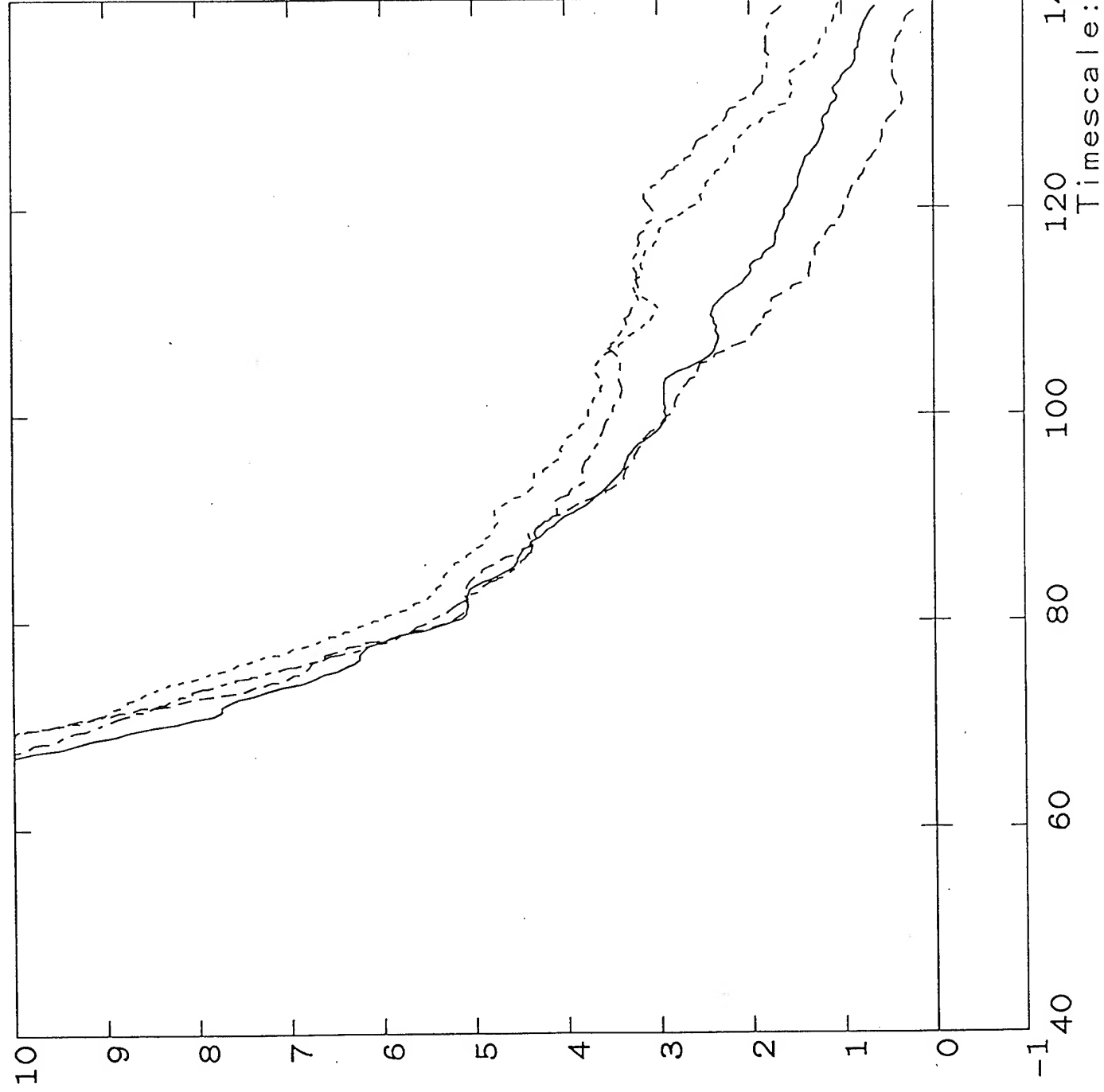
Shot 5893

_____ z5900 Ohms
Units: 1.00E+00
Max: 1.00E+01
Ts(ns): 2.00E+00

----- z5908 Ohms
Units: 1.00E+00
Max: 1.00E+01
Ts(ns): 2.00E+00

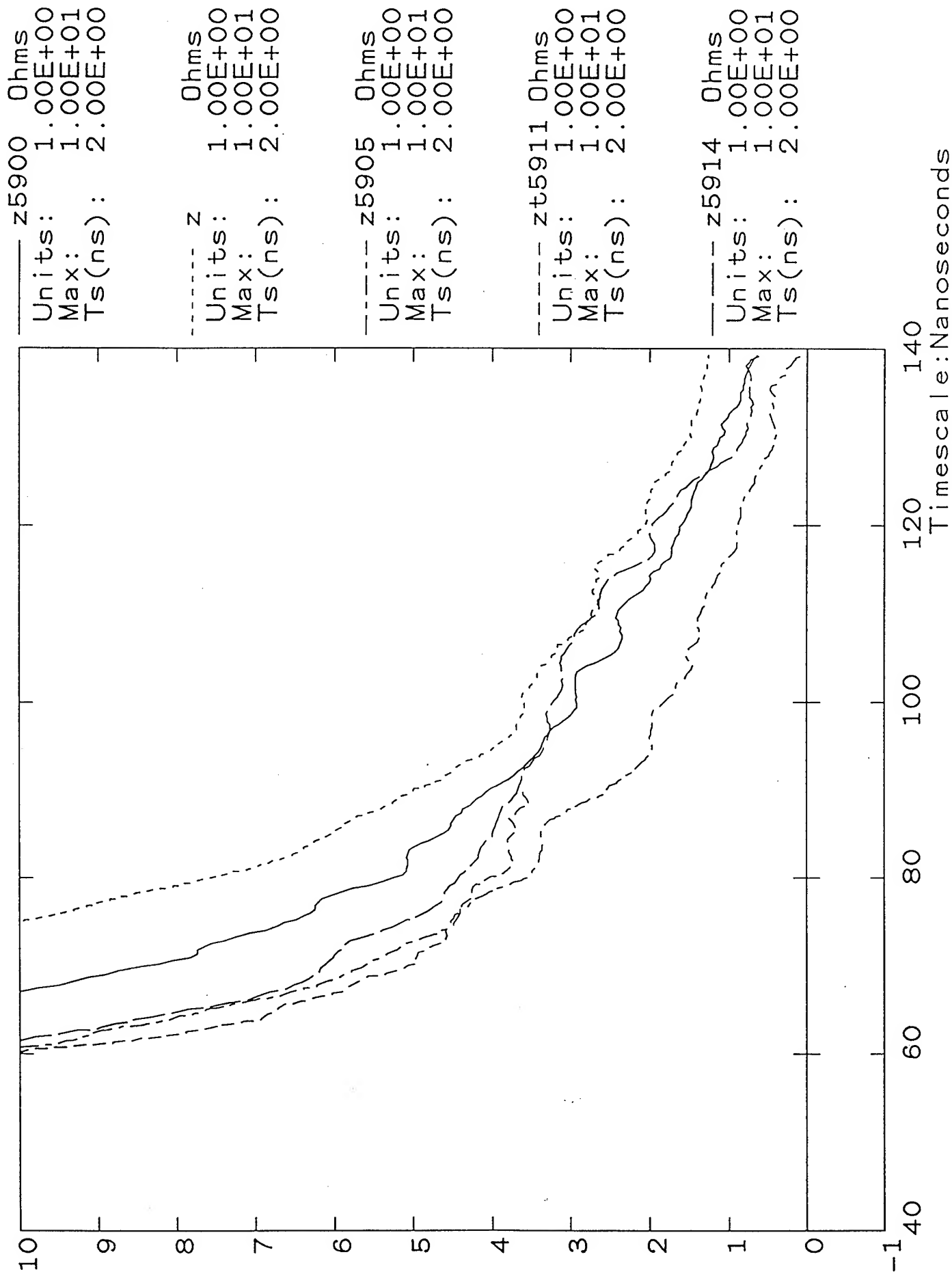
----- z5913 Ohms
Units: 1.00E+00
Max: 1.00E+01
Ts(ns): 2.00E+00

----- z5907 Ohms
Units: 1.00E+00
Max: 1.00E+01
Ts(ns): 2.00E+00



Shot 5903

Fig 10



5915

Aperture ~ 4" from anode

film ~ 1.5" from aperture

spot
displacement,
mm

ring 1 —
2 -1
3 -2
4 -3
5 -4

⇒

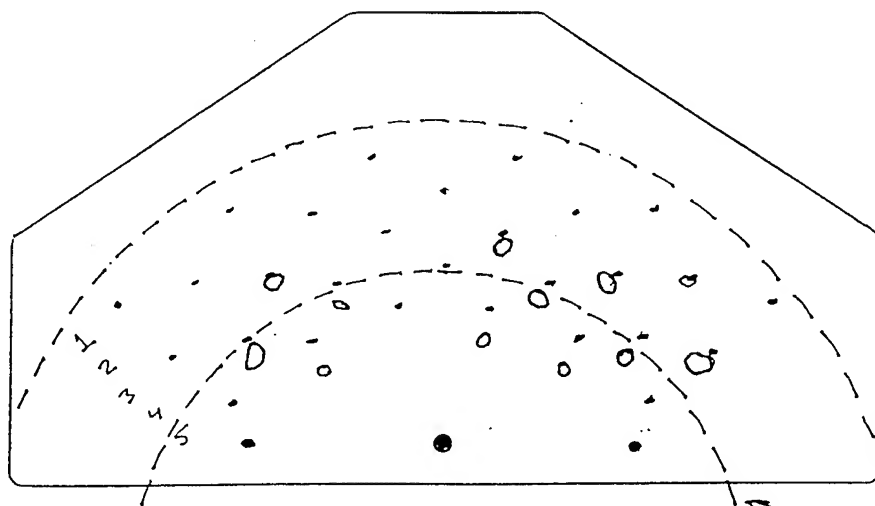
initial
radius



5.3 cm
5.1
4.9
4.7

peak
current
density

$$\text{average bending} = \frac{2.5 \text{ mm}}{38 \text{ mm}} = 65 \text{ mR}$$



cathode
locations

hollow circles = traces of spots

spot
width

$$\left\{ \begin{array}{l} \Delta r_{\text{spot}} \sim 2 \text{ mm, or say } 3 \text{ mm} \\ \Delta r_{\text{hole}} \sim 1 \text{ mm} \end{array} \right.$$

$$\Rightarrow \frac{2 \text{ mm}}{38 \text{ mm}} \approx .05$$

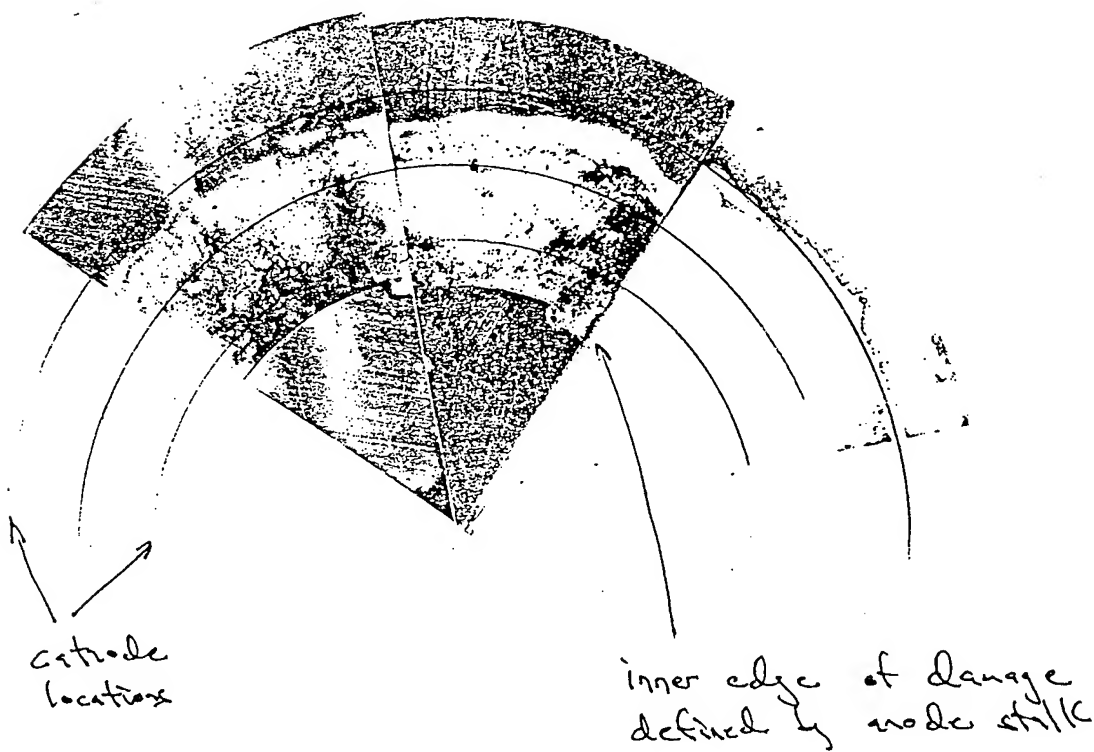
$$\Rightarrow \approx 25 \text{ mR min } \mu\text{Div}$$

Shot 5915

witness plates ~ 4" from anode

brass + Al

Fig 12



PULSED POWER PHYSICS TECHNOTE 94-19

TITLE: ANALYSIS OF RUTHERFORD SCATTERING AND FARADAY CUP DATA
FROM APPLIED-B DIODE RUNS 7 AND 8

Author: D. Hinshelwood

Date: September 21, 1994

Abstract: Rutherford scattering has been used to diagnose the ion beam on some of the shots during applied-B diode runs 7 (spring 1994) and 8 (recently). A new Faraday cup, developed at Cornell, was also used on the last shot of run 8. Data from these diagnostics are discussed and compared with predictions in this note. While there are some unexplained features in these data, and indications that on some shots the ion voltage and/or current may be incorrect later in time, the overall picture is that the extracted ion beam is roughly $2/3$ protonic and consistent with the diode electrical waveforms. Both diagnostics are easy to field, and are seen to work reasonably well in this difficult, high-current-density environment. Future refinements are also possible. The scattering foil can be expanded to sample a larger fraction of the beam, and both diagnostics are well-suited to being fielded in multiple arrays that allow spatial resolution of the beam. Therefore, information on both the total ion current and its distribution can be obtained in the future. I am enthusiastic about the potential of both diagnostics for diagnosing transported ion beams in all of our ion beam research programs.

Rutherford scattering has been used to diagnose the ion beam on some of the shots during applied-B diode runs 7 (spring 1994) and 8 (recently). A new Faraday cup, developed at Cornell, was also used on the last shot of run 8. Data from these diagnostics are discussed and compared with predictions in this note.

The relevant shots are summarized in the spreadsheet on the following page. Columns 5 AND 6 refer to the anode foil, and are described in TN 94-16. Column 7 is the ion beam energy as determined from VCOR and IION. The column "RS" refers to the scattering arrangement used. In arrangement 1, a single, NRL p-i-n was used. This arrangement allowed for some shot-to-shot variation in geometry, so the one useful shot taken has not been analyzed. Arrangements 2 and 3 are shown at the top of Fig 1. Here, 3, 1.9-cm diam apertures defined the beam area on the scattering foil. The 3 SNL p-i-n's were centered in 2.1-cm ID tubes. With arrangement 2, all 3 scatterers were 1.8- μ Al, and the p-i-n's were located 18 cm from the scatterers. Arrangement 3 used 2 thick-Al scatterers and 1 thick-Ta scatterer. The p-i-n's were located 18 cm from the Al scatterers and 88 cm from the Ta scatterer. Arrangement 4 was used during run 8, and is shown at the bottom of Fig. 1. Here, the beam scattered off a piece of thick Al foil glued to a 1.3-cm wide Al bar that was cut to 45 degrees. The p-i-n was located 18 cm from this bar. In all cases the p-i-n's were covered with a 2.5- μ Ti foil. In arrangements 2 and 3, this foil usually survived, as the aperture plate stopped most of the diode debris. With arrangement 4, where this plate was not used, enough debris blew into the tubes to break the foils on most shots.

CALCULATIONS

The predicted, absolute p-i-n signals were calculated in ANALYSIS using VCOR and IION. Flashover is often seen to produce a spurious spike in VCOR. Therefore, on flashover shots (see column 2), VCOR was artificially truncated by drawing a straight line between its value at the time of flashover to zero at the time of impedance collapse. This represents a reasonable guess of the correct voltage. (Note: the ion energy in column 7 of the spreadsheet was calculated using VCOR, rather than the truncated version, so the values given are probably too high for the flashover shots.) The Ti foil thickness on the p-i-n was increased from 2.5 to 3 μ in the code to approximate the additional stopping by the diode dead layer. The code asks for a geometrical factor, which is the product of the fraction of the beam area that is scattered, times the detector solid angle. The factors used here are: 1.1×10^{-6} and 4.6×10^{-8} for the Al and Ta foils in arrangements 2 and 3; and 1×10^{-6} for arrangement 4. Calculated and observed signals for a typical shot are shown at the top of Fig. 2.

Columns 9 and 10 give the ratio of the time-integrated p-i-n signal to the time-integrated predicted signal. Departures of this ratio from unity occur due to some combination of the following: uncertainty in the geometry, stopping coefficients, ion current, and voltage; beam nonuniformity; and the presence of non-protonic ions in the beam. (The p-i-n foil and Kimfol together will stop all carbon ions at these diode voltages.)

shot	comnts	fields	TFM	eff th	delay,ns	ei(kj)	RS	ratio AI	ratio Ta	AI*1.1	Ta*1.1	comnts
5992	lt flash	5992	950	200	47	12.7	1					saturated
5993		~5992	1800	360	60	8.5	2					weak sigs
5994		5994	950	160	73	11.5	2					weak sigs
5995		5994	950	205	84	7.8	2	0.17		0.19		cent ques
5996		5994	950	150	45	10.1	2	0.31		0.34		cent ques
5997	no pulser	5994	950	213	0	5.7	2	0.34		0.37		cent ques
5998		5994	180	25	59	9	2	0.31		0.34		
6003	flash, no pulser	no field, plug	950	215	0	7.8	3	0.08	0.09	0.09	0.10	weird shot
6004		x5584, no plg	950	160	38	8.8	1					
6005	lt flash, no puls	~6004, plug	950	200	0	10.3	3	0.04	0.07	0.04	0.08	pin1 possibly
6006	lt flash, no puls	~6005, thn plg	950	160	0	5.4	3	0.09	0.07	0.10	0.08	out of
6007	lt flash, no puls	6006, plug	950	211	0	10.4	3	0.08	0.06	0.09	0.07	alignment
6010	flash	5992	950	182	30	10.6	3	0.63	1	0.69	1.10	on shots
6011	flash	6011	360	72	50	12.3	3	0.48	0.61	0.53	0.67	5998-6013
6012		6011	1800	261	74	8.3	3	0.38	0.31	0.42	0.34	
6013	flash	6011	950	268	58	10.3	3	0.44	0.5	0.48	0.55	
6091	flash	opt	950	165	19	7.6	4	0.74		0.81		
6092	flash	opt, K x .95	950	200	33	7.2	4	0.6		0.66		
6093	flash	opt, K x .95	950	240	59	9.6	4	0.63		0.69		tail (2nd hump)
6094	flash	6019	950	160	63	7.3	4	0.85		0.94		tail (2nd hump)
6095	flash, no pulser	6019	950	257	0	6.1	4	0.29		0.32		
6096	flash	6019	950	85	60	7.9	4	0.89		0.98		
6097	flash	sim 6019	950	250	76	7.7	4	0.59		0.65		
6098	6 mm gap	6019	950	225	79	7	N					no pin
6099	wider area	6019	950	130	64	4.5	4	0.29		0.32		
6100	wider area	6019	950	275	58	8.9	4	0.82		0.90		tail
6101	slightly wider	6019	320	50	72	8.8	4	2.6		2.86		
6102	area here on	6019	320	20	78	7.3	4	0.82		0.90		
6103		6019	950	216	81	8.9	4	0.47		0.52		tail (2nd hump)
6104	no pulser	6019					4	0.27		0.30		tail
6105	no pulser	6019	360	9	0	4.8	4	0.43		0.47		tail
6106		6019	360	37	33	4.2	4	0.17		0.19		
6107		6019	950	225	0	11.1	4					no HP
6108		6019			91	8.7	4	0.46		0.51		tail
6109		prefire					4					
6110		6019	300	6	104	6.2	4	1		1.10		tail

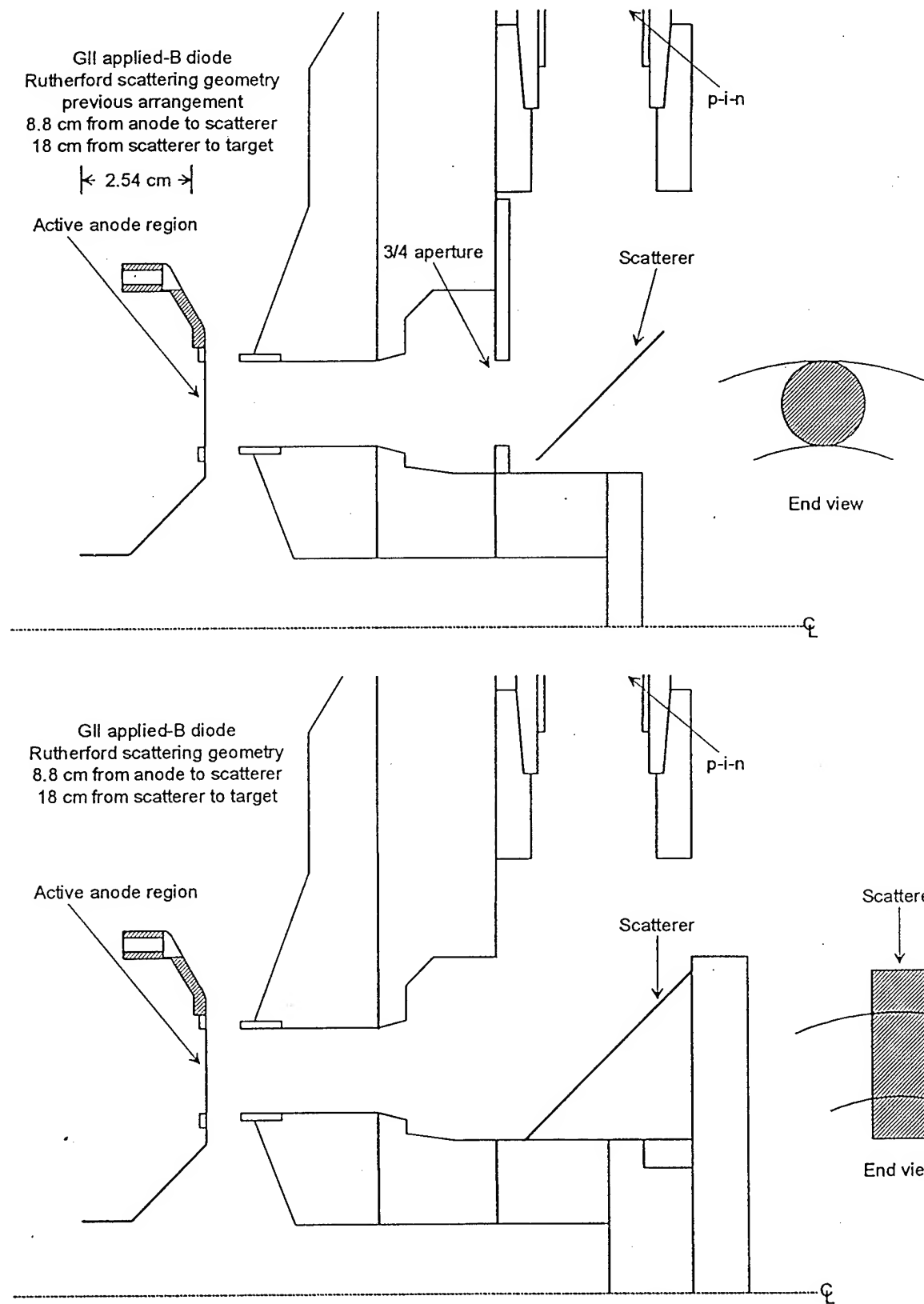


Fig. 1: Rutherford scattering arrangements used in runs 7 (top) and 8 (bottom).

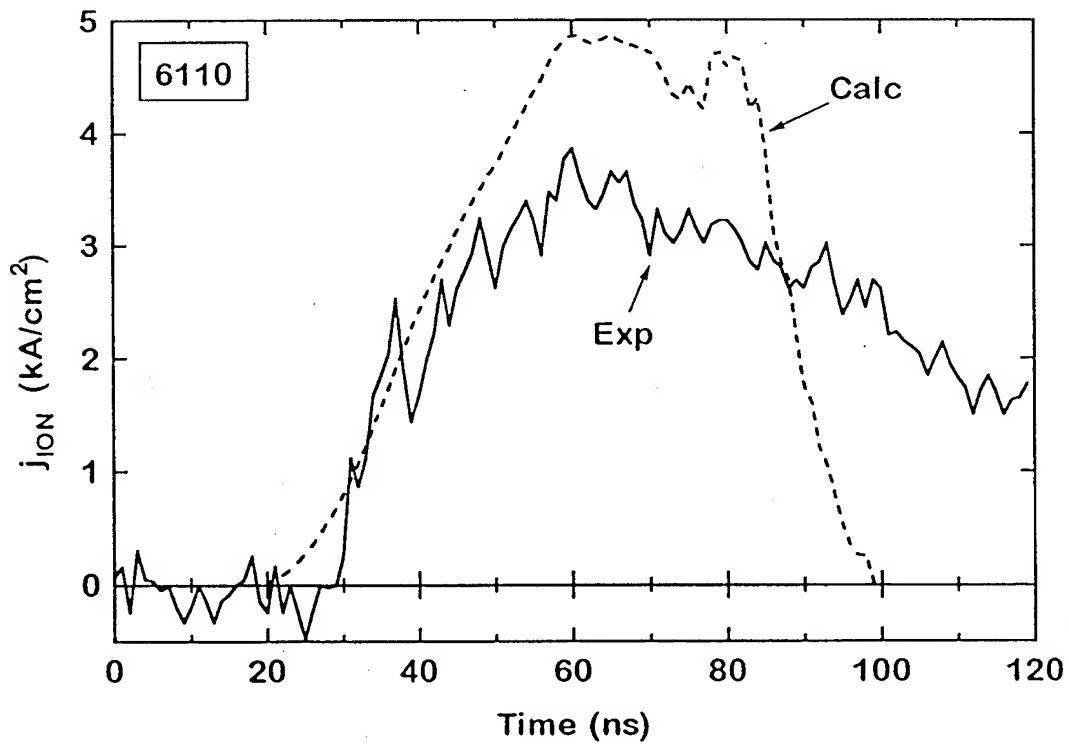
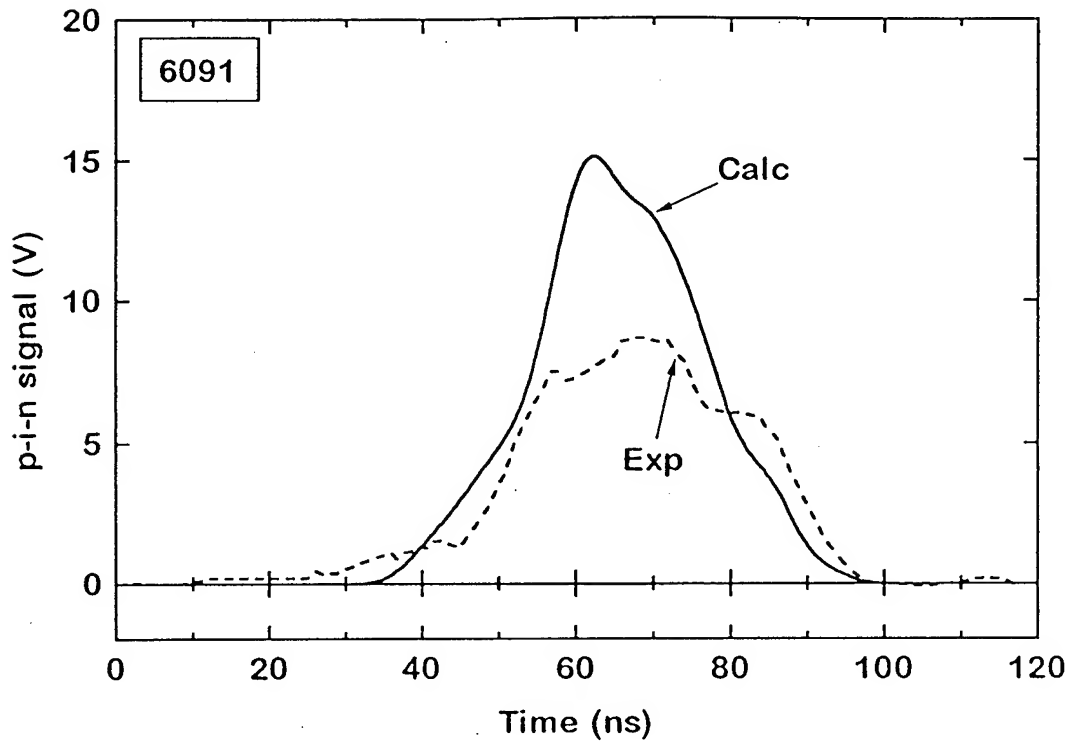


Fig. 2: Calculated and observed signals from Rutherford scattering (top) and the Cornell Faraday cup (bottom).

UNCERTAINTIES

Calculation of the yield requires the fraction of the beam intercepted by the detector, the detector solid angle, and the scattering angle. Inspection of the end views in Fig. 1 shows that with arrangements 2 and 3, the intercepted beam fraction depends on the beam width and radius. If the beam bends inward, as was observed on this run, the intercepted fraction will decrease. This results in an estimated uncertainty of 10-20 percent. The scatterer shape in arrangement 4 was chosen to reduce this problem. (Ideally, a pie-shaped scatterer would be used, eliminating this uncertainty completely). The uncertainty in the detector solid angle is estimated at about 5 percent.

The average scattering angle depends on the distribution of ion initial radii and trajectories, which may well vary as the field geometry is changed. (The possible scattering angles in these arrangements range from about 76 to 96 degrees, representing a factor of two variation in the predicted yield.) One shot, 6098, was taken with a shadowbox plate at the Kimfol location. The data from this shot indicates an average scattering angle of 86 degrees, which results in a 10 percent decrease in the predicted yield from that at the nominal 90 degrees. The ratios in columns 9 and 10 are based on calculations for a 90-degree scattering angle. The ratios are multiplied by 1.1 in columns 11 and 12 to account for the assumed, average angle of 86 degrees. The uncertainty in the yield associated with the scattering angle is estimated to be about 15 percent. Taking everything together, geometry-related uncertainties of 15-20 percent for arrangement 4 and 20-25 percent for arrangements 2 and 3 are assumed.

Since the ions scattered from a thick target have an average energy on the order of half of the initial energy, which is itself rather low on these shots, attenuation by the Kimfol, air, and p-i-n foil has a big effect. This results in a calculated scattering yield that is more than proportional to the ion voltage and strongly affected by the assumed dE/dx of the target, foils, and air. For example, the yields calculated for these shots using the upgraded stopping coefficients (see TN 94-17) were 20-30 percent less than those calculated using the old values. Based on Ziegler's claim of 3-5-percent accuracy in dE/dx , an uncertainty of 5-10 percent is assumed here.

The current and voltage waveforms have calibration uncertainties on the order of 5 percent each. In addition to this are possible waveshape errors. For example, the inductive voltage correction is susceptible to noise on the diode current, and the ion current measurement is susceptible to shielding of the dB/dt loops. The total current- and voltage-related uncertainty in the calculation is estimated to be about 15 percent.

The composite uncertainty in the yield calculation is thus about 25 percent for arrangement 4 and 25-30 percent for arrangements 2 and 3. This uncertainty has both random and systematic components, although I believe that the former dominate.

On run 8, the p-i-n foils were destroyed on most shots, allowing debris to deposit on the detectors. The small, recessed detectors are difficult to clean and it is possible that debris may have been left on some shots. This may explain, for example, the very low yield on shot 6106.

A timing uncertainty of roughly 3 ns is assumed.

RESULTS

The p-i-n's were shielded with about 1/4 in of Pb which virtually eliminated Brems pickup.

Arrangement 2 allowed three identical measurements that can be compared with each other and with the three ion current signals. The average variation among the three p-i-n signals on shots 5995-5998 was 10-20 percent. Similar variations in the current signals were observed, but the two were not azimuthally correlated. (The three dB/dt loops were located at 12, 4, and 8:00, and the scattering apertures were located at 11, 3, and 7:00). Since these variations are within the experimental uncertainty discussed above, the lack of correlation may not be meaningful.

Figure 3 shows calculated and observed signals for four shots. These shots are chosen to illustrate the range of agreement in shape and timing, and in these graphs the two traces are normalized to each other so that the shapes may be easily compared. The first few shots in run 7 had a much larger predicted/observed signal ratio late in time, while the reverse was observed on a few shots in run 8 (see shots 5998 and 6103 in the figure). The level of shape agreement seen on shot 6013 is representative of most shots. On some of the shots at the end of run 8 (see the last column in the spreadsheet) the observed signal has an unphysically-long tail. On these shots the signal level was not particularly high, so the detector was not saturated. Perhaps the detector was beginning to fail.

In general, the shape and timing discrepancies observed with the pinch-reflex diode are not observed here. On run 7, the observed signal is delayed 5 ns on the average relative to the predicted signal. This is seen at both detector distances (as in shot 6013) and may result from some timing error. On run 8, the timing agreement is better.

Subject to the abovementioned uncertainties, the ratios in columns 11 and 12 of the spreadsheet can give information on the proton content in the beam. By averaging enough shots, the random errors, including beam non-uniformity, can be smoothed out. The comparison of integrals may not be meaningful for shots with poor shape agreement, or especially the shots with tails on the observed signal. Nonetheless, here goes: First, note that the shots with no pulser exhibited lower ratios on the average. This is encouraging as it suggests that the EMFAPS is increasing the proton content of the beam. Shots 6010-6013 give average ratios of 0.53 for the Al and 0.67 for the Ta targets. The difference may not be statistically significant for the small number of shots, and is within the experimental uncertainty. The average ratio for all pulser shots in run 8 is 0.82. Eliminating the shots with tails, and the two shots with the highest and lowest (shots 6101 and 6106), leaves 7 shots with an average ratio of 0.66.

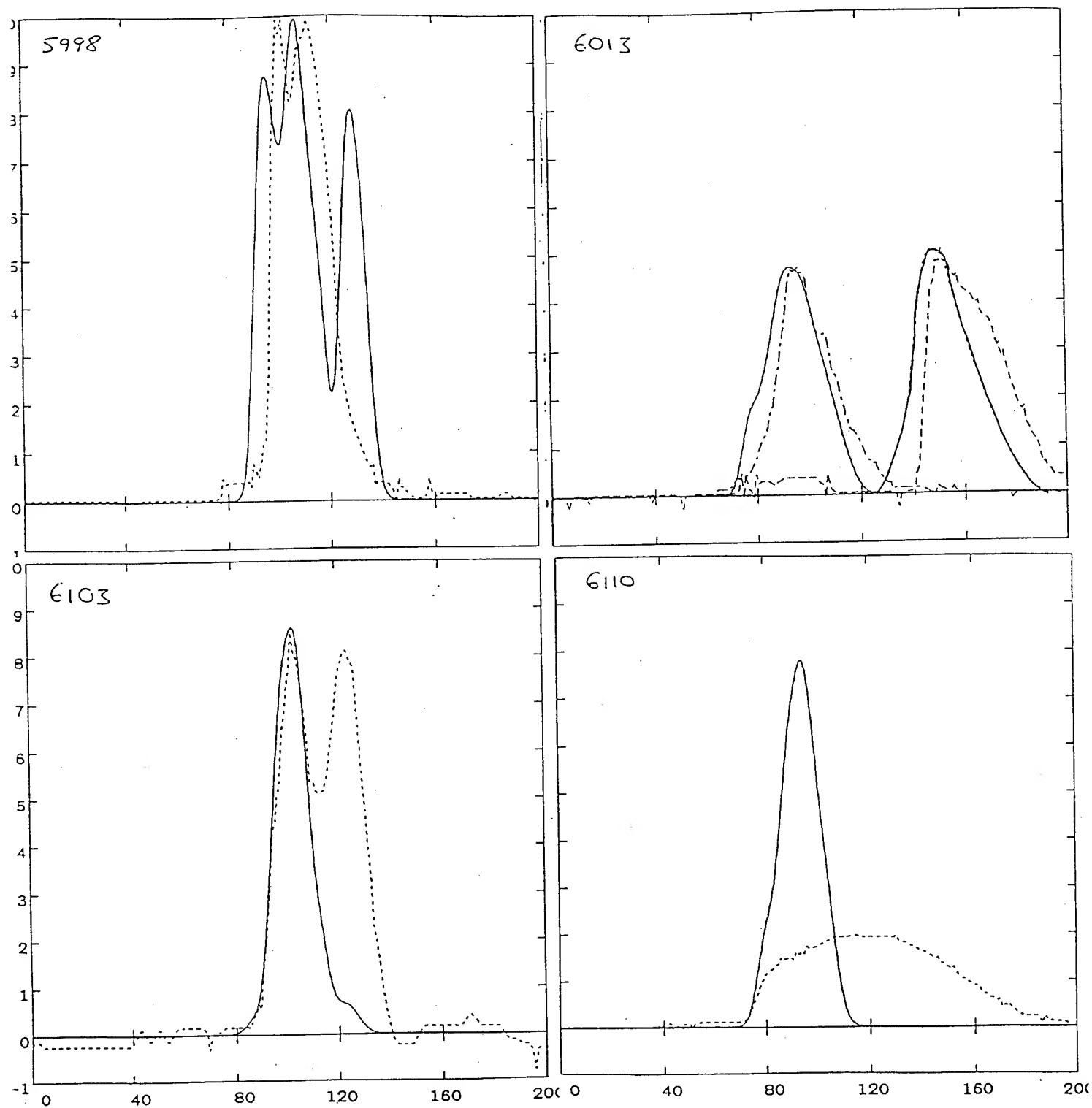


Fig. 3: Calculated (solid) and observed (dashed) Rutherford scattering signals from four shots. In this figure, the signals are normalized in amplitude to illustrate shape fidelity.

FARADAY CUP

The calculated and observed signals from our one shot with the Cornell Faraday cup are shown at the bottom of Fig. 2. The design of this cup was provided by Joe Olson. The main features of this cup are the large (5-mm diam) aperture, the lack of bias voltage, and the low ($0.05\text{-}\Omega$) shunt resistor. The cup was located in 1-Torr air, about 1.5 cm behind the Kimfol. The tail on the observed signal is not understood at present. Other than this, the agreement with prediction is good, and consistent with the Rutherford scattering results. (The Kimfol will stop all singly-, and most of the doubly-, charged carbon ions, but the cup should record higher charge states. Therefore, a somewhat higher ratio of observed to predicted signal might be expected, relative to that from Rutherford scattering.) The Faraday cup is an attractive diagnostic because the signal is relatively independent of the diode voltage, and most of the geometric uncertainties involved in Rutherford scattering are avoided.

CONCLUSIONS

While there are some unexplained features in these data, and indications that on some shots the ion voltage and/or current may be incorrect later in time, the overall picture is that the extracted ion beam is roughly $2/3$ protonic and consistent with the diode electrical waveforms. Both diagnostics are easy to field, and are seen to work reasonably well in this difficult, high-current-density environment. Future refinements are also possible. The scattering foil can be expanded to sample a larger fraction of the beam, and both diagnostics are well-suited to being fielded in multiple arrays that allow spatial resolution of the beam. Therefore, information on both the total ion current and its distribution can be obtained in the future. The use of permanent magnets may allow the Faraday cup to be used outside the cathode return flux, and even in experiments with the pinch-reflex diode. I am enthusiastic about the potential of both diagnostics for diagnosing transported ion beams in all of our ion beam research programs.

PULSED POWER PHYSICS TECHNOTE 95-01

TITLE: ANALYSIS OF APPLIED-B DIODE RUN 5

Author: D. Hinshelwood

Date: January 22, 1994

Abstract: This is one of a series of teknotes, composing a first cut at analysis of the reams of applied-B diode (MID) data we have acquired so far. The purpose here is to get the data out on the table and to identify the best shots, obvious trends, and any unexpected results.

There is a clear hastening of the ion-current onset with an increase in the delay time, reduction in the gap, and decrease in the field. Before closure, the impedance is higher at higher fields and shorter delays. For very short, or zero, delays, the impedance is markedly higher and closure appears to be significantly reduced. For most of the shots examined here, the time of closure appears to be independent of the field magnitude, gap, or pulser delay (for delays of 60 ns or more). The seeming independence of closure time of field amplitude may be reasonable, assuming that the electrode plasmas are collisional enough to move across the field lines. What is unexpected is the seeming independence of closure time on diode gap. Even more interesting is the strong delay in closure that occurs when the foil is not pulsed, or pulsed soon before the shot.

For proper MID performance, we need fairly rapid current onset, an ability to control the impedance, efficient ion production, and a relatively slow impedance collapse. The shots in this run show that the first three are achievable. The main problem is the rapid impedance collapse, and this is where our thoughts should focus.

INTRODUCTION

This is one of a series of teknotes, composing a first cut at analysis of the reams of applied-B diode (MID) data we have acquired so far. The purpose here is to get the data out on the table and to identify the best shots, obvious trends, and any unexpected results. No attempt will be made to draw final conclusions yet. To date there have been ten MID runs. The first three runs used wax-filled-groove, hereafter referred to as passive, anodes. Run 4 was our only attempt with POS-driven, EMFAPS anodes. Run 5 was the first run using a pulser to drive the EMFAPS anodes. On run 6, EMFAPS anodes were used without the pulser. In this case the early electron loss current returning through the anode foil is used to form the anode plasma. These will be referred to as limiter-EMFAPS anodes, although a physical limiter was rarely used. Runs 7-10 used pulser-EMFAPS anodes. Results from run 8 have already been presented in TN 94-16.

MASTER SPREADSHEET

The enclosed spreadsheet lists all shots of this run other than short-circuit shots. This is part of an evolving master spreadsheet that will summarize all of our MID data. The first page gives the basic shot parameters. The second and third columns refer to the distances, in mm, between the cathode and anode surfaces, and the extension of the cathode tips (see Fig. 1). The difference between these numbers gives the closest A-K distance. The next four columns give the voltages, in kV, of the four magnetic field banks.

In analyzing MID data, the characteristics of the anode foil are somewhat of a question mark. Not only have the foils not been completely characterized, but we don't know exactly how the foil characteristics affect diode operation. The anode foils are described by at least two parameters: the thickness and resistivity. The sputter-deposition rate of the anode foil is roughly proportional to the power fed to the sputtering guns. The eighth column refers to the Watt-minutes of the sputtering process and is thus a measure of the anode film thickness. A nearby thin-film monitor is used to diagnose the deposition process, and indicates a film thickness of about 2 \AA/W-min . (I am working with John K. to measure the resulting film thicknesses directly.) Subsequent to this run, we began characterizing the foils by four-probe resistance measurements, which give an effective thickness (column 9) much less than the physical value. The increased resistivity of the foils is seen to depend on the vacuum conditions during deposition. The origin of, or practical effect of, the foil resistivity is not known at present. Data from later runs affords comparisons of foils with both different thicknesses and resistivities, and indicates that diode behavior is not strongly affected by these parameters.

The tenth column refers to the presence of a flux-excluding insert embedded in the anode, not used for this run. Column 11 gives the peak foil current in kA. The next six columns give some shot parameters in normalized units; these are better displayed on the second sheet. Finally, columns 18 and 19 give the corrected voltage and ion current at peak ion power.

The second sheet presents some of the shot parameters in more useful form. (Obvious dud shots, such as 5828, are not included on this sheet.) Columns 7-9 give the ratios of the other field settings to IOC. These three numbers are sufficient to describe the shape of the applied field. Column 10 gives the delay, in ns, from the start of the anode foil current to the start of the diode open-circuit voltage waveform. The next three columns give the diode and ion beam energies, in kJ, and the energy efficiency, e_i/e .

Columns 14 and 15 give the ion and total energies, normalized to shot 6019 by assuming that the energies scale as the peak open-circuit voltage squared. Shot 6019 had a typical open-circuit voltage for a 32 kV Marx charge, so the values in columns 14 and 15 might be expected if the shots were repeated at 32 kV. (A 26 kV Marx charge was used for this run.)

Column 16 gives the ratio of diode corrected voltage to ion current at peak ion power.

ELECTRICAL WAVEFORMS

Several key waveforms describe the diode behavior. VD is the voltage at the insulator. IK4T is the average of three B-dot loops located just outside the outer cathode tip (see Fig. 1) and is thus the total diode current. IK3T is the average of three loops located just inside the outer tip, and represents the sum of the ion current and the electron current emitted from the inner tip. The six IK4 and IK3 loops are recorded individually. IK2T is the analog sum of three loops just outside the inner tip, and gives the electron current emitted from that tip. Other diode waveforms include the shunt and door currents, ISHT and IOUT. From these, several traces are calculated. VCOR is the corrected voltage, and Z is the ratio of VCOR to IK4T. The ion current, IION, is given by the difference of IK3T and IK2T. The diode and ion power and energy are also calculated.

Calibration of the diode monitors based on short-circuit shots is discussed in TN 94-09. On short-circuit shots the calibrations are constant to within about 5 percent. Other factors may come into play on diode shots, such as possible bombardment of the monitors by the ion beam.

Other waveforms recorded include the pulser output, the foil current (measured close to the foil), and the magnetic field coil currents.

RUN FIVE OVERVIEW

A Marx charge of 26 kV was used on this run, as compared to 32 kV on recent runs, and 36 kV on other Gamble II experiments.

This run comprised 23 shots with one dud. For most MID shots on other runs, cathode tips with 4-mm extension were used, but 6-mm tips were used on the shots in this run. The first five shots were taken with a smaller A-K gap. The 8-mm gap used on succeeding shots is typical of that used on the passive shots.

All anode foils on this run were nominally similar, and relatively thin compared to most anodes used on later shots. Also, the foils on this run were coated at higher base pressures than later foils and so were probably relatively resistive. Concurrent bench measurements indicate fairly uniform foil breakdowns. The active anode region (nominally defined by the width of the aluminum that is masked from deposition of the copper current contacts) was about 1.5 cm wide on this run. Pickup problems prevented an accurate measurement of the foil current on this run, so the values given in the spreadsheet are approximate. The first of several pulser versions was used on this run, producing a peak current of about 30 kA. Cable breakdowns over the course of the run reduced this to about 20 kA by the end.

The measured field coil currents on this run are consistent with the bank charging voltages.

The shunt and door currents agree with IK4T to within the measurement accuracy. This gives confidence in the total diode current measurement and indicates that measurable current does not flow in vacuum upstream of the diode. Also, the inner cathode current IK2T is small on all shots in this run, so that possible errors in this measurement are not a concern. IK3T is thus the key diagnostic. Emission of electrons from the Kimfol would cause the ion current to be over-estimated, although the consensus is that this is not likely. Any ion current to the outer tip would be recorded as electron current. Also, ion bombardment of the loops could cause them to fail. I believe that these are both unlikely, but not impossible, on this run: The outer edge of the ion emission area was inside the outer cathode diameter, and data from later shots indicates that the ion trajectories were inward.

No beam diagnostics were used on this run.

ELECTRICAL DATA

Figures 2-5 show electrical data from shot 5818. These are typical waveforms from the main field configuration used on this run. Fig. 2 gives the ion and total currents, corrected voltage, and impedance. This is the standard graph format used to characterize MID shots. The diode produces a healthy ion current with high efficiency, but with a quickly falling impedance that reduces the voltage to an uninteresting value. Analysis shows that energy coupling from the machine is hurt more by the low, late-time impedance than by the early, high impedance. The ion and total currents appear to start at the same time. Figures 3 and 4 show the individual IK4 and IK3 signals. The variations here are typical of the run. Figure 5 compares the insulator and corrected voltages, and the diode, door, and shunt currents. The peak insulator voltage on this shot is close to the flashover limit. Thus, while the early, high impedance does not have a large, direct effect on energy coupling to the diode, it has a large indirect effect in preventing operation at higher Marx charge.

Note that the electrical behavior beyond 120 ns is unphysical: the corrected voltage reverses sign while the current does not. This is also seen with the pinch-reflex diode, but in that case the action is already over by then and nobody worries about it. I do not understand the cause of this discrepancy at present. Since the three current monitors all agree, I would suspect some late-time phenomena in the diode voltage monitor. The bottom line here is that we have to be careful in interpreting the final impedance fall. On shot 5818, the time of apparent shorting-out is consistent with an extrapolation of the earlier impedance (when the waveshapes are reasonable) and so may be correct.

Figure 6 shows a composite of IK2T traces from all other shots on this run (except 5829 and 5830, where there were problems with the scope channel). On most of these shots the electron current emitted from the inner cathode was negligible. These shots all had the same field shape. The other shots used a different field configuration as discussed below.

Thirteen of the 22 shots had the same field shape, and seven of those had the same field amplitude. These seven, 5817, 5816, 5818, 5824, 5830, 5829, and 5823, will be discussed first. They differ only in the pulser-to-generator delay. Shot 5817 (Fig. 7), with a short delay, is typical of limiter-EMFAPS shots: the diode current onset is quite late, and the diode impedance remains higher than when the pulser is used. Shot 5816 had conditions and results similar to 5818. Shot 5824 (Fig. 8), with a longer delay than 5818, had a very high efficiency and gave the best normalized ion beam energy of this run. Shots 5823, 5829, and 5830 all had the longest delay. Shot 5830 (Fig 9) shows a more rapid current onset than 5818, with similar overall results. Shot 5823 (Fig. 10) is an interesting comparison with 5830. The two are similar except that 5823 shows a very low ion efficiency. One explanation is that for some reason the IK3 loops failed on this shot and the ion current was actually much larger (all three loops gave a similar, small signal). However, the ion current is low from the very beginning, so the loops must have failed very early. If the ion current is correct, we have to explain why the electron current increased to provide the same total current. Such phenomena would be indicative of a significant role for the self-magnetic field. Shot 5823 is one of three shots in this run exhibiting anomalous behavior. Shot 5829 is another one, as it shows a very high early impedance typical of limiter-EMFAPS shots. On this shot there may have been a problem with the foil breakdown.

Impedance traces for the above shots are compared in Fig. 11. As the delay increases, the current onset begins earlier. Except for the earliest delay, the apparent time of diode closure is not correlated with delay. This is also seen in the data from run 8 (TN 94-16) and suggests that diode closure is not exacerbated by using a long pulser delay.

The next six shots had the same shape but different field amplitudes. Shots 5825, 5826, and 5827 had a 10 percent higher field. (Actually, the field shape on these shots was not exactly the same, but I believe that the difference in IOA here is not significant.) On shots 5825 and 5827 (Fig. 12) the pulser did not fire. They exhibit the expected behavior with a late-falling impedance. It is interesting that the early electron current which may have flown through the foil is small, smaller than that produced by the pulser. Could there be

another explanation for the anode plasma formation that must have occurred? As stated above, the foils have a much higher resistivity than the bulk metallic value. Could this resistivity result from microscopic regions of aluminum oxide that form a microscopic, flashover diode? This seems far-fetched but may be worth considering. Shot 5826 shows behavior very similar to 5825 and 5827, even though the pulser fired on this shot. This is the third anomalous shot, and I would guess that there was some problem with the foil breakdown here.

Shot 5815 (Fig. 13) had a 20 percent higher field than 5818. The results are not too different than 5818, and although the early impedance is higher, the electron loss current is no lower, the apparent closure is not delayed, and the normalized ion beam energy is lower.

Shot 5813 (fig. 14) had a 40 percent higher field than 5818. Again, the early impedance is much higher but closure and electron loss are not reduced. Shot 5814 had the same field but no pulser, resulting in a very high impedance and an early flash.

Impedance histories for three field strengths are compared in Fig. 15. As the field is raised, the impedance starts higher but crashes faster. In retrospect, a shot with a lower field than 5818 might have been interesting.

Shots 5819-22 had a different field shape than the above shots, with lower anode fields, particularly IOA. This would be expected to place the separatrix toward the anode coils and to tilt the lines back to the anode at large radii. Shots 5819 (Fig. 16) and 5821 showed similar behavior, with a slower impedance collapse but lower average ion efficiency than shot 5818. Shot 5820 (fig. 17), with a long delay, had the best diode impedance for this run, i.e., a rapid initial fall followed by a relatively slow collapse. However, the ion efficiency was relatively poor. Shot 5822, with no pulser, was very similar to 5817. As seen in Fig. 6, these shots tended to have higher inner cathode currents than the former series of shots. Impedance histories for shots 5816, 5818, and 5819 are compared in Fig. 17a. The impedance for shot 5819 falls more slowly, which is odd considering that this shot had two of the fields turned down. On these shots, the ion efficiency starts out similar to those in the first series, but then gets worse after about 20 ns.

The remaining five shots had a smaller (5 mm rather than 8) A-K gap. Shot 5812 had the same field settings as 5813, although the field configurations may have been different because of the different coil-set spacing. It is interesting to compare the impedances on these two shots (Figs. 18 and 14). The initial impedance fall occurs much earlier on shot 5812, as might be expected, but both shots appear to short out at about the same time. Shot 5812 shows a lower ion efficiency than the shots at the larger gap.

Shots 5808-11 had the same field shape. These shots showed similar electrical behavior as summarized in Fig. 19. Shot 5811, with a short delay, does not show the later current onset that occurs on short-delay shots at the larger gap. Also, the impedance history is

less influenced by the applied field (compare Figs. 19 and 15). The inner-cathode currents varied on these shots but were typically of the level on shots 5819-22 (dashed lines in Fig. 6).

One feature of shots 5808-5812 is that, similar to shots 5819-5822, they start out with efficiencies similar to those on shots in the first series, but show a transition to much less efficient behavior after 20 ns (except for shot 5809, where the transition occurs after 60 ns).

ENERGY COUPLING

The total ion beam energy is probably the best single metric of diode performance, because we want voltage, ion current, and a reasonable pulsewidth. Key shots have been excerpted from the spreadsheet and re-ordered in Fig. 20. One caveat is that the energies are normalized based on the peak open-circuit voltage, without considering the open-circuit voltage waveshape which can differ shot-to-shot. Also, normalizing the energy to a higher Marx charge may not be valid for the higher-impedance shots, because they might flash at the higher charge.

Shots 5814 and 5829 are not listed because the flashovers that occurred will distort the energy comparison. Shot 5825, which had a high ion beam energy, is not listed because on this shot one of the three IK3 signals was suspiciously large. Shot 5826 is not listed because, as stated earlier, its behavior looks like that of a limiter-EMFAPS shot and it is not clear what happened when the foil was pulsed. Shot 5823 is not listed because of the beforestated unusually low (apparent) ion beam efficiency. The remaining shots are listed in order of increasing field and increasing delay.

Consider the first five shots, which had the same fields but different delays. Shot 5824 has the best normalized ion beam energy and one of the highest total energies. However, the dependence of coupled energy on delay is not strong. For example, on shot 5817, with a very different impedance history (see Fig. 15), the high late-time impedance compensates for the slow current onset. These five shots have average normalized ion and total energies of 18.6 and 25.2 kJ.

Now consider shot 5827, with a slightly different field shape and no pulser (which is probably the important difference). This shot has very similar normalized energies. Again, running without the pulser produces a markedly different impedance history, but little difference in energy coupling, at least in this field geometry.

Shots 5815 and 5813, with increasing fields, show declining normalized energies.

Now, consider shots 5819-5822. Here the total normalized energy is higher, as would be expected from the flatter impedance profiles (Fig. 17a). However, the normalized ion energies tend to be lower, reflecting the lower ion efficiency.

Likewise, The smaller-gap shots have reasonable normalized energies but lower normalized ion energies, because of the low efficiencies on these shots.

KEY PHENOMENA

Another way to look at these data is to consider separately the key phenomena that affect diode performance. These are: ion current initiation, efficiency, impedance tuneability, and impedance collapse. These aspects are best examined by looking at Figs. 11, 15, 17a, and 19.

The current onset begins earlier at longer pulser delays, lower fields, and the smaller gap.

On the first series of shots examined the ion efficiency is good. At the smaller gap and with the different field shape of shots 5819-5822, the ion efficiency starts off similarly but seems to show a transition, at about 20 ns, to a lower value.

Increasing the applied field is seen to raise the impedance (Fig. 15) but not to impede the eventual collapse - the impedance starts to fall later and then comes crashing down, and the ion beam energy is not increased. Above 60 ns, the delay shows little effect on the impedance other than hastening the initial fall. At the smaller gap, the impedance history shows no strong dependence on applied field or delay. The impedance histories in Fig. 19 are not too different from those (at all but the shortest delays and highest fields) at the larger gap (obviously, this is a bit of an apples-to-oranges comparison).

As stated above, we have to take the apparent diode closure time with a grain of salt because of the unphysical monitor behavior at the end of the pulse. Nonetheless, it is instructive to compare the apparent closure times. Figures 11, 15, and 19 imply that, except at the shortest delays, closure occurs at about 130 ns, independent of delay, magnetic field, or gap. Plasma closure might not be expected to be affected by the field, but one would certainly expect the smaller gap to be associated with an earlier closure. Shot 5827, with no pulser, and 5817, with a short delay, show markedly later apparent closure. Figure 17a also shows that shot 5819, with reduced anode fields, appears to close later, although the difference is not as dramatic as with shots 5817 and 5827. Figure 21 shows impedances for the four shots with the field shape of shot 5819. All show the apparent later closure, and shot 5822, with no pulser, shows the even later closure of shots 5817 and 5828.

SUMMARY

In this first cut at revisiting the MID data, I will attempt to answer four questions for each run:

(1) What are the key shots, in terms of performance, for each run?

I would say that the three best shots here are 5824, 5819, and 5827. Shot 5824 had the highest normalized ion energy and a peak ion current density exceeding 6 kA/cm^2 . Shot 5819 had a lower ion efficiency but a more-slowly falling impedance and gave the second-highest normalized ion energy. Shot 5827, a limiter-EMFAPS shot, had a reasonable ion efficiency and normalized energy, and a higher voltage. Extrapolating this shot to 32 kV would imply an ion current of about 200 kA and voltage of 1-1.2 MV for close to 40 ns.

(2) Which field configurations should we concentrate on mapping out?

(Except for the slight change on shots 5825-27,) in this run we only used four configurations, so we might as well map them all out. Because of the apparent delay in closure on shots 5819-21, it will be very interesting to compare the field geometry on those shots with that on shots in the first group.

(3) What are the significant trends in the data?

As mentioned above, there is a clear hastening of the ion-current onset with an increase in the delay time, reduction in the gap, and decrease in the field. Before closure, the impedance is higher at higher fields and shorter delays. For very short, or zero, delays, the impedance is markedly higher and closure appears to be significantly reduced. For most of the shots examined here, the time of closure appears to be independent of the field magnitude, gap, or pulser delay (for delays of 60 ns or more).

(4) What are the most puzzling features to these data?

The seeming independence of closure time of field amplitude may be reasonable, assuming that the electrode plasmas are collisional enough to move across the field lines. What is unexpected is the seeming independence of closure time on diode gap. Another interesting comparison is shots 5819 and 5818 (Fig. 17a), where a reduction in two of the fields seems to cause a delay in closure. The latter is suggestive of a picture John Greenly and I are considering, where in the presence of strong self-magnetic fields, the applied field acts to direct electrons more than to insulate them. Even more interesting is the strong delay in closure that occurs when the foil is not pulsed, or pulsed soon before the shot. Is this directly related to the effect of the foil current? Or is it an indirect effect, related to the reduced ion current that occurs at short or zero delays? Also interesting is the possible interpretation of shots 5823 and 5830, where the electron loss seems to increase as the ion current is reduced.

CONCLUSIONS

For proper MID performance, we need fairly rapid current onset, an ability to control the impedance, efficient ion production, and a relatively slow impedance collapse. The shots in this run show that the first three are achievable. The main problem is the rapid impedance collapse, and this is where our thoughts should focus.

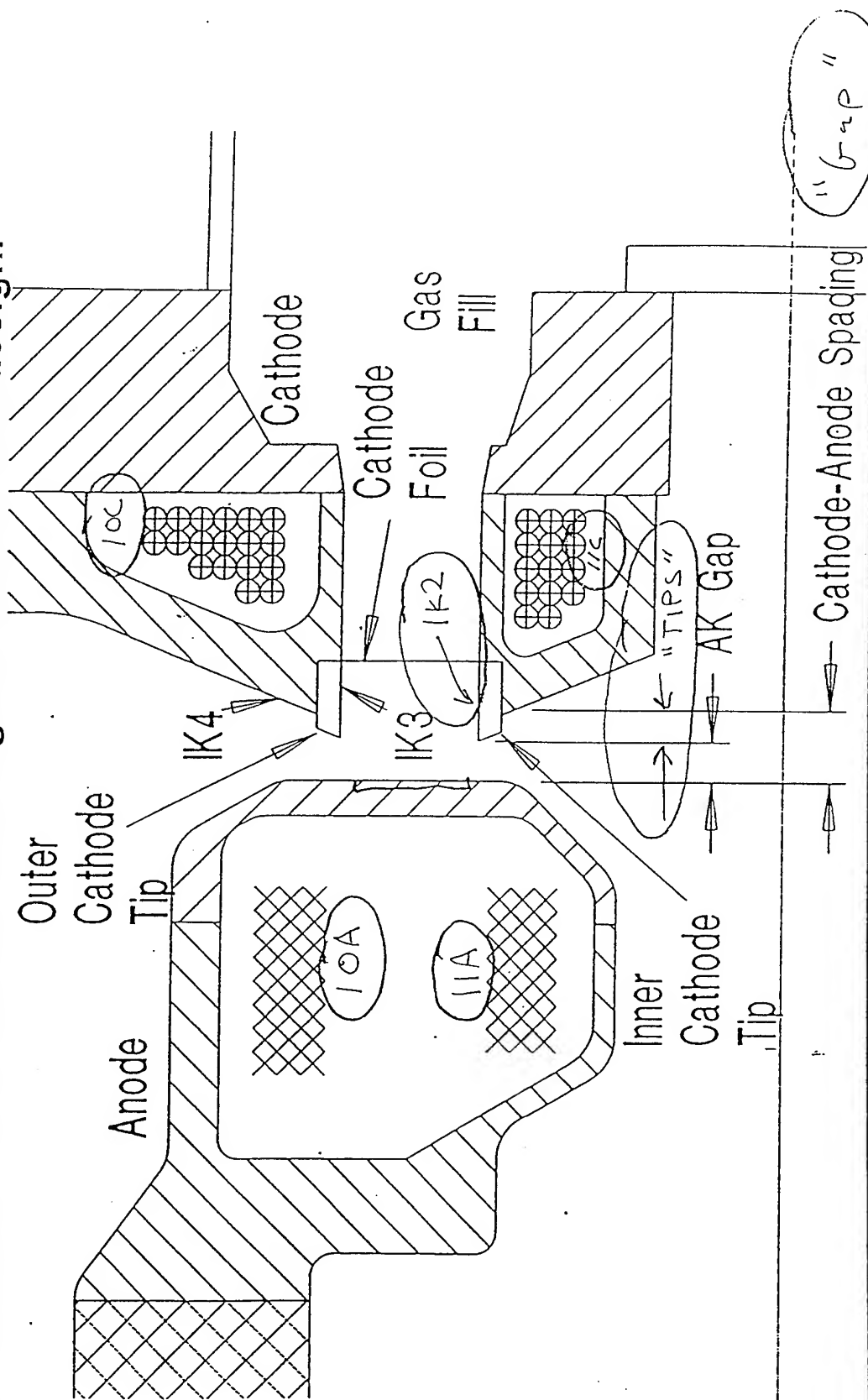
shot	gap	lips	lIA	lOA	lIC	lOC	lW-m	eff th	ins	lf	delay, r	z=10	zd, mm	VOC	e(k)	e(k)	Vpp	lipp	comnts
5808	11	6	2.30	1.58	2.22	2.78	200	NA	N	30	52	19	69	54	7.4	12.7	56	30	note: If monitor has pickup shots 5808-30, so ampl approx
5809	11	6	2.76	1.89	2.64	3.34	200	NA	N	30	46	22	56	55	7.1	10	46	25	
5810	11	6	3.30	2.27	3.16	4.00	200	NA	N	25	52	17	68	56	5.6	13.5	70	17	
5811	11	6	2.76	1.89	2.64	3.34	200	NA	N	30	15	24	55	57	4.8	11.5	65	18	
5812	11	6	2.76	2.72	2.64	3.34	200	NA	N	30	47	19	60	56	5.8	11.9	63	22	
5813	14	6	2.76	2.72	2.64	3.34	200	NA	N	30	37	36	49	56	6.5	9.8	83	23	opened gap, local damage outer anode
5814	14	6	2.76	2.72	2.64	3.34	200	NA	N	0	0	57	200	56	3.7	5.7	97	14	no pulser, flash, Z never 0
5815	14	6	2.30	2.26	2.22	2.78	200	NA	N	30	42	30	60	63	10.9	15.3	88	18	
5816	14	6	1.92	1.88	1.83	2.33	200	NA	N	30	51	25	56	57	8.8	12.1	57	40	
5817	14	6	1.92	1.88	1.83	2.33	200	NA	N	30	17	35	65	54	8	12.5	86	18	
5818	14	6	1.92	1.88	1.83	2.33	200	NA	N	30	63	24	58	64	11	14.4	57	33	
5819	14	6	1.54	1.00	1.83	2.33	200	NA	N	25	54	19	77	62	11.8	17.9	75	33	
5820	14	6	1.69	1.10	2.01	2.56	200	NA	N	20	116	9	83	55	7	16.4	72	23	
5821	14	6	1.69	1.10	2.01	2.56	200	NA	N	25	75	16	75	59	7.8	16.5	66	26	
5822	14	6	1.69	1.10	2.01	2.56	200	NA	N	0	0	34	75	58	8.3	14.5	87	19	no pulser, slight ding outer anode
5823	14	6	1.92	1.88	1.83	2.33	200	NA	N	20	102	15	87	63	5.6	18.4	74	18	
5824	14	6	1.92	1.88	1.83	2.33	200	NA	N	25	80	23	67	61	12.9	15.7	74	42	
5825	14	6	2.11	1.88	2.01	2.56	200	NA	N	0	0	35	69	58	12.4	12.6	82	33	no pulser
5826	14	6	2.11	1.88	2.01	2.56	200	NA	N	25	49	33	73	56	10	14.1	75	27	
5827	14	6	2.11	1.88	2.01	2.56	200	NA	N	0	0	30	76	66	12.8	17.9	87	32	no pulser
5828	24	6	1.92	1.88	1.83	2.33	500	NA	N	20									extra spacer, gap way too large, open circ and early flash
5829	14	6	1.92	1.88	1.83	2.33	500	NA	N	20	102	26	61	58	9.1	9.9	90	32	flash
5830	14	6	1.92	1.88	1.83	2.33	500	NA	N	20	102	14	71	66	13.1	17.5	79	43	

shot	gap	IIA	IOA	IIIC	IOC	IC/OC	IA/OC	OA/OC	delns	ei(kj)	e(kj)	eneff	eIV2	eV2	ZIPP	comnts
5808		2.30	1.58	2.22	2.78	0.80	0.83	0.57	61	7.4	12.7	0.6	16.2	27.9	1.9	note: If monitor has pickup shots 5808-30, so ampl approx
5809		2.76	1.89	2.64	3.34	0.79	0.83	0.57	54	7.1	10.0	0.7	15.0	21.2	1.8	
5810		3.30	2.27	3.16	4.00	0.79	0.83	0.57	61	5.6	13.5	0.4	11.4	27.6	4.1	
5811		2.76	1.89	2.64	3.34	0.79	0.83	0.57	18	4.8	11.5	0.4	9.5	22.7	3.6	
5812		2.76	2.72	2.64	3.34	0.79	0.83	0.81	55	5.8	11.9	0.5	11.8	24.3	2.9	
5813		2.76	2.72	2.64	3.34	0.79	0.83	0.81	44	6.5	9.8	0.7	13.3	20.0	3.6	opened gap, local damage outer anode
5814		2.76	2.72	2.64	3.34	0.79	0.83	0.81	0	3.7	5.7	0.6	7.6	11.6	6.9	no pulser, flash, Z never 0
5815		2.30	2.26	2.22	2.78	0.80	0.83	0.81	50	10.9	15.3	0.7	17.6	24.7	4.9	
5816		1.92	1.88	1.83	2.33	0.79	0.82	0.81	60	8.8	12.1	0.7	17.3	23.8	1.4	
5817		1.92	1.88	1.83	2.33	0.79	0.82	0.81	20	8.0	12.5	0.6	17.6	27.4	4.8	
5818		1.92	1.88	1.83	2.33	0.79	0.82	0.81	74	10.6	14.4	0.7	16.6	22.5	1.7	
5819		1.54	1.00	1.83	2.33	0.79	0.66	0.43	64	11.8	17.9	0.7	19.6	29.8	2.3	
5820		1.69	1.10	2.01	2.56	0.79	0.66	0.43	137	7.0	16.4	0.4	14.8	34.7	3.1	
5821		1.69	1.10	2.01	2.56	0.79	0.66	0.43	89	7.8	16.5	0.5	14.3	30.3	2.5	
5822		1.69	1.10	2.01	2.56	0.79	0.66	0.43	0	8.3	14.5	0.6	15.8	27.6	4.6	no pulser, slight ding outer anode
5823		1.92	1.88	1.83	2.33	0.79	0.82	0.81	120	5.6	18.4	0.3	9.0	29.7	4.1	
5824		1.92	1.88	1.83	2.33	0.79	0.82	0.81	94	12.9	15.7	0.8	22.2	27.0	1.8	
5825		2.11	1.88	2.01	2.56	0.79	0.82	0.73	0	12.4	12.6	1.0	23.6	24.0	2.5	no pulser
5826		2.11	1.88	2.01	2.56	0.79	0.82	0.73	58	10.0	14.1	0.7	20.4	28.8	2.8	
5827		2.11	1.88	2.01	2.56	0.79	0.82	0.73	0	12.8	17.9	0.7	18.8	26.3	2.7	no pulser
5829		1.92	1.88	1.83	2.33	0.79	0.82	0.81	120	9.1	9.9	0.9	17.3	18.8	2.8	flash, IK2 is gibberish
5830		1.92	1.88	1.83	2.33	0.79	0.82	0.81	120	13.1	17.5	0.7	19.2	25.7	1.8	IK2 signal is gibberish

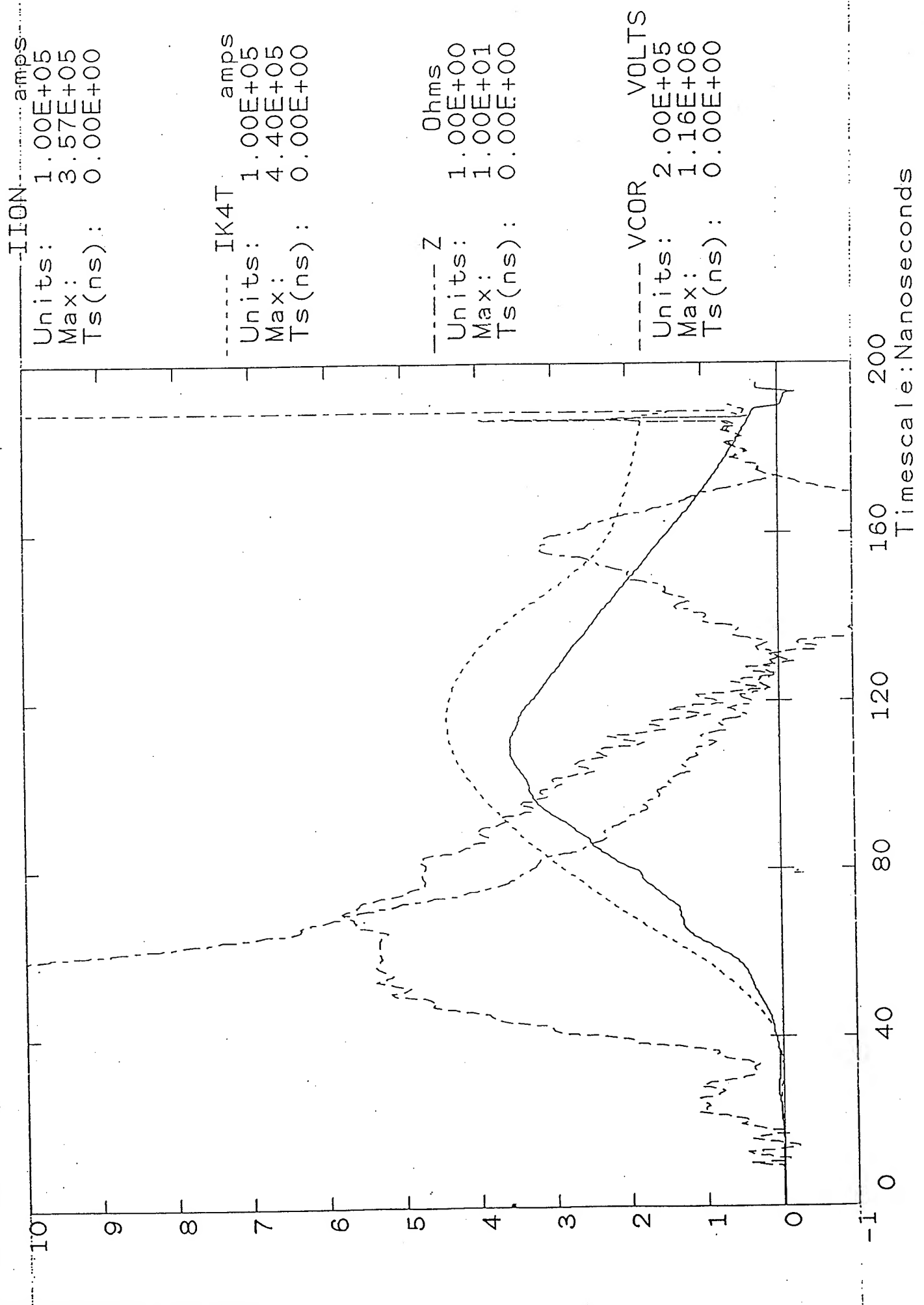
F16-1

SABRE MID Design

SABRE is 10 MV, 250 kA accelerator at Sandia National Labs. The diode on GAMBLE II is a clone of the original SABRE MID design.

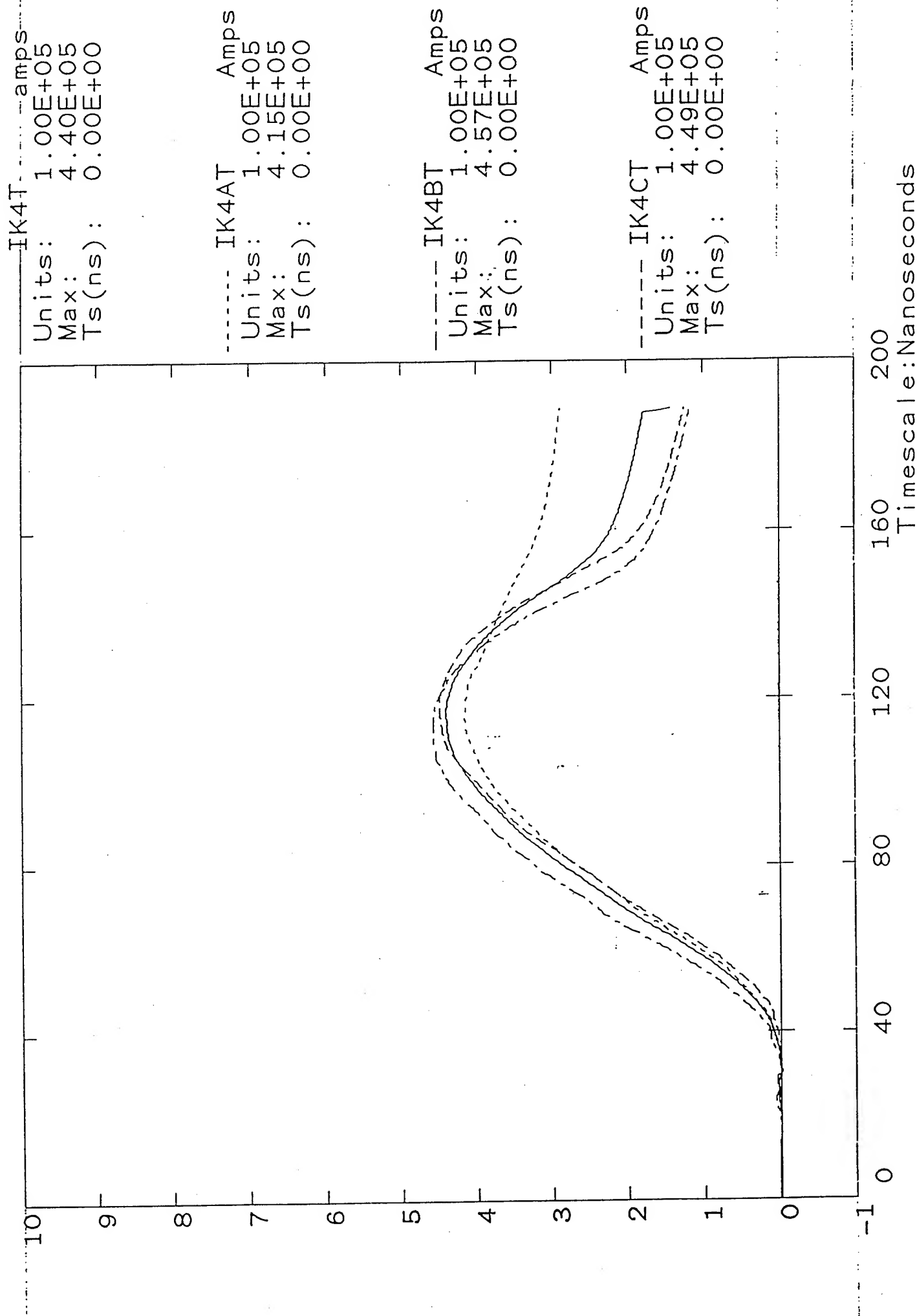


NRL



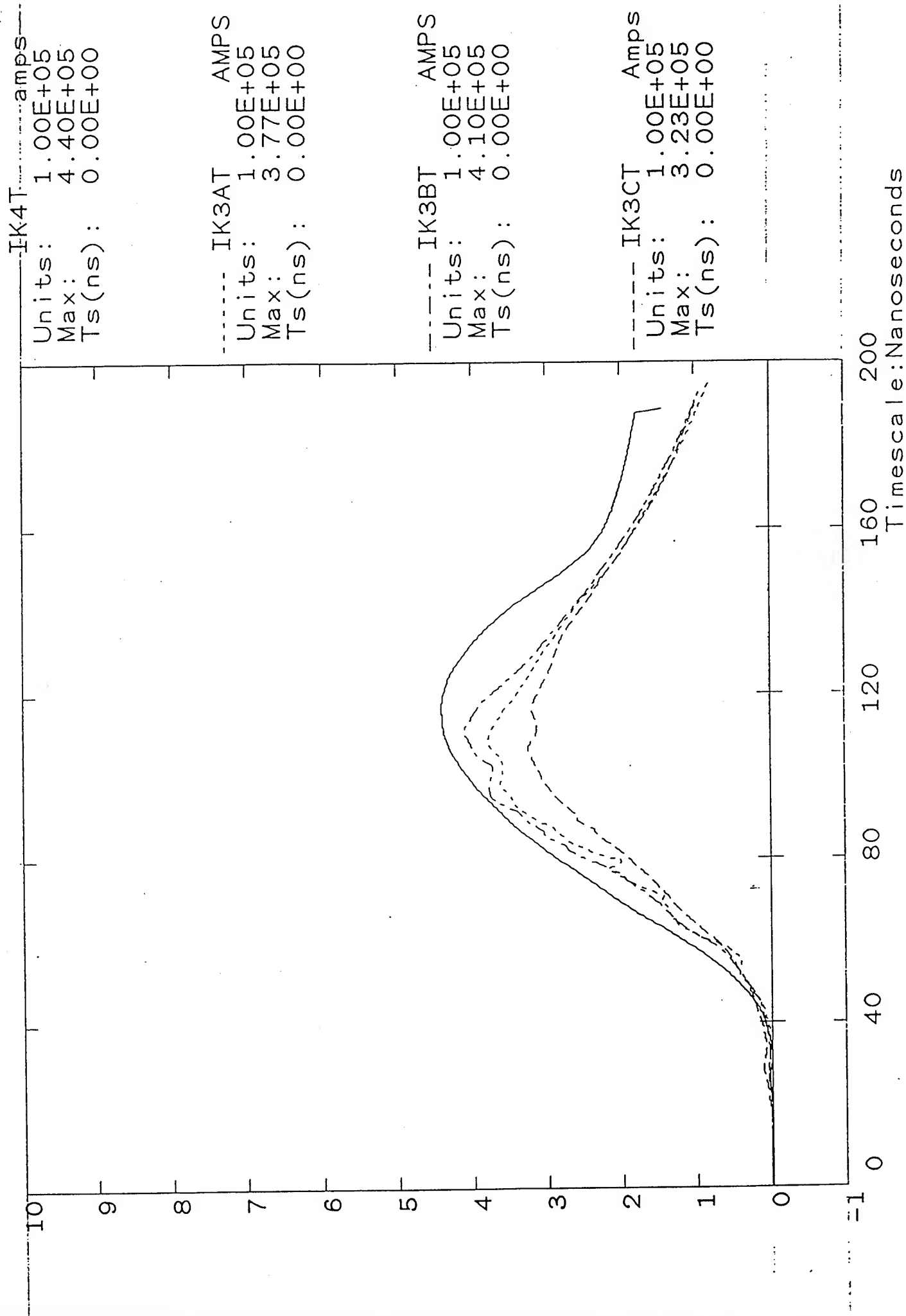
Shot 5818

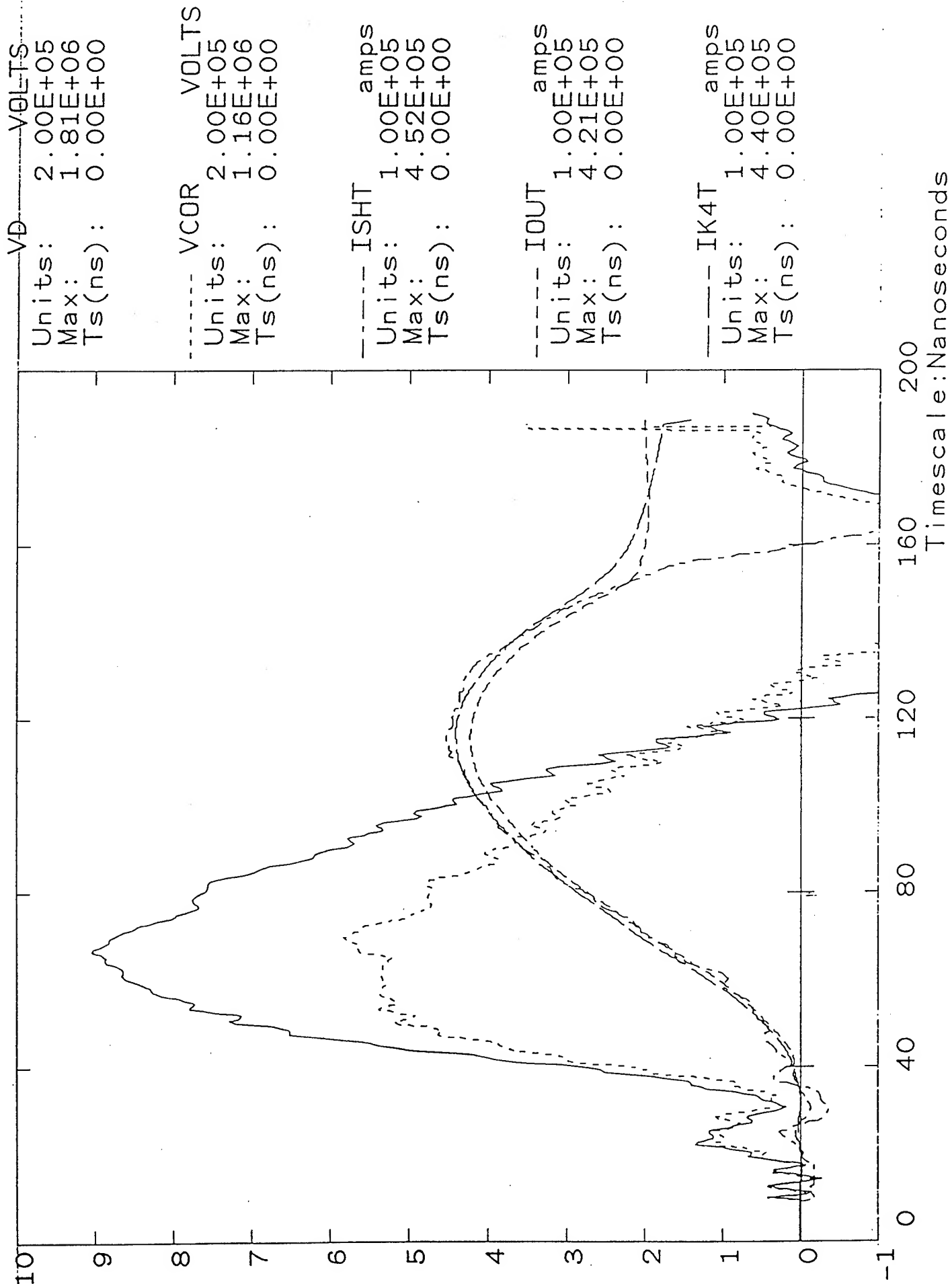
F16-3



Shot 5818

FIG-4

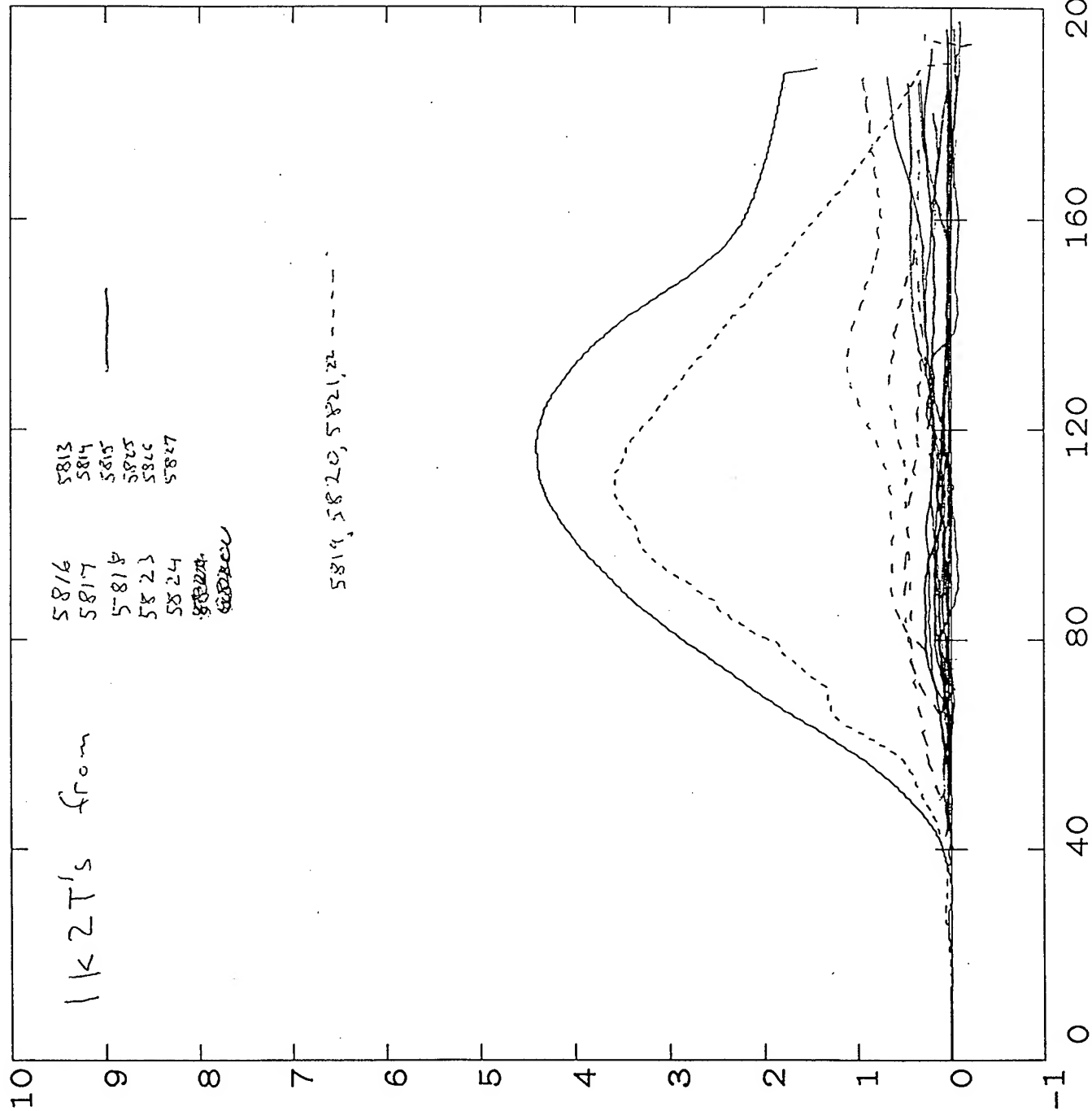




Shot 5818

Flg-6

Units: ik4t
Max: 1.00E+05
Ts(ns): 4.40E+05
0.00E+00



Shot 5817

Fig 7

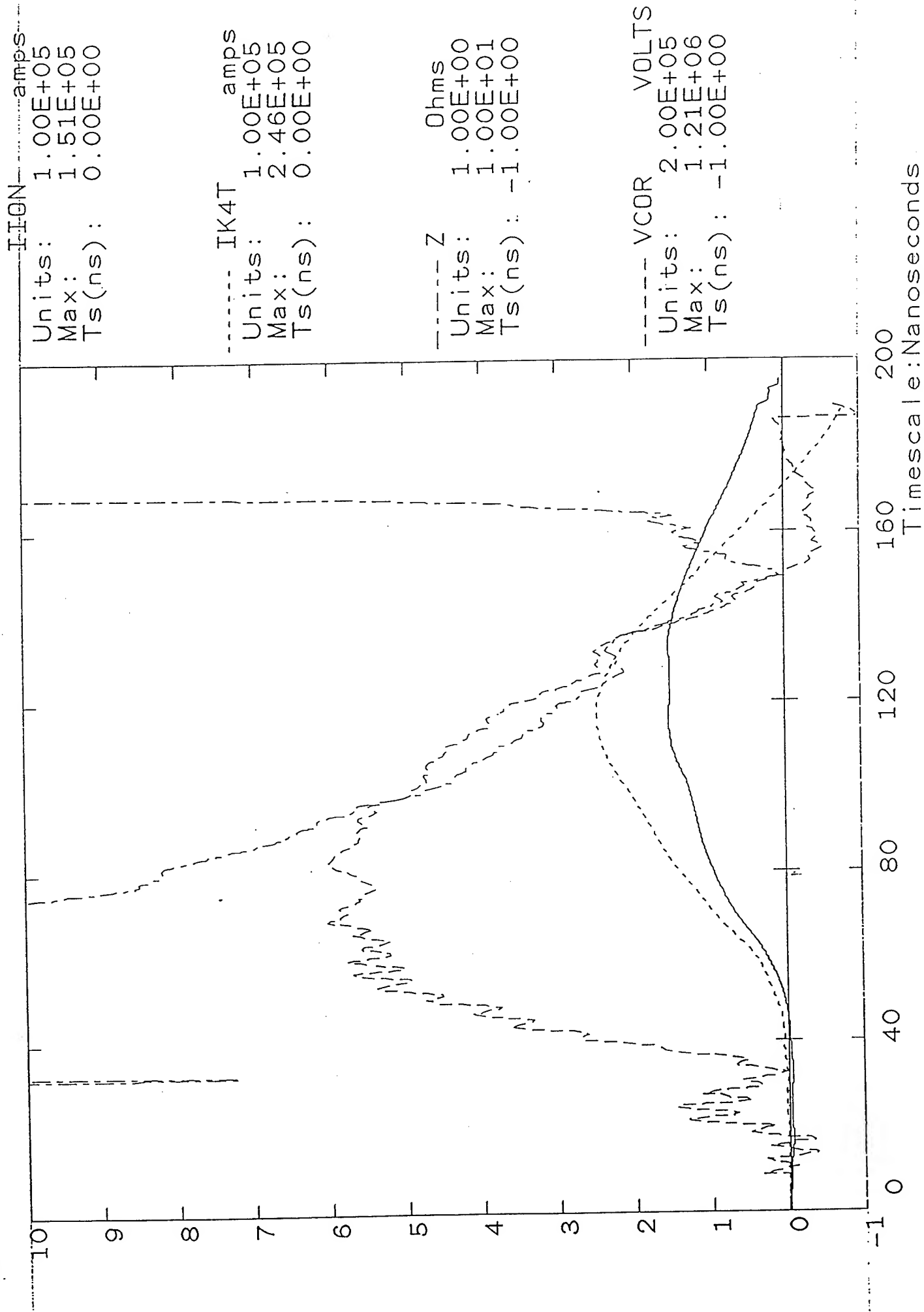
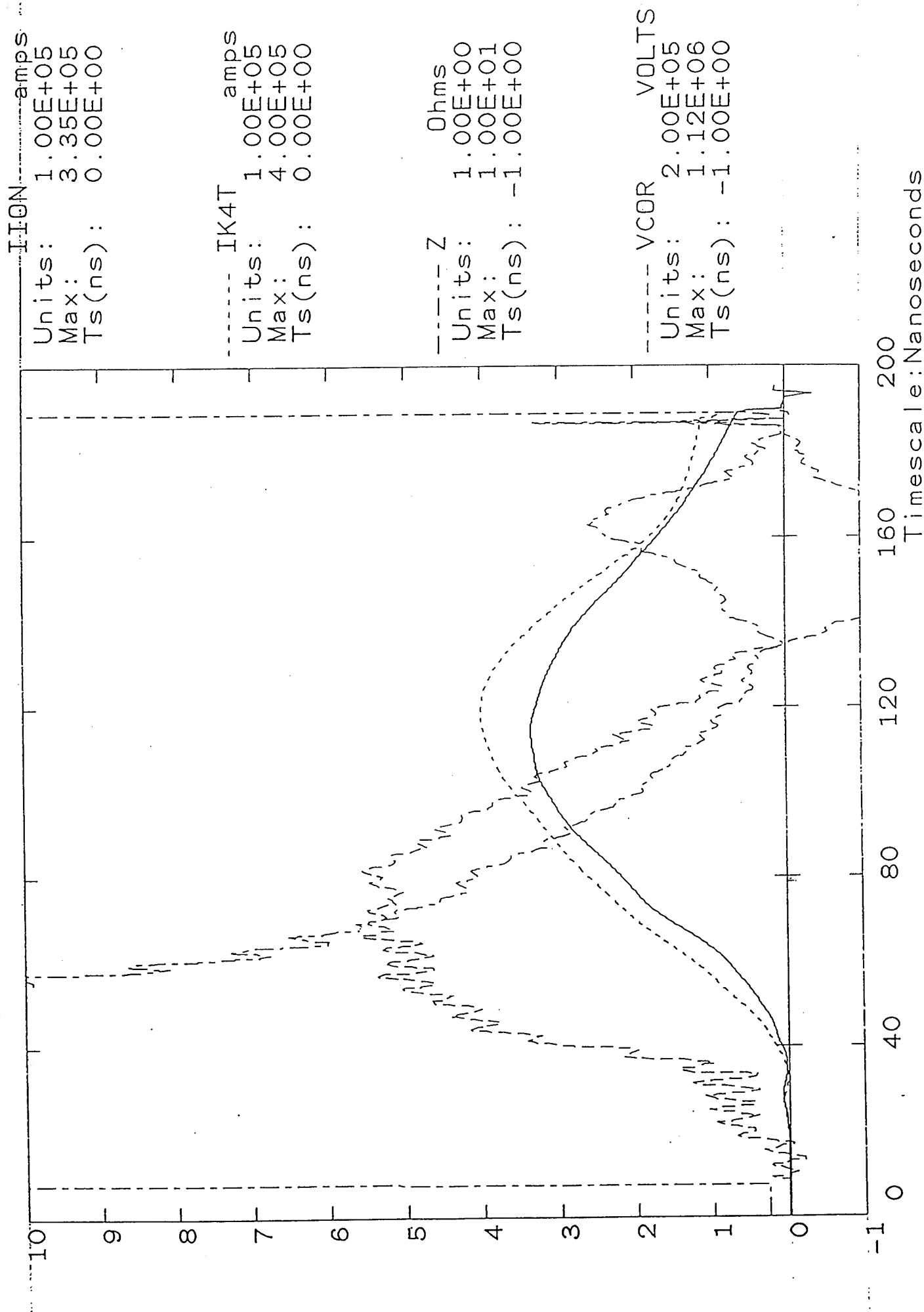
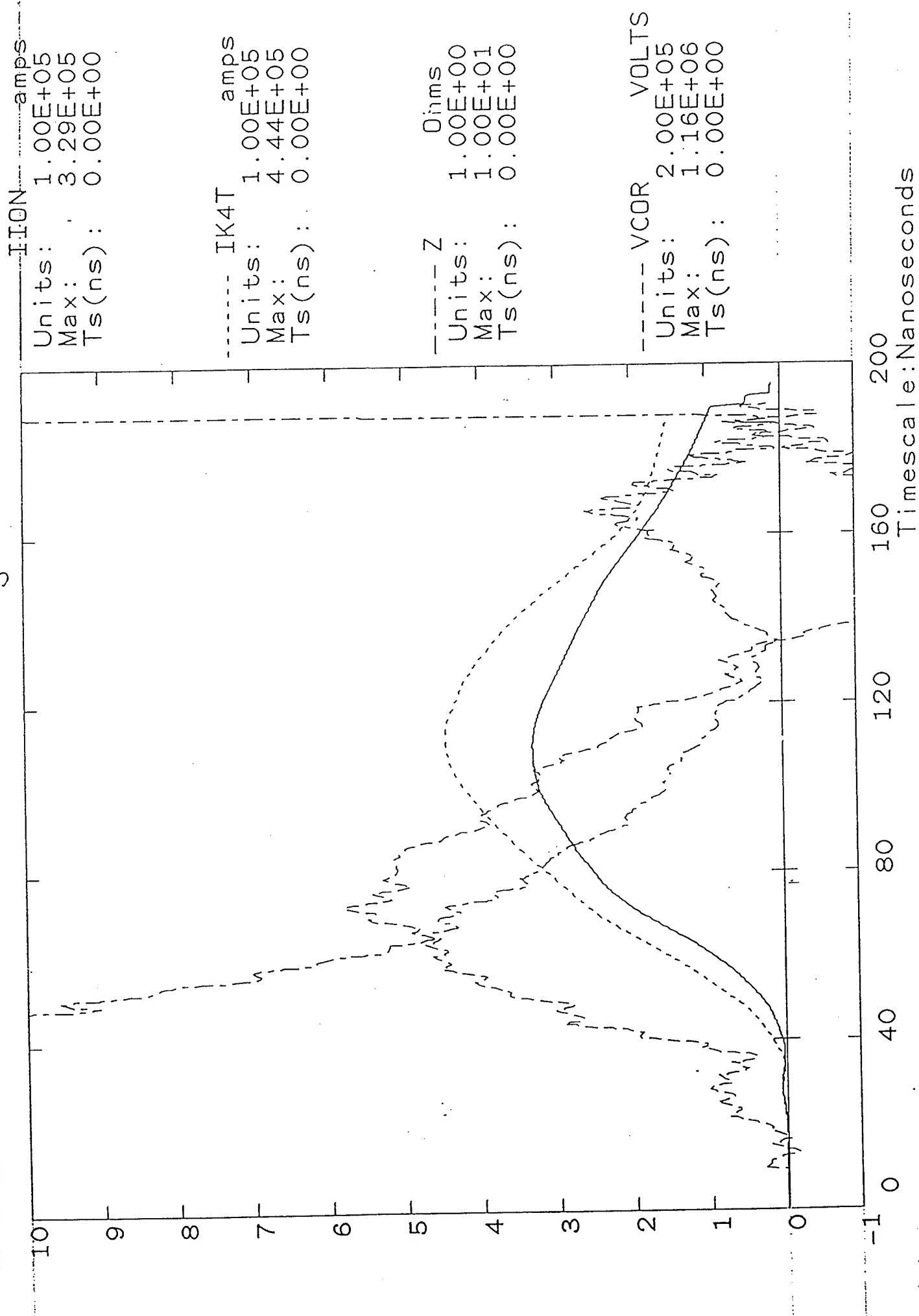


Fig 8

Shot 5824





Shot 5823

Fig 910

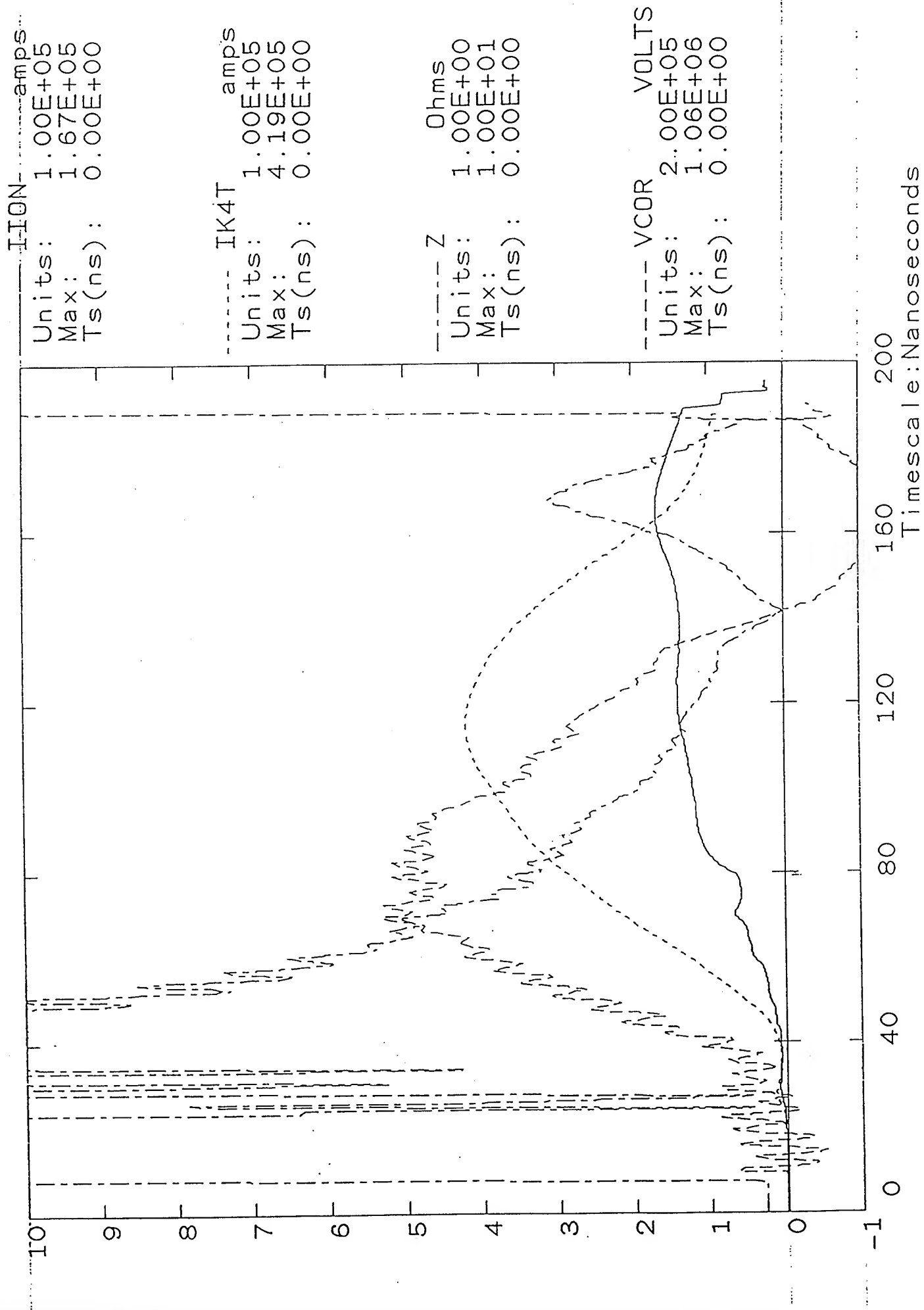
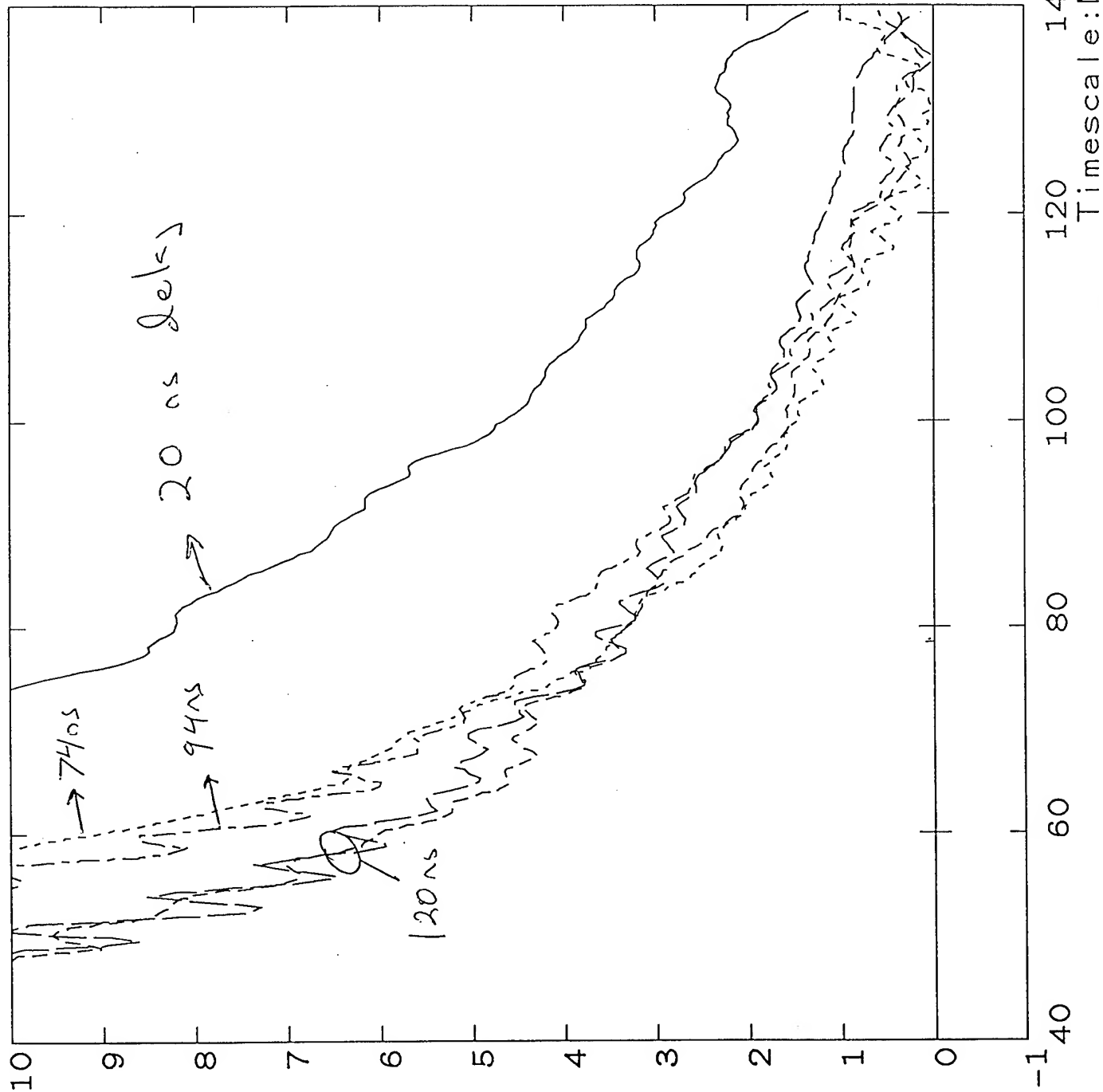
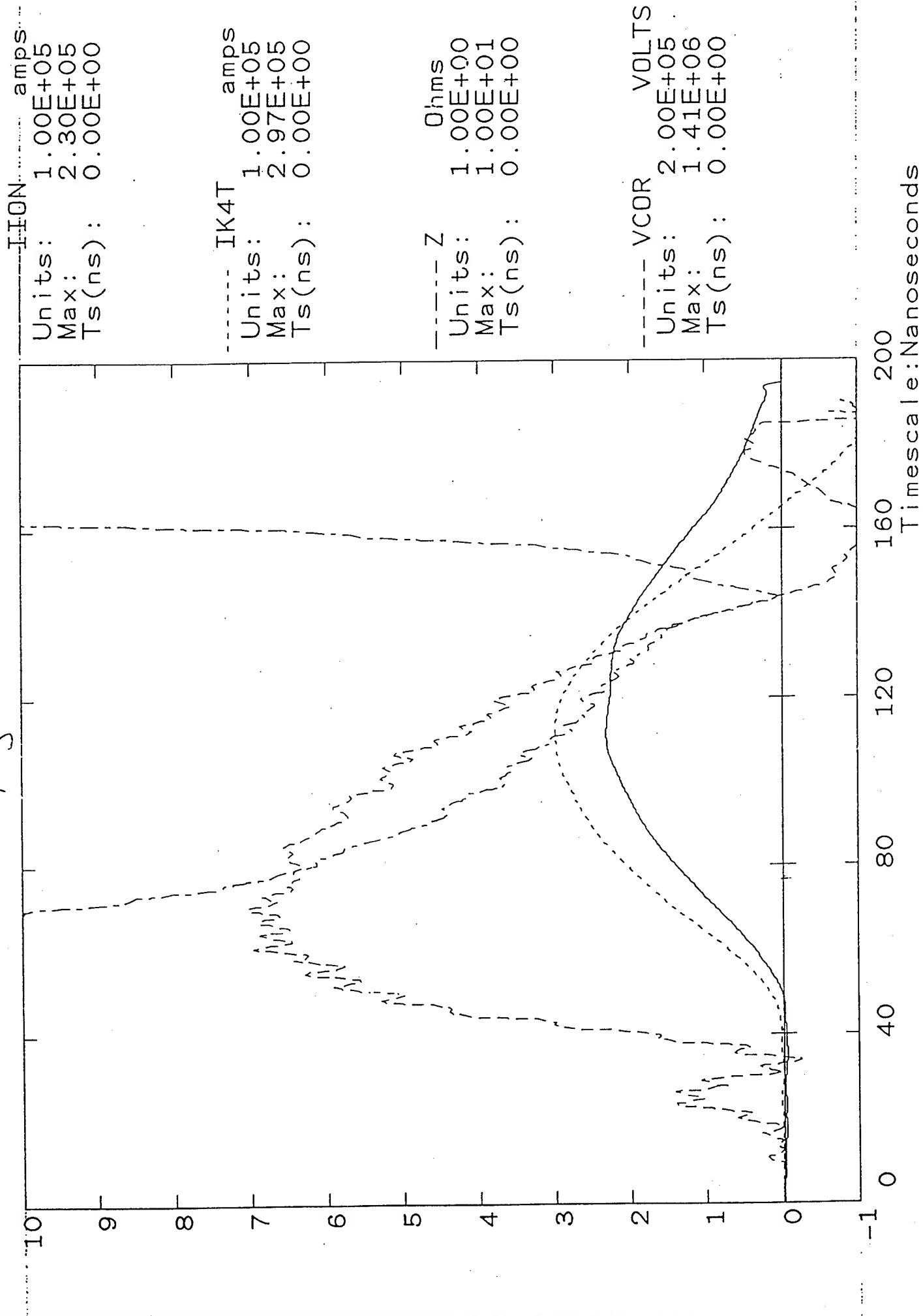


Fig 11

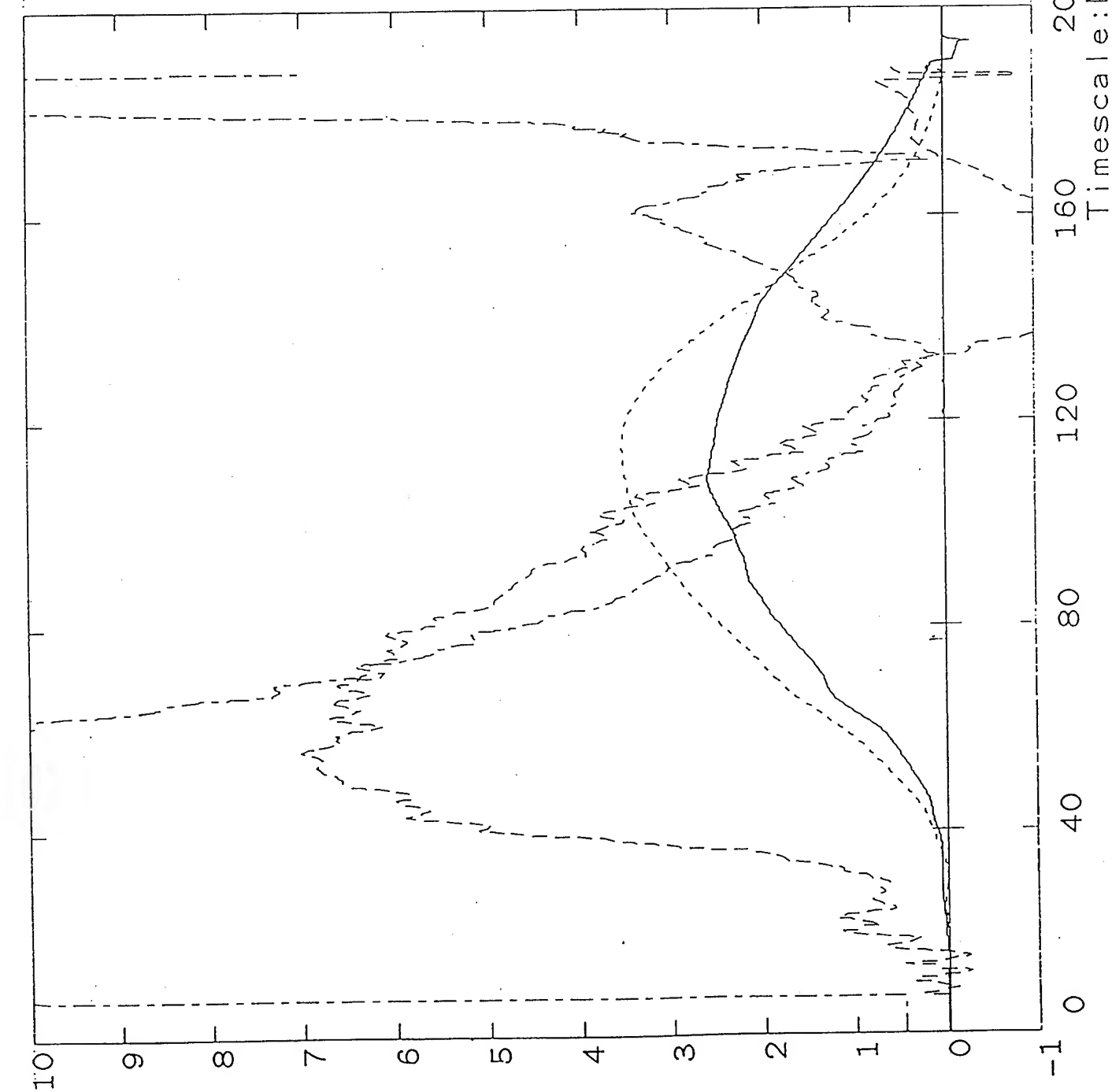
Shot 5818





Shot 5815

Fig 13



----- IION ----- amps
Units: 1.00E+05
Max: 2.57E+05
Ts(ns): 0.00E+00

----- IK4T ----- amps
Units: 1.00E+05
Max: 3.53E+05
Ts(ns): 0.00E+00

----- Z ----- Ohms
Units: 1.00E+00
Max: 1.00E+01
Ts(ns): -2.00E+00

----- VCOR ----- VOLTS
Units: 2.00E+05
Max: 1.40E+06
Ts(ns): -2.00E+00

F-314

Shot 5813

II-ION amps
Units: 1.00E+05
Max: 2.24E+05
Ts(ns): 0.00E+00

IK4T amps
Units: 1.00E+05
Max: 3.43E+05
Ts(ns): 0.00E+00

Z Ohms
Units: 1.00E+00
Max: 1.00E+01
Ts(ns): 0.00E+00

VCOR VOLTS
Units: 2.00E+05
Max: 3.53E+06
Ts(ns): 0.00E+00

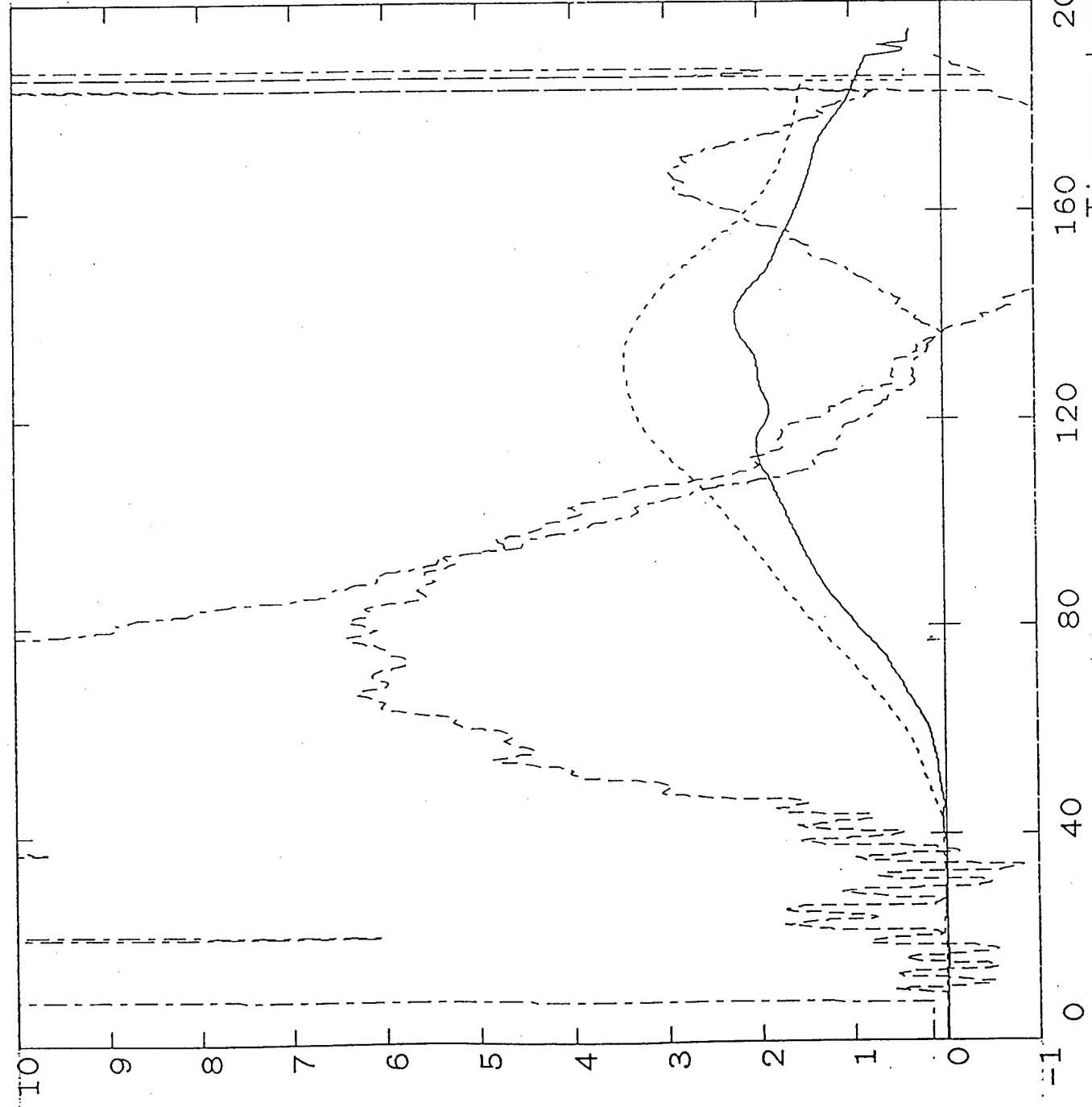


Fig 15

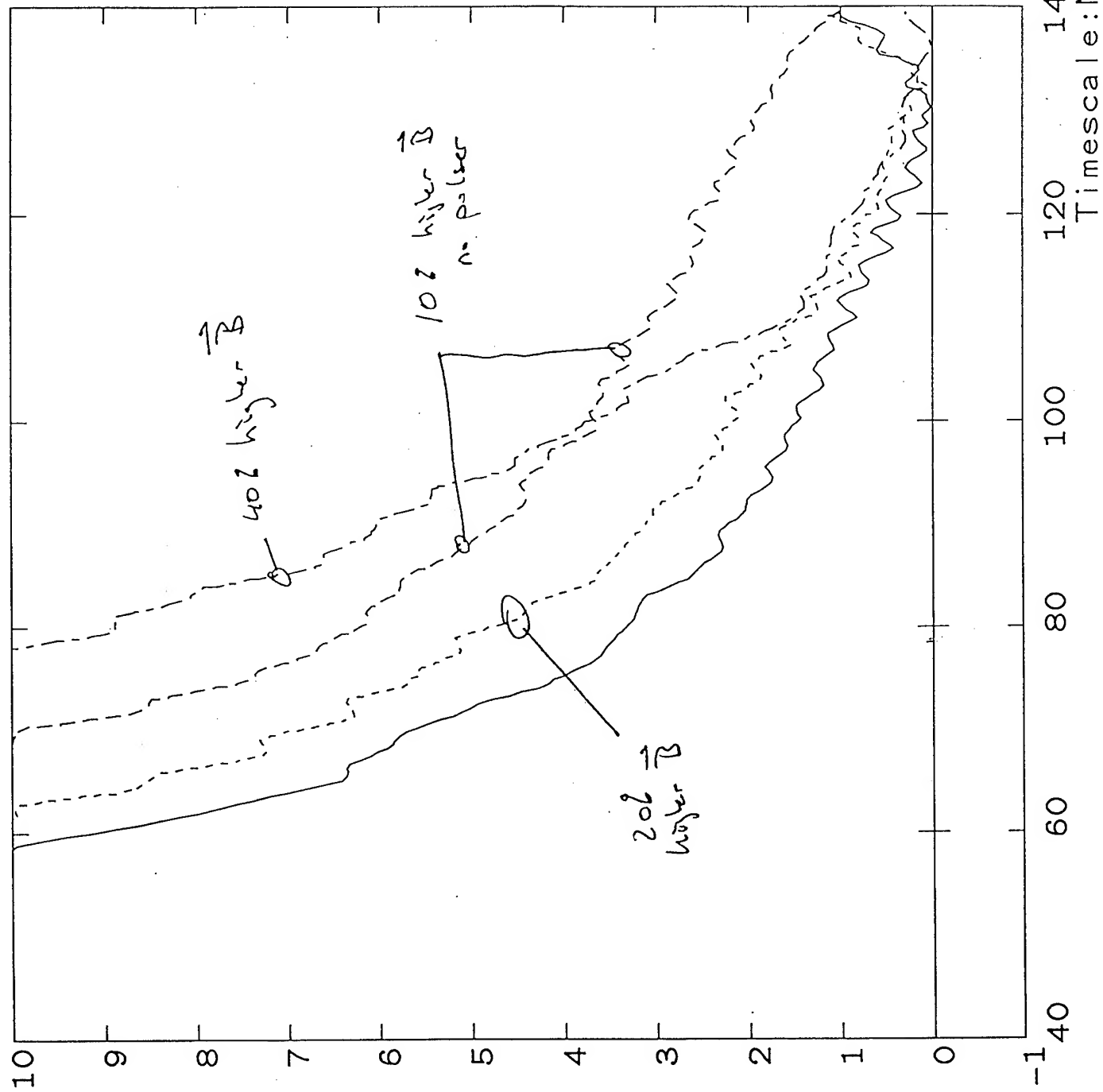
Shot 5818

Units: 1.00E+00
Max: 1.00E+01
Ts(ns): 0.00E+00

Units: 1.00E+00
Max: 1.00E+01
Ts(ns): -2.00E+00

Units: 1.00E+00
Max: 1.00E+01
Ts(ns): 0.00E+00

Units: 1.00E+00
Max: 1.00E+01
Ts(ns): 0.00E+00



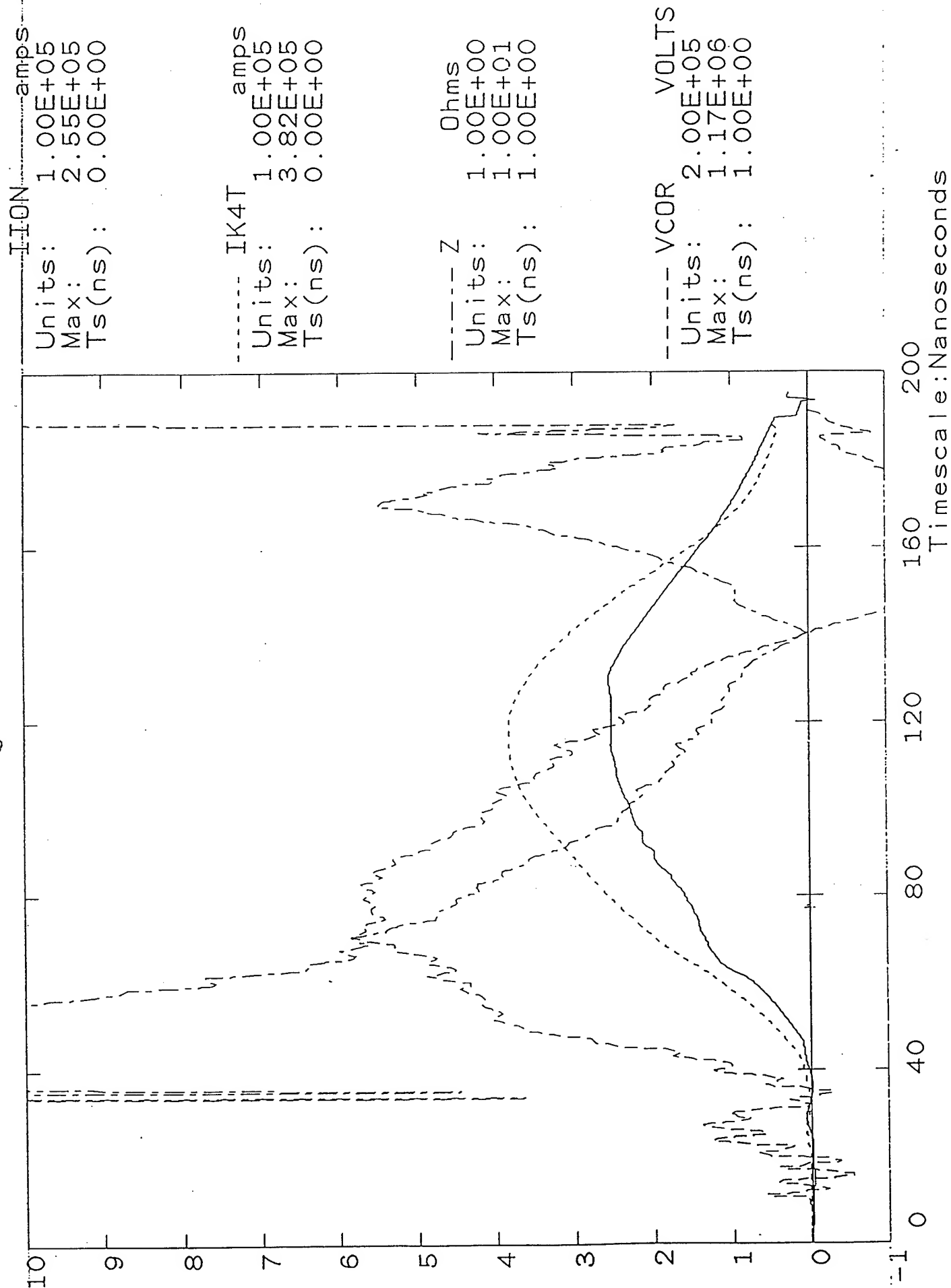
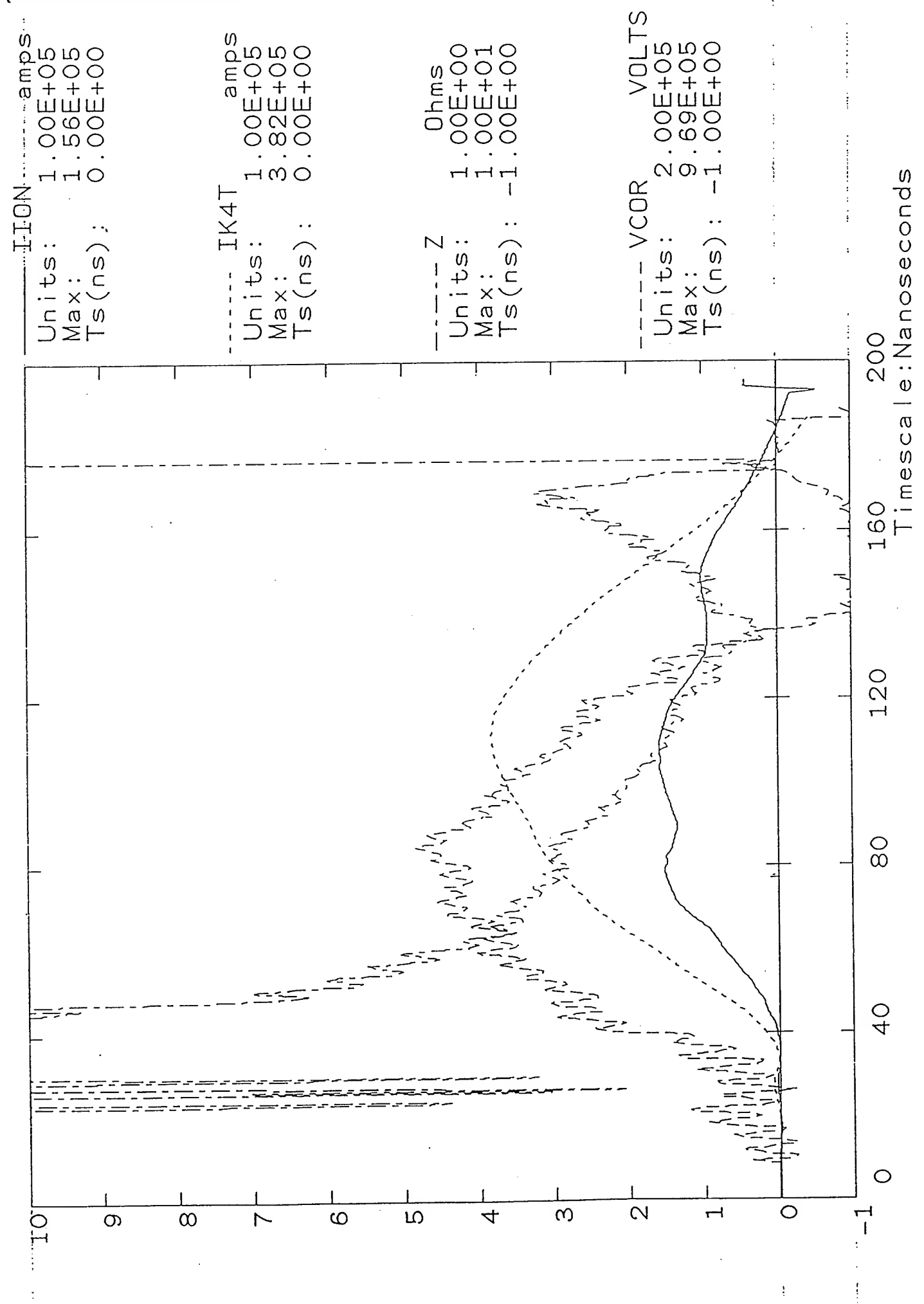


Fig 17

Shot 5820



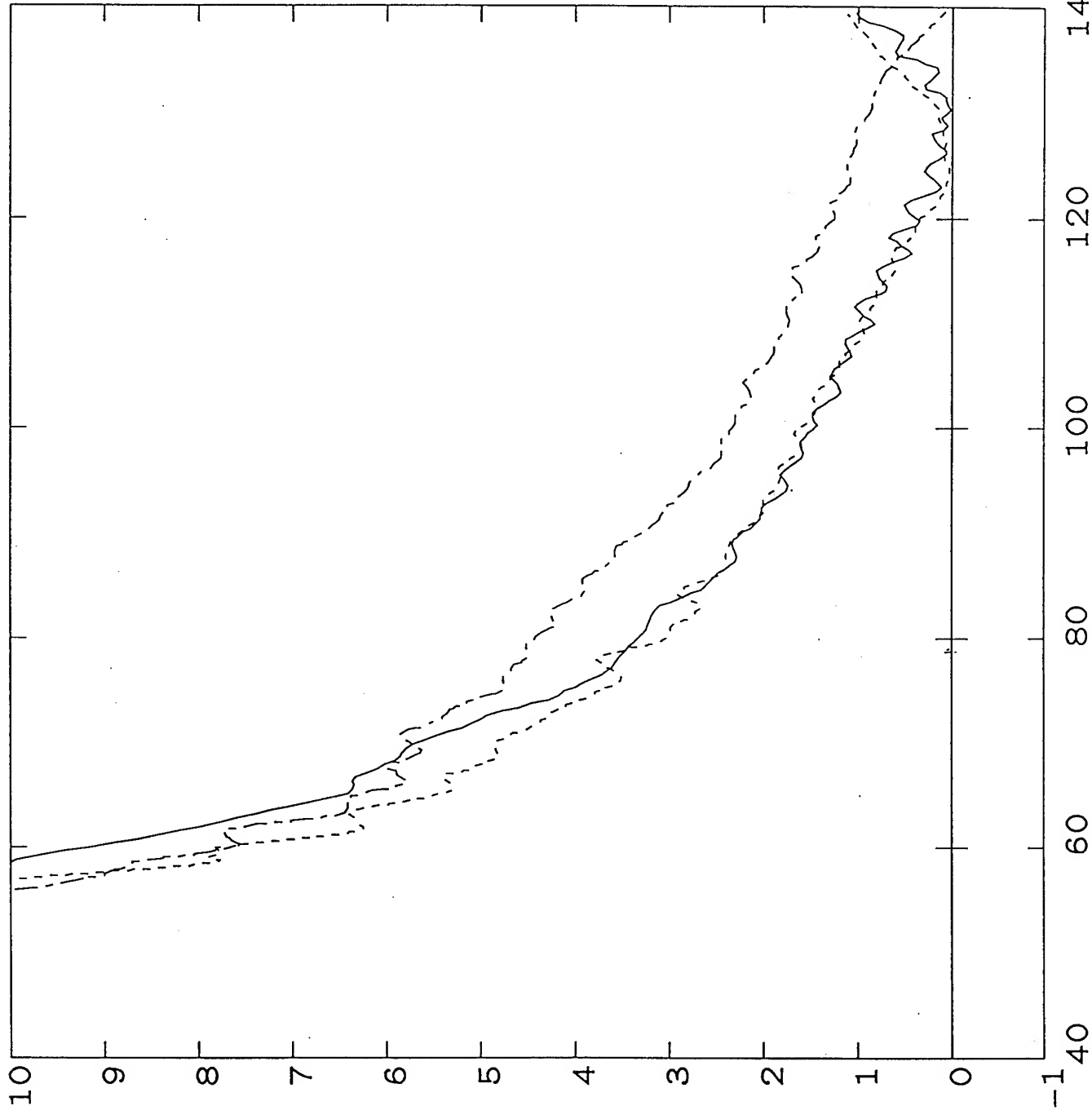
Shot 5818

Fig 17a

Units: 1.00E+00
Max: 1.00E+01
Ts(ns): 0.00E+00

----- z5816 Ohms
Units: 1.00E+00
Max: 1.00E+01
Ts(ns): -1.00E+00

----- z5819 Ohms
Units: 1.00E+00
Max: 1.00E+01
Ts(ns): 1.00E+00



Timescale:Nanoseconds

Shot 5812

Fig 18

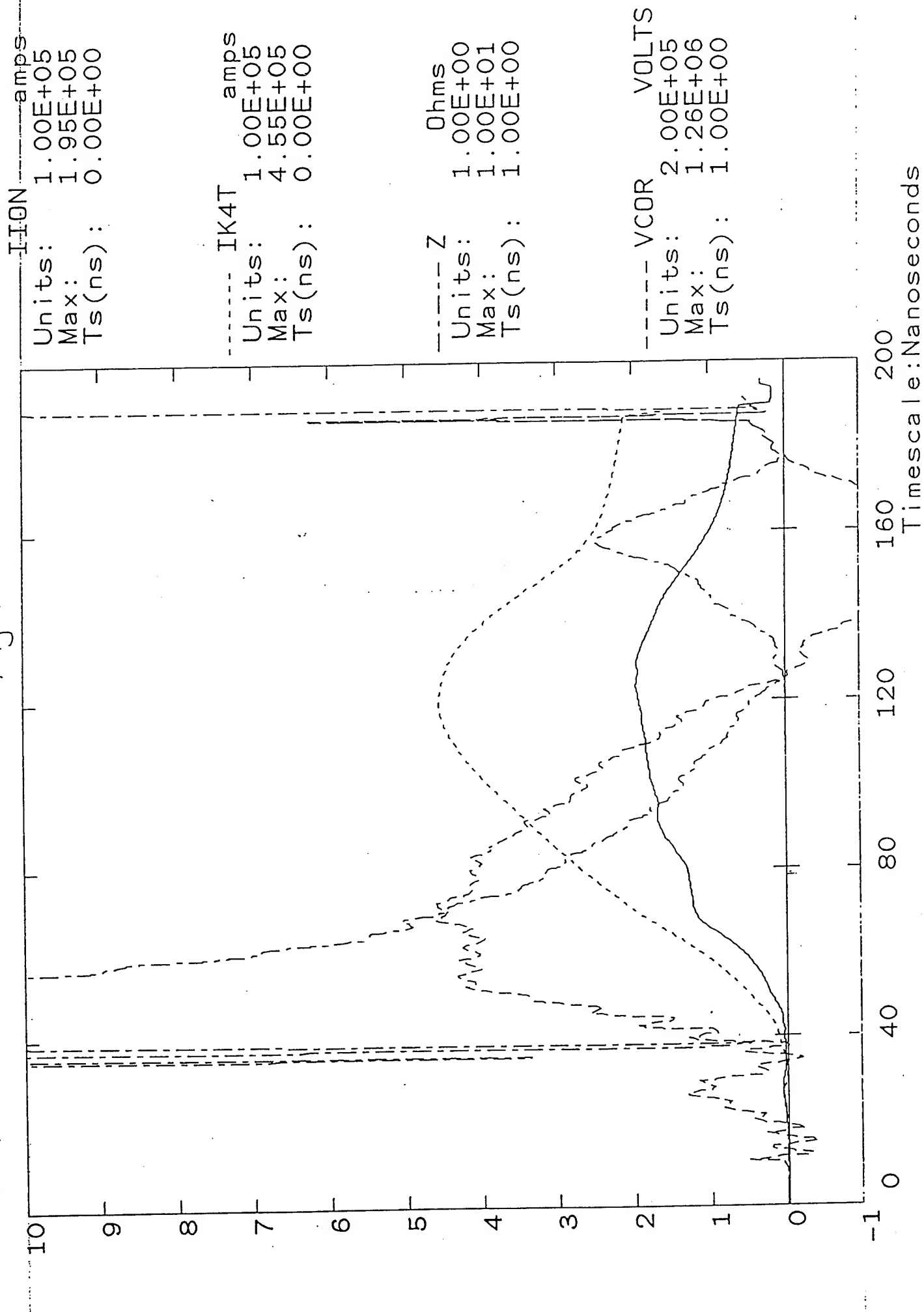
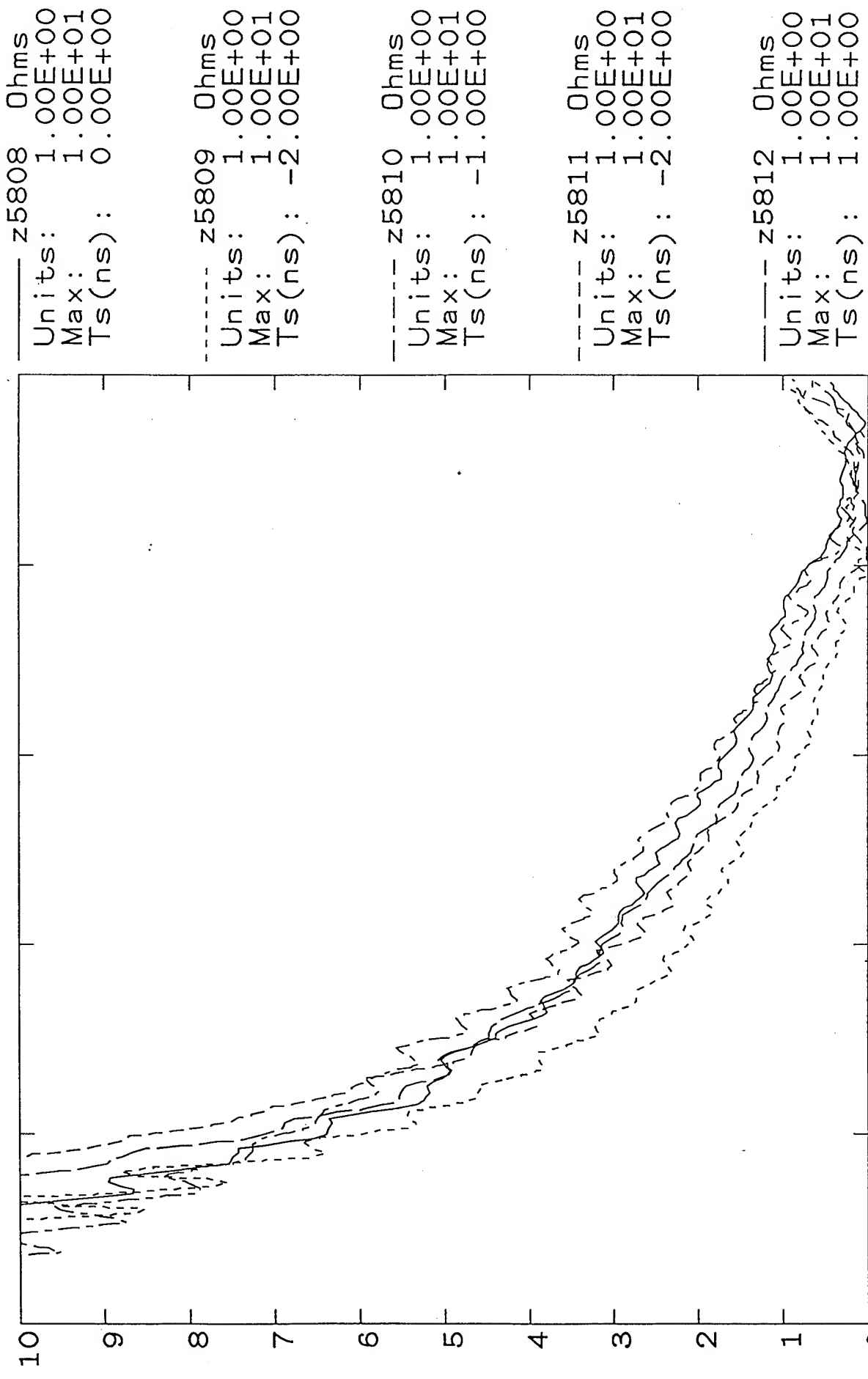


Fig 19

Shot 5824



Timescale:Nanoseconds

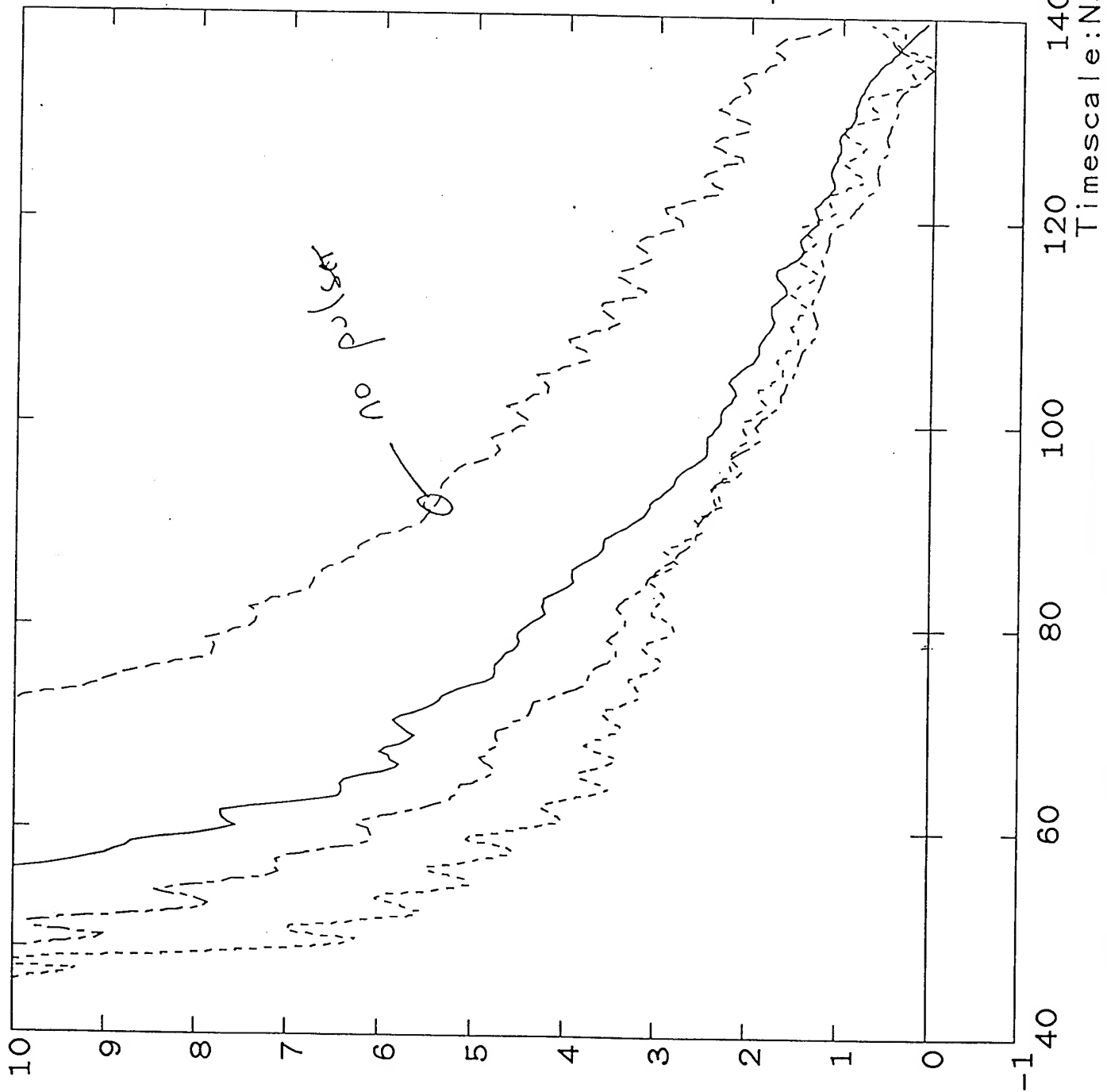
Fig 20

run5

shot	IOC	lc/oc	la/oc	oa/oc	delns	e(kj)	eneff	e/v2	e/v2	ZIP	comnts
5817	2.33	0.79	0.82	0.81	20	8.0	12.5	0.6	17.6	27.4	4.8
5816	2.33	0.79	0.82	0.81	60	8.8	12.1	0.7	17.3	23.8	1.4
5818	2.33	0.79	0.82	0.81	74	10.6	14.4	0.7	16.6	22.5	1.7
5824	2.33	0.79	0.82	0.81	94	12.9	15.7	0.8	22.2	27.0	1.8
5830	2.33	0.79	0.82	0.81	120	13.1	17.5	0.7	19.2	25.7	1.8 IK2 signal is gibberish
5827	2.56	0.79	0.82	0.73	0	12.8	17.9	0.7	18.8	26.3	2.7 no pulser
5815	2.78	0.80	0.83	0.81	50	10.9	15.3	0.7	17.6	24.7	4.9
5813	3.34	0.79	0.83	0.81	44	6.5	9.8	0.7	13.3	20.0	3.6 opened gap, local damage outer anode
5819	2.33	0.79	0.66	0.43	64	11.8	17.9	0.7	19.6	29.8	2.3
5822	2.56	0.79	0.66	0.43	0	8.3	14.5	0.6	15.8	27.6	4.6 no pulser, slight ding outer anode
5821	2.56	0.79	0.66	0.43	89	7.8	16.5	0.5	14.3	30.3	2.5
5820	2.56	0.79	0.66	0.43	137	7.0	16.4	0.4	14.8	34.7	3.1
5812	3.34	0.79	0.83	0.81	55	5.8	11.9	0.5	11.8	24.3	2.9
5808	2.78	0.80	0.83	0.57	61	7.4	12.7	0.6	16.2	27.9	1.9 note: If monitor has pickup shots 5808-30, so ampl approx
5811	3.34	0.79	0.83	0.57	18	4.8	11.5	0.4	9.5	22.7	3.6
5809	3.34	0.79	0.83	0.57	54	7.1	10.0	0.7	15.0	21.2	1.8
5810	4.00	0.79	0.83	0.57	61	5.6	13.5	0.4	11.4	27.6	4.1

Shot 5818

Fig 21



z5819 Ohms
Units: 1.00E+00
Max: 1.00E+01
Ts(ns): 1.00E+00

z5820 Ohms
Units: 1.00E+00
Max: 1.00E+01
Ts(ns): -1.00E+00

z5821 Ohms
Units: 1.00E+00
Max: 1.00E+01
Ts(ns): 0.00E+00

z5822 Ohms
Units: 1.00E+00
Max: 1.00E+01
Ts(ns): 0.00E+00

PULSED POWER PHYSICS TECHNOTE 94-16

TITLE: ANALYSIS OF APPLIED-B DIODE RUN 8

Author: D. Hinshelwood

Date: August 24, 1994

Abstract: This note contains an analysis of results from the recent applied-B/EMFAPS diode run on Gamble II (run 8). These results allow the multidimensional parameter space of the applied-B/EMFAPS diode to be collapsed, permitting a more controlled set of experiments on the next run. These results suggest that diode performance is still limited, at least in part, by the EMFAPS behavior. The results point to a path for achieving ion beam conditions with this diode that are suitable for initial transport experiments.

INTRODUCTION

Toward the end of applied-B run 7, we had two shots (6017 and 6019) whose electrical behavior was getting close to that desired. After the run, ATHETA calculations were performed using a more accurate description of the experimental geometry. These calculations showed that the magnetic field was different than we had previously believed. Jess then used ATHETA to determine the field currents required for a more optimum field geometry. Run 8 was to be carried out using these fields, with the hope of improved diode performance. After seeing no improvement with the optimized field, shots were taken during this run with the fields of shots 6017-6019. None of these shots had results quite as good as those obtained previously. This note represents an attempt to analyze the electrical data from run 8. Beam data, such as Rutherford scattering and shadowbox results, will be described in a future note. Briefly, Rutherford scattering indicates that the beam at present is 50-70% protonic. The results of the analysis here suggest that a path to the diode performance required for transport experiments does indeed exist. The multidimensional parameter space of the applied-B/EMFAPS diode can be collapsed, allowing a more limited variation of parameters on the next run.

SHOT 6017 RESULTS

Electrical signals from shot 6017 in run 7 are shown in figure 1 as a point of reference. Ion current begins within 10 ns of the open-circuit voltage arrival, and reasonable ion efficiency occurs early in time. Eventually, however, the electron current increases and loads down the diode voltage. This loading is both resistive and inductive, although the latter is a larger effect. Our desired operating condition of roughly 1 MV and 250 kA is obtained, but only for about 1 ns. The ion beam energy for this shot is 15 kJ, compared with our typical PRD results of 30-40 kJ. Part of this difference results from the 12% lower Marx charge and open-circuit voltage used on the applied-B diode shots.

Obviously, we would like to reduce the electron loss. For example, if there were no electron loss on this shot, 27 kJ of ions would have been obtained based on the open-circuit voltage waveform. However, the general electron loss behavior seen on this shot has been so typical that this may not be possible. (Perhaps the electron loss is a byproduct of the relatively extreme enhancements required on Gamble II as compared with LION, SABRE, and KALIF.) Reducing the inductance is also difficult. Of the 65 nH in this geometry, 33 nH are inherent to Gamble II, 11 nH are inherent to the diode, 6 nH result from a door spacer that has been required to inhibit flashover, and 16 nH result from the extension we use to improve diagnostic access. Thus, an inductance reduction of more than about 15 nH does not seem feasible.

We have sufficient ion current, however, that decent results could be obtained even without eliminating the electron loss. Figure 2 shows calculated waveforms assuming a 30% reduction in both the electron and ion current. Here we get an acceptable 200 kA of ions at a healthy 1-1.4 MV. Operating at our normal (12% higher) Marx charge, still better results would be expected. The problem is that the calculated insulator voltage in

Fig. 2 has increased from 1.8 to 2.2 MV, and flashover would be expected. So, while on shot 6017 it is the late-time impedance that degrades the diode operation, in principle this problem could be solved by operating at higher impedance if only the early time insulator voltage could be reduced.

All of this points to a road map toward obtaining diode performance sufficient for transport experiments: (1) operate with a higher diode impedance, and try to reduce the early-time insulator voltage by improving the EMFAPS; (2) try to reduce the late-time electron loss by optimizing the field geometry, etc., but don't depend on this being possible; (3) if all else fails, use power conditioning, such as an upstream POS/PFD, to keep the insulator voltage down early in time. This plan will be discussed further after the following analysis of the data from run 8.

RUN 8 RESULTS

Figures 3 and 4 show the magnetic fields calculated for shots 6017-9 ("6019 fields") and 6090 ("optimized fields"). The optimized fields are produced by a 15% reduction in cathode coil currents and 5% increase in anode coil currents, relative to those on shot 6019. Figure 5 shows a summary of shots in run 8, along with shots 6019 and 6017 (on the second page). The early part of this run was star-crossed, as indicated in the second column. The run was preceded by a 3-week down time due to major Marx problems. Residual Marx problems also caused shots 6075-8 to fire late relative to the magnetic field, and several other shots to prefire. For the first 18 shots the inner and outer anode coil connections were reversed. The resulting field has not been calculated yet but will have a much greater inner/outer flux ratio than usual.

(Regarding ATHETA, we have just finished a direct, in situ measurement of rA_{θ} , using a technique suggested by Mike Cuneo. Jess is presently analyzing the results.)

The first several shots were taken with a 5 mm, rather than the standard 7-mm, gap. A 1-mm-smaller gap was used on shot 6098. In these cases the gap was changed by moving the coil assemblies. Therefore, incomplete field diffusion would have resisted the change in V_{crit} by partially conserving the flux. Shots 6091, 6108, and 6110 had fields equal in shape but reduced 10% in amplitude from shot 6090. Shots 6092,3 had cathode fields reduced by a further 5%.

The next column gives the Al film thickness as measured by a nearby thin-film monitor - the actual thickness is estimated to be about 30% greater. The following column gives the thickness calculated from the foil resistance and the bulk resistivity of Al. The standard foil was thus about 1200 Å thick and had a resistance about 5 times greater than the bulk value. On some shots a 3-mil Cu, flux-conserving insert was cast in the anode about 2 mm behind the foil.

The following columns list the time: between the start of the foil current and the arrival of the open-circuit voltage; between the voltage arrival and the moment when the impedance

drops below ten Ω ; the time between $z=10\Omega$ and the diode shorting; the time between the voltage arrival and the diode shorting. The final three columns give the ion beam energy, the open-circuit voltage, and the ion beam energy normalized to that of shot 6019, by scaling as VOC squared.

Data from all shots are presented in the two graphs at the bottom. As these shots were taken under disparate conditions, scatter is to be expected. The left graph plots the diode shorting time against the diode turn-on time. The two do not increase together: shots that turn on early do not short early. This points to different phenomena behind turn-on and shorting. The right graph plots the turn-on time against the delay time. The data are noted separately because of the scatter. For both the 6019 and optimized fields, there is a general trend toward earlier turn-on as the pulser delay is increased, which is reasonable. Note that shots 6017 and 6019 lie off the general trend, as if there were some difference in the anode plasma formation, i.e., a more efficient formation, on those shots. The noted shots, 6078, 6103, and 6108 represent some of the best shots from run 8 and are described further in the next section. The remaining three squares at the bottom of the graph correspond to shots with the smaller gap and reversed anode coil connections.

BEST SHOTS FROM RUN 8

Waveforms from the three best shots from run 8 are shown in Figs 6-8, and the impedance histories are compared in Fig 9. Shot 6103, the best of the run, has a similar impedance history, and 85% of the ion beam energy, as shot 6017. Almost equal results were obtained on shots 6108 (optimized fields) and 6078 (wrong connection, late machine). It is interesting to note that good results are obtained for three different field configurations, and it will be quite useful to calculate the field on shot 6078. In particular, it would be interesting to repeat shot 6078 with a larger gap or stronger field. All of these shots had relatively rapid turn-on. Figure 10 shows the results of a shot taken without firing the pulser: the foil current is clearly seen to have an effect.

MORE COMPARISONS

Shots with different pulser delays are compared in Fig 11. Increasing the delay here hastens the turn-on but not shorting, as shown previously on the two graphs. These data indicate that we may not be driving the foil hard enough. Figures 12-13 show that for two field configurations, reducing the gap does not reduce the turn-on time but does reduce the subsequent impedance. Again, without running ATHETA we do not know precisely how much V_{crit} changes when the gap is changed. These figures suggest that improved performance might be possible with larger gaps.

Figure 14 shows similar impedance behavior from shots with two different field strengths (see the table). These data, along with the good results obtained for three field configurations, indicate that diode performance is not strongly affected by 10%-level changes in the field configuration.

Finally, figure 15 shows results from similar shots with different foil thicknesses and resistivities. Thinner foils are associated here with faster impedance collapse, although this is not always observed.

Over the course of this run, as well as on a few shots during run 7, no consistent effect of the flux-excluding insert has been observed.

ROAD MAP TO TRANSPORT RESEARCH

As discussed earlier, future plans comprise two near-term and one or two more distant (~4-6 months) steps. Further bench tests of the source with a new pulser are beginning now. The next Gamble II run is planned for late September. Depending on the outcome of these experiments, we may wish to investigate power conditioning and/or further diode optimization.

The upcoming bench experiments will be carried out using our new Marx/water-line pulser and higher-voltage cables. This pulser, which will be described in a future note, produces a pulse of similar amplitude (35 kA) and risetime (20 ns) as the previous version, but with a narrower pulsewidth of 30 ns FWHM. By changing the Marx capacitors and/or line length, it should be possible to produce currents up to 50 kA and pulselengths from 30-60 ns. We plan to use Stark broadening and/or two-color interferometry to better diagnose the plasma density, and a new, gated intensifier to better observe the breakdown uniformity. The use of copper and steel foils will be studied, and targets for titanium foils will be ordered shortly.

This work has been a challenge because the applied-B/EMFAPS diode has such a huge parameter space. However, the results of runs 7 and 8 help to narrow down the optimization process, and suggest a series of more-controlled experiments for run 9. Since minor changes in the field configuration are not seen to affect greatly the diode performance, it makes sense to stay with the 6019 fields, which have given the best results, for the near term. While flux-excluding inserts have so far shown no effect, we might as well keep using them. Unless the upcoming bench tests show otherwise, we should stay with our standard, 950 TFM, ~250 Å effective thickness Al foils. Assuming that we wish to keep using the maximum foil current possible, the remaining variables are the pulser delay, the foil current pulselength, and the diode gap. The latter can be varied either by moving the coil assemblies or by changing the cathode tips. For the first few shots, I would suggest using the same tips with a 1 to 2 mm wider coil spacing, the maximum possible pulser delay, and varying the drive pulse length.

By restricting ourselves to the above four variables, we will be able to begin looking at reproducibility also.

If we are not able to obtain an early time low impedance by optimizing the EMFAPS, power conditioning will be necessary. This approach is less attractive because of the added complexity. On the other hand, it may make our diode more relevant to

experiments on SABRE.. If power conditioning becomes necessary, the work required can be performed partly under the auspices of our 6.1 program on plasma-filled diode research, thus minimizing the diversion of SNL-supplied resources from our major goal of transport research.

Fig 1

Shot 6017

$E_i = 15 \text{ kJ}$
 $V_D = 1.8 \text{ mV}$

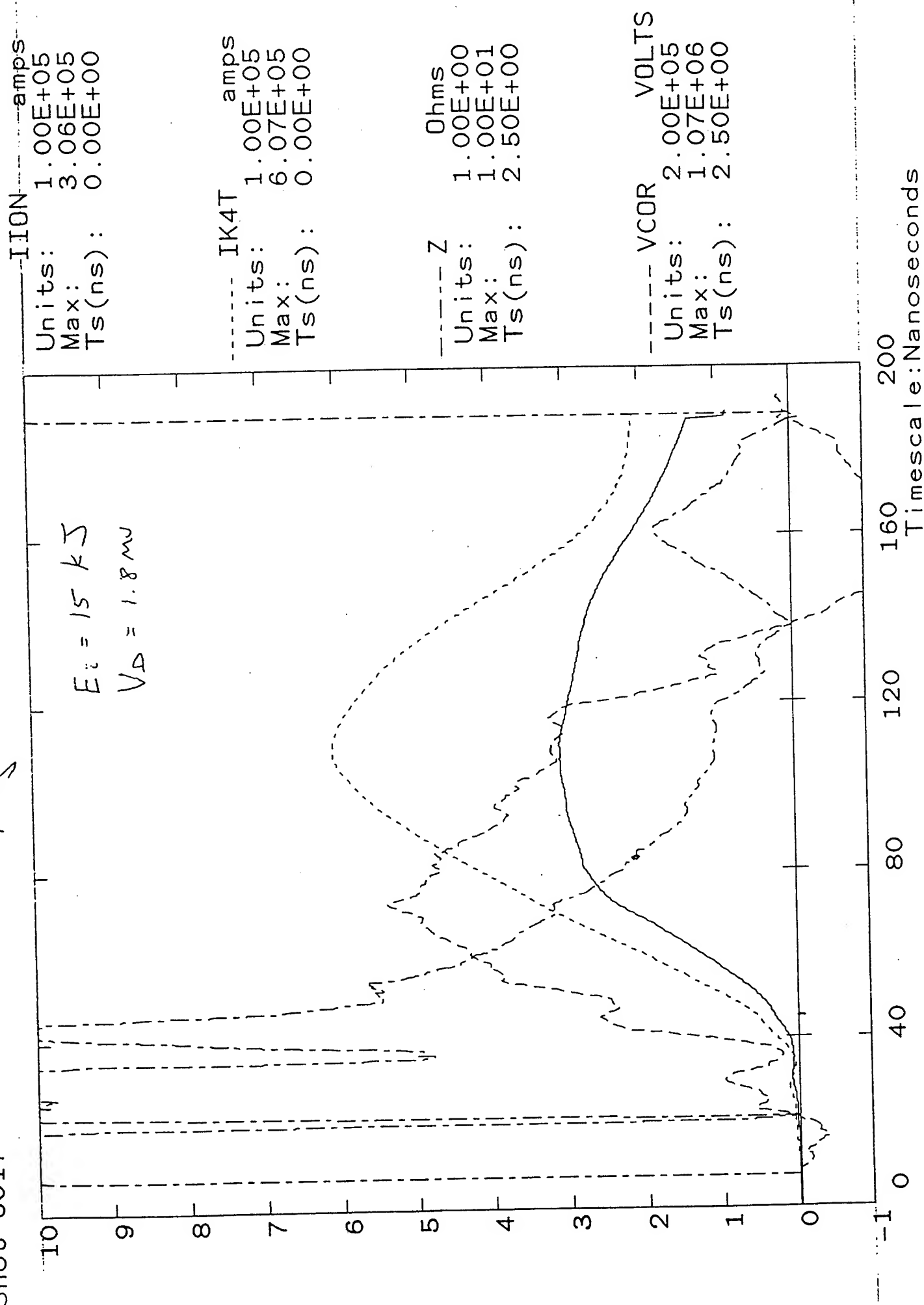


Fig 2 hypothetical waveforms

Shot 6017

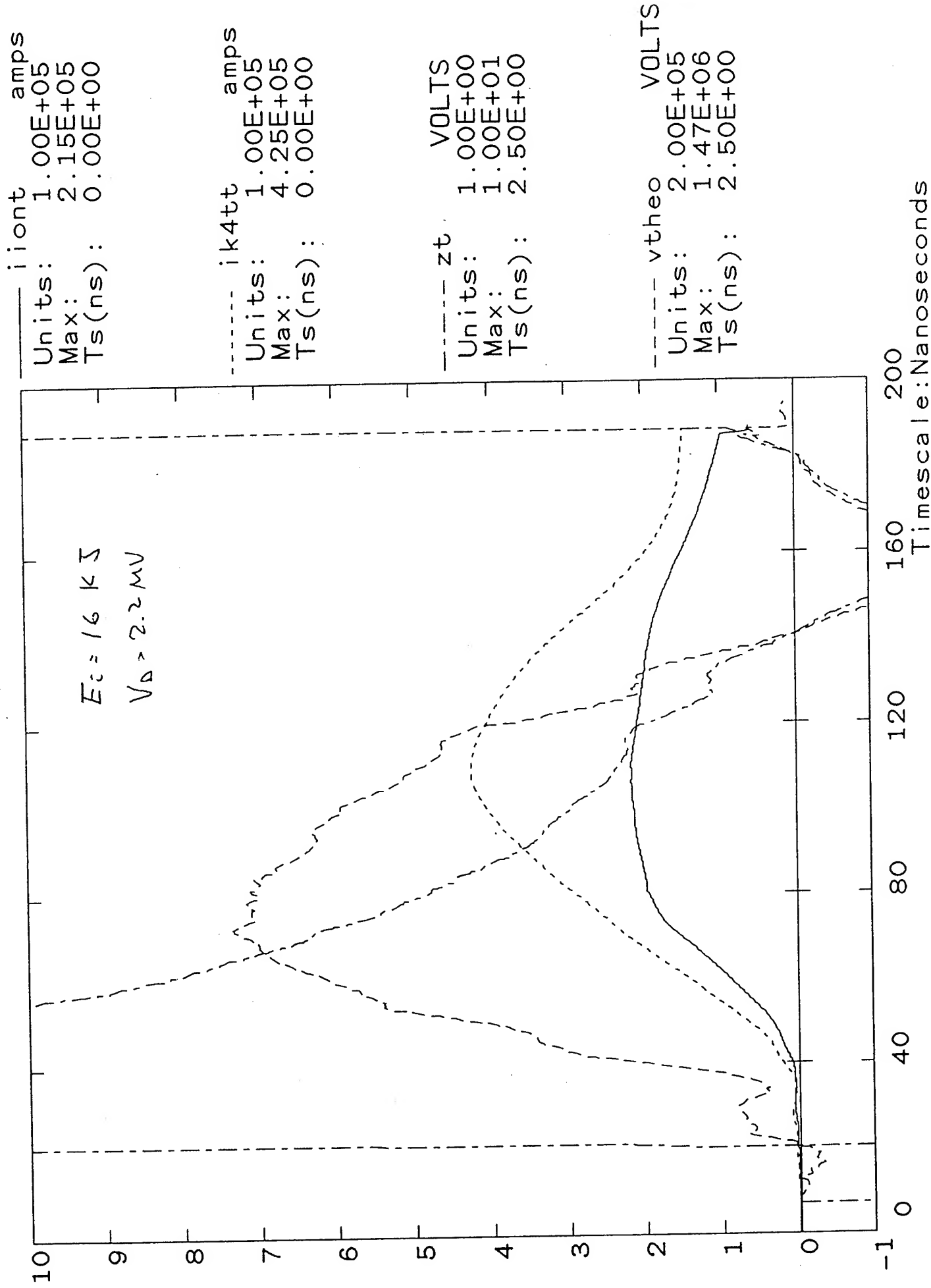


FIG 3 6019 field contours: 20
 min: -2.0386E-03
 max: 2.2322E-03

at0826091314.arc

- buf: 1 mult: 0.000E+00
- buf: 2 mult: 0.000E+00
- buf: 3 mult: 0.000E+00
- buf: 4 mult: 0.000E+00
- buf: 5 mult: 1.000E+00
- buf: 6 mult: 1.000E+00
- buf: 7 mult: -1.000E+00
- buf: 8 mult: -1.000E+00

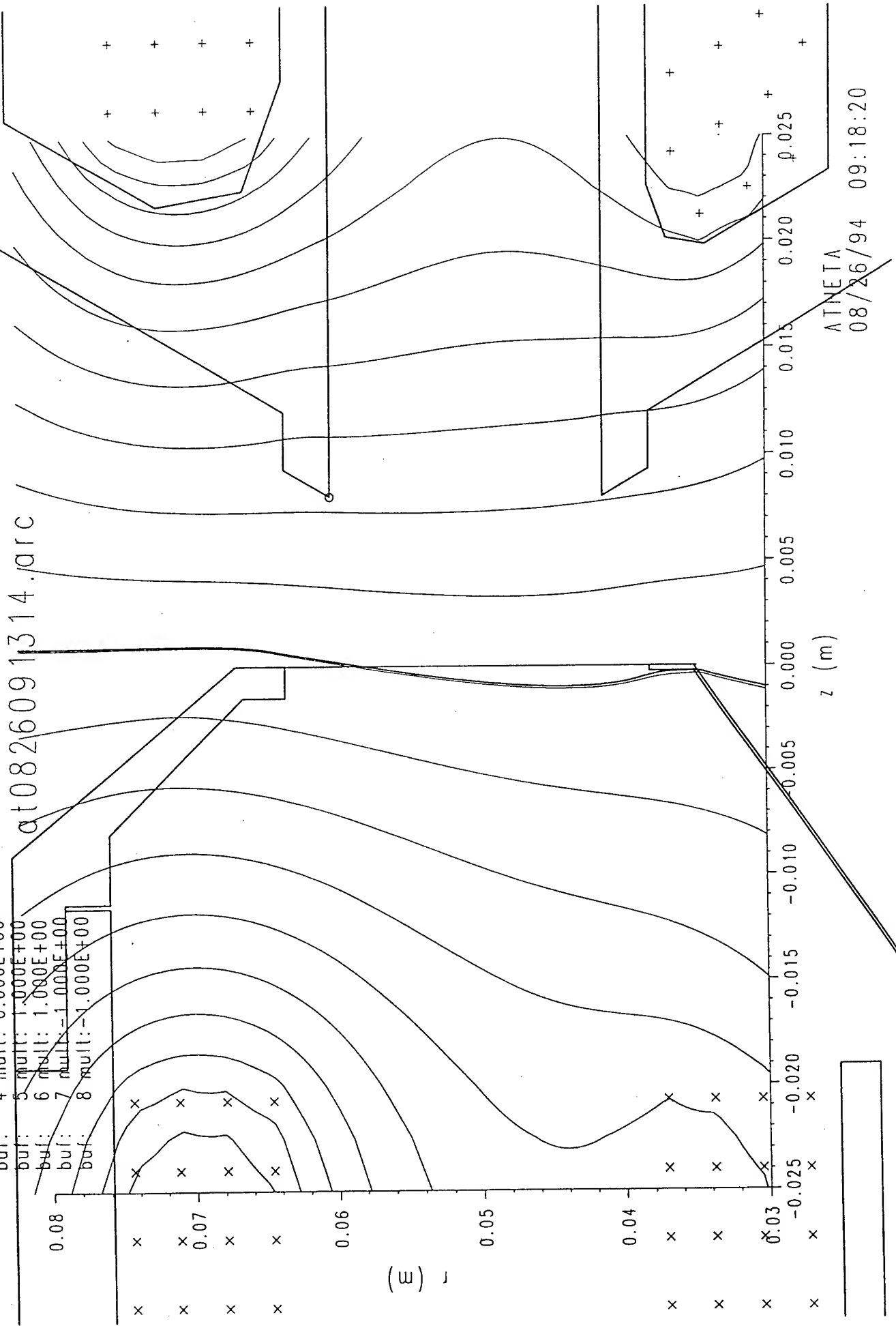
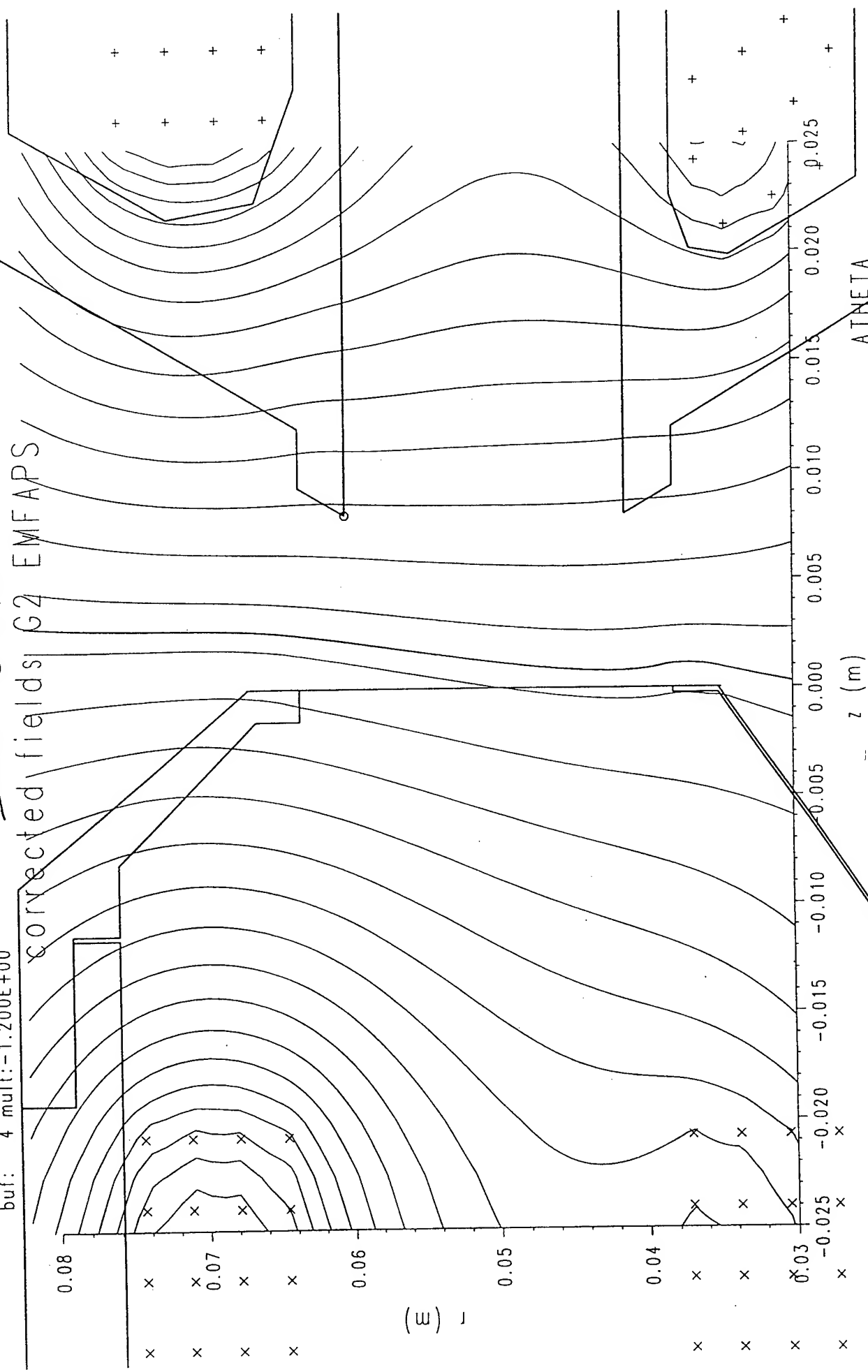


Fig 4 'optimized' fields
 shot 6090

buf: 1 mult: 1.000E+00
 buf: 2 mult: 1.000E+00
 buf: 3 mult: -1.150E+00
 buf: 4 mult: -1.200E+00

corrected fields G2 EMFAPS



ATHETA
 06/02/94 16:25:03

Fig 5

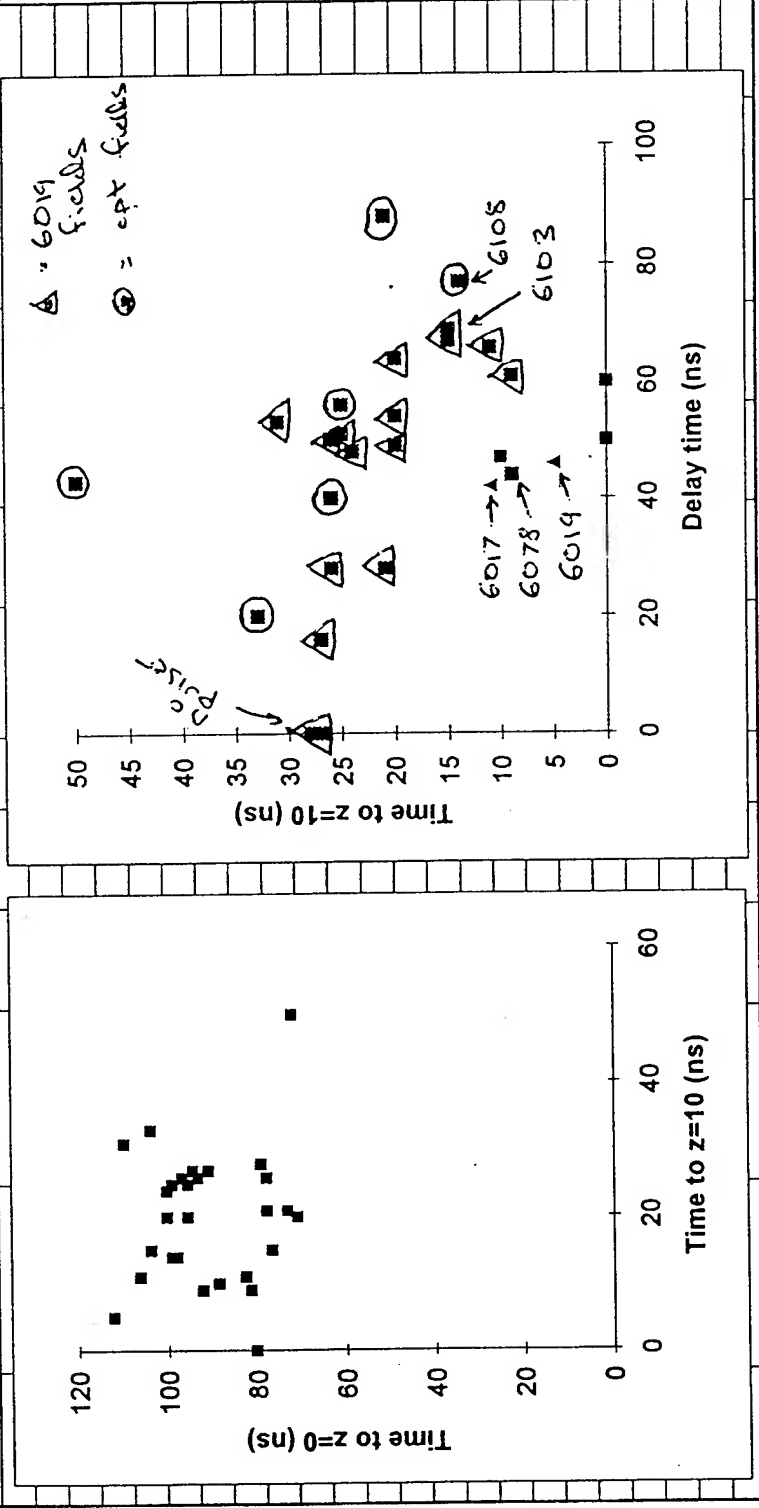
APPB.XLS

shot	comnts	fields	TFM	eff th	ins	delay,ns	Z=10	Z dur	Z=0	ei(kj)	vocMV	E:6019
6072	5 mm gap	no field										
6073	5 mm gap	no field										
6074	5 mm gap	prefire										
6075	5 mm gap	wrong, late	?	?	?	52	11	71	81	4.6	2.2	6.4
6076	5 mm gap	wrong	950	155 ?	?	71	0	80	80	5.1	2.4	6.0
6077	5 mm gap	wrong, v late	?	?	?	59	0	80	80	5.2	2.2	7.4
6078		wrong, late	?	?		55	12	77	89	11.8	2.5	12.7
6079		prefire										
6080		prefire										
6081		prefire										
6082	flash	wrong	950	153 Y	?	51	59	13	72	2.9	2.0	4.7
6083	flash	wrong	950	224 ?	?	24	39	65	104	9.3	2.2	12.9
6084	flash	wrong	950	242 ?	?	47	31	63	93	8.4	2.3	10.4
6085	no pulser	wrong										
6086		prefire										
6087	flash	wrong x.9	950	220 ?	?	66	30	66	96	6.8	2.3	8.4
6088	no pulser	wrong										
6089	no pulser	wrong										
6090	flash	opt x 1.1	950	212 N	N	57	28	72	100	7.5	2.2	10.7
6091	flash	opt	950	165 N	N	19	32	59	91	7.6	2.4	8.9
6092	flash	opt, K x.95	950	200 Y	Y	33	31	47	78	7.2	2.5	8.0
6093	flash	opt, K x.95	950	240 N	N	59	31	66	97	9.6	2.3	12.2
6094	flash		950	160 N	N	63	37	73	110	7.3	2.3	9.3
6095	flash, np		950	257 ?	?	0	32	63	94	6.1	2.2	8.7
6096	flash		950	85 ?	?	60	30	70	99	7.9	2.2	10.9
6097	flash	slm 6019	950	250 N	N	76	24	77	100	7.7	2.2	11.0
6098	6 mm gap		950	225 N	N	79	18	59	77	7	2.4	8.4
6099	wider area		950	130 Y	Y	64	24	47	71	4.5	2.4	5.4
6100	wider area		950	275 N	N	58	24	72	96	8.9	2.4	10.1
6101	slightly wider		320	50 N	N	72	11	81	92	8.8	2.2	12.2
6102	area here on		320	20 Y	Y	78	13	70	83	7.3	2.2	9.8
6103			950	216 N	N	81	18	86	104	8.9	2.0	14.4
6104	no pulser											
6105	no pulser		360	9 Y	Y	0	33	46	79	4.8	2.5	5.2
6106			360	37 Y	Y	33	25	48	73	4.2	2.5	4.5
6107			950	225 N	N	0	17	83	99	11.1	2.5	12.3
6108					N	91	17	81	98	8.7	2.3	11.0
6109		prefire										
6110			300	6 Y	Y	104	25	53	78	6.2	2.3	7.9

Fig 5, (cont)

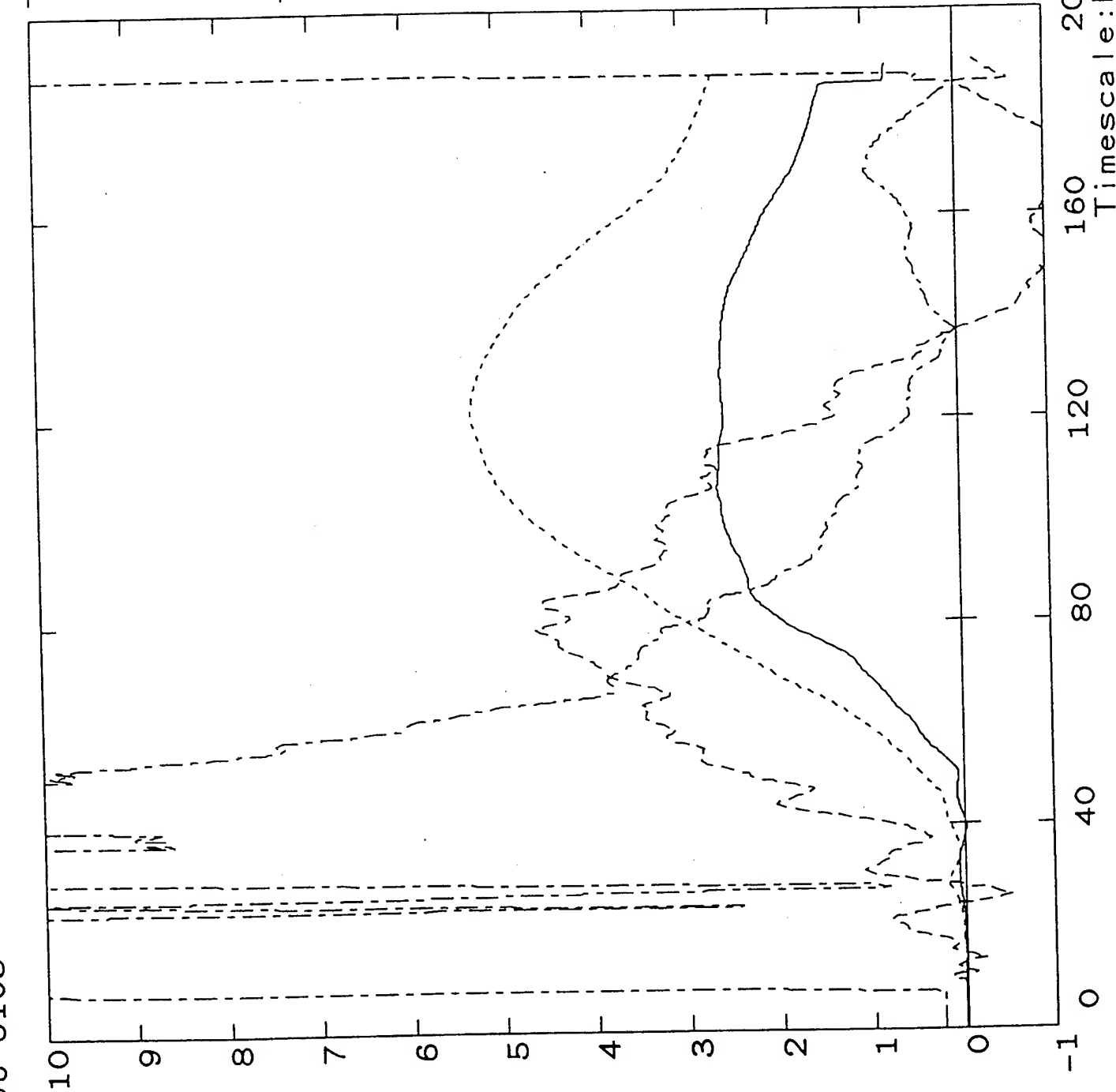
APPB.XLS

6017	6019	950	300 N	50	13	93	106	15	2.5	16.6
6019	6019	950	83 N	54	6	106	112	16	2.6	16.0



F. 2 6

Shot 6103



Units: 1.00E+05
Max: 2.62E+05
Ts(ns): 0.00E+00

Units: 1.00E+05
Max: 5.28E+05
Ts(ns): 0.00E+00

Units: 1.00E+00
Max: 1.00E+01
Ts(ns): 0.00E+00

Units: 2.00E+05
Max: 9.23E+05
Ts(ns): 0.00E+00

FIG 7

Shot 6078

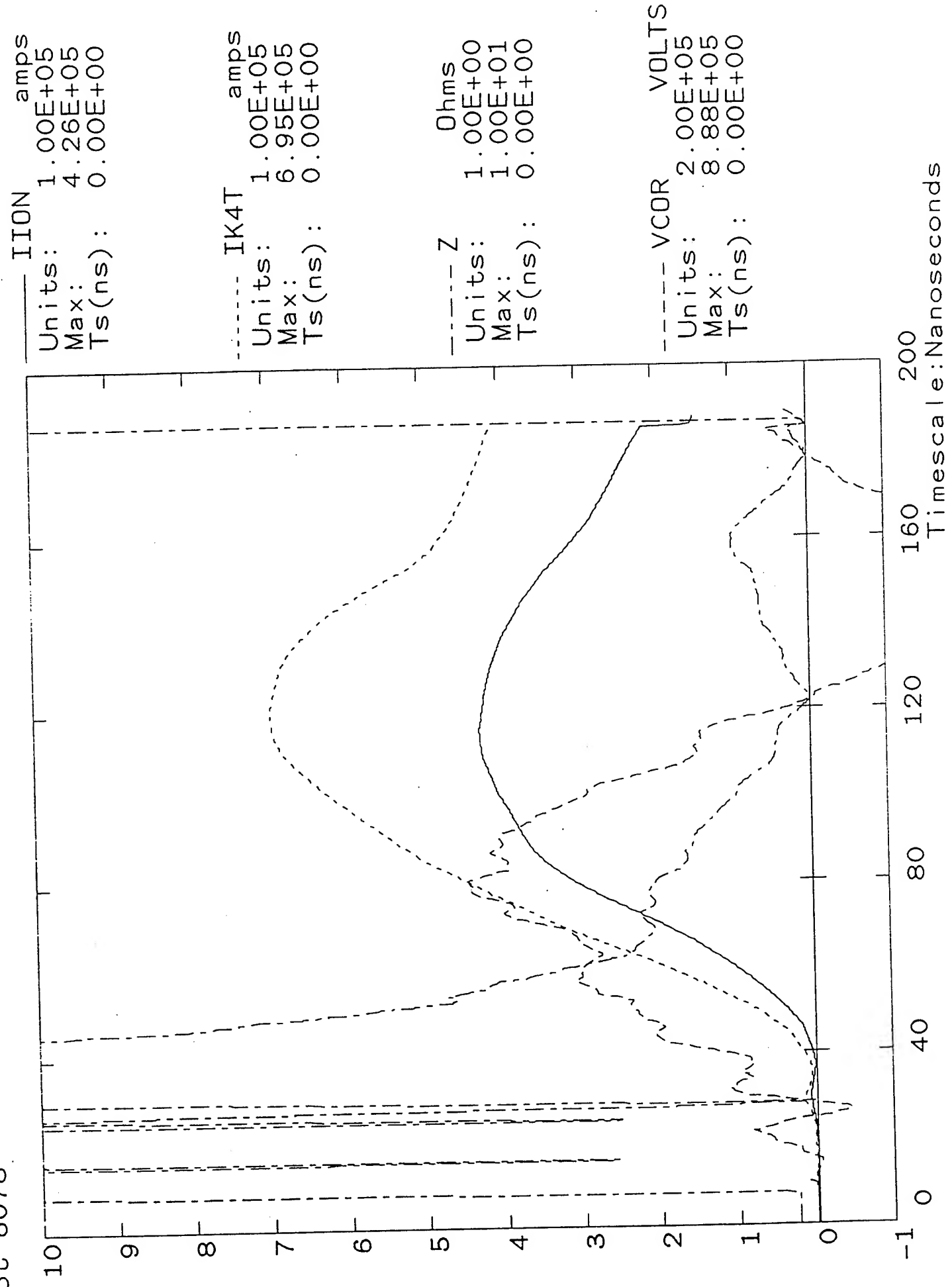


FIG 8

Shot 6108

IION amps
 Units: 1.00E+05
 Max: 2.89E+05
 Ts(ns): 0.00E+00
 IK4T amps
 Units: 1.00E+05
 Max: 6.40E+05
 Ts(ns): 0.00E+00
 Z Ohms
 Units: 1.00E+00
 Max: 1.00E+01
 Ts(ns): 0.00E+00
 VCOR VOLTS
 Units: 2.00E+05
 Max: 9.32E+05
 Ts(ns): 0.00E+00

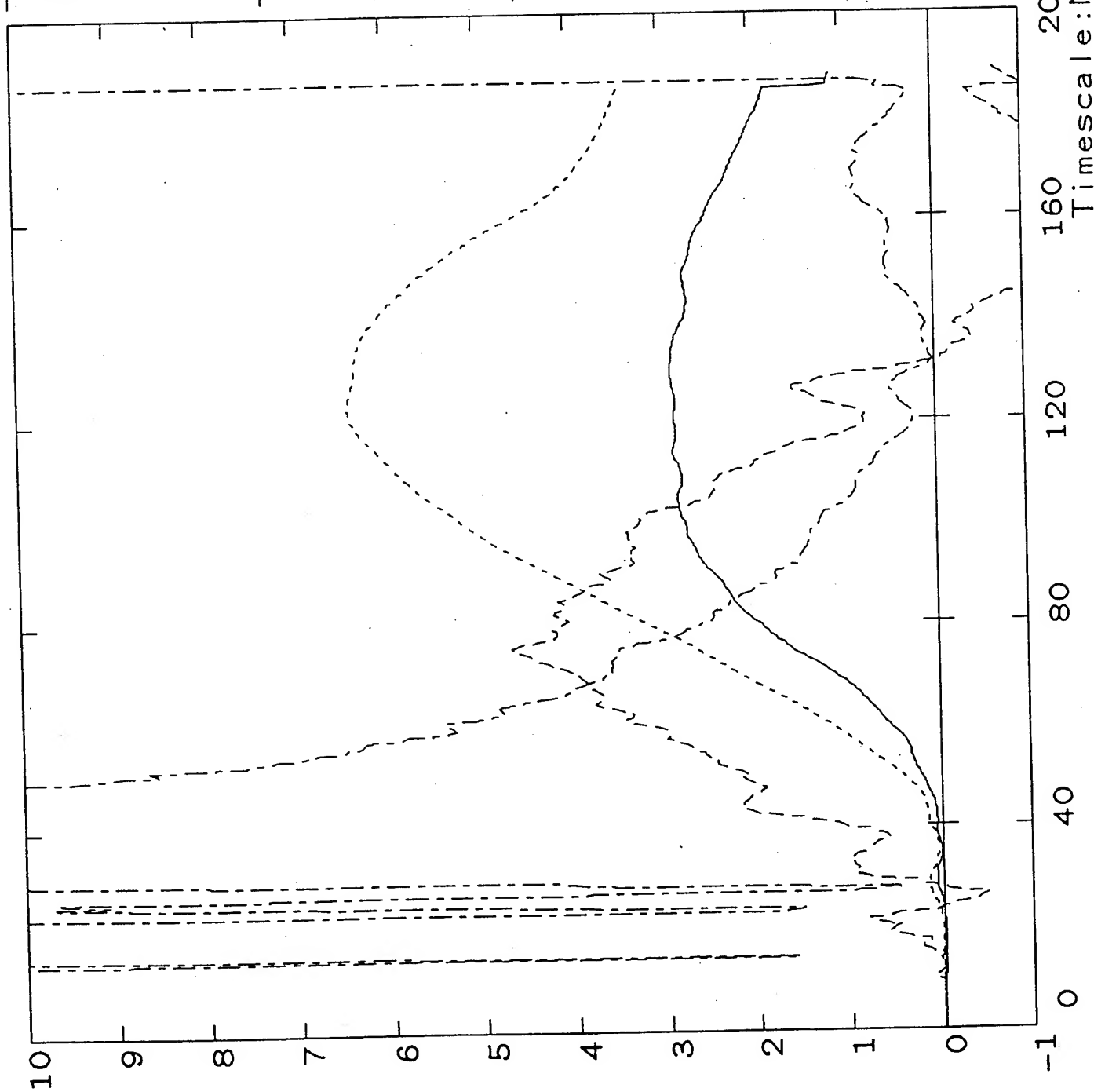


Fig 9

Shot 6017

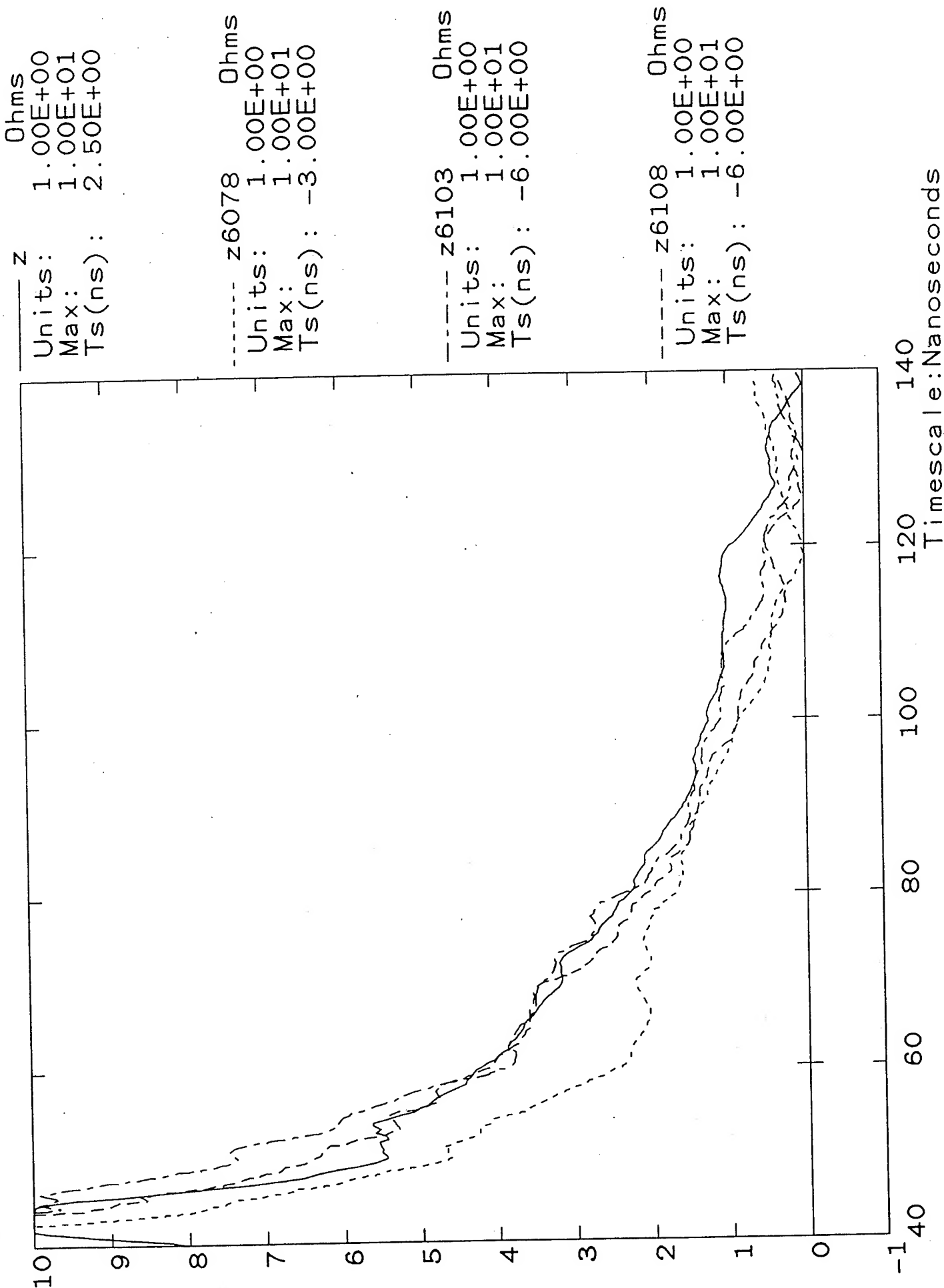
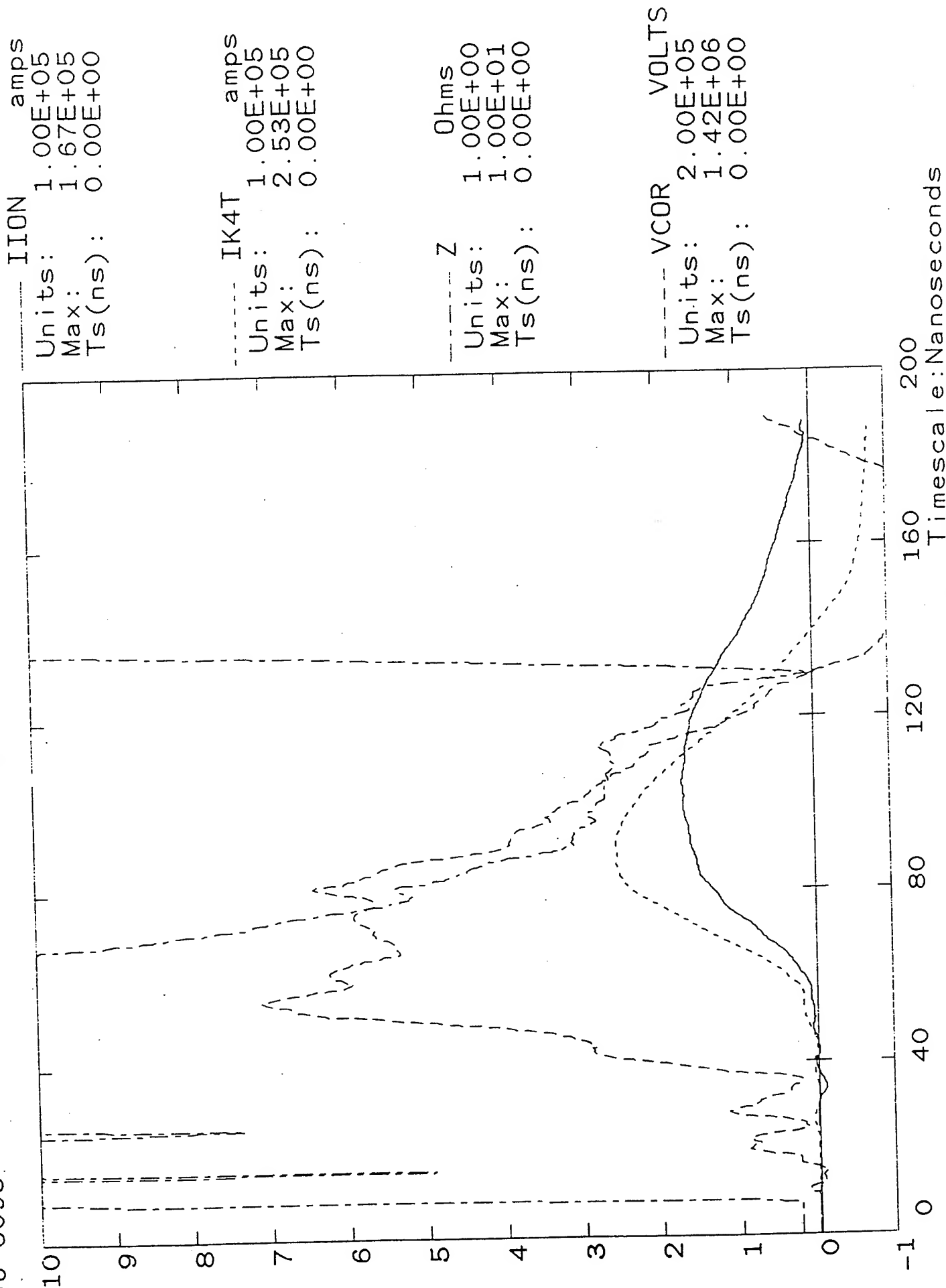


Fig 10

Shot 6095



Shot 6103

Fig 11

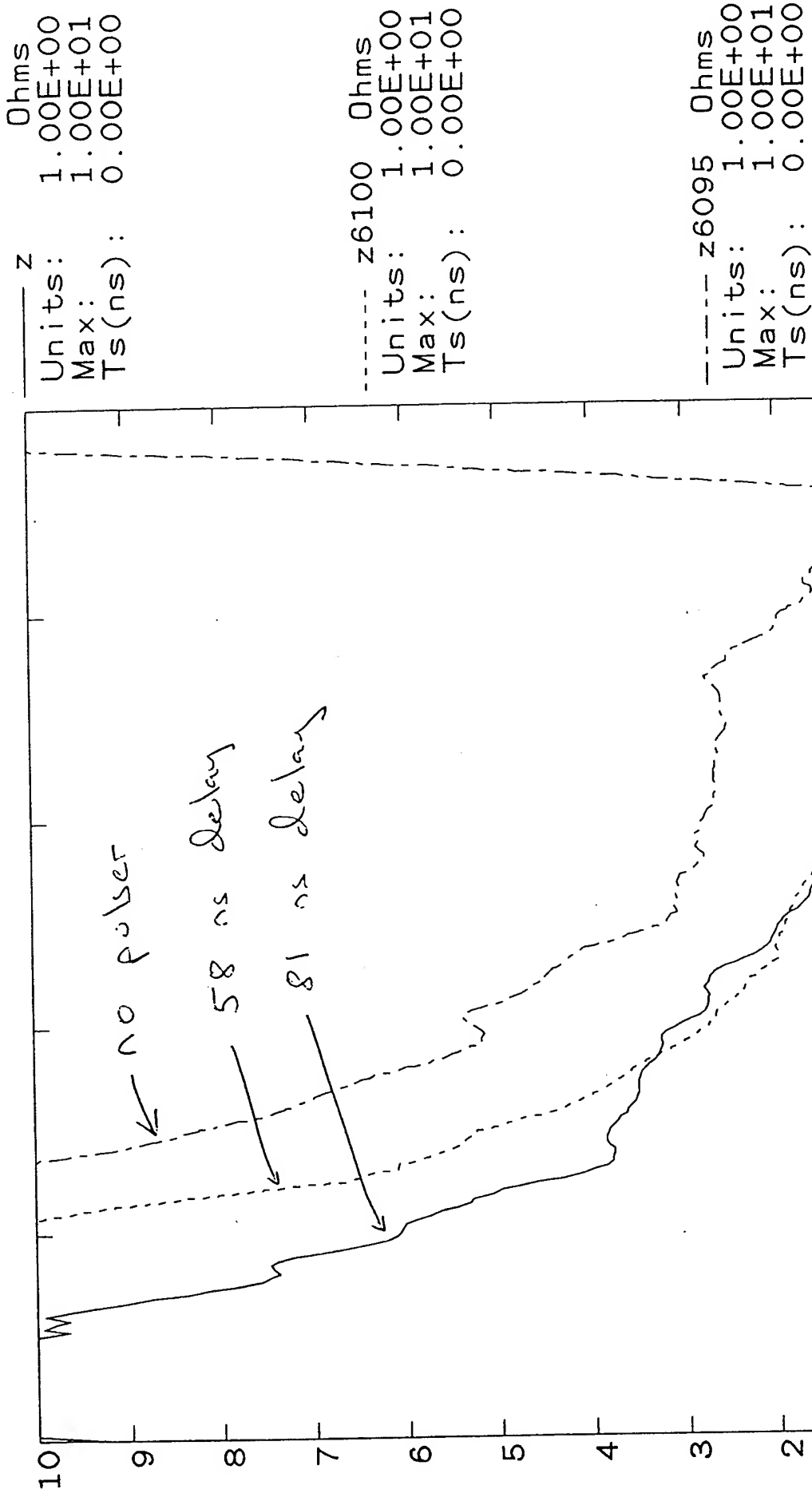


Fig 12

Shot 6078

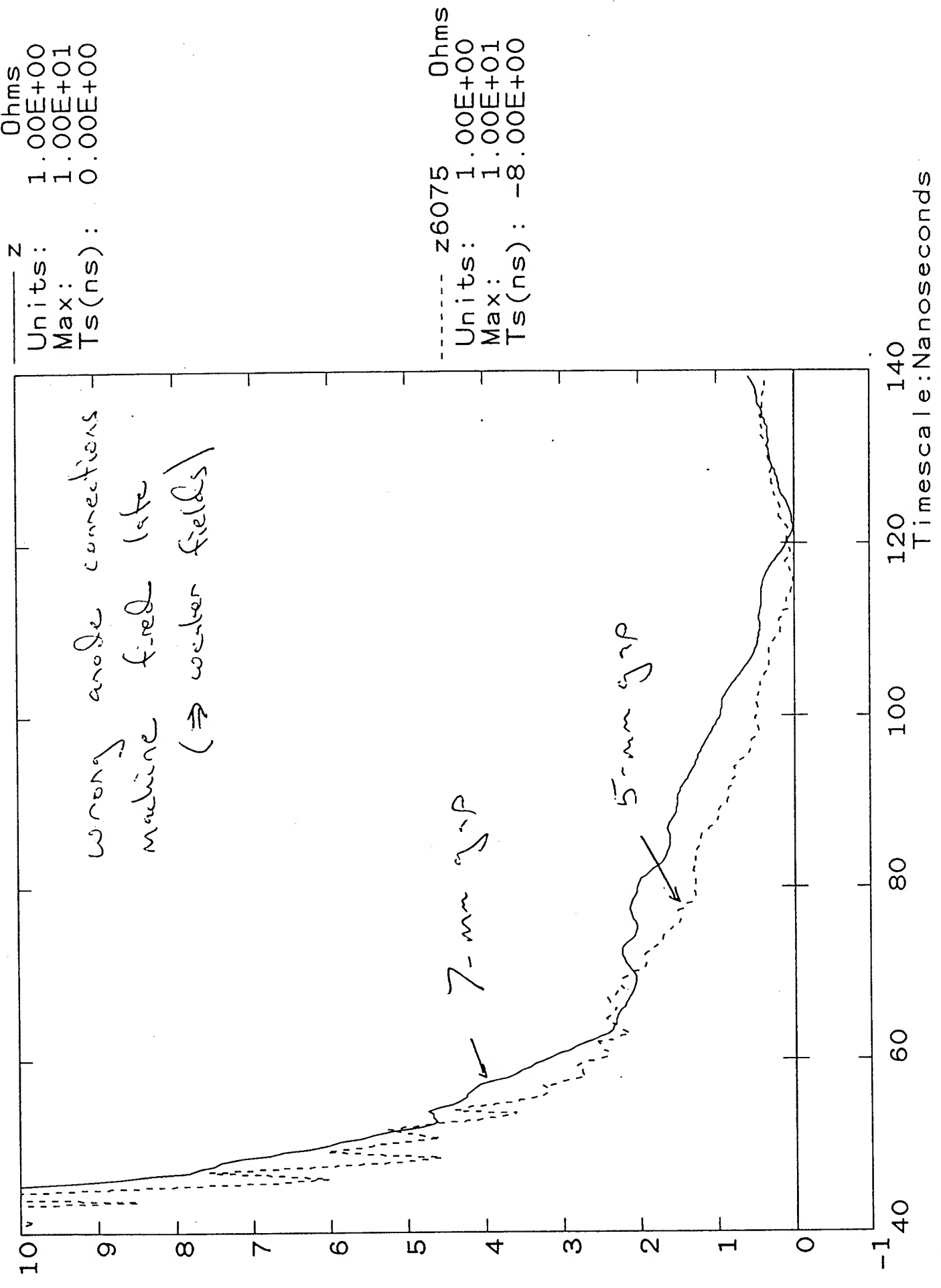
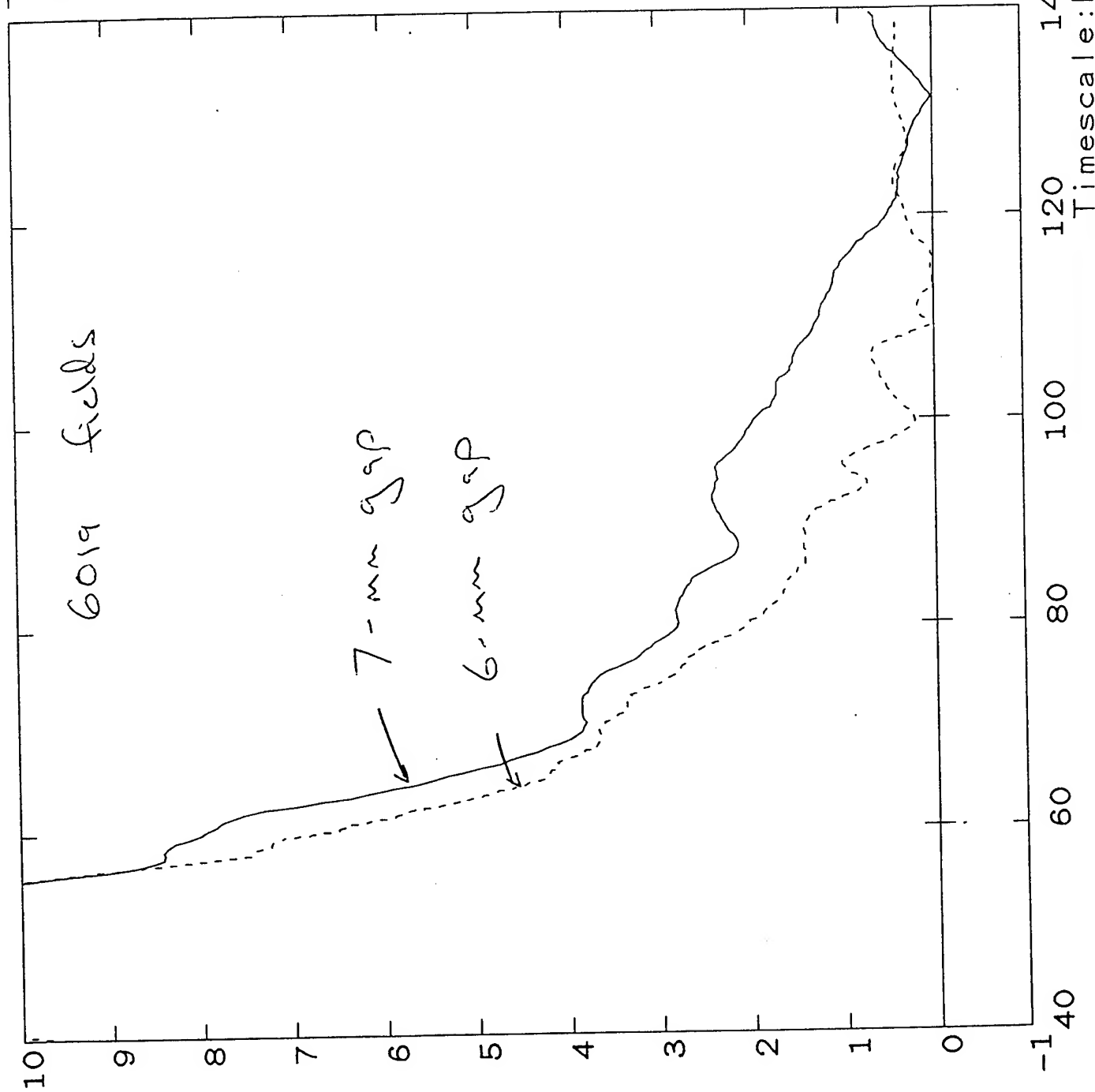


Fig 13

Shot 6097



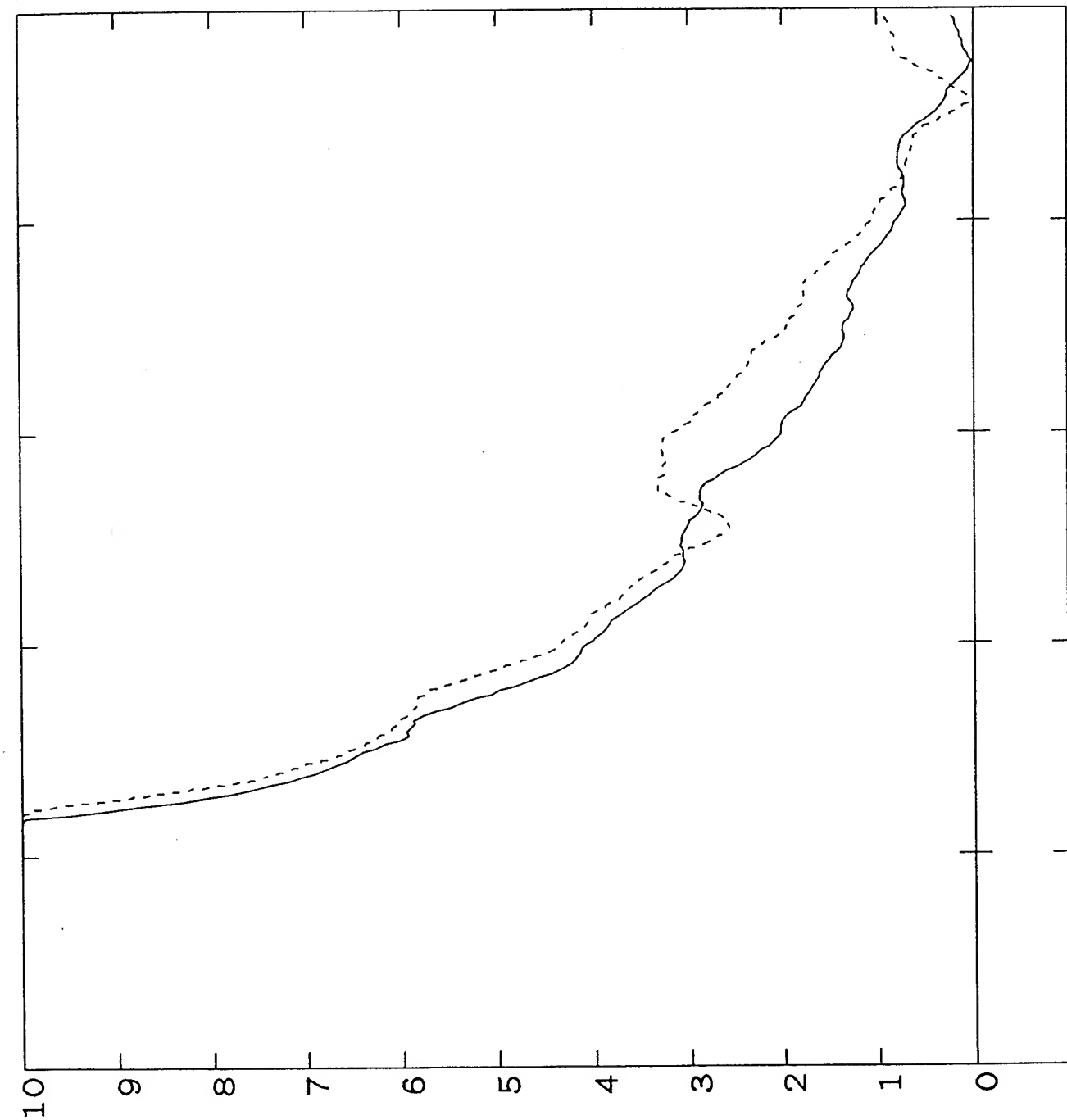
Units: 1.00E+00
Max: 1.00E+01
Ts(ns): 0.00E+00

----- z6098 Ohms
Units: 1.00E+00
Max: 1.00E+01
Ts(ns): 0.00E+00

Figure 14

Shot 6090

Units: 1.00E+00
Max: 1.00E+01
Ts(ns): 0.00E+00

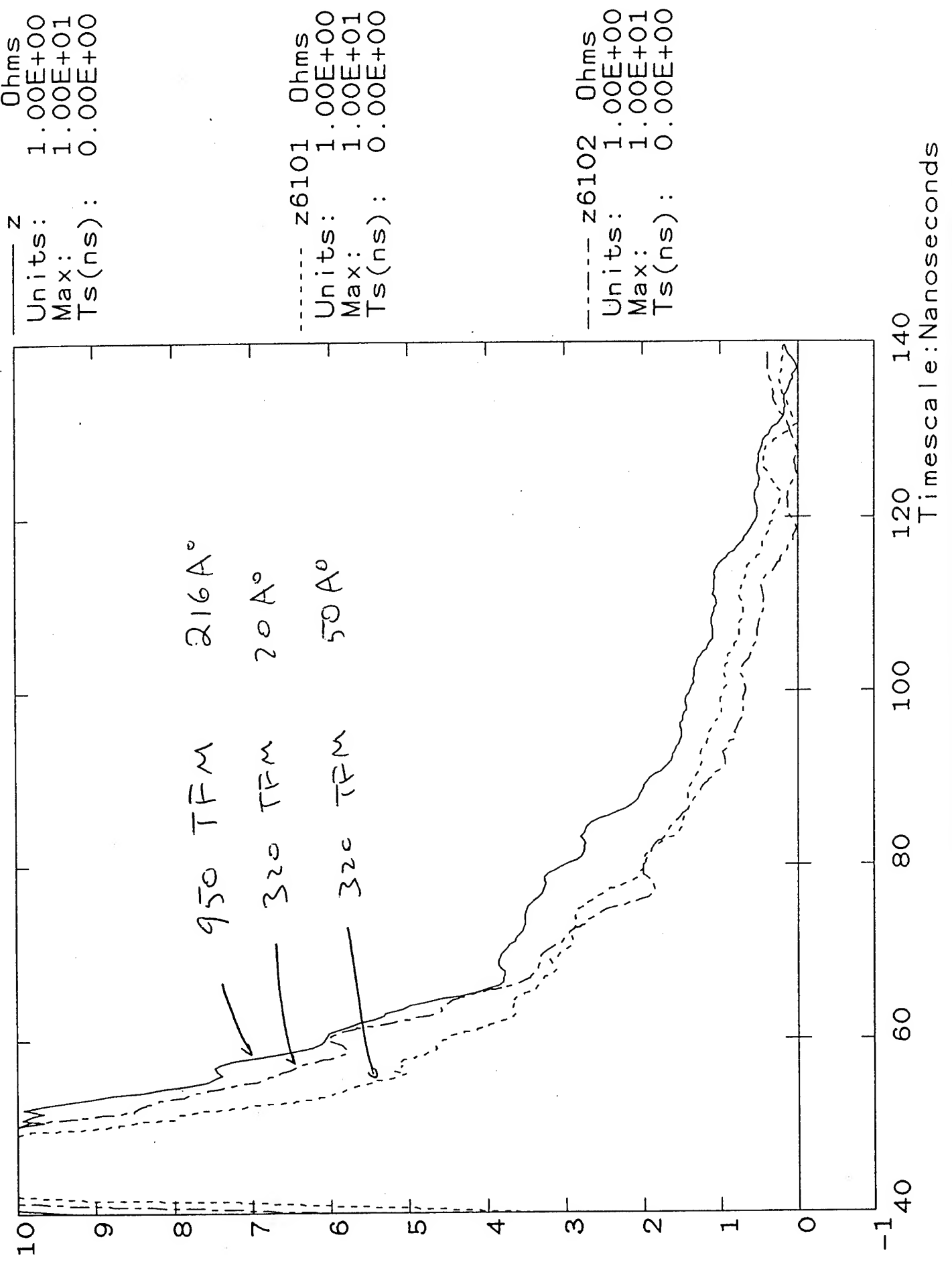


Units: 1.00E+00
Max: 1.00E+01
Ts(ns): 0.00E+00

Timescale: Nanoseconds

Fig 15

Shot 6103



PULSED POWER PHYSICS TECHNOTE 94-19

TITLE: ANALYSIS OF RUTHERFORD SCATTERING AND FARADAY CUP DATA
FROM APPLIED-B DIODE RUNS 7 AND 8

Author: D. Hinshelwood

Date: September 21, 1994

Abstract: Rutherford scattering has been used to diagnose the ion beam on some of the shots during applied-B diode runs 7 (spring 1994) and 8 (recently). A new Faraday cup, developed at Cornell, was also used on the last shot of run 8. Data from these diagnostics are discussed and compared with predictions in this note. While there are some unexplained features in these data, and indications that on some shots the ion voltage and/or current may be incorrect later in time, the overall picture is that the extracted ion beam is roughly $2/3$ protonic and consistent with the diode electrical waveforms. Both diagnostics are easy to field, and are seen to work reasonably well in this difficult, high-current-density environment. Future refinements are also possible. The scattering foil can be expanded to sample a larger fraction of the beam, and both diagnostics are well-suited to being fielded in multiple arrays that allow spatial resolution of the beam. Therefore, information on both the total ion current and its distribution can be obtained in the future. I am enthusiastic about the potential of both diagnostics for diagnosing transported ion beams in all of our ion beam research programs.

Rutherford scattering has been used to diagnose the ion beam on some of the shots during applied-B diode runs 7 (spring 1994) and 8 (recently). A new Faraday cup, developed at Cornell, was also used on the last shot of run 8. Data from these diagnostics are discussed and compared with predictions in this note.

The relevant shots are summarized in the spreadsheet on the following page. Columns 5 AND 6 refer to the anode foil, and are described in TN 94-16. Column 7 is the ion beam energy as determined from VCOR and IION. The column "RS" refers to the scattering arrangement used. In arrangement 1, a single, NRL p-i-n was used. This arrangement allowed for some shot-to-shot variation in geometry, so the one useful shot taken has not been analyzed. Arrangements 2 and 3 are shown at the top of Fig 1. Here, 3, 1.9-cm diam apertures defined the beam area on the scattering foil. The 3 SNL p-i-n's were centered in 2.1-cm ID tubes. With arrangement 2, all 3 scatterers were 1.8- μ Al, and the p-i-n's were located 18 cm from the scatterers. Arrangement 3 used 2 thick-Al scatterers and 1 thick-Ta scatterer. The p-i-n's were located 18 cm from the Al scatterers and 88 cm from the Ta scatterer. Arrangement 4 was used during run 8, and is shown at the bottom of Fig. 1. Here, the beam scattered off a piece of thick Al foil glued to a 1.3-cm wide Al bar that was cut to 45 degrees. The p-i-n was located 18 cm from this bar. In all cases the p-i-n's were covered with a 2.5- μ Ti foil. In arrangements 2 and 3, this foil usually survived, as the aperture plate stopped most of the diode debris. With arrangement 4, where this plate was not used, enough debris blew into the tubes to break the foils on most shots.

CALCULATIONS

The predicted, absolute p-i-n signals were calculated in ANALYSIS using VCOR and IION. Flashover is often seen to produce a spurious spike in VCOR. Therefore, on flashover shots (see column 2), VCOR was artificially truncated by drawing a straight line between its value at the time of flashover to zero at the time of impedance collapse. This represents a reasonable guess of the correct voltage. (Note: the ion energy in column 7 of the spreadsheet was calculated using VCOR, rather than the truncated version, so the values given are probably too high for the flashover shots.) The Ti foil thickness on the p-i-n was increased from 2.5 to 3 μ in the code to approximate the additional stopping by the diode dead layer. The code asks for a geometrical factor, which is the product of the fraction of the beam area that is scattered, times the detector solid angle. The factors used here are: 1.1×10^{-6} and 4.6×10^{-8} for the Al and Ta foils in arrangements 2 and 3; and 1×10^{-6} for arrangement 4. Calculated and observed signals for a typical shot are shown at the top of Fig. 2.

Columns 9 and 10 give the ratio of the time-integrated p-i-n signal to the time-integrated predicted signal. Departures of this ratio from unity occur due to some combination of the following: uncertainty in the geometry, stopping coefficients, ion current, and voltage; beam nonuniformity; and the presence of non-protonic ions in the beam. (The p-i-n foil and Kimfol together will stop all carbon ions at these diode voltages.)

shot	comnts	fields	TFM	eff th	delay,ns	ei(ki)	RS	ratio AI	ratio Ta	AI*1.1	Ta*1.1	comnts
5992	lt flash		5992	200	47	12.7	1					saturated
5993			~5592	360	60	8.5	2					weak sigs
5994			5994	160	73	11.5	2					weak sigs
5995			5994	205	84	7.8	2	0.17		0.19		cent ques
5996			5994	150	45	10.1	2	0.31		0.34		cent ques
5997	no pulser		5994	213	0	5.7	2	0.34		0.37		cent ques
5998			5994	25	59	9	2	0.31		0.34		
6003	flash, no pulser	no field, plug	950	215	0	7.8	3	0.08	0.09	0.09	0.10	weird shot
6004		x5584, no plg	950	160	38	8.8	1					
6005	lt flash, no puls	~6004, plug	950	200	0	10.3	3	0.04	0.07	0.04	0.08	pin1 possibly
6006	lt flash, no puls	~6005, thn plg	950	160	0	5.4	3	0.09	0.07	0.10	0.08	out of
6007	lt flash, no puls	6006, plug	950	211	0	10.4	3	0.08	0.06	0.09	0.07	alignment
6010	flash	5992	950	182	30	10.6	3	0.63	1	0.69	1.10	on shots
6011	flash	6011	360	72	50	12.3	3	0.48	0.61	0.53	0.67	5998-6013
6012		6011	1800	261	74	8.3	3	0.38	0.31	0.42	0.34	
6013	flash	6011	950	268	58	10.3	3	0.44	0.5	0.48	0.55	
6091	flash	opt	950	165	19	7.6	4	0.74		0.81		
6092	flash	opt, K x .95	950	200	33	7.2	4	0.6		0.66		
6093	flash	opt, K x .95	950	240	59	9.6	4	0.63		0.69		tail (2nd hump)
6094	flash	6019	950	160	63	7.3	4	0.85		0.94		tail (2nd hump)
6095	flash, no pulser	6019	950	257	0	6.1	4	0.29		0.32		
6096	flash	6019	950	85	60	7.9	4	0.89		0.98		
6097	flash	sim 6019	950	250	76	7.7	4	0.59		0.65		
6098	6 mm gap	6019	950	225	79	7	N					no pin
6099	wider area	6019	950	130	64	4.5	4	0.29		0.32		
6100	wider area	6019	950	275	58	8.9	4	0.82		0.90		tail
6101	slightly wider	6019	320	50	72	8.8	4	2.6		2.86		
6102	area here on	6019	320	20	78	7.3	4	0.82		0.90		
6103		6019	950	216	81	8.9	4	0.47		0.52		tail (2nd hump)
6104	no pulser	6019					4	0.27		0.30		tail
6105	no pulser	6019	360	9	0	4.8	4	0.43		0.47		tail
6106		6019	360	37	33	4.2	4	0.17		0.19		
6107		6019	950	225	0	11.1	4					no HP
6108		6019			91	8.7	4	0.46		0.51		tail
6109		prefire					4					
6110		6019	300	6	104	6.2	4	1		1.10		tail

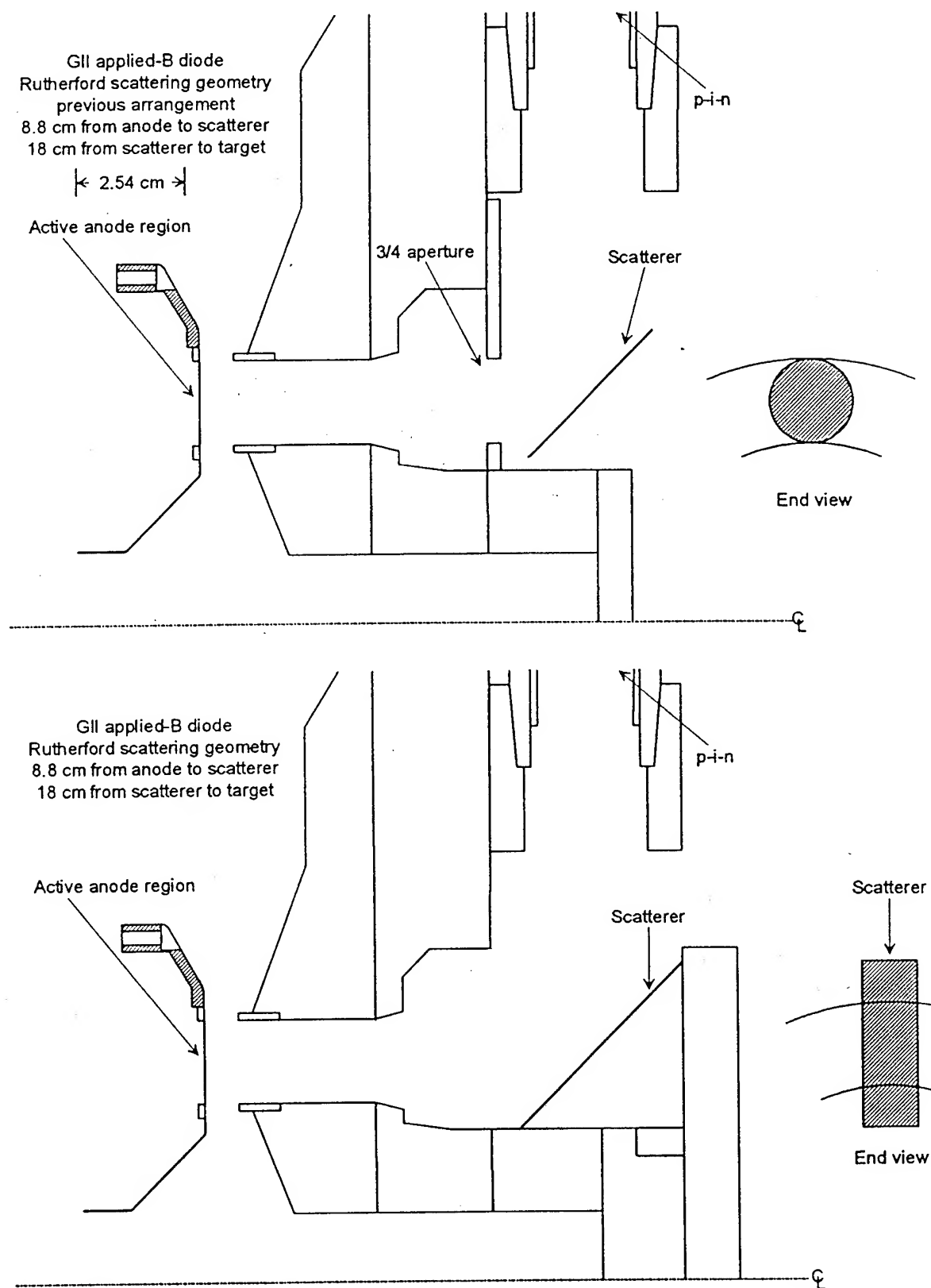


Fig. 1: Rutherford scattering arrangements used in runs 7 (top) and 8 (bottom).

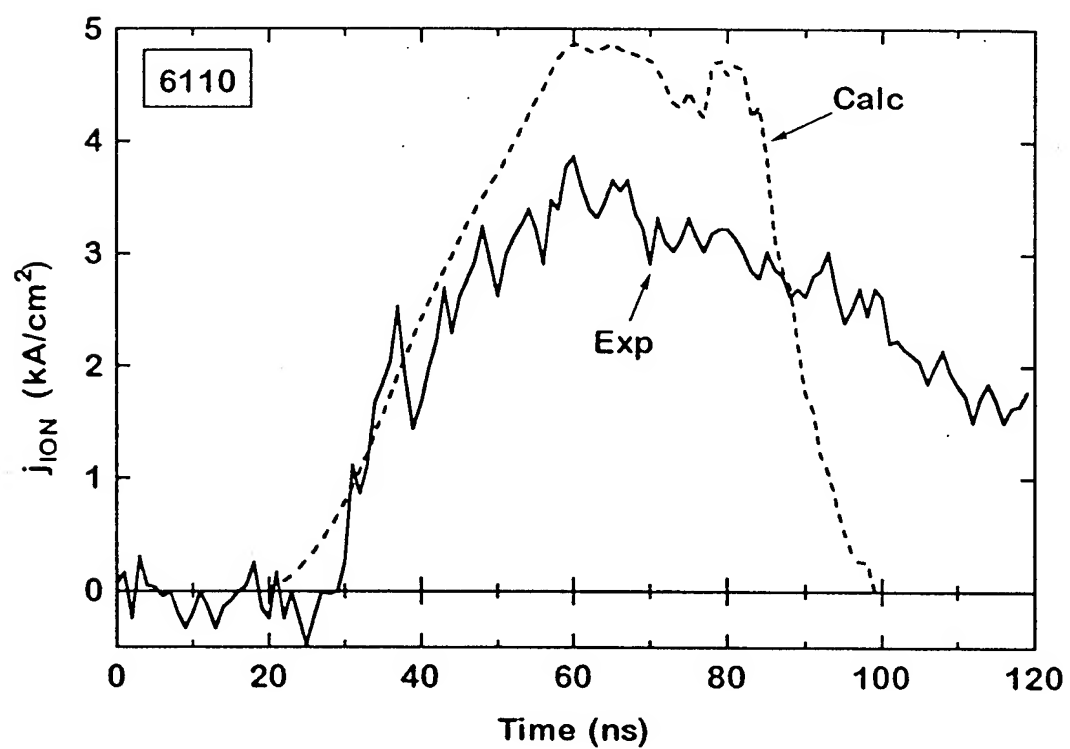
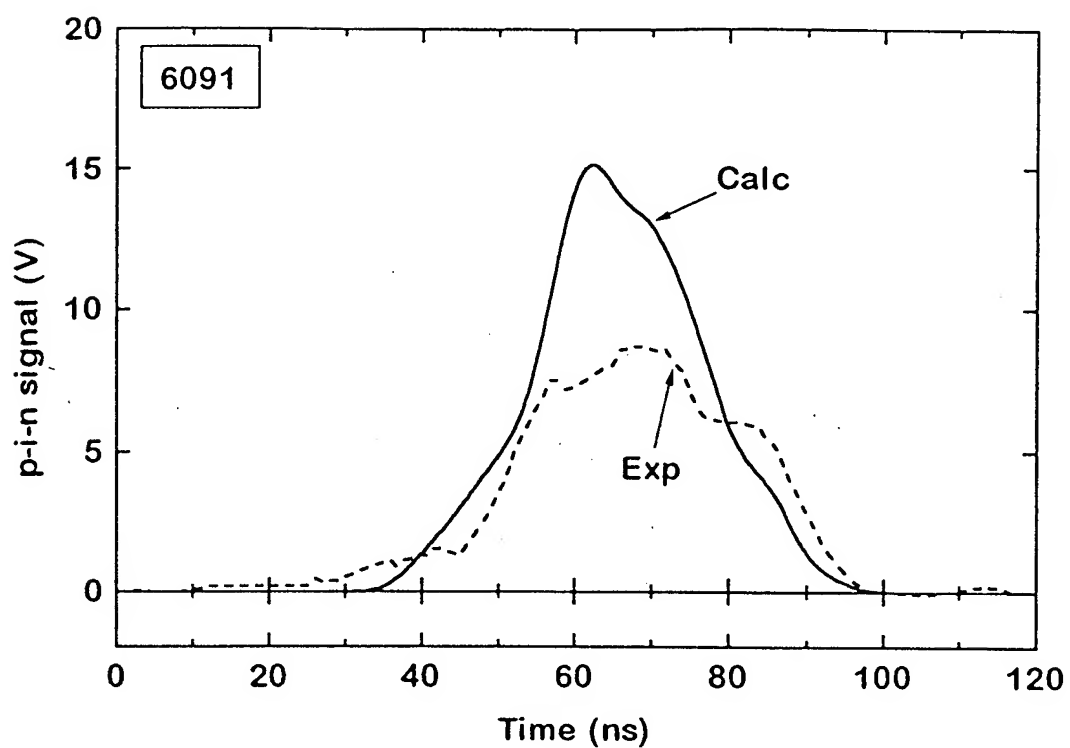


Fig. 2: Calculated and observed signals from Rutherford scattering (top) and the Cornell Faraday cup (bottom).

UNCERTAINTIES

Calculation of the yield requires the fraction of the beam intercepted by the detector, the detector solid angle, and the scattering angle. Inspection of the end views in Fig. 1 shows that with arrangements 2 and 3, the intercepted beam fraction depends on the beam width and radius. If the beam bends inward, as was observed on this run, the intercepted fraction will decrease. This results in an estimated uncertainty of 10-20 percent. The scatterer shape in arrangement 4 was chosen to reduce this problem. (Ideally, a pie-shaped scatterer would be used, eliminating this uncertainty completely). The uncertainty in the detector solid angle is estimated at about 5 percent.

The average scattering angle depends on the distribution of ion initial radii and trajectories, which may well vary as the field geometry is changed. (The possible scattering angles in these arrangements range from about 76 to 96 degrees, representing a factor of two variation in the predicted yield.) One shot, 6098, was taken with a shadowbox plate at the Kimfol location. The data from this shot indicates an average scattering angle of 86 degrees, which results in a 10 percent decrease in the predicted yield from that at the nominal 90 degrees. The ratios in columns 9 and 10 are based on calculations for a 90-degree scattering angle. The ratios are multiplied by 1.1 in columns 11 and 12 to account for the assumed, average angle of 86 degrees. The uncertainty in the yield associated with the scattering angle is estimated to be about 15 percent. Taking everything together, geometry-related uncertainties of 15-20 percent for arrangement 4 and 20-25 percent for arrangements 2 and 3 are assumed.

Since the ions scattered from a thick target have an average energy on the order of half of the initial energy, which is itself rather low on these shots, attenuation by the Kimfol, air, and p-i-n foil has a big effect. This results in a calculated scattering yield that is more than proportional to the ion voltage and strongly affected by the assumed dE/dx of the target, foils, and air. For example, the yields calculated for these shots using the upgraded stopping coefficients (see TN 94-17) were 20-30 percent less than those calculated using the old values. Based on Ziegler's claim of 3-5-percent accuracy in dE/dx , an uncertainty of 5-10 percent is assumed here.

The current and voltage waveforms have calibration uncertainties on the order of 5 percent each. In addition to this are possible waveshape errors. For example, the inductive voltage correction is susceptible to noise on the diode current, and the ion current measurement is susceptible to shielding of the dB/dt loops. The total current- and voltage-related uncertainty in the calculation is estimated to be about 15 percent.

The composite uncertainty in the yield calculation is thus about 25 percent for arrangement 4 and 25-30 percent for arrangements 2 and 3. This uncertainty has both random and systematic components, although I believe that the former dominate.

On run 8, the p-i-n foils were destroyed on most shots, allowing debris to deposit on the detectors. The small, recessed detectors are difficult to clean and it is possible that debris may have been left on some shots. This may explain, for example, the very low yield on shot 6106.

A timing uncertainty of roughly 3 ns is assumed.

RESULTS

The p-i-n's were shielded with about 1/4 in of Pb which virtually eliminated Brems pickup.

Arrangement 2 allowed three identical measurements that can be compared with each other and with the three ion current signals. The average variation among the three p-i-n signals on shots 5995-5998 was 10-20 percent. Similar variations in the current signals were observed, but the two were not azimuthally correlated. (The three dB/dt loops were located at 12, 4, and 8:00, and the scattering apertures were located at 11, 3, and 7:00). Since these variations are within the experimental uncertainty discussed above, the lack of correlation may not be meaningful.

Figure 3 shows calculated and observed signals for four shots. These shots are chosen to illustrate the range of agreement in shape and timing, and in these graphs the two traces are normalized to each other so that the shapes may be easily compared. The first few shots in run 7 had a much larger predicted/observed signal ratio late in time, while the reverse was observed on a few shots in run 8 (see shots 5998 and 6103 in the figure). The level of shape agreement seen on shot 6013 is representative of most shots. On some of the shots at the end of run 8 (see the last column in the spreadsheet) the observed signal has an unphysically-long tail. On these shots the signal level was not particularly high, so the detector was not saturated. Perhaps the detector was beginning to fail.

In general, the shape and timing discrepancies observed with the pinch-reflex diode are not observed here. On run 7, the observed signal is delayed 5 ns on the average relative to the predicted signal. This is seen at both detector distances (as in shot 6013) and may result from some timing error. On run 8, the timing agreement is better.

Subject to the abovementioned uncertainties, the ratios in columns 11 and 12 of the spreadsheet can give information on the proton content in the beam. By averaging enough shots, the random errors, including beam non-uniformity, can be smoothed out. The comparison of integrals may not be meaningful for shots with poor shape agreement, or especially the shots with tails on the observed signal. Nonetheless, here goes: First, note that the shots with no pulser exhibited lower ratios on the average. This is encouraging as it suggests that the EMFAPS is increasing the proton content of the beam. Shots 6010-6013 give average ratios of 0.53 for the Al and 0.67 for the Ta targets. The difference may not be statistically significant for the small number of shots, and is within the experimental uncertainty. The average ratio for all pulser shots in run 8 is 0.82. Eliminating the shots with tails, and the two shots with the highest and lowest (shots 6101 and 6106), leaves 7 shots with an average ratio of 0.66.

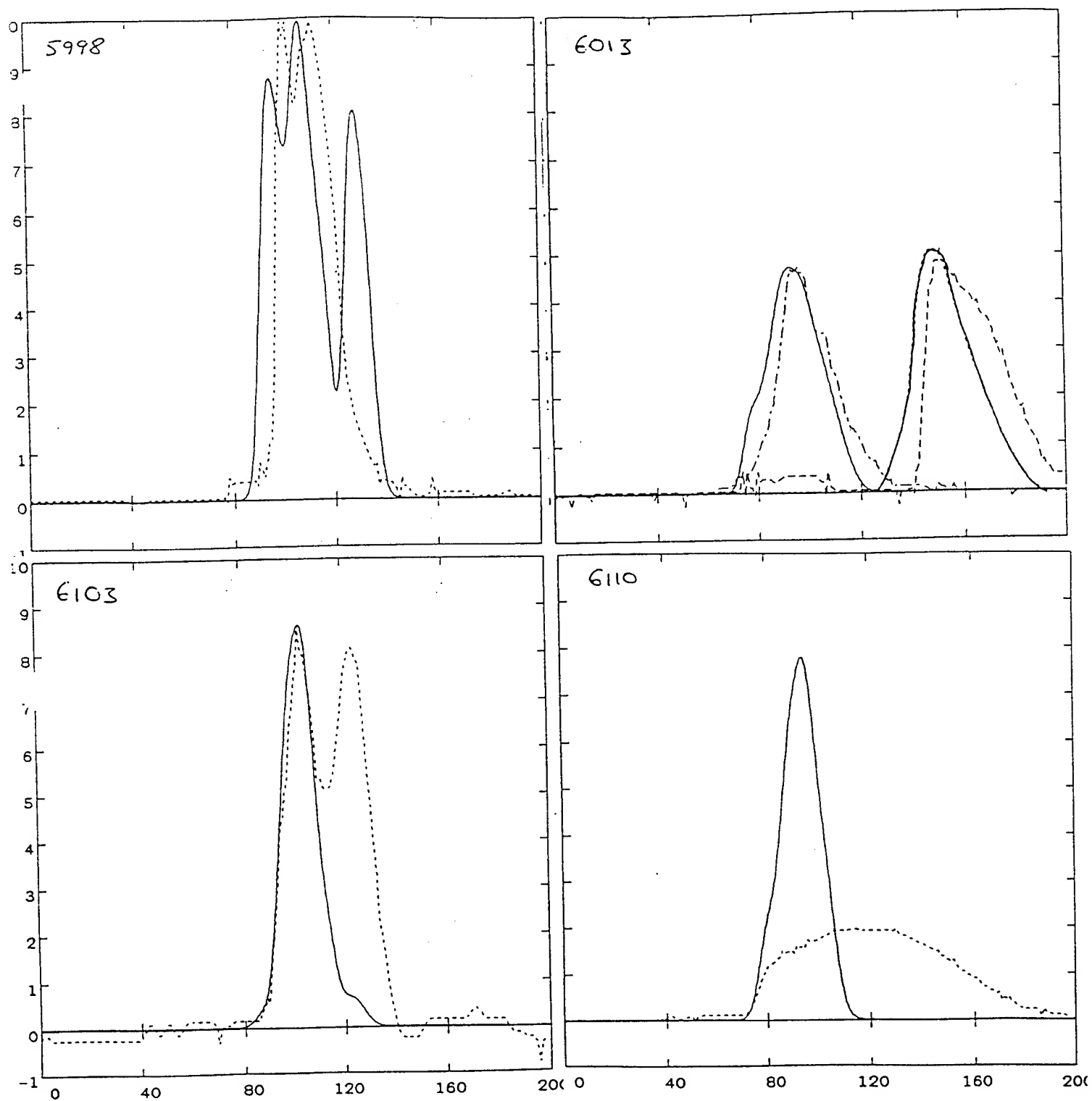


Fig. 3: Calculated (solid) and observed (dashed) Rutherford scattering signals from four shots. In this figure, the signals are normalized in amplitude to illustrate shape fidelity.

FARADAY CUP

The calculated and observed signals from our one shot with the Cornell Faraday cup are shown at the bottom of Fig. 2. The design of this cup was provided by Joe Olson. The main features of this cup are the large (5-mm diam) aperture, the lack of bias voltage, and the low ($0.05\text{-}\Omega$) shunt resistor. The cup was located in 1-Torr air, about 1.5 cm behind the Kimfol. The tail on the observed signal is not understood at present. Other than this, the agreement with prediction is good, and consistent with the Rutherford scattering results. (The Kimfol will stop all singly-, and most of the doubly-, charged carbon ions, but the cup should record higher charge states. Therefore, a somewhat higher ratio of observed to predicted signal might be expected, relative to that from Rutherford scattering.) The Faraday cup is an attractive diagnostic because the signal is relatively independent of the diode voltage, and most of the geometric uncertainties involved in Rutherford scattering are avoided.

CONCLUSIONS

While there are some unexplained features in these data, and indications that on some shots the ion voltage and/or current may be incorrect later in time, the overall picture is that the extracted ion beam is roughly 2/3 protonic and consistent with the diode electrical waveforms. Both diagnostics are easy to field, and are seen to work reasonably well in this difficult, high-current-density environment. Future refinements are also possible. The scattering foil can be expanded to sample a larger fraction of the beam, and both diagnostics are well-suited to being fielded in multiple arrays that allow spatial resolution of the beam. Therefore, information on both the total ion current and its distribution can be obtained in the future. The use of permanent magnets may allow the Faraday cup to be used outside the cathode return flux, and even in experiments with the pinch-reflex diode. I am enthusiastic about the potential of both diagnostics for diagnosing transported ion beams in all of our ion beam research programs.

PULSED POWER PHYSICS TECHNOTE 93-03

TITLE: INITIAL RESULTS WITH AN EMFAPS ON GAMBLE II

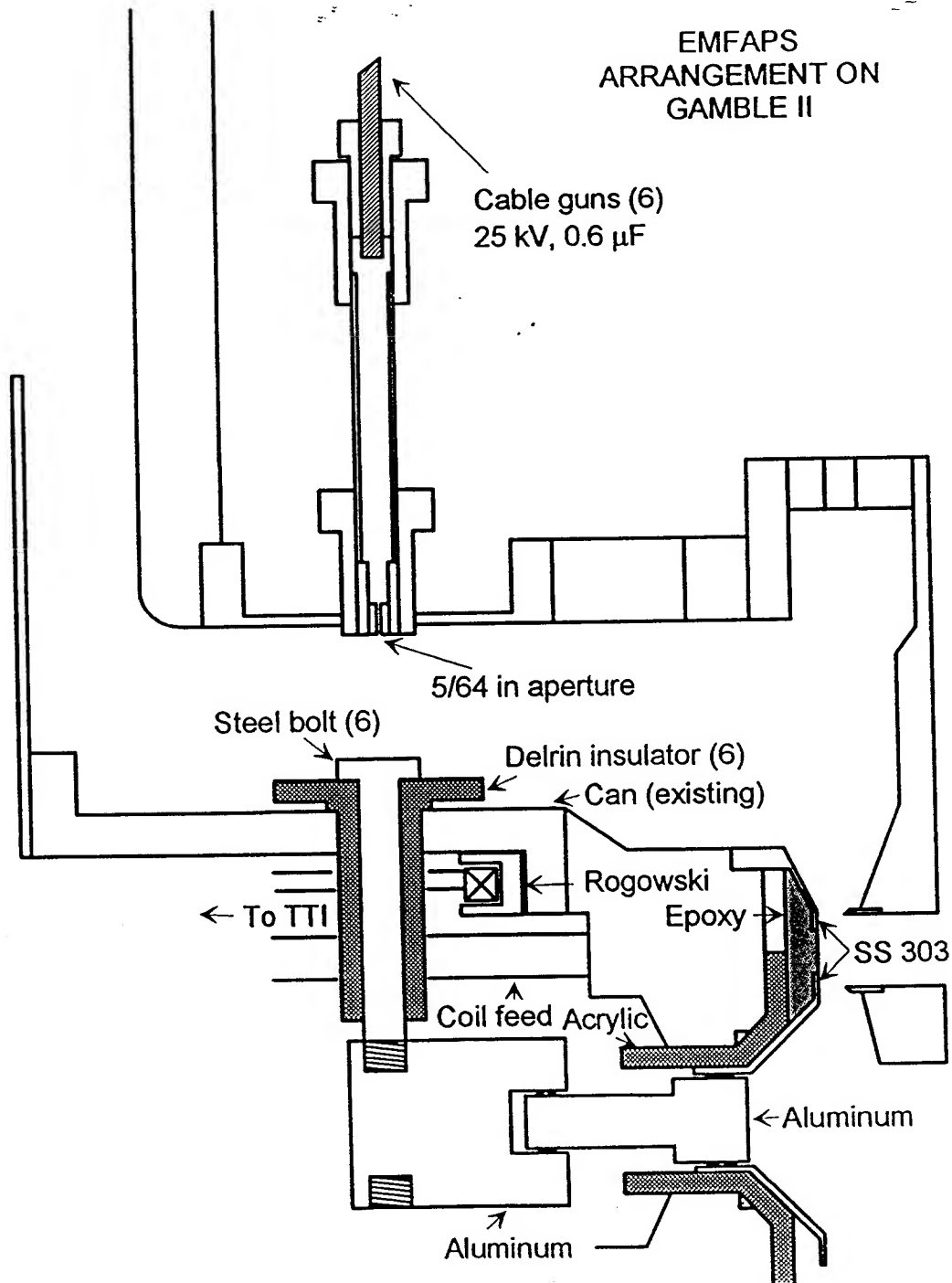
AUTHOR: D. Hinshelwood

DATE: March 23, 1993

ABSTRACT: This note describes the results of our first shots with an EMFAPS (Exploding metallic foil anode plasma source) installed on the Sandia magnetically insulated diode on Gamble II. The main purpose of this run was to relate the POS conditions (plasma delay and injection geometry) to the foil and POS currents, and the metallic foil arrangement used was not expected to produce a very uniform ion source. Nonetheless, on two shots we did obtain significantly improved diode performance. Compared to non-EMFAPS shots, these shots exhibit a faster-rising, higher ion current, a much faster initial impedance drop, a slower subsequent impedance collapse, a reduced peak insulator voltage, and an increased ion beam energy. Plans for future work are also described here.

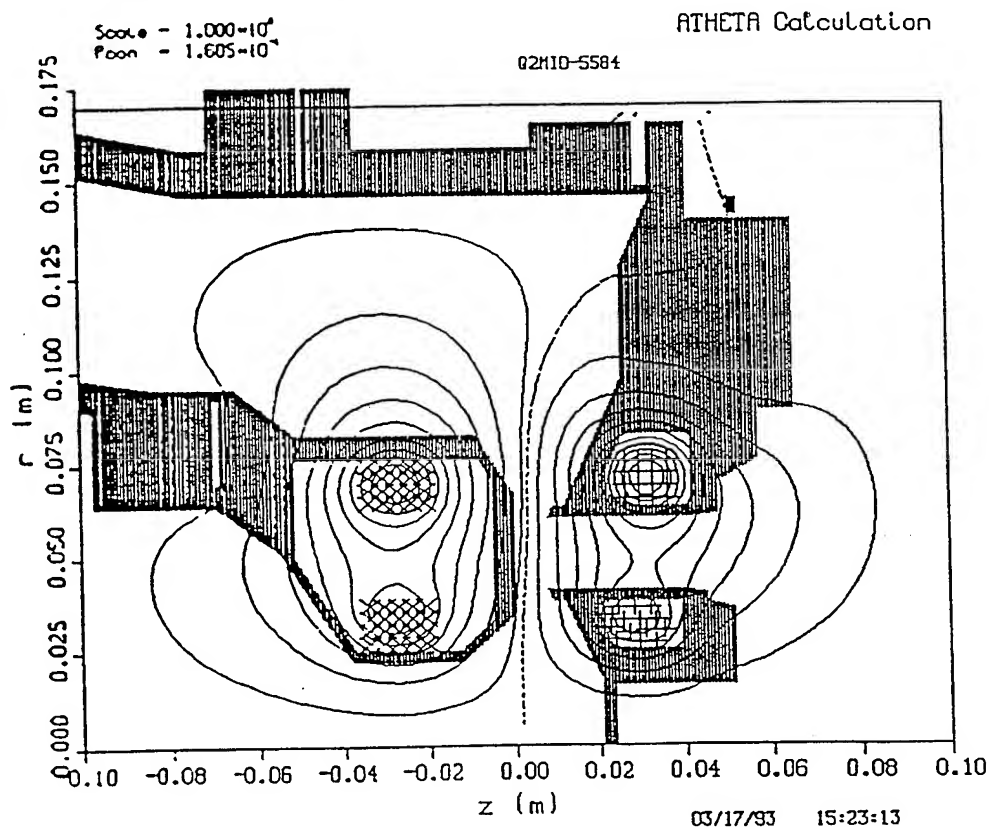
This note describes the results of our first shots with an EMFAPS (Exploding metallic foil anode plasma source) installed on the Sandia magnetically insulated diode on Gamble II. The main purpose of this run was to relate the POS conditions (plasma delay and injection geometry) to the foil and POS currents, and the metallic foil arrangement used was not expected to produce a very uniform ion source. Nonetheless, on two shots we did obtain significantly improved diode performance.

A drawing of the experiment is shown below:



Six plasma guns inject plasma from the cathode to six steel bolts which are located on the anode, but insulated from it by Delrin bushings. The anode tip comprises two concentric stainless rings connected by Thermoset (600/70) epoxy. A metallic foil on the epoxy surface bridges these rings. The inner ring is connected to the six bolts. When the generator is fired the current flows along the anode, past the bushings, through the foil, out the bolts, and through the plasma across to the cathode. This current heats the metal foil, desorbing adsorbed gases and/or surface contaminants. This material is subsequently ionized by the voltage across the foil, resulting in an anode plasma. Eventually the bushings flash over due to the inductive and resistive voltage drop and because MHD forces push the plasma channels forward from the bolts and off the bushings. At this point the foil current crowbars and subsequent generator current flows in a standard POS arrangement. Finally, the switch opens and energy is transferred to the diode. Performance of this source depends critically on the timings of both the foil current crowbarring and the switch opening.

Because of a bug in the ATHETA program we were not able to calculate the exact applied magnetic field configuration in this experiment. Sandia personnel are fixing this bug; in the mean time, the calculated configuration used immediately prior to this run was used as a starting point. This configuration is shown below:



The EMFAPS anode tip extends 6.4 mm beyond the tip in the configuration above. To compensate for this in the absence of a code calculation, the cathode coil currents were left unchanged while the outer and inner anode coil currents were increased by 25 and 18 percent, respectively. To reduce cost and fabrication time, stainless rather than titanium

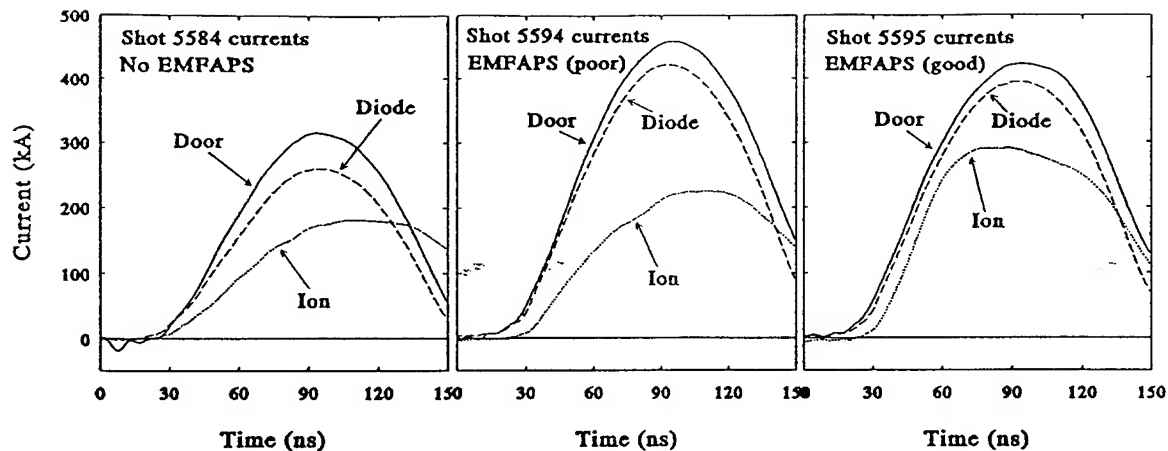
was chosen for the EMFAPS anode tip. Most of the tip is fairly thin, and in particular the inner ring is spun from 0.004-cm sheet. With a coil current rise time of about 100 μ s, the calculated skin depth is about 0.8 cm so that field penetration should not be a problem. The EMFAPS diode gap is 0.4 mm smaller than the 8-mm gap in the configuration above.

Since we do not yet have a coating capability, the vapor-deposited metallic foil was replaced by an aluminized mylar foil which was attached to the stainless anode rings with conducting epoxy. The epoxy was not expected to provide a suitable current contact and indeed the measured resistance was about 1 Ω , much greater than that expected from the foil alone. This may be due in part to a low-voltage contact resistance, but in general, arcing and asymmetrical current flow through the foil would be expected.

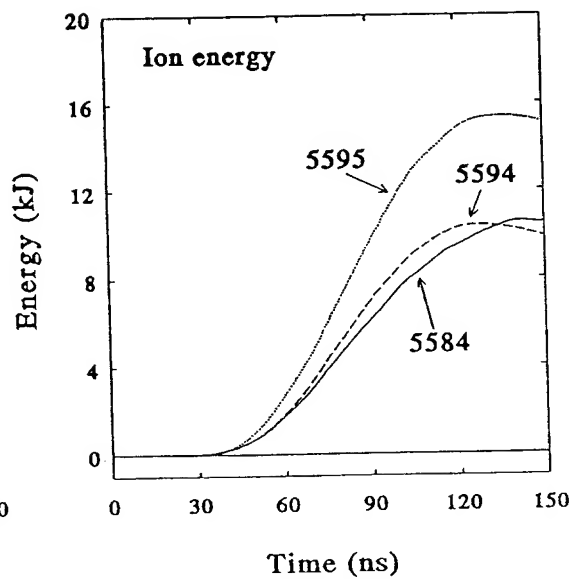
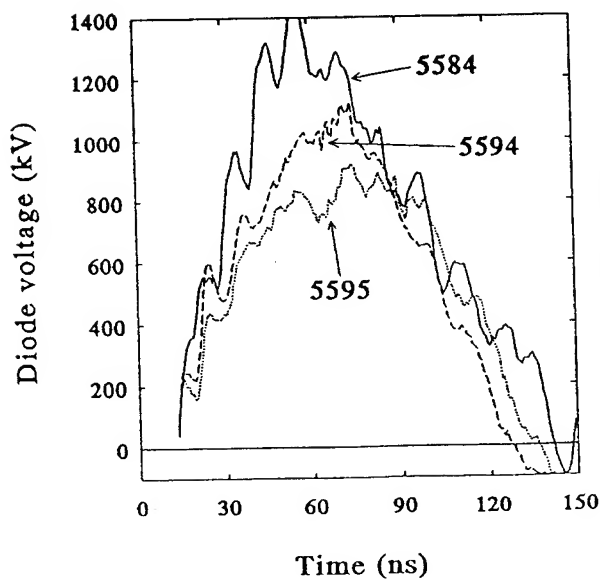
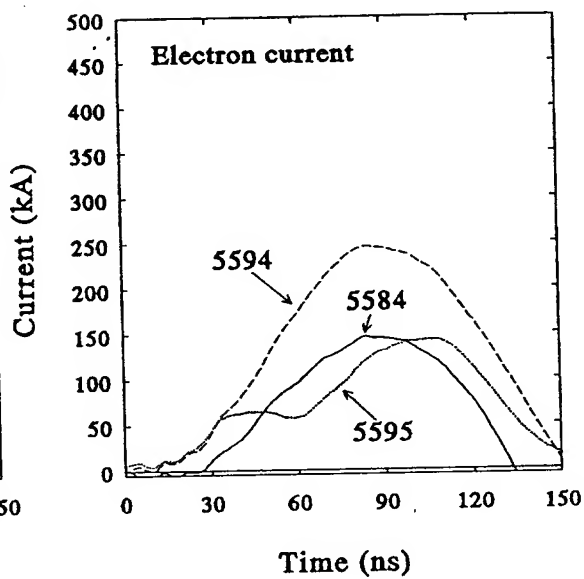
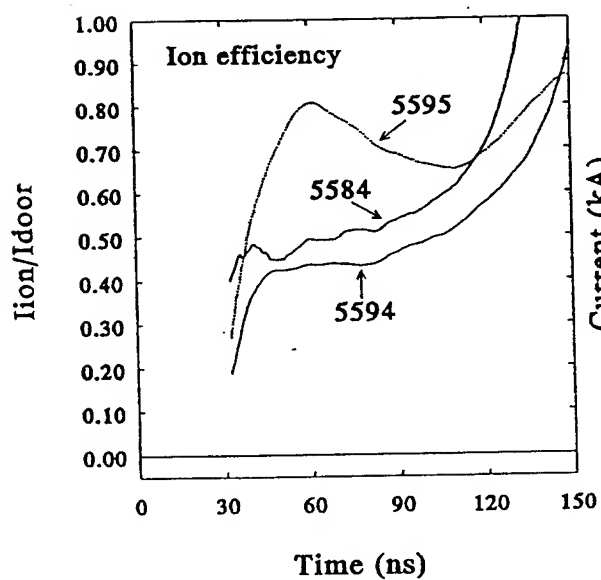
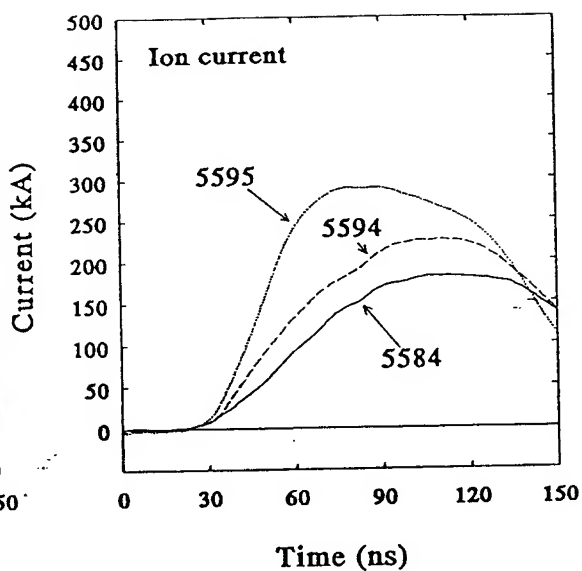
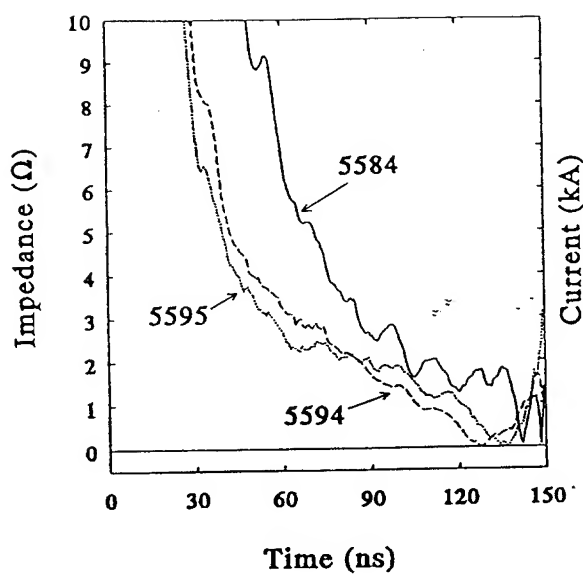
The Delrin bushings have steps so that additional insulation can be placed under them if needed. The insulation used at Cornell extends farther from the POS current contact than these bushings do, and premature flashover of the bushings may be a problem here. Because our transit time isolator is not well shielded, we have had trouble in the past extracting signals through it. Since measurement of the foil current is so important, the Rogowski was wound with about 50, 5-mm diam turns and integrated in the screen room. During calibration the time response was observed to be better than 10 ns, sufficient for this experiment.

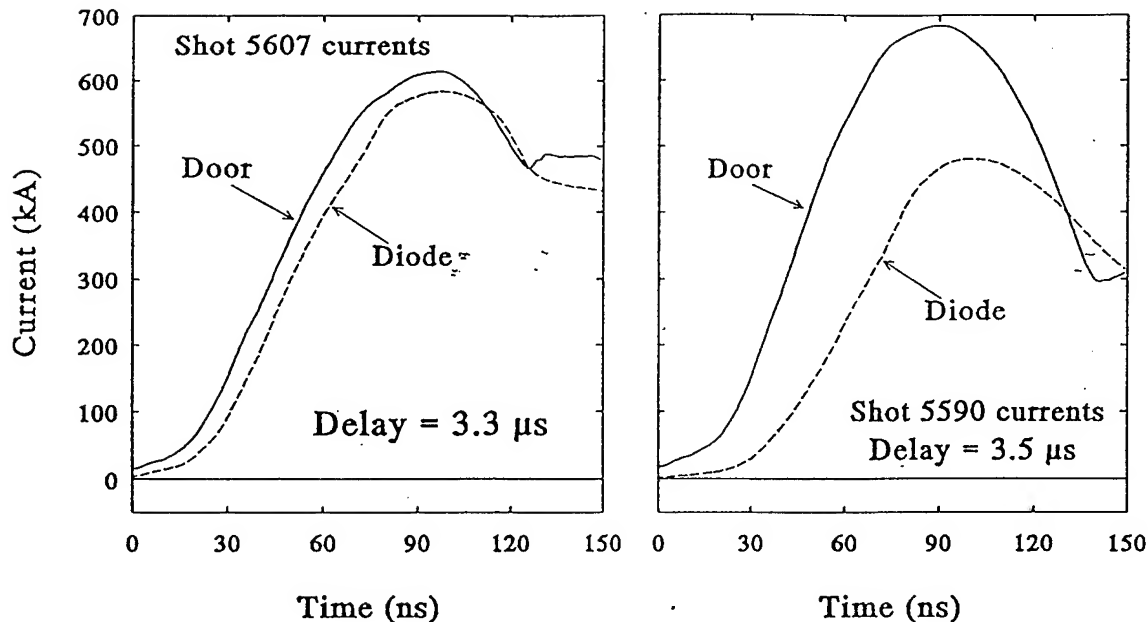
Cable guns, developed by John Goyer at PL, are used for the plasma source. These have a 60° cone machined in them which greatly increases the resulting plasma density relative to that produced by Mendel guns (we used cable guns because our old Mendel guns are in dubious condition). Therefore, the plasma flow into the POS region must be highly attenuated in order to have a reasonable gun-to-generator timing window for this experiment. A large part of this run comprised short circuit shots to determine POS timing scans for several gun arrangements. For these shots, the Delrin bushings were replaced by metal washers and a short circuit was placed in the diode. Initially, the guns were recessed in the 8-cm tubes shown in the drawing, with 6-mm apertures at the ends. This produced too much plasma. Next, only three guns were used and the doghouse voltage was reduced to 17.5 kV. Our two good shots were obtained with this arrangement although the timing window was narrow. No conduction at all was observed when the 0.6 μ F doghouse capacitors were replaced with 0.02 μ F caps. Finally, the apertures were reduced to 2-mm diam as shown in the drawing, and all six guns were used with a 25 kV doghouse voltage. The timing window is still narrow with this arrangement and even smaller apertures will be used in the future.

Typical short circuit shots are shown below: These shots were taken using different gun configurations so the timings can not be compared directly, but they are representative of all the short circuit data. At small delays (for a given configuration) the load current is simply delayed, at longer delays poor switching is indicated, and risetime sharpening is never observed. Poor switching would be expected in positive polarity at such a large radius, but also note that there are no anode monitors in this experiment and some of the "loss" could be vacuum electron flow.



Diode behavior on these three shots is compared further in the next six graphs. The impedance is defined here as the corrected voltage divided by the door current. The electron current is obtained by subtracting the ion current from the door current, and thus includes any vacuum electron flow from the switch. The efficiency is defined as the ion current divided by the door current. The most prominent feature of these graphs is the much faster initial impedance drop on the two EMFAPS shots. These two exhibit relatively similar impedance behavior although shot 5595 shows a slightly faster initial drop and significantly slower subsequent collapse. This similarity is interesting in view of the great difference in ion current between these two shots. While shot 5594 shows a higher ion current than shot 5584, the ion efficiency is actually reduced relative to the non-EMFAPS shot. One possibility is that the difference in impedance behavior between the EMFAPS and non-EMFAPS shots is not due to the improved ion source but is related rather to some subtle difference between the magnetic field contours of the two configurations. This could allow more electron loss on shot 5594. On shot 5595, the additional ion current could conceivably help to insulate the electron loss, maintaining the same total current, analogous to the critical current of a self-insulated diode. Alternatively, the similar impedance behavior on the EMFAPS shots could be fortuitous: On shot 5595 the rapid drop results from the ion current. On shot 5594 the total ion current is presumably reduced because of a poorly formed ion source, and John Greenly has pointed out that any azimuthal asymmetry in the ion current could also cause an increased electron loss.





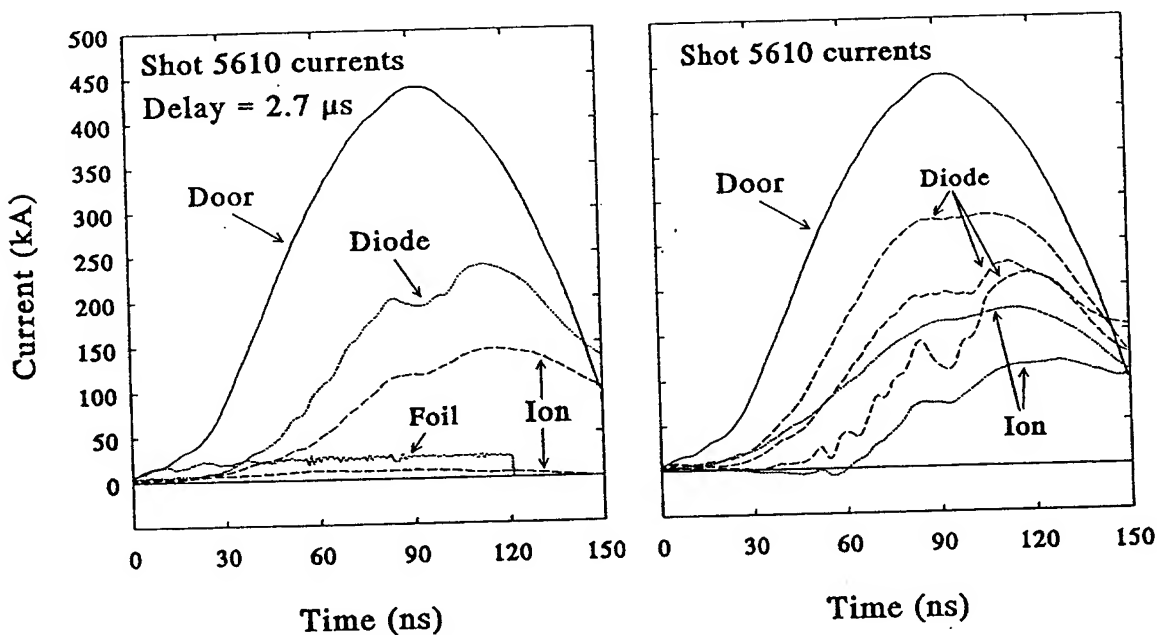
Results from the diode shot below show an interesting feature. Shot 5610 had the same switch configuration as shot 5607 above and a smaller delay. However, the switch appears to conduct more current on shot 5610. Similar behavior was observed on other pairs of shots. John Greenly has observed this feature at Cornell also. In the graphs which follow, the door current is measured by four summed B-dots located in the first part of the vacuum section and upstream of the switch. The diode current is measured by three summed B-dots located just outside the outer cathode. The ion current is obtained by subtracting signals from two sets of three summed B-dots, located just inside the outer cathode and just outside the inner cathode. In practice, the latter signal is almost negligible as seen below, indicating that little electron current is emitted from the inner cathode. (John Greenly has suggested that this is a good operating situation for an MID.) The B-dot signals are integrated and then an ad hoc correction is applied to compensate for the time response degradation resulting from field diffusion around the monitors. This consists of an RC time constant correction using a negative time constant whose value is chosen to give the best waveshape match on short circuit shots.

On the MID shots taken before this run the calibration for the diode current signal appeared to change from shot to shot, as if one of the individual B-dots was not working, and this monitor was basically useless. After the first few shots on this run things seemed to settle down but still the calibration (as determined from periodic short circuit shots without plasma) varied by ten percent or so during the run. With the POS this diagnostic is vital and by the end of this run all three B-dots on both sides of the outer cathode were recorded individually. This will be continued in the future so that if one B-dot is obviously unphysical its signal can be discarded. The anode current monitors were not useable because of our noisy transit time isolator. In the future a high priority should be placed on

installing a better isolator so that at least the total diode anode current can be measured to characterize better the POS.

On shot 5610 the foil current reaches about 25 kA before it crowbars. On some shots it reached as high as 50 kA, so that premature flashover of the Delrin bushings may not be a problem

The right hand graph shows signals from individual B-dots, both outside and inside the outer cathode. Note the great asymmetry - one of the ion currents begins well before one of the diode currents. This asymmetry is likely associated with the poor switching and large foil current, and is hopefully not representative of a shot with lower POS conduction.



Three shots are compared in more detail in the following graphs. Shot 5584 is the last shot taken before the EMFAPS hardware was installed. The magnetic field contours shown previously were calculated for coil currents used on this shot. Shots 5594 and 5595 were taken during this run. These shots had the same switch configuration and delay time and show no measureable switch conduction (I believe that the discrepancy between the door and diode currents arises from problems with the diode monitor). On both shots a crowbarred foil current of about 5 kA is observed, indicating that some small current conduction through the switch did occur. These two shots differ in that a much higher ion current is observed on shot 5595. Since everything else was the same this difference is attributed to the foil conditions; evidently the foil current on shot 5594 flowed in such a way as to produce a poor anode source. Such a shot to shot variation could be expected for the relatively crude foil arrangement used in this run.

The calculated open circuit voltages for these three shots have the same timing, shape, and amplitude so that waveforms from each shot may be compared directly. Note the much smaller current on the non-EMFAPS shot.

In any event the results so far are encouraging. Even with the rather crude foil current contacts, on two shots (one other like shot 5595 occurred) we have obtained a much improved impedance behavior (which may not be due completely to the ion source), both in terms of the faster initial drop and slower subsequent collapse, and a much greater ion efficiency. The faster initial impedance drop results in a greatly reduced peak diode voltage. Since the peak ion current occurs earlier, the average ion voltage is not reduced and the ion beam power is increased, as shown in the last two graphs. The ion beam energy has been increased by 50 percent. The reduced peak insulator voltage should allow operation without flashover at an increased machine charge and thus allow higher ion voltages to be achieved. With a proper (i.e., vacuum deposited) foil arrangement, further improvement in the ion current onset and fraction may be expected.

The main thrust of work in the immediate future will be to develop a coating capability here. The deposition so far at both Cornell and KfK has been performed using thermal evaporation. While suitable for aluminum and copper, this technique is generally difficult for titanium and palladium (although Hans Bluhm says that they have had no difficulty). While we were first told that anything other than a thermal evaporation system would be too costly, I now see that a sputter deposition system should be quite affordable and will give much greater capability than a thermal evaporation system. I am in contact with the Sandia technician who will be assisting Mike Cuneo and should have the necessary equipment ordered soon. Also, a local contractor has offered both to coat some anodes in the interim and to help us (as a paid consultant) get started.

Beyond this, as soon as ATHETA is available we should model the EMFAPS configuration with the goal of optimizing the field configuration. And, as stated before the transit time isolator should be improved to the point where we can monitor the anode currents in the diode.

Finally, Ron and Steve have suggested that we should consider trying to drive the foil with an external pulser. After discussing this idea we have some thoughts on how to do this and may get around to trying them. If successful, this approach would add a large measure of control to the EMFAPS technique.

PULSED POWER PHYSICS TECHNOTE 95-33

TITLE: EMFAPS PULSER DEVELOPMENT

Author: D. Hinshelwood and R. Fisher

Date: Dec. 5, 1995

Abstract: We have developed an EMFAPS pulser that satisfies our initial design goal of 50 kA and a <10 -ns risetime. The pulser consists of a 3-stage Marx, water PFL, solid stab output switch, and multiple-cable feed to the diode. This note describes the goals and design process, briefly recounts earlier versions of the pulser, and then describes in detail the present pulser and feed arrangement. Finally, thoughts on how to increase the output in the future are given.

INTRODUCTION

We have developed an EMFAPS pulser that satisfies our initial design goal of 50 kA and a <10 -ns risetime. We have just sent a duplicate pulser to Mike Cuneo at SNL, and this seems like a good time to document its design and summarize the work done so far. This note describes the goals and design process, briefly recounts earlier versions of the pulser, and then describes in detail the present pulser and feed arrangement. Finally, thoughts on how to increase the output in the future are given. Some of what follows is being written just so I won't forget it, and most readers will want to skim over parts of it.

DESIGN GOALS

The main objective of our EMFAPS development is to improve the performance of the Gamble II applied-B diode for transport experiments, by increasing the proton fraction and hopefully by decreasing the ion turn-on time. Until recently, we planned to use the SABRE diode furnished to us by SNL. While not the highest priority, we also hoped to be able to assist the development of an EMFAPS on SABRE. For both objectives we envisioned the need for bench experiments.

The first step was to establish design goals for the foil current pulse. At Cornell, a POS is used to divert about 100 kA through the foil with a 5-10 ns risetime. At KfK, a similar scheme is used to drive 200-kA level currents, also with a 5-10 ns risetime. The minimum current and maximum risetime for satisfactory operation were (and are) not well established. Since the SABRE diode has about half the circumference as the LION diode, John Greenly and I agreed that roughly 50 kA current, with a 5-10 ns risetime, would be a good goal for our experiment.

Three approaches for providing this current were considered: (1) diverting some of the machine pulse through a POS, as is done in the other experiments; (2) diverting some of the machine pulse through a direct connection, using some sort of pickoff; and (3) using an external pulser.

We began by trying the POS approach, using the same arrangement used at Cornell and KfK. This approach did not work on Gamble II because of difficulties in synchronizing the POS plasma source with the generator, arising from the ~ 1 μ s Marx jitter. In principle, this difficulty could be overcome. The sequence of a Gamble II shot is as follows: The Marx fires, with large jitter; about 1.4 μ s later, the water switch closes, with about 200 ns jitter; about 200 ns later, the oil switch closes, with ~ 10 ns jitter; and power reaches the load 80-90 ns later. One could envision developing either a slow plasma source that could tolerate the Marx jitter, or a fast source that could tolerate the water switch jitter. Developing such a source might be no more difficult than developing a suitable external pulser for (3) above. Nonetheless, we decided to abandon the POS approach and to proceed with (3). The main reason for this was that an external pulser would allow the foils to be driven on the bench with the same waveform used on machine

shots. We were further motivated by the fact that this was also the direction chosen by KfK.

Before proceeding with the pulser, Ron, Steve, and I spent some time considering the possibility of driving the foil directly from some sort of machine pickoff. Such an approach could be simple to field and should eliminate jitter between the foil current and the generator pulse. However, we could not come up with a good way of producing the necessary current pulse. The arrangements we considered that would provide sufficient current through the foil early in the pulse, would drive excessive currents later in the pulse. Our analysis was not exhaustive and this problem perhaps could have been solved, but there were other arguments against this approach. It probably would not be transferrable to SABRE, because the two machines are so different. Also, any pickoff would presumably be mounted on the inside of the center conductor. Gaining access requires removal of the generator front end, with a 2-way turnaround time of at least a day. This would greatly complicate the debugging, optimization, and adjustment that would be needed initially. And most important, the driving pulse again would not be replicated on the bench.

Once we decided to develop an external driver, the next question was where to locate it. Locating the driver close to the load could allow more efficient coupling of energy to the load and would eliminate the need for a complicated feed arrangement. The pulser could perhaps be located in vacuum, with its output ~10 cm from the foil. However, because of the difficulty in designing a pulser to operate in a vacuum ambient, this option was rejected. Another possibility would be to locate the pulser in the water, immediately behind the evacuated section of the center conductor. This was rejected because of the access problems mentioned above. (As it turned out, we ended up using solid switches that need replacing every shot, which would have made this option virtually impossible.) In addition, locating the pulser in vacuum or in nearby water would be incompatible with the smaller center conductor of SABRE. Finally, limited BERTHA runs did not show a large advantage from locating the pulser so close.

Therefore, we decided to locate the pulser outside the machine, and to run the pulse in through the transit-time isolator. (Because of the need for frequent debugging during the development process, this was a wise choice.) Such an arrangement simplifies the design somewhat, in that the pulser sees only a fixed-impedance load for times of interest, and the foil sees only a fixed-impedance source. It also allows the possibility for further pulse conditioning at the load, for example by using a surface-flashover closing switch to sharpen the risetime.

FEED DESIGN

The next step was to design the feed. One option is to use a parallel array of high-voltage coaxial cables. Another option is to use a single, low-impedance coaxial feed. Finally, one or more (parallel) striplines could be used. For the latter two (homemade) options,

polyimide (Kapton) is the dielectric of choice, laminated with either attached, heat-sensitive adhesive, or low-viscosity epoxy.

The EMFAPS foil starts out with a very low ($< 1\Omega$) resistance, and so ideally the feed and pulser should have as low an impedance as possible. Two factors, however, limit how low the feed impedance can be: size limitations posed by the transit-time isolator; and the L/R time resulting from the small inductance at the feed-foil connection. In the system being built at KfK, six polyimide/epoxy striplines are used, giving a feed impedance of 0.35Ω . However, the SABRE diode has a relatively small inner diameter. Because of this, any demountable connection will have an inductance of at least a few nH. The output switch and connection on the pulser will also have at least 1-2 nH. For 5 nH total inductance, a 1Ω feed will give a risetime of at least 5 ns. Therefore, 1Ω is about the lower limit from inductance considerations. In addition to forcing a higher feed impedance, the small inner diameter of the SABRE diode makes a multiple stripline connection more difficult.

The Gamble II transit time isolator is about 5 cm in diameter. This size is just sufficient for 30, ~6-mm diam cables plus the anode coil cables and one or two foil diagnostic cables. With 50Ω cables, this gives an impedance of 1.67Ω . The minimum impedance obtainable with a single, laminated coax is on this order also.

So, from both inductance and access considerations, the feed will be about 1-2 Ω .

A cable array is obviously more attractive than a single, laminated coax: bends are trivial and do not involve impedance discontinuities; the system is robust - only a small current loss results from a single cable failure unless that failure occurs right next to the pulser or load; the flexible cables will not be affected by machine shock and need not be sized to a few mm; and fabrication is much simpler. Striplines can be made flexible to some extent, but still suffer from the lack of robustness, and would be more difficult to fabricate and install. Therefore, we decided to use a cable feed if at all possible.

Reynolds type-C cables were used at first, because of their low, 30Ω impedance. We have used them in the past at up to 50 kV. However, during our first EMFAPS run on the machine (run 5, with 20-30 kA foil currents), a few cables failed and soon after that they all failed. At Bruce's suggestion I spoke with John Thompson at MLI, who had looked at several types of cables for the ACE flashboards. He recommended Reynolds P/N 1679785. This is a 50Ω cable similar in size to type-C and RG-223.

Breakdown of this cable was compared with that of RG-223 and type-C cable in a short test using the EMFAPS pulser. By using only one cable output, and open-circuiting the other end of that cable, high voltages could be produced. The 1679785 cable was the best, as expected. No breakdown was observed, including one shot with a peak voltage of about 180 kV! The RG-223 also worked surprisingly well, surviving one shot at 110 kV before failing at 160 kV. The type-C cable performed much worse than RG-223, even when scaling for the lower impedance was taken into account.

(These tests used positive polarity, which John Thompson found gave better results. According to JCM, negative polarity is better, at least for polyethylene and polypropylene. The reason for this discrepancy might be that at John's relatively long pulse length, corona around the center conductor plays a larger role than bulk breakdown of the solid.)

The above tests did not include lifetime testing, different polarities, or multiple samples of each cable, but were sufficient to confirm the Reynolds cable as superior. While waiting for these (long lead-time) cables, we replaced the type-C cables with a 30-cable, RG-223 array which survived EMFAPS runs 7 and 8 (~40 kA foil currents). An array of 30 Reynolds cables was then used for runs 9, 10, and 11 (40-55 kA foil currents).

A number of cable-to-foil connections have been used. Initially, cables were used all the way to the foil, with multiple-Cajon vacuum joints. This worked OK but proved to be unwieldy. The present arrangement, shown in Fig. 1, uses a short section of laminated coax for the vacuum portion of the feed. This coax consists of a 1.5-in diam stainless tube covered with ~0.35-in-thick Kapton/epoxy laminate, as developed for the low-mass channel work. This wall thickness gives a nominal match to the 1.7Ω cable array. A square of Kapton is taped to the tubing, the tubing is held in a lathe and rotated by hand, and epoxy is painted on while the Kapton is pulled tight. Copper tape forms the outer conductor. A section of Al tube over this forms a vacuum seal with a single Cajon fitting. At the foil, a 2-3 nH slip connection is used. The lexan insulator is formed into a funnel shape by pressing lexan tube against a rotating, conical form while heating it with a heat gun.

The cables are connected to the coax in water, as shown in Fig. 1. Making the connection in water is advantageous for two reasons: (1) the good insulation of water allows the spacings to be small; and (2) the capacitance of the water in principle can offset any inductance. With an optimized design, it should be possible to achieve an almost constant impedance between the cables and the coax. The cables are terminated with bored-out BNC connectors which allow the center conductor to pass through. Connectors designed for RG-59 will fit the Reynolds cable. We found the brand (see Fig. 1) to be important - our first batch quickly corroded in the water. Mini banana plugs are used at the center conductor ends. On bench tests, the cable harness is sealed and filled with water. (Water leaking out through the BNC fittings is continually pumped back in.)

Even the Reynolds cables fail occasionally, at traveling-wave voltages of 50-70 kV. This is well below the 180 kV value mentioned above. The lower breakdown voltage could be a lifetime effect (which solid dielectrics exhibit), or due to the inevitable trauma the results from periodically inserting and removing the cables from the transit-time isolator. Another possibility, that I don't have enough data to confirm, is that the cables are damaged by the voltage reversal that occurs in the normal arrangement but was not present in the cable tests. Depending on the specific pulser circuit used, this reversal was at times greater than 100%. According to JCM, this can be a problem in some situations, and Joe Burton long ago mentioned reversal effects. There is some circumstantial evidence for reversal being a problem: breakdown is often observed to occur at the location where the forward and

reverse pulse would just separate; failure of one cable tends to increase the chance of others failing (sharp reversals would be expected from a short in a cable); and voltage monitors have shown that breakdown often happens at the time of reversal.

In summary, the present feed arrangement is fairly simple and easy to field, and is adequate for 50-kA level foil currents. However, it is the weakest link in the system. To achieve much higher currents, we will probably have to bite the bullet and build a laminate-type feed. This is discussed further at the end of this note.

PULSER OPTIONS

The simplest driver would consist of a charged capacitor or transmission line connected to the load by a closing switch. However, for the parameters here, and taking into account resistive and inductive voltage drop across the switch, DC charges of 100 kV or more would be required. This is not very practical, and so some form of voltage multiplication is necessary. A Marx alone would be far too inductive. One possibility is to use a simple Marx/PFL combination, as sketched in Fig. 2a. Another is to use a lumped-element, LC-inversion circuit, as in Fig. 2b. With this circuit the main switches are outside of the output circuit. Finally, a transmission-line LC circuit, i.e., a Blumlein, could be used. Here, if the initial switch is fast enough, no output switch is needed. This approach can be scaled to multiple lines, by either using multiple switches or a single switch with convolutes.

Water is the obvious choice for dielectric because of its high energy density, self-healing properties, and relative ease of use. However, a water line cannot be DC-charged, and thus requires circuit 2a. Oil is not attractive because of the volume (both transverse and longitudinal) needed. Arrays of coaxial cables have been used in the past, but many cables would be needed at these impedances, and capacitive coupling between grounds of adjacent stages would force the pulser to be rather large and unwieldy. Kapton striplines are another possibility. They offer no advantage over water in circuit 2a, but allow circuit 2c, with its simpler triggering (see below) to be used. High-dielectric-constant solid material (i.e., titanates) is yet another possibility. I could not find an easy source of BaTiO_3 raw material for a stripline, but arrays of ceramic capacitors could be used in circuit 2b.

Therefore, three circuits were worth considering: a Marx/water-PFL; an LC-inversion circuit using ceramic capacitors; and a Kapton Blumlein. The first two could be adapted to either a single-coax, parallel-plate, or parallel-cable feed, while the last would be difficult to adapt to a single-coax feed without adding too much inductance.

The output switch remains to be considered. (The primary switches in 2a and 2b do not have stringent requirements on inductance. Commercial gas switches will work fine and can be triggered with negligible jitter. Indeed, this has been seen in practice with both circuits.) Note that the output switches in 2a and 2b are pulse-charged, while that in 2c is DC-charged. The breakdown strength of gases and liquids increases for short pulses so

that a pulsed-charged gas or liquid switch will have lower inductance and resistance than the DC-charged versions. This effect is not seen with solids. On the other hand, it is a little easier to design a trigger circuit for a DC-charged switch, since the trigger on a pulse-charged switch cannot be capacitively blocked.

The pulser now being built at KfK uses circuit 2c. The simpler triggering of this circuit is an advantage, but I decided against using this circuit for several reasons. The main objection was that for the range of feed impedances considered here, it might be difficult to achieve the necessary traveling-wave output voltage using only two stages. With more than two stages, either complicated convolutes are needed, or multiple, solid switches must be triggered with low jitter (otherwise the risetime would be too long). Also I wanted to keep the option of using a gas or liquid switch. As mentioned above, static-charged gas or liquid switches would be too lossy. Finally, circuit 2c would be the least compact of the three, although this was not a major concern.

PREVIOUS PULSER DESIGNS

The first version of an output switch was the multichannel surface tracking switch used by Doucet's group. This switch can have an inductance as low as 2 nH and is easier to use than a solid switch. However, even though many channels were observed, the risetime produced by this switch here was no better than that provided by standard, MLI pancake switches. I believe that the problem was caused by resistive effects. With the much-higher-capacitance, ~800-ns-timescale circuit at Palaiseau, the switch resistive phase would be insignificant, whereas here it could well dominate.

After this, a low-inductance (MLI 40044) pancake switch was used for runs 7-10.

The timing on Gamble II, described above, is such that there is not enough time to trigger either circuit 2a or 2b from beyond the oil switch. Therefore, I used a capacitive pickoff in the PFL, which supplies a ~100 kV pulse into 50 Ω . Even this far back, timing is tight. BERTHA modeling showed that circuit 2b would be a bit faster than circuit 2a, and so this circuit was chosen in order to allow longer delays if desired. Other than this, similar pulses were predicted with either circuit. A simple, four-stage version of 2b was used on run 5, with a typical foil current shown in Fig. 3a. Next, a larger, four-stage pulser was built for runs 7 and 8. This used special capacitors which had their insulation removed for lower inductance. A typical foil current pulse from this pulser is also shown in Fig. 3a, and a drawing of the pulser is shown in Fig. 3b.

In retrospect, the decision to use circuit 2b was a mistake. EMFAPS results showed that a long delay between the pulser and the generator is neither necessary nor desirable, which makes circuit 2b unnecessary, and less attractive than 2a because of its greater complexity. Also, the capacitors were delivered very late, and then were found to be improperly fired, with an uncooked region in the center that left them susceptible to breakdown. Because of this, the charge voltage had to be derated, and foil currents were limited to about 40 kA

rather than the hoped-for 50. (This pulser is now in use as a calibration source at Phoenix.)

Next, a Marx/water-line pulser, shown in Fig. 3c, was constructed. Because of time constraints for an upcoming run, we used components at hand. The re-entrant geometry of the water line was used to allow an oil output switch, and to accommodate existing hardware. Both 20-nF and 80-nF capacitors were available. Initially, a 3-stage, 20-nF/stage Marx was coupled to a matched, 1.3Ω , 9-ns line. The output from this pulser, still with the gas output switch and a 50-kV charge, is also shown in Fig. 3a. The Marx capacitance and line length were varied: 80-nF capacitors and an 18-ns line were also examined. With the larger caps and longer line, the line charge time was too long for the available delay on Gamble II. With the larger caps and shorter line, ringing gain increased the line charge, resulting in foil currents of 50-55 kA. This arrangement was used in runs 9 and 10.

With the LC-, and 20-nF-capacitor-water-line pulsers, the output switch was pressurized to 55 PSIG and broke down at about 120 kV. This is about twice the breakdown voltage expected for a DC charge. With the 80-nF-capacitor water-line pulser, the switch was pressurized with a $N_2/10\%SF_6$ mixture to 40 PSIG, and broke down at about 160 kV.

PRESENT PULSER DESIGN

The next step was to improve the output switch. The pulser was reconfigured slightly into a straight, rather than reentrant geometry. This was done to reduce the output inductance and because tests suggested that at these voltages, a water switch might work as well as an oil switch. It was designed to accommodate gas, water, or solid switches. BERTHA modeling was used to optimize the design. Because we want the current into the foil quickly, there was nothing to be gained by using a line longer than about 10 ns (one-way). For output and foil inductances of a few nH, BERTHA showed that using lines shorter than about 5 ns also offered no advantage. The line impedance should be lower than the 1.67Ω feed impedance to get some voltage gain from the mismatch. Mismatch has diminishing returns, however, above factors of 2-3. I decided to use a 0.68Ω line, with outer and inner diameters of 7.75 and 7 in. The outer conductor could then be made from ISO200 vacuum hardware, which is readily available and would make any future modifications easy. The inner conductor would also be a readily available size, which we happened to have on hand as well. The ~1-cm gap would be large enough to prevent breakdown, even with small air bubbles present. With the output switch on the axis, using a much-larger-diameter line might introduce unwanted radial-transit-time effects. With a 5-ns line, the existing Marx could be used, with either 20-nF, 40-nF, or 80-nF capacitors. The former would give a good match to the line, while the latter two would give some ringing gain. The water line details are shown in Fig. 4a.

I also used BERTHA to examine several ways of reducing the amplitude of the reflected wave, including shortening the feed length, varying the line impedance and Marx

capacitance, and even adding a crowbar switch in various locations. Nothing I tried made much difference, however.

OUTPUT SWITCH TESTS

I first tried a water analog of Doucet's surface-tracking switch by placing a disk of TFE between the output electrodes. I had hoped that this would induce multichanneling and would be reusable. However, switching was no better than with a simple water gap (below) and the switch tracked every shot.

Next, a water switch, consisting of four bolts projecting from the ground (negative) electrode, at 10-cm-diameter, was tried. Breakdown was reasonably consistent with JCM. The jitter was about 10 ns, with a ~12-ns risetime. This was better than with the gas switch, but slower than with the solid switches (below).

The first attempt at solid switching used one or more sheets of plastic between the output electrodes. Sheets of Kapton, mylar, TFE, and polyethylene were used, in thicknesses from .003 to .016 in. Switching was quite fast, with risetimes of 8 ns or better. However, the jitter was tremendous, at least with Kapton and mylar, as shown in Fig. 5. Perhaps the jitter could be improved somewhat by taking great care with the foils and electrodes, but this approach does not seem well-suited to a self-break switch.

Finally, at Rick's suggestion, we went to polyethylene stab switches. As used by JCM, we stabbed multiple holes to a controlled depth in 1/16 in polyethylene, and then covered both sides with copper tape. The stab and sheet switches were not compared under identical conditions, but the stab switches seem to switch almost as rapidly as the sheet switches, with greatly improved jitter. Typical data are compared with JCM (from Ihor's book, although Ihor has the polarities reversed in his text) in Fig. 6. I estimate the RMS jitter with this switch at about 10 ns. Recent data is shown in Fig. 6. We have been using rather coarse, compass needles from NRL supply. It is possible that better switching and/or reduced jitter could be obtained by using sharper needles.

PULSER DETAILS

The pulser was operated with 20-nF capacitors in run 11, with foil currents of about 40 kA, ~8 ns 10-90 risetimes, and 30 ns typical widths. I have switched to 40-nF capacitors (MLI 31165) for both our and Mike's pulsers in order to boost the current by ringing up the PFL. (The 80-nF caps ring up the line to voltages higher than I feel comfortable switching into the cables, and just add extra energy rattling around the pulser.) This gives a Marx energy of 150 J. We have recently switched from the old MLI 40065 switches to their replacements, model 40264. These feature an irradiated gap. For 50-kV charge, they are pressurized to 26-30 PSIG and have an RMS jitter of about 5 ns when triggered by a PT55. This is better than obtained with the 40065 switches. When the PT55 is replaced by the higher-voltage, lower-impedance, PFL pickoff on Gamble II, the jitter should be reduced further. The Marxes are housed in the blue tanks we inherited from

MLI. The bias and trigger components are located on a plate mounted on top of the Marx. The circuit schematic is shown in Fig. 4b. The water line (Fig. 4a) is mounted on a hinged top. After replacing the cable header with a blank-off plate, the lid is easily lifted to gain access to the Marx.

The Marx output is connected to the line with 8 pairs of silicone HV wires (Newark 96F5269WA). I used aluminum tube for the line inner conductor because we had some available - it might be better to use stainless in the future to reduce corrosion. As it is, the water should be changed every week or so. Side ports were added to the outer tank to allow trigger access to the output switch in the future. I use stainless KF blankoffs as output switch electrodes to save wear on the line. The nylon rod in the center is tightened to compress the switch lightly. An acrylic plate is placed over the top of the line, outside the switch area, to reduce prepulse. The cables are connected using the same BNC/mini-banana plug design mentioned earlier. I estimate the effective switch and output inductance as being 2-5 nH (the value is not obvious because most of the "inductance" is pre-loaded with electrostatic energy).

The PFL voltage is measured with a simple resistive divider. Eight, 330 Ω resistors connect the bottom of the PFL, in the oil, to the center pin of a BNC connector mounted on the oil tank top. For faster pulses, I have seen some problems with capacitive coupling through such chains, but this should not be a problem for the relatively slow PFL waveform. The output voltage is measured with a capacitive/resistive divider mounted on the water line top. This comprises a 4.5-nF disk capacitor and a 510 Ω resistor. This monitor has only intermittent reliability and needs to be improved, but is not that important. The foil current is measured with a ~30-turn, externally-integrated Rogowski near the foil (see Fig. 1). This design was chosen to provide a large signal that would survive the noise inherent in the Gamble II transit-time isolator. To minimize capacitive coupling, the ground is not returned through the coil as is often done. The signal level is large enough to necessitate MHV cable ends and bulkhead connectors at the vacuum-water boundary.

RESULTS

The Rogowski was first calibrated at low current and slower risetime using a fast Tektronix current transformer. Then, as a check, an IPC current transformer was installed at the foil location and the pulser was fired normally. The IPC signal is compared with the integrated Rogowski signal in Fig. 7. The two agree well, although the Rogowski is seen to be just a bit slow. The current is lower than usual on this shot because of the added load inductance of the IPC mounting.

Figures 8-9 show the PFL voltage, output voltage, and foil current for a 50-kV Marx charge and .015 stab depth (from the positive, ground side). The foil current reaches 60 kA, with a peak dI/dt in excess of 5 kA/ns. The apparent 10-90 time is about 10 ns, indicating (based on Fig. 7) a real time of about 8 ns. This output meets the pulser design

goals. This pulser was used in run 11 on Gamble II, but at lower PFL switching voltages, and 40-kA typical currents.

A check on these waveforms is provided by using the load current and estimated feed inductance of 4 nH to calculate the forward-going voltage at the pulser. This is compared with the PFL and output voltages in Fig. 10. Good agreement with the PFL voltage is seen until the two-way transit time, as expected. The output voltage, as mentioned above, is seen to be distorted on this shot.

I have made some attempt at modeling this pulser with BERTHA. First, the PFL was rung for several cycles by open-circuiting the output switch and reducing the Marx charge. This waveform was used to obtain the Marx series resistance, PFL shunt resistance, and Marx inductance. With the proper values, excellent agreement with the data was achieved. Next, the entire circuit was modeled. All inductances and impedances are known to the needed accuracy - the only unknown is the variable switch resistance. I used Tom Martin's switch model. In this model, switching is determined by one number $LC_B/N^{1/3}$, where L is the length, N the number of channels, and C_B the Braginskii constant. In principle, these may all be determined beforehand, giving predictive capability, but as I do not know the Braginskii constant for polyethylene, this parameter was treated as free.

I found that in order to reproduce the measured current, I had to add a constant, series resistance of 0.4-0.6 Ω to the variable switch resistance. Apparently, this circuit does not supply enough energy to drive the solid switch to a very low resistance. This is consistent with the solid-switch results at KfK. The circuit used to model this pulser is shown in Fig. 11. The rather large Marx series resistance is probably due to resistive time effects; I did not try Martin's model for the Marx switches.

The calculated PFL voltage and load current are compared with the measured values, for the shot in Figs. 9-10, in Figs. 12-13. Reasonable agreement is achieved, but there is room for improvement. I will try to refine this in the future.

FUTURE WORK

This pulser meets our original design goals and is adequate for our upcoming EMFAPS bench experiments, and hopefully for Mike Cuneo's needs at SNL. For operational use on Gamble II, however, the pulser-generator jitter needs to be reduced, and the current probably needs to be increased.

With the present trigger arrangement, the jitter arises from both the self-breaking pulser output switch, and the machine oil switch. Both problems can be addressed by triggering the pulser output switch from a pickoff located just beyond the oil switch. The delay between the oil switch and the diode should be sufficient for this approach to work. As mentioned previously, a different trigger arrangement must be used for a pulse-charged switch. John Shipman long ago developed a trigger circuit for a pulse-charged solid switch like the one here, which had an auxiliary solid switch in the trigger circuit. A

simpler arrangement, shown in Fig. 14, might be possible here. This scheme can be tested on the bench.

There are two reasons why the present, 50-kA current may not be enough. First, we have recently decided to build a new applied-B diode with a larger outer radius. This means that a higher current will be needed to provide the same current/width. Second, there is as yet no consensus on the necessary foil current; it may turn out that the $\sim 2X$ larger currents/width in the KfK experiments are needed. It may also turn out that even smaller current/width (and/or longer risetimes) will suffice, with the existing pulser being adequate for the new diode. Hopefully, upcoming EMFAPS experiments here will answer this question. In the meantime, we should assume that at least 100 kA foil current, with a 5-10 ns risetime, will be required.

Improving the feed is the key to increasing the foil current. For example, BERTHA modeling, using the circuit in Fig. 11, shows that by dropping the feed impedance slightly to 1.5Ω , going back to the 80-nF capacitors (easy), and charging to 60 kV (we have such a supply), almost 100 kA would be produced. The feed would then have to hold off 90 kV. It should be possible to make a 1.5Ω laminated coax that will possess the needed strength, and will fit through the existing transit-time isolator. A sketch of such a system is shown in Fig. 14b (some mechanical details remain to be worked out, but should be straightforward). The only difficulty will be the right-angle bend, but the low-impedance, water ambient makes the task easier by allowing larger spacings. It should be possible to build a feed that has almost no additional inductance ($<3-4$ nH) all the way from the output switch to the load.

If we need still higher current, then either the transit-time isolator must be enlarged (not too difficult) or we must use multiple striplines a la KfK. I would worry that capacitive effects will limit how close striplines can be packed in water. Triplates could be used, at the expense of a little more inductance at the pulser and foil. I will be talking with Peter Hoppe next week at SNL about these issues.

Fig 1

EMFAPS FEED ARRANGEMENT

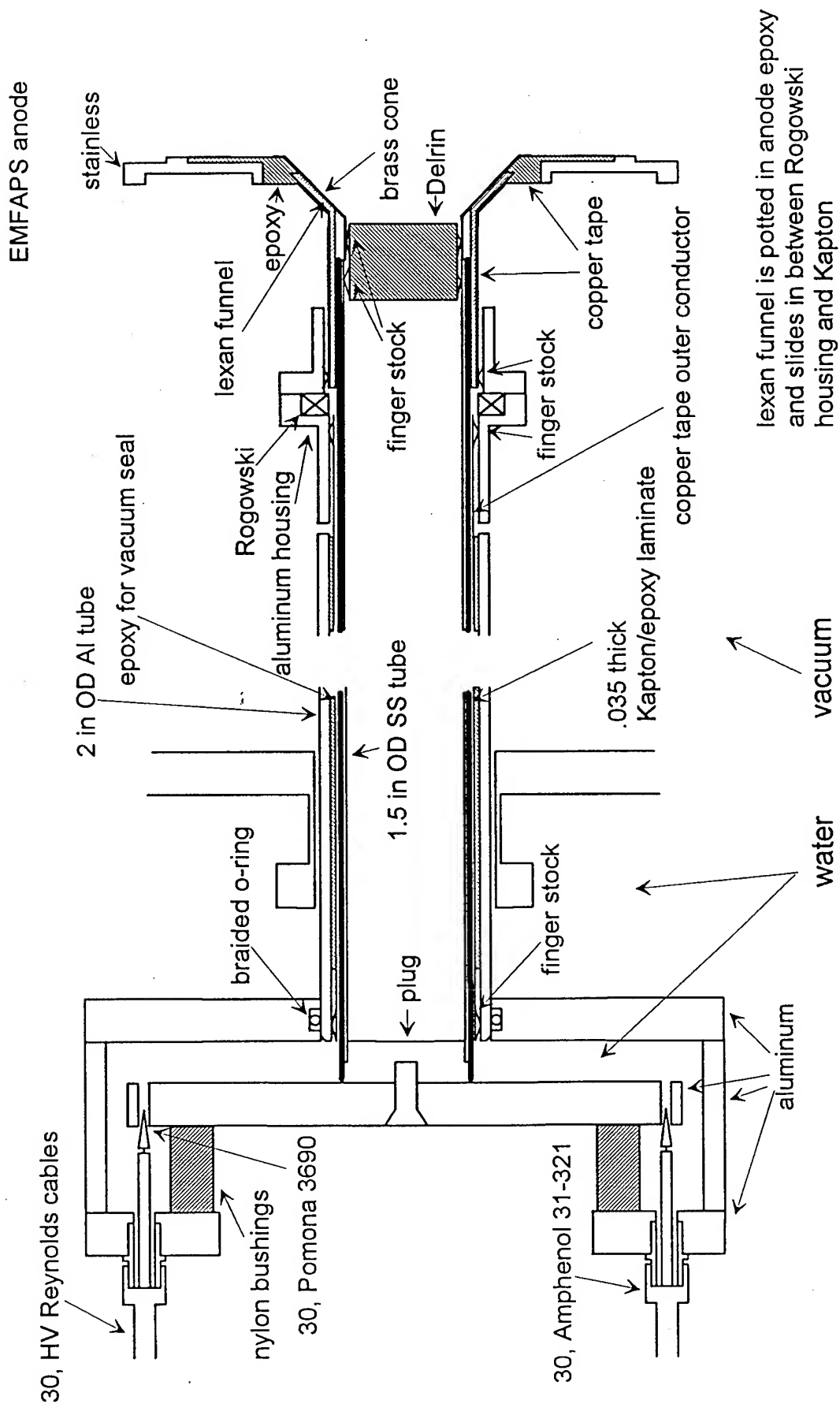
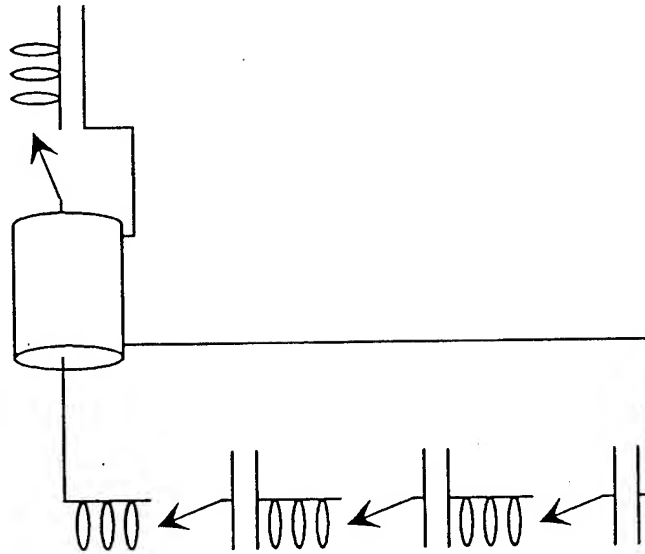


Fig 2

GENERIC EMFAPS CIRCUITS

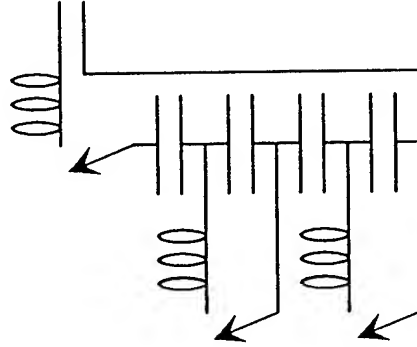
A

Marx/PFL
pulse-charged
water dielectric



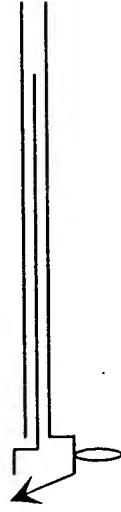
B

L-C inversion
pulse-charged
ceramic dielectric



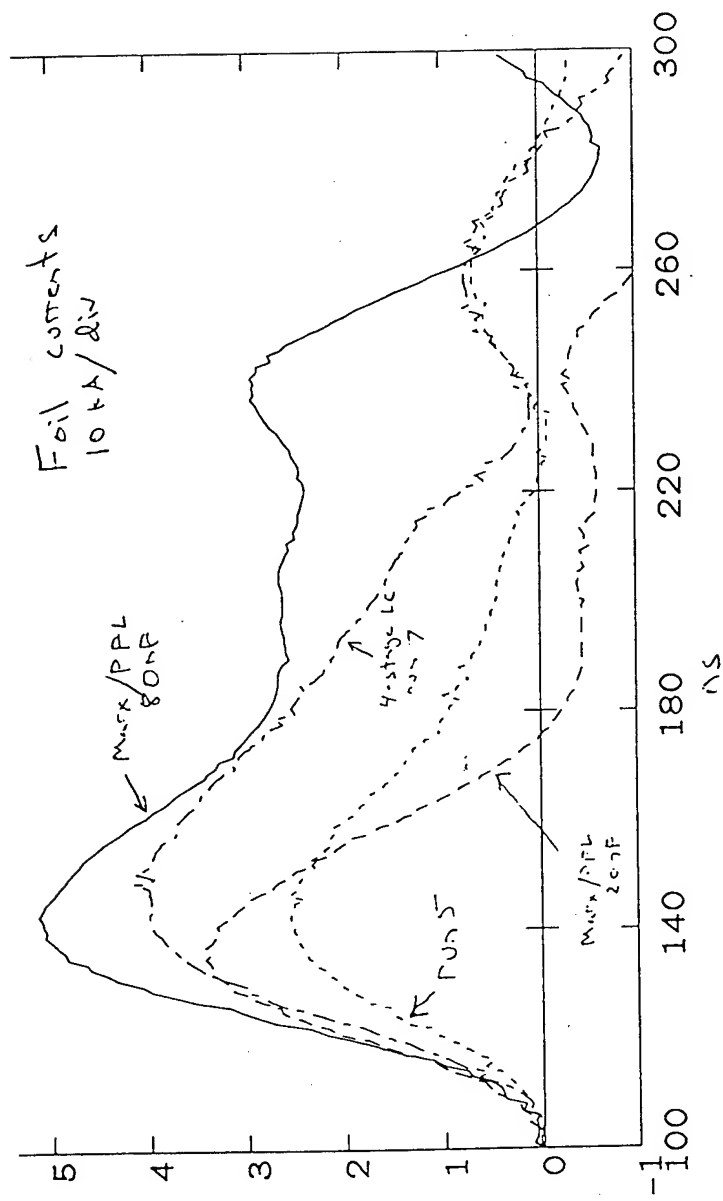
C

Blumlein
static-charged
Kapton dielectric

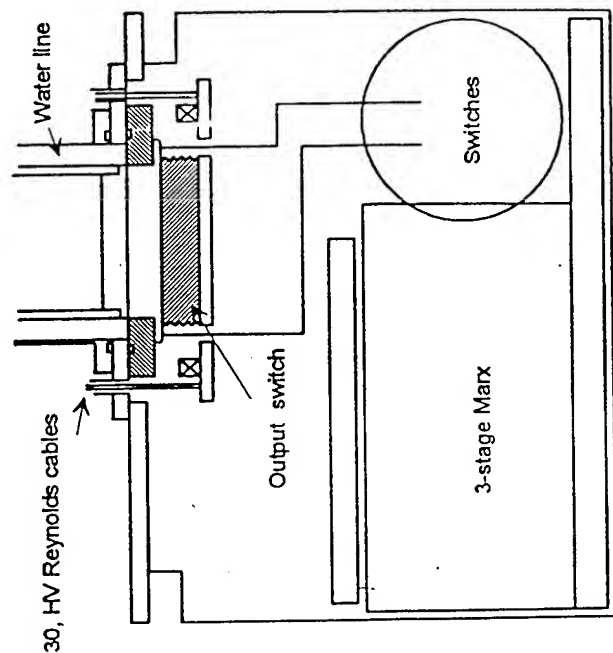


FOIL →

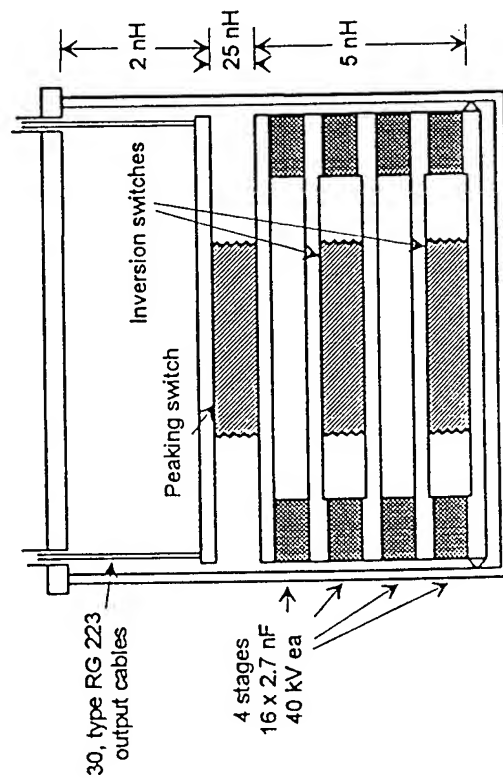
Fig 3
Previous Pulsers
+ Results



A



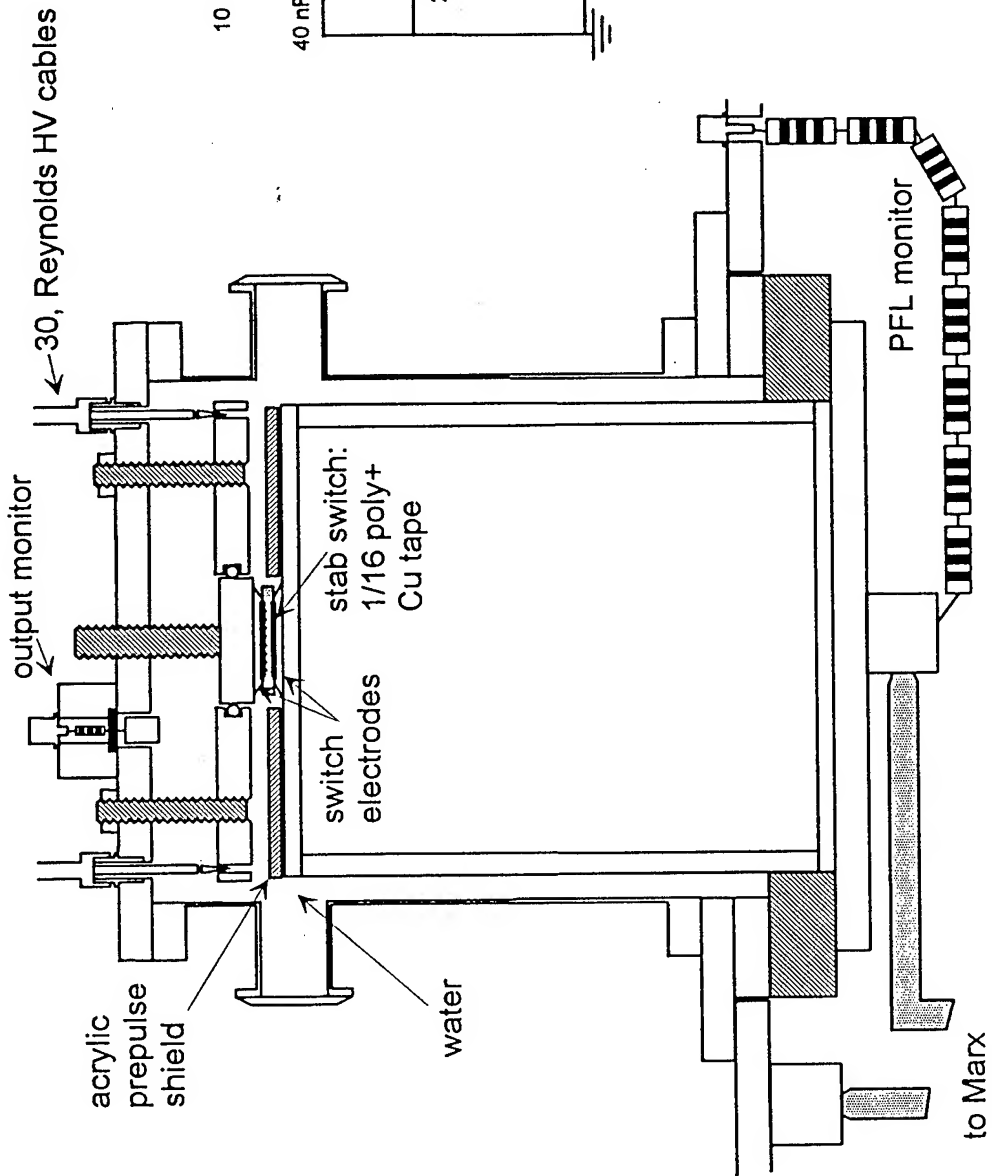
L-C Inversion pulser



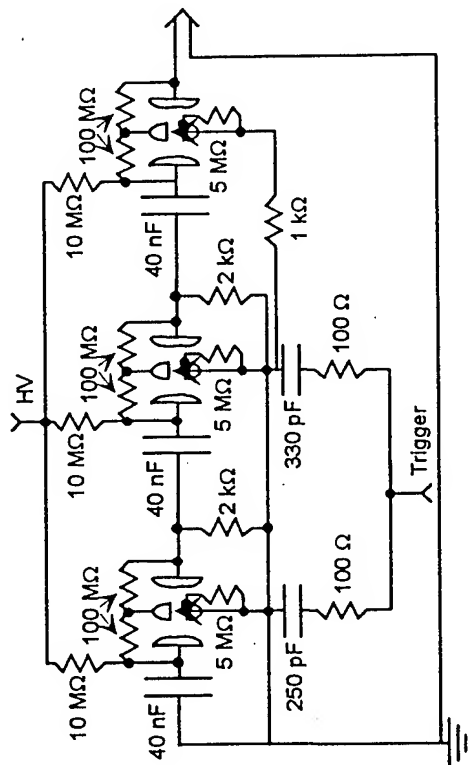
B

Fig 4

EMFAPS pulser details



A



Marx circuit

B

Fig 5

Sheet1 Chart 1

Breakdown of thin sheets

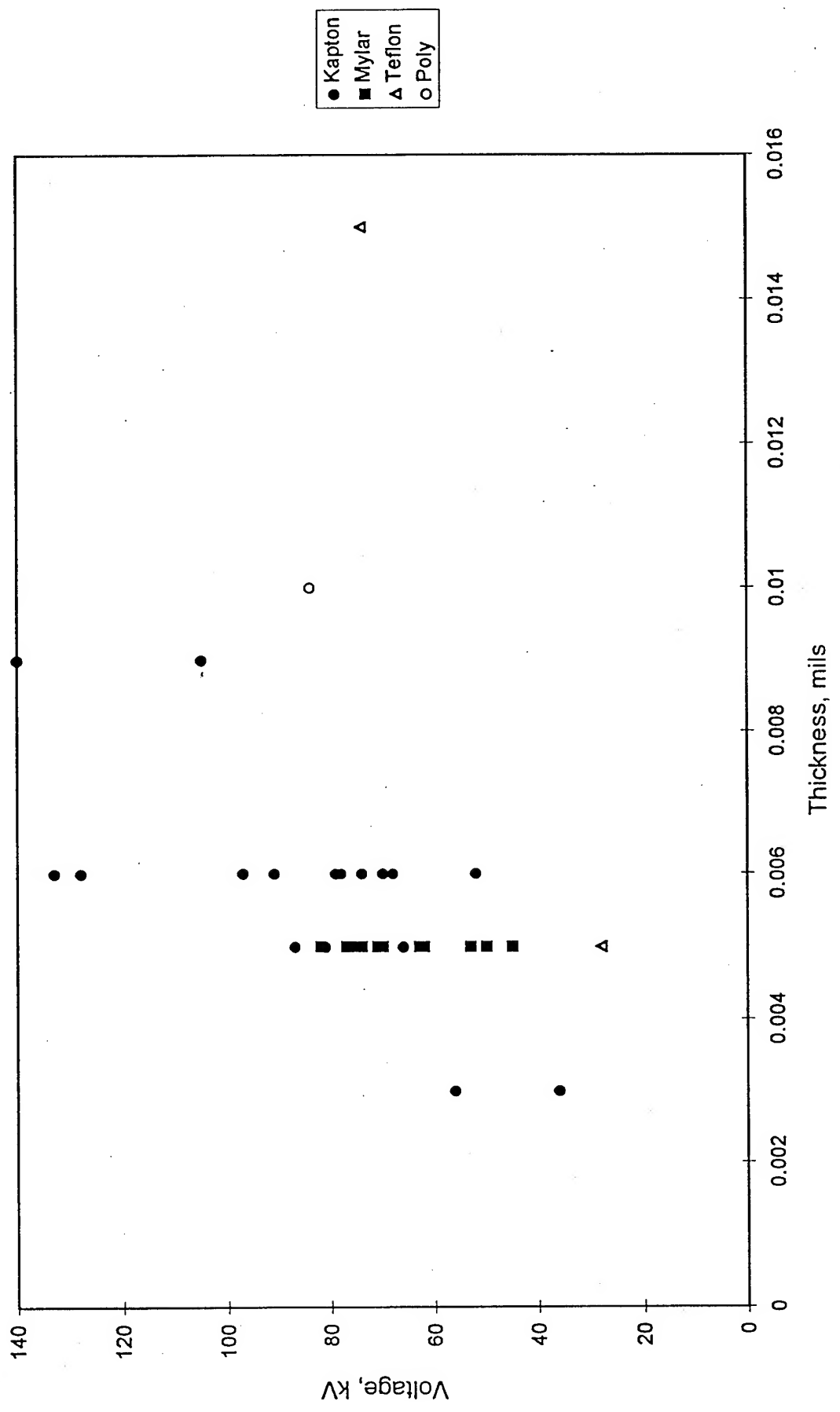
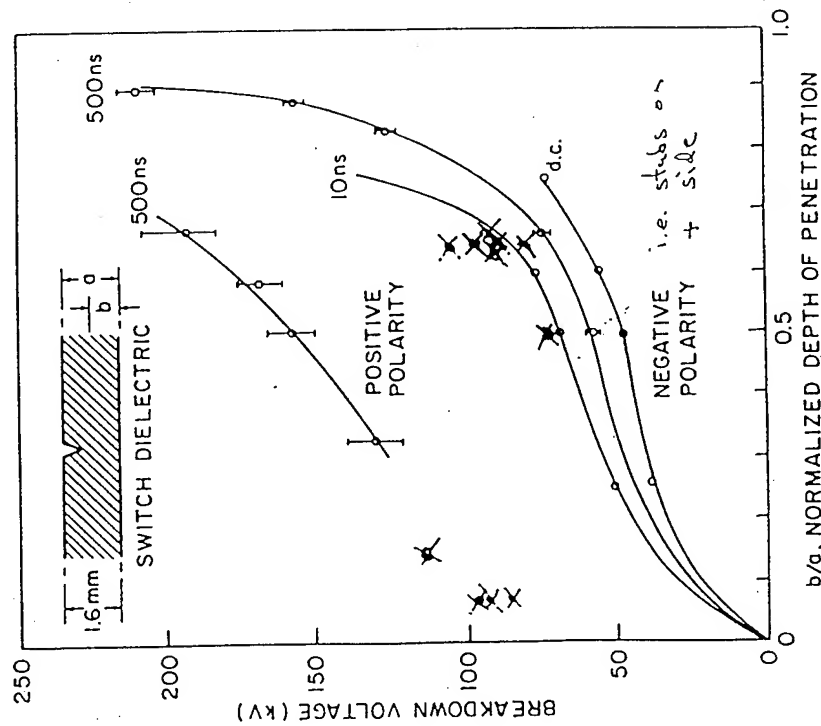


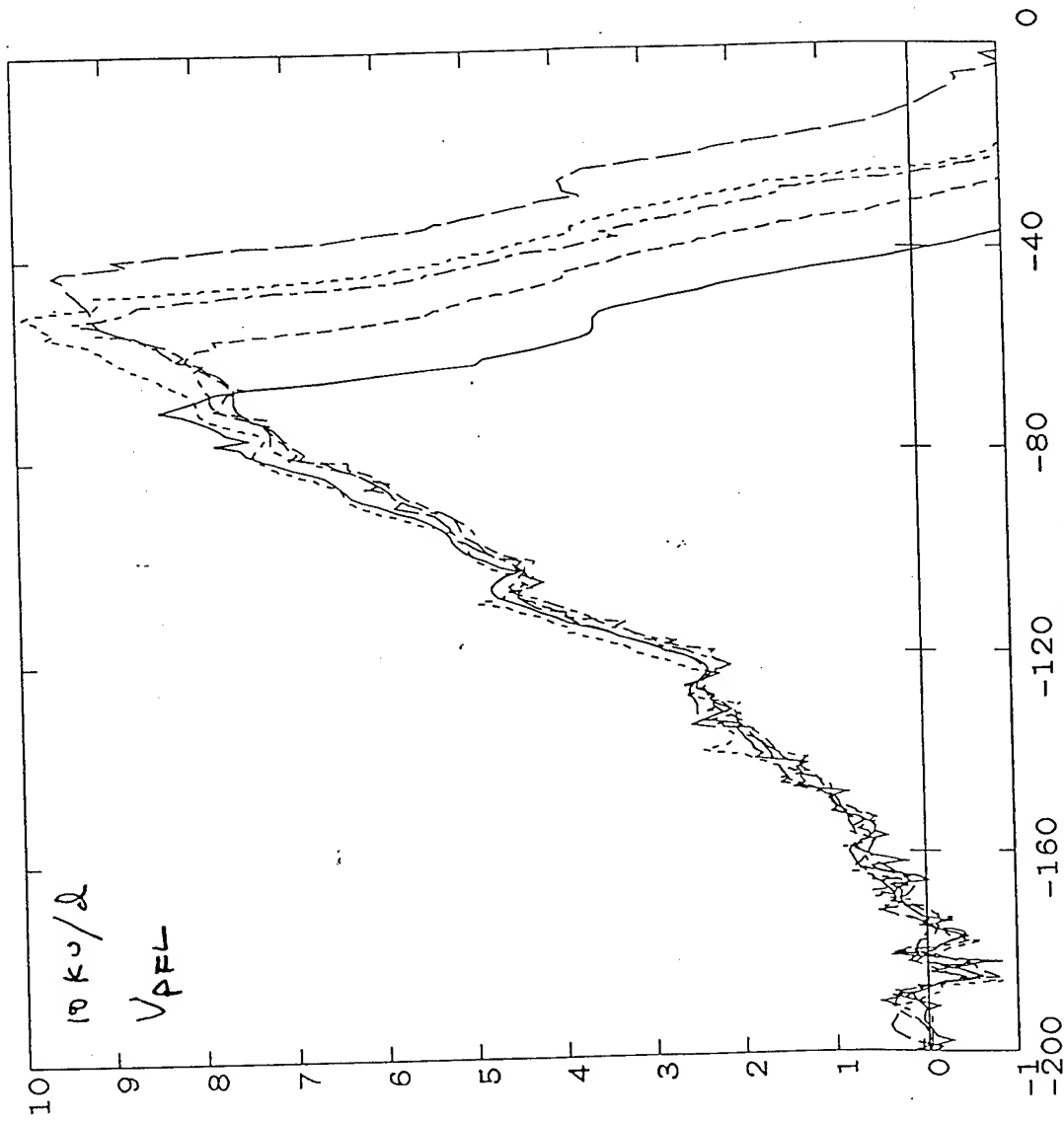
Fig 6

Stub

switch like



comp w SCM
(ref: Thor)



signals aligned to match rise
ns

Fig 7

Shot hs87

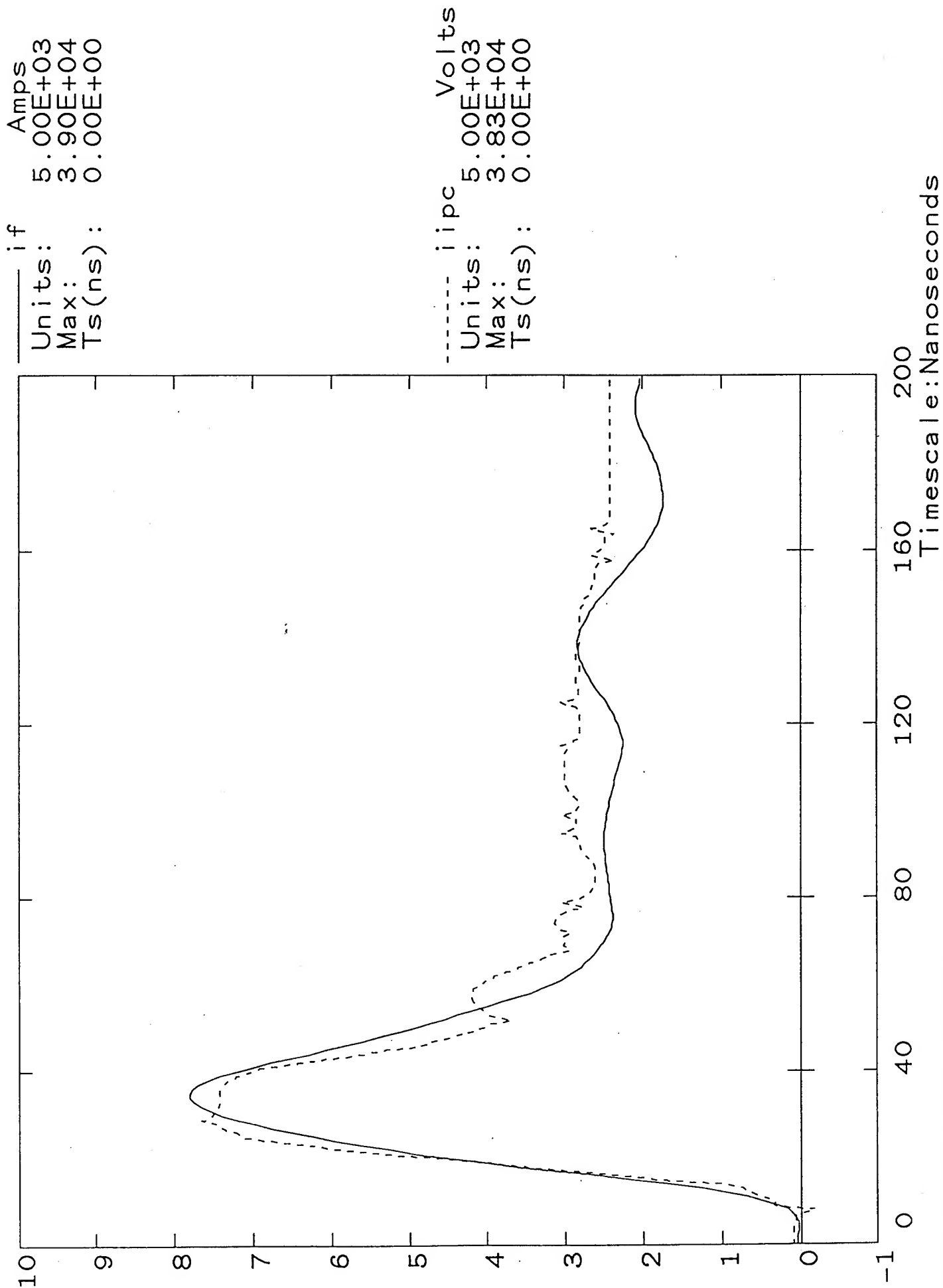


Fig 8

Shot hs90

Units: 2.00E+04
Max: 1.23E+05
Ts(ns): 0.00E+00

vg1

Volts

PFL

Units: 2.00E+04
Max: 7.84E+04
Ts(ns): 0.00E+00

vg2

Volts

body

Timescale: Nanoseconds

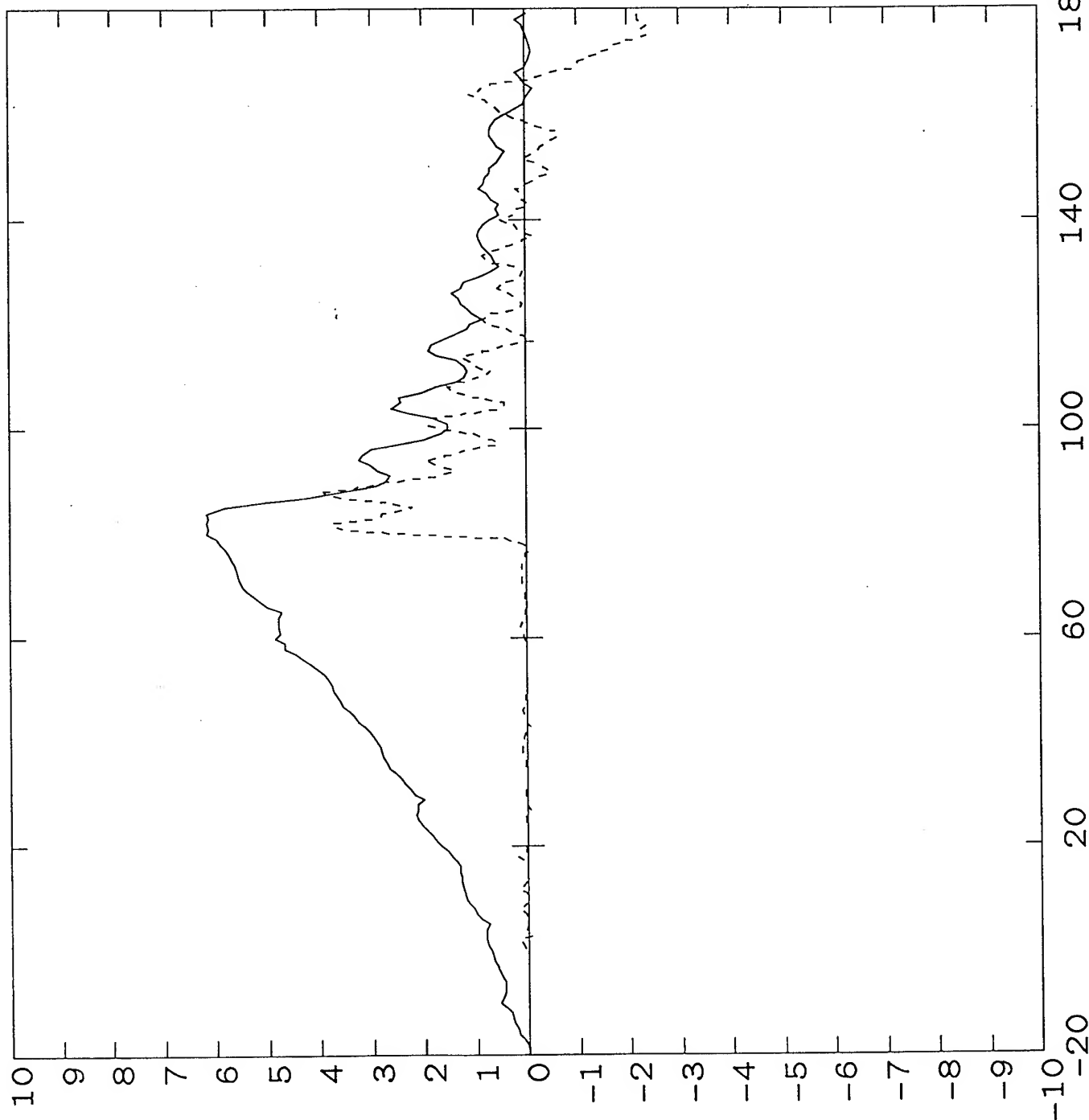


Fig 9

Shot hs90

Units: Amps
Max: 1.00E+04
Ts(ns): 6.00E+04
0.00E+00

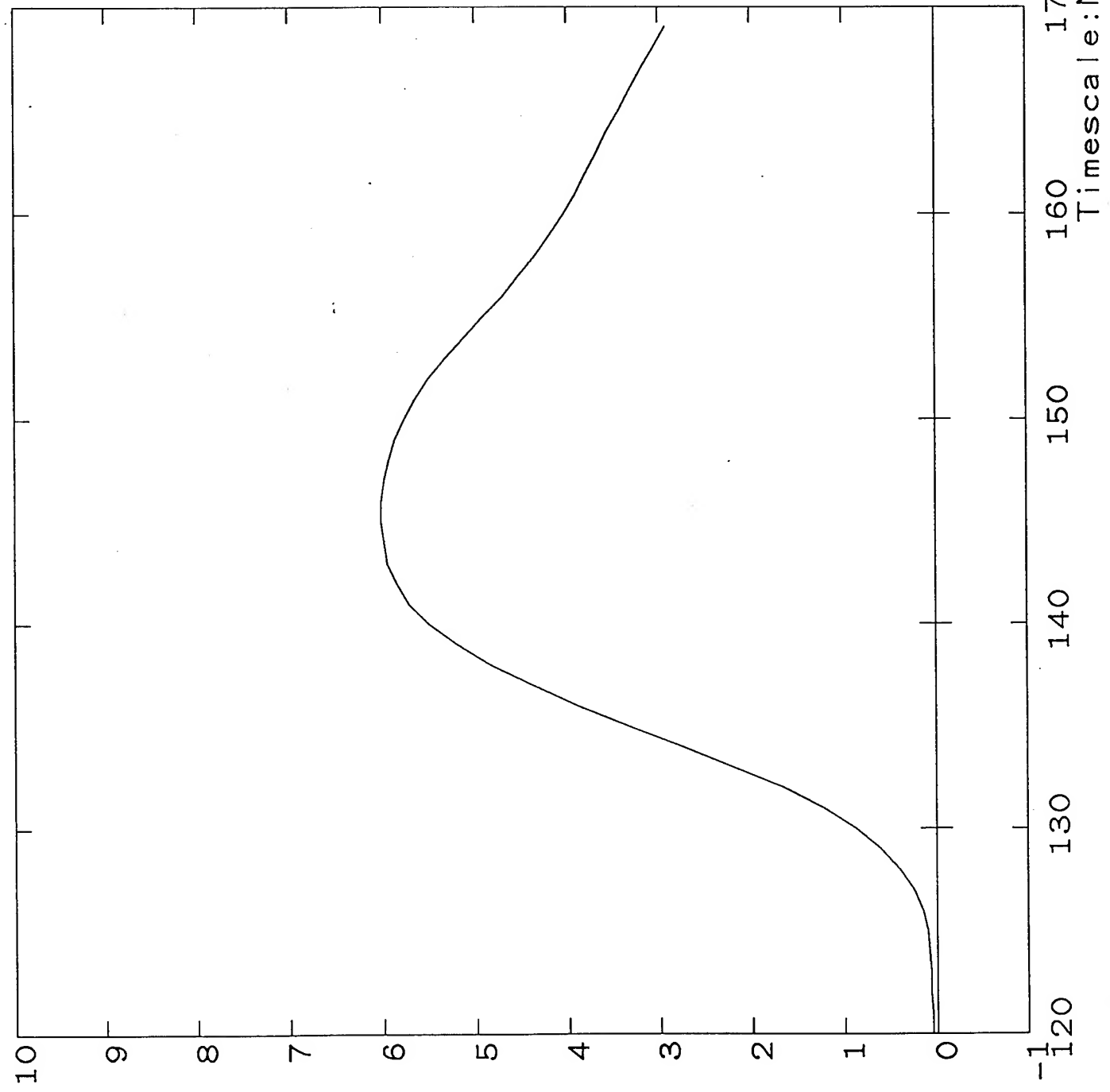
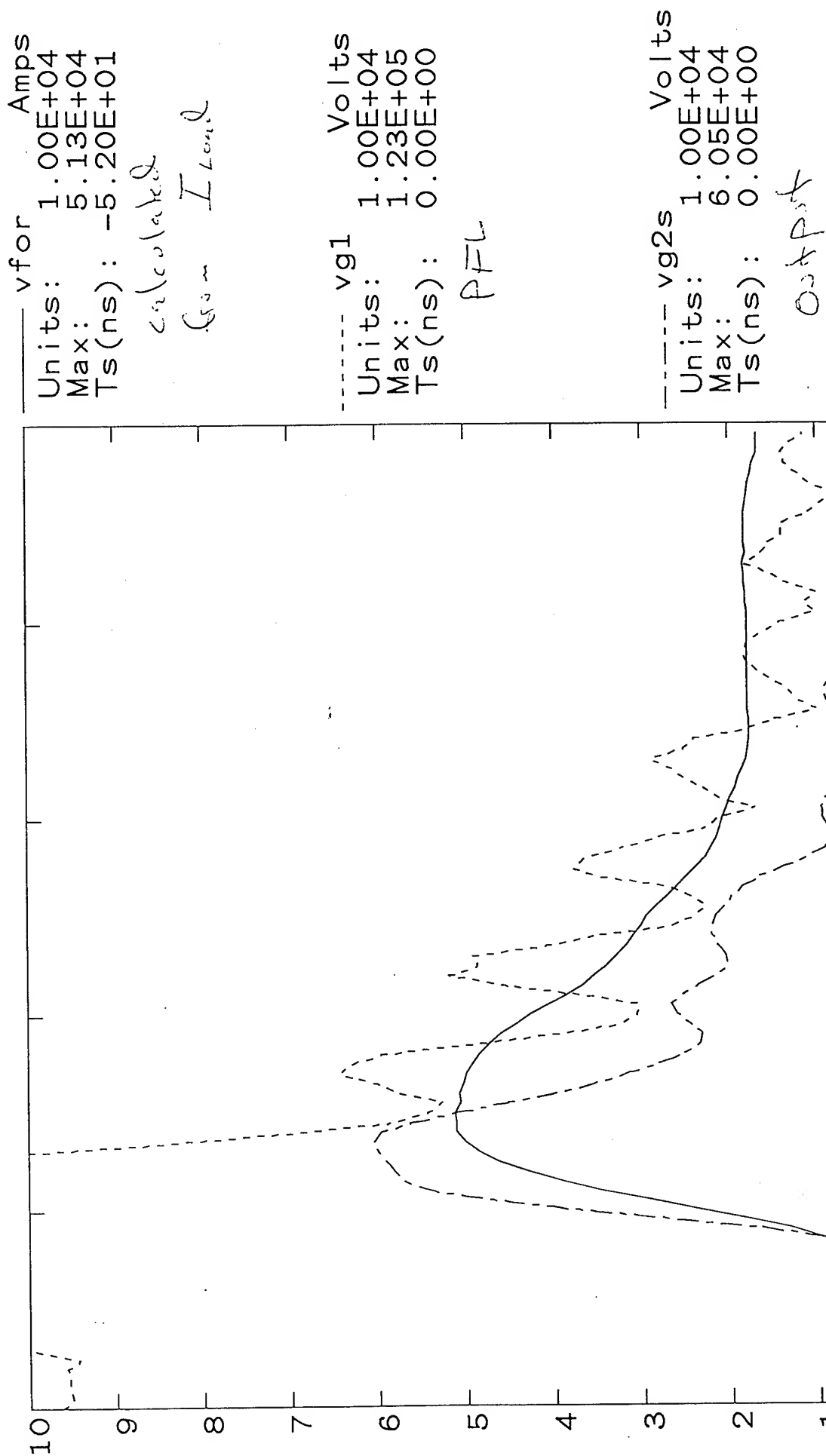


Fig 10

Shot hs90



Timescale: Nanoseconds

Fig 11

BERTHA pulser model

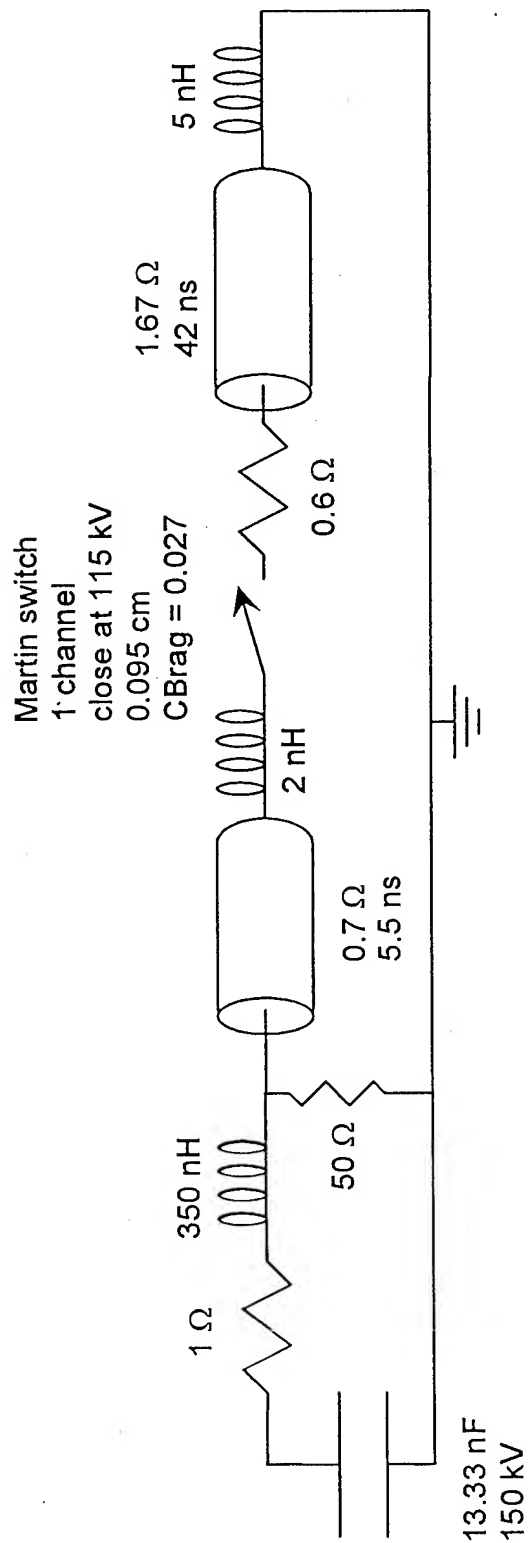


Fig 12

Shot pul1

vg190 Volts
Units: 2.00E+04
Max: 1.23E+05
Ts(ns): 2.50E+01

exp

vo005 VOLTS
Units: 2.00E+04
Max: 1.22E+05
Ts(ns): 0.00E+00

BERTHA

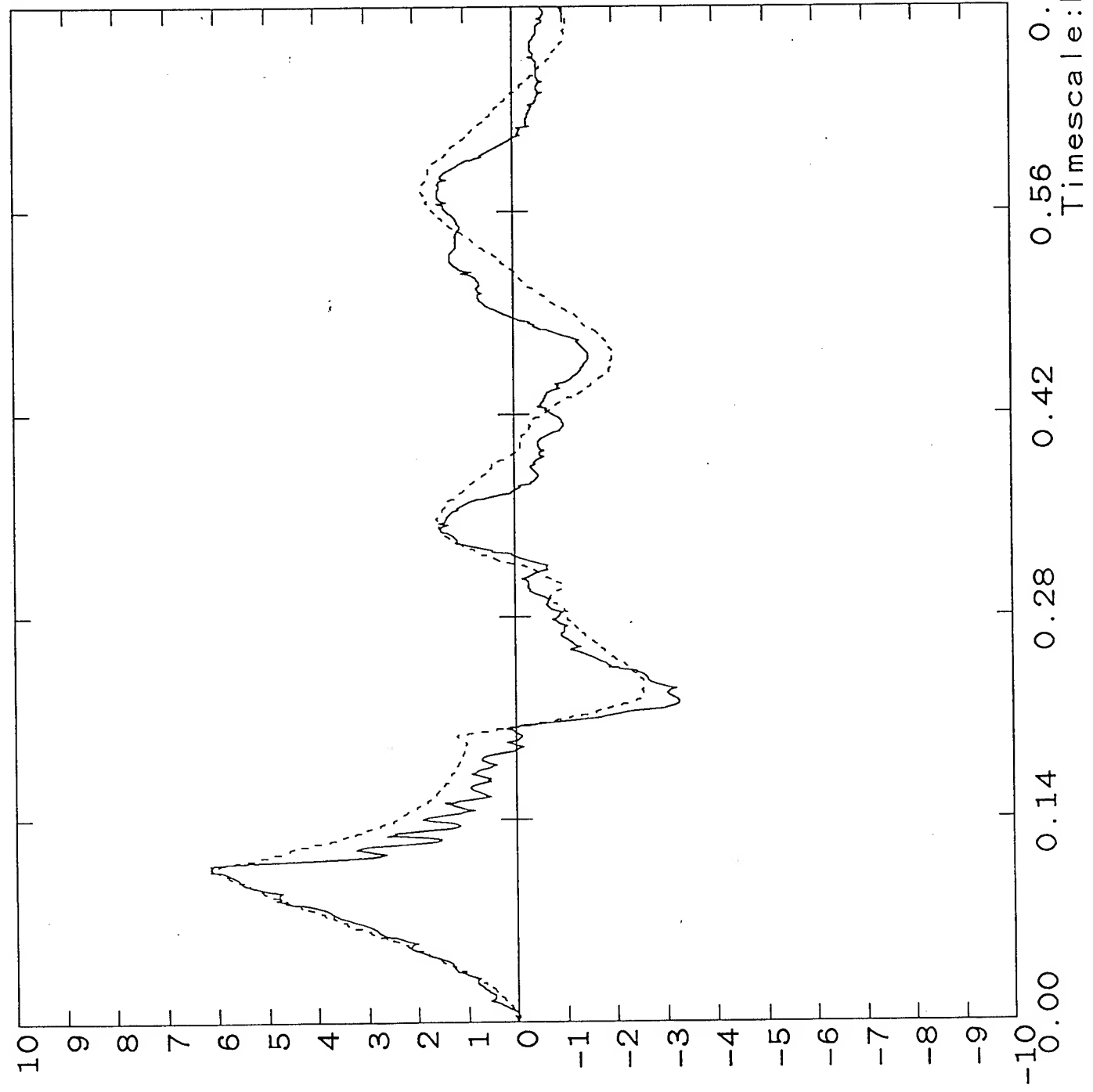


Fig 13

Shot pul1

if90 Amps
Units: 1.00E+04
Max: 6.00E+04
Ts(ns): 1.90E+01

Exp

cu012 AMPS
Units: 1.00E+04
Max: 6.01E+04
Ts(ns): 0.00E+00

BETA4A

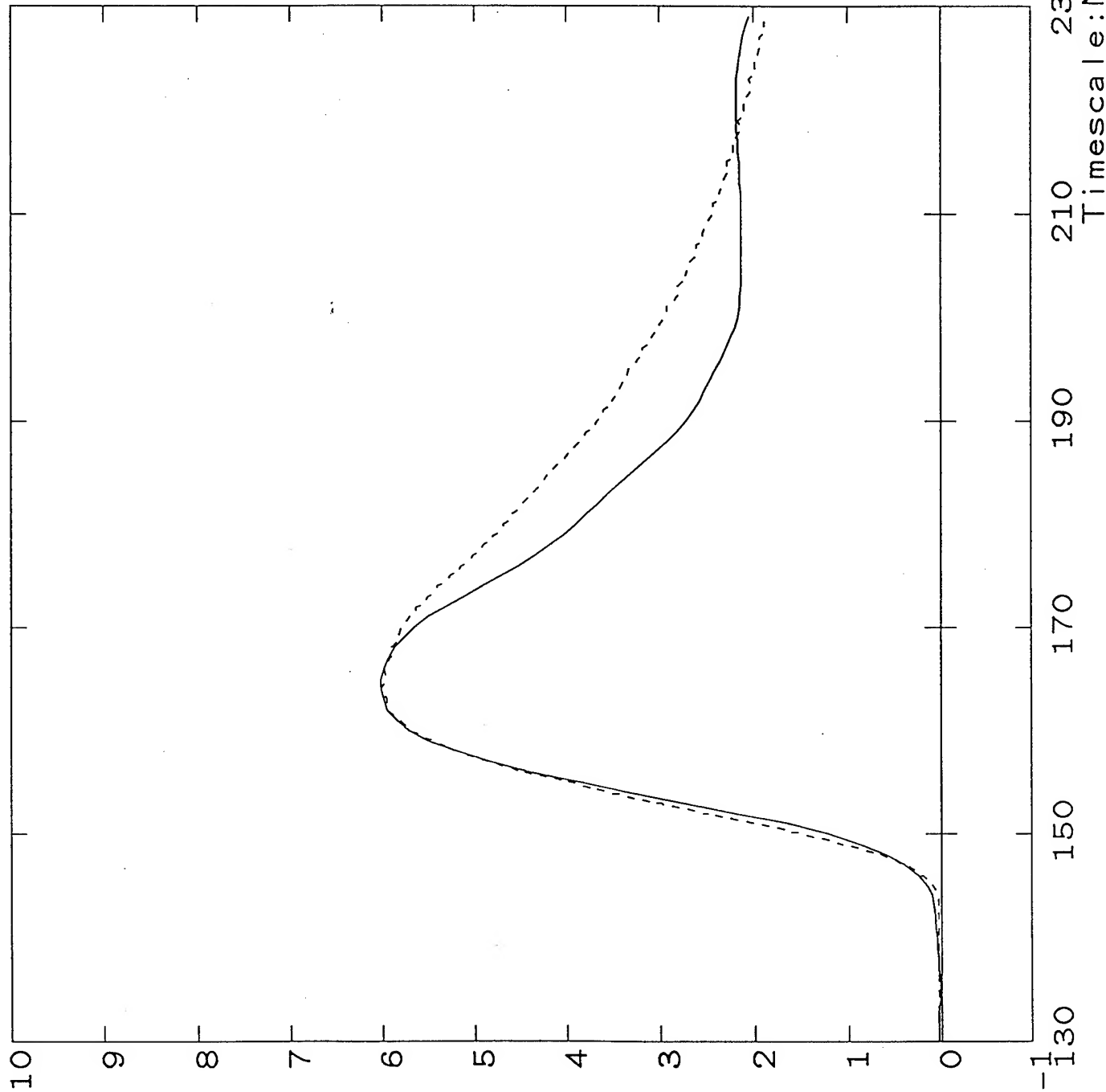
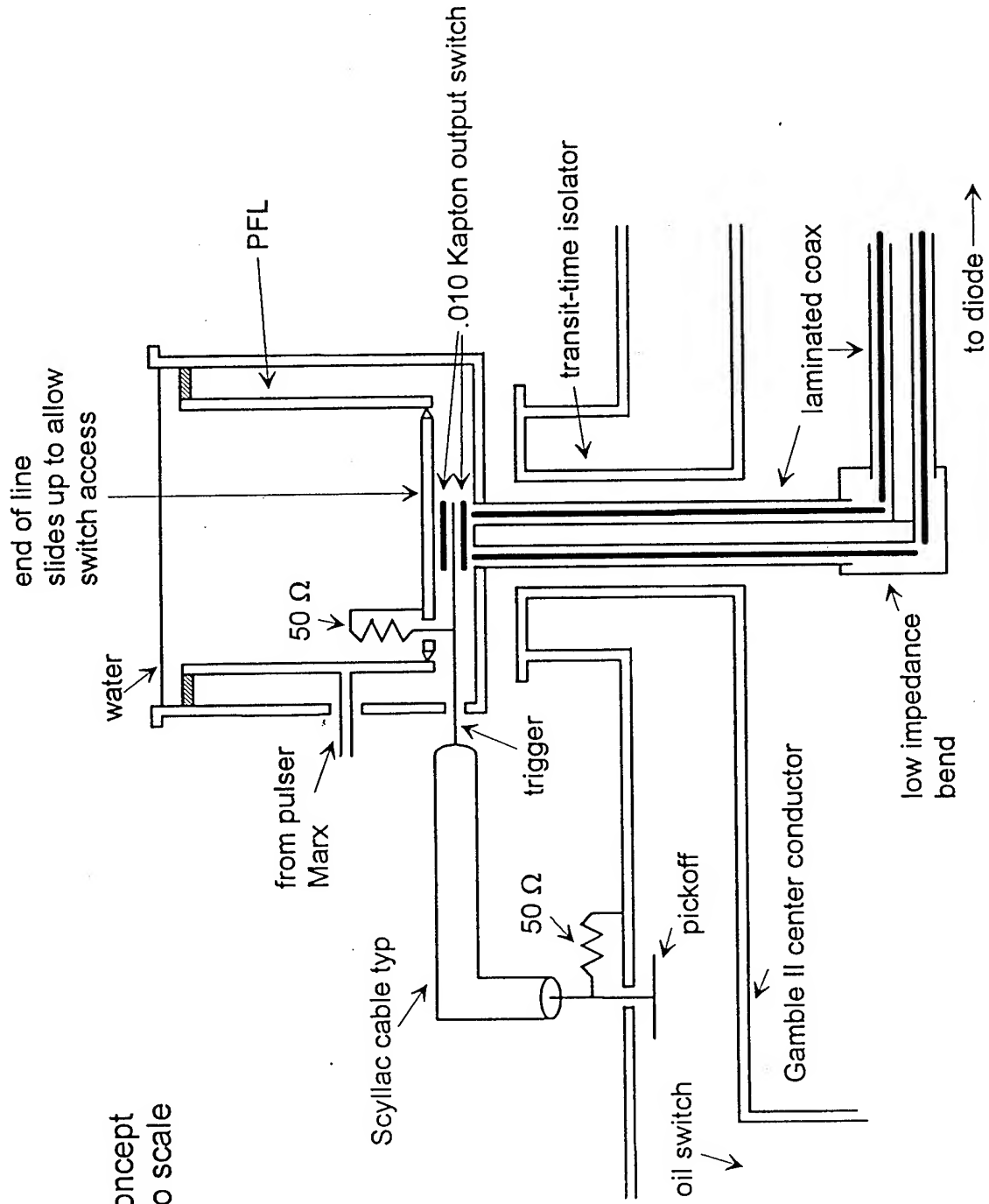


Fig 14

100 kA pulser concept
schematic, not to scale



PULSED POWER PHYSICS TECHNOTE 93-19

TITLE: INITIAL PULSER-DRIVEN EMFAPS RESULTS

Author: D. Hinshelwood, R. Fisher, and J. Neri

Date: November 18, 1993

Abstract: This note describes our work on pulser-driven EMFAPS to date. Anodes have been coated and vaporized, both on the bench and in an experimental run on Gamble II. The results of that run are presented in TN 93-18; this note describes our pulser and coating system status and presents the results of our bench studies. The foils have been diagnosed using electrical measurements, interferometry, spectroscopy, photography, and photometry. We see that the foils vaporize at actions lower than expected, which we attribute to semi-microscopic non-uniformities in the foil. This early vaporization may limit the proton inventory available to the diode. Planned improvements are discussed.

INTRODUCTION

This note is a companion to Jess's TN 93-18: together these describe the current status of our EMFAPS effort. This note focuses on the development of a pulser to drive the foil externally, and bench tests of exploding foils.

Our EMFAPS effort was first suggested by Mike Cuneo as a technique for obtaining a high-quality proton beam from the SABRE diode on Gamble II, in order to facilitate relevant ion beam transport experiments. Later, the goal was expanded to include the study of EMFAPS technology in general with the goal of fielding a source on SABRE. EMFAPS operation requires a current of tens of kA to be driven rapidly through a thin metallic foil on the anode surface. This current can be supplied by a partial diversion of the pulsed power to the diode, by an early diversion of the electron flow in the diode (limiter-EMFAPS), or by an external pulser. All of these approaches have advantages and disadvantages. With only a small fraction of the incoming pulsed power, a high current can be supplied quickly to the foil. In the successful implementations of EMFAPS to date, at Cornell and KfK, a POS in re-entrant geometry is used to divert the early portion of the machine current through the foil. This scheme was also used in our first EMFAPS experiments on Gamble II. The drawback to the POS approach is the difficulty in obtaining reproducible operation. This was particularly true in our first experiment, but even at KfK they are not completely satisfied with this approach and eventually plan to use an external pulser. We have also considered more passive means of diverting the early pulsed power, using inductive, resistive, or capacitive division, and have concluded that it would be very difficult to divert enough current quickly to drive the foil. Limiter-EMFAPS is particularly attractive on Gamble II because of the low generator impedance which gives us plenty of current, and because of the other beneficial effects that result from the use of a limiter. However, this approach may be less attractive on a higher-impedance machine such as SABRE, and serves to constrain diode design. The use of an external pulser offers several advantages: the foil current, and the delay between foil current and machine current, may be varied independently to allow better control of EMFAPS operation; the source may be studied and developed on the bench under the same driving conditions as on machine shots; and in principle the source may be easily transferred to other machines. Pulser-EMFAPS suffers from the difficulty of developing a pulser that can supply the required current, and possible difficulties in synchronizing the pulser to the machine. However, we believe that pulser-EMFAPS has the best long-term potential and have concentrated on this approach.

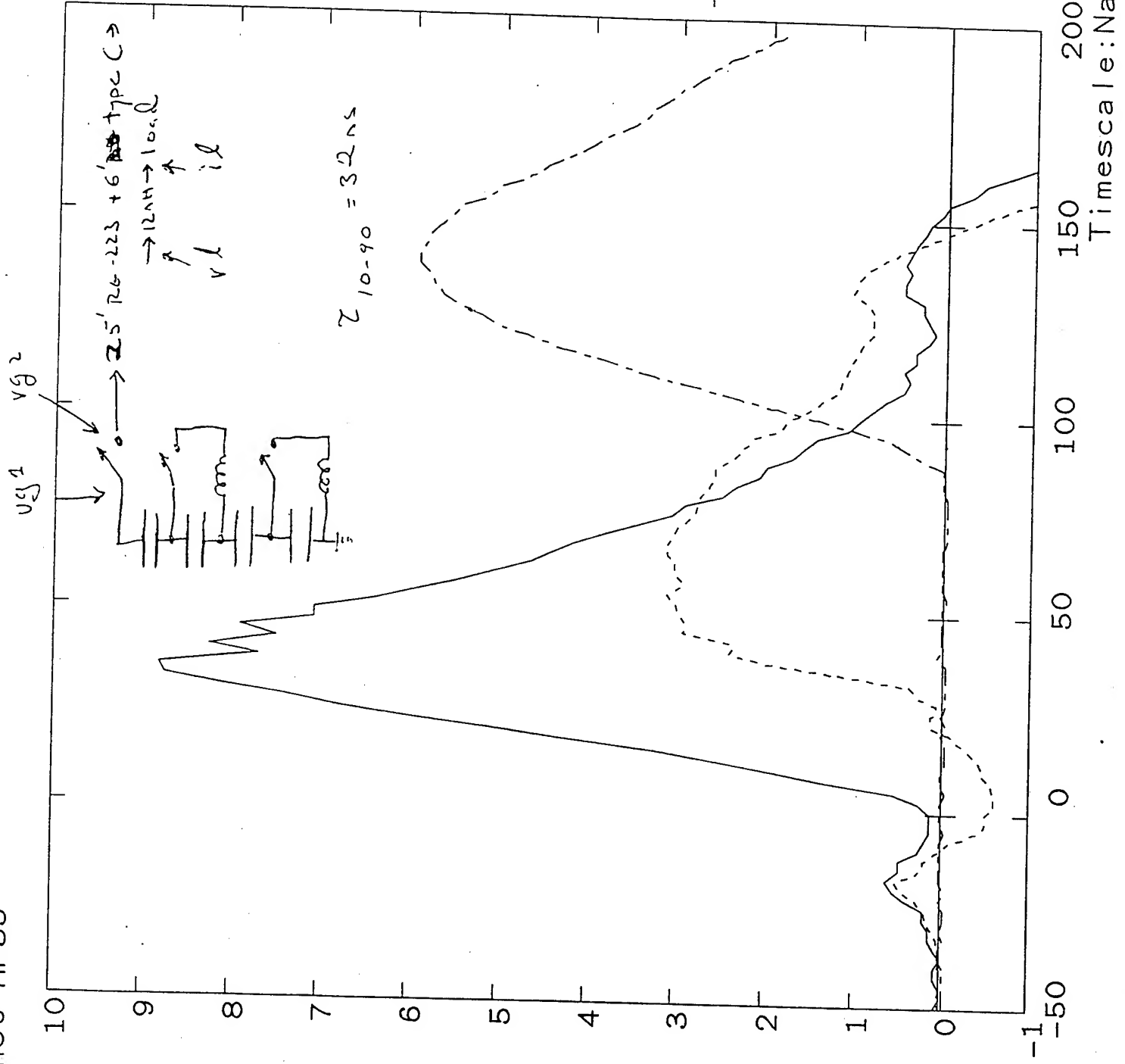
PULSER DESIGN

Pulser-EMFAPS can itself be pursued by two approaches. Either a very compact pulser, that can be located close to the foil, can be designed, or a low-impedance cable feed can be used to supply current from outside the machine. For now we have chosen the latter, because the pulser design is simplified (it need not be built for vacuum or water immersion), because access to the pulser (if needed during a run) will not be a problem, and because this scheme will be the easiest to adapt to SABRE.

Our pulser design is still evolving and the gory details will be presented in a later note. Initially, 15, type-C cables were used to provide a $2\text{-}\Omega$ feed. However, we had troubles with cable breakdowns during the run and after some testing found that RG-223 has (surprisingly to us) superior breakdown strength. Now we use 30, RG-223 cables to give a $1.6\text{-}\Omega$ feed (although we have not yet replaced a 9-ns section of the $2\text{-}\Omega$ feed at the load). This is about the maximum number that will fit through the Gamble II transit-time isolator. Our present pulser comprises a four stage LC inversion network, with 8, 2.7-nF , 45 kV doorknob capacitors per stage. A sketch of the circuit, and the waveforms for a roughly 42-kV charge, are shown in Fig. 1. The pulser produces 30 kV across the $1.6\text{-}\Omega$ load with a rise time of about 10 ns. This relatively low voltage is the result of energy losses in the spark gaps and an overmatch between the pulser and line impedances. More, lower-inductance capacitors have been ordered to correct the latter problem, and we plan to operate with a 50-kV voltage wave on the cables. Figure 2 compares the calculated forward-going voltage waves at the pulser and at the load. Substantial degradation of the pulse is seen to occur. Reflections at the $2\text{-}\Omega$ section near the load probably account for part of this degradation. Most of the degradation, however, appears to be caused by dispersion in the cables. If so, this could be a problem for SABRE where the cables must be even longer. The greater diameter of the SABRE line, however, should allow the use of better (i.e., RG-214), or more, cables. If necessary, a peaking circuit could also be added near the load. For Gamble II, we could always locate the pulser close to the load if necessary. In summary, while this pulser arrangement has allowed a partially successful EMFAPS on Gamble II (see Jess's Technote), further improvement is required. With the new capacitors and a uniform cable feed, we should be able to obtain 50-60 kA through the foil with a rise time of 20-25 ns. If necessary, this rise time could be reduced with a peaking circuit.

Figure 3 shows the current and voltage measured at the load for a short circuit in the foil location. VCOR is the voltage across the foil itself, corrected for the 12 nH between the voltage divider and the foil. The finite corrected voltage calculated for this short circuit results from small errors in the current and voltage measurement and illustrates the uncertainty in determining the foil voltage.

The pulser must be triggered from Gamble II with a minimum of jitter, which we had anticipated to be a potential difficulty. In addition, with the LC circuit used, simultaneous triggering of the two stages is a concern. Gamble II consists of a Marx, intermediate store, water switch, PFL, oil switch, transformer section, and diode. The transformer input is a fast-rising pulse which has no jitter relative to the diode. However, it does not come early enough for the pulser to erect and for the pulser output to reach the diode. The use of a signal derived from the PFL dV/dt provides for a sufficient delay, but this signal has a ~ 50 ns rise time, and the oil switch jitter now comes into play. In practice, however, we found that the pulser could be triggered quite reliably. An air-gap peaking switch sharpened the trigger pulse, and the use of a $50\text{ }\Omega$ trigger cable provided plenty of current so that both of the initial switches on the pulser (see the sketch in Fig. 1) closed together. The output switch was operated in a self-break mode. With this



V
0.00E+00
8.80E+04
0.00E+04

VG2
Units: V
Max: 1.00E+04
Ts(ns): 3.08E+04

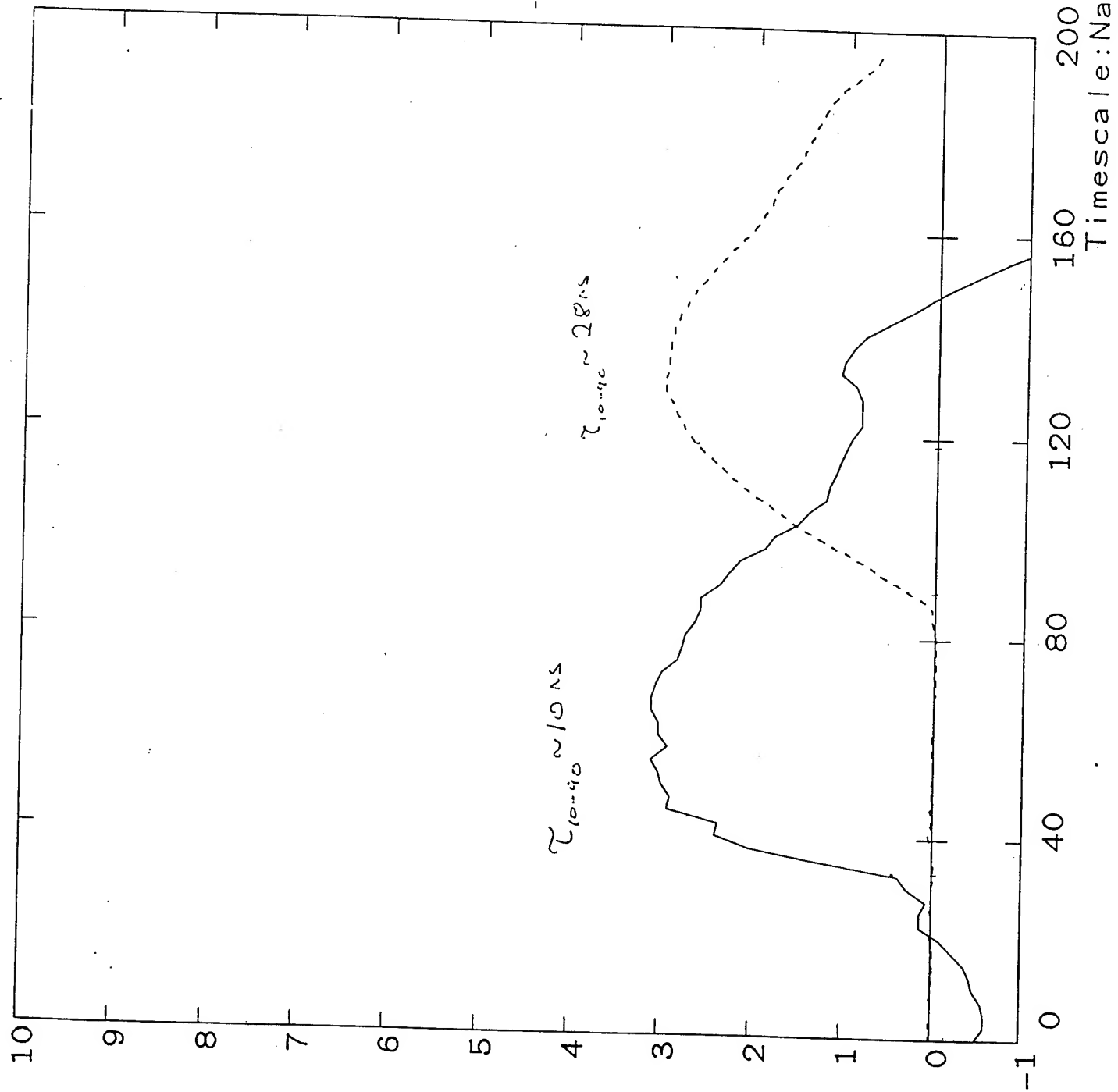
IL
Units: A
Max: 5.00E+03
Ts(ns): 2.96E+04

Shot HP35

5

VG2 V
Units: 1.00E+04
Max: 3.08E+04
Ts(ns): 0.00E+00

VF0R V
Units: 1.00E+04
Max: 2.98E+04
Ts(ns): 1.00E+00



Shot HP35

CCR

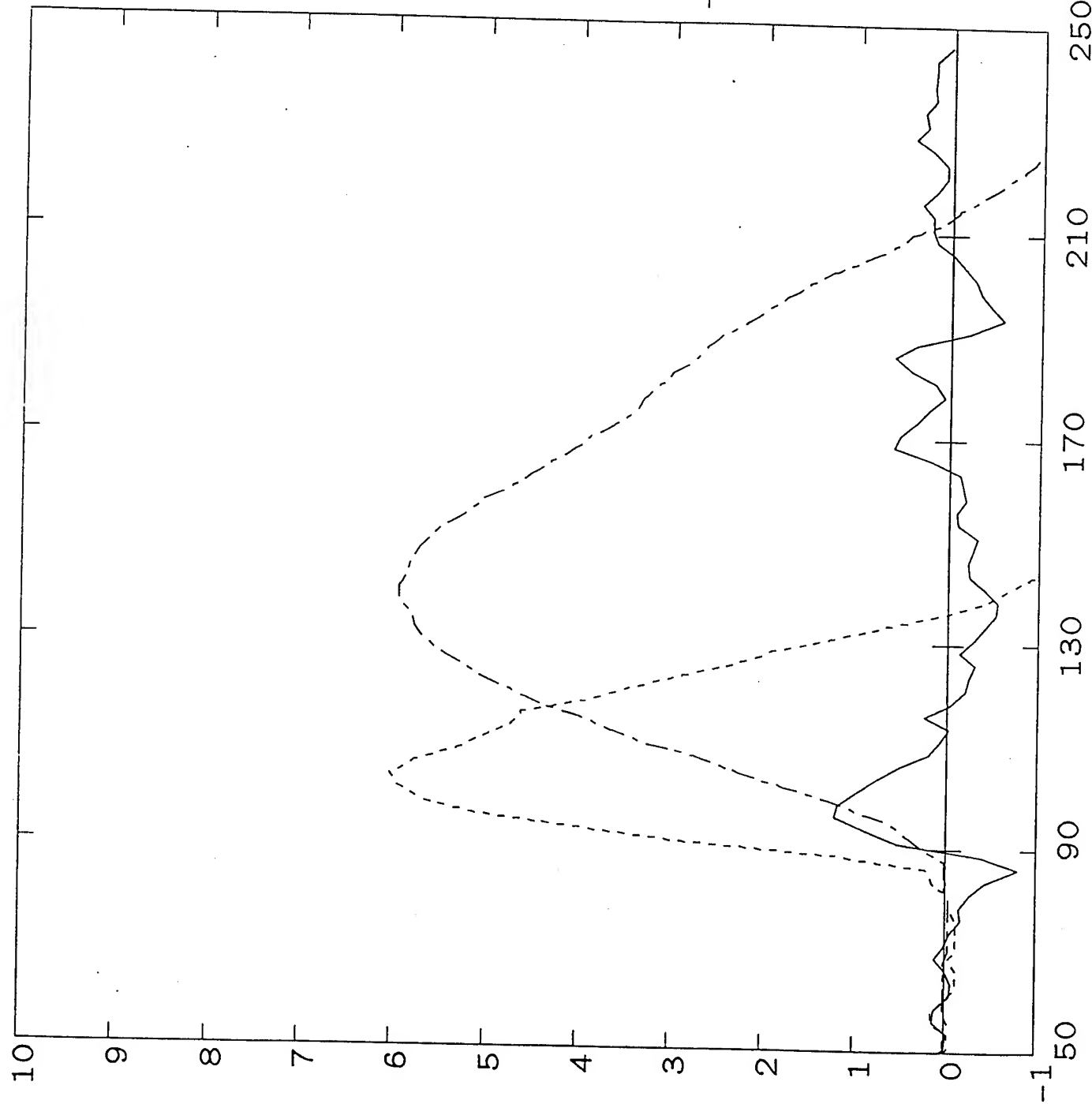
Units: V
Max: 2.51E+03
Ts(ns): 1.00E+00

VL

Units: V
Max: 1.20E+04
Ts(ns): 1.00E+00

IL

Units: A
Max: 2.96E+04
Ts(ns): 0.00E+00



Timescale: Nanoseconds

arrangement, the combined jitter of the oil switch, two initial pulser switches, and pulser output switch was about 10 ns. If necessary, this could be reduced still further by triggering the pulser output switch from the transformer input signal.

COATING SYSTEM

Our EMFAPS anode design is shown in Figure 4. The anodes consist of two stainless rings held together by low-viscosity epoxy. First, copper contacts are coated at the boundaries of the anode emission area, which extends from about 4.5 to 5.5 cm in radius. Then, aluminum is coated over the emission area and the contacts. Mini-mak sputtering guns, supplied by US Gun, are used to apply the coating (Kerry Lampa from SNL guided us to this manufacturer and has provided invaluable advice in setting up our sputtering system.) The guns are arranged on the emission area circumference and the anode is rotated above them to insure azimuthally uniform deposition. A masking arrangement allows both coatings to be applied without opening up. We had some troubles at first in maintaining a steady discharge. These were resolved after conversations with the manufacturer by reducing the thickness of our targets. The coating system is now working quite well. At present, we coat with copper for 20 minutes at 100 W discharge power and then with aluminum for 4-20 minutes at 50 W. Most of the shots on Gamble II were taken with 4-minute anodes. We will soon calibrate the system using our thin-film monitor. The copper films are estimated to be about 2000 Å thick and the aluminum films estimated to be about 200 Å thick for 4-minute coatings.

Our technology for preparing the anodes for coating is still evolving. The anodes used in the Gamble II shots were prepared by sanding the epoxy and then waxing the surface lightly as was done at Cornell. As at Cornell, this method still results in some visible scratches in the emission surface region and discontinuities at the epoxy-metal boundaries. We are now trying different metal edge profiles, types of epoxy, casting arrangements, and finishing techniques with the goal of reducing these potential problems. Our anodes now are similar to those at Cornell in this regard, but as discussed later, the use of a (longer current rise time) external pulser may place more demands on the foil quality and thus the anode smoothness. One of the goals of our bench tests is to determine just how critical the foil and current-contact smoothness is.

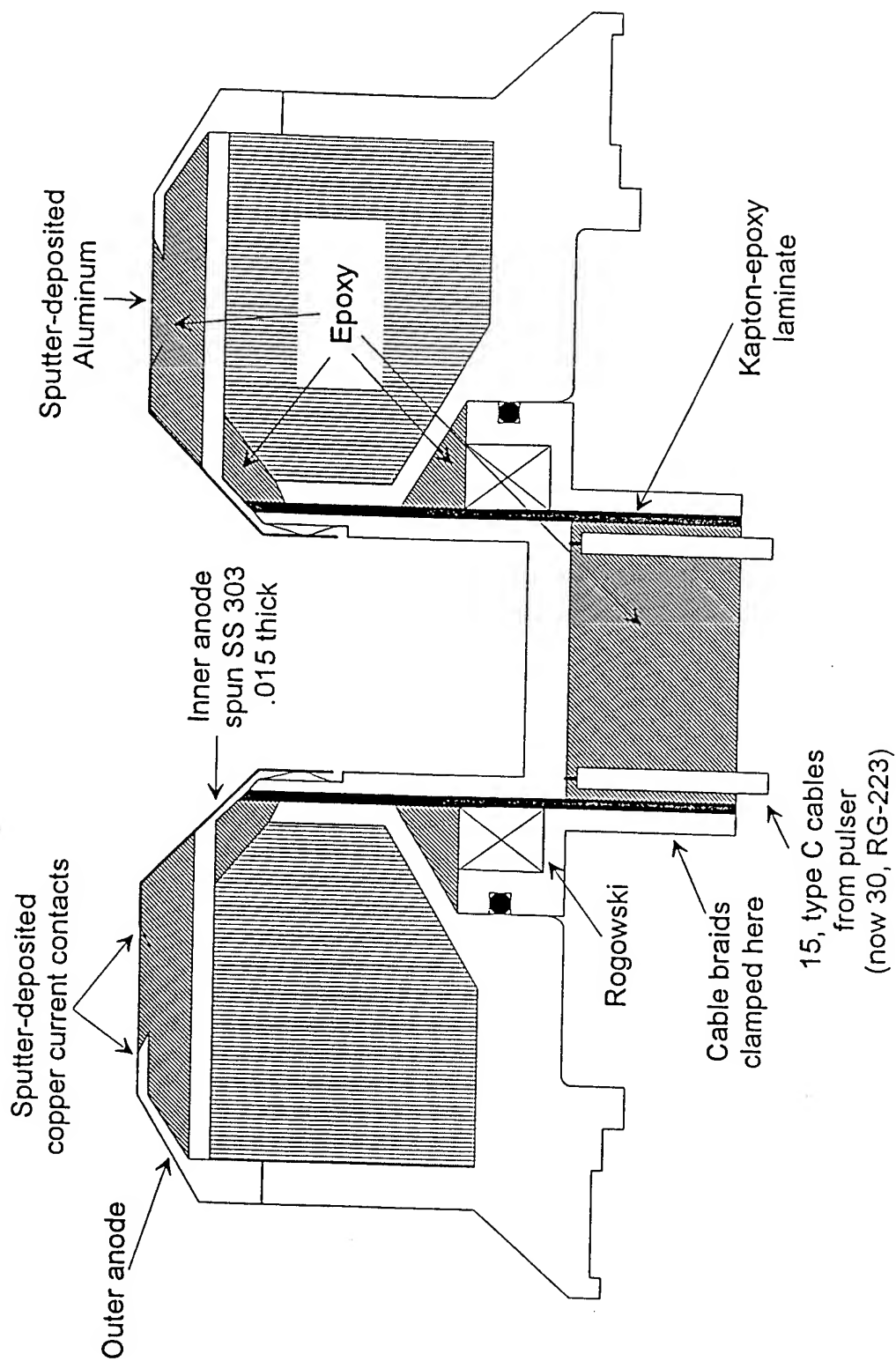
At present, we find that the growth rate of our films is strongly dependent on the anode epoxy surface smoothness, and that slight variations in finishing can lead to variations in the film thickness. This may be due to the relatively low deposition rates used, on the order of 50 Å/minute. We will be discussing this issue with deposition experts at NRL and SNL.

FOIL MEASUREMENTS

The foils were diagnosed using current and voltage measurements, open shutter photography, time-integrated spectroscopy, time resolved measurement of aluminum light emission, streak photography, and interferometry. A typical open shutter picture is shown

EMFAPS arrangement on Gamble II

External pulser used to heat foil



in Fig. 5. (The dark ring is the shadow of a quartz viewport.) A reasonably uniform luminosity is seen over the foil region. At the boundaries of this region, where the copper contacts begin, increased luminosity is observed as if arcs are occurring. At the further edges of the copper contacts, particularly at the inner diameter, further spotty light is observed. The degree of uniformity and of apparent arcing varied from shot to shot, in part because of differences in anode preparation, and this picture represents an "average" shot. The degree of arcing seen here is similar to that seen in published data from KfK, and may not be a problem. This shot was taken without an applied field; there is some indication that radial striations in the luminosity are observed when shots are taken with the field coils energized. John Greenly has seen a similar phenomenon at Cornell.

Time-integrated, spatially-resolved spectrograms show only two sets of strong spectral lines: the neutral aluminum resonance lines at 3944 and 3966 Å, which originate mainly from the anode emission area; and neutral copper lines at 3247 and 3274 Å, which originate from the current contacts. One line attributed to Al II was observed, but other lines expected from that species were not. Faint continuum and other line emission is also recorded, and no line emission from hydrogen is observed. The fact that copper light is observed indicates that some form of arcing is occurring at the current contacts since the copper contacts should be much too thick to vaporize under the action applied here.

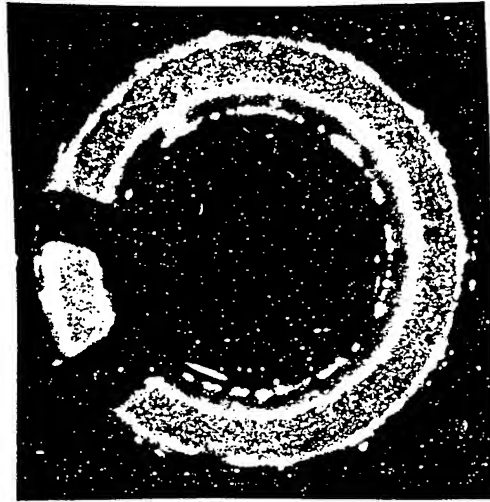
Electrical characteristics for a shot with a 4-minute aluminum coating are shown in Figure 6. Comparison with Fig. 3 shows that the corrected voltage never rises greatly above the noise level, but the two sets of traces suggest a foil resistance that rises from near zero to a value of about 0.4Ω before dropping to a much lower value.

Optical and interferometric data for this shot is shown in Fig. 7. A large-diameter photodiode (PD) is used to record visible light emission without spatial or spectral resolution. When the photodiode was covered with an interference filter for the Al I line at 3961 Å no signal was observed, indicating that light emission is dominated by the continuum and lines that appear only faintly on the film. A photomultiplier (PMT) is used with a spectrometer to record the Al I line emission. In this case no measurable signal is observed when the spectrometer is detuned. These data are corrected for all optical path lengths and for the photomultiplier tube intrinsic delay. Both broad-band and neutral aluminum light are observed to begin at about the moment of foil voltage collapse.

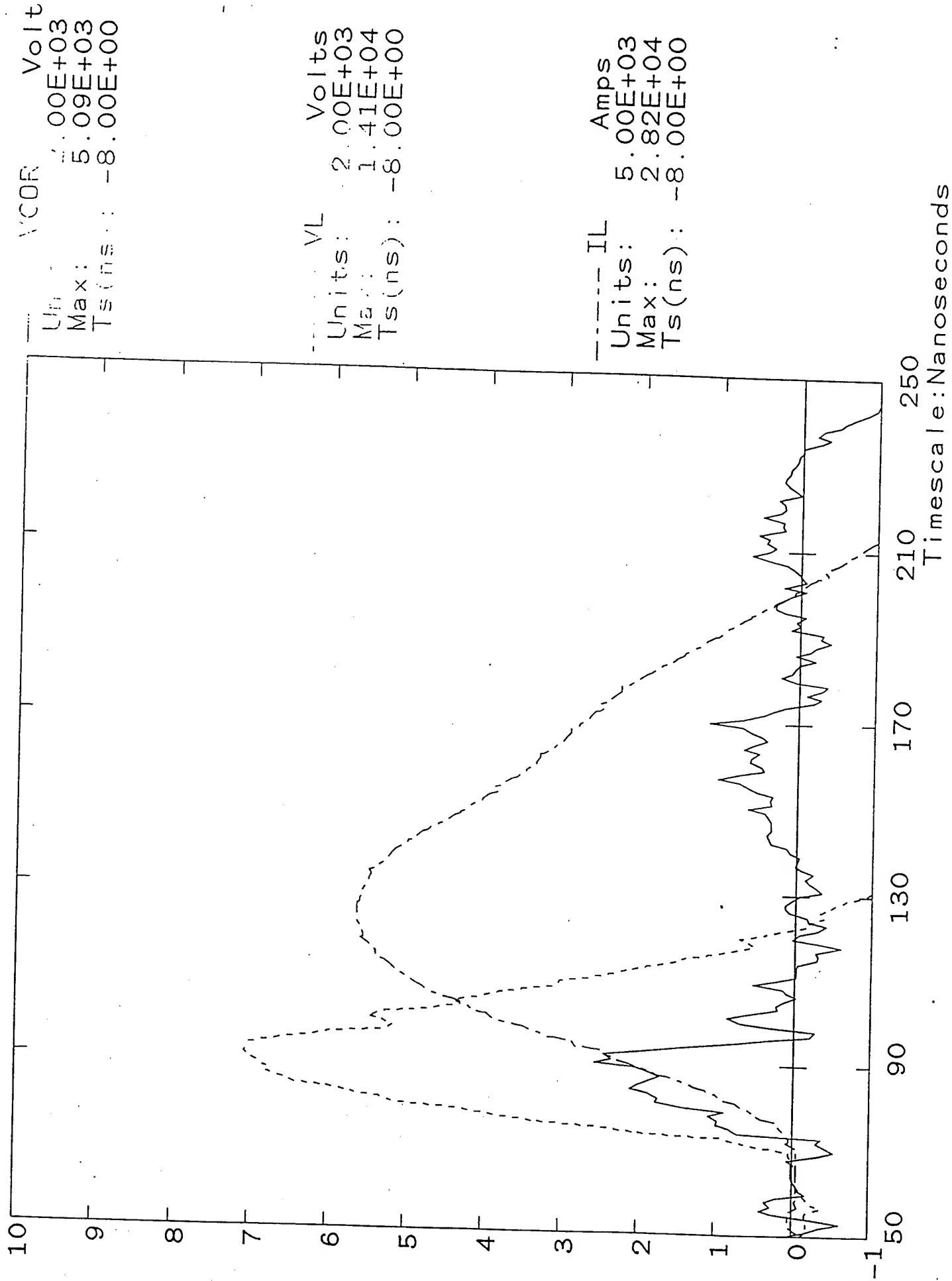
The electron density is measured using our standard, 40-MHz heterodyne-phase-detection interferometer. The ~3-mm diam beam was aligned to graze the anode. The short (2-cm) path length here leads to a relatively large noise-equivalent average density, and on this shot the electron density barely exceeds that value, rising to $1 \times 10^{15} \text{ cm}^{-3}$ well after the pulse.

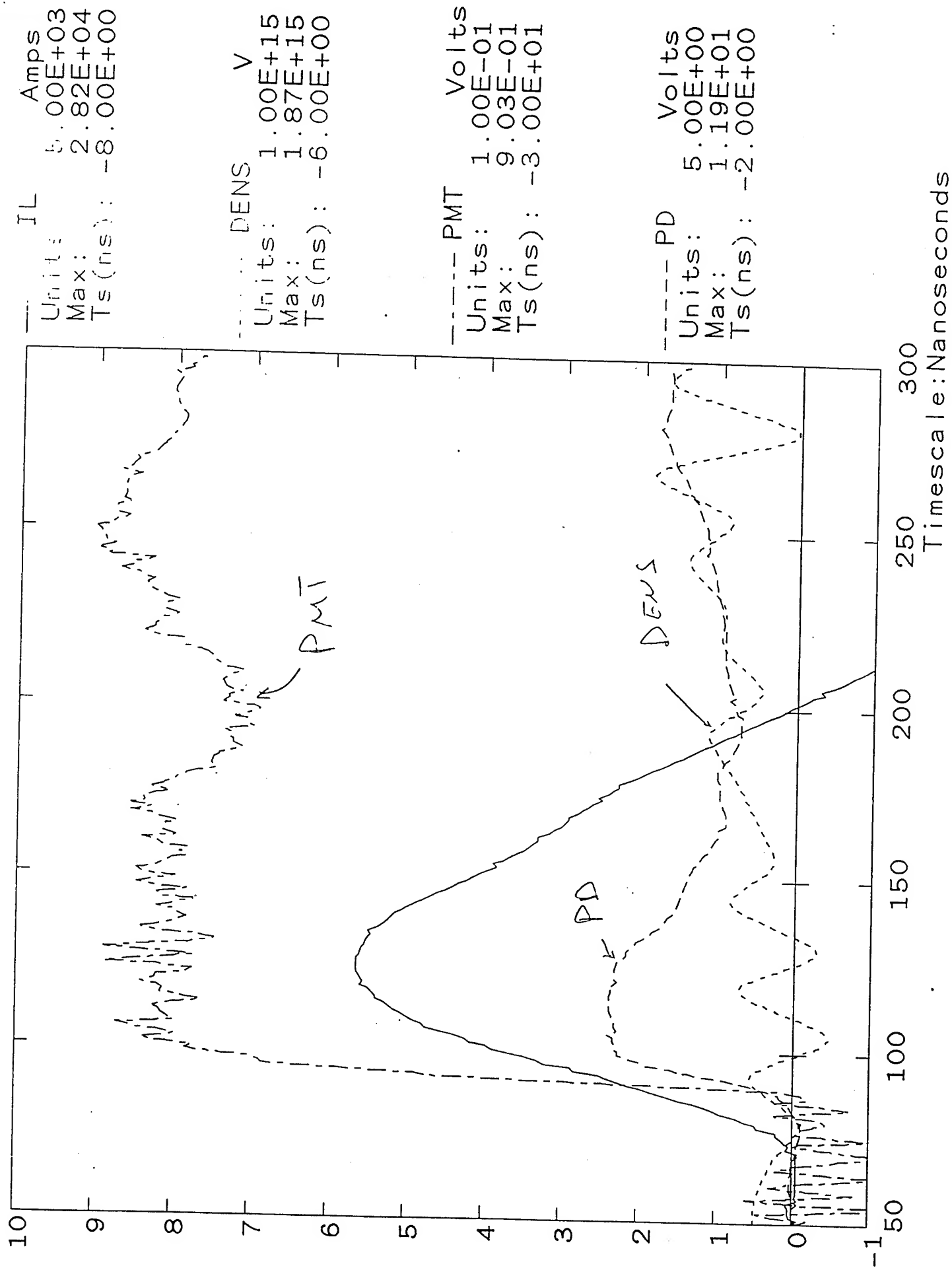
Figures 8-10 compare total light, Al I emission, and the calculated electron density for shots using anodes with aluminum coating times of 4, 10, 16, and 30 minutes, giving approximate foil thicknesses of 200, 400, 600, and over 1000 Å. In comparison with the 4-minute anode, the 10-minute anode shows a later onset of both total and aluminum light

FIG 5



Shot HP49





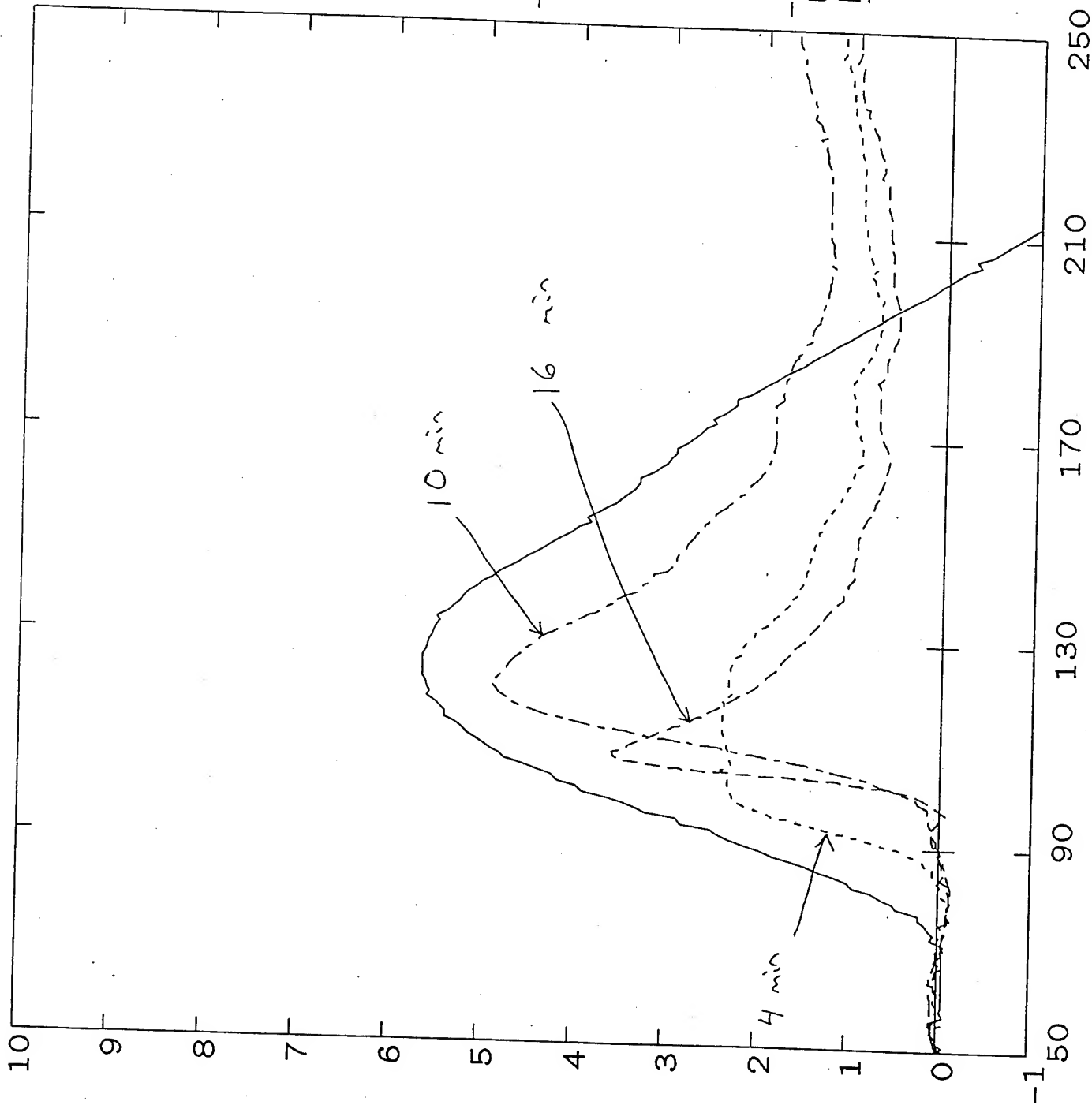
13

IL
Units: 00E+03
Max: 2.82E+04
Ts(ns): -8.00E+00

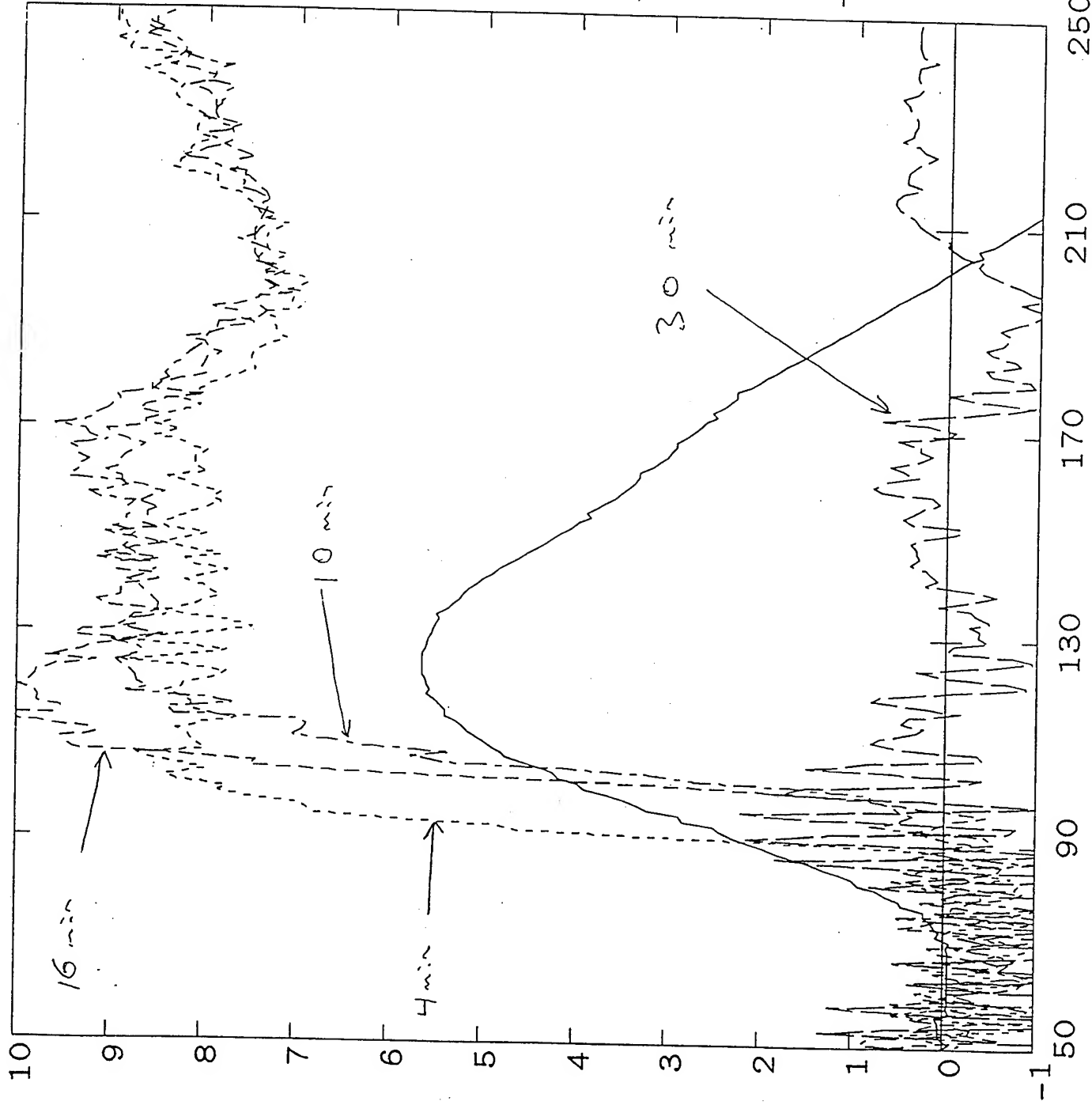
PP
Units: 5.00E+00
Max: 1.19E+01
Ts(ns): -2.00E+00

----- PDHP50 Volts
Units: 5.00E+00
Max: 2.45E+01
Ts(ns): -2.00E+00

----- PDHP51 Volts
Units: 5.00E+00
Max: 1.79E+01
Ts(ns): -2.00E+00



Timescale: Nanoseconds



IL

Units: 00E+03
 Max: 2.82E+04
 Ts(ns): -8.00E+00

PMT

Units: 1.00E-01
 Max: 9.03E-01
 Ts(ns): -3.00E+01

PMTHP50 Volts

Units: 1.00E-01
 Max: 9.63E-01
 Ts(ns): -3.00E+01

PMTHP51 Volts

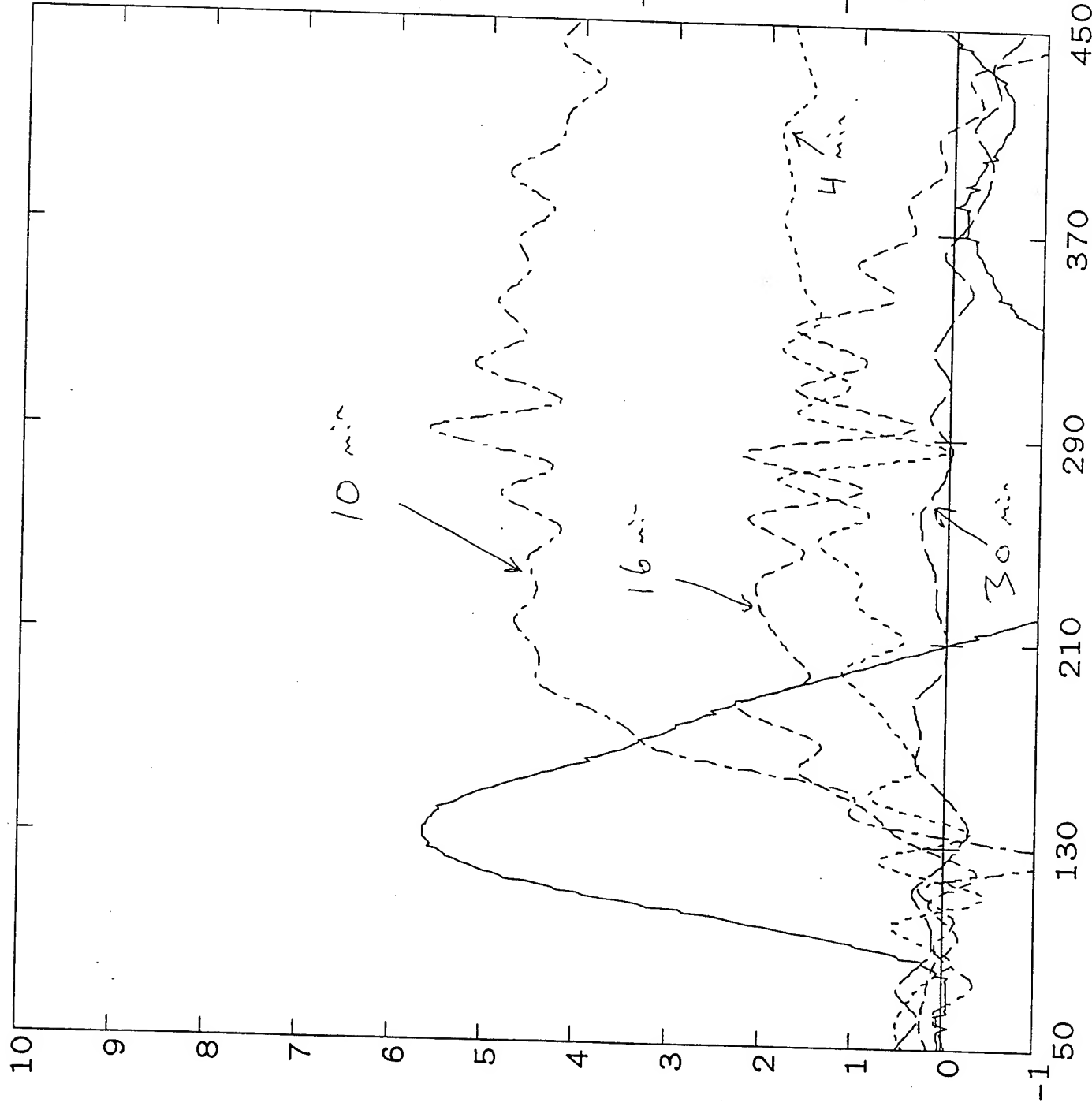
Units: 1.00E-01
 Max: 1.04E+00
 Ts(ns): -3.00E+01

PMTHP54 Volts

Units: 1.00E-01
 Max: 3.22E-01
 Ts(ns): -3.00E+01

Timescale: Nanoseconds

Shot hp49



Units: 5.00E+03
Max: 2.82E+04
Ts(ns): 0.00E+00
Amps

Units: 1.00E+15
Max: 1.87E+15
Ts(ns): 0.00E+00
dens V

Units: 1.00E+15
Max: 5.62E+15
Ts(ns): 0.00E+00
denshp50 V

Units: 1.00E+15
Max: 4.05E+15
Ts(ns): 0.00E+00
denshp51 V

Units: 1.00E+15
Max: 4.40E+15
Ts(ns): 0.00E+00
denshp54 V

Timescale: Nanoseconds

emission and a roughly four-fold higher electron density. With the higher density the S/N ratio improves and the density can be seen to start near the time of peak current, about 30 ns after the onset of light emission. The later apparent vaporization time and higher density seen here would be expected for the thicker coating. With the 16 minute anode, no further increase in time of light emission onset is observed and the electron density is actually lower, relative to the 10 minute anode. For the 30 minute anode, neither aluminum light nor measurable electron density is ever observed. The corrected voltages for these shots are consistent with the light emission traces: for the 10 and 16 minute anodes the corrected voltage drops at the time emission begins, and no noticeable corrected voltage is observed for the 30 minute anode.

INTERPRETATION

Tucker and Toth present resistivity and phase transition occurrences for various metals as functions of specific action ($A^2\text{-s/cm}^4$) and specific energy density in a SNL report (SAND-75-0041). The former is a more useful quantity for comparison with the present experimental results because of the uncertainty in the foil voltage. For aluminum, vaporization begins at a specific action of $4.9 \times 10^8 A^2\text{-s/cm}^4$ and a resistivity of $42 \mu\Omega\text{-cm}$. By the end of vaporization, or burst, these values become 6.6×10^8 and 390, respectively. The calculated actions and resistances corresponding to the beginning of vaporization are compared with those measured at the time of light emission and voltage collapse for the four shots above in the following table (neither occurred on HP54 so the action is that at the end of the current pulse):

Shot	Thickness (Å)	Pred action ($A^2\text{-s}$)	Meas action ($A^2\text{-s}$)	Pred res (Ω)	Meas res (Ω)
HP49	200 +/-100	0.5-4.5	0.2-0.8	.5-1.4	0.2-0.6
HP50	400 +/-150	2.8-14	1-3	.25-.6	0.1-0.4
HP51	600 +/-200	7.2-29	1-3	.17-.35	0.1-0.4
HP54	1000 +/-200	29-65	>40		

At least on two shots, aluminum is vaporized much sooner than predicted. The foil resistance is also lower than expected, especially since the predicted values correspond to the beginning of vaporization; those predicted for burst are almost ten times greater. A likely explanation for the early vaporization is that the foils are not completely uniform. Polishing the anodes prior to waxing leaves a very fine pattern of azimuthal scratches resembling a phonograph record. These persist in the coated films as areas of variable transparency, indicating a non-uniform film thickness, i.e., a radial scan of the film thickness would have a sawtooth profile. The thinner regions would then vaporize at an action much lower than the value predicted for the average foil thickness, and yet these regions may contribute little to the total resistance if they constitute a small fraction of the foil radial extent. The early vaporization may be exacerbated in our experiments because of the relatively slow current rise time.

The collapse of the foil voltage on these shots occurs at values of 5-10 kV, which seems low for a rapid gas breakdown to occur. One possibility is that arcs at the current contacts produce electrons to initiate this breakdown. To examine the breakdown evolution, a few shots have been taken using a streak camera, with the slit aligned in the radial direction. The resolution of this measurement is limited by the low light levels involved, but indications are that light is observed from the foil emission region before the contacts light up. This indicates that arcs at the contacts are not the cause. Another possibility is that if small regions of the foil vaporize first, breakdown may be added by the semi-microscopic field enhancement that would result.

The above data point to two possible factors that may have limited the diode performance on the past Gamble II run: the vaporized foils may not have supplied enough protons, resulting in a source-limited ion current; and, the relatively long delays between foil breakdown and the diode pulse may have allowed plasma and/or neutrals to move out into the diode, possibly causing parallel load losses. Both of these problems should be corrected if the foils could hold off until past the peak of the pulser current pulse, since that would increase the plasma (and thus proton) inventory, and allow a shorter foil-current/diode-current delay to be used. Premature foil vaporization should be impeded by either a faster current rise or a greater foil uniformity, and both of these approaches will be pursued.

FUTURE WORK

Work at present is proceeding in parallel in three areas: (1) A limiter-EMFAPS run will begin on Gamble II next week. In addition to furthering our study of EMFAPS physics, this will allow our programs that require an MID source to proceed. (2) We will continue to investigate the coating process and to study foil explosions on the bench. (3) An improved pulser will be constructed. Progress in these areas should allow us to field a successful pulser-driven EMFAPS source on Gamble II.

PULSED POWER PHYSICS TECHNOTE 94-09

TITLE: CALIBRATION OF APPLIED-B DIODE MONITORS

Author: D. Hinshelwood

Date: May 5, 1994

Abstract: This note gives a detailed analysis of all short-circuit shots taken with the applied-B diode, from which monitor calibrations and their uncertainties are obtained. With a few exceptions, the monitor calibrations have remained fairly stable over time and with the correct calibrations, we can have a fair degree of confidence regarding data taken during previous runs.

Calibration summary:

VO	1.22 E6	up to 5610	
	1.15 E6	after 5806	
IK1	2.5 E11,	-3 E-7	
IK2	3.94 E11,	-1.7 E-7	
IK3 A	-6.76 E11	-1.7 E-7	IK3T = -6 E11, -1.7 E-7
IK3 B	-7.43 E11	-1.7 E-7	ON 5595-5610
IK3C	-7.34 E11	-1.7 E-7	
IK3T	-7.2 E11	-1.7 E-7	
IK4A	-4.72 E11	-5 E-7	
IK4B	-3.46 E11	-3 E-7	
IK4C	-3.77 E11	-3 E-7	
IK4T	-3.98 E11	-3 E-7	
L	75 nH	correction on diode shots	
	80 nH	correction on short-circuit shots	

The following is an attempt to analyze in gory detail the short-circuit shots taken during several runs with the applied-B diode. During these runs we have seen some apparent changes in calibrations for some of the monitors, which has caused concern. For this experiment the calibrations of current monitors are particularly important because the ion current efficiency involves both a ratio and a difference of current signals. After a thorough review of the data, it appears that the calibrations have been fairly stable with a few exceptions. This note contains few waveforms but those referred to are collected in a notebook in my office.

Shots with the applied-B diode were taken during seven separate runs to date. Passive anodes only were used on the first three runs. I was not involved with these runs and Jess should be contacted with specific questions. The first run comprised shots 5358-5385. Shot 5360 was a short-circuit shot with good signals. No further short-circuit shots were taken during these three runs. The second and third runs comprised shots 5514-5529, and shots 5571-5584.

The fourth run involved our studies of POS-driven EMFAPS, and comprised shots 5585-5610. Most of the shots during this run were devoted to optimizing the POS and had short-circuit loads. As will be discussed, many calibration inconsistencies were observed at this time. On shots 5585-90 the short-circuit connection was made at the outer cathode ring so that calibrations of most monitors were not possible. Shots 5596-5598 were short-circuit shots with no plasma. Initially, all four monitors IK1-4 consisted of sets of three dB/dt loops, summed at the machine. Because of shifting values of the apparent IK4 calibrations which were noticed at this time (see below), the 3, IK4 loops were monitored on separate channels from shot 5597 on. Shots 5601-5605, 5607, and 5608 had injected POS plasma but sufficiently short conduction that calibrations could be obtained.

The fifth run consisted of our first attempt at pulser-driven EMFAPS, shots 5806-5830. Shots 5806-7 were short-circuit shots. The sixth run was devoted to limiter-driven EMFAPS and involved shots 5887-5915. No short-circuit shots were taken during this run.

The seventh, current run is our second attempt at pulser-driven EMFAPS using a more powerful pulser and (hopefully) better foils, and consists of shots 5980-6020. Shots 5980-5981 were short-circuit shots although many signals were off-scale on the former. Shot 5981 gave significantly different calibrations for IK3 and IK2 than shot 5807. As a consistency check, shot 5999 was also a short-circuit shot. This gave similar calibrations to those from shot 5807. We then realized that shot 5981 was taken without the cathode rings. (This had been done to make sure that we did not get emission from them.) To study this further, short-circuit shots 6000-6002 were taken. Shot 6000 also had no cathode tips, shot 5999 had the cathode tips and Kimfol ring but no Kimfol, and shots 6001-2 had the cathode tips and a thin aluminum disk to simulate the Kimfol. All shots gave similar calibrations for IK4 and IK1, as would be expected. Shots 6000 and 5981 gave similar calibrations for IK3. Finally, shots 6008 and 6009 were taken. Both had the

cathode tips in, but no Kimfol ring was used on shot 6008. They also gave similar calibrations to shot 5807.

In retrospect, it is not surprising that the cathode tips have a big effect because their presence increases the depth of the loops relative to the surface over which current flows. It was a little surprising to note that the Kimfol ring has a negligible effect (see the Table below), since without it the current is forced to flow radially through the three struts, rather than through the uniform foil.

After noticing the effect of the cathode tips' presence, I spoke with Mike Cuneo to make sure that there was not something else that we were forgetting. He said that they calibrated their monitors in the same way that we had been doing, and that it is important to have the cathode tips in place. They also observe no significant effect from the presence of the Kimfol, which he attributes to the placement of the three loops: they are offset by 30 degrees from the struts. Mike also said that the arches in the cathode tips are actually a bit too small and that they slightly occlude the B-dot holes in the cathode. I looked carefully at our hardware and noticed a very small amount of azimuthal play in the cathode tip placement. This play could allow a small shot-to-shot variation in the B-dot sensitivity by allowing a slight occlusion of the holes on some shots. I think this effect will be very small, but perhaps the arches should be enlarged before the next run.

The B-dots, particularly those for IK2 and IK3, suffer signal distortion caused by field penetration into the titanium during the current pulse. This results in an apparent increase in the signal amplitude toward the end of the pulse. Early on, we found that we could approximately match the IOUT waveform by applying a negative time constant correction to the B-dot signals. The time constant was chosen to optimize the matching of signal shapes. Mike said that they use a similar technique at Sandia. However, this is not an exact correction and some error in the B-dot signals can still be expected late in time.

It seems that the design of these current monitors could be improved significantly. If we were building hardware from scratch, I would locate the B-dot loops in an azimuthal slot and fasten the cathode tips on from the front. By using a slot rather than separate holes, the B-dot sensitivity would be increased greatly, and there would be no distortion of the signal shape resulting from field penetration into the titanium.

This table gives calibrations derived from all Applied-B short circuit shots. IK3T and IK4T refer to the composite averages of the three individual signals. All calibrations are in units of 10^{11} and those for IK3 and IK4 are multiplied by -1. These calibrations are based on the time constant corrections given at the bottom, in units of 10^{-7} , except for IK1, where the calibrations are based on -2×10^{-7} . The average calibration for IK1 is based on a more correct time constant of -3×10^{-7} .

Shot	IK1	IK2	IK3A	IK3B	IK3C	IK3T	IK4A	IK4B	IK4C	IK4T
5360	3.73	4.03	nr	nr	nr	6.99	nr	nr	nr	3.94
5596	os	os,~4	nr	nr	nr	os,~6	nr	nr	nr	4.44
5597	nr	nr	nr	nr	nr	6.17	5.26	3.84	3.84	4.31
5598	nr	nr	nr	nr	nr	5.92	5.23	3.64	3.79	4.22
5601	os	os	nr	nr	5.99	-	nr	nr	3.61	-
5602	2.66	3.84	nr	nr	6.06	-	nr	nr	3.74	-
5603	2.6	3.8	nr	nr	5.62	-	nr	nr	3.76	-
5604	2.8	3.8	nr	nr	5.88	-	nr	nr	3.66	-
5605	(1)	(1)	nr	nr	6.49	-	nr	nr	3.72	-
5607	2.74	3.95	x	6.53	5.92	-	3.95	3.56	x	-
5608	2.62	3.84	x	6.76	5.92	-	3.74	3.38	3.69	3.60
5806	os	x	x	7.24	7.24	-	5.17	os	os	-
5807	2.8	x	6.83	7.68	7.50	7.34	5.12	3.03	3.78	3.98
5981	2.46	3.1	4.86	5.41	5.86	5.38	4.50	3.53	3.69	3.90
5999	2.58	os,~4	6.84	7.25	7.40	7.16	4.55	3.47	3.75	3.92
6000	2.56	os	5.02	5.24	5.59	5.28	4.33	3.37	3.70	3.80
6001	2.78	os,~4	6.70	8.20	7.05	7.32	4.69	3.58	3.89	4.05
6002	2.56	4.5	6.60	7.46	6.94	7.00	4.42	3.46	3.56	3.81
6008	2.53	3.66	6.62	6.49	7.58	6.90	4.78	3.53	3.85	4.05
6009	2.77	4.06	6.99	7.69	7.69	7.46	4.95	3.68	3.92	4.18
AVG	2.5	3.94	6.76	7.43	7.34	7.20	4.72	3.46	3.77	3.98
τ	-3	-1.7	-1.7	-1.7	-1.7	-1.7	-5	-3	-3	-3.7

Notes:

use 6 as calibration for IK3T on shots 5594-5600

nr signal not recorded

os signal off scale

x scope troubles or signal strange shape

- can't average because one or two signals missing

(1) termination troubles with HP prevent calibration

The calibrations will now be discussed in more detail.

IK1:

These loops, located inside the inner cathode ring, never show any current. There is really little reason to even record these signals. However, it is useful to go through the exercise of checking the calibration over time, as sort of a consistency check. Except for shot 5360, the calibrations show a variation of about \pm ten percent, and there is no constant variation with time. As mentioned above, the values in the table were calculated based on a time constant of -2×10^{-7} . Inspection of the waveforms shows that this slightly over-corrects the signals. A value of -3×10^{-7} was chosen to match the value used for IK4 below (IK1 and IK4 have similar loop geometries). Using this time constant would give the average calibration listed at the bottom.

IK2:

These loops are located on the outside of the inner cathode and they measure electron current emitted from the inner cathode. This current tends to be small but not negligible, and its measurement is important because this current must be subtracted from that of IK3 to get the ion current. Calibrations were obtained using a time constant of -1.7×10^{-7} . This was seen to be the optimum value for the IK3 loops, which have the same geometry as the IK2 loops. Looking over the data, this time constant gives reasonable agreement with the shape of IOUT. Shot 5981, taken without the cathode rings in place, gives a low calibration as expected. The other calibrations indicate that the cathode rings were in place for all previous calibration shots. The average calibration is obtained from the remaining 9 shots where the signal was not off scale. Seven shots gave calibrations within five percent of the average, with the remaining two deviating by seven and 14 percent. In addition, there are three shots, where the signal was off scale, that are consistent with the average calibration. It is particularly encouraging to note that there is no steady "drift" in the calibrations over the entire duration of the applied-B runs.

IK3:

These loops are located on the inside of the outer cathode. The ion current is given by the difference between IK3 and IK2, so that IK3 is the most important of the four loop sets. Because of calibration uncertainties noticed in the fourth run, the three loops were monitored individually starting with shot 5601. Consider first shots 5806-onward. The average calibration values listed at the bottom of the table were derived from these shots. As with IK2, shots 5981 and 6000, taken without the cathode rings in place, give low calibrations. On several of these shots, different values of the time constant were checked and -1.7×10^{-7} was found to give the best shape agreement overall. The degree of waveshape agreement varies somewhat from shot to shot, but this may be due in part to uncertainty in baselining the traces. One trouble is that these signals have been recorded on 7912's, whose short record length does not permit a long lead-in from which accurate baseline values may be obtained. The calibrations from these shots are within ten percent (with one exception, which deviates by 13 percent) of the average for individual loops and within five percent for the three-loop composite. The average calibrations from shots

5806-5807 are within about one percent of the total average. This is encouraging because of the large number of shots, taken over a large expanse of time, between the short-circuit shots 5807 and 5999. It is also encouraging to note that the composite calibration from shot 5360 is within three percent of the average value for the composite calibration. These results also indicate that the presence of Kimfol has no significant effect, in agreement with Mike's results at SNL. Shot 5999 had the Kimfol ring but no Kimfol, and shot 6008 had neither. The first gave calibrations close to the average, and the latter gave calibrations (for both IK2 and IK3) that are only a bit low.

Thus, if the fourth run (shots 5596-5608 on the table) is ignored, the calibrations for IK3 look quite consistent. The problem is that while the fourth run had only a few applied-B diode shots, it does include shot 5595, our best results to date. Two other shots, 5594 and 5600, also showed good performance.

Shots 5596-5598 indicate a composite calibration that is 15 percent low, i.e., the signals are higher than usual. One possibility is that the cathode tips were left out, and thus the "standard" calibration would apply on the applied-B diode shots. I don't think the cathode tips were left out for two reasons: (1) the calibrations for IK2 during this run are not consistent with this (the inner tip would not have been installed without the outer tip); (2) the results on the diode shots during this run are not consistent with this - using the standard calibration gives ion currents at times larger than the total current. On shots 5601-5608 the loops were monitored separately although only IK3C was recorded on most shots. The fact that the IK3C calibrations on these shots are also low (by about the same amount) indicates that the different calibration did not result from a single loop, or the splitter box. On shots 5607-5608, the IK3C signal was recorded on the HP and a 7912. Both gave the same amplitudes, indicating that there was not a scope problem. This leaves the attenuators. The composite signal on 5596-5598 and the IK3C signals on the following shots probably used the same 20 dB attenuator. On the other hand, I seem to remember checking all attenuators at the time of the run. It is probably not possible at this time to go back and resolve the problem. However, the consistent results of the short-circuit shots during this run leave me comfortable with using a composite calibration of 6×10^{11} for IK3. This calibration also gives physically reasonable signals on the applied-B shots during the run.

IK4:

These B-dots are located on the outside of the outer cathode ring and measure the total diode current. On Gamble II, we do not expect any vacuum electron flow from upstream of this monitor. Therefore, this monitor should agree with the machine current monitors IOUT and ISHT, and in effect every shot is a calibration shot. This also means that the IK4 signal is not as important as IK3 and IK2. The time constants used give reasonable waveshape agreement with IOUT. The use of a different time constant for IK4A is supported by the data. The averages given in the table are derived from shots 5806-on. Over these shots, the individual calibrations agree with the average to within about ten percent, and the composite calibrations match the average within five percent.

All actual shots taken during this time also show agreement between IK4T and IOUT to within five percent. Similar agreement is obtained on the short-circuit shot 5360 and on all diode shots up to shot 5517 in the second run. However, over shots 5520-5596, the composite calibrations, derived from IK4T-IOUT comparisons, vary greatly shot to shot, increasing from the average by up to a factor of 2.5. After shot 5596, the three signals were recorded individually, although only IK4C was actually recorded after shot 5598. By that time, the IK4C calibration was consistent with the final average. Actually, there is a general trend from shot 5594 on, where the calibration seems to be settling down to the usual value. One possibility is that some debris was not being completely removed from the epoxy potting around these loops for some period of time. In any event, the problem seems to have gone away.

In summary, the B-dot loops on the applied-B cathode show calibrations that are consistent over time within about five percent, which is all the accuracy that can be expected, with two exceptions. During the fourth run the IK3 loops had a 20 percent lower calibration for reasons that are not exactly clear. And during a longer period of time the IK4 loops had a varying, higher calibration. The latter problem is not serious since the IK4 loops are essentially redundant with IOUT. I now believe that with these calibrations we can have a good deal of confidence in the key current waveforms on all previous applied-B diode shots. With our present SOP, which includes frequent short-circuit shots, great care in cleaning around the loops, and verification of attenuator values, even greater confidence is warranted. At present, the accuracy of current measurement is limited primarily by two effects: (1) imperfect reconstruction of the waveshapes by the use of time-constant correction; (2) integration errors resulting from incorrect baselining. The former is unavoidable without a complete hardware redesign. The latter could be reduced greatly by recording the signals with a longer lead-in, and in the future we should consider using the HP for the more important signals.

Inductance:

Examining the inductance, derived from short-circuit shots, over time can give a consistency check on the machine monitors VD, ISHT, and IOUT. For most of the short-circuit shots, as well as most of the diode shots, ISHT and IOUT are in reasonable agreement. The following table lists the inductances calculated from the short-circuit shots. Nominally, the inductance would be obtained by comparing DIOUT and VD, and these values are given in the third column. The problem with this is that the shapes of the two signals never exactly agree. This may be due to transmission line effects, as the short is located about 3 ns from the voltage monitor. Indeed, DIOUT is usually seen to have a ringing imposed on it that is missing on VD. (This problem for some reason seems to have gotten worse on the most recent run.) By comparing the integral of VD to IOUT some of this gets smoothed over and better shape agreement is obtained. Inductances derived in this way are given in the second column, and inductances similarly derived from the integral of VD and ISHT are given in the third column. The last column lists inductances derived from VD and the (9 point) derivative of IK4T, normalized to IOUT on that shot. On many shots DIK4T has a smoother signal than DIOUT, which suggests

that the ringing on DIOUT may be due in part to pickup rather than transmission line effects.

The diode hardware has been essentially unchanged since the very first shots, so that the inductance should be constant to within 1 nH. The exception is shot 5360, which was taken without the 3-cm door spacer and with a 2-mm farther coil spacing. These two effects combine to reduce the inductance by about 6 nH. The values for shot 5360 in the table have had 6 nH added to them to correct for this. The average inductance over shots 5806-6009 is 85 nH, and the variation is within seven percent, which is reasonable considering the uncertainties involved. The value for shot 5360 is also consistent with this. The values over shots 5597-5608 are lower, however, averaging to 75 nH. It would be tempting to simply disregard these shots since other calibration troubles were present at this time.

However, calibrations of the diode voltage monitor support this difference. At shot 5407 the monitor was calibrated, giving 1.22 MV/V, which was essentially unchanged from a previous measurement. This number has been used to obtain the values in the table. After shot 6020 the monitor was calibrated again, yielding a factor of 1.15 MV/V. Using this value for shots 5806-6009 (the values after the "/" in the average column) gives an average inductance of 80 nH, a number which is still consistent with shot 5360 and within ten percent of the results from shots 5597-5605.

Shot	IOUT	DIOUT	ISHT	DIK4T	AVG	Comments
5360	82	83	82	83	82	corr for missing door spacer; reas sh agr
5596	58	-	58	65		poor shape agreement
5597	79	79	78	-	79	reasonable shape agreement
5598	76	76	75	-	76	reasonable shape agreement
5601	-	-	-	-		very poor shape agr, problems with VD?
5602	-	-	-	-		very poor shape agr, problems with VD?
5603	-	-	-	-		very poor shape agr, problems with VD?
5604	74	75	74	-	75	reasonable shape agreement
5605	-	-	74	-	74	can't use IOUT, term error
5607	65	66	64	-		not so good shape agreement
5608	70	72	68	73	71	reasonable shape agreement
5806	80	~80	80	-	80/75	poor shape agr on differential signals
5807	88	92	88	92	90/84	reasonable shape agreement
5981	88	-	88	86	87/82	reasonable shape agreement
5999	86	89	85	88	87/82	ISHT higher than IOUT
6000	86	92	82	92	88/83	IOUT higher than ISHT, not so gd sh agr
6001	80	86	84	81	85/80	IOUT higher than ISHT, not so gd sh agr
6002	85	88	81	85	85/80	IOUT lower than ISHT, reas shape agr
6008	86	-	83	87	85/80	not so good shape agreement
6009	78	-	79	79	79/74	DIOUT useless on 6008, 6009

Motivated by these inductance calculations, I will (somewhat arbitrarily) assume a calibration for VD of 1.22 MV/V for the first four runs (up to shot 5610) and 1.15 MV/V

Shot 6017

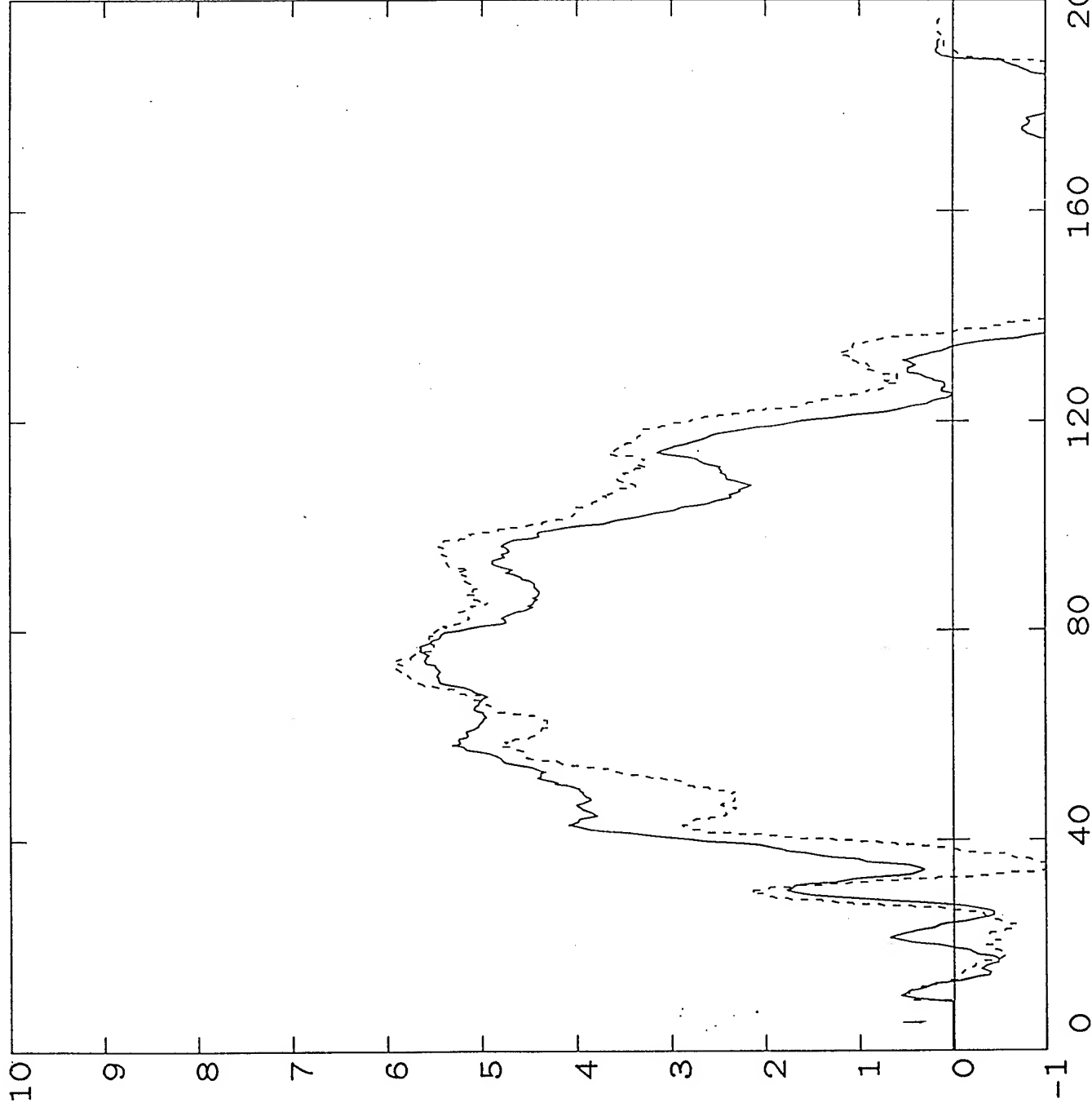
VD uses 1.15 e6
Vcor = VD - (75nH) DI00T

----- vcor ----- VOLTS
Units: 2.00E+05
Max: 1.13E+06
Ts(ns): 5.00E-01

shift VD - 2ns

----- vcorp ----- VOLTS
Units: 2.00E+05
Max: 1.19E+06
Ts(ns): 4.50E+00

shift VD + 2ns



Timescale: Nanoseconds

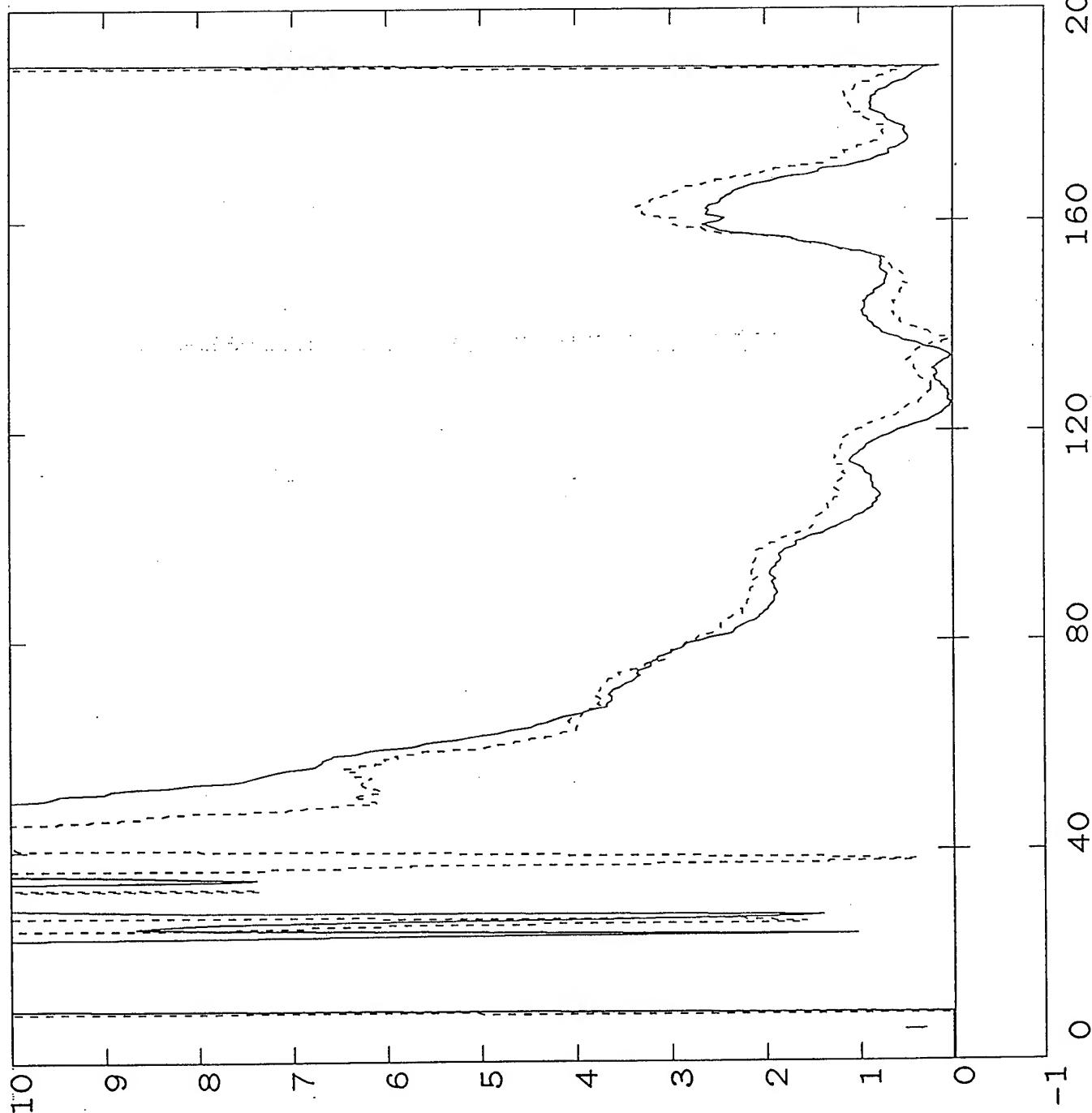
Shot 6017

-----zm----- Ohms
Units: 1.00E+00
Max: 1.00E+01
Ts(ns): 5.00E-01

$V_{load} / 100 \Omega$

-----zp----- Ohms
Units: 1.00E+00
Max: 1.00E+01
Ts(ns): 4.50E+00

$V_{load} / 100 \Omega$



Timescale: Nanoseconds

for the subsequent shots. The nominal inductance is 80 nH. Of course, this is the inductance up to the short. The actual inductance (to IK4) is expected to be about 5 nH less than this, and so a value of 75 nH will be used in the inductive correction.

Open-circuit voltage:

In principle, the calculated open-circuit voltage can be compared with the transformer input to provide another consistency check on the diagnostics. I tried this, however, and got poor waveshape agreement and so this does not appear fruitful.

Timing:

Possible timing errors arise from three sources: (1) scope time base inaccuracies; (2) uncertainties in determining the fiducial position; (3) unequal cable lengths. We have never really worried about (1), although in the future the scopes should probably be calibrated at least before each run. The uncertainty produced by (2) is on the order of 1 ns. Regarding (3), all signals are sent to the screen room via equal-length cables, but several monitors have additional short lengths of cables at the machine. These may not always have been correctly taken into account by adjusting the fid delay. In addition, there is a possible fundamental uncertainty associated with the 3-ns separation of VD and ISHT from the rest of the monitors. BERTHA modeling in the past, however, has shown that this delay does not appear on the waveforms (since they respond to standing-wave amplitudes). Taking everything into account, I feel fairly confident in assigning a 2-ns uncertainty to signal timing, as long as the cable lengths are equal.

On the most recent run, the PIN's, IOUT, and IK1-4 all had an additional ~1.5 feet of cable at the machine. Therefore, on this run all signals can be timed correctly by timeshifting VD forward by 2.5 ns. (I won't worry about ISHT or the pulser diagnostics, since the former is not that important and a 2.5-ns shift in the latter is negligible.) On the previous three runs, IOUT and VD had the same length, and so IK1-4 should be shifted back by 2.5 ns.

The results will not be very sensitive to a possible ± 2 ns relative timing error between different current waveforms, but they may be sensitive to an error in the relative timing of VD and IOUT. Synchronization of these is necessary first to obtain VCOR and then to get the impedance, power, calculated Rutherford signal, etc. The following two graphs show VCOR and Z calculated based on a ± 2 ns timeshift of VD from its correct time. A small but noticeable change in the impedance behavior results. For this experiment (unlike shots with the PRD where the impedance is more stable) we have to realize that there is an uncertainty of the order shown here in the waveforms derived from both voltage and current.

SECTION THREE

INTENSE BEAM TRANSPORT

JAYCOR personnel were directly involved in all aspects of the NRL intense beam transport program during the contract period. Theoretical and experimental studies of beam transport were carried out in support of the Sandia National Laboratories light-ion inertial confinement fusion program. Investigations performed under the contract period are summarized below.

3.1 Transport of Intense Ion Beams in Gas

Present designs for a light-ion inertial-confinement-fusion reactor indicate that intense ion-beams must be ballistically transported and focused over a distance of several meters in a low-pressure, background gas. These reactor designs are referred to as either the Laboratory Microfusion Facility (LMF) or the High-Yield Facility (HYF). During the previous contract period, ion beam transport experiments in low-pressure gases were conducted at NRL with JAYCOR participation. During this contract period, additional analyses were performed, with JAYCOR participation, in order to understand the evolution of the background gas/plasma parameters. A detailed theoretical analysis has been completed that provides scaling relations between parameters obtained on the Gamble II experiments and the required LMF/HYF parameters.

Another beam transport method, self-pinched transport, is under consideration as a backup transport scheme for light-ion inertial-confinement-fusion designs. JAYCOR personnel are working with NRL and SNL to design self-pinch transport experiments (to be performed at NRL) and to conduct theoretical analysis of this transport method. Detailed analytic and computational modeling using the three-dimensional particle-in-cell code IPROP (written by D. Welch, Mission Research Corp.) are underway. Once again, JAYCOR personnel are involved with all aspects of the self-pinch transport experiments and analysis.

3.2 Analysis of Ion Beam Transport Constraints

A detailed study of ion beam transport constraints, conducted by JAYCOR personnel in collaboration with NRL, was performed during the contract period. These constraints can define a region in parameter space in which ion beam transport is possible (i.e., an operational window). Constraints identified and analyzed during this study include beam-driven instabilities, plasma hydrodynamics, beam energy loss during transport, module packing (the reactor design is multimodular), and beam transport efficiency. In addition, system design parameters such as time-of-flight bunching of the beams, background gas species, and background gas pressure, were factored into the analysis. A methodology for analyzing other transport schemes and reactor designs was established. The results of the analysis for the ballistic transport with solenoidal lens focusing scheme indicate that baseline reactor design

parameters may be too limiting and thus some design changes will have to be considered. This work is summarized in an accompanying internal report.

3.3 Diagnostic Development

Diagnostic development in support of intense ion beam transport experiments continued during the contract period with JAYCOR participation. A proton beam diagnostic, based on Rutherford scattering, has been extensively evaluated. Fielded on Gamble II pinched-beam ion diode experiments at NRL, this diagnostic continues to show promise as an accurate method of determining beam energy losses during transport. JAYCOR personnel were also involved with the development of other beam diagnostics including Faraday cup detectors, shadowboxes, etc. When applicable, new subroutines were added into the main NRL experimental data analysis program. These subroutines include stopping power calculations, detailed in an enclosed report (3.5.13).

3.4 Additional Beam Transport Work

In addition to the tasks described above, JAYCOR personnel were involved in several other beam transport related projects. Follow-up work from the previous contract period on a survey of radioactivities induced by proton and deuteron beams in common accelerator and laboratory materials was completed and submitted for publication. JAYCOR personnel in collaboration with NRL and Los Alamos National Laboratories conducted experiments in surface modification of materials and thin-film deposition using ion beams. Finally, a theoretical study of relativistic charged-particle limiting currents was carried out. The study of limiting currents is especially important in very-low pressure regime transport experiments, a topic of potentially future importance to other research areas supported under this contract.

3.5 List of Papers

- 3.5.1 "Current neutralization of intense MeV proton beams transported in low-pressure gas," F.C. Young, D.D. Hinshelwood, R.F. Hubbard, M. Lampe, J.M. Neri, C.L. Olson, P.F. Ottinger, D.V. Rose, S.P. Slinker, S.J. Stephanakis, and D.R. Welch, *Phys. Rev. Lett.* **70**, 2573 (1993).
- 3.5.2 "Interaction of intense MeV light-ion beams with low-pressure gases," F.C. Young, R.F. Hubbard, M. Lampe, J.M. Neri, P.F. Ottinger, S.J. Stephanakis, S.P. Slinker, D.D. Hinshelwood, D.V. Rose, C.L. Olson, and D.R. Welch, *Phys. Plasmas* **1**, 1700 (1994).
- 3.5.3 "Physics of gas breakdown for ion beam transport in gas," C.L. Olson, D.D. Hinshelwood, R.F. Hubbard, M. Lampe, J.M. Neri, P.F. Ottinger, J.W. Poukey, D.V. Rose, S.P. Slinker, S.J. Stephanakis, D.R. Welch, and F.C. Young, *Il Nuovo Cimento* **106A**, 1705 (1993).
- 3.5.4 "Evolution of a Maxwellian plasma driven by ion-beam-induced ionization of a gas," B.V. Oliver, P.F. Ottinger, and D.V. Rose, *Phys. Plasmas*, *accepted for publication* (1996).

- 3.5.5 "Constraints on intense light-ion-beam transport for inertial confinement fusion," D.V. Rose, P.F. Ottinger, B.V. Oliver, D. Mosher, C.L. Olson, and J.U. Guillory, Pulsed Power Physics Branch Technote 95-24 (1995).
- 3.5.6 "Effect of time-of-flight bunching on efficiency of light-ion-beam inertial-confinement-fusion transport schemes," P.F. Ottinger, D.V. Rose, and C.L. Olson, J. Appl. Phys. **75**, 4402 (1994).
- 3.5.7 "Transport efficiency studies for light-ion inertial confinement fusion," D.V. Rose, P.F. Ottinger, and C.L. Olson, Naval Research Laboratory Memorandum Report #7609 (1994).
- 3.5.8 "Transport efficiency studies for light-ion inertial confinement fusion systems using ballistic transport with solenoidal lens focusing," D.V. Rose, P.F. Ottinger, and C.L. Olson, IEEE Trans. Plasma Sci. **PS-23**, 163 (1995).
- 3.5.9 "Beam transport," C.L. Olson, M.E. Cuneo, M.P. Desjarlais, D.L. Hanson, D.D. Hinshelwood, R.F. Hubbard, G.L. Kulcinski, M. Lampe, T.R. Lockner, J.E. Maenchen, M.G. Mazarakis, J.M. Neri, B.V. Oliver, J.C. Olson, R.E. Olson, P.F. Ottinger, R.R. Peterson, T.D. Pointon, J.W. Poukey, D.V. Rose, T.W.L. Sanford, S.P. Slinker, S.A. Slutz, S.J. Stephanakis, D.R. Welch, and F.C. Young, *Laser Interaction and Related Phenomena, AIP Conf. Proceedings 318*, G.H. Miley, ed. (American Institute of Physics, New York, 1994), p. 557.
- 3.5.10 "Light-ion-beam transport research at NRL," P.F. Ottinger, D.D. Hinshelwood, R.F. Hubbard, M. Lampe, D. Mosher, J.M. Neri, W. Noonan, C.L. Olson, D.V. Rose, S.P. Slinker, S.J. Stephanakis, D.R. Welch, and F.C. Young, in the Proceedings of the Tenth International Conference on High-Power Particle Beams (June 20-24, 1994, San Diego, Ca), p. 112.
- 3.5.11 "LIF standoff research," C.L. Olson, M.E. Cuneo, M.P. Desjarlais, A.B. Filuk, J.B. Greenly, D.L. Hanson, D.D. Hinshelwood, R.F. Hubbard, M. Lampe, T.R. Lockner, J.E. Maenchen, M.G. Mazarakis, C.W. Mendel, Jr., P.R. Menge, D. Mosher, T.J. Nash, J.M. Neri, W. Noonan, B.V. Oliver, J.C. Olson, R.E. Olson, P.F. Ottinger, R.R. Peterson, T.D. Pointon, J.W. Poukey, J.P. Quintenz, D.V. Rose, T.W.L. Sanford, S.P. Slinker, S.A. Slutz, J.R. Smith, S.J. Stephanakis, D.R. Welch, and F.C. Young, in the Proceedings of the Tenth International Conference on High-Power Particle Beams (June 20-24, 1994, San Diego, Ca), p. 104.
- 3.5.12 "Development of Rutherford scattering to diagnose proton beams from Gamble II," F.C. Young, D.D. Hinshelwood, W.A. Noonan, and S.J. Stephanakis, Pulsed Power Physics Technote 94-06 (1994).
- 3.5.13 "Incorporation of TRIM ion energy loss calculations into ANALYSIS routines," D. Hinshelwood, Pulsed Power Physics Technote 94-17 (1994).
- 3.5.14 "Radioactivities produced by proton and deuteron beams up to 10 MeV," F.C. Young and D.V. Rose, Atomic Data Nuclear Data Tables, *accepted for publication* (1996).

- 3.5.15 "Survey of radioactivities induced by intense pulsed ion beams," F.C. Young and D.V. Rose, in the Proceedings of the International Conference on Nuclear Data for Science and Technology (May 9-13, 1994, Gatlinburg, TN), p. 386.
- 3.5.16 "Film deposition and surface modification using intense pulsed ion beams," C.A. Meli, K.S. Grabowski, D.D. Hinshelwood, S.J. Stephanakis, D.J. Rej, and W.J. Waganaar, J. Vac. Sci. Technol. A **13**, 1182 (1995).
- 3.5.17 "Numerical simulation of limiting currents for transport of intense relativistic electron beams in conducting waveguides," J. Appl. Phys. **78**, 5787 (1995).

Current Neutralization of Intense MeV Proton Beams Transported in Low-Pressure Gas

F. C. Young,⁽¹⁾ D. D. Hinshelwood,⁽²⁾ R. F. Hubbard,⁽¹⁾ M. Lampe,⁽¹⁾ J. M. Neri,⁽¹⁾ C. L. Olson,⁽³⁾
P. F. Ottinger,⁽¹⁾ D. V. Rose,⁽²⁾ S. P. Slinker,⁽¹⁾ S. J. Stephanakis,⁽¹⁾ and D. R. Welch⁽⁴⁾

⁽¹⁾Plasma Physics Division, Naval Research Laboratory, Washington, D.C. 20375

⁽²⁾JAYCOR, Incorporated, Vienna, Virginia 22182

⁽³⁾Sandia National Laboratories, Albuquerque, New Mexico 87185

⁽⁴⁾Mission Research Corporation, Albuquerque, New Mexico 87106

(Received 4 February 1993)

(P)184

This paper reports on the first experiments designed to study ion-beam-induced gas ionization and subsequent conductivity growth using intense proton beams transported through various gases in the 1-Torr pressure regime. Net-current fractions of 2% to 8% are measured outside the beam channel. Ionization is confined predominantly to the beam channel with ionization fractions of a few percent. Analysis suggests that net currents are larger inside the beam channel and that fast electrons and their secondaries carry a significant fraction of the return current in a halo outside the beam.

PACS numbers: 52.40.Mj, 41.85.Ja, 52.25.Jm, 52.65.+z

In ion-driven inertial confinement fusion (ICF), it is necessary to transport intense ion beams over several meters to isolate the ion source from the target explosion and to allow for focusing and time-of-flight bunching. Several light-ion ICF schemes [1], as well as some heavy-ion ICF schemes [2,3], envision ballistic (i.e., field-free) transport and focusing of the beam in neutral gas. This is possible if rapid beam-induced gas ionization leads to formation of a plasma with conductivity sufficient to charge and current neutralize the beam during the pulse duration [4]. Complete charge neutrality is expected; however, large net currents could arise which would shift, and possibly degrade, the beam focal spot [5,6]. The conductivity must also be sufficient to avoid beam filamentation instabilities [7,8] which could disrupt the beam tail. The required conductivity growth results from ion impact ionization, secondary electron impact ionization, electron avalanche breakdown, and late-time Ohmic heating.

The primary light-ion scheme for the proposed Laboratory Microfusion Facility uses ballistic transport with solenoidal lens focusing of 1-MA, 30-MeV, 40-ns lithium beams [9]. A typical beam current density before focusing is of order 1 kA/cm². Helium at 1-Torr pressure is suggested for the background gas to satisfy the above requirements while minimizing collisional energy loss and scattering of the beam. Transport in this 1-Torr regime is not well understood. This paper reports on the first experiments designed to study ion-beam-induced gas ionization and subsequent plasma conductivity growth in this regime.

This pressure range falls between the high-density regime treated by resistive models, and the low-density regime treated by collisionless models. To understand this intermediate regime, additional physics must be considered. Fast electrons created by beam-ion impact ionization (i.e., knockon electrons [10] or delta rays), which act to neutralize beam current for ion beams, could be important for intense beams. Also, runaway electrons

can result from high electric fields at the beam front. Fast electrons created by these processes can have mean free paths on the order of the beam radius, leading to nonlocal secondary ionization. A significant nonthermal electron population, which persists for the beam pulse duration, can also alter the plasma conductivity. Thus, collisional processes involving both thermal and fast electrons are important in this intermediate regime, and resistive models, which do not treat fast electron effects, are inadequate. Results of theoretical modeling of these experiments using the DYNAPROP [11] and IPROP [12] codes are presented to evaluate the importance of these effects. These codes are described when the modeling results are presented.

The experimental arrangement is shown in Fig. 1. A 1-MeV proton beam, generated in vacuum with a pinch-reflex diode [13] on the Gamble II generator is injected through a 2- μ m-thick polycarbonate foil into a collimator consisting of two 3-cm-diam apertures separated by 40 cm. The collimator region is maintained at 1-Torr air to provide reproducible injection into the transport region. A 1-kA/cm² beam exits the collimator through another 2- μ m-thick polycarbonate foil, and the interaction of this

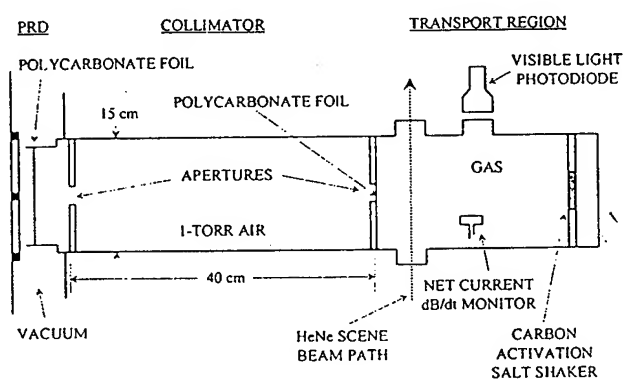


FIG. 1. Experimental arrangement of the pinch-reflex diode (PRD), the collimator, and the transport region.

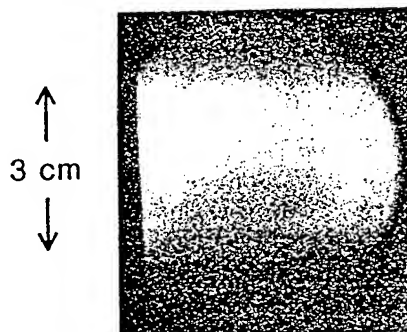


FIG. 2. Visible-light image of the ion-beam excitation of helium at 5 cm into the transport region. The beam is incident from the left.

beam with different gases in the transport region is studied.

The beam itself is characterized using several diagnostics at various distances from the collimator exit. The number of protons in the beam is measured by carbon activation [14]. A "salt shaker" detector located 26 cm beyond the collimator exit is used to minimize blowoff loss of radioactivity [15]. The beam size and uniformity in the transport region are determined from ion-induced $K\alpha$ x-ray images of aluminum targets, and from damage patterns on plastic witness plates. The beam profile is also recorded after transport over 170 cm in gas using chlorostyrene radiachromic film shielded by a $6.4\text{-}\mu\text{m}$ thickness of aluminum. These measurements indicate a uniform beam of 50-mrad divergence with a penumbra extending to 75 mrad, consistent with the collimator geometry. The energy distribution of ions in the beam is measured using a stacked-foil diagnostic as described below.

Interaction of the beam with the gas is diagnosed using photometry, magnetic-field measurements, and interferometry. Visible light emitted from the gas is monitored with a photodiode and a framing camera. A visible-light image, recorded 5 cm beyond the collimator exit with a 400-ns gated camera, is shown in Fig. 2. This image is uniform with no apparent structure. Net currents are recorded with a dB/dt monitor located 13 cm downstream of the collimator exit and outside the beam envelope at 4 cm radius. A HeNe interferometer using heterodyne phase detection is used to determine the electron density [16]. This technique provides high sensitivity and signal-to-noise ratio at the expense of time resolution. The sensitivity for this setup is limited by the noise-equivalent-average density of $5 \times 10^{14} \text{ cm}^{-3}$, with a time resolution of 25 ns. The path of the interferometer scene beam is 5 cm from the collimator exit as shown in Fig. 1.

Data from a typical shot are shown in Fig. 3. Current and voltage traces in the diode [Fig. 3(a)] indicate that a 50-ns-duration, $> 400\text{-kA}$ ion pulse is generated with most of the ions in the range of 1.0 to 1.2 MV. Adjusting

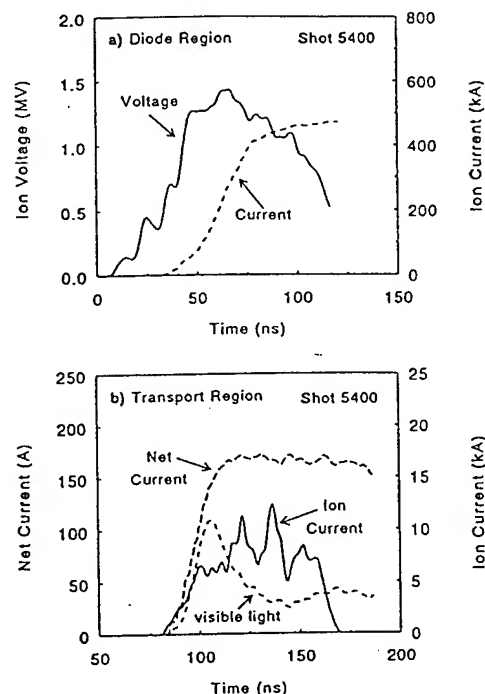


FIG. 3. (a) Ion-voltage and ion-current traces in the diode and (b) time-of-flight shifted ion current compared with measured net-current and visible-light traces.

this pulse for proton time of flight results in the ion-current pulse in Fig. 3(b) in the transport region. This pulse includes only protons above the 460-keV thick-target carbon-activation threshold and is normalized to the number of protons determined from this activation. This pulse duration is evaluated for each shot to determine the average proton current in the transport region. The net-current trace and the visible-light emission begin when the ion beam reaches the transport region.

The energy spectrum of the proton beam is measured in 1-Torr air with a carbon-activation foil stack located at 170 cm from the collimator exit. At this distance, a stack of ten $2\text{-}\mu\text{m}$ -thick polycarbonate foils with a $1.8\text{-}\mu\text{m}$ -thick aluminum cover survives, and the ^{13}N activity in each foil can be measured after the shot. A foil area of 124 cm^2 is used to provide measurable activity. The activity in each foil, produced by the 37-keV FWHM $^{12}\text{C}(p,\gamma)^{13}\text{N}$ resonance at 460 keV, is unfolded using the range-energy relation for protons in polycarbonate ($\text{C}_{16}\text{H}_{14}\text{O}_3$) to give the solid histogram in Fig. 4. The width of each step in this histogram corresponds to the energy interval over which protons activate that foil in the stack. This spectrum has been shifted up in energy to correct for energy loss in the aluminum cover on the stack. The dashed histogram is the spectrum determined from the diode current and voltage for this shot. It has been shifted down in energy to correct for energy loss in the two polycarbonate foils and air in the collimator and transport regions. Note the 400 \times difference in these two scales. The spectral intensity in the transport region is

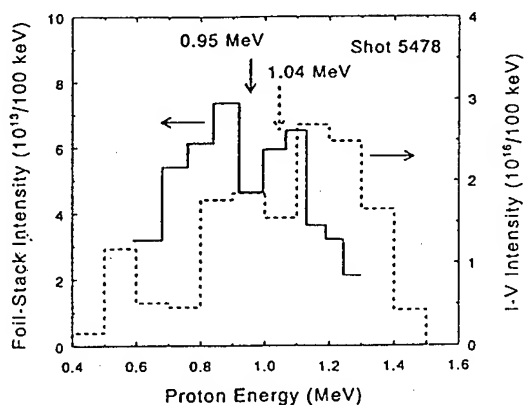


FIG. 4. Histograms of proton number vs proton energy in the transport region deduced from stacked-foil activations (solid) and from the diode current and voltage (dashed). Average energies for these histograms are indicated.

only a small fraction of that in the diode and corresponds to somewhat lower-energy protons. Average energies for these two spectra differ by about 100 keV. Since most of the protons have energies less than 1 MeV and the deuteron fraction in the beam is unknown, no correction is made for carbon activation by deuterons [14].

Simulations using a ray-trace code and a diode model [17] for the pinch-reflex diode have been carried out to calculate beam transport through the collimator and into the transport section. Experimental diode voltage and current wave forms and a beam microdivergence of 125 mrad at the anode were used to generate the time-dependent ion distribution function. Complete charge and current neutralization of the beam are assumed and ion energies are corrected for losses in the foils and gas. Ions which hit aperture plates or walls are removed from the simulation. Results predict beam currents, radial density profiles, and divergences which agree with those observed in the transport region. The predicted energy spectrum, however, agrees with the dashed curve in Fig. 4 rather than the measured spectrum (solid curve). An electric field induced at the beam front by a rising net current could explain the lower energy of the measured spectrum. Higher-energy ions, which reside at the beam head, would be slowed by this induced field. Because complete current neutralization is assumed, this energy loss is precluded in the simulations. If this is the correct explanation for the observed energy spectrum, the downshift would be considerably less at the collimator exit than at 170 cm downstream where the measurement was made.

Net currents and electron densities were measured for helium, neon, and air at pressures ranging from 0.25 to 4 Torr. Peak values of these measurements are given in Table I. From shot to shot the average current of the incident proton beam ranged from about 5 to 7 kA corresponding to current densities of about 0.7 to 1 kA/cm² at

TABLE I. Net current and electron density measurements.

Gas	Pressure (Torr)	Proton current (kA)	Peak net current (kA)	Electron density (10 ¹⁵ cm ⁻³)
Ne	0.34	4.5	0.11	...
	1.0	6.3	0.20	1.6
	1.25	6.4	0.22	...
	4.0	4.6	0.17	2.6
Air	0.25	4.8	0.18	...
	1.0	6.9	0.21	0.9
	4.0	5.5	0.28	1.8
He	0.25	6.2	0.31	...
	1.0	6.8	0.32	0.7
	4.0	5.9	0.47	1.5

the collimator exit. Net current wave forms from the dB/dt monitor have current rise times of 15 to 50 ns and decay times of several hundred ns. The uncertainty in the peak net currents is estimated to be $\pm 10\%$. Net-current fractions range from 2.3% to 8.0%. The local electron density is obtained by dividing the interferometrically measured line density by the 3-cm beam diameter. Peak electron densities are of order 10^{15} cm⁻³ and correspond to ionization fractions of 0.6% to 4.6%. For 0.25-Torr gas pressure, electron densities are too small to be measured. Negligible line density (less than the instrument sensitivity) was observed when the scene beam was located about 1.5 cm off center, indicating that ionization is largely confined to the beam diameter.

DYNAPROP and IPROP simulations were carried out to evaluate beam-induced net currents and electron densities in helium. DYNAPROP is a 1D code which uses a resistive model to treat plasmas created by beam interaction with high-density collisional gases. Beam dynamics is described by envelope and emittance equations; the plasma density, temperature, and conductivity are determined by rate equations; and the net current is calculated with a circuit equation. IPROP is a 3D hybrid code which treats beam ions and fast electrons (above 100 eV) as particles. The remaining electrons are treated as a resistive medium, while plasma ions are represented as a stationary background. Rate equations are used to create electron-ion pairs and Maxwell's equations are used to solve for the fields. Because azimuthal symmetry is assumed, IPROP was used in 2½ D mode.

Results are compared with the measurements in Table II. For all three pressures, IPROP predicts a net current inside the dB/dt probe ($r=4$ cm) that is within 30% of the measured value. However, IPROP predicts a net current within the 1.5-cm beam radius that is a factor of 3 larger than the measured values. DYNAPROP calculates the effective net current (a radially averaged current weighted by the beam current density), which is predicted to be somewhat larger than the IPROP current within

TABLE II. Comparisons with theory for helium.

Pressure (Torr)	Measured ($r=4$ cm)	Net currents (kA)			Measured (line average)	Electron densities (10^{15} cm $^{-3}$)		
		IPROP ($r=4$ cm)	IPROP ($r=1.5$ cm)	DYNAPROP ($r \approx 1.5$ cm)		IPROP ($r=0$)	IPROP ($r=1.5$ cm)	DYNAPROP ($r=0$)
0.25	0.31	0.31	0.9	1.3	...	0.2	0.2	0.2
1.0	0.32	0.39	1.0	1.5	0.7	1.0	0.6	0.7
4.0	0.47	0.63	1.6	2.1	1.5	3.2	1.8	1.9

the beam radius. The small net current at the probe location observed in IPROP is a consequence of fast electrons carrying a significant fraction of the return current in a halo outside the beam. These electrons create additional ionization at large radius which contributes to the return current. These comparisons suggest that fast electrons play an important role in return-current conduction, and that the magnetic field within the beam channel is larger than that measured outside the beam envelope. An effective net-current fraction of about 25% in the ray-trace calculations mentioned earlier would be required to down-shift the high energy edge of the calculated spectrum to match the solid histogram in Fig. 4. This fraction is consistent with IPROP and DYNAPROP predictions within the beam. Both IPROP and DYNAPROP predict electron densities that are in reasonable agreement with the measured values.

In summary, 1-MeV, 1-kA/cm 2 proton beams have been transported through helium, neon, and air at pressures of 0.25 to 4 Torr. Small net current fractions of 2% to 8%, are measured outside the beam channel. Ionization is confined predominantly to the beam channel where ionization fractions are only a few percent. Analysis of the beam energy spectrum after transport suggests that larger effective net currents exist inside the beam channel. Similarly, IPROP and DYNAPROP calculations predict net currents in the beam channel 3 to 5 times larger than measured net currents. Outside the beam channel, IPROP predicts small net currents in agreement with measurements. Fast electrons and their secondaries carry a significant fraction of the return current outside the beam (although their density is low compared with the plasma electron density within the beam channel). More extensive experiments and modeling are required to develop sufficient understanding of beam-induced gas ionization and conductivity growth in this pressure regime to confidently scale results to ICF scenarios.

The expert assistance of J. R. Boller and B. Roberts in supporting these experiments is appreciated. This work was supported by the U.S. Department of Energy through Sandia National Laboratories.

- [1] D. Mosher *et al.*, in *Proceedings of the Eighth International Conference on High-Power Particle Beams*, edited by B. N. Breizman and B. A. Knyazev (World Scientific, Singapore, 1991), p. 26.
- [2] C. L. Olson, *J. Fusion Energy* 1, 309 (1982).
- [3] *Proceedings of the Conference on Heavy Ion Inertial Fusion, Washington, DC, 1986*, AIP Conf. Proc. No. 152 (American Institute of Physics, New York, 1986).
- [4] C. L. Olson, in *Proceedings of the 1990 Linear Accelerator Conference, Albuquerque, New Mexico, September 1990* (LANL Report No. LA-12004-C), p. 396.
- [5] J. A. Swegle and S. A. Slutz, *J. Appl. Phys.* 60, 3444 (1986).
- [6] D. J. Johnson *et al.*, *J. Appl. Phys.* 58, 12 (1985).
- [7] C. L. Olson, in *Proceedings of the 1991 IEEE Conference on Plasma Science, Williamsburg, Virginia, June 1991*, *IEEE Conference Records-Abstracts*, edited by K. Schoenbach (IEEE, New York, 1992), p. 165.
- [8] E. P. Lee *et al.*, *Phys. Fluids* 23, 2095 (1980).
- [9] P. F. Ottinger, D. V. Rose, J. M. Neri, and C. L. Olson, *J. Appl. Phys.* 72, 395 (1992).
- [10] R. F. Hubbard, S. A. Goldstein, and D. Tidman, in *Proceedings of the Heavy Ion Beam Fusion Workshop, Berkeley, California, 1979*, edited by W. B. Hermannsfeldt (Lawrence Berkeley Laboratory Report No. LBL-10301, 1980), p. 488.
- [11] See R. F. Hubbard *et al.*, NRL Memorandum Report No. 7112, 1992 (National Technical Information Service Document No. ADA256070). Copies may be ordered from the National Technical Information Service, Springfield, VA 22161. The price is \$17.50 plus a \$3.00 handling fee. All orders must be prepaid.
- [12] B. B. Godfrey and D. R. Welch, in *Proceedings of the Twelfth Conference on Numerical Simulations of Plasmas* (Lawrence Livermore National Laboratory, San Francisco, CA, 1987), Paper CM1.
- [13] S. J. Stephanakis *et al.*, *Phys. Rev. Lett.* 37, 1543 (1976).
- [14] F. C. Young, J. Golden, and C. A. Kapetanakis, *Rev. Sci. Instrum.* 48, 432 (1977).
- [15] A. E. Blaugrund and S. J. Stephanakis, *Rev. Sci. Instrum.* 49, 866 (1978).
- [16] B. V. Weber and D. D. Hinshelwood, *Rev. Sci. Instrum.* 63, 5199 (1992).
- [17] J. M. Neri *et al.*, *Phys. Fluids B* 5, 176 (1993).

Interaction of intense MeV light-ion beams with low-pressure gases*

F. C. Young,[†] R. F. Hubbard, M. Lampe, J. M. Neri, P. F. Ottinger, S. J. Stephanakis, and S. P. Slinker

Plasma Physics Division, Naval Research Laboratory, Washington, D.C. 20375

D. D. Hinshelwood and D. V. Rose

JAYCOR, Inc., Vienna, Virginia 22182

C. L. Olson

Sandia National Laboratories, Albuquerque, New Mexico 87165

D. R. Welch

Mission Research Corporation, Albuquerque, New Mexico 87106

(Received 3 November 1993; accepted 20 January 1994)

The interaction of intense proton beams with low-pressure (0.25 to 4 Torr) background gases is studied to evaluate beam-current neutralization during transport. Electrons to neutralize the beam are provided by beam-induced ionization of the gas. In experiments with 1 MeV, 1 kA/cm² protons, net currents outside the beam envelope and electron densities within the beam envelope are measured for helium, neon, argon, and air. Net-current fractions are 2% to 8% and ionization fractions are 0.6% to 5% for 5 to 7 kA beams. Simulations of the experiments for helium and argon suggest that fast electrons play an important role in generating a significant fraction of the return current in a halo outside the beam. As a result, net currents inside the beam may be larger than inferred from magnetic-field measurements outside the beam. Ions at the head of the beam are observed to lose more energy than expected from collisional energy losses in the background gas.

I. INTRODUCTION

The transport of intense ion beams over several meters is required for ion-driven inertial confinement fusion (ICF) in order to isolate the ion source from the target explosion. This standoff also allows for focusing and time-of-flight (TOF) bunching of the ion beam. Several ICF schemes for transporting either light ions^{1,2} or heavy ions^{2,3} envision ballistic transport and focusing of the beam in a low density gas. Rapid ionization of the gas by the intense beam is expected to form a background plasma with a conductivity sufficient to charge and current neutralize the beam during the pulse duration.⁴ Then, the ions travel in straight-line paths through the plasma provided there are no external fields. Complete charge neutrality is expected; however, significant net currents could arise which would shift and possibly degrade the beam focal spot.^{5,6} In addition, the plasma conductivity must be large enough to avoid beam filamentation instabilities⁷⁻⁹ which could disrupt the tail of the beam. Ionization of the gas and growth of the plasma conductivity result from collisional energy deposition and impact ionization by the ion beam, secondary electron impact ionization, electron avalanching, and late-time Ohmic heating.

The primary light-ion ICF scheme uses ballistic transport with solenoidal lens focusing of 1 MA, 30 MeV, 40 ns lithium beams.^{7,10} A typical beam current density before focusing is of order 1 kA/cm². Helium at a pressure of 1 Torr is suggested for the background gas to satisfy the above requirements on conductivity while minimizing col-

lisional energy loss and scattering of the beam. Transport in this 1 Torr regime is not well understood, and experiments have not been carried out to investigate beam-induced gas ionization and subsequent conductivity growth in this regime. This paper reports on experiments designed to measure net currents and electron densities induced by kA/cm² proton beams in various gases at pressures in the range from 0.25 to 4 Torr.

This pressure range falls between the high-density regime treated by resistive models and the low-density regime treated by collisionless models. To understand this intermediate regime, additional physics must be considered. Fast electrons created by beam-ion impact ionization (i.e., knock-on electrons¹¹ or delta rays), which act to neutralize the ion beam current could be important for intense beams. Also, runaway electrons can result from high electric fields at the beam front. Fast electrons created by these processes can have mean-free paths on the order of the beam radius leading to nonlocal secondary ionization. Finally, a significant nonthermal electron population, which persists for the beam pulse duration, can alter the plasma conductivity. Thus, contributions from both thermal and fast electrons may be important in the intermediate regime. Modeling of the present experiments has been carried out with the codes, DYNAPROP,¹² which does not treat fast-electron effects, and IPROP,¹³ which incorporates a fast-electron component. The experimental results are compared with predictions from these two codes in order to quantify the importance of fast-electron effects in this intermediate regime. Initial results of this research have been reported recently in Ref. 14.

*Paper 214, Bull. Am. Phys. Soc. 38, 1902 (1993).

[†]Invited speaker.

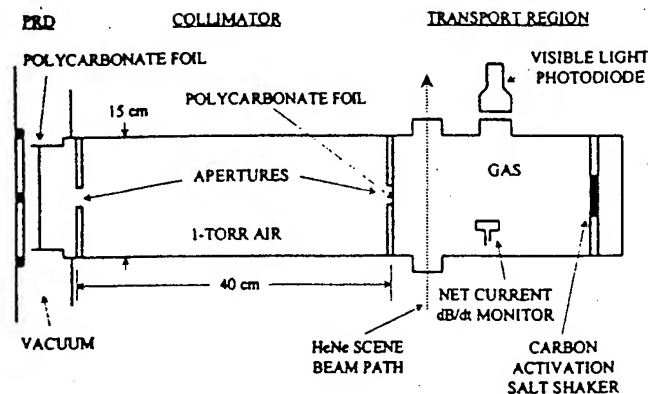


FIG. 1. Experimental arrangement of the PRD, the collimator region, and the transport region.

II. EXPERIMENT

The experimental setup is divided into three regions as shown in Fig. 1. The ion beam is generated with a pinch-reflex diode¹⁵ (PRD) on the Gamble II pulsed-power generator.¹⁶ This beam is injected into a collimator region to produce a highly directional "cool" beam. After the collimator, the beam is injected into a transport region where its interaction with different gases is studied. Each of these regions is identified in Fig. 1 and described below.

A. Ion diode

A 12 cm diam planar PRD with a polyethylene anode foil is used to produce an intense proton beam in vacuum. Typical ion voltage and current waveforms, presented in Fig. 2, indicate that a 50 ns duration, > 400 kA ion pulse is generated with most of the protons in the range from 1.0 to 1.2 MeV. These ions are weakly focused radially in the vacuum gap between the anode and a 2 μm thick polycarbonate foil (Kimfol) located within the hollow cathode of the PRD.¹⁵ This converging ion beam passes through the 11 cm diam Kimfol and free streams in 1 Torr air behind the Kimfol toward the entrance of the collimator.

B. Collimator

The collimator is used to reduce the beam divergence prior to injection into the transport region. It consists of two 3 cm diam apertures separated by 40 cm, and its entrance is located 5 cm behind the Kimfol. Less than 10% of the beam is transmitted through this collimator because the beam from the PRD has a large microdivergence (125 to 150 mrad). The collimator region is maintained at 1 Torr air to neutralize the ion beam for efficient and reproducible injection into the transport region. Protons with current densities of 0.5 to 1 kA/cm² exit the collimator through another 2 μm thick Kimfol.

C. Transport region

In the transport region, the interaction of the beam with different gases is studied. This region consists of a 15 cm diam cylindrical chamber which is filled with helium, neon, argon, or air before each shot. Diagnostics in this

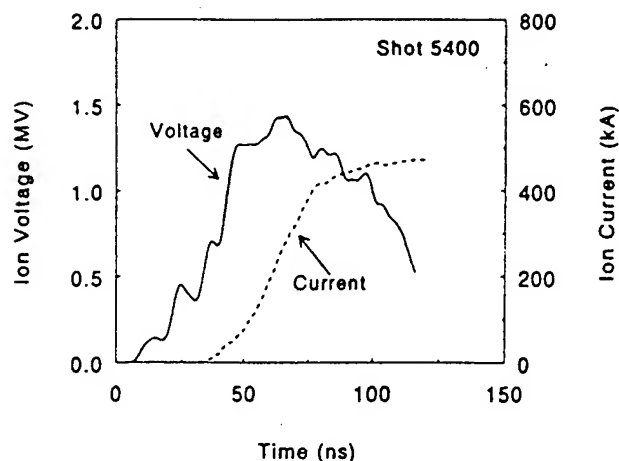


FIG. 2. Ion-voltage and ion-current traces in the PRD.

region include carbon activation to determine the incident proton intensity, a photodiode to measure visible-light emission from the gas, dB/dt monitors to record net currents, and a HeNe interferometer to measure electron density. These diagnostics are illustrated in Fig. 1.

The diameter and uniformity of the beam in the transport region are determined with an array of diagnostics located at different distances from the exit of the collimator. Ion-induced K- α x-ray images are obtained from aluminum targets at 20 cm.¹⁷ Damage patterns from plastic witness plates are also obtained at 20 cm. These diagnostics indicate that in traveling 20 cm the beam increases in diameter from 3 to 5 cm. At 170 cm, radiachromic film¹⁸ is exposed behind 6.4 μm thick aluminum. For this measurement, the diameter of the transport region at 30 cm beyond the collimator exit is increased from 15 to 50 cm in order to allow for radial expansion of the beam. A radial distribution of the ion-beam energy obtained from radiachromic film measurements is presented in Fig. 3. This profile is smooth and exhibits a mild asymmetry. The full width at half-maximum (FWHM) (19 cm) of this distribution corresponds to a beam divergence of 50 mrad, and its full width (28 cm) corresponds to a divergence of 75 mrad. Measurements with all of these diagnostics indicate a beam divergence of 50 mrad with a penumbra extending to 75 mrad. This divergence is consistent with the collimator geometry. There is no evidence of beam nonuniformities in time-integrated x-ray images or radiachromic film exposures. Also, a visible-light image recorded 5 cm beyond the collimator exit is uniform with no indication of any filaments or structure in the beam.¹⁴

The beam intensity in the transport region is measured by carbon activation.¹⁹ A salt shaker is used to minimize blowoff loss of radioactivity.²⁰ A 5.4 cm diam salt shaker located 20 cm from the collimator exit samples the total ion intensity. Even with only 8.7% transmission into the salt shaker, the uncertainty in this measurement from counting statistics is less than 2%. To determine the pulse duration at the salt shaker, current and voltage traces in the diode (e.g., see Fig. 2) are TOF adjusted and corrected for energy losses in the two Kimfols and the gas between

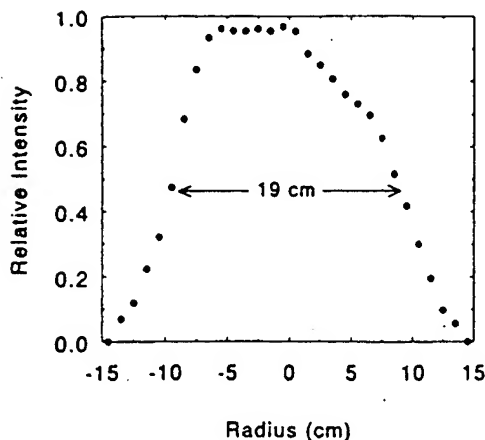


FIG. 3. Radial distribution of the ion beam energy at 170 cm from the exit of the collimator.

the diode and the salt shaker. The proton current in the transport region, corresponding to the traces in Fig. 2, is shown in Fig. 4 along with net-current and visible-light measurements for this shot. This current pulse includes only protons above the 460 keV thick-target carbon-activation threshold and is normalized to the number of protons determined from this activation. This pulse duration increases to 70 ns due to TOF dispersion of the protons. The pulse duration determined in this way is combined with the carbon-activation measurement for each shot to evaluate the average proton current in the transport region. The structure of the ion current pulse in Fig. 4 is associated with small variations in the voltage waveform and may not be real. However, higher energy ions are shifted to the front of the beam due to temporal dispersion in flight from the diode to the transport region. The net current and the visible-light emission begin when the ion beam reaches the transport region, as indicated in Fig. 4. Net-current measurements for different gases are presented in Sec. III B.

III. RESULTS

A. Ion energy measurements

The proton energy spectrum at 170 cm from the collimator exit has been measured with a carbon-activation foil stack and has been compared with the spectrum expected from measured diode current and voltage traces.¹⁴ The average proton energy in the transport region is about 100 keV less than expected, and the shape of the spectrum suggests that the higher energy portion of the spectrum has been downshifted by 200 to 300 keV.

The precision of these carbon-activation measurements is limited by counting statistics of radioactivity. For the measurements in Ref. 14, these uncertainties range from 12% to 18% depending on the intensity of the activity induced in each foil. Attempts to field this diagnostic closer to the collimator exit were unsuccessful because the foil stack was damaged by higher energy-density beams. When the beam intensity was attenuated with screens, the foil

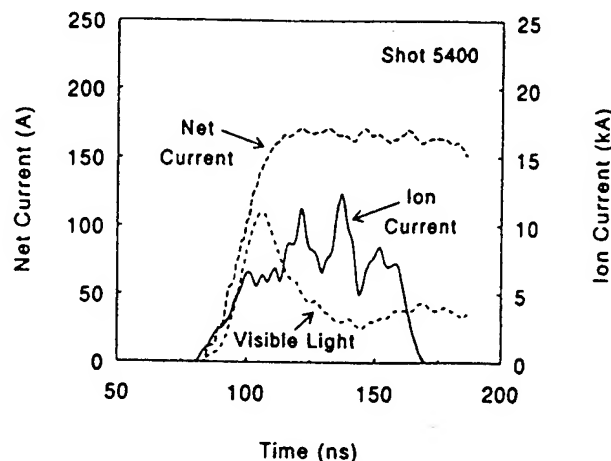


FIG. 4. Ion-current trace from Fig. 2 shifted by TOF to the transport region and compared with net-current and visible-light traces recorded on the same shot. The net current is measured at 11 cm beyond the collimator, while the ion current and visible-light traces are at 5 cm.

stack survived, but the induced activations were too small to provide meaningful spectral measurements.

Independent measurements of the ion energy in the transport region were carried out using a $d(d,n)$ neutron TOF technique. For these measurements, the anode is coated with deuterated polyethylene (CD_2) to produce a beam which is primarily deuterons. Neutrons from two CD_2 targets are detected with a scintillator-photomultiplier detector located 3.8 m from the collimator exit at 0° to the beam direction. This detector is shielded with lead to attenuate intense bremsstrahlung from the diode. The first CD_2 target is a 3 cm i.d., 3 cm wide annulus centered on the exit aperture at the collimator exit, while the second is a large-area target (15 cm diam) located 1.9 m beyond the collimator exit on axis. Target thicknesses of 0.8 to 1.0 μm are used to minimize temporal dispersion of the neutrons due to deuteron energy loss in the target.

A typical TOF signal recorded by the scintillator-photomultiplier detector is presented in Fig. 5 along with calculated TOF traces. Neutrons from the two targets are separated in time and superimposed on the tail of the (saturated) bremsstrahlung pulse. The onset of each neutron signal is compared with calculated neutron traces based on ion current and voltage traces.²¹ The neutron onset is used for this comparison because it represents the most energetic deuterons. These calculations include corrections for deuteron and neutron flight times and for deuteron energy loss in the Kimfol and gas between the diode and the target. Also a correction is made to account for temporal dispersion due to lead shielding on the detector.²² The magnitudes of the calculated signals are scaled to be comparable with the measured signals. Uncertainty in the voltage of $\pm 7\%$ corresponds to flight-time uncertainties of ± 4 ns for the first target and ± 10 ns for the second target. For the first target, the calculated signal in Fig. 5 is consistent in time with the onset of the measured signal, while the calculated signal for the second target occurs about 40 ns earlier than the measured signal. This discrep-

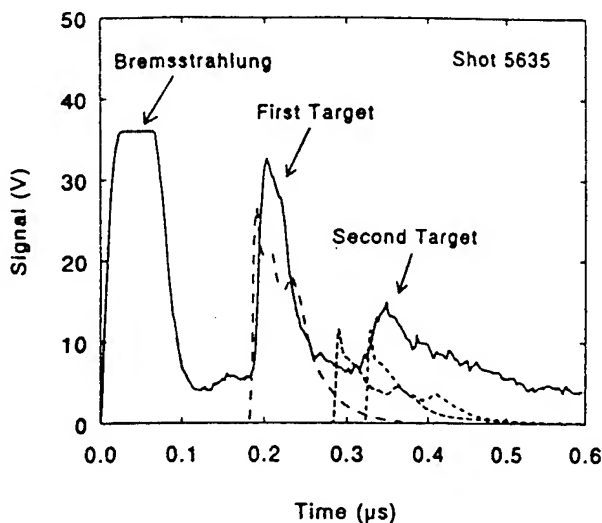


FIG. 5. Neutron TOF trace (solid line) for $d(d,n)$ neutrons measured with two CD_2 targets separated by 1.9 m. Calculated neutron TOF traces (dashed lines) for the first target, the second target, and for the second target with 2 keV/cm continuous ion slowing.

any indicates that deuterons, in traveling from the diode to the second target, lose energy in addition to collisional energy losses. This downshifted deuteron energy is insensitive to the type of gas or its pressure in the transport region. In particular, the trace in Fig. 5 was obtained with 1 Torr air in the transport region, but similar traces were recorded with either 0.25 Torr neon or 4 Torr helium in this region.

These observations support the speculation¹⁴ that downshifted ion energies may result from electric fields induced at the front of the beam by the rising net current. Fields of only ≈ 2 kV/cm are sufficient to account for the observed energy loss as indicated by the trace in Fig. 5 which is calculated for this field continuously slowing the beam from the diode to the target. In this case, the additional energy loss up to the first target is < 100 keV and corresponds to a only a 4 ns time shift of the calculated signal. This shift is within the uncertainty in fitting the measured first-target signal in Fig. 5. In addition to induced fields, electric fields at the head of the beam may also arise from space-charge effects and/or from large plasma resistivity early in the beam pulse. These effects are being studied.

The shapes of the calculated neutron traces can also be compared with the measured neutron signals. For the first target, the rise time and duration of the calculated trace are consistent with the measured signal. For the second target, the duration of the calculated trace agrees with the measured signal, but the measured signal has a significantly longer rise time. The increased rise time is consistent with the change in shape of the ion energy spectrum observed with stacked-foil activation.

B. Net-current measurements

Net currents were measured in the transport region with a linear array of three dB/dt monitors located at 5,

11, and 17 cm from the collimator exit. The signals from these monitors are electronically integrated in order to reduce uncertainties associated with baseline drifts that are encountered when measured differential signals are computationally integrated. Each dB/dt loop is 4 cm in axial length by 2 cm in radial extent and has a 1 ns time response. This relatively large loop area is required to provide adequate sensitivity in the integrated mode. The inner edge of each loop is 3 cm from the ion-beam axis and just outside the ion-beam envelope to give maximum sensitivity for net current but to avoid interference with the ion beam. The monitors are mounted on a dielectric support in the transport region and are calibrated absolutely *in situ* with a 40 A current source.

These monitors are sensitive to the presence of nearby conducting surfaces or electron sources which can perturb the magnetic field associated with the net current. For example, if a Kimfol is not used at the collimator exit, the monitor at 5 cm recorded a factor-of-2 less current. Similar variations are observed for the monitor at 17 cm if the carbon activation diagnostic at 20 cm is replaced with an aluminum target at 24 cm for K- α x-ray measurements. In both cases the net current recorded by the 11 cm monitor is not altered by such changes. Therefore, this monitor is used for net-current measurements reported in this paper.

Peak values of the net currents for helium, neon, argon, and air are given in Table I for pressures ranging from 0.25 to 4 Torr. The average incident proton current for each shot is also listed. For each gas, the shots are selected to maintain nearly constant proton current. From shot to shot, the proton current ranges from about 5 to 7 kA corresponding to current densities of about 0.7 to 1 kA/cm² at the collimator exit. The uncertainty in the peak net current is estimated to be $\pm 10\%$. Net-current fractions for each shot are also listed in Table I. These fractions range from 2% to 8% and tend to increase with pressure. These fractions are smaller for neon and air and larger for helium and argon.

Net-current waveforms corresponding to the values in Table I are presented in Fig. 6. These waveforms have been corrected for the 1 μ s integration time used on the monitor. This correction is minimal ($< 5\%$) at peak current, but is quite large toward the end of the current pulse. For each gas, the shape of the current does not change much with pressure. Current rise times range from 15 ns for air to 50 ns for argon. Decay times are 100 to 300 ns for helium and argon, but much longer for neon. The net currents increase with the incident beam current until the plasma conductivity becomes sufficiently large to provide neutralization of additional beam current, and the net current becomes frozen in the plasma. After the ion beam pulse shuts off, the current resistively decays. Late in time the plasma conductivity is also decreasing as suggested by the decrease in visible-light emission from the plasma. The temporal evolution of these currents is not analyzed in this report. For this initial work, we focus on understanding the magnitude of the net currents. For this purpose, peak values in Table I are compared with simulations.

TABLE I. Net current and electron density measurements.

Gas	Pressure (Torr)	Proton current (kA)	Peak net current (kA)	Net-current fraction (%)	Electron density ($10^{15}/\text{cm}^3$)	Ionization fraction (%)
He	0.25	6.2	0.31	4.9		
	1.0	6.8	0.32	4.6	0.5	1.4
	4.0	5.9	0.47	8.0	1.5	1.1
Ne	0.34	4.5	0.11	2.3		
	1.0	6.3	0.20	3.2	1.2	3.4
	1.25	6.4	0.22	3.4		
	4.0	4.6	0.16	3.5	2.6	1.8
Ar	0.25	5.0	0.17	3.5		
	1.0	4.7	0.35	7.4	1.1	3.1
	4.0	4.5	0.23	5.0	6.2	4.4
Air	0.25	4.8	0.18	3.8		
	1.0	6.9	0.21	3.0	0.9	1.3
	4.0	5.5	0.27	4.9	1.8	0.64

C. Electron-density measurements

A HeNe interferometer with heterodyne phase detection is used to determine electron density.²³ This technique provides high sensitivity and signal-to-noise ratio at the expense of time resolution. The sensitivity for this setup is limited by the noise-equivalent-average density of $5 \times 10^{14} \text{ cm}^{-3}$ with a time resolution of 20 ns. The path of the interferometer scene beam is 5 cm from the collimator exit as shown in Fig. 1. The local electron density is obtained by dividing the interferometrically measured line density by the 3 cm beam diameter. Negligible line density (less than the measurement sensitivity) was observed when the scene beam was located about 1.5 cm off center, indicating that ionization is largely confined to the beam diameter.

Electron densities unfolded from the interferometer signals are shown for two shots in Fig. 7. Calculated densities based on ion-impact ionization are also shown for comparison. Each calculation uses the TOF shifted ion-current wave shape, the proton intensity exiting the collimator as determined by carbon activation, and the ion-impact ionization cross section.²⁴ Reasonable agreement between calculation and experiment is obtained. The difference for the argon shot is within uncertainties of the electron-density and proton-intensity measurements. Measured electron densities agree with densities calculated for shots with helium, neon, or argon in the transport region, for shots with different proton intensities, and for shots with either 1 Torr or 4 Torr pressure in the transport region. For 0.25 Torr pressure, the electron densities are too small to be measured. These results suggest that ion impact is the dominant ionization mechanism for the conditions of this experiment. The resulting ionization fractions are only a few percent. Peak electron densities and ionization fractions are listed in Table I. In contrast with the current measurements in Table I, these densities represent average values obtained from several shots at each pressure for the different gases.

IV. SIMULATIONS OF THE BEAM-PLASMA INTERACTION

The DYNAPROP¹² and IPROP¹³ codes were used to investigate beam-induced gas ionization. These codes have

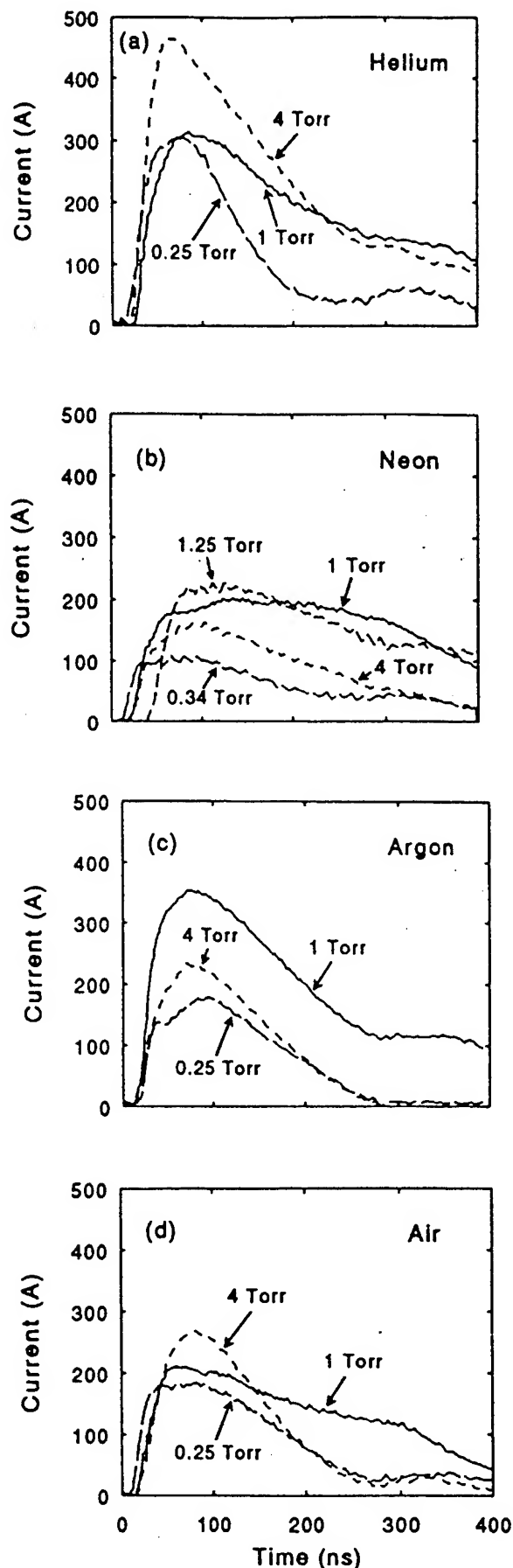


FIG. 6. Net-current traces for (a) helium, (b) neon, (c) argon, and (d) air in the transport region at pressures ranging from 0.25 to 4 Torr.

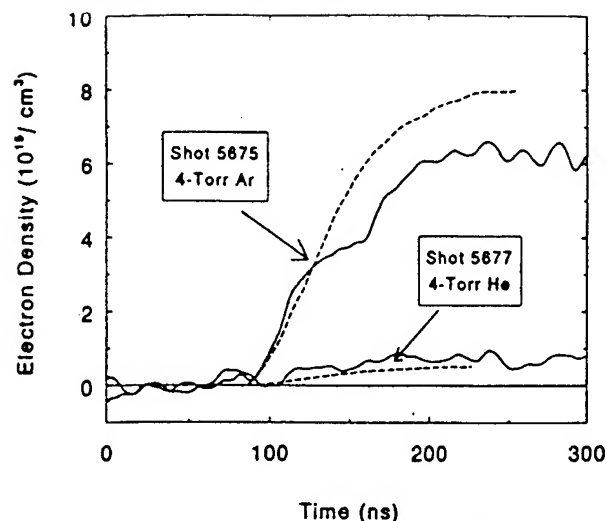


FIG. 7. Electron densities for 4 Torr helium and 4 Torr argon in the transport region. The dashed lines are calculations based on ion-impact ionization cross sections.

been widely used to model electron beams with currents comparable to this experiment, and code predictions have agreed reasonably well with experimental net currents. DYNAPROP is a 1-D code which uses a resistive model to treat plasmas created by beam interactions with high-density collisional gases. Beam dynamics is described by envelope and emittance equations; the plasma density, temperature, and conductivity are determined by rate equations; and the net current is calculated with a circuit equation. DYNAPROP calculates the effective net current (a radially averaged current weighted by the ion-beam current). On the other hand, IPROP is a 3-D hybrid code which treats beam ions and fast electrons (above 100 eV) as particles. The remaining electrons are treated as a resistive medium. Plasma ions are represented as a stationary

background. Rate equations are used to create electron-ion pairs and Maxwell's equations are used to solve for the fields.

DYNAPROP and IPROP simulations were run to model beam-induced net currents and electron densities in helium using the transport-region geometry with conducting walls at $r=7.5$ cm. Results are compared with the measurements in Table II. Electron densities predicted by both codes for helium are in agreement with measured densities. DYNAPROP predicts effective net currents four to five times larger than observed experimentally at $r=4$ cm. IPROP predicts somewhat smaller net currents within $r=1.5$ cm (i.e., net current within the beam radius), but these currents are also about three times larger than the measurements. However, IPROP with fast electrons predicts net currents within 30% of the measurements at the radial location of the dB/dt monitor ($r=4$ cm). This result is a consequence of the fast electrons carrying a significant fraction of the return current in a halo outside the beam. These fast electrons create additional ionization at large radius which also contributes to the return current.

The contribution of the fast electrons in the IPROP simulations for neutralizing ion-beam current is important. With mobile fast electrons in the code, the electron density increases more rapidly initially than observed with a pure fluid model of the plasma. As the ion beam enters neutral gas, the rising net current induces an electric field which can be large enough to cause electrons to run away. However, the space-charge electric field ahead of the beam effectively prevents these electrons from outrunning the beam. Because these electrons are energetic, traveling at roughly the beam velocity, their momentum transfer frequency is low and their mean-free path is comparable to the beam radius. Comparison of the IPROP simulations in Fig. 8 indicates that fast electrons play an important role in return-current conduction. Also, these results indicate that the magnetic field within the beam channel may be much

TABLE II. Comparison of net currents and electron densities with simulations.

Gas	Pressure (Torr)	Net current (kA)			
		Measured ($r=4$ cm)	IPROP ($r=4$ cm)	IPROP ($r=1.5$ cm)	DYNAPROP ($r \approx 1.5$ cm)
He	0.25	0.31	0.31	0.9	1.3
	1.0	0.32	0.39	1.0	1.5
	4.0	0.47	0.63	1.6	2.1
Ar	0.25	0.17	0.32	0.9	
	1.0	0.35	0.33	1.1	
	4.0	0.23	0.23	1.8	
		Electron density ($10^{15}/\text{cm}^3$)			
		Measured (average)	IPROP ($r=0$)	IPROP ($r=1.5$ cm)	DYNAPROP ($r=0$)
He	0.25		0.2	0.2	0.2
	1.0	0.7	1.0	0.6	0.7
	4.0	1.5	3.2	1.8	1.9
Ar	0.25		1.2	0.7	
	1.0	1.1	5.0	3.2	
	4.0	6.2	25.0	30.0	

larger than that measured outside the beam envelope.

IPROP was also used to model beam-induced net currents and electron densities for argon. These results are also summarized in Table II. Again, predicted net currents at the dB/dt monitor location ($r=4$ cm) are in good agreement with the measurements (with the exception of the 0.25 Torr case), and net currents at the beam radius ($r=1.5$ cm) are three to eight times larger than the measurements. However, the maximum calculated electron densities are three to four times larger than the values measured for argon. This disagreement is in contrast with the good agreement obtained for helium. Because this discrepancy between helium and argon does not occur for the net-current calculations, it is suspected that the plasma density is modeled accurately at early time, but that late-time effects are not being modeled properly. The source of this discrepancy for electron densities in argon is being investigated.

V. DISCUSSION

Only shots with relatively constant ion-beam current are included in Table I. However, variations of the average ion current of up to a factor of 2 from shot to shot are observed in the experiment. Within this variation, little change of the net-current fraction is observed. Also, the net currents are relatively insensitive to the gas density over the range of this experiment. These observations are consistent with the net current becoming frozen in the plasma early in the pulse. In addition, measured electron densities increase with incident ion current and with gas density as expected from ion-impact ionization. The net currents are sensitive to the type of gas with larger values for helium and argon and smaller values for neon and air.

To make more detailed comparisons of the net-current traces with results from the simulations requires a direct measurement of the ion current in the transport region. In the present experiments, only the average proton current in

this region was measured. A variety of charge-collecting diagnostics have failed to provide a reliable time-resolved measure of this current due to the large current density (kA/cm^2) in a low-pressure background gas. Initial tests with a Rutherford scattering technique to time resolve the particle current scattered from a high-atomic-number target in the transport region are promising. Such direct ion-current measurements can be used as input to simulations to make time-resolved comparisons of measured net currents and electron densities with simulations.

Additional experiments are required to address two issues identified in the present study. Energy losses are observed at the front of the beam, but the mechanism causing this energy loss is not understood. The IPROP simulations suggest that it may be associated with larger magnetic fields and induced electric fields within the beam envelope. Resistive and space-charge electric fields also may slow the head of the beam, and space-charge fields may cause the beam head to blow up. Ion energy spectrum measurements (with a magnetic spectrometer) at different axial locations in the transport region are planned to address this issue. The second issue is to determine experimentally if the net current is substantially larger within the beam as predicted by IPROP. Efforts to measure magnetic fields (and net currents) within the beam with magnetic probes have been unsuccessful. New novel diagnostics may be required to make such measurements within the beam envelope.

For light-ion ICF, several 1 MA level beams must be transported from individual diodes to the target. If a high degree of current neutralization can be achieved, then these beams can be focused and transported ballistically in a background gas. The present experimental results must be scaled to higher total ion-beam current to evaluate this possibility. For larger ion-beam currents, the net-current fractions should be smaller than in the present experiment so that the degree of current neutralization may be sufficient to allow ballistic transport for light-ion ICF. On the other hand, if further experiments establish that the net current will be large enough to affect ICF transport, proper system design can compensate for this effect because the net current acts as a distributed lens. However, this requires the predictive capability being developed by this work.

In summary, intense 1 MeV, $1 \text{ kA}/\text{cm}^2$ proton beams have been transported through helium, neon, argon, and air at pressures in the range of 0.25 to 4 Torr. Small net currents (2%–8%) have been measured outside the beam channel. Interferometric measurements across the channel indicate that these gases are only weakly ionized (0.6%–5%) and that the ionization is confined predominately to the beam channel. Electron densities predicted by both DYNAPROP and IPROP simulations are consistent with the measured densities for helium. Simulations which include both thermal and fast electrons (IPROP) predict net currents outside the beam at the dB/dt monitor location which agree with experiment. In these simulations, fast electrons carry a significant fraction of the return current at the beam edge. Simulations with both codes, however, predict net currents at the beam radius that are substan-

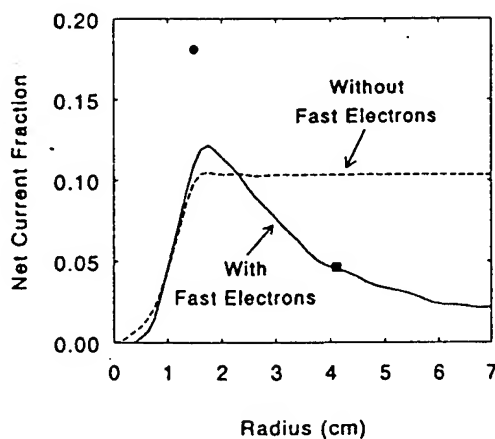


FIG. 8. Radial distributions of net currents from IPROP simulations for 1 Torr helium with and without fast electrons. The currents occur 70 ns after injection at 11 cm into the transport region. The square point at 4 cm radius corresponds to the measurement in Table I. The circular point at 1.5 cm radius corresponds to the DYNAPROP result in Table II.

tially larger than net currents measured outside the beam. These comparisons indicate that simple resistive models are inadequate for ion beams in this region. Measurements of ion energies after transport also suggest that the effective net current within the beam channel is larger than the measured current, but no direct measurement of this effective current has been made. More extensive experiments and modeling, including effects of fast electrons and non-local ionization, are required to develop a thorough enough understanding of beam-induced gas ionization, breakdown, and conductivity growth in this pressure regime to confidently scale results to light-ion fusion scenarios.

ACKNOWLEDGMENTS

The assistance of J. R. Boller in making electrical measurements, of W. A. Noonan in preparing deuterated polyethylene targets, and of B. Roberts with Gamble II operations is appreciated.

This work was supported by the U.S. Department of Energy through Sandia National Laboratories.

- ¹D. Mosher, D. D. Hinshelwood, J. M. Neri, P. F. Ottinger, J. J. Watrous, C. L. Olson, and T. A. Mehlhorn, in *Proceedings of the 8th International Conference on High-Power Particle Beams*, edited by B. N. Breizman and B. A. Knyazev (World Scientific, Singapore, 1991), p. 26.
- ²C. L. Olson, *J. Fusion Energy* **1**, 309 (1982).
- ³*Proceedings of the Conference on Heavy Ion Inertial Fusion*, Washington, DC, 1986, AIP Conf. Proc. 152 (American Institute of Physics, New York, 1986).
- ⁴See National Technical Information Service Document No. DE91009298 (C. L. Olson, in *Proceedings of the 1990 Linear Accelerator Conference*, LANL Report No. LA-12004-C, p. 396). Copies may be ordered from the National Technical Information Service, Springfield, Virginia 22161.
- ⁵J. A. Swegle and S. A. Slutz, *J. Appl. Phys.* **60**, 3444 (1986).
- ⁶D. J. Johnson, R. J. Leeper, W. A. Stygar, R. S. Coats, T. A. Mehlhorn, J. P. Quintenz, S. A. Slutz, and M. A. Sweeney, *J. Appl. Phys.* **58**, 12 (1985).
- ⁷C. L. Olson, in *Conference Record - 1991 IEEE International Conference on Plasma Science*, edited by K. Schoenbach, Williamsburg, Virginia (Institute of Electrical and Electronic Engineers, Piscataway, NJ, 1991), p. 165, IEEE Catalog No. 91CH3037-91.
- ⁸E. P. Lee, S. S. Yu, H. L. Buchanan, F. W. Chambers, and M. N. Rosenbluth, *Phys. Fluids* **23**, 2095 (1980).
- ⁹P. F. Ottinger, D. Mosher, and S. A. Goldstein, *Phys. Fluids* **24**, 164 (1981).
- ¹⁰P. F. Ottinger, D. V. Rose, J. M. Neri, and C. L. Olson, *J. Appl. Phys.* **72**, 395 (1992).
- ¹¹H. A. Bethe and J. Ashkin, in *Experimental Nuclear Physics*, edited by E. Segre (Wiley, New York, 1953), Vol. 1, p. 231.
- ¹²See National Technical Information Service Document No. ADA256070 (R. F. Hubbard *et al.*, NRL Memorandum Report No. 7112, 1992). Copies may be ordered from the National Technical Information Service, Springfield, Virginia 22161.
- ¹³D. R. Welch, C. L. Olson, and T. W. L. Sanford, *Phys. Plasmas* **1**, 764 (1994).
- ¹⁴F. C. Young, D. D. Hinshelwood, R. F. Hubbard, M. Lampe, J. M. Neri, C. L. Olson, P. F. Ottinger, D. V. Rose, S. P. Slinker, S. J. Stephanakis, and D. R. Welch, *Phys. Rev. Lett.* **70**, 2573 (1993).
- ¹⁵G. Cooperstein, S. A. Goldstein, D. Mosher, R. J. Barker, J. R. Boller, D. G. Colombant, A. Drobot, R. A. Meger, W. F. Oliphant, P. F. Ottinger, F. L. Sandel, S. J. Stephanakis, and F. C. Young, in *Laser Interaction and Related Plasma Phenomena*, edited by H. Schwarz, H. Hora, M. Lubin, and B. Yaakobi (Plenum, New York, 1981), Vol. 5, p. 105.
- ¹⁶J. D. Shipman, Jr., *IEEE Trans. Nucl. Sci.* **NS-18**, 243 (1971); see National Technical Information Service Document No. DE8500613 (J. R. Boller, J. K. Burton, and J. D. Shipman, Jr., "Status of upgraded version of the NRL Gamble II pulse power generator," in *Digest of 2nd IEEE International Pulsed Power Conference*, Lubbock, Texas, 1979, edited by A. H. Guenther and M. Kristiansen). Copies may be ordered from the National Technical Information Service, Springfield, Virginia 22161.
- ¹⁷R. D. Bleach, D. J. Nagel, D. Mosher, and S. J. Stephanakis, *J. Appl. Phys.* **54**, 3064 (1981).
- ¹⁸W. P. Bishop, K. C. Humpherys, and P. T. Randtke, *Rev. Sci. Instrum.* **44**, 443 (1973).
- ¹⁹F. C. Young, J. Golden, and C. A. Kapetanakis, *Rev. Sci. Instrum.* **48**, 432 (1977).
- ²⁰A. E. Blaugrund and S. J. Stephanakis, *Rev. Sci. Instrum.* **49**, 866 (1978).
- ²¹F. C. Young, *Proceedings of the Workshop on Measurement of Electrical Quantities in Pulse Power Systems*, Boulder, Colorado, edited by R. H. McKnight and R. E. Hebner, Jr., NBS Special Publication 628 (US Government Printing Office, Washington, DC, 1982), p. 104 (Library of Congress Catalog No. 82-600535).
- ²²R. J. Leeper and J. Chang, *IEEE Trans. Nucl. Sci.* **NS-29**, 798 (1982).
- ²³B. V. Weber and D. D. Hinshelwood, *Rev. Sci. Instrum.* **63**, 5199 (1992).
- ²⁴E. W. McDaniel, *Collision Phenomena in Ionized Gases* (Wiley, New York, 1964), p. 185.

Physics of Gas Breakdown for Ion Beam Transport in Gas(*)(**).

C. L. OLSON⁽¹⁾, D. D. HINSHELWOOD⁽²⁾, R. F. HUBBARD⁽³⁾, M. LAMPE⁽³⁾
J. M. NERI⁽³⁾, P. F. OTTINGER⁽³⁾, J. W. POUEY⁽¹⁾, D. V. ROSE⁽²⁾
S. P. SLINKER⁽³⁾, S. J. STEPHANAKIS⁽³⁾, D. R. WELCH⁽⁴⁾ and F. C. YOUNG⁽³⁾

⁽¹⁾ Sandia National Laboratories - Albuquerque, NM 87185

⁽²⁾ JAYCOR, Inc. - Vienna, VA 22182

⁽³⁾ Naval Research Laboratory - Washington, DC 20375

⁽⁴⁾ Mission Research Corporation - Albuquerque, NM 87106

(ricevuto il 25 Maggio 1993; approvato l'1 Giugno 1993)

Summary. — Detailed analysis, experiments, and computer simulations are producing a new understanding of gas breakdown during intense ion beam transport in neutral gas. *Charge neutralization* of beam micro clumps is shown to limit the net clump potentials to a non-zero value ϕ_{\min} , which can lead to divergence growth and axial energy spreading. At pressures ≥ 1 Torr, plasma shielding should substantially reduce this effect. *Current neutralization* has been studied in experiments on the GAMBLE II accelerator. The importance of fast electrons (knock-ons and runaways) has been established in IPROP simulations, which are in agreement with the experiments. For light-ion fusion parameters with pressures ≥ 1 Torr, very small net current fractions ($\ll 1\%$) appear feasible, permitting ballistic transport in gas. *Self-pinched transport* requires higher net current fractions ($\geq 2\%$) and preliminary IPROP code results indicate that this appears achievable for small-radius intense beams in lower-pressure gases (≤ 1 Torr). Several self-pinched transport concepts look promising. The importance of these results for both light-ion fusion and heavy-ion fusion is discussed.

PACS 28.50.Re — Fusion reactors and thermonuclear power studies.

PACS 52.40.Mj — Particle beams interactions in plasma (including intense charged-particle beams).

PACS 52.25.Jm — Ionization of plasmas.

PACS 41.85.Ja — Beam transport.

(*) Paper presented at the International Symposium on Heavy Ion Inertial Fusion, Frascati, May 25-28, 1993.

(**) This work was supported by the U.S. Department of Energy under Contract No. DE-AC04-76DP00789.

1. - Introduction.

The propagation of an intense ion beam from an accelerator to a fusion target plays an important role in the feasibility of both light-ion fusion (LIF) and heavy-ion fusion (HIF). Several possible ion beam propagation modes involve transport in neutral gas [1, 2]. For ballistic propagation in gas, it is generally assumed that perfect charge and current neutralization occur. For self-pinch propagation it is generally desired that a sizeable net current be achieved. This paper discusses research designed to understand gas breakdown, and to examine fundamental limits on charge neutralization and current neutralization. Based on GAMBLE II gas breakdown experiments and IPROP simulations, a new understanding of gas breakdown is evolving [3]. Results summarized here suggest that both ballistic transport and self-pinch transport may be feasible in appropriate parameter regimes for LIF. Implications of these results for HIF are also discussed.

2. - Charge neutralization.

For transport of intense ion beams in neutral gas, it is generally assumed that charge neutralization is perfect. Complete charge neutralization means that there is a neutralizing background of electrons with density n_e exactly equal to the total ion density (beam density n_b plus background ion density n_i) everywhere in space and time. In reality, there may be deviations from perfect charge neutrality. These can be referred to as macro or micro charge non-neutrality. *Macro* charge non-neutrality refers to global charge non-neutrality which, if uniform, leads to linear spreading of the beam; this effect can, within limits, be accommodated for by initial over-focusing of the beam. If macro charge non-neutrality is non-uniform, it may lead to serious distortions of the beam. *Micro* charge non-neutrality refers to local non-neutral clumps in the beam that can produce local transverse and axial spreading; these effects can produce emittance increases that may result in larger spot sizes. In this section, we examine the effects of micro charge non-neutrality.

The fundamental concept is that small charge clumps can only be charge neutralized down to some minimum potential ϕ_{\min} [4]. Such charge clumps may be produced by noise, instabilities, or other non-uniform beam effects. Consider first the effects of electron trapping to reduce the net potential (later, we will consider plasma shielding effects). Trappable electrons may be available from walls, hot electron plasmas (created by the beam), or by gas ionization near the bottom of the potential well. A physical picture of how ϕ_{\min} occurs is most easily seen by transforming to the moving ion clump frame. In that frame, a stationary potential well of depth ϕ occurs. Electrons born in the potential well (e.g., by gas ionization) will have a velocity $-v_i$ and kinetic energy $1/2 m_e v_i^2$, where v_i is the original ion velocity and m_e is the electron mass. Electrons will be trapped only if $e\phi > (1/2) m_e v_i^2$. Therefore, the self-consistent net potential will not be reduced below $e\phi_{\min} = (1/2) m_e v_i^2$. (Detailed calculations and simulation results show $e\phi_{\min}$ may actually be larger by a factor of 1-4 [5].)

If there are no other neutralizing mechanisms, a spherical ion charge clump of radius ξ and potential $e\phi_{\min}$ will simply expand to a radius $\gg \xi$. The resultant transverse microdivergence will be $\theta_u = [(m_e/M_p)(Z_t/A)]^{1/2}$ where Z_t is the ion charge state during transport, M_p is the proton mass, and A is the atomic number.

Simultaneously, the resultant axial energy spread is $\Delta\varepsilon_{\parallel}/\varepsilon_{\parallel} = \pm 2\theta_{\mu}$. The characteristic clump expansion time is $\tau = (2\xi/v_i)/\theta_{\mu}$ and the characteristic transit length is $L = 2\xi/\theta_{\mu}$. These results are based solely on electron trapping arguments. The effects of plasmas, collisions, and an external magnetic field may enhance or reduce these results. Typically at the higher gas pressures (1–10 Torr), plasma shielding should reduce these results, whereas at lower pressures (≤ 0.1 Torr) these results may have significant consequences.

Computer simulations in 2D with plasma-to-bunch density ratios of 0–100 have been performed. In general, wakes form and rapid oscillations occur, but the peak potential is still $\sim \phi_{\min}$ and the peak electric fields are still $\sim \phi_{\min}/\xi$. Emittance growth and axial energy spreading are observed [4].

For LIF parameters (electrical current density $J_i = 5 \text{ kA/cm}^2$ and $\beta = v_i/c = 0.1$ corresponding to 5 MeV p or 30 MeV Li) we only need $\xi \geq 0.02 \text{ cm}$ and a clump electrical current $\sim 9 \text{ A}$ to produce $e\phi_{\min} = 1/2 m_e v_i^2 = 2.6 \text{ keV}$. The basic results predict i) no dependence of θ_{μ} on diode voltage, ii) proton $\theta_{\mu} = (m_e/M_p)^{1/2} \approx 23 \text{ mrad}$ iii) (non-protonic $\theta_{\mu}) \geq (\text{proton } \theta_{\mu})$ for proton-contaminated beams, and iv) $\Delta\varepsilon_{\parallel}/\varepsilon_{\parallel} \approx \pm 2\theta_{\mu} = \pm 4.6\%$. The characteristic clump expansion time is $\tau \approx 0.6 \text{ ns}$ and the transit length is $L = 1.7 \text{ cm}$. The mechanism could easily occur in the "charge-neutral" region inside the diode, or in the gas transport region. Predictions i)-iv) are consistent with LIF data. It should be noted that this contribution to θ_{μ} would add in quadrature with other contributions to θ_{μ} . To fully assess this mechanism for LIF, further research is needed (*e.g.*, measurements of ion source micro-nonuniformities) to evaluate potential micro clump levels.

For HIF parameters (particle current 4 kA, particle current density $J_i^p = 12.7 \text{ A/cm}^2$, electrical current density (assuming $Z_t = 40$) $J_i = 508 \text{ A/cm}^2$, $Z = 55$, $A = 133$, and $\beta = 0.3$ corresponding to $\sim 6 \text{ GeV Cs}$), we would need $\xi \geq 0.4 \text{ cm}$ and a clump electrical current $\sim 230 \text{ A}$ to produce $e\phi_{\min} = 1/2 m_e v_i^2 = 23 \text{ keV}$. Results predict $\theta_{\mu} = 12.7 \text{ mrad}$, a characteristic clump expansion time of $\tau \approx 7 \text{ ns}$, and a transit length of $L = 63 \text{ cm}$. Note that the mechanism for LIF occurs on a microscale ($\xi \sim \text{sub mm}$, $\tau \sim \text{sub ns}$, $L \sim \text{cm}$), whereas for HIF it occurs on a macroscale ($\xi \sim \text{cm}$, $\tau \sim 10 \text{ ns}$, $L \sim \text{meter}$). For HIF it would be unlikely to have a high level of macro ion clumps, because the beam should be well phase-mixed by the time it reaches the final transport region. Also, the most likely instability to generate bunches is the ion-electron two-stream instability, and this has been shown to be benign [6]. Thus, for HIF, this mechanism does not appear to be troublesome; however this conclusion should be verified, especially for the lower pressures ($\leq 10^{-1} \text{ Torr}$).

3. - Current neutralization.

For ballistic transport of ion beams in gas, it is generally desired that current neutralization be perfect. Complete current neutralization means that there is a neutralizing background electron current density J_p that exactly matches the ion beam current density J_b . Overall, the net current is $I_{\text{net}} = I_b + I_p$, where I_b is the beam current and I_p is the plasma current. To achieve a small I_{net} means that the background electrical conductivity σ must rise quickly so that $t_d \gg t_b$ is achieved very early in the beam risetime ($< 1 \text{ ns}$ typically). Here the magnetic diffusion time is $t_d = 4\pi\sigma r_b^2/c^2$, t_b is the beam pulse length, r_b is the beam radius, and c is the speed of

light. In addition, τ must be high enough throughout the pulse to avoid the filamentation instability.

The physical processes involved in gas breakdown and the growth of τ include ion impact ionization, secondary electron impact ionization, electron avalanching, and late time Ohmic heating[7]. Energetic electrons can be created in ionizing collisions between beam ions and neutral gas atoms (ion compact ionization), in momentum-changing collisions between beam ions and free electrons (knock-on collisions), and from free electron acceleration in electric fields (avalanching). In the 1 Torr pressure regime, the mean free path between collisions can be of the order of the beam radius; then the gas breakdown processes are «non-local» and they must be followed accurately in space and time.

The first experiments designed to study beam-induced gas breakdown and conductivity growth have been performed on the GAMBLE II accelerator at NRL[3]. In these experiments, a 1 MeV proton beam produced in a pinch reflex diode is injected through a 2 μ m polycarbonate foil into a 40 cm long collimator section, and then through another 2 μ m polycarbonate foil into an experimental transport section. The collimator section has entrance and exit apertures of 1.5 cm radius, and is filled with 1 Torr air. A 1 kA/cm² beam enters the experimental section which is filled with helium, air, or neon at pressures in the range of 0.25–4.0 Torr. Diagnostics include carbon activation, K_α X-ray imaging of aluminum targets, a visible light photodiode, a framing camera, net current B -dot monitors, HeNe interferometry to measure electron density, and diode voltage and current monitors. Net current fractions ranged from 2.3% to 8% and peak electron densities were of order 10^{15} cm⁻³ corresponding to ionization fractions of 0.6% to 4.6%.

IPROP and DYNAPROP simulations were performed to evaluate net currents and electron densities. IPROP is a 3D EM hybrid code[8]. Beam ions are treated as particles, and fast electrons (> 100 eV) are also treated as particles. Slow electrons (< 100 eV) are treated as a tensor conductivity, while plasma ions are treated as a stationary background. Maxwell's equations are used to solve for the fields. The important unique feature is that the fast electrons (*e.g.*, knock-ons and runaways) are followed explicitly, and that these are the particles responsible for non-local breakdown effects. Because azimuthal symmetry was assumed, IPROP was used in a 2-1/2-D mode. DYNAPROP is a 1D code based on a resistive plasma model in which the beam dynamics are described by an envelope equation[9]. The plasma properties (density, temperature) are determined by rate equations, and the net current is calculated from a circuit equation.

Figure 1 shows a comparison of the net current in the GAMBLE II experiments with IPROP and DYNAPROP results. Many such comparisons have been made; this examples illustrates the main effects. If fast electrons are not included, note that both IPROP and DYNAPROP predict a net current much higher than that observed in the experiment by the B -dot monitor at $r = 4$ cm. By including fast electrons in IPROP, good agreement is obtained with the experiments. Note that fast electrons outside the beam radius contribute significantly to the return current, so that the net current at $r = 4$ cm is considerably smaller than the net current at the beam radius of 1.5 cm. These comparisons show that fast electrons and non-local effects play an important role in gas breakdown and that the magnetic field within the beam channel can be larger than that measured outside the beam channel.

IPROP has also been used to compare with net current measurements for the barrel diode geometry of PBFA II, including applied magnetic field effects. IPROP

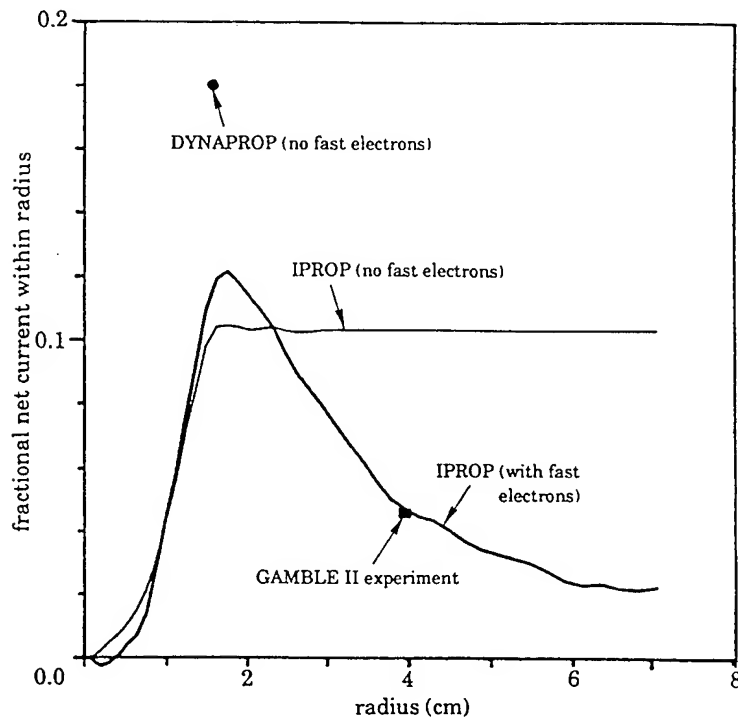


Fig. 1. - Net current fraction contained within a given radius for the GAMBLE II experiments, IPROP 2 1/2D simulations, and DYNAPROP 1D simulations (1 MeV p, ~ 6 kA, ~ 1 kA/cm², $r_b = 1.5$ cm, B-dot at $r = 4$ cm, 1 Torr He).

predicts $\geq 99.8\%$ neutralization for 6 MeV Li ions in 4 Torr argon on PBFA II. It is important to note that the net current fraction here is even smaller than in the GAMBLE II experiments because the total current is higher (~ 1 MA instead of ~ 7 kA), the ions are Li^{+3} which ionize faster than protons, and the gas is argon which is easier to ionize than helium.

The results are extremely encouraging and suggest that, from a net current view point, ballistic transport in gas appears to be a viable option for both LIF and HIF.

4. - Self-pinch propagation.

For self-pinch transport, the ion beam is focused down to a small radius and then transported at small radius to the target. The ion beam is contained by the net self magnetic field. Different versions of this mode use, *e.g.*, a low-pressure gas, a laser performed channel with radius larger than the beam radius, an annular preformed plasma, etc. For all cases, the required net current in the «channel» is $I_c = 1/2(R/r_s)^2 \theta_\mu^2 I_m$ where R is the initial beam radius, r_s is the channel spot radius, θ_μ is the beam microdivergence, and $I_m = \beta\gamma(A/Z)M_p c^3/e$ is the Alfvén current. Typically net currents of about 50 kA are needed for LIF beams, and somewhat smaller net currents are needed for pre-stripped HIF beams.

The strategy for LIF is to note that for typical LMF parameters only $\sim 2\%$ net

currents are needed for self-pinch transport. Since many parameters control the net current (beam radius, total current, ion species, gas type, gas pressure, etc.), it is conceivable that self-pinch transport may work. Past work at LLNL, LBL, SNL, and NRL has always indicated that gas breakdown is too good in the 1 Torr regime and that net currents are too small for self-pinch transport for LIF or HIF. However, by going to lower pressures, and/or by using a special laser preformed plasma, sufficiently large net currents may be achievable.

Recent IPROP simulations with protons indicate that sizeable net currents should be achievable[10]. As the beam intensity increases ($50 \rightarrow 500$ kA, $3 \rightarrow 0.75$ cm radius) and the pressure decreases below 1 Torr, IPROP simulations show a trend toward higher net current fractions in the range of 1–12%. A different self-pinch transport scheme uses a preformed annular plasma (with inner radius about equal to the beam radius) in < 0.1 Torr gas. For a 50 kA, 45 MeV proton beam in 0.001–0.1 Torr nitrogen, IPROP simulations predict net current fractions of 10–40% for this annular plasma transport scheme. These preliminary results are encouraging.

5. – Conclusions.

Gas breakdown research has produced the following results of importance to both LIF and HIF:

1) Charge neutralization of beam micro clumps will be limited to finite values of ϕ_{\min} , which can lead to divergence growth and axial energy spreading. At pressures ≥ 1 Torr, plasma shielding should substantially reduce this effect.

2) Current neutralization for beam injection into neutral gas has been studied in the GAMBLE II experiments. The importance of fast electrons (knock-ons and runaways) has been established in IPROP simulations, which are in agreement with the experiments. For LIF parameters with pressures ≥ 1 Torr, very small net current fractions ($\ll 1\%$) appear feasible, permitting ballistic transport in gas.

3) Self-pinch transport requires higher net current fractions ($\geq 2\%$) and preliminary IPROP code results indicate that these appear achievable for small-radius intense beams in lower-pressure gases (≤ 1 Torr). Several self-pinch transport concepts look promising.

REFERENCES

- [1] C. L. OLSON: *J. Fusion Energy*, 1, 309 (1982).
- [2] P. F. OTTINGER, D. V. ROSE, J. M. NERI and C. L. OLSON: *J. Appl. Phys.*, 72, 395 (1992).
- [3] F. YOUNG, D. D. HINSHELWOOD, R. F. HUBBARD, M. LAMPE, J. M. NERI, C. L. OLSON, P. F. OTTINGER, D. V. ROSE, S. P. SLINKER, S. J. STEPHANAKIS and D. R. WELCH: *Phys. Rev. Lett.*, 70, 2573 (1993).
- [4] C. L. OLSON and J. W. POUEY: *Proceedings of the IX International Conference on High-Power Particle Beams Washington, D.C., May 25-29, 1992*, p. 897 (1993).
- [5] J. W. POUEY: SNL Report SAND80-2545 (1980); J. W. POUEY, J. P. QUINTENZ and C. L. OLSON: *J. Appl. Phys.*, 52, 3016 (1981).
- [6] P. D. STROUD: *Laser Part. Beams*, 4, 230 (1986).

- [7] C. L. OLSON: *Proceedings of the 1990 Linear Accelerator Conference, Albuquerque, N.M., September 10-14, 1990*, p. 396 (1991); J. A. SWEGLE and S. A. SLUTZ: *J. Appl. Phys.*, 60, 3444 (1986).
- [8] B. B. GODFREY and D. R. WELCH: *Proceedings of the XII Conference on Numerical Simulation of Plasmas, San Francisco, Cal., 1987*, paper CM1.
- [9] R. F. HUBBARD *et al.*: NRL Memorandum Report No. 7112, 1992.
- [10] D. WELCH: *Proceedings of the 1993 Particle Accelerator Conference, Washington, D.C., May 17-20, 1993*, paper Pa 123.

Evolution of a Maxwellian plasma driven by ion-beam-induced ionization of a gas

*B.V. Oliver**, *P.F. Ottinger*, and *D.V. Rose†*

Plasma Physics Division, Naval Research Laboratory, Washington D.C. 20375

Abstract

The ionization of gas by intense (MeV, kA/cm²) ion beams is investigated for the purpose of obtaining scaling relations for the rate of rise of the electron density, temperature, and conductivity of the resulting plasma. Various gases including He, N, and Ar at pressures of order 1 torr have been studied. The model is local and assumes a drifting Maxwellian electron distribution. In the limit that the beam to gas density ratio is small, the initial stage of ionization occurs on the beam impact ionization time and lasts on the order of a few nanoseconds. Thereafter, ionization of neutrals by the thermal electrons dominates electron production. The electron density does not grow exponentially, but proceeds linearly on a fast time-scale $t_{th} = U/(v_b \rho \, dE/dx)$ associated with the time taken for the beam to deposit energy U into the plasma electrons, where U is the ionization potential of the gas, ρ is the gas mass density, dE/dx is the stopping power, and v_b is the beam velocity. This results in a temperature with a logarithmically decreasing time dependence and a conductivity with a linear rise-time proportional to t_{th} .

PACS numbers: 52.25.Jm, 41.75.-i, 52.40.Mj

*National Research Council Associate at NRL

†JAYCOR, Vienna, VA.

I. INTRODUCTION

The transport of intense ion beams with currents near or above the Alfvén current requires charge and current neutralization. This is typically achieved by propagating in gas or a pre-formed plasma. For propagation in gas, provided the gas density is larger than the beam density, rapid ionization by the beam head is sufficient for charge neutralization, but not necessarily current neutralization. The degree to which current neutrality is achieved is a function of the risetime of the local plasma conductivity, which in turn is a function of the electron density and temperature. It is important then, to understand how gas ionization scales with the gas and beam parameters so that appropriate environments can be chosen for systems which need complete current neutrality (e.g., ballistic transport) or for those which rely on collective effects where partial neutralization is desired (e.g., self-pinched transport).

The physics of gas breakdown by charged particle beams is an active area of research. Among the many publications, experimental studies of plasma production and neutralization for electron beam transport in gas have been reported by Hammer and Rostoker [1], Miller and Gerardo [2,3], Stallings and Schneider [4], and Haan *et al.* [5]. Theoretical modeling by Swain [6], Olson [7], and Iyyengar *et al.* [8–10] are also of note. More recently work by Gladyshev, *et al.* [11] and Sanford *et al.* [12] have been reported.

Ion-beam-induced breakdown studies by Swegle and Slutz [13], Olson and Welch [14,15], Hubbard *et al.* [16] and Young *et al.* [17,18], have been conducted in the context of ion beam driven inertial confinement fusion (ICF). Various schemes including ballistic transport and solenoidal lens focusing [19,20], wire-guided transport [21], self-pinched transport [22,23], and z-discharge transport [24,25] will rely on background plasma to maintain partial if not complete neutrality. Although empirical studies and modeling have been presented, analytic scaling relations for the plasma temperature and density with respect to beam and gas parameters have yet to be developed and is, therefore, the subject of this paper. The results should find application to electron, as well as ion beam propagation in gas.

In experiments at the Naval Research Laboratory (NRL) [17], net current and plasma

electron inventory were measured on the Gamble II accelerator with 1 MeV, 1 kA/cm² proton beams impinging various gases in the 0.25 - 4 torr pressure regime. The measured net-current fractions outside the beam envelope were within 2% to 8% and ionization fractions within the beam envelope were within 0.6% to 5%. Plasma production with similar beam and gas parameters is studied here. In particular, attention is paid to systems with a low amount of ionization and a low degree of beam energy loss. In this case various simplifying assumptions can be made and yet the essential physics of ionization can be maintained such that scaling to relevant ICF parameters is possible.

For the above parameters, the beam velocity and density are $v_b \sim 10^9$ cm/s and $n_b \sim 3 \times 10^{12}$ cm⁻³, respectively. At these energies and densities, beam energy loss per unit distance traveled is small (< 50 eV/cm) and one can consider the beam impact parameters to remain constant throughout the pulse duration. On the other hand, plasma electron densities and temperatures are changing on timescales associated with the instantaneous, time dependent collision frequencies.

For 10% ionization of 1 torr He with an electron temperature $T_e \sim 10$ eV the characteristic collision frequencies are $\sim 10^9$ s⁻¹ and the thermal equilibration time between electrons and ions is approximately 1 μ s. Since beam pulselengths are only ~ 40 ns, it is expected that the energy deposited in the gas will be absorbed primarily by ionization of gas neutrals and stopping by the free electrons; the neutral gas and plasma ions should remain cold. In this case, only the plasma electrons obtain enough energy, along with the injected beam ions, to contribute to ionization.

In a classical model of impact ionization, the interaction between the bombarding particle and the target particle is described in terms of binary Coulomb collisions [26]. The maximum cross-section for ionization occurs for velocities of the impact particle which are close to the velocities of the orbital electrons of the target atom. For 1 MeV protons impinging He, the beam energy E_b satisfies $E_b \gg MU/m$, where U is the first ionization potential (~ 25 eV for He) and m and M are the electron and beam ion masses, respectively. In this case, once a sufficient population of thermal electrons is created they become more efficient at

ionization than the beam ions because their velocities are more closely in resonance with those of the bound electrons. The time rate of change of the electron density primarily becomes a function of the electron temperature. The beam provides the free energy to heat the plasma electrons to temperatures sufficient for ionization.

During breakdown the electrons can drive an "avalanche" since their contribution to the continued ionization of the gas results in exponential growth of the electron population [27]. Exponential growth is only possible, however, when the electron ionization frequency is constant in time. This is generally not the case since the cross-section is a function of the energy distribution. For a Maxwellian plasma the distribution is a function of the temperature and, therefore, temporal evolution of the collision frequency is determined in part by the time dependence of the temperature. Indeed, it is found that for a low degree of ionization such that the electron (n_e) to neutral gas (n_0) density ratio satisfies $n_e/n_0 \ll 1$, the ionization frequency decreases nearly proportional to $1/t$, resulting in a density which increases nearly linear in time. This in turn results in a plasma conductivity growth which is also secular.

In Sec. II, a generic model of gas breakdown is presented which is similar to previous models [6-8,14]. We are primarily concerned with systems where the beam density satisfies $n_b \ll n_0$ such that, for the times of interest, a relatively low degree of ionization occurs and only ground state ionization of the gas is modeled. In Sec. III, truncations of the model equations and scalings for the electron temperature and density evolution are presented. The results are then used to predict the behavior of the conductivity and estimate net currents in Sec. IV. A summary of the analytic relations and a discussion with respect to ion-beam transport experiments is presented in Sec. V. In addition, a comparison of the analytic results to numerical integration of the model equations is also included. Conclusions are presented in Sec. VI.

II. MODEL EQUATIONS

As mentioned in the introduction, for systems with a low degree of ionization ($n_e/n_0 \ll 1$), beam parameters can be assumed constant and only the first ionization state of the gas need be considered. In this instance, the plasma electrons remain cool ($T_e < U$) and effects due to thermal radiation, recombination, and multiple ionization are negligible. A qualitative discussion of expected trends when a high degree of ionization occurs is presented in Sec. VI. The ion beam is assumed to be monoenergetic with constant density and to enter the gas charge and current neutral. Only impact ionization by the beam and the background electrons is modeled. The assumption of neutrality frees us from having to consider the early acceleration of electrons due to space-charge effects and inductive electric fields. It is expected that at the diode where the beam is generated, sufficient co-moving electrons (driven by just such fields) will be drawn from the surrounding walls into the beam region and provide this neutrality. Additionally, the results presented here are valid for beams with time dependent parameters (e.g., energy and current) when the time rate of change is slow compared to the timescales of ionization. This is almost always the case since ionization occurs on a nanosecond timescale and beam pulselengths are an order of magnitude longer.

The rate equation for the electron density is

$$\frac{dn_e}{dt} = \frac{n_e}{t_e} + \frac{n_b}{t_b}, \quad (1)$$

where,

$$\frac{1}{t_e} = (n_0 - n_e) \langle v_e \sigma_e \rangle, \quad (2a)$$

$$\frac{1}{t_b} = (n_0 - n_e) v_b \sigma_b. \quad (2b)$$

The subscripts e and b refer to the electron and beam ions respectively. The coefficients $t_{e,b}$ are the ionization times and are a function of the cross-sections for ionization $\sigma_{e,b}$, the velocity of the ionizing species $v_{e,b}$, and the background neutral population $(n_0 - n_e(t))$. Here, n_0 is the initial gas density. The symbol $\langle \dots \rangle$ denotes the ensemble average over

the electron distribution which is assumed to be a drifting Maxwellian of temperature T_e with

$$f_e(\mathbf{v}_e) = \left(\frac{m}{2\pi T_e}\right)^{3/2} \exp\left(-\frac{m}{2T_e}(\mathbf{v}_e - \mathbf{v}_d)^2\right), \quad (3)$$

where the drift velocity $\mathbf{v}_d = Zn_b v_b \hat{\mathbf{z}}/n_e$ is obtained from the assumption of current neutral propagation. The beam is injected in the $\hat{\mathbf{z}}$ direction and Z is the beam ion charge state.

The electron temperature in Eq. (3) is determined by calculating the energy deposited by the beam by integration of the stopping power less that expended in ionization of the gas

$$T_e = \frac{2}{3} \left[\frac{Zn_b}{n_e} \int \rho v_b \frac{dE}{dx} dt - U \left(1 - \frac{n_e(0)}{n_e}\right) \right] \quad (4)$$

where dE/dx (eV cm²/g) is the gas stopping power, ρ (g/cm³) is the gas mass density, and $n_e(0)$ is the initial electron density. The ionization cross-sections σ_e and σ_b are calculated from formulae derived by Gryzinski [26]

$$\sigma_e = \left(\frac{b\pi e^4}{U^2}\right) g_i(E_e/U), \quad (5a)$$

$$\sigma_b = \left(\frac{Z^2 b\pi e^4}{U^2}\right) G_i(mE_b/MU), \quad (5b)$$

where E_e is the bombarding electron energy, e is the electron charge, U is the potential energy for single ionization of the gas, and b is the number of electrons occupying the outer shell of the ground-state atom (e.g., $b = 2$ for He). All quantities are in Gaussian units, except energy which is in units of eV. The functions $g_i(x)$ and $G_i(x)$ are universal functions characterizing the energy dependence of the cross-sections and are defined in Appendix A. A plot of $g_i(E/U)$ for electron ionization is shown in Fig. (1). Both $g_i(x)$ and $G_i(x)$ are similar in structure, rising linearly from 0 at $x = 1$, having a maximum around $x \sim 4$, and decreasing as $\ln(x)/x$ for large x .

For given beam parameters, numerical integration of Eqs. (1)-(5) with the initial conditions $T_e(0) = 0$ and $n_e(0) = Zn_b$ (corresponding to charge neutral injection) gives the temporal evolution of the density and temperature of the electron population. Background plasma ions and neutrals are assumed immobile on the timescales of interest and therefore, do not contribute to electron production.

In general, the coefficient t_e is complicated by the fact that there may exist separate populations of electrons, each having unique cross-sections for interaction. Indeed, hybrid particle in cell simulations [15] have demonstrated the existence of a non-thermal component of electrons traveling at velocities near the beam velocity for a large portion of the beam injection phase. However, their contribution to plasma production is considerably smaller than the cool thermal component (see Fig. 1). This is due to their decreased cross-section at higher velocities and their low density. Their role is primarily important in the ionization of gas away from the beam since their mean free path is substantially greater (~ 1 cm) than the thermal electrons. This creates plasma and therefore the possibility of current paths outside of the beam envelope. *Albeit* important, such non-local behavior is beyond the scope of this paper and is not addressed.

III. DENSITY AND TEMPERATURE EVOLUTION

The large number of beam and gas parameters make it difficult to obtain scaling relations for the temporal evolution from numerical integration of Eqs. (1)-(5). It is useful to consider truncations of the model equations to develop a more thorough understanding of the dynamics. First, the initial stage is considered where beam ions and co-moving electrons contribute to ionization. Then, ionization driven by the thermal electrons is considered.

A. Initial ionization by beam ions and co-moving electrons

In the very early stages of ionization the ionization fraction is low enough that $n_b \leq n_e \ll n_0$. The plasma is very cool and only the beam ions and co-moving current neutralizing electrons contribute to the ionization. For beam (electron) energies satisfying $E_b \gg MU/m$ ($E_e \gg U$) the ionization cross-sections defined in Eqs.(5) are approximately

$$\sigma_e \approx \frac{5b\pi e^4}{3U^2} \frac{U}{E_e}, \quad \text{for } E_e \gg U, \quad (6a)$$

$$\sigma_b \approx \frac{5Z^2b\pi e^4}{3U^2} \frac{MU}{mE_b}, \quad \text{for } mE_b \gg MU. \quad (6b)$$

In determining the expressions (6), the energy dependent part of the $\ln(x)$ terms in the functions $g_i(x)$ and $G_i(x)$ (see Eqs. (A2) and (A4)) have been neglected since they do not greatly affect the physics and it allows for a less complicated analysis. However, their contribution has been considered and a brief discussion is presented following Eq. (11).

The electron drift velocity $v_d = Zn_b v_b / n_e \gg \sqrt{T_e/m}$ and the ionization frequencies in Eqs. (2) become

$$\frac{1}{t_e} \simeq \frac{n_0 \sigma_b v_b}{Z^2} \left(\frac{n_e}{Zn_b} \right), \quad (7a)$$

$$\frac{1}{t_b} \simeq n_0 \sigma_b v_b. \quad (7b)$$

The electron energy $E_e = mv_d^2/2 = m(Zn_b v_b / n_e)^2/2$ has been used to determine σ_e in Eq. (6a) and the beam ionization frequency t_b is assumed constant. Normalizing the density and time as $n = n_e / Zn_b$ and $\tau = t/t_b$ and substituting Eqs. (7) into Eq. (1), the electron density evolves according to

$$\frac{dn}{d\tau} = \frac{1}{Z^2} n^2 + 1, \quad (8)$$

with solution

$$n(\tau) = \frac{1 + Z \tan(\tau/Z)}{1 - \frac{1}{Z} \tan(\tau/Z)}, \quad (9)$$

for the initial condition $n(0) = 1$. Equation (9) demonstrates a very rapid production of electrons on the beam impact time t_b .

The evolution governed by Eq. (8) is only valid for times when the electron kinetic energy is greater than U , implying that the solution (9) only applies for

$$n_e \leq Zn_b \sqrt{\beta}, \quad (10)$$

or equivalently for times

$$t < t_b Z \arctan \left(\frac{Z\sqrt{\beta} - Z}{Z^2 + \sqrt{\beta}} \right). \quad (11)$$

The parameter $\beta = (mE_b/MU)$ is a measure of the beam injection velocity relative to the orbital velocity of the bound electron in the gas. For injection into various gases (e.g. He,

N, and Ar), β ranges from ~ 30 for 1 MeV protons to ~ 100 for 30 MeV Li^{+3} ions. The arctangent function multiplying t_b in Eq. (11) will have a range from $0.6 \rightarrow 1.0$ and is therefore relatively insensitive to the beam and gas parameters.

One can show that by retaining the logarithmic terms in σ_e from Eqs. (2) and (A4), the functional multiplying t_b in Eq. (11) has a $\ln(\sqrt{\beta})$ dependence, making its scaling with β even weaker than the arctangent function. It is concluded then, that, even with more accurate truncations of the cross-sections $\sigma_{e,b}$, the very initial stages of ionization will last for a time $t \simeq t_b$ and will produce a density $n_e \simeq Zn_b\sqrt{\beta}$. Similar arguments have been presented by Olson [14]. After a time t_b , continued ionization is primarily accomplished by electrons in the tails of the thermal distribution.

B. Ionization by the thermal electrons

Once the electron density is larger than the beam density by the factor $\sqrt{\beta}$, the electron drift energy $mv_d^2/2$ is small and rapidly decreases below the background temperature T_e . In the limit $v_d \ll (T_e/m)^{1/2}$ the electron ionization frequency (2a) becomes

$$\frac{1}{t_e} = \frac{\gamma}{t_b} \left(1 - f \frac{n_e}{Zn_b} \right); \quad (12)$$

where

$$\gamma(\tau) = \frac{3}{Z^2} \frac{(\beta T_e / \pi U)^{1/2}}{6.0 + T_e / U} \exp\left(-\frac{U}{T_e}\right), \quad (13a)$$

$$\frac{T_e}{U} = \frac{2}{3} \left(\frac{t_b}{t_{th}} \frac{\tau}{n} + \frac{n(0)}{n} - 1 \right), \quad (13b)$$

$$t_{th} = U / (v_b \rho \, dE/dx). \quad (13c)$$

Here, $f = Zn_b/n_0$ is the ratio of the beam-charge to initial-neutral density and the thermal time t_{th} is the time it takes the beam to dump energy equal to the ionization potential into the gas. For the parameters assumed in this work $f \ll 1$. The weighting function for thermal electron induced ionization $\gamma(\tau)$, is obtained by considering an approximate form of Gryzinski's ionization cross-section [28] and integrating $\langle v_e \sigma_e \rangle$ over the Maxwellian

distribution in the limit $(T_e/m)^{1/2} \gg v_d$. Equation (13b) is obtained from integration of Eq. (4), assuming dE/dx , n_b , and v_b remain constant throughout propagation. Substituting Eq. (12) into Eq. (1) yields

$$\frac{dn}{d\tau} = \gamma(1 - fn)n - fn + 1, \quad (14)$$

for the normalized variables. The first term on the right hand side (rhs) is the contribution from ionization by the thermal electrons, the other terms are the beam contribution. Solutions are obtained for different cases.

1. Solutions for constant γ

For a constant value of the function γ , closed form solutions to Eq. (14) are easily obtained. For the initial condition $n(0) = \sqrt{\beta}$, corresponding to the time after the initial ionization phase

$$n(\tau) = \frac{\sqrt{\beta} \left(\gamma + f - (f - \gamma) \tanh\left(\frac{\gamma+f}{2}\tau\right) \right) + 2 \tanh\left(\frac{\gamma+f}{2}\tau\right)}{\left(\gamma + f + (f - \gamma + 2\gamma f \sqrt{\beta}) \tanh\left(\frac{\gamma+f}{2}\tau\right) \right)}. \quad (15)$$

The asymptotic solution of Eq. (15) results in $n \rightarrow 1/f$ on a timescale $t > 2t_b/(\gamma + f)$.

In the limit $[\gamma, (4\beta)^{-1/2}] \gg f$, the solution (15) becomes

$$n(\tau) = \left(\sqrt{\beta} + \frac{1}{\gamma} \right) \exp(\gamma\tau) - \frac{1}{\gamma}, \quad (16)$$

which demonstrates exponential growth on a timescale $t = t_b/\gamma$. The limit $f \rightarrow 0$ implies an infinite supply of neutral atoms for ionization. Hence, electron growth can proceed unimpeded on a timescale established by the temperature. Note that in the limit $\gamma > 1$, the effect of beam impact ionization is negligible.

Figure 2 shows γ/κ vs T_e/U , where $\kappa = (3/Z^2)(\beta/\pi)^{1/2}$. The maximum value at $T_e/U = 10$ corresponds to a value of $\gamma_{max} = 0.175\kappa$. For β in the range $30 \rightarrow 100$, the maximum growth rate will not exceed $\sim (1.5/Z^2 t_b)$ and in general will be much lower since we are concerned with situations where $T_e/U < 1$.

In the opposite limit, $[f, (4\beta)^{-1/2}] \gg \gamma$, Eq. (15) is completely determined by beam impact ionization:

$$n(\tau) = (\sqrt{\beta} - \frac{1}{f}) \exp(-f\tau) + \frac{1}{f}. \quad (17)$$

In this case, the electron density approaches n_0 on the timescale $t = (n_0/Zn_b)t_b$ and will grow approximately as $n_e = Zn_b t/t_b$ until such time.

For beam injection into 1 torr of gas, $f = Zn_b/n_0$ will typically be of order $\sim 10^{-4}$. According to Sec. III A, directly after the initial ionization phase $n \sim \sqrt{\beta}$ and $\tau \sim 1$ which implies an initial temperature

$$\frac{T_e(1)}{U} = \frac{2}{3} \left(\frac{t_b}{\sqrt{\beta}t_{th}} + \frac{1}{\sqrt{\beta}} - 1 \right).$$

The ratio (t_b/t_{th}) is only a function of the gas parameters and for He, N, and Ar is in the range $8 < t_b/t_{th} < 15$. For $\beta = 30$, the temperature after the initial ionization will be of order U and γ will be approximately $\simeq 0.5$, which satisfies $\gamma \gg f$. Thus, the electron density should first proceed in a manner similar to that described by the solution (16). In this case, according to Eq. (13b) the temperature will decrease as

$$\frac{T_e}{U} \simeq \frac{2}{3} \left(\frac{t_b/t_{th}}{\sqrt{\beta} \exp(0.5\tau)} - 1 \right).$$

However, according to Eq.(13), if γ is assumed to remain constant at ~ 0.5 , it will only take a time δt satisfying

$$\frac{\delta t}{t_b} \exp(-0.5(\delta t)/t_b) \simeq \frac{t_{th}}{t_b} \sqrt{\beta}$$

for the electron temperature to drop near zero, such that γ becomes less than f . Beam injection into He, for example, with $\beta = 30$ yields a value for $t_{th}\sqrt{\beta}/t_b$ of $\simeq 0.7$. This implies that within a time $\delta t \simeq 1.4t_b$, γ will have decreased more than three orders of magnitude from ~ 0.5 to 10^{-4} . According to Eq. (13a) and Fig. (2), this also implies a temperature drop from $T_e \sim U$ to $T_e \sim U/10$. The rapid change in γ on the timescale t_b justifies a time-dependent treatment of Eq. (14).

2. Solutions with time dependent γ

In the limit $n \ll 1/f$, the term fn in the electron contribution to Eq. (14) can be neglected and the formal solution to Eq. (14) is

$$n(\tau) = \int_0^\tau dt \exp[\lambda(\tau) - \lambda(t)] + n(0) \exp[\lambda(\tau)], \quad (18)$$

where

$$\lambda(\tau) = \int_0^\tau dt [\gamma(t) - f],$$

and $\gamma(\tau)$ is defined in Eq. (13a). The form of the solution given in Eq. (18) is misleading. Although $\gamma(\tau)$ depends explicitly on time, it depends implicitly on the density through the temperature. Hence, Eq. (14) is nonlinear in the variable n even in the limit $n \ll 1/f$. Substituting Eq. (18) into Eq. (13b) for the temperature, results in an inhomogeneous, integral (Volterra) equation for $\lambda(\tau)$:

$$\int_0^\tau dt \exp[-\lambda(t)] + n(0) = \frac{\alpha\tau + n(0)}{\mathcal{C}(\tau)} \exp[-\lambda(\tau)], \quad (19)$$

where

$$\mathcal{C}(\tau) = \frac{3}{2} \frac{T_e}{U} + 1, \quad (20a)$$

$$\alpha = \frac{t_b}{t_{th}}. \quad (20b)$$

The coefficient α generally satisfies $\alpha \gg 1$. The function $\mathcal{C}(\tau)$ is bounded below by $\mathcal{C}(\tau) > 1.0$ since the plasma temperature cannot become less than zero. One also expects $\mathcal{C}(\tau) < 2.5$ since for a low degree of ionization, the temperature should satisfy $T_e/U < 1$. Making the *ansatz* that $\mathcal{C}(\tau)$ varies adiabatically such that $(\tau \dot{\mathcal{C}}/\mathcal{C}) \ll 1$, Eq. (19) is then integrable and yields

$$\lambda(\tau) = \ln[(\alpha\tau + n(0))^{(1-\mathcal{C}/\alpha)}] - \ln[n(0)]. \quad (21)$$

Substituting Eq. (21) into Eq. (18) yields

$$\gamma(\tau) = \frac{\alpha - \mathcal{C}}{\alpha\tau + n(0)} + f, \quad (22a)$$

$$n(\tau) = \frac{\alpha\tau + n(0)}{\mathcal{C}}. \quad (22b)$$

For adiabatic variations of $\mathcal{C}(\tau)$, n grows linearly in time with slope $(\alpha/\mathcal{C}) = (t_b/Ct_{th}) \gg 1$. The electron distribution adjusts itself such that when the beam deposits energy U into the gas via collisional stopping, a neutral atom is ionized.

According to Eq. (22) and the definition of γ given in Eq. (13a), the temperature must satisfy

$$\frac{(\alpha - 3T_e/2U - 1)(6.0 + T_e/U)}{\kappa(T_e/U)^{1/2} \exp[-U/T_e] - f(6.0 + T_e/U)} = \alpha\tau + n(0). \quad (23)$$

In the limits $f \ll T_e/U < 1$ and $\alpha \gg 1$, a rough estimate of $T_e(\tau)$ yields

$$T_e(\tau) \simeq \frac{U}{\ln[\kappa(\alpha\tau + n(0))/6\alpha]}. \quad (24)$$

A check on the accuracy of the adiabatic assumption for $\mathcal{C}(\tau)$ is obtained from T_e with

$$\left| \frac{\tau \dot{\mathcal{C}}}{\mathcal{C}} \right| = \frac{3/2}{(\ln[\kappa(\alpha\tau + n(0))/6\alpha])^2 + 3/2 \ln[\kappa(\alpha\tau + n(0))/6\alpha]} \ll 1,$$

which is satisfied for $\tau \gg (6/\kappa)$. For the parameters of interest $6/\kappa < 1$.

In the static solution given in Eq. (15), the density begins to asymptote to its maximum value around $n = 1/2f$. At such time, electron production slows down and the temperature begins to rise. Assuming evolution close to that described by Eq. (22), one can estimate a minimum temperature at the time $\alpha\tau + n(0) = \mathcal{C}/2f$ from Eq. (24) and the definition of \mathcal{C} . Expanding the logarithmic terms in the variable T_e/U yields

$$\left. \frac{T_e}{U} \right|_{min} \simeq \frac{1}{3} \ln[\kappa/12\alpha f] \left(\left(1 + \frac{6}{(\ln[\kappa/12\alpha f])^2} \right)^{1/2} - 1 \right). \quad (25)$$

Table I gives values of the important time constants t_b and t_{th} and minimum temperatures for various gases at pressures of 1 torr. The values are calculated assuming injection of a Gamble II parameter beam (1 MeV, 1.2 kA/cm², protons). Also presented are the corresponding times for injection of an ICF parameter beam (30 MeV, 5 kA/cm², Li⁺³) into 1

torr He. Helium gas fill has been chosen for ICF since it minimizes beam/gas scattering and thus reduces beam emittance growth. It is observed that $(T_e/U)_{min} \simeq 0.15$ for the various gases and pressures. The temperature scales weakly with the density and stopping power of the gas and is primarily determined by the ionization potential. Note that the Gamble II ionization times for injection into Ar are similar to injection of the ICF beam into He.

Interestingly, the result given in Eq. (22) could have been obtained by assuming unconstrained evolution of n and minimizing the energy density such that

$$\frac{d}{dt}\left(\frac{3}{2}nT_e\right) = \frac{3}{2}\left(\frac{\partial}{\partial t} + \frac{dn}{dt}\frac{\partial}{\partial n}\right)nT_e = 0.$$

In which case, upon substitution of $3nT_e/2$ from Eq. (13), one finds that n must satisfy Eq. (22) with $C = 1$. Hence, although the density must rigorously obey Eq. (14), because systems are considered where $n_b \ll n_0$, there is essentially an unlimited supply of neutrals available for ionization and the electron dynamics are not constrained. This continues until their population approaches the available neutral population.

IV. PLASMA CONDUCTIVITY AND NET CURRENTS

For classical diffusion in a homogeneous, isotropic plasma, the net current is determined by the scalar resistivity η [29]

$$\eta = \frac{c^2 m (\nu_{en} + \nu_{ei})}{4\pi e^2 n_e}. \quad (26)$$

The electron collision frequency is a combination of elastic scattering with gas neutrals ν_{en} and Coulomb collisions with ions ν_{ei} where

$$\nu_{en} = (n_0 - n_e) 1.2 \times 10^{-6} \sigma_n \left(\frac{T_e}{m}\right)^{1/2}, \quad (27a)$$

$$\nu_{ei} = 2.9 \times 10^{-6} \Lambda n_e T_e^{-3/2}, \quad (27b)$$

and σ_n is the neutral collision cross-section (typically of order $5 \times 10^{-16} \text{ cm}^2$), Λ is the Coulomb logarithm, c is the speed of light, and again T_e is in units of eV. The inelastic

component of electron neutral scattering is neglected in Eq. (26) since, according to Eqs. (12) and (22) in the limit $f \ll 1$, the electron ionization frequency satisfies

$$1/t_e \simeq \frac{\alpha - \mathcal{C}}{\alpha t + t_b}, \quad (28)$$

which, after a couple nanoseconds and typical values of α , is much smaller than either ν_{en} or ν_{ei} .

When the conditions of Sec. III are valid, the electron temperature evolves slowly and is nearly constant (of order U) and the electron density n_e evolves linearly, with time constant t_{th} . For a very low degree of ionization (less than 1%), the electron neutral collision frequency ν_{en} dominates. In this case, the resistivity decreases with time proportional to t_{th}/t since $\nu_{en} \simeq n_0 \langle \sigma_n v_e \rangle$ is constant for constant temperature. For 1% ionization of 1 torr He, the temperature will be ~ 8 eV and $\nu_{en} \sim 3 \times 10^9 \text{ s}^{-1}$. However, once the electron density is large such that $\nu_{ei} > \nu_{en}$, the collisionality will be density dependent and hence, the resistivity should asymptote to a value determined by the temperature. The cross-over from neutral to Coulomb dominated collisions occurs when the electron density becomes larger than a critical density n_{ec} satisfying

$$\frac{n_{ec}}{(n_0 - n_{ec})} = 0.41 \frac{\sigma_n T_e^2}{\Lambda \sqrt{m}}. \quad (29)$$

For ionization of He, the critical density is $(n_{ec}/n_0) = 0.04$, and for Ar $(n_{ec}/n_0) = 0.017$.

From the definitions (26) and (27), the resistivity as a function of density can be rewritten as

$$\eta(t) = 2.9 \times 10^{-6} \frac{\Lambda c^2 m}{4\pi e^2 T_e^{3/2}} \left[1 + \frac{(n_0 - n_e)}{n_e} \frac{0.41 \sigma_n T_e^2}{\Lambda \sqrt{m}} \right]. \quad (30)$$

If the evolution of n_e is determined by Eq. (22) then the resistivity evolves according to

$$\eta(t) = \eta_0 \left(1 - \frac{n_{ec}}{n_0} + \frac{n_{ec} \mathcal{C}}{Z n_b} (n_e(0)/Z n_b + t/t_{th})^{-1} \right) \quad (31)$$

where $\eta_0 \equiv (2.9 \times 10^{-6} \Lambda c^2 m / 4\pi e^2 T_e^{3/2})$. The resistivity decreases at the rate

$$t_r = \left(\frac{n_{ec} \mathcal{C}}{Z n_b} \right) t_{th}.$$

The initial value of the resistivity satisfies $\eta_i = \eta(0) > \eta_0$.

The net current (beam plus plasma) is related to the magnetic field via Ampere's law. If the plasma is resistive and currents are only carried by the electrons then for a one dimensional Cartesian system, diffusion of the \hat{y} component of the magnetic field satisfies

$$\frac{\partial B_y}{\partial t} - \eta(t) \frac{\partial^2 B_y}{\partial x^2} = \eta(t) \frac{\partial j_{bz}}{\partial x}, \quad (32)$$

where j_{bz} is the \hat{z} component of beam current density. The time dependent solution to the Fourier transformed field \tilde{B}_y is

$$\tilde{B}_y(k, t) = -\frac{i}{k} \int_0^t dt' \eta(t') \tilde{j}_{bz}(k, t') \exp(k^2[\zeta(t') - \zeta(t)]), \quad (33)$$

where

$$\zeta(t) = \int_0^t dt' \eta(t') = \eta_0 t \left((1 - (n_{ec}/n_0) + \frac{C n_{ec} t_{th}}{Z n_b t} \ln(\frac{Z n_b t}{n_e(0) t_{th}} + 1) \right),$$

k is the transform variable, and it is evident that $B_y(k, 0) = 0$ in accordance with the assumption of current neutral beam injection. For a beam current density of the form

$$\tilde{j}_{bz}(k, t) = \tilde{j}_{bz}(k) \Theta(t) \quad \text{for } t < t_p,$$

where $\Theta(t)$ is the step function, the solution to Eq. (33) is

$$\tilde{B}_y(k, t) = -\frac{i \tilde{j}_{bz}}{k^3} (1 - \exp[-k^2 \zeta(t)]) \quad \text{for } t < t_p. \quad (34)$$

Three parameters determine the net field characteristics. These include the initial and asymptotic values of the resistivity, η_i and η_0 respectively, and the rate of decrease of η (determined by t_r) relative to the beam pulselength t_p . For a beam with transverse dimension $k \sim \pi/a$, the asymptotic diffusion time $t_d \equiv (a^2/4\eta_0)$ is determined by the asymptotic temperature, the initial diffusion time $t_o \equiv a^2/4\eta_i$ is determined by the initial temperature and the ratio of the beam to critical electron density $Z n_b/n_{ec}$, and the rate of decrease of η is determined by t_{th} and $Z n_b/n_{ec}$. To limit net currents to very small values, it is necessary to satisfy $t_r \ll t_p \ll t_d$ and therefore have the conductivity rise as quickly as possible, to

as high a value as possible. Since the plasma temperature is nearly a linear function of the ionization potential and most gases have first ionization potentials which lie within the range $13 \text{ eV} < U < 25 \text{ eV}$, the asymptotic value η_0 will not vary much with gas species. On the other hand, according to Eq. (29), gases like Ar should reach the asymptotic values of η more rapidly than gases like He since less ionization is needed and the thermal ionization time t_{th} is faster. Thus, a choice of gas with a maximum stopping power for given ionization potential energy (i.e., t_{th} is a minimum) is desired in order to increase the rise time t_r to as large a value as possible. A plot of \tilde{B}_y from Eq. (34) for a beam propagating through 1 torr of gas is shown in Fig. 3. The two different curves represent propagation in He and Ar. The corresponding times of t_o , t_r , and t_d for the different gases are given in Table II for injection of a Gamble II parameter beam (1 MeV, 1.2 kA/cm², protons) and for injection of an ICF parameter beam (30 MeV, 5 kA/cm², Li⁺³).

V. DISCUSSION

A summary of the scaling relations derived in Sec. III and a comparison of the theory to numerical integration of the model equations are presented and application of the results to specific NRL Gamble II proton beam experiments and light ion driven ICF scenarios are given.

A. Scaling relations

In the initial stages of ionization, both the beam ions and co-moving electrons contribute to ionization. In a time $t \sim t_b = (n_0 \sigma_b v_b)^{-1}$, electron densities of order

$$n_e \simeq Z n_b \beta^{1/2} = Z n_b (m E_b / M U)^{1/2} \quad (35)$$

will be produced. When $\beta \gg 1$ the beam ionization cross-section σ_b is given by Eq. (6b) such that t_b scales as

$$\begin{aligned}
t_b &= \left[1.3 \times 10^{-6} \frac{5\pi e^4}{3m} \frac{Z^2 n_0 b}{U} \left(\frac{2M}{E_b} \right)^{1/2} \right]^{-1} \\
&= \left[2.1 \times 10^8 \left(\frac{Z^2 n_0 b}{U} \right) \left(\frac{M}{E_b} \right)^{1/2} \right]^{-1}.
\end{aligned} \tag{36}$$

For a 1.0 MeV proton beam impinging 1 torr He gas, the beam impact time $t_b \simeq 1.5$ ns and $(\beta)^{1/2} \simeq 5$. Hence, within a couple nanoseconds the plasma electron density will be five times the beam density. For light-ion driven ICF beam parameters of 30 MeV, Li^{+3} ions, $t_b = 0.3$ ns and $(\beta)^{1/2} \sim 10$ in 1 torr He. After 0.3 ns, $n_e \simeq 30n_b$.

The primary contribution to electron production follows the initial stage and results from ionization by the background thermal electrons. Growth is not exponential but proceeds nearly linear with time as $n_e = Zn_b (t/t_{th}C)$, where t_{th} is defined in Eq. (13c). Because $C(t)$ scales weakly with the parameters β and t_b (see Eqs. (20a) and (24)), the rate of electron production following the initial stage (i.e., for $t > t_b$), scales as

$$\frac{dn_e}{dt} \propto Zn_b \frac{v_b \rho dE/dx}{U}. \tag{37}$$

The electron temperature decreases slowly with a logarithmic time dependence (see Eq. (24)). It is expected to have a minimum value around

$$T_e|_{min} \simeq \frac{U}{\ln[\kappa/12\alpha f]}, \tag{38}$$

where Eq. (25) has been expanded in the limit $6/(\ln[\kappa/12\alpha f])^2 \ll 1$. According to Eqs. (38) and (24), to reach $T_e|_{min}$ will take a time

$$t_{min} \simeq t_b \frac{C(T_{min})}{2\alpha f}. \tag{39}$$

For 1.0 MeV protons impinging 1 torr He, t_{min} is $\simeq 1 \mu\text{s}$. For 30 MeV, Li^{+3} in 1 torr He, $t_{min} \simeq 0.3 \mu\text{s}$. Since the beam pulselength t_p is generally much shorter than t_{min} , one can expect the temperature to evolve according to Eq. (24) throughout the pulse and the temperature to be a fraction of the ionization potential.

If the evolution of the electron return current is determined by classical diffusion as described by Eq. (32), then for a time dependent scalar resistivity, the magnetic fields

generated by the net current (beam plus plasma) can grow secularly in time. When the plasma electron density rises linearly in time, the azimuthal magnetic field evolves as in Eq. (34). When the conditions $(t_p, t_r) \ll t_d$ are satisfied, one can expand Eq. (34) in the small parameter t/t_d to obtain

$$\left| \frac{\tilde{B}_y k^3}{\tilde{j}_{bz}} \right| \simeq \left(1 - \left(1 - \frac{t}{t_d} \right) \left(\frac{t}{\sqrt{\beta} t_{th}} + 1 \right)^{-t_r/t_d} \right), \quad (40)$$

where $t_d = 1/k^2 \eta_0 \simeq a^2/4\eta_0$, $t_r = (n_{ec} C t_{th}/Z n_b)$, and, since the time behavior of $\eta(t)$ is described for times following the initial ionization phase, the initial electron density is approximately $n_e(0) \simeq Z n_b (\beta)^{1/2}$. For times short compared to $\beta^{1/2} t_{th}$ a binomial expansion of Eq. (40) yields

$$\left| \frac{\tilde{B}_y k^3}{\tilde{j}_{bz}} \right| = \frac{t}{t_d} \left(1 + \frac{t_r}{\sqrt{\beta} t_{th}} \right) = \frac{t}{t_d} \left(1 + \frac{n_{ec} C}{n_e(0)} \right) \quad (41)$$

which is equivalent to the early stages of diffusion when the plasma has a resistivity $\eta = \eta_i$. In the limit $t_r/t_d \rightarrow 0$, the field governed by Eq. (40) grows linearly with slope $1/t_d$ which is determined by η_0 and scales as $U^{3/2}$ since T_e is proportional to U (see Eq. (24)).

It proves useful to consider an effective resistivity η_{eff} which is the time averaged resistivity over the beam pulselength

$$\begin{aligned} \eta_{eff} &= \frac{1}{t_p} \int_0^{t_p} \eta(t) dt \\ &= \eta_0 \left(1 + \frac{t_r}{t_p} \ln \left[1 + \frac{t_p}{\epsilon t_r} \right] \right), \end{aligned} \quad (42)$$

where

$$\epsilon = (n_e(0)/n_{ec} C) \quad (43)$$

is the ratio $(n_e(0) t_{th}/Z n_b t_r)$ and is $\sim \sqrt{\beta} t_{th}/t_r$ for $t > t_b$. The parameter ϵ is generally much less than 1 and dependent on both gas and beam parameters. A plot of η_{eff} as a function of t_p/t_r for different values of ϵ is shown in Fig. 4. For beam pulselengths much greater than the time t_r , η_{eff} approaches η_0 . For shorter pulselengths, however, the value of η_{eff}

is approximately given by the initial resistivity (the limit of Eq. (42) for $t_p/t_r \ll 1$) which scales like

$$\eta_{eff} \simeq \eta_i = \frac{\eta_0}{\epsilon}(1 + \epsilon).$$

Hence, in order to reduce net-fields to as small a value as possible, not only does one want $t_r \ll t_p \ll t_d$, but also to have ϵ as large as possible.

B. Numerical examples

The analytic results of Sec. III are compared to numerical integration of equations similar to Eqs. (1) - (5) but which also include physics explicitly assumed negligible in the model equations of Sec. II. In particular, effects due to secondary ionization, ohmic heating, and radiative cooling have been included. A brief outline of the model equations used in the numerical calculation is found in Appendix B. Results are presented for injection of a 1 MeV, 1.2 kA/cm² proton beam into various gases with pressures ranging from 0.25 to 4 torr. For these beam and gas parameters, $n_b = 5.6 \times 10^{12} \text{ cm}^{-3}$ and the condition $f \ll 1$ is always satisfied. These beam and gas parameters are similar to the experimental conditions of Ref. [18].

Typical evolution of the electron density and temperature as a function of time is shown in Fig. 5, for propagation in 1 torr He. Nearly complete ionization of the first state occurs for times $t > 2 \mu\text{s}$. The temperature decreases monotonically after the initial ionization phase ($t > t_b$) and then rises once $n_e \sim 1/2f$. Overall the density evolution is not unlike the solution given in Eq. (15) but with a time constant equivalent to $(\gamma + f)/2 \sim 10^{-2}$. The temperature is observed to evolve slowly with time and have a minimum $(T_e/U)_{min} \simeq 0.2$ at $t_{min} = 800 \text{ ns}$, in close agreement with the Table I results and Eq. (39).

For times less than 100 ns, the gas is only partially ionized (for ICF purposes, beam pulselengths will typically be $\sim 10 - 50 \text{ ns}$). In this limit the scalings presented in Sec. III B are valid. In Fig. 6 the electron density normalized to the initial gas density n_0 is plotted

as a function of time for various gases at a pressure of 1 torr. The beam pulselength is 45 ns. After the initial ionization phase the density is observed to rise linearly with time in accordance with the solution (22). The rate of rise is proportional to t_{th} . From Table I the ratio of the rate of rise of Ar:He $\simeq 8$ and Ar:N $\simeq 2$ as is evidenced in Fig. 6. Figure 7 plots the ionization fraction at the end of the beam pulse ($t_p = 45$ ns) as a function of initial gas density. According to Eq. (22), since $1/t_{th}$ is proportional to n_0 , the ionization fraction should be independent of n_0 .

In Figs. 8 and 9 the temperature is plotted as a function of time for various gas environments. Figure 8 demonstrates that the initial ionization phase lasts for a time $\sim t_b$ for each gas and that the slow evolution during the linear growth phase of the electron density yields temperatures which are a fraction of the ionization potential and scale directly with the ionization potential. Figure 9 demonstrates the same behavior in Ar at various gas pressures. Note the small variation in minimum temperature as the initial gas pressure is varied from 0.25 \rightarrow 2 torr. Also, note the slow $1/\ln[t]$ dependence of the temperature on time as predicted by the solution given in Eq. (24).

VI. CONCLUSIONS

A simple model for gas ionization by an ion beam which includes contributions from beam impact and a background of thermal electrons has been presented. Scalings for the plasma temperature and density have been obtained for cases when a low degree of ionization occurs. It is found that the primary component of ionization is driven by the thermal electrons and it occurs on a time associated with the time taken for the beam to deposit energy equal to the ionization potential into the electrons via classical stopping. This is generally much faster than the beam-impact ionization time. Additionally, it is found that the plasma temperature is usually a fraction ($\sim 25 - 30\%$) of the gas ionization potential.

At present, ICF driven by light ions envisions the use of 30 MeV, 1 MA, Li beams. At this energy and current, the beam particle density will be approximately $n_b \sim 3 \times 10^{12}$

cm^{-3} at the diode. For ballistic transport schemes, beam transport will probably occur in a background gas with pressures in the range 0.1 - 1 torr such that $f = n_b/n_0 \ll 1$ and the results of Sec. III should be valid. According to Eqs. (10) and (11), the electron density will rise to $\sim 3(\beta)^{1/2}n_b = 1.2 \times 10^{14} \text{ cm}^{-3}$ after a time $t \sim t_b = 2.5 \text{ ns}$, for injection into 1 torr He. Thereafter, the density will grow linearly with time at a rate $1/t_{th} = 2.5 \times 10^{10} \text{ s}^{-1}$. Hence, in approximately 50 ns the electron density will be $n_e = Zn_bt/t_{th} = 1.5 \times 10^{16} \text{ cm}^{-3}$ and the gas will be half ionized.

The characteristics of ionization and the role of the background electrons when $f \leq \gamma$ is currently a topic of further study. This can occur for propagation near the target, or for self-pinch transport, where the beam density relative to the background gas density is expected to be at least a factor 10^2 times larger than for ballistic transport prior to focusing. In this instance, it is expected that following the initial ionization stage, the electron density (for the above beam parameters) will be $Z^2(\beta)^{1/2} \sim 90$ times larger than the beam density and the assumption of a low degree of ionization $n_e \ll n_0$ is not valid. Ionization of the first ionization state will occur quickly, similar to the constant coefficient solution (15), since γ will be on the order or less than f . Thereafter the plasma will heat at a rate given by Eq. (13b) of $n_bt/(n_et_{th}) \ll t/t_{th}$ to some fraction of the second ionization potential. For ionization of the second state, depending on whether or not γ is less than or greater than f one should expect growth governed by Eq. (15) or Eq. (22) respectively, where U now corresponds to the ionization potential of the second level.

The possibility exists that for certain conditions the neutral ionization time can become longer than t_{th} (i.e., for $\gamma < f$, $T_e > 0$). In this instance, the electrons cannot ionize the gas faster than the beam dumps energy into them and the free electrons experience a type of thermal runaway. As they heat they can become too hot for efficient coupling to the bound electrons of the neutrals, thereby decreasing their ionization cross-section and increasing the ionization time further. Of course, one should consider in greater detail the coupling of energy from the beam to the hot electrons to determine if such a state can, in fact, be induced.

ACKNOWLEDGEMENTS

We would like to thank D. Mosher for the use of a code on gas ionization and D. Welch for useful discussions on this and related topics. We also thank J. Guillory for helpful discussions during the testing of the gas ionization code. This work is supported by the U.S. Department of Energy through Sandia National Laboratories. One of us (BVO) was a National Research Council Research Associate during the course of this work.

APPENDIX A: Electron and Beam Ionization Cross-Sections

For ionization by electron impact, the cross-section as found in Gryzinski [26] is

$$\sigma_e = \left(\frac{b\pi e^4}{U^2}\right) g_i(E/U), \quad (\text{A1})$$

where

$$g_i(x) = \frac{1}{x} \left(\frac{x-1}{x+1}\right)^{3/2} \left[1 + \frac{2}{3} \left(1 - \frac{1}{2x}\right) \ln(2.7 + \sqrt{x-1})\right]. \quad (\text{A2})$$

The function $g_i(E/U)$ is shown in Fig. 1.

For ionization by heavy particles ($M \gg m$), with energies larger than the ionization potential U , the cross-section is

$$\sigma_b = \left(\frac{Z^2 b\pi e^4}{U^2}\right) G_i(mE/MU), \quad (\text{A3})$$

where

$$G_i(x) = \frac{1}{x} \left(\frac{x}{x+1}\right)^{3/2} \left(1 - \frac{1}{\alpha}\right) \times \left(1 - \left(\frac{1}{\alpha}\right)^{1+x}\right) \left[\frac{x}{x+1} + \frac{2}{3} \left(1 + \frac{1}{\alpha}\right) \ln(2.7 + \sqrt{x})\right], \quad (\text{A4})$$

and

$$\alpha = 4x(1 + 1/\sqrt{x}).$$

The variables in the above expressions are defined in Sec.II.

APPENDIX B: Numerical Algorithm

A zero-dimensional, one temperature model of ion beam induced gas breakdown is presented. It includes ionization of the first and second ionization states of the gas atom, ohmic heating of the plasma, and radiative cooling. This model was originally developed [30] to study instability growth in light-ion ICF reactor systems [31]. The normalized (to the initial gas density) ionization populations, f_i , satisfy

$$f_o + f_1 + f_2 = 1, \quad (\text{B1})$$

and

$$n_e = \langle Z \rangle n_o = \langle f_1 + 2f_2 \rangle n_o, \quad (\text{B2})$$

where n_e is the electron density, n_o is the initial neutral gas density, $\langle Z \rangle$ is the average ionization state, f_o is the neutral population fraction, and f_1, f_2 are the first and second ionization populations, respectively. The coupled rate equations are

$$\frac{df_1}{dt} = \langle Z \rangle ([-S_1 f_1 - \alpha_1 f_1] + [S_o f_o + \alpha_2 f_2]), \quad (\text{B3})$$

and

$$\frac{df_2}{dt} = \langle Z \rangle ([-\alpha_2 f_2] + [S_1 f_1]), \quad (\text{B4})$$

where S_i is the ionization coefficient and α_i is the electron-ion radiative recombination coefficient (expressed here in units of sec^{-1});

$$S_i = 10^{-5} \frac{(T_e/U_i)^{1/2} n_o}{U_i^{3/2} (6 + T_e/U_i)} \exp\left(-\frac{U_i}{T_e}\right), \quad (\text{B5})$$

and

$$\alpha_i = 5.2 \times 10^{-14} Z_i n_o \left(\frac{U_{i-1}}{T_e}\right)^{1/2} \left[0.43 + \frac{1}{2} \ln\left(\frac{U_{i-1}}{T_e}\right) + 0.47 \left(\frac{U_{i-1}}{T_e}\right)^{-1/3}\right]. \quad (\text{B6})$$

In Eqs. (B5) and (B6), T_e is the electron temperature in eV, U_i is the ionization potential of the i^{th} ionization state in eV, and $Z_i = i$.

The rate equations are coupled to an energy balance relation

$$\frac{d\epsilon_i}{dt} = P_S + P_\Omega - P_R, \quad (\text{B7})$$

where

$$\epsilon_i = \frac{3}{2} (1 + \langle Z_i \rangle) T_e + f_1 U_0 + f_2 (U_1 + U_0). \quad (\text{B8})$$

Here, P_S is the heating power due to beam ion stopping in the background gas, P_Ω is the ohmic heating power and is dependent on the electron-ion and electron-neutral collision

frequencies, and P_R is the radiated power. P_S is determined using stopping data from Ref. [32] plus a correction for enhanced stopping by free electrons in a plasma. The model for P_R includes both a continuum term (optically thin approximation) and a line radiation term. Over the temperature ranges observed in this work (≤ 30 eV), P_R yields values in good agreement with experimental values found in Ref. [33].

REFERENCES

- [1] D.A. Hammer and N. Rostoker, Phys. Fluids **13**, 1831 (1970).
- [2] P.A. Miller and J.B. Gerardo, J. Appl. Phys. **43**, 3001 (1972).
- [3] P.A. Miller and J.B. Gerardo, J. Appl. Phys. **43**, 3008 (1972).
- [4] C.H. Stalling and R.L. Schneider, Plasma Physics **18**, 791 (1976).
- [5] P.H. de Haan, G.C.A.M. Janssen, H.J. Hopman, and E.H.A. Granneman, Phys. Fluids **25**, 592 (1982).
- [6] David W. Swain, J. Appl. Phys. **43**, 396 (1972).
- [7] C.L. Olson, Phys. Rev. A **11**, 288 (1975).
- [8] S.K. Iyyengar and V.K. Rohatgi, IEEE Trans. on Plasma Sci. **PS-14**, 277 (1986).
- [9] S.K. Iyyengar and V.K. Rohatgi, Phys. Fluids B **1**, 1860 (1989).
- [10] G.Venugopala Rao and S.K. Iyyengar, J. Appl. Phys. **71**, 2503 (1992).
- [11] M.V. Gladyshev, M.G. Nikulin, and A.B. Sionov, Sov. J. Plasma Phys. **17**, 546 (1991).
- [12] T.W.L. Sanford, D.R. Welch, and R.C. Mock, Phys. Plasmas **1**, 404 (1994).
- [13] J.A. Swegle and S.A. Slutz, J. Appl. Phys. **60**, 3444 (1986).
- [14] See National Technical Information Service Document No. DE91009298. (C.L. Olson in Proceedings of the 1990 Linear Accelerator Conference, LANL Report No. LA-12004-C, p. 396). Copies may be ordered from the National Technical Information Service, Springfield, VA 22161.
- [15] D.R. Welch, C.L. Olson, and T.W.L. Sanford, Phys. Plasmas **1**, 764 (1994).
- [16] See National Technical Information Service Document No. ADA256070. (R.F. Hubbard *et al.*, NRL Memorandum Report No. 7112, 1992). Copies may be ordered from the

National Technical Information Service, Springfield, VA 22161.

- [17] F.C. Young, D.D. Hinshelwood, R.F. Hubbard, M. Lampe, J.M. Neri, C.L. Olson, P.F. Ottinger, D.V. Rose, S.P. Slinker, S.J. Stephanakis, and D.R. Welch, *Phys. Rev. Lett.* **70**, 2573 (1993).
- [18] F.C. Young, R.F. Hubbard, M. Lampe, J.M. Neri, P.F. Ottinger, S.J. Stephanakis, S.P. Slinker, D.D. Hinshelwood, D.V. Rose, C.L. Olson, and D.R. Welch, *Phys. Plasmas* **1**, 1700 (1994).
- [19] P.F. Ottinger, D.V. Rose, J.M. Neri, and C.L. Olson, *J. Appl. Phys.* **72**, 395 (1992).
- [20] B.V. Oliver and R.N. Sudan. In *Proceedings of the X International Conference on High Power Particle Beams*, page 678, June 20-24, 1994.
- [21] J.J. Watrous, D. Mosher, J.M. Neri, P.F. Ottinger, C.L. Olson, J.T. Crow, and R.R. Peterson, *J. Appl. Phys.* **69**, 639 (1991).
- [22] R.F. Hubbard, M. Lampe, G. Joyce, S.P. Slinker, I. Haber, and R.F. Fernsler, *Part. Accel.* **75**, 161 (1992).
- [23] D.R. Welch, M.E. Cuneo, C.L. Olson, and T.A. Mehlhorn. "Gas Breakdown Effects in the Generation and Transport of Light Ion Beams for Fusion", 1996. to be published in *Phys. Plasmas*.
- [24] P.F. Ottinger, D.V. Rose, D. Mosher, and J.M. Neri, *J. Appl. Phys.* **70**, 5292 (1991).
- [25] J.M. Neri, P.F. Ottinger, D.V. Rose, P.J. Goodrich, D.D. Hinshelwood, D. Mosher, S.J. Stephanakis, and F.C. Young, *Phys. Fluids B* **5**, 176 (1993).
- [26] M. Gryzinski, *Phys. Rev. A* **138**, A322 (1964).
- [27] R.B. Miller. *Intense Charged Particle Beams*, page 195. Plenum Press, New York, 1982.
- [28] R.W.P. McWhirter. "Spectral Intensities". In *Plasma Diagnostic Techniques*, chapter 5.

Academic Press, New York, 1965.

- [29] L. Spitzer, *Physics of Fully Ionized Gases*. Wiley, New York., 1962.
- [30] D. Mosher. (private communication, 1994).
- [31] D.V. Rose, P.F. Ottinger, B.V. Oliver, D. Mosher, C.L. Olson, and J.U. Guillory, Bull. Am. Phys. Soc 40, 1752 (1995).
- [32] L.C. Northcliffe and R.F. Schilling, Nucl. Data Tables A7, 233 (1970).
- [33] D.E. Post, R.V. Jansen, C.B. Tarter, W.H. Grasberger, and W.A. Lokke, Atom. Data Nucl. Data Tables 20, 397 (1977).

TABLES

TABLE I. The ionization potential, the time-scales t_b and t_{th} , and the minimum temperature calculated from Eq. (25) for various gases at a pressure of 1 torr. Calculations are for injection of uniform current density, Gamble II (1 MeV, 1.2 kA/cm² proton beam) and ICF (30 MeV, 5 kA/cm², Li⁺³) parameter beams.

TABLE II. The critical density fraction and the resistive times $t_d = (a^2/4\eta_0)$, $t_o = (\beta^{1/2}/n_{ec}C)t_d$, and $t_r = (n_{ec}C/Zn_b)t_{th}$ for various gases at a pressure of 1 torr. Calculations are for injection of beam parameters given in Table I. A temperature $T_e/U = 0.3$, beam radius $a = 1$ cm, and neutral cross-section $\sigma_n = 5 \times 10^{-16}$ cm² is assumed in the calculation of η_0 and n_{ec} .

FIGURES

FIG. 1. The function $g_i(x)$ for electron ionization.

FIG. 2. The weighting function for thermal electron induced ionization γ as a function of T_e .

FIG. 3. The Fourier transformed field $k^3 \tilde{B}_y / j_{bz}$ vs. time for a Gamble II parameter beam (1 MeV, 1.2 kA/cm², proton) propagating in 1 torr He and Ar.

FIG. 4. The effective resistivity normalized to the asymptotic resistivity as a function of t_p/t_r for different values of ϵ as defined in Eq. (43). The typical values for the Gamble II parameter beam in He and Ar are also shown.

FIG. 5. The numerically calculated electron density and temperature as a function of time for ionization in 1 torr He by the Gamble II parameter beam (1 MeV, 1.2 kA/cm², protons).

FIG. 6. The electron density as a function of time for various gases at a pressure of 1 torr. Beam parameters are the same as in Fig. (5).

FIG. 7. The calculated electron density at the end of the beam pulse ($t_p = 45$ ns) for various gases at pressures of 0.25, 1, and 2 torr. Beam parameters are the same as in Fig. (5).

FIG. 8. The electron temperature as a function of time for various gases at a pressure of 1 torr. Beam parameters are the same as in Fig. (5).

FIG. 9. The electron temperature as a function of time for Ar at various pressures. Beam parameters are the same as in Fig. (5).

	Gas	U (eV)	$(T_e/U)_{min}$	t_b (ns)	t_{th} (ns)
GII	He	24.6	0.15	1.3	0.23
	N	14.5	0.15	0.5	0.05
	Ar	15.8	0.15	0.27	0.03
ICF	He	24.6	0.17	0.3	0.04

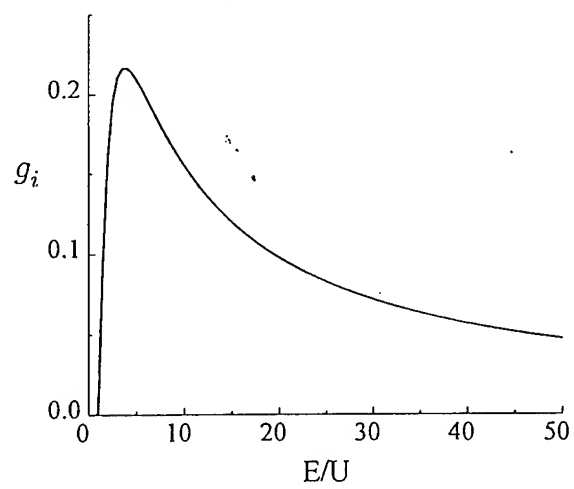
original

Oliver : Table I

	Gas	n_{ec}/n_0	t_d (ns)	t_o (ns)	t_r (ns)
GII	He	0.04	690	9	85
	N	0.016	270	17	5
	Ar	0.017	340	13.5	4.5
ICF	He	0.04	690	30.5	9

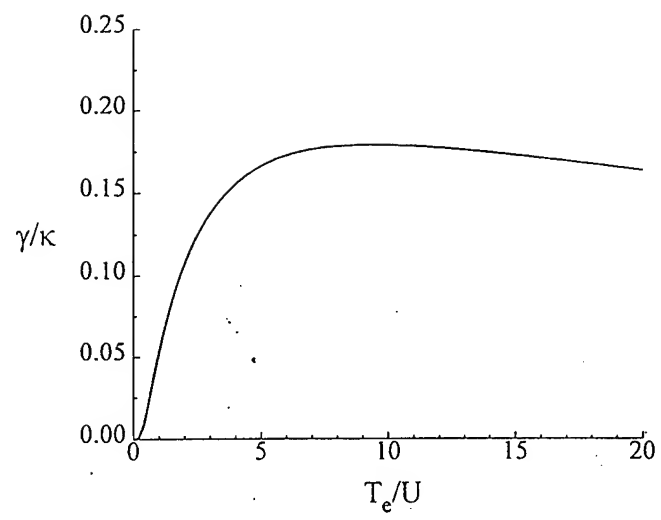
original

Oliver: Table II



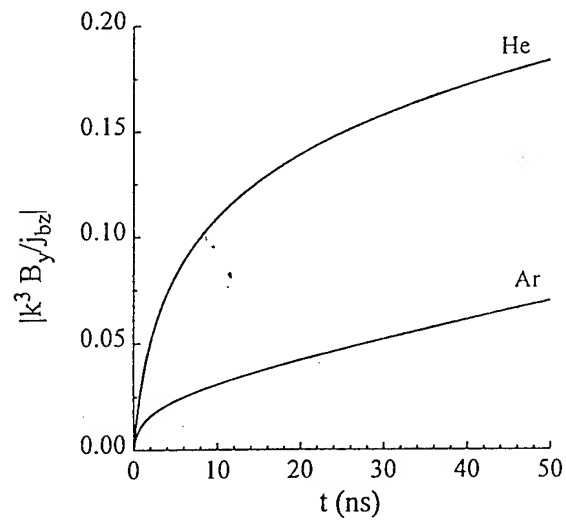
original

Oliver's Fig. 1



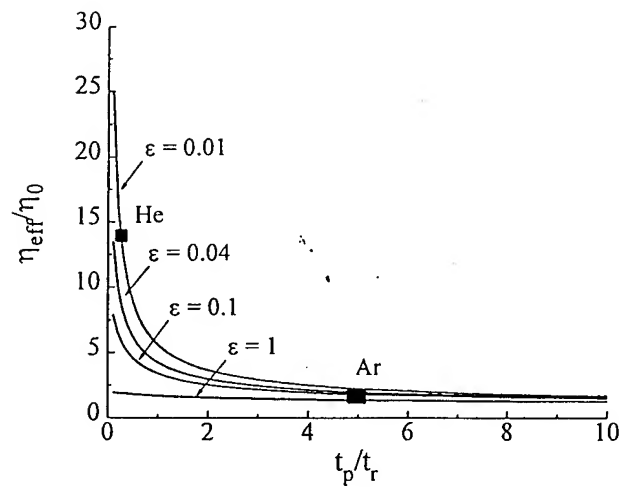
original

dimer: Fig. 2



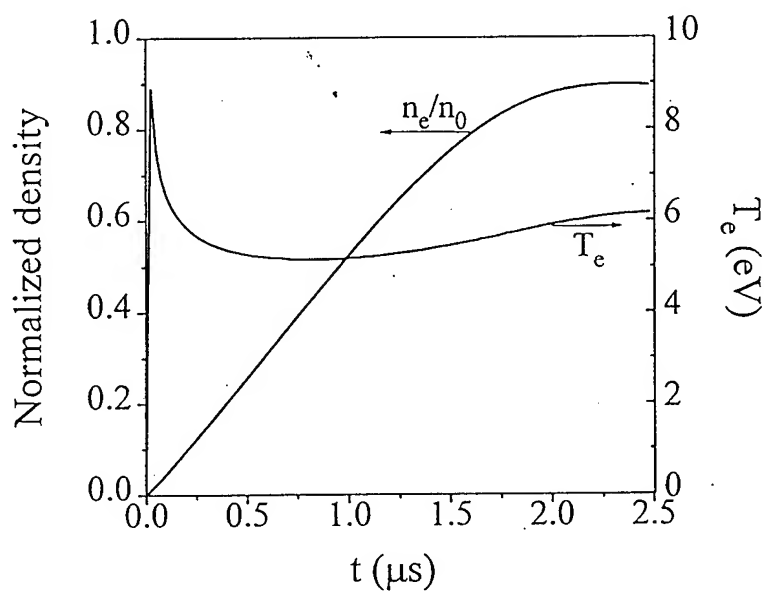
original

duer: Fig. 3



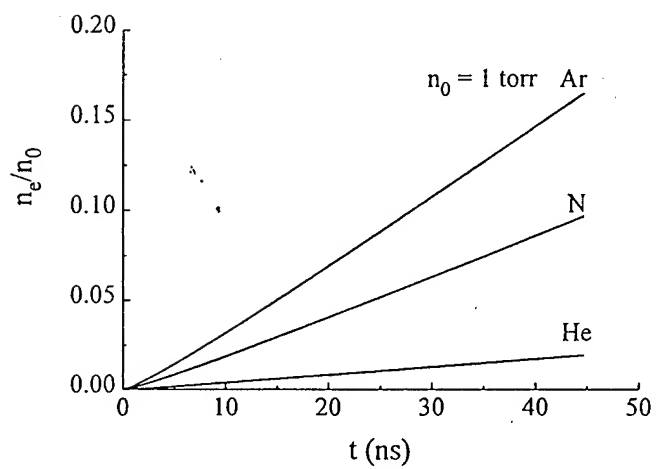
original

Oliver: Fig. 4



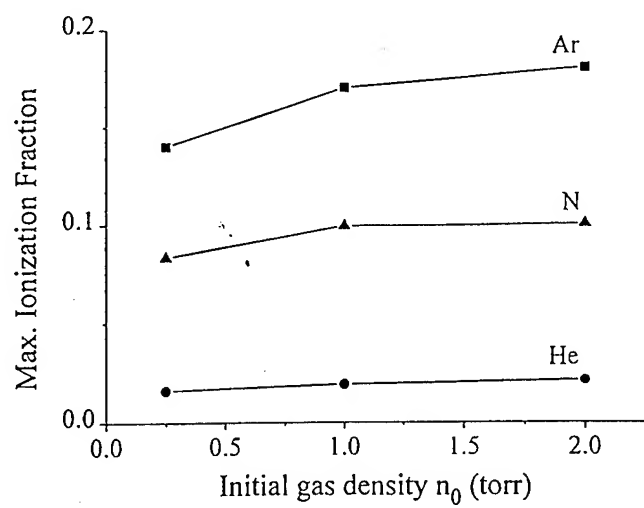
Original

Oliver: Fig. 5

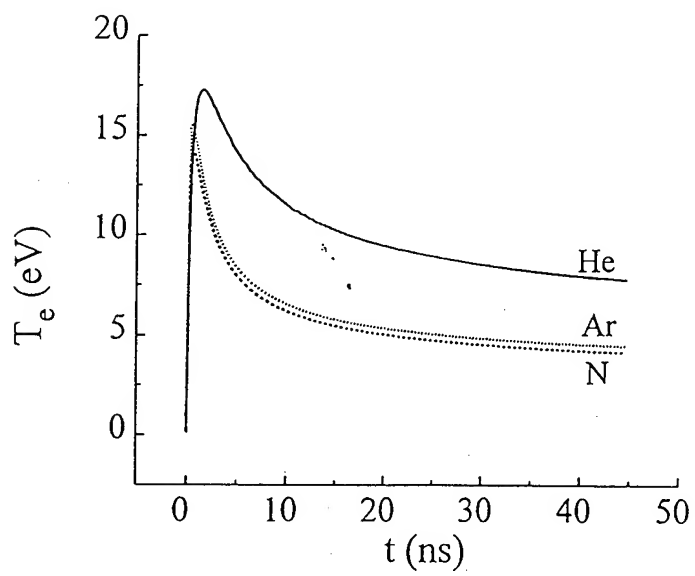


original

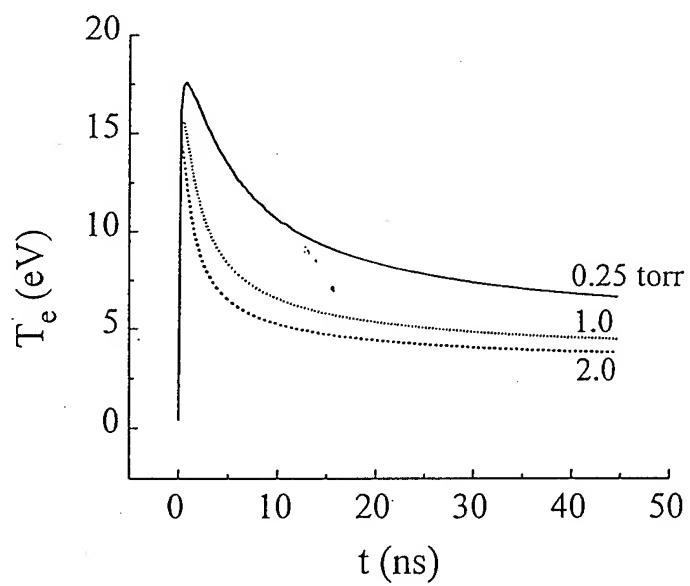
Oliver: Fig. 6



original
Oliver: Fig. 7



original
Oliver: Fig. 8



original

Oliver: Fig. 9

PULSED POWER PHYSICS BRANCH TECHNOTE TN95-24.

Title: Constraints on intense light-ion-beam transport for inertial confinement fusion.

Authors: D.V. Rose,^{a)} P.F. Ottinger, B.V. Oliver,^{b)} D. Mosher, C.L. Olson,^{c)} and J.U. Guillory.^{d)}

Date: November 12, 1995.

Abstract: A summary of a presentation made at the APS Plasma Physics Meeting, Nov. 6-10, 1995 [Bull. Am. Phys. Soc. 40, 1752 (1995)]. The proposed Laboratory Microfusion Facility (LMF) will require > 10 MJ of 30-MeV lithium ions to be transported and focused onto a high-gain, high-yield inertial confinement fusion target. The light-ion LMF approach uses a multimodular system with individual ion extraction diodes as beam sources. Given a set of parameters associated with a ballistic transport and solenoidal lens focusing design, constraints on transportable ion beam power are examined to define an operational window. Beam-driven instabilities, plasma hydrodynamics, beam energy losses during transport, module packing, and beam transport efficiency are considered. System design parameters include time-of-flight bunching of the beams, background gas species and pressures, etc. Preliminary results for other transport schemes, such as self-pinched transport, will be discussed.

^{a)} JAYCOR, Inc., Vienna, VA 22182

^{b)} NRL-NRC Research Associate

^{c)} Sandia National Laboratories, Albuquerque, NM

^{d)} George Mason University, Fairfax, VA 22030

**THIS REPORT REPRESENTS UNPUBLISHED INTERNAL WORKING
DOCUMENTS AND SHOULD NOT BE REFERENCED OR DISTRIBUTED
WITHOUT CONSENT OF THE AUTHORS**

Constraints On Intense Light-Ion-Beam Transport For Inertial Confinement Fusion*

D.V. Rose,^{a)} P.F. Ottinger, B.V. Oliver,^{b)} D. Mosher,
C.L. Olson,^{c)} and J.U. Guillory^{d)}

Plasma Physics Division, Naval Research Laboratory
Washington, DC 20375

APS Division of Plasma Physics Meeting, Nov. 1995

* Work supported by US DOE through Sandia National Laboratories.

^{a)} JAYCOR, Inc., Vienna, VA 22182

^{b)} NRL-NRC Research Associate

^{c)} Sandia National Laboratories, Albuquerque, NM

^{d)} George Mason University, Fairfax, VA 22030.

Fig. 1

In this talk, various constraints on transportable ion beam power are presented. These constraints determine an "operational window" in parameter space in which stable ion beam propagation of sufficient energy is possible. The results of this and similar analyses can be used in the design of light-ion inertial confinement fusion (ICF) facilities. One such ICF facility is the proposed Laboratory Microfusion Facility (LMF). Parameters from a preliminary LMF design are used in this analysis.

Objective is to explore the constraints on transportable ion beam power for light-ion ICF

- Will only discuss the diode-to-lens region of the baseline LMF transport scheme (ballistic transport with solenoidal lens focusing)
- Important constraints
 - Beam-driven instabilities
 - Module packing (system is multimodular)
 - Beam transport efficiency
- Additional constraints (not of consequence for this case)
 - Beam energy losses during transport
 - Plasma hydrodynamics

Fig. 2

Of the several different transport schemes under consideration for light-ion LMF, we consider only the ballistic transport with solenoidal lens focusing scheme (see Fig. 5). As a first step we will treat the diode-to-lens region where the beam is at large radius and low density. For this transport scheme, the significant constraints are; beam-driven instabilities, module packing, and beam transport efficiency. Additional constraints include beam energy losses during transport, and plasma hydro-motion, however these constraints are not significant for the ballistic transport/solenoidal lens focusing scheme.

Light-Ion LMF Parameters	
Driver	Target
<ul style="list-style-type: none"> • Ion diode radius, R = 6 - 20 cm. • Ion currents (Li⁺¹) ~1 MA. • Beam transport (and focusing) over 4 m. • N modules (diodes) = 12. • Time-of-flight bunching factor, $\alpha = 2$. • Peak power efficiency at 3/4 pulse length. 	<ul style="list-style-type: none"> • 30 MeV Lithium ions. • Target radius, $r_t = 1$ cm. • Energy on target, $E_t = 14$ MJ. • Pulse duration on target, $\tau_t = 20$ ns. <div style="border: 1px solid black; padding: 5px; margin-top: 10px;"> Focal length (lens-to-target), $F = 1.5$ m, implying $\theta_\mu = 5$ mrad. </div>

Fig. 3

The LMF parameters that are used in the constraint calculations are given in Fig. 3. Of these, the ion diode radius (R) and the ion beam current will be varied in this study. We assume here that the voltage V rises in time to achieve time-of-flight bunching and that the beam current scales as V^k . Thus the beam pulse rises monotonically from the head to the tail of the beam. Since we will be plotting the constraints as a function of R and the beam power at the end of the pulse (P_{tail}), the following expression relates these two quantities to the beam density, n_b :

$$n_b \text{ (m}^{-3}\text{)} = 2.6 \times 10^3 P_{tail} \text{ (W)} / [R \text{ (m)}^2] .$$

For $P_{tail} = 43$ TW and R ranging from 6 to 20 cm, we find that $n_b = 2.8 \times 10^{12} - 3.1 \times 10^{13} \text{ cm}^{-3}$.

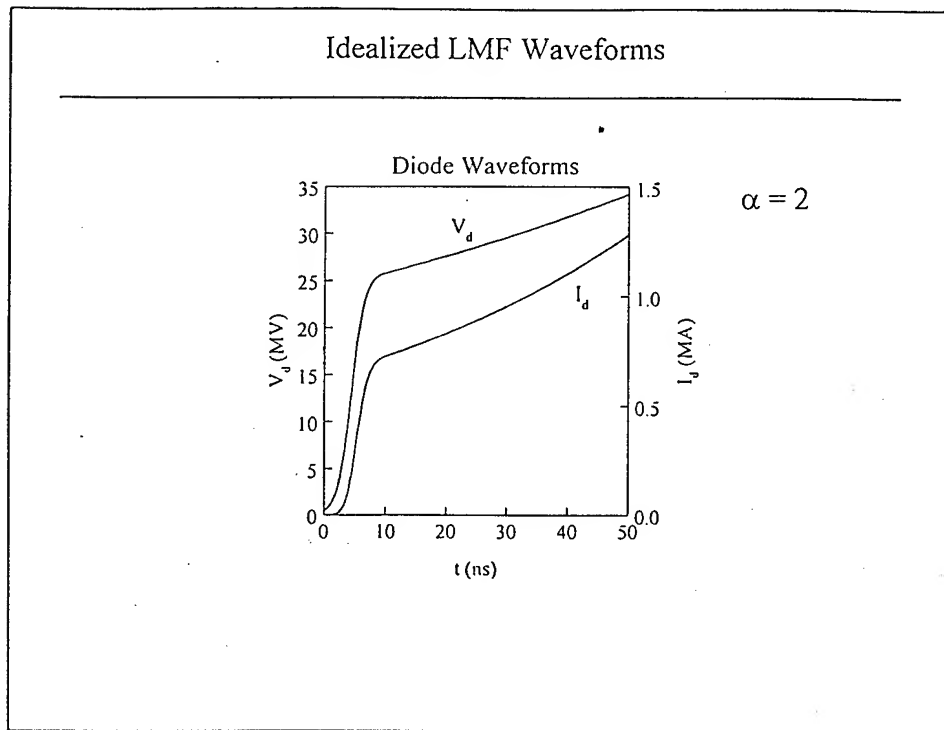


Fig. 4

The idealized LMF waveforms used in this analysis are shown. The first 10 ns of these waveforms is included to aid in the integration of the rate equations in the 0-D conductivity model.

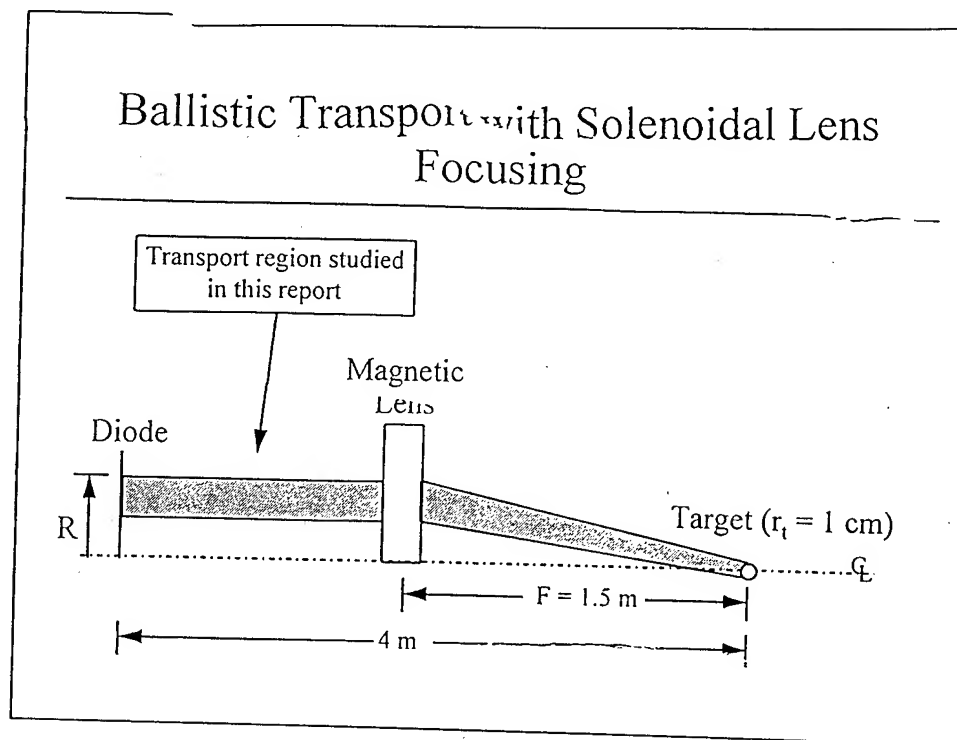


Fig. 5

A schematic for the LMF ballistic transport/solenoidal lens focusing scheme is given. This drawing is *not* to scale. Note that the extracted beam is annular. For this report, we assume the inner radius of the beam to be $R/2$. All constraint calculations presented in this report are for the diode-to-lens section of the transport system only. Work is underway to address the constraints on beam transport in the focusing section.

0-D model for background gas response to the ion beam pulse has been developed in order to calculate instability constraints

- Rate equations for ionization populations
- Plasma electron heating by collisional beam stopping
- Resistive heating of the plasma electrons (assumes $J_p = -J_b$, and Spitzer resistivity)
- Radiative cooling
- Initiated with sub-eV electron temperatures and electron densities of ~ 5 -20 times the beam density.

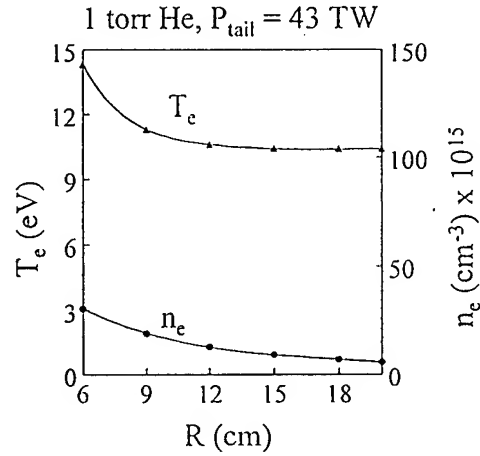


Fig. 6

A 0-D “conductivity” model has been developed to calculate the response of the background gas to the ion beam pulse. The computed plasma conductivity is in turn used to compute the instability constraints. This model is in “qualitative” agreement with results of NRL gas breakdown experiments. (The measured net fields on the Gamble II experiments suggest conductivities that are in reasonable agreement with this 0-D model). Typical plasma parameters for 1-2 torr helium at the end of the beam pulse (for $R = 12$ cm, $P_{tail} = 43$ TW) are:

$$\nu_e = \nu_{ei} + \nu_{en} = 8.6 \times 10^9 - 2.1 \times 10^{10} \text{ sec}^{-1},$$

$$\sigma = 4.1 \times 10^{14} - 3.7 \times 10^{14} \text{ sec}^{-1},$$

$$T_e = 10.2 - 8.2 \text{ eV},$$

$$n_e = 9.3 \times 10^{15} - 2.0 \times 10^{16} \text{ cm}^{-3}.$$

Two-Stream Instability

- Collisionally stabilized if:

$$v_e \geq 1.52 \frac{\omega_{pb}^2}{\omega_{pe}} \left(\frac{V_b}{\Delta V_{bz}} \right)^2$$

v_e = electron collision
freq.

ω_{pb} = beam ion plasma
freq.

ω_{pe} = electron plasma
freq.

V_b = beam velocity.

ΔV_{bz} = spread in the
beam ion axial velocity.

- Tail of beam (after beam heats plasma) is most vulnerable.

Fig. 7

The stabilization condition for the two-stream instability is given. This constraint will be analyzed by computing the required axial beam velocity spread as a function of beam and plasma density at the tail of the beam. For $R = 12$ cm, $P_{tail} = 43$ TW and 1-2 torr helium, we find $\omega_{pe} = 5.4 \times 10^{12} - 8.0 \times 10^{12}$ rad/sec and $\omega_{pb} = 4.2 \times 10^9$ rad/sec. This results in a required axial beam velocity spread for stabilization of 2.4 - 1.3 %, for 1-2 torr helium, respectively.

Filamentation Instability

- Significant growth is prevented if:

$$\sigma \geq \frac{\tau_b \omega_{pb}^2}{2\pi\theta^2 n}$$

σ = plasma conductivity.

τ_b = beam pulse duration.

θ = beam microdivergence (before focusing) or R/F (after focusing).

n = number of e-fold growth times.

- Tail of beam could be disrupted if plasma conductivity does not grow quickly enough.

Fig. 8

The filamentation instability constraint is given. The factor of 2π as used here [derived from solving the dispersion relation, P.F. Ottinger, et. al., Phys. Fluids 24, 164 (1981)] is not the same as used in other analysis [8π , in E.P. Lee, et. al., Phys. Fluids 23, 2095 (1980) and C.L. Olson, unpublished]. For this study, we have considered 10 e-folds. For $R = 12$ cm, $P_{tail} = 43$ TW, $\tau_b = 40$ ns, and 1-2 torr helium, we find the required conductivity to stabilize the beam, $\sigma_* = 4.5 \times 10^{14} \text{ sec}^{-1}$, assuming $\theta_\mu = 5$ mrad and $n = 10$ e-folds.

Beam Energy Loss Constraint

- Required power for LMF system:

$$P \geq \frac{E_t}{\eta_t \eta_{loss} N \tau_b}$$

η_t = energy transport efficiency.
 η_{loss} = energy loss efficiency due to collisional stopping as well as resistive and inductive slowing ($\eta_{loss} = 1$ for this work).

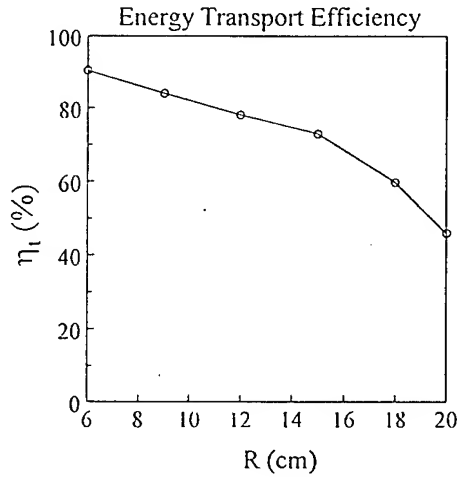


Fig. 9

The beam energy loss constraint is presented. This constraint is expressed as the required power on target at the tail of the beam in the results to be shown later. For the ballistic transport/solenoidal lens focusing scheme presented here, the combined resistive, inductive and collisional stopping energy loss mechanisms, η_{loss} , are estimated to be less than 1% of the beam energy and are not included in the calculations. However, the energy transport efficiency [see. P.F. Ottinger, et. al., J. Appl. Phys. 75, 4402 (1994) and D.V. Rose, et. al., IEEE Trans. Plasma Sci. 23, 163 (1995)] is included in the constraint calculations and is plotted as a function of R above. The reduction in η_t for larger R is due primarily to the effect of the temporal change in the focusing distance as a result of the voltage ramp required for time-of-flight bunching of the beam.

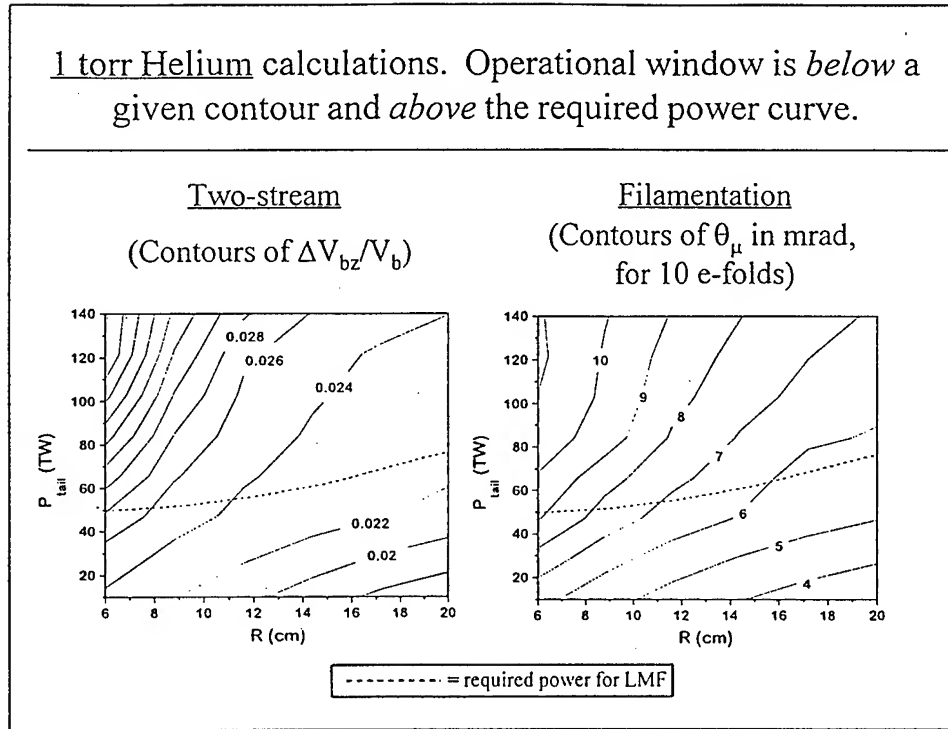


Fig. 10

Contour plots of the two-stream and filamentation instabilities are expressed as the beam parameters $\Delta V_{bz}/V_b$ and θ_μ respectively. The dashed line includes the energy loss constraints and represents the required power for the system parameters shown in Fig. 3. The calculations presented here are for 1 torr helium. The operational window is below a given contour and above the required power curve.

1 torr Helium calculations. Operational window is *below* a given contour and *above* the required power curve.

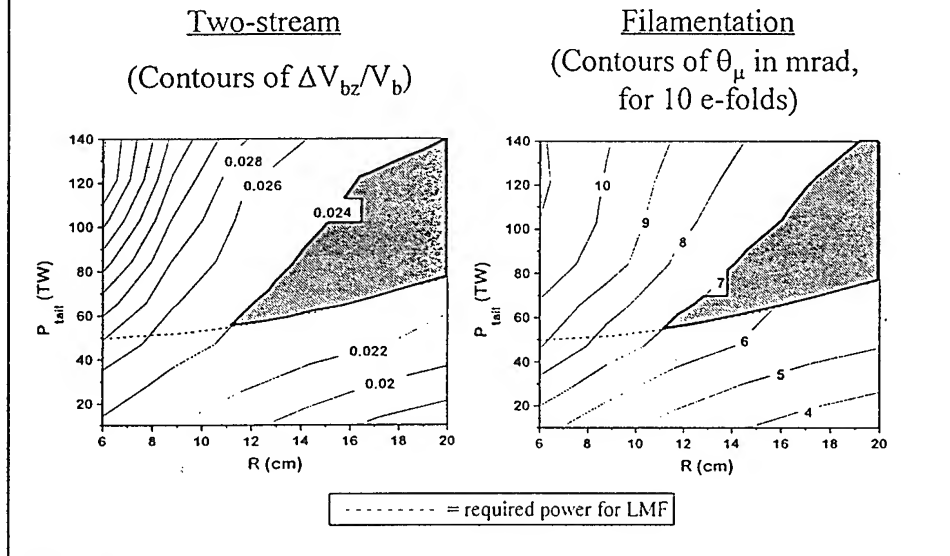


Fig. 11

Contour plots from Fig. 10 are shown again with sample “operation windows” indicated by shaded regions. Note that the energy loss constraint curve shown here (the dashed line) is computed assuming a beam with 5 mrad of microdivergence. This figure is only intended to illustrate how operational windows are defined.

2 torr Helium calculations. Operational window is *below* a given contour and *above* the required power curve.

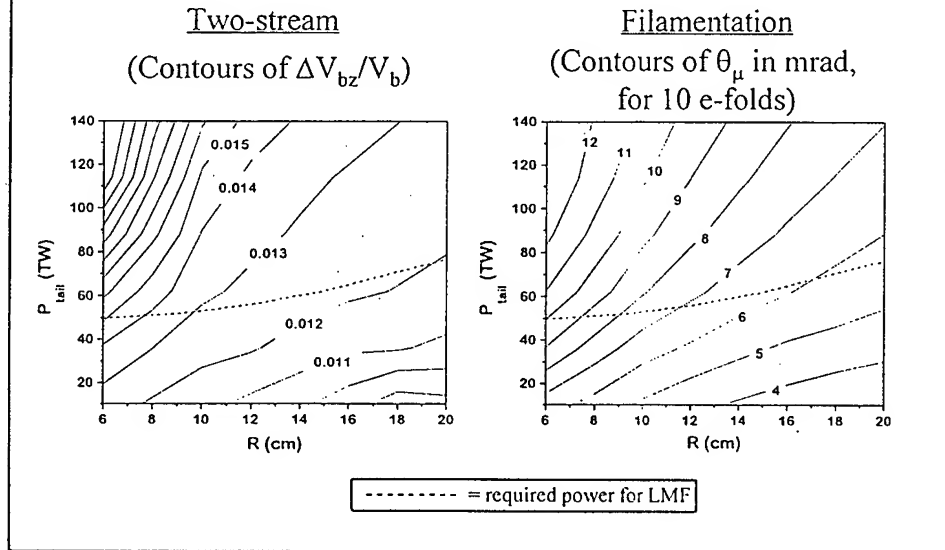


Fig. 12

Similar to the previous figure, stability constraint contours are shown for 2 torr helium. For 2 torr helium, the required axial beam velocity spread is reduced. The filamentation constraint contours do not differ significantly between 1 and 2 torr helium because the conductivity does not vary significantly between the two pressures.

Summary and Conclusions

- Constraints for operational window identified.
- Plasma conductivity model developed for helium.
- Calculations of constraints on diode-to-lens transport indicate system design parameters may be too limiting.
- Operational windows will help to determine appropriate system parameters for LMF transport.
- Experiments and numerical simulations are planned at NRL and SNL to investigate growth of beam instabilities.
- Operational windows for other transport schemes being addressed (self-pinched and z-discharge transport).

Fig. 13

In this report, constraints on transportable ion beam power have been identified and analyzed for light-ion LMF parameters. These calculations will be used to identify an operation window for ion beam transport. These results in turn will be used to determine appropriate system parameters for LMF transport.

The transport region between the lens and target is currently being evaluated for the ballstic transport/solenoidal lens scheme. Additional transport schemes, including self-pinch and z-dischare transport are also being addressed.

Ongoing experiments, supported by numerical simulation and analytic analysis, at NRL and SNL will address the issue of beam stability in low pressure background gases, enabling more detailed determination of appropaite system design parameters for LMF.

Effect of time-of-flight bunching on efficiency of light-ion-beam inertial-confinement-fusion transport schemes

P. F. Ottinger

Plasma Physics Division, Naval Research Laboratory, Washington, DC 20375

D. V. Rose

JAYCOR, Inc., Vienna, Virginia 22182

C. L. Olson

Sandia National Laboratories, Albuquerque, New Mexico 87185

(Received 7 September 1993; accepted for publication 13 January 1994)

The Laboratory Microfusion Facility (LMF) has been proposed for the study of high-gain, high-yield inertial-confinement-fusion targets. The light-ion LMF approach uses a multimodular system with applied- B extraction diodes as ion sources. A number of ion-beam transport and focusing schemes are being considered to deliver the beams from the diodes to the target. These include ballistic transport with solenoidal lens focusing, z -discharge channel transport, and wire-guided transport. The energy transport efficiency η_t has been defined and calculated as a function of various system parameters so that point designs can be developed for each scheme. The analysis takes into account target requirements and realistic constraints on diode operation, beam transport, and packing. The effect on η_t of voltage ramping for time-of-flight beam bunching during transport is considered here. Although only 5 mrad microdivergence calculations are presented here, results for bunching factors of ≤ 3 show that transport efficiencies of $>50\%$ can be obtained for all three systems within a range of system parameters which seem achievable (i.e., for diode microdivergence within 5–10 mrad, for diode radius within 10–15 cm, and for diode-ion-current density within 2–10 kA/cm²). In particular, the point design for the baseline LMF system using ballistic transport with solenoidal lens focusing and a bunching factor of 2 was calculated to have $\eta_t = 84\%$. Other factors affecting the overall system efficiency, but not included in the analysis, are also identified and estimated.

I. INTRODUCTION

A multimodular light-ion inertial-confinement-fusion (ICF) system directs energy from a number of intense ion beams onto a target for implosion. Each beam is transported, and focused over a distance of a few meters from the ion diode to the target. This standoff allows for packing the pulsed power generators around the target chamber. It also provides for isolation of the diode hardware from the target explosion and for beam power compression by time-of-flight (TOF) bunching.

The Laboratory Microfusion Facility (LMF) has been proposed for the study of high-gain, high-yield ICF targets.¹ A multimodular light-ion approach, based on Hermes-III accelerator technology, is presently under investigation.^{1,2} A number of transport and focusing schemes are being considered for LMF.^{3,4} The baseline approach is ballistic transport with solenoidal lens focusing (BTSF).^{5–7} Advantages of this system include its engineering simplicity, the absence of hardware requirements in the target chamber, and that the diode and solenoidal lens can be adjusted to form a nearly achromatic lens system. Alternate approaches include z -discharge channel transport⁸ (ZDT), wire-guided transport⁹ (WGT), and pinched transport.¹⁰ Either a wall-stabilized z -discharge channel with a low-mass wall design¹¹ or a laser-initiated free-standing z -discharge channel^{12–14} could be used for ZDT. Advantages of these alternative approaches are that they provide positive beam guidance until the beam is very near the target, and that they allow larger radius target cham-

bers, an important consideration for ICF reactor concepts.^{15,16} Due to the presence of transport system hardware inside the target chamber, neither wall-stabilized ZDT nor WGT are appropriate for an ICF reactor, but both could be used for LMF.

Previous analyses^{7–9} considered transport efficiency for monoenergetic beams. This article evaluates transport efficiency when voltage ramping for TOF beam bunching is used. For this purpose, the energy transport efficiency η_t is defined here as the ratio of total ion energy which is delivered to the target to the total ion energy produced in the diode. Because they have been most extensively studied, only BTSF, ZDT, and WGT will be considered. This work is an extension of a preliminary analysis presented earlier.¹⁷ Schematics for one module of a LMF system using each of the three transport schemes are shown in Figs. 1–3. For the BTSF scheme (Fig. 1), the beam is transported ballistically at large radius (i.e., at the diode radius) and then is focused inside the target chamber onto the target by a solenoidal lens located in the target chamber wall. For ZDT and WGT (Figs. 2 and 3, respectively), the beam is ballistically focused before entering the target chamber and then is propagated to the target in the transport system at small radius (i.e., at the target radius).

An extraction applied- B ion diode will be used to generate a beam of lithium ions.^{18–20} A combination of geometric shaping of the anode and self-magnetic field focusing of the beam in the vacuum region of the diode are used to extract

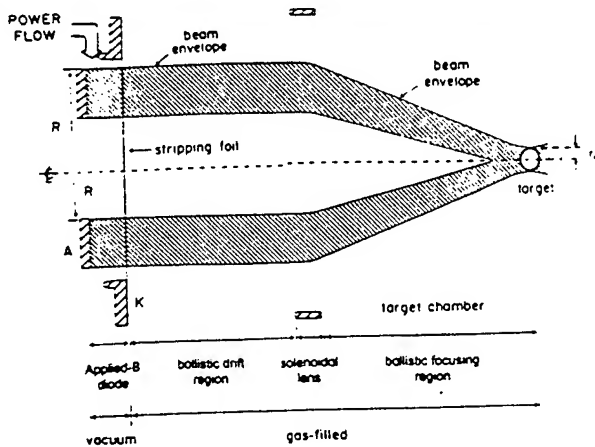


FIG. 1. Schematic of BTSF system.

the beam in an appropriate fashion for each transport scheme. The Li ions are produced in the diode in charge state $Z_d=1$, and are accelerated across an average diode voltage of $V_0=30$ MV. A foil separating the diode vacuum region and the gas-filled ballistic drift region will strip the Li^{+1} beam to Li^{+3} , so that the beam is transported to the target in charge state $Z_t=3$. Once through the foil, the beam-induced gas breakdown provides charge and current neutralization of the beam allowing the beam to propagate ballistically.²¹ The gas must also be chosen to prevent excessive energy loss due to classical slowing down. Consideration of these and other constraints suggests 1 Torr of helium as a background gas.²² These constraints are not addressed in this article.

The multimodular LMF approach positions a number of such beam generation/transport systems around a high-gain fusion target. The number of modules N is expected to be in the range of 10–30; however, packing constraints can limit N . With a target radius r_t of about 1 cm, a total energy E_t of about 10–20 MJ of 30 MeV Li ions will be required on target at a total average power P_t of about 1000 TW.¹ The total equivalent ion current (flux of Li ions) on target, $I_{eq}=Z_d I_i/Z_t=P_t/V_0$, is then about 33 MA, while the total electrical current on target I_t is 100 MA because of stripping from Li^{+1} to Li^{+3} when passing through the foil (i.e., the effective voltage drops to $Z_d V_0/Z_t=10$ MV after stripping).

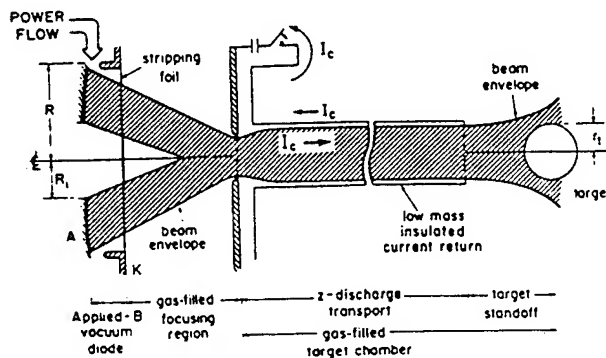


FIG. 2. Schematic of ZDT system.

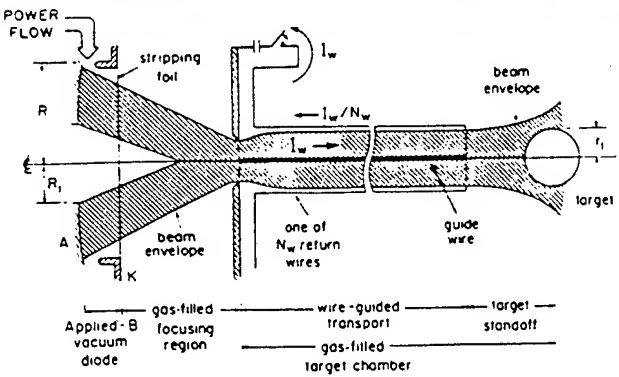


FIG. 3. Schematic of WGT system.

When an appropriate voltage ramp is applied to the ion diode, beam transport over a distance of a few meters allows for TOF bunching of the beam so that the original beam pulse duration τ_d is reduced during flight to that appropriate for target implosion τ_t .^{23–25} Since the total beam energy remains nearly constant during flight, the beam power increases roughly as $\alpha \equiv \tau_d/\tau_t$. Implosion physics considerations suggest pellet driver times of 10–15 ns, so that beam compression factors in the range of 2–3 will be required for proposed accelerator pulse durations of 30–45 ns. Defining the energy transport efficiency η_t as the ratio of total ion energy which is delivered to the target to the total ion energy produced in the diodes, and assuming $N=20$, $\alpha=2$, and $\eta_t=50\%$, the diode of each module will need to produce an average ion current, $I_{d0}=Z_d I_i/\alpha \eta_t N Z_t$, of about 1.7 MA. Because the diode is expected to be hollow,¹⁹ the active ion emitting area extends from an inner radius R_i to the outer radius R . Since it is difficult to achieve the correct applied magnetic-field profile for $R_i < R/2$ in an extraction geometry for the applied-B diode,² and since the ion emitting area increases slowly as R_i is reduced to small values, it will be assumed that $R_i=R/2$. Thus, the average ion current density at the diode surface J_i is given by

$$J_i = I_{d0}/\pi(R^2 - R_i^2) = 4Z_d I_i/(3\pi\alpha\eta_t N Z_t R^2), \quad (1)$$

where all variables are expressed in CGS units unless explicitly noted. Using $R=2R_i=15$ cm with $I_{d0}=1.7$ MA from the previous example, Eq. (1) yields $J_i=3$ kA/cm². Experimental measurements of J_i have demonstrated values as high as 6–10 kA/cm² for the applied-B diode.^{26,27}

Transport efficiency has been calculated as a function of various system parameters for each scheme so that LMF point designs can be developed. The analyses take into account target requirements and realistic constraints on diode operation, beam transport, and packing. Previous analyses have considered transport efficiencies of monoenergetic beams for LMF systems using BTSF,⁷ ZDT,⁸ and WGT.⁹ Here, the effect on η_t of voltage ramping for time-of-flight beam bunching during transport is considered for these same systems. Since self-magnetic-field ion bending in the diode varies in time as $I_d/V^{1/2}$, where $V(t)$ is the diode accelerating voltage, anode shaping (which is fixed in time) can only compensate for this bending at one point in time. Thus,

the steering angle for ions exiting the diode varies in time. For ZDT and WGT, this causes the focus to move inward (i.e., toward the diode) as a function of time. Because the beam is annular, the BTSF diode and solenoidal lens pair is only achromatic for one radial position. With optimum achromatic matching, the best focus at the target for BTSF is found to move outward (i.e., away from the diode) as a function of time. Because this voltage ramping causes the location of the beam focal spot to move axially as a function of time (or voltage), its effect on η_t will be called the "focus sweep" effect. The codes developed for the previous analyses⁷⁻⁹ were modified to treat time variations in the voltage and current to study the focus sweep effect. These codes are three-dimensional, nonrelativistic, single-particle orbit codes and 20 000 particles per simulation are used to provide adequate statistics. This number of particles typically results in less than 1% variation in transport efficiency statistics.

Although only 5 mrad microdivergence calculations are presented here, results for bunching factors of ≤ 3 show that transport efficiencies of $> 50\%$ can be obtained for all three systems within a range of system parameters which seem achievable (i.e., for diode microdivergence within 5–10 mrad, for diode radius within 10–15 cm, and for diode-ion-current density within 2–10 kA/cm²). In particular, the point design for the base-line LMF system using ballistic transport with solenoidal lens focusing and a bunching factor of 2 was calculated to have $\eta_t = 84\%$. Not included in the analysis is ion-beam-species purity, waveform efficiency, and beam energy losses. LMF beams are expected to be greater than 90% pure. The waveform efficiency accounts for energy in the head and tail of the power pulse which is not usable. The LMF waveform efficiency is expected to be greater than 80%. Beam energy losses, which are typically on the order of 10%, are due to beam ion deceleration in the self-consistent electric fields and collisional stopping of the beam in the background gas and foils.

Section II of this article provides the details of the ion-source model used in the analysis. This includes a discussion of the beam properties (defined in terms of ion-beam-current density and microdivergence at the diode, and the steering angle of ions as they exit the diode), the diode impedance model (relating the beam current and the diode voltage), and the voltage waveform required for bunching. The results of the transport efficiency calculations for BTSF, ZDT, and WGT are given in Secs. III, IV, and V, respectively. Finally, a summary and conclusions from this work are provided in Sec. VI.

II. ION-SOURCE MODEL

It is assumed that the ion current density is uniform across the annular anode emitting surface of the applied- B diode which has been assumed to extend from a radius of $R/2$ to R . Ions orbits are bent toward the axis in the diode vacuum region by the self-magnetic field of the beam. For small angles, the bending angle $\theta_b(r, t)$ is $\omega_c \Delta / v$, where ω_c is the beam ion cyclotron frequency associated with the self-magnetic field in the diode region, so that $\omega_c = 2eZ_d I_d / r m_i c^2$. Here, $I_d(t)$ is the ion current in the diode, $Z_d e$ and m_i are the beam ion charge (in the diode) and

mass, and c is the speed of light. Also, $v(r)$ is the ion speed, and Δ is the distance from the anode to a foil which separates the diode vacuum region and the gas-filled, charge- and current-neutralized transport region. There is no bending at the inner edge of the annular beam, where the self-magnetic field is zero. Anode shaping is used to compensate for the magnetic bending in the diode to provide a forward-directed beam for BTSF or a focused beam for ZDT and WGT.

The foil separating the diode vacuum region from the gas-filled transport region is referred to as the stripping foil because the Li^{+1} ions generated in the diode are stripped to Li^{+3} as they pass through it. For an applied- B extraction diode, ion-beam angular momentum arguments dictate the position and shape of the stripping foil in order to achieve a small beam spot size at the target.¹⁸ Because of the extraction geometry, the Li^{+1} ions are born at the anode with nonzero canonical angular momentum. When the applied magnetic field is configured to provide uniform magnetic insulation across the anode (and, therefore, uniform J_z), the ion canonical angular momentum must vary in radius across the anode. The stripping foil is positioned downstream so that, when stripping occurs, the ion canonical angular momentum is removed and focusing to the axis is possible. The actual foil position will depend on the detailed LMF diode design which is unknown at this time. In addition to this effect on the ion angular momentum, the diode applied magnetic field can also affect the other ion velocity components. However, these changes in v_r and v_z will be negligibly small and, again, will depend on the detailed LMF diode design, which is undetermined at this time. Thus, only applied-field effects on the ion angular momentum are considered here.

For ZDT and WGT, it is assumed here that Δ is fixed at a some typical value and is independent of radius.

For BTSF, the picture is more complicated since the diode and solenoidal lens should be matched to form an achromatic lens pair in order to optimize transport efficiency. It is shown in Sec. III that fixing Δ by angular momentum arguments and then applying this achromatic matching condition will generally fix the diode radius at a smaller value than desired. Efficiency decreases for diode radii different from this matched radius because chromatic effects begin to dominate (i.e., ions with different energy focus at different axial positions). This difficulty for BTSF may be avoided by techniques such as using two foils separated by vacuum. The first foil strips the beam and satisfies the angular momentum condition, and the second foil is located further downstream to satisfy the achromatic matching condition. This assumes that the vacuum between the foils allows beam ion orbit bending to continue in the beam self-magnetic field (but now with ions in a charge state of Z_i after stripping). This is possible because the ion beam can draw electrons off nearby walls along the transverse applied magnetic-field lines for charge neutralization but electron flow across these magnetic-field lines for beam current neutralization is inhibited.⁵

Two cases are examined for BTSF. The first case assumes the angular momentum and the achromatic matching conditions can be satisfied separately (e.g., by using two foils separated by vacuum) and thus determines the optimum

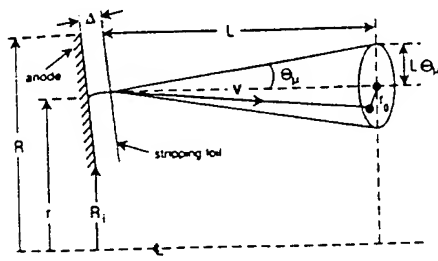


FIG. 4. Injection geometry for BTSF.

BTSF performance without constraining the choice of diode radius. For this first case, an effective Δ is used for a single foil placed where the achromatic matching condition is satisfied. Since the results only depend on the ion steering angle exiting the diode, using this effective gap rather than the actual foil positions does not effect the results. Calculating the actual positions of the two foils depends again on the detailed LMF diode design as well as the degree of current neutralization between the two foils. Such a calculation is beyond the scope of this work. The second case assumes there is one foil placed at the same value of Δ (set by the angular momentum condition) as used for ZDT and WGT. This study determines the diode radius which satisfies the achromatic matching condition for a given system and how rapidly transport efficiency drops off away from this matched radius because of chromatic effects.

As illustrated in Fig. 4, ions are assumed to leave the diode region distributed uniformly in a cone of half-angle θ_μ about the steering angle $\theta_s(r, t) = \theta_b(r, t) + \theta_a(r)$, where θ_μ is the source microdivergence, and $\theta_a(r)$ results from the anode surface shaping. It is assumed for simplicity that θ_μ has a square profile in velocity space and is independent of radius and time. A distribution for the microdivergence with the same half-width at half-maximum but a smoother profile could have somewhat lower efficiency because ions in the tail of the distribution could be lost. The actual reduction in efficiency from those quoted here will depend on the system parameters but could be as much as 25% for a Gaussian distribution. Figure 4 shows the beam extracted parallel to the axis as needed for BTSF and Fig. 5 shows a focused beam appropriate for ZDT or WGT. Since θ_b varies in time as $I_d/V^{1/2}$, where $V(t)$ is the diode accelerating voltage, θ_a can only compensate for θ_b at one point in time. At this time, the power transport efficiency (i.e., the instantaneous energy transport efficiency) is optimized. For this analysis, it is cho-

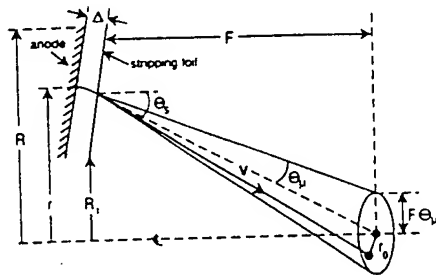


FIG. 5. Injection geometry for ZDT and WGT.

sen to be the time t_0 when the average voltage V_0 is reached. Since t_0 is near midpulse, this choice also approximately optimizes η_i . Choosing some other time during the pulse (e.g., the end of the pulse in order to maximize power coupling to the target when the voltage and power are highest) would optimize the instantaneous energy transport efficiency for that chosen time at the expense of lowering the overall energy transport efficiency η_i .

The model assumes that V increases monotonically in time for TOF bunching, and that the diode impedance characteristics lead to an ion current that scales⁹ as

$$I_d(t) = I_{d0} \left(\frac{V(t)}{V_0} \right)^k. \quad (2)$$

It is also assumed that changes in θ_a due to anode plasma motion are negligible. Using the assumption of uniform current density in the annular diode and the diode impedance model given in Eq. (2), θ_b can be written as

$$\theta_b(r, t) = -\theta_0 \left(\frac{V(t)}{V_0} \right)^{k-1/2} \left(\frac{r}{R} - \frac{R}{4r} \right), \quad (3)$$

where

$$\theta_0 = \frac{8I_{d0}\Delta}{3c^2R} \left(\frac{eZ_d}{2m_iV_0} \right)^{1/2}. \quad (4)$$

For $k > 1/2$, θ_a overcompensates for θ_b early in time [when $V(t) < V_0$] and undercompensates late in time [when $V(t) > V_0$]. This will lead to an inward sweeping of θ_s over the duration of the pulse.

At t_0 the steering angle is set equal to $\theta_s(r, t_0) = -r/F$, so that the beam is ballistically focused a distance F from the diode for ZDT and WGT. For BTSF, F is set to equal ∞ , so that the beam is extracted parallel to the axis. Combining this condition on the steering angle with Eq. (3) evaluated at t_0 , yields the appropriate anode shape which is given by

$$\theta_a(r) = -\frac{r}{F} + \theta_0 \left(\frac{r}{R} - \frac{R}{4r} \right). \quad (5)$$

The time-dependent steering angle is now found by combining Eqs. (3) and (5) which yields

$$\theta_s(r, t) = -\frac{r}{F} + \theta_0 \left[1 - \left(\frac{V(t)}{V_0} \right)^{k-1/2} \right] \left(\frac{r}{R} - \frac{R}{4r} \right). \quad (6)$$

The second term on the right-hand side of Eq. (6) describes the time-dependent diode focus sweeping. Note that the radial dependance of this term may be more complicated in an actual LMF system than that used here because Δ will most likely depend on r [where $\theta_0 \propto \Delta$ as given in Eq. (4)]. For an actual LMF diode design, an iterative ray tracing procedure will be required to determine the anode shape and foil position which optimize proper beam extraction. Errors in these calculations introduced by this geometric correction will be evaluated when actual LMF designs become available. Again, this level of detail is beyond the scope of this work.

If D is the total path length for the beam from the diode to the target, then the ideal voltage ramp for TOF bunching²³ is given by

$$V(t) = \frac{V(0)}{\{1 - (t/T)[(\alpha - 1)/\alpha]\}^2}, \quad (7)$$

where $T \equiv D/v(0)$. The average voltage is defined as $V_0 \equiv [V(0) + V(\tau_d)]/2$. Evaluating Eq. (7) at $t = \tau_d$ and substituting the resulting expression for $V(\tau_d)$ into this definition of V_0 yields

$$V(0) = 2V_0 - V(\tau_d) = \frac{2V_0\xi^2}{(1 + \xi^2)}, \quad (8)$$

where

$$\xi = 1 - \left(\frac{\tau_d}{T} \right) \left(\frac{\alpha - 1}{\alpha} \right). \quad (9)$$

Equation (8) along with the definition of V_0 relates $V(0)$ and $V(\tau_d)$ to V_0 for given values of $\xi(\alpha, \tau_d, T)$. Since the beam can be treated nonrelativistically, $v(0) = [2eZ_d V(0)/m_i]^{1/2}$. Substituting Eq. (8) into the definition of D yields

$$T^2 = \frac{m_i D^2}{4eZ_d V_0} \left(\frac{1 + \xi^2}{\xi^2} \right), \quad (10)$$

which is a transcendental equation for T in terms of given values for m_i , D , V_0 , and $\xi(\alpha, \tau_d, T)$. Using Eq. (2) for I_d and setting the total beam energy per module,

$$E_d = \int_0^{\tau_d} I_d V dt = \frac{I_{d0}}{V_0^k} \int_0^{\tau_d} [V(t)]^{k+1} dt, \quad (11)$$

equal to (E_s/N) , specifies I_{d0} for given values of V_0 , E_s , N , k , and $\xi(\alpha, \tau_d, T)$. Here, E_s is the total ion energy available from the N diodes and is related to the energy on target E_t through $E_t = \eta E_s$. Substituting for $V(t)$ from Eq. (7) into Eq. (11) and performing the integration yields

$$\begin{aligned} I_{d0} &= \frac{(2k+1)E_s}{2^{k+1}NV_0\tau_d} \left(\frac{1-\xi}{\xi} \right) \frac{(1+\xi^2)^{k+1}}{(1-\xi^{2k+1})} \\ &= \frac{5E_s}{8NV_0\tau_d} \left(\frac{1-\xi}{\xi} \right) \frac{(1+\xi^2)^3}{(1-\xi^5)}, \end{aligned} \quad (12)$$

where the last result applies when $k=2$ as is assumed in this analysis.

Thus, for given values of the system parameters V_0 , k , D , Δ , τ_i , α , N , and E_s , the TOF voltage shape $V(t)$ is specified by Eq. (7) and the ion-beam current $I_d(t)$ is specified by Eq. (2). In specifying $V(t)$ and $I_d(t)$, $V(0)$ [or $V(\tau_d)$], T , and I_{d0} are also determined through Eqs. (8), (10), and (12), respectively. For a given diode radius R , the ion steering angle $\theta_s(r, t)$ is determined by Eq. (6) with θ_0 given in Eq. (4). $V(t)$, $I_d(t)$, $\theta_s(r, t)$, R , θ_μ , and F completely specify the diode source model for a given system.

For the calculations that are presented here, it is assumed that Li^{+1} ions are accelerated in the diode and are stripped to Li^{-3} as they pass through the foil. It is also assumed that $V_0 = 30$ MV, $k=2$, $D=400$ cm, $\Delta=4$ cm, $\tau_i=15$ ns, $\alpha=1$, 2, or 3 (so that $\tau_d=15$, 30, or 45 ns), $N=10$, 20, or 30 modules, and $E_s=10$, 20, or 30 MJ. In addition, R is varied from 6 to 20 cm and it is assumed that $\theta_\mu=5$ mrad and $F=150$ cm for ZDT and WGT (or $F=\infty$ for BTSF). As illustrated in Fig. 5, this corresponds to a beam focal spot

in MJ and R expressed in cm. In deriving these values it was assumed that $V_0=30$ MV, $k=2$, $D=400$ cm, $\Delta=4$ cm, $\tau_i=15$ ns, $Z_d=1$, and $m_i=7m_p$, for lithium ions, where m_p is the mass of a proton.

α	$V(0)$ (MV)	$V(\tau_d)$ (MV)	T (ns)	I_{d0} (MA)	θ_0 (rad)
1	30.0	30.0	140	$2.22E_s/N$	$1.13E_s/NR$
2	26.8	33.2	148	$1.12E_s/N$	$0.57E_s/NR$
3	23.7	36.3	157	$0.76E_s/N$	$0.39E_s/NR$

size of $\theta_\mu F = 0.75$ cm. As is discussed in Sec. III, the spot size for BTSF is also $F_{so}\theta_\mu = 0.75$ cm, where F_{so} is the focal length of the solenoidal lens. The target radius should be somewhat larger and is assumed to be $r_t = 1$ cm. One exception to these values occurs for BTSF when the achromatic matching condition is used to determine Δ . These parameter values are typical of those determined in previous LMF design studies.^{1,2,7-9}

Table I shows the values of $V(0)$, $V(\tau_d)$, T , I_{d0} , and θ_0 for the diode voltage wave forms that are considered. These diode voltage waveforms are given by Eq. (7) with appropriate values of α , $V(0)$, and T from Table I. The ion current in the diode and the ion power in the diode,

$$P_d(t) = I_d(t)V(t) = I_{d0}V^3(t)/V_0^2,$$

are obtained from Eq. (2) for $I_d(t)$ with I_{d0} given in Table I and $k=2$. The values for θ_0 given in Table I are needed in Eq. (6) for the steering angle to calculate the effect on η_t of focus sweeping. For the cases where the achromatic matching condition is satisfied for BTSF, Δ is different from 4 cm. For these cases, the values of θ_0 given in Table I must be appropriately adjusted by multiplying by the actual Δ in centimeters and dividing by 4 cm. Note that E_s/N varies from 0.33 to 3 MJ/module for the range of values considered for E_s and N . This implies from Table I that both I_{d0} and $\theta_0 R$ will vary by as much as a factor of 27.

III. BALLISTIC TRANSPORT WITH SOLENOIDAL LENS FOCUSING

For BTSF, the beam is extracted from the diode parallel to the axis as shown in Fig. 4 and is maintained at large radius for a propagation distance $L=250$ cm. Then the solenoidal lens, which is located in the target chamber wall, focuses the beam over a distance $F_{so}=150$ cm onto a target of radius r_t . F_{so} is chosen as the smallest practical target chamber radius in order to maximize allowable θ_μ values, where $F_{so}\theta_\mu$ should be less than r_t so that most of the beam strikes the target. Beam-induced breakdown of the background gas provides beam charge and current neutralization,²¹ which is assumed to be complete. This system is illustrated in Fig. 1.

The focal length of the solenoidal lens is given by⁷

$$F_s = \frac{4v^2(t)}{\omega_c^2 L_s}, \quad (13)$$

where $v(t) = [2eZ_d V(t)/m_i]^{1/2}$ is the ion speed and $\omega_c = eZ_p B_{z0}/m_i c$ is the ion cyclotron frequency. The

magnetic-field strength is adjusted to provide a 100 cm focal length at V_0 for the solenoid length $L_s = 30$ cm used here. Typically, B_{z0} (the magnetic-field strength on axis at the center of the solenoid) is about 20 kG. With voltage ramping for TOF bunching, ions at the head and tail of the beam will have a slightly different solenoidal lens focal length. Tuning the lens to the average voltage V_0 maximizes the time-integrated transport efficiency by minimizing the variation in focal length over the pulse.

The parameters of the diode and solenoidal lens pair can be matched to further minimize chromatic effects due to the TOF voltage ramp. The total ion bending angle of the diode and solenoidal lens is $\theta_T = \theta_s - r/F_s$. Assuming that the diode voltage can be written as $V(t) = V_0[1 + \delta(t)]$, where $|\delta| \ll 1$, θ_T can be expanded in powers of δ . Using Eq. (6) for θ_s with $F = \infty$ and Eq. (13) for F_s , yields

$$\theta_T = -\frac{r}{F_{so}} + \left[\frac{r}{F_{so}} - \left(k - \frac{1}{2} \right) \left(\frac{r}{R} - \frac{R}{4r} \right) \theta_0 \right] \delta(t) + O(\delta^2), \quad (14)$$

where $F_{so} = 4v_0^2/\omega_c^2 L_s$ is the solenoidal lens focal length for V_0 and $v_0 = (2eZ_d V_0/m_i)^{1/2}$. The diode and solenoidal lens would comprise an achromatic lens pair to first order in $\delta(t)$ if the coefficient of $\delta(t)$ [i.e., the terms in the square brackets in Eq. (14)] could be set equal to zero. However, the beam is annular rather than solid so that the terms in coefficient vary differently in r . Thus, the lens pair can only be made achromatic for one value of r . Since the individual terms in the coefficient of $\delta(t)$ are largest for $r=R$ in the range of interest (i.e., $R/2 \leq r \leq R$), the lens pair should be matched at $r=R$. This choice also maximizes the number of ions which are focused achromatically, because J_i is uniform. For $r=R$, the matching condition becomes

$$\theta_0 = \frac{4R}{3F_{so}(k - \frac{1}{2})}, \quad (15)$$

where θ_0 is given in Eq. (4). Note also that $k > 1/2$ is required for achromatic matching. For the BTSF system discussed here ($V_0 = 30$ MV, $F_{so} = 150$ cm, $k = 2$, $Z_d = 1$, and $m_i = 7m_p$, where m_p is the proton mass), this results in the condition

$$\Delta = \frac{0.047R^2}{I_{d0}(\text{MA})}, \quad (16)$$

where I_{d0} changes with the choices of α , E_s , and N (see Table I).

Substituting the matched value of θ_0 from Eq. (15) into Eq. (14) yields the total focusing angle for the achromatic matched system θ_{Tm} which is given by

$$\theta_{Tm} = -\frac{r}{F_{so}} + \frac{r}{3F_{so}} \left(\frac{R^2}{r^2} - 1 \right) \delta(t) + O(\delta^2). \quad (17)$$

Because the BTSF system is nearly achromatic under these conditions, the reduction in η_i due to focus sweeping should be less for BTSF than for either ZDT or WGT. Note that the coefficient of δ vanishes for $r=R$ so that the system is achromatic to first order in δ for $r=R$. For $r < R$, the coefficient is positive. Since $\delta < 0$ at the beginning of the pulse and $\delta > 0$

at the end of the pulse, the beam is focused outward (i.e., away from the diode) in time for ions with $r < R$ for BTSF. This is opposite to the inward focus sweep (i.e., toward the diode) due to the diode steering angle alone (see discussion of Fig. 6) before the beam passes through the solenoidal lens.

As discussed in Sec. II, two cases are examined for BTSF. The first case assumes that the angular momentum and the achromatic matching conditions can be satisfied separately and thus determines the optimum BTSF performance without constraining the choice of diode radius. For this first case, the effective Δ (or matched value) is set by Eq. (16). Note that in this case the value of Δ increases as R^2 . The second case assumes there is one foil placed at the same fixed value of Δ (set by the angular momentum condition) as used for ZDT and WGT. In this case, $\Delta = 4$ cm and does not vary with R . In this study the achromatic matching condition is only satisfied at one diode radius for a given system and shows how rapidly transport efficiency drops off away from this matched radius because of chromatic effects.

The code ATHETA²⁸ is used to create the solenoidal magnetic-field map used for the transport efficiency calculations. Flux excluding shields are used on either side of the solenoid to confine the field to the vicinity of the lens. These shields have an inner radius of $5R_s/6$ and extend radially outward for 25 cm. The diode region is protected from the target blast by a center plug in the solenoid (not shown in Fig. 1). The outer radius of this plug is determined by the line of sight from the center of the target chamber to the outer edge of the diode. Ions at small radius are removed from the beam if they strike this plug.

In addition to chromatic effects, nonideal lens effects can reduce transport efficiency. For the magnetic-field structure used here, the radial gradient in B_z significantly alters the focal length of ions which pass through the lens at a radius greater than about $R_s/3$.⁷ Thus, the solenoid radius is generally set at $R_s = 3R$. However, packing constraints in the target chamber wall limit R_s to a value of $2F_{so}(f/N)^{1/2}$, where f is the fraction of the target chamber surface area which is enclosed by the N solenoids. For the cases considered here and assuming $f = 0.5$, R_s is limited to 45 cm for $R \geq 15$ cm with $N = 20$ and to 36 cm for $R \geq 12$ cm with $N = 30$. Cases considered with $N = 10$ are unaffected by this packing constraint.

Figure 6 illustrates beam transport, focusing, and bunching for BTSF. The plot shows $rP(r, z)$ (i.e., the beam power density multiplied by r) for the beam pulse at four times during transport for the matched beam case [$\Delta = 9.44$ cm from Eq. (16)] with $N = 20$, $E_s = 20$ MJ, $R = 15$ cm, and $\alpha = 2$. Because the beam radius changes by an order of magnitude, $rP(r, z)$ is plotted rather than $P(r, z)$ for ease of viewing in cylindrical geometry. Ions which hit the center plug are lost and not included in calculating $P(r, z)$. The first snapshot on the left-hand side shows the beam as it exits the diode. The second snapshot shows the beam in the ballistic drift region. Note that, due to the diode focus sweep [see Eq. (6)], the front of the beam is expanding outward, while the tail is compressing. The third snapshot shows the beam as it is exiting the solenoidal lens, and the fourth snapshot shows

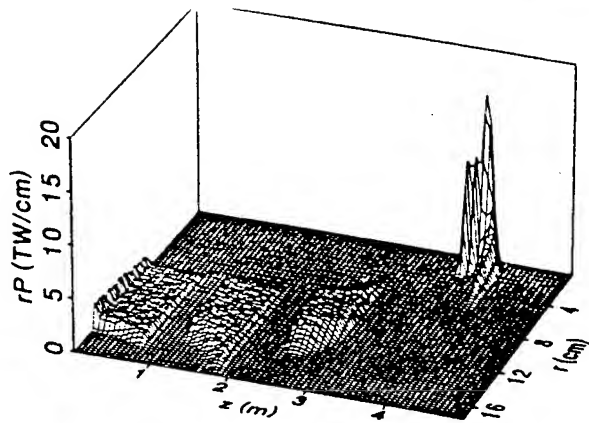


FIG. 6. Plot of $rP(r,z)$ at four snapshots in time during transport for BTSF. The diode, solenoidal lens, and target are located at $z=0, 2.5$, and 4 m, respectively. This case corresponds to $N=20$, $E_s=20$ MJ, $R=15$ cm, $\alpha=2$, and Δ is matched.

the beam as it is passing through the target region. The center of the lens is at 2.5 m and the target is at 4 m. For BTSF, the power density increases rapidly near the target where the beam both bunches and focuses. Although the 20 000 particles used in these simulations provide good statistics for calculated η_t , the power density plots are somewhat statistically noisy because these particles are distributed over a large number of grid cells in two dimensions. Since these plots are only meant to illustrate the basic features of BTSF, no attempt was made to smooth the data or reduce the noise with more particles. The power density plots for ZDT and WGT exhibit similar statistical noise.

Figure 7 shows results of η_t calculations for the first BTSF case where Δ is matched to satisfy Eq. (16) for the achromatic focusing condition. The cases shown are for $N=20$ and $E_s=20$ MJ, and the three curves correspond to bunching factors of $\alpha=1, 2$, and 3 . The points refer to the actual simulation results, while the lines are smooth curve fits. The fall off in η_t for $R>15$ cm with $\alpha=1$ is caused by the packing constraint which limits R_s to 45 cm for $N=20$. The drop off in efficiency as α increases is due to the focus sweep effect, and is no more than about 13% for $\alpha=2$ and

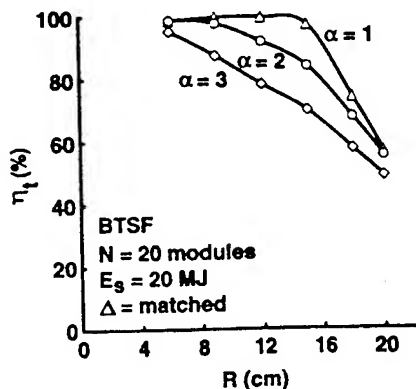


FIG. 7. Plot of η_t vs R with $N=20$ and $E_s=20$ MJ for the first BTSF case where Δ is matched. The individual curves are for $\alpha=1, 2$, and 3 .

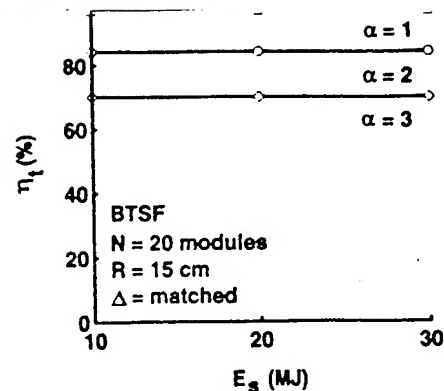


FIG. 8. Plot of η_t vs E_s with $N=20$ and $R=15$ cm for the first BTSF case where Δ is matched. The individual curves are for $\alpha=1, 2$, and 3 .

about 28% for $\alpha=3$. As shown in Fig. 7, the focus sweep effect reduces η_t at $R=15$ cm from 97.4% for the case with no focus sweep (i.e., $\alpha=1$) to 84.3% for $\alpha=2$ and 70.2% for $\alpha=3$. Figure 8 shows that η_t varies very little over the range of E_s under consideration for a matched system with $N=20$ and $R=15$ cm, and Fig. 9 shows that η_t drops slightly as N increases from 10 to 30 modules for a matched system with $E_s=20$ MJ and $R=15$ cm. This slight drop results from the packing constraint which limits R_s .

For the second BTSF case, Δ is fixed at 4 cm so that each system is achromatically matched for only one value of R . For $N=20$ and $E_s=20$ MJ, Eq. (16) shows that this matched radius is $R=9.76$ cm for $\alpha=2$ and $R=8.04$ cm for $\alpha=3$. Figure 10 shows the calculated values of η_t for this case. As expected, the values of η_t for $\alpha>1$ are lower than those shown in Fig. 7 for all values of R except those near the matched radii quoted above. For example, at $R=15$ cm η_t is 78.5% for $\alpha=2$ and 54.5% for $\alpha=3$ when $\Delta=4$ cm, compared with 84.2% and 70.2% , respectively, when the Δ is matched. Although the reduction is not severe, mismatching Δ can significantly affect η_t with the effect worse for larger α .

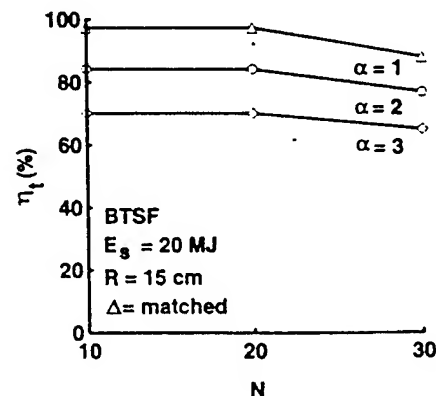


FIG. 9. Plot of η_t vs N with $E_s=20$ MJ and $R=15$ cm for the first BTSF case where Δ is matched. The individual curves are for $\alpha=1, 2$, and 3 .

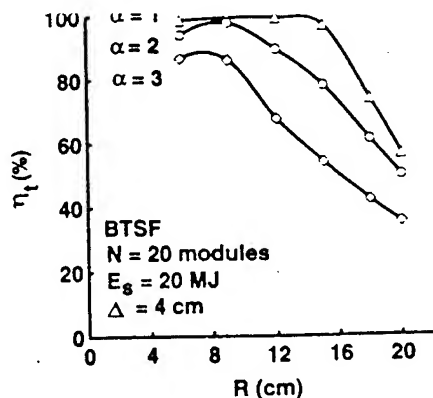


FIG. 10. Plot of η_t vs R with $N=20$ and $E_s=20$ MJ for the second BTSF case where $\Delta=4$ cm. The individual curves are for $\alpha=1, 2$, and 3 .

IV. BALLISTIC FOCUSING WITH Z-DISCHARGE TRANSPORT

For ZDT, the anode is shaped to ballistically focus the beam onto the aperture of the transport channel located a distance F from the diode. The ZDT system is illustrated in Fig. 2 and diode extraction geometry is illustrated in Fig. 5. For ZDT, Δ is fixed at 4 cm. Inside the channel, the magnetic field associated with the discharge current radially confines the ions. Once focused, the beam then propagates down the channel with a small radius on the order of the target size. At the exit, the beam expands slightly over the pellet standoff distance d . The low-mass current return wall provides stability for the discharge and results in a small but tolerable amount of debris for LMF.¹¹ Unlike the BTSF case where F is restricted by the target chamber size, F is allowed to vary for ZDT to maintain a channel size on the order of the target size as θ_μ varies. Thus, the aperture radius is chosen to be $r_a = F\theta_\mu$ so that at V_0 the full beam enters the channel. To allow for trapping of the expanding portion of the beam,⁸ the channel radius is generally chosen so that $r_c^2 = 2r_a^2$. Here, $r_c = r_t = 1$ cm, which is slightly smaller than $2^{1/2}F\theta_\mu = 1.06$ cm for $F=150$ cm and $\theta_\mu=5$ mrad. Finally, a typical channel current of $I_c=40$ kA is chosen, which confines the entire beam for $\alpha=1$ and $R \leq 10.5$ cm.⁸ As R increases beyond 10.5 cm ions will be lost to the channel wall.

Because of the time dependence of θ , when TOF bunching is required ($\alpha > 1$), the axial location of the focus sweeps inward in time. Early in the pulse the beam is focused beyond the channel entrance, at V_0 it is focused at the aperture, and late in the pulse it is focused before the aperture. Thus, early and late in the pulse some ions will strike the aperture and be lost. This focus sweep effect reduces η_t for $\alpha > 1$. First, the focus sweep effect on η_t is calculated for the standard system described above. At the end of this section, an alternative ZDT system is considered which reduces the focus sweep effect at the expense of requiring a higher channel current.

For these calculations, the discharge current density is assumed to be uniform and complete beam charge and current neutralization is assumed in both the gas-filled ballistic focusing region and in the transport channel. Packing con-

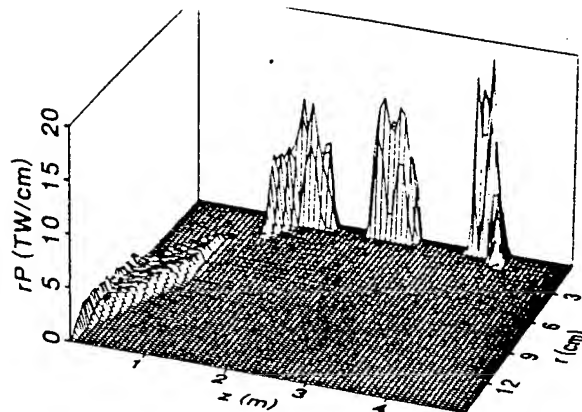


FIG. 11. Plot of $rP(r,z)$ at four snapshots in time during transport for ZDT. The diode, channel entrance, and target are located at $z=0, 1.5$, and 4 m, respectively. This case corresponds to $N=20$, $E_s=20$ MJ, $I_c=40$ kA, $R=15$ cm, and $\alpha=2$.

siderations determine a standoff distance of $d=r_t(N/2)^{1/2}$ between the channel exit and the target.⁸ The length of the transport channel is given by $D-F-d$ and is on the order of about 250 cm.

Figure 11 shows a plot of $rP(r,z)$ at four snapshots in time during transport for ZDT. Ions which hit the aperture or the channel wall are lost and are not included in calculating $P(r,z)$ beyond the point where they are lost. The diode, channel entrance, and target are located at $z=0, 1.5$, and 4 m, respectively. This case corresponds to $N=20$, $E_s=20$ MJ, $I_c=40$ kA, $R=15$ cm, and $\alpha=2$. Note that the beam focuses as it leaves the diode and then is transported at small radius. Unlike the BTSF case, $rP(r,z)$ increases first near the channel aperture where the beam focuses and continues to increase as the beam bunches approaching the target.

The calculated transport efficiency for ZDT is plotted as a function of R in Fig. 12 for the case with $N=20$, $E_s=20$ MJ, and $I_c=40$ kA. The individual curves are for $\alpha=1, 2$, and 3 . Since ZDT is not achromatic the drop off in η_t due to the focus sweep effect is significant. This is particularly evident for small R where diode bending is accentuated by the large self-fields in the diode which scale as $1/R$ (see θ_0 in

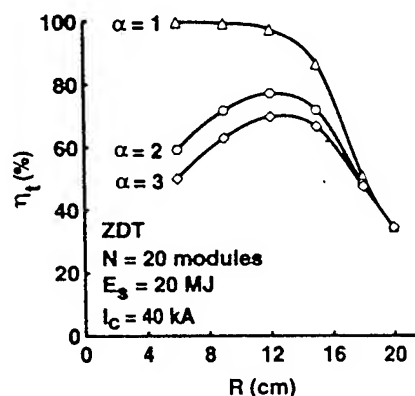


FIG. 12. Plot of η_t vs R with $N=20$, $E_s=20$ MJ, and $I_c=40$ kA for ZDT. The individual curves are for $\alpha=1, 2$, and 3 .

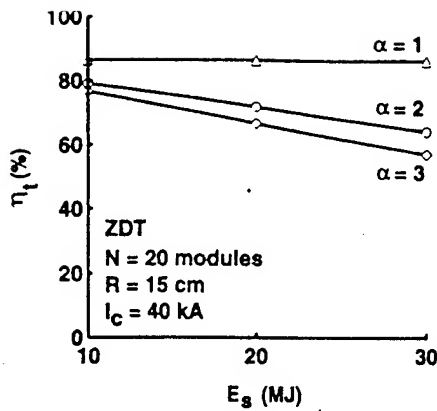


FIG. 13. Plot of η_t vs E_s with $N=20$, $R=15$ cm and $I_c=40$ kA for ZDT. The individual curves are for $\alpha=1, 2$, and 3 .

Table I). The drop off in η_t at large R is due to losses to the channel wall at fixed I_c as the ion transverse velocity ($v_r \sim R/F$) increases. High efficiency can be extended to larger R by increasing I_c (to reduce losses to the wall), however, more rapid beam expansion in the stand-off region eventually limits this.⁸

As shown in Fig. 12, the focus sweep effect reduces η_t at $R=15$ cm from 86.6% for the case with no focus sweep (i.e., $\alpha=1$) to 71.9% for $\alpha=2$ and 66.7% for $\alpha=3$. The packing constraint has little effect on ZDT transport efficiency. Figure 13 shows the variation of η_t with E_s for the case with $N=20$, $R=15$ cm, and $I_c=40$ kA. The individual curves are for $\alpha=1, 2$, and 3 . The focus sweep effect increases as E_s increases because the time variation in the steering angle as shown in Eq. (6) is proportional to θ_0 which scales as E_s (see Table I). Figure 14 shows the variation of η_t with N for the case with $E_s=20$ MJ, $R=15$ cm, and $I_c=40$ kA. The focus sweep effect increases as N decreases because θ_0 scales as $1/N$ (see Table I). The variations of η_t with E_s and N are more pronounced for ZDT compared with BTSF because ZDT is not achromatic.

An alternative ZDT system can be designed which reduces the focus sweep effect; however, higher channel current is required. If F were reduced to $F^*(R)$ so that the

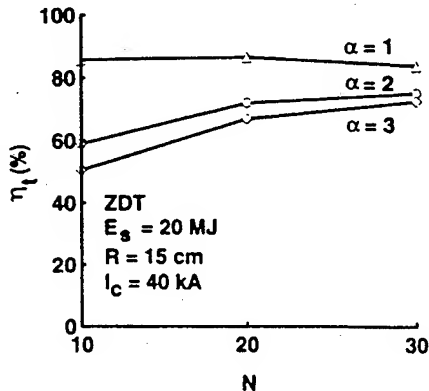


FIG. 14. Plot of η_t vs N with $E_s=20$ MJ, $R=15$ cm and $I_c=40$ kA for ZDT. The individual curves are for $\alpha=1, 2$, and 3 .

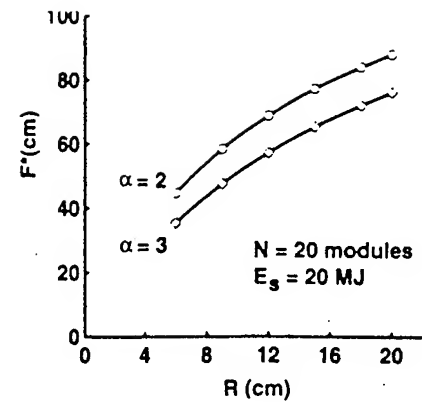


FIG. 15. Plot of $F^*(R)$ from Eq. (18). The individual curves are for $\alpha=2$ and 3 .

largest spot size at $F^*(R)$ during the pulse were less than the aperture size, then ion losses to the aperture could be eliminated; however, I_c would have to be increased to confine the larger transverse energy of the beam ions. A similar approach could also be appropriate for WGT. In Sec. V, however, it is shown that the larger wire radius required to avoid melting the wire with the larger current will severely reduce η_t for WGT. The maximum beam radius at a fixed $F^*(R)$ occurs at $t=\tau_d$ and is given by

$$r_b^{\max} = R - \theta_s(R, \tau_d) F^*(R) + \theta_\mu F^*(R).$$

Substituting for $\theta_s(R, \tau_i)$ from Eq. (6) and solving for $F^*(R)$, yields

$$F^*(R) = \frac{(r_d/\theta_\mu)}{1 + (3\theta_0/4\theta_\mu)[(V(\tau_d)/V_0)^{3/2} - 1]}, \quad (18)$$

where $\theta_0(R)$ and $V(\tau_d)$ are given in Table I for the cases considered here. Figure 15 shows a plot of $F^*(R)$ for $\alpha=2$ and 3 . Since $v_r \sim R/F$ and the channel (or wire) current required to confine the beam^{8,9} scales as $I_{c,w} \sim (R/F)^2$, the channel (or wire) current should be scaled up by $[F/F^*(R)]^2$ so that

$$I_{c,w}^*(R) = \left\{ 1 + \frac{3\theta_0}{4\theta_\mu} \left[\left(\frac{V(\tau_d)}{V_0} \right)^{3/2} - 1 \right] \right\}^2, \quad (19)$$

where again $\theta_0(R)$ and $V(\tau_d)$ are given in Table I for the cases considered here. The new channel (wire) current $I_{c,w}^*(R)$ is plotted in Fig. 16. This current increases with α and becomes prohibitively large for small R .

The transport efficiency is plotted as a function of R with $N=20$ and $E_s=20$ MJ for ZDT with $I_c = I_c^*(R)$ and $F = F^*(R)$ in Fig. 17. The individual curves are for $\alpha=1, 2$, and 3 . As expected, by eliminating the losses to the aperture the transport efficiency for both the $\alpha=2$ and $\alpha=3$ cases approach that of the $\alpha=1$ case. This is accomplished at the expense of higher channel current. Results of Ref. 11 suggest that the ZDT channel current may be limited by engineering and physics considerations to about 100 kA for low-mass wall-stabilized channels appropriate for LMF. Thus, this technique may only be useful for ZDT at large R where little improvement in η_t is seen.

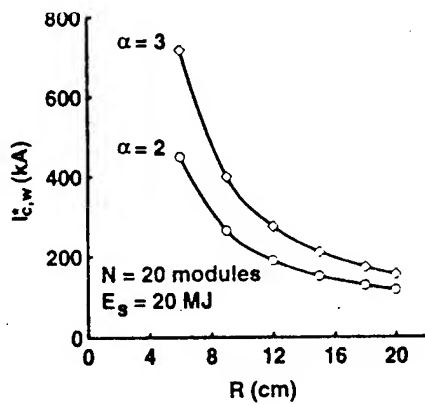


FIG. 16. Plot of $I_{c,w}^*(R)$ from Eq. (19). The individual curves are for $\alpha=2$ and 3.

V. BALLISTIC FOCUSING WITH WIRE-GUIDED TRANSPORT

The WGT system is similar to the ZDT system and is illustrated in Fig. 3. The anode is shaped to ballistically focus the beam onto the aperture of the transport system located at a distance F from the diode. The diode extraction geometry is illustrated in Fig. 5 with Δ fixed at 4 cm. Inside the transport system, the magnetic field associated with the current in the gas-embedded central guide wire confines the ion beam to a small radius on the order of r_f . The focal distance and aperture size are chosen for a given θ_μ in the same way as for ZDT so that $r_a = F\theta_\mu$. For WGT, there is no confining wall and the transported beam radius is given by⁹

$$r_b = F\theta_\mu \exp\left(\frac{v_0 R^2}{2v_w F^2}\right), \quad (20)$$

where $v_w = 2ZeI_w/m_i c^2$. Beam-induced breakdown of the gas in the ballistic focusing region and in the gas surrounding the guide wire results in beam charge and current neutralization during transport. Ions with small angular momen-

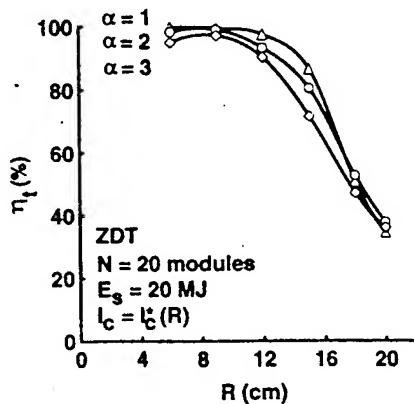


FIG. 17. Plot of η_t vs R with $N=20$ and $E_s=20$ MJ for ZDT with $I_c = I_c^*(R)$ and $F=F^*(R)$. The individual curves are for $\alpha=1, 2$, and 3.

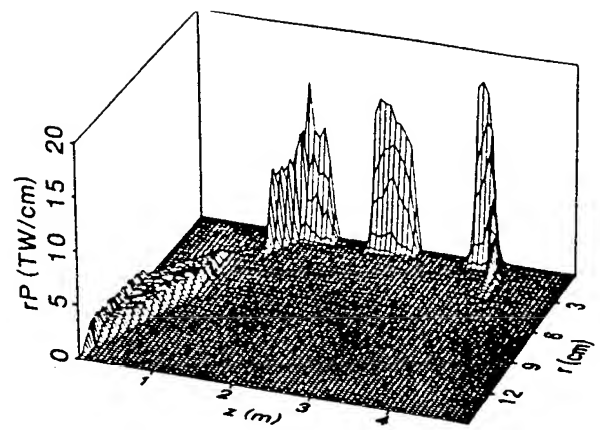


FIG. 18. Plot of $rP(r,z)$ at four snapshots in time during transport for WGT. The diode, transport system entrance, and target are located at $z=0, 1.5$, and 4 m, respectively. This case corresponds to $N=20, E_s=20$ MJ, $I_w=40$ kA, $R=15$ cm, and $\alpha=2$.

tum hit the wire and are lost. The wire radius is specified as the minimum radius required to avoid melting and is given by⁹

$$r_w = 5.6 \times 10^{-3} I_w^{1/2} \text{ (kA)}. \quad (21)$$

For the standard case where the wire current is $I_w=40$ kA, $r_w=0.035$ cm. Return-current wires are placed around the central guide wire at a radius of about $1.4r_b$ in order to minimize losses due to chaotic orbit effects while maintaining as compact as possible WGT system radius for packing.⁹ Because the return wires are placed at $1.4r_b$, the standoff distance becomes $d=r_b N^{1/2}$ for WGT,⁹ which is $2^{1/2}$ times larger than the standoff required for ZDT.⁸ At the exit, the beam expands over this pellet standoff distance. The length of the transport system is given by $D-F-d$ and is on the order of about 250 cm.

As with ZDT, the axial location of the focus sweeps inward in time for WGT. For $\alpha>1$, early and late in the pulse some ions strike the aperture and are lost. First, the focus sweep effect on η_t is calculated for the standard WGT system described above. At the end of this section, an alternative WGT system similar to the alternate ZDT system described in Sec. IV is considered.

Figure 18 shows a plot of $rP(r,z)$ at four snapshots in time during transport for WGT. Ions which hit the aperture or the guide wire are lost and are not included in calculating $P(r,z)$ beyond the point they are lost. The diode, transport system entrance, and target are located at $z=0, 1.5$, and 4 m, respectively. This case corresponds to $N=20, E_s=20$ MJ, $I_w=40$ kA, $R=15$ cm, and $\alpha=2$. Note that the beam focuses as it leaves the diode and then is transported at small radius. As with ZDT, $rP(r,z)$ increases first near the aperture to the transport system where the beam focuses and continues to increase as the beam bunches approaching the target. Also note that the beam expands in the standoff region more rapidly for WGT than for ZDT. The more rapid expansion is a result of larger transverse ion energies because of the larger average magnetic field with the centrally located current in WGT than with the distributed current in ZDT.^{8,9}

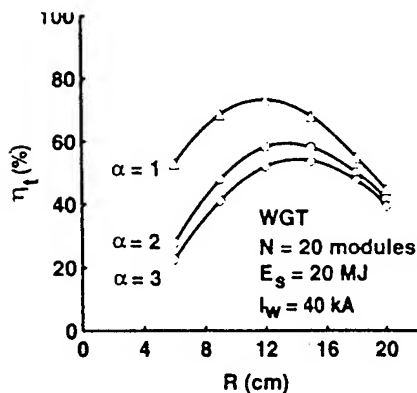


FIG. 19. Plot of η_t vs R with $N=20$, $E_s=20$ MJ, and $I_w=40$ kA for WGT. The individual curves are for $\alpha=1, 2$, and 3 .

The calculated transport efficiency for WGT is plotted as a function of R in Fig. 19 for the case with $N=20$, $E_s=20$ MJ, and $I_w=40$ kA. The individual curves are for $\alpha=1, 2$, and 3 . Since WGT is not achromatic the drop off in η_t due to the focus sweep effect is significant. As with ZDT, this is particularly evident for small R . Unlike ZDT, η_t is also reduced at small R because more ions with small angular momentum hit the central guide wire.⁹ The drop off in η_t at large R (at fixed I_w) is due to larger r_b [see Eq. (20)], larger d , and more rapid beam expansion in the standoff region ($v_r \sim R/F$) as R increases. High efficiency can be extended to larger R by increasing I_w (to reduce r_b), however, beam expansion in the standoff region eventually limits this.⁹ Because beam expansion is more rapid and the standoff distance is larger for WGT compared with ZDT, increasing I_w for WGT is not as effective as increasing I_c for ZDT in extending high efficiency to larger R .⁹ In addition, a larger wire radius is required for higher I_w to prevent melting the wire. This increases the losses to the wire.

As shown in Fig. 19, the focus sweep effect reduces η_t at $R=15$ cm from 67.9% for the case with no focus sweep (i.e., $\alpha=1$) to 57.9% for $\alpha=2$ and 53.6% for $\alpha=3$. Figure 20 shows the variation of η_t with E_s for the case with $N=20$,

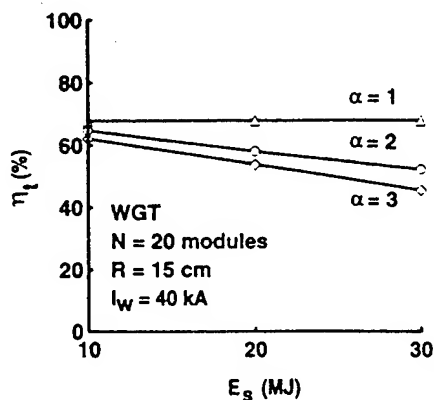


FIG. 20. Plot of η_t vs E_s with $N=20$, $R=15$ cm, and $I_w=40$ kA for WGT. The individual curves are for $\alpha=1, 2$, and 3 .

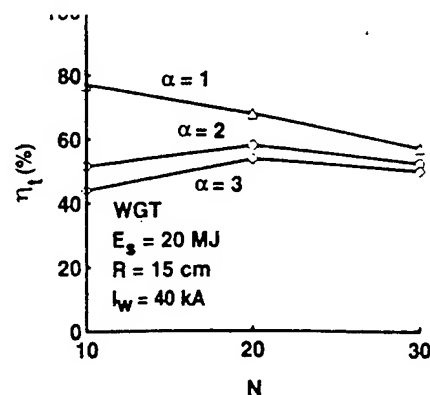


FIG. 21. Plot of η_t vs N with $E_s=20$ MJ, $R=15$ cm, and $I_w=40$ kA for WGT. The individual curves are for $\alpha=1, 2$, and 3 .

$R=15$ cm, and $I_w=40$ kA. The focus sweep effect increases as E_s increases because the time variation in the steering angle [as shown in Eq. (6)] is proportional to θ_0 which scales as E_s (see Table I). Figure 21 shows the variation of η_t with N for the case with $E_s=20$ MJ, $R=15$ cm, and $I_w=40$ kA. The focus sweep effect increases as N decreases because θ_0 scales as $1/N$ (see Table I). As with ZDT, the variations of η_t with E_s and N are more pronounced for WGT compared with BTSF because WGT is not achromatic.

An alternative transport system, similar to that discussed for ZDT at the end of Sec. IV, can also be designed for WGT. However, for WGT a larger wire radius is needed [see Eq. (21)] to avoid melting the wire with the larger wire current that is required. Because of this, more ions will be lost to the wire. The transport efficiency is plotted as a function of R in Fig. 22 with $N=20$ and $E_s=20$ MJ for WGT with $I_w = I_w^*(R)$ from Eq. (18) and $F=F^*(R)$ from Eq. (19). The individual curves are for $\alpha=1, 2$, and 3 . Unlike ZDT, eliminating losses at the aperture by this technique does not improve the transport efficiency for either $\alpha=2$ and $\alpha=3$ cases. This results from increased losses to the wire and in the standoff region.

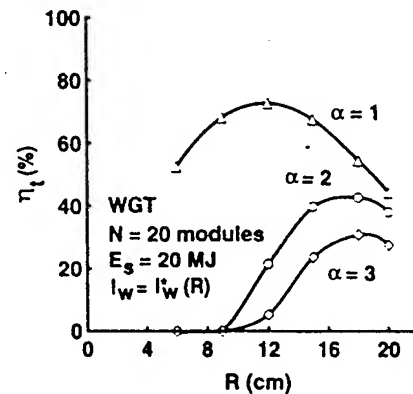


FIG. 22. Plot of η_t vs R with $N=20$ and $E_s=20$ MJ for WGT with $I_w = I_w^*(R)$ and $F=F^*(R)$. The individual curves are for $\alpha=1, 2$, and 3 .

VI. SUMMARY AND CONCLUSIONS

Transport efficiency has been calculated as a function of various system parameters (namely, R , α , E_s , and N) so that LMF point designs can be developed for BTSF, ZDT, and WGT schemes. Typical point design values are $\theta_\mu = 5$ mrad, $R = 15$ cm, $F = 150$ cm, $E_s = 20$ MJ, $N = 20$ cm, $\alpha = 2$, $r_t = 1$ cm, and $\tau_t = 15$ ns for 30 MeV lithium ions. The analysis takes into account target requirements and realistic constraints on diode source brightness, packing, and beam transport. Focus sweeping due to a voltage ramp for TOF bunching has been considered. Because the standard BTSF system is nearly achromatic, the focus sweep effect reduces η_t the least for BTSF. Results shown in Figs. 7, 12, and 19 indicate that reasonably high transport efficiency ($>50\%$) can be obtained for all three systems for bunching factors as large as $\alpha = 3$ with $R \leq 15$ cm. In particular, the point design for LMF using the base-line BTSF system with $R = 15$ cm and $\alpha = 2$ is calculated to have $\eta_t = 84\%$. At the same values of R and α , the ZDT system has the next highest η_t (71.9%) and WGT has the lowest η_t (59.5%). High η_t can be extended to larger R than displayed in Figs. 7, 12, and 19 by increasing R_s for BTSF,⁷ I_c for ZDT,⁸ and I_w for WGT.⁹ Eventually this is limited by the packing constraint for BTSF and by the more rapid beam expansion in the target standoff region for ZDT and WGT. WGT also suffers from higher losses to the wire at higher I_w because of the larger wire radius that is required to avoid melting the guide wire.

The focus sweep effect increases as E_s increases and N decreases because the time variation in the steering angle is proportional to θ_0 which scales as E_s/N . Because BTSF is nearly achromatic, the variations of η_t with E_s and N are more pronounced for ZDT and WGT than for BTSF. However, η_t remains acceptably high (above 50%) for all three transport systems over the relevant range of values for E_s and N when typical point design values are used for the other system parameters.

A second BTSF system was considered where Δ was fixed at 4 cm so that the achromatic matching condition is only satisfied for one value of R . This one matched value of R is typically smaller than the desired value. Although the focus sweep effect is larger at values of R different from that one matched value, the decrease in η_t (from that obtained in the achromatically matched system) is not prohibitive. In the future, adjustments of the solenoidal lens magnetic field map will be studied to optimize η_t for BTSF with focus sweeping.

Alternate systems for ZDT and WGT were also analyzed. For these systems, the beam was focused onto an aperture at F^* (see Fig. 15) so that the beam spot size was smaller than the aperture during the entire pulse. This eliminates losses to the aperture due to the focus sweep effect at the expense of a larger current $I_{c,w}^*$ (see Fig. 16) which is required to confine the hotter (i.e., larger R/F^*) beam. High η_t is recovered for ZDT, but losses both to the larger guide wire (required to avoid wire melting at the higher I_w^*) and in the longer standoff region preclude improvements in η_t for WGT. Results of Ref. 11 suggest that the ZDT channel current may be limited by engineering and physics consider-

ations to about 100 kA for low-mass wall-stabilized channels appropriate for LMF. Thus, this technique may only be useful for ZDT at large R where little improvement in η_t is seen. Therefore, these alternative systems do not hold promise for significant improvements in η_t over those obtained for the standard ZDT and WGT systems. In the future, other variations on the standard ZDT and WGT systems will be considered to optimize η_t .

The purpose of this article was to evaluate the basic aspects of ion-beam transport efficiency for LMF when TOF bunching is used. In the future, other issues associated with a specific LMF design will have to be addressed in order to accurately determine η_t for that design. Ion-beam species purity, waveform efficiency, and beam energy losses during transport have not been considered and will reduce the overall efficiency. Detailed measurements of beam microdivergence are needed to provide an accurate model for θ_μ . A LMF diode impedance model must be defined to establish the appropriate value for k in Eq. (3). Also, the details of the stripping foil position and anode shape need to be worked out so that the effect of the radial dependence of Δ can be properly folded into the calculation of η_t for a specific LMF diode design. And finally, the assumption of complete beam current neutralization is very stringent. Net currents as small as 0.1% of the beam current can have a significant effect on beam transport and η_t . However, since a small net current acts on the beam as a distributed lens, its effect on transport can be corrected if the net current is predictable. Work is presently underway to evaluate beam current neutralization²⁹ for LMF applications.

ACKNOWLEDGMENT

This work was supported by the U.S. DOE through Sandia National Laboratories.

- ¹J. J. Ramirez, R. W. Stinnett, D. L. Johnson, C. L. Olson, T. A. Mehlhorn, J. T. Crow, J. P. Quintenz, K. R. Prestwich, M. P. Desjarlais, R. E. Olson, G. O. Allshouse, T. H. Martin, J. P. VanDevender, D. L. Cook, S. A. Slutz, K. B. Coachman, T. R. Lockner, B. N. Turman, S. A. Goldstein, and J. N. Olsen, *Fusion Tech.* 15, 350 (1989).
- ²D. L. Johnson, J. J. Ramirez, R. W. Stinnett, and K. B. Coachman, in the *Proceedings of the 1989 Particle Accelerator Conference*, edited by F. Bennett and J. Kapt, Chicago, IL, March 20–23, 1989, p. 1017.
- ³C. L. Olson, in the *Proceedings of the 1989 Particle Accelerator Conference*, edited by F. Bennett and J. Kapt, Chicago, IL, March 20–23, 1989, p. 1011.
- ⁴D. Mosher, D. D. Hinshelwood, J. M. Neri, P. F. Ottinger, J. J. Watrous, C. L. Olson, and T. A. Mehlhorn, in the *Proceedings of the 8th International Conference on High-Power Particle Beams*, edited by B. N. Breizman and B. A. Knyazev, Novosibirsk, U.S.S.R., July 2–5, 1990, p. 26.
- ⁵C. L. Olson, in the *Proceedings of the 1988 Linear Accelerator Conference*, edited by C. Leemann, Newport News, VA, October 3–7, 1988, p. 34.
- ⁶T. A. Mehlhorn and J. P. Quintenz, in the *Proceedings of the 1989 Particle Accelerator Conference*, edited by F. Bennett and J. Kapt, Chicago, IL, March 20–23, 1989, p. 1014.
- ⁷P. F. Ottinger, D. V. Rose, J. M. Neri, and C. L. Olson, *J. Appl. Phys.* 72, 395 (1992).
- ⁸P. F. Ottinger, D. V. Rose, D. Mosher, and J. M. Neri, *J. Appl. Phys.* 70, 5292 (1991).
- ⁹J. J. Watrous, D. Mosher, J. M. Neri, P. F. Ottinger, C. L. Olson, J. T. Crow, and R. R. Peterson, *J. Appl. Phys.* 69, 639 (1991).
- ¹⁰R. F. Hubbard, M. Lampe, G. Joyce, S. P. Slinker, I. Haber, and R. F. Fernsler, *Part. Accel.* 37–38, 161 (1992).
- ¹¹D. D. Hinshelwood, *J. Appl. Phys.* 72, 4581 (1992).

- ¹²J. N. Olsen and R. J. Leeper, *J. Appl. Phys.* **53**, 3397 (1982).
- ¹³S. Nakai, K. Imasaki, S. Miyamoto, S. Higaki, T. Ozaki, A. Yoshinouchi, H. Fujita, K. Mima, K. Nishihara, T. Yabe, S. Ido, Y. Ohgaki, and C. Yamanaka, *Laser and Particle Beams* **1**, 29 (1983).
- ¹⁴J. R. Freeman, L. Baker, and D. L. Cook, *Nucl. Fusion* **22**, 383 (1982).
- ¹⁵G. A. Moses, G. L. Kulcinski, D. Bruggink, R. Engelstad, E. Lovell, J. MacFarlane, Z. Musicki, R. Peterson, M. Sawan, I. Sviatoslavsky, L. Wittenberg, G. Kessler, U. von Mollendorff, E. Stein, D. Cook, R. Olson, I. Smith, P. Corcoran, H. Nishimoto, and J. Fockler, *Fusion Tech.* **15**, 756 (1989).
- ¹⁶R. R. Peterson and G. A. Moses, in the Proceedings of the 7th International Conference on High-Power Particle Beams, edited by W. Bauer and W. Schmidt, Karlsruhe, Germany, July 4–8, 1988, p. 625.
- ¹⁷P. F. Ottinger, D. Mosher, J. M. Neri, D. V. Rose, and C. L. Olson, in the Proceedings of the 9th International Conference on High-Power Particle Beams, edited by D. Mosher and G. Cooperstein, Washington, DC, May 25–29, 1992, p. 60.
- ¹⁸D. J. Johnson, R. J. Leeper, W. A. Stygar, R. S. Coats, T. A. Mehlhorn, J. P. Quintenz, S. A. Slutz, and M. A. Sweeney, *J. Appl. Phys.* **58**, 12 (1985).
- ¹⁹S. A. Slutz and D. B. Seidel, *J. Appl. Phys.* **59**, 2685 (1986).
- ²⁰D. L. Hanson, M. E. Cuneo, P. F. McKay, R. S. Coats, and S. E. Rosenthal, *IEEE Trans. Plasma Sci.* **PS-19**, 831 (1991).
- ²¹C. L. Olson, in Proceedings of the 1990 Linear Accelerator Conference, edited by S. O. Schriber and C. Beckmann, Albuquerque, NM, September 1990, LANL Report LA12004-C, p. 396.
- ²²C. L. Olson, in IEEE Conference Record Abstracts, the 1991 IEEE International Conference on Plasma Science, edited by K. Schoenbach, Williamsburg, VA, June 3–5, 1991, p. 165.
- ²³F. Winterberg, *Plasma Phys.* **17**, 69 (1975).
- ²⁴S. A. Goldstein, G. Cooperstein, R. Lee, D. Mosher, and P. F. Ottinger, in IEEE Conference Record Abstracts, the 1978 IEEE International Conference on Plasma Science, edited by F. Schwirzke, Monterey, CA, May 15–17, 1978, p. 112.
- ²⁵G. Cooperstein, S. A. Goldstein, D. Mosher, R. J. Barker, J. R. Boller, D. G. Colombant, A. Drobot, R. A. Meger, W. F. Oliphant, P. F. Ottinger, F. L. Sandel, S. J. Stephanakis, and F. C. Young, in *Laser Interaction and Related Plasma Phenomena*, edited by J. J. Schwartz, H. Hora, M. Lubin, and B. Yaakobi (Plenum, New York, 1981), Vol. 5, p. 105.
- ²⁶J. P. VanDevender, J. A. Swegle, D. J. Johnson, K. W. Bieg, E. J. T. Burns, J. W. Poukey, P. A. Miller, J. N. Olsen, and G. Yonas, *Laser and Particle Beams* **3**, 93 (1985).
- ²⁷P. L. Dreike, E. J. T. Burns, S. A. Slutz, J. T. Crow, D. J. Johnson, P. R. Johnson, R. J. Leeper, P. A. Miller, L. P. Mix, D. B. Seidel, and D. F. Wenger, *J. Appl. Phys.* **60**, 878 (1986).
- ²⁸J. P. Quintenz and D. B. Seidel, Sandia National Laboratories Report SAND84-1336, June 1984.
- ²⁹F. C. Young, D. D. Hinshelwood, R. F. Hubbard, M. Lampe, J. M. Neri, C. L. Olson, P. F. Ottinger, D. V. Rose, S. P. Slinker, S. J. Stephanakis, and D. R. Welch, *Phys. Rev. Lett.* **70**, 2573 (1993).

REPORT DOCUMENTATION PAGE			Form Approved OMB No. 0704-0188	
Public reporting burden for this collection of information is estimated to average 1 hour per response, including the time for reviewing instructions, searching existing data sources, gathering and maintaining the data needed, and completing and reviewing the collection of information. Send comments regarding this burden estimate or any other aspect of this collection of information, including suggestions for reducing this burden, to Washington Headquarters Services, Directorate for Information Operations and Reports, 1215 Jefferson Davis Highway, Suite 1204, Arlington, VA 22202-4302, and to the Office of Management and Budget, Paperwork Reduction Project (0704-0188), Washington, DC 20503.				
1. AGENCY USE ONLY (Leave Blank)	2. REPORT DATE September 30, 1994	3. REPORT TYPE AND DATES COVERED Interim		
4. TITLE AND SUBTITLE Transport Efficiency Studies for Light-Ion Inertial Confinement Fusion		5. FUNDING NUMBERS 67-0879-0-2		
6. AUTHOR(S) D.V. Rose, ¹ P.F. Ottinger, and C.L. Olson ²				
7. PERFORMING ORGANIZATION NAME(S) AND ADDRESS(ES) Naval Research Laboratory Washington, DC 20375-5320		8. PERFORMING ORGANIZATION REPORT NUMBER NRL/MR/6770-94-7609		
9. SPONSORING/MONITORING AGENCY NAME(S) AND ADDRESS(ES) Sandia National Laboratories Albuquerque, NM 87185		10. SPONSORING/MONITORING AGENCY REPORT NUMBER SNL FAO AI-7233 DOE DE-AC04-94AL8500		
11. SUPPLEMENTARY NOTES ¹ JAYCOR, Inc., Vienna, VA 22182 ² Sandia National Laboratories, Albuquerque, NM 87185				
12a. DISTRIBUTION/AVAILABILITY STATEMENT Approved for public release; distribution unlimited.			12b. DISTRIBUTION CODE	
13. ABSTRACT (Maximum 200 words) The proposed Laboratory Microfusion Facility (LMF) will require ≥ 10 MJ of 30 MeV lithium ions to be transported and focused onto high-gain, high-yield inertial confinement fusion targets. The light-ion LMF approach used a multimodular system with individual ion extraction diodes as beam sources. Several transport schemes are being considered to deliver the individual ion beams to the centrally located target. Previous work [P.F. Ottinger, D.V. Rose, and C.L. Olson, J. Appl. Phys. 75, 4402 (1994)] examined the effect of time-of-flight bunching on energy transport efficiency, η_t , under realistic constraints on diode operation, beam transport, and packing. Target design considerations suggest that the instantaneous power efficiency, Γ_t , be maximized near peak power. Because of time-of-flight bunching, peak power occurs at the end of the power pulse for LMF designs. This work examines the effect of power efficiency tuning on η_t for three transport schemes. Results indicate that tuning the power pulse to maximize Γ_t , at about three-quarters through the pulse provides high power efficiency at the end of the pulse while still maintaining high η_t . In addition to power efficiency tuning, effects on η_t from variations of the diode impedance model and the diode voltage waveform are also examined.				
14. SUBJECT TERMS Light-ion Inertial confinement fusion			15. NUMBER OF PAGES 51	
			16. PRICE CODE	
17. SECURITY CLASSIFICATION OF REPORT UNCLASSIFIED	18. SECURITY CLASSIFICATION OF THIS PAGE UNCLASSIFIED	19. SECURITY CLASSIFICATION OF ABSTRACT UNCLASSIFIED	20. LIMITATION OF ABSTRACT UL	

CONTENTS

I. Introduction	1
II. Ion Source Model	6
III. Power Efficiency Tuning	17
IV. Impedance Model Variations and Non-Ideal Accelerator Wave Forms	28
V. Summary and Conclusions	40
VI. Acknowledgments	44
VII. References	45
VIII. List of Variables	47

TRANSPORT EFFICIENCY STUDIES FOR LIGHT-ION INERTIAL CONFINEMENT FUSION

I. Introduction

The Laboratory Microfusion Facility (LMF) has been proposed for the study of high-gain, high-yield inertial confinement fusion (ICF) targets.¹ A multimodular light-ion approach, based on Hermes-III technology, is under investigation.^{1,2} This approach requires the transport and focusing of a number of intense ion beams over distances of several meters to a centrally located, high-gain, high-yield ICF target. The distance between the target and beam generators provides for packing of the beam generators around a target chamber of > 100 cm radius, and isolation of the diode hardware from the explosion. In addition, the transport distance allows for time-of-flight (TOF) bunching of the beams to achieve power multiplication. Several beam transport and focusing schemes are being evaluated for LMF,^{3,4} including ballistic transport with solenoidal lens focusing (BTSF),⁵ and ballistic focusing with z-discharge transport (ZDT),⁶ or wire-guided transport (WGT).⁷ The baseline approach for LMF utilizes the BTSF scheme with a ballistic transport distance L (diode to lens) of 250 cm and a focal distance F (lens to target) of 150 cm. The LMF system is schematically illustrated for BTSF in Fig. 1. The alternate transport schemes, ZDT and WGT are shown in Figs. 2 and 3, respectively. In both of these transport schemes, the beam is ballistically focused over a distance F of 150 cm onto the transport channel entrance and transported a distance L of 250 cm to the target. In addition to these three transport schemes, self-pinched transport has been proposed for transporting intense ion beams for LMF.⁸ Since the BTSF, ZDT, and WGT schemes have been the most extensively studied to date, self-pinched transport will not be discussed in this work. However, results for self-pinched transport should be similar to those of ZDT.

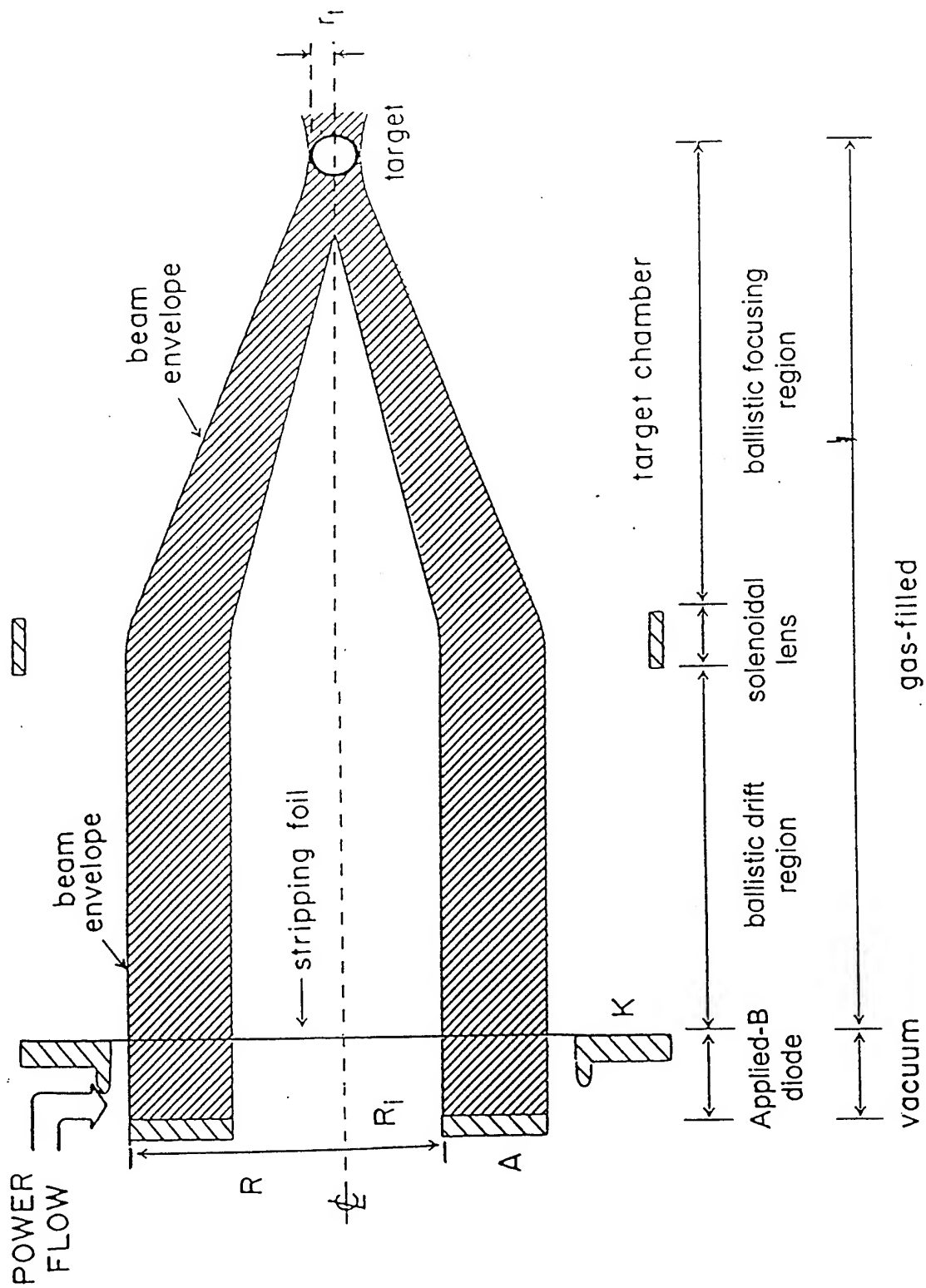


Fig. 1 - Schematic of BTSF system.

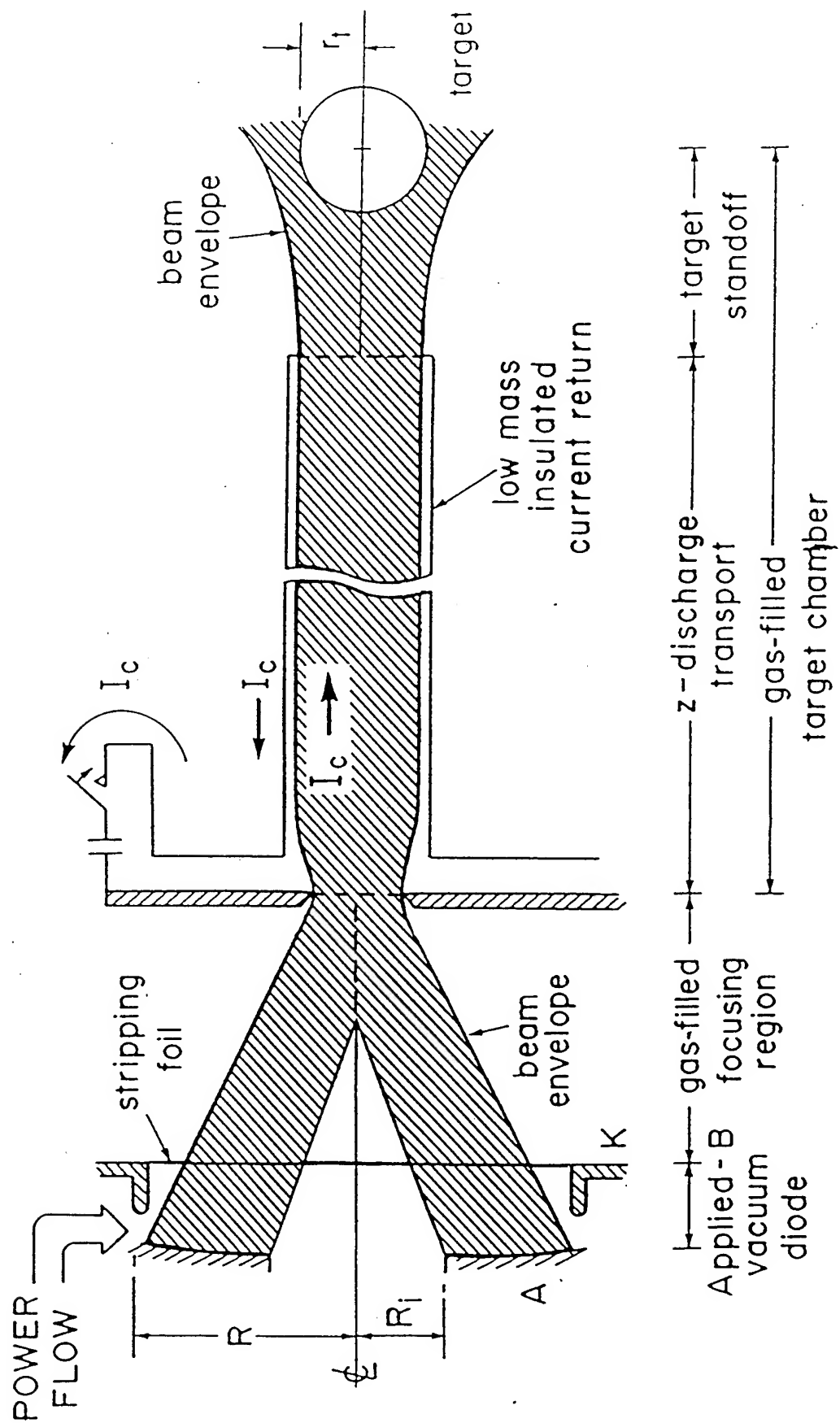


Fig. 2 - Schematic of ZDT system.

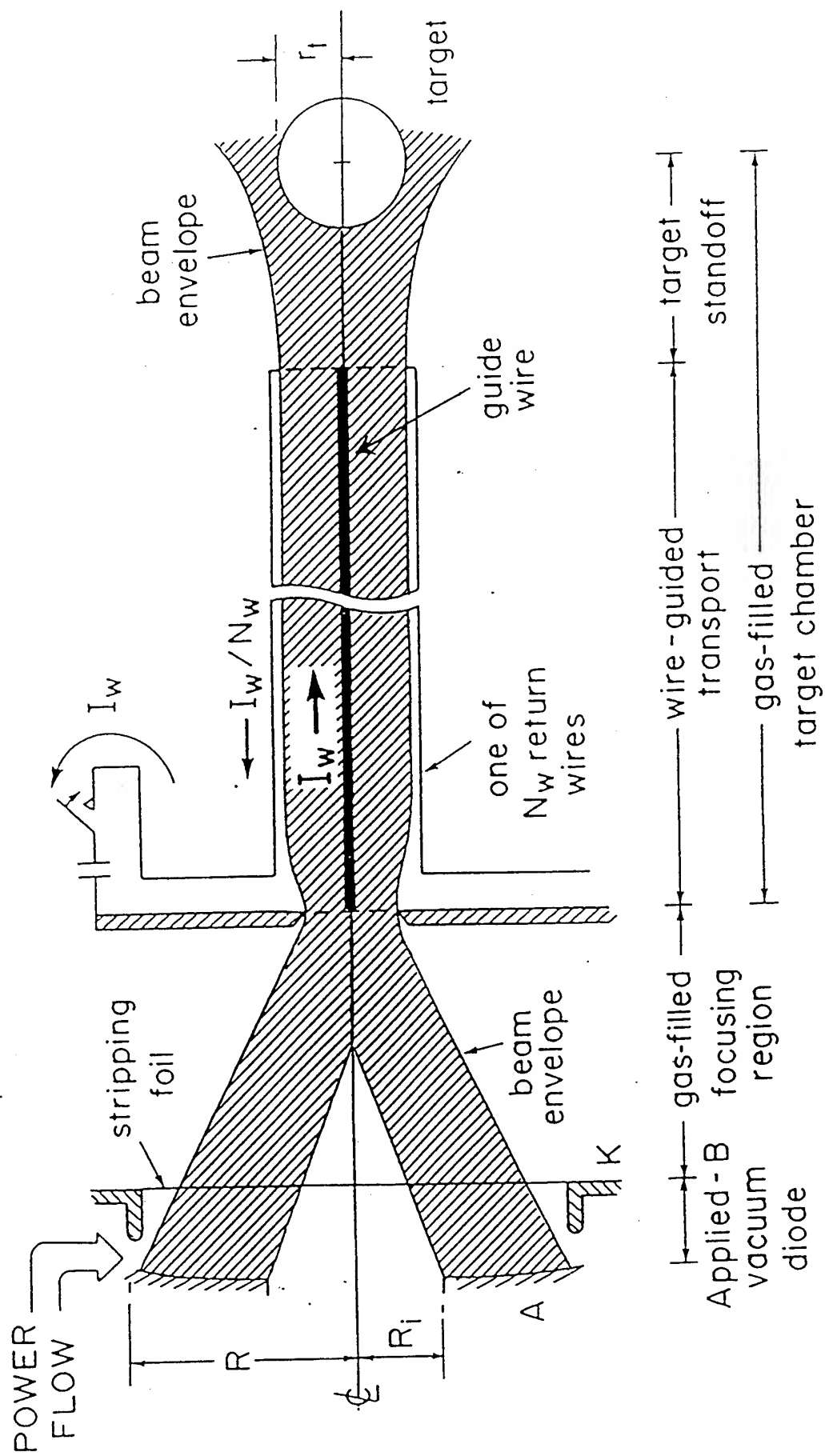


Fig. 3 - Schematic of WGT system.

A previous analysis⁹ examined the effect of time-of-flight bunching on energy transport efficiency, η_t , under realistic constraints on diode operation, beam transport, and packing. The energy transport efficiency η_t is defined here as the ratio of total ion energy delivered to the target to the total ion energy produced in the diodes. This effort extends the previous analysis to examine the impact of systematic variations in several key model parameters. These parameters include tuning the peak power coupling between the beam and the target, current scaling for the diode impedance model, and diode voltage variations about the ideal voltage ramp for TOF bunching. The square microdivergence profile for the ion source model, used in the previous analysis, has also been replaced with a Gaussian microdivergence profile.

Power efficiency Γ_t is defined as the ratio of the instantaneous transported ion power on target to the power at that same instant of an ideal bunched beam pulse at the target location as defined by the product of current and voltage will be given in Eqs. (15) and (16). Because of chromatic focusing effects, Γ_t changes in time as the voltage changes. Typically, the achromatic matching condition (for BTSF) or the ballistic focal length (for ZDT and WGT) are fixed at mid-pulse to optimize η_t . In this case Γ_t peaks near mid-pulse. However, Γ_t can be tuned to peak at other times at the expense of lower η_t . Previous work⁹ examined chromatic effects on η_t with power efficiency tuned to peak at mid-pulse. Target design considerations indicate that peak power should be delivered at the end of the pulse.¹⁰ In this paper, the time of peak power efficiency is varied between the mid-point and the end of the voltage pulse to determine the effect on η_t . Results indicate that tuning the power pulse to maximize Γ_t at about three-quarters through the pulse provides high power efficiency at the end of the pulse while still maintaining high η_t . For BTSF, this yields 89 % instantaneous power efficiency at the tail of the pulse with η_t of 73 % for parameters of interest ($L = 250$ cm, $F = 150$ cm, a diode radius of 15 cm, and a microdivergence of 5 mrad) for a system with 20 modules and 20 MJ of ion energy available at the diodes.

Section II of this paper reviews the ion source model used in this work and highlights changes from the previous analysis. The effect on η_i due to modifying the microdivergence profile for all three transport schemes is also examined in this section. In Sec. III, the effect of power efficiency tuning on η_i is examined. Section IV of this paper examines the impact on η_i due to variations in the diode impedance model and the diode voltage waveform. This paper is summarized in Sec. V. Note that when comparing two efficiency numbers, absolute differences (in %) are quoted rather than percentage changes.

II. Ion Source Model

The ion source model is based on the extraction applied- B diode with an annular emitting surface extending from outer radius R to inner radius $R_i = R/2$. Ions accelerated across the vacuum gap, Δ , in the diode are bent toward the axis by the self-magnetic field of the beam. For small angles, this bending angle $\Theta_b(r, t)$ is $\omega_c \Delta / v$, where $v(t)$ is the ion speed, and ω_c is the beam ion cyclotron frequency associated with the self-magnetic field in the diode region so that $\omega_c = 2eZ_d I_d / r m_i c^2$. Here, $I_d(t)$ is the ion current in the diode, eZ_d and m_i are the beam ion charge in the diode and the ion mass, and c is the speed of light. Uniform current density is assumed in the annular emitting region of the diode.

A stripping foil separates the diode vacuum region from the gas-filled transport region. Singly charged lithium ions accelerated across the vacuum gap are stripped to Li^{+3} as they enter the gas-filled region. For applied- B extraction diodes, the position and shape of this stripping foil are determined by ion beam angular momentum considerations. This topic is addressed in detail in Ref. 9. For the purposes of this work, the width of the vacuum gap, Δ , in the BTSF case is determined solely from the achromatic matching condition⁵ and it will be assumed that both achromatic and angular

momentum conditions have been satisfied.⁹ For ZDT and WGT, it is assumed that Δ is fixed at 4 cm, independent of radius.

As illustrated in Figs. 4 and 5, ions are assumed to leave the diode region distributed in a cone of half-angle Θ_μ about a steering angle $\Theta_s = \Theta_b(r, t) + \Theta_a(r)$, where Θ_μ is the source microdivergence, and $\Theta_a(r)$ is due to the anode surface shape (assuming no anode plasma motion). Unlike the previous analysis⁹, Θ_μ is assumed to have a Gaussian profile in velocity space and is independent of radius and time. The impact of this change is discussed at the end of this section. Figure 4 shows the beam extracted parallel to the axis for BTSF and Fig. 5 shows a focused extraction of the beam appropriate for ZDT and WGT. Since Θ_b varies as $V_d^{(k-1/2)}$, where $V_d(t)$ is the diode accelerating voltage, and diode current scales as V^k (typically k is assumed to be 2.0), Θ_a can compensate for Θ_b at only one point in time. At this time, referred to as the tuning time, the instantaneous power transport efficiency is optimized. The previous analysis used a tuning time near mid-pulse, when the average voltage V_o is reached, optimizing η_t . For this analysis, the tuning time, expressed in terms of the tuned diode voltage V_{tune} , is varied between the middle and the end of the pulse in order to study the impact of changing the time of optimal power efficiency (delivered to the target) on η_t .

The ideal ramped voltage and current pulses produced by the diode are

$$V_d(t) = \frac{V_d(0)}{\left(1 - \frac{t}{T} \frac{\alpha - 1}{\alpha}\right)^2}, \quad (1)$$

and

$$I_d(t) = I_{do} \left(\frac{V_d(t)}{V_o} \right)^k, \quad (2)$$

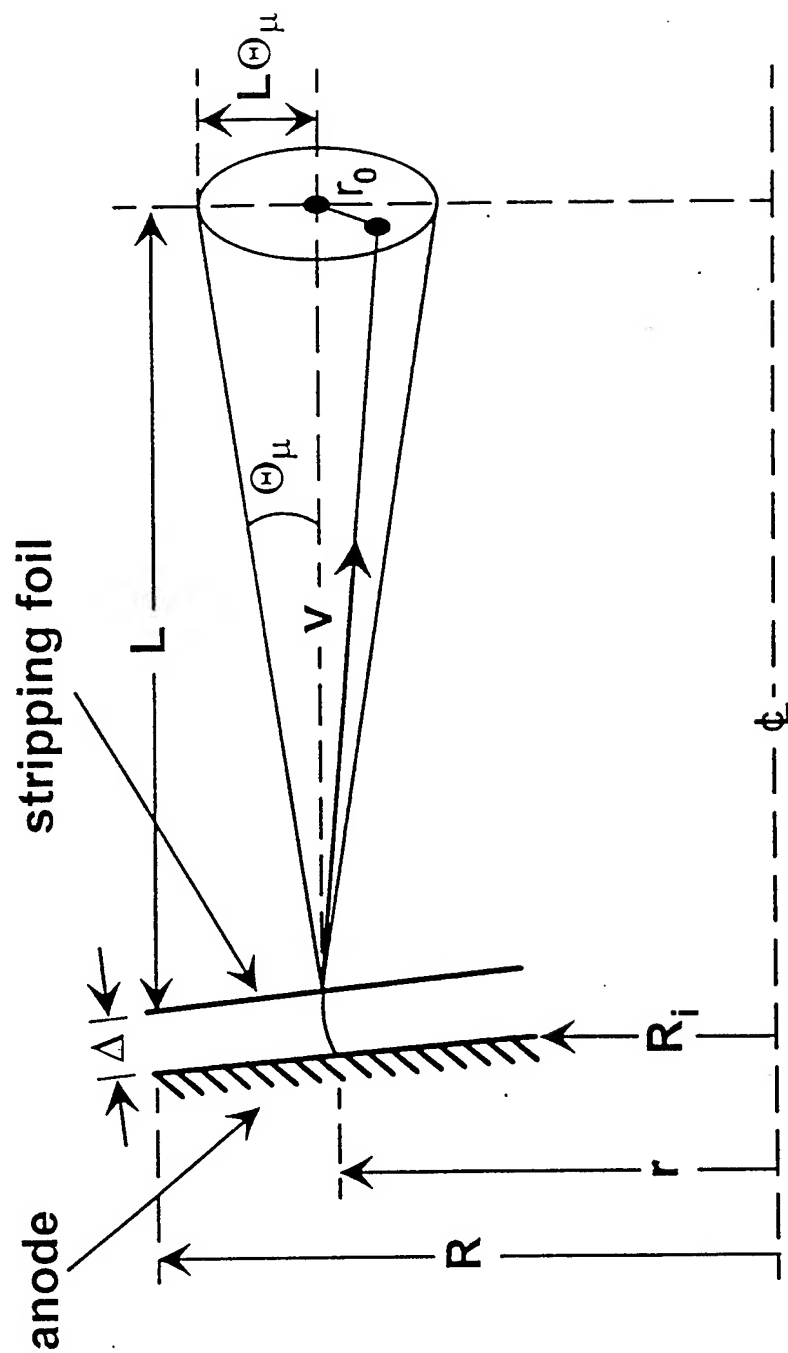


Fig. 4 - Injection geometry for BTSE.

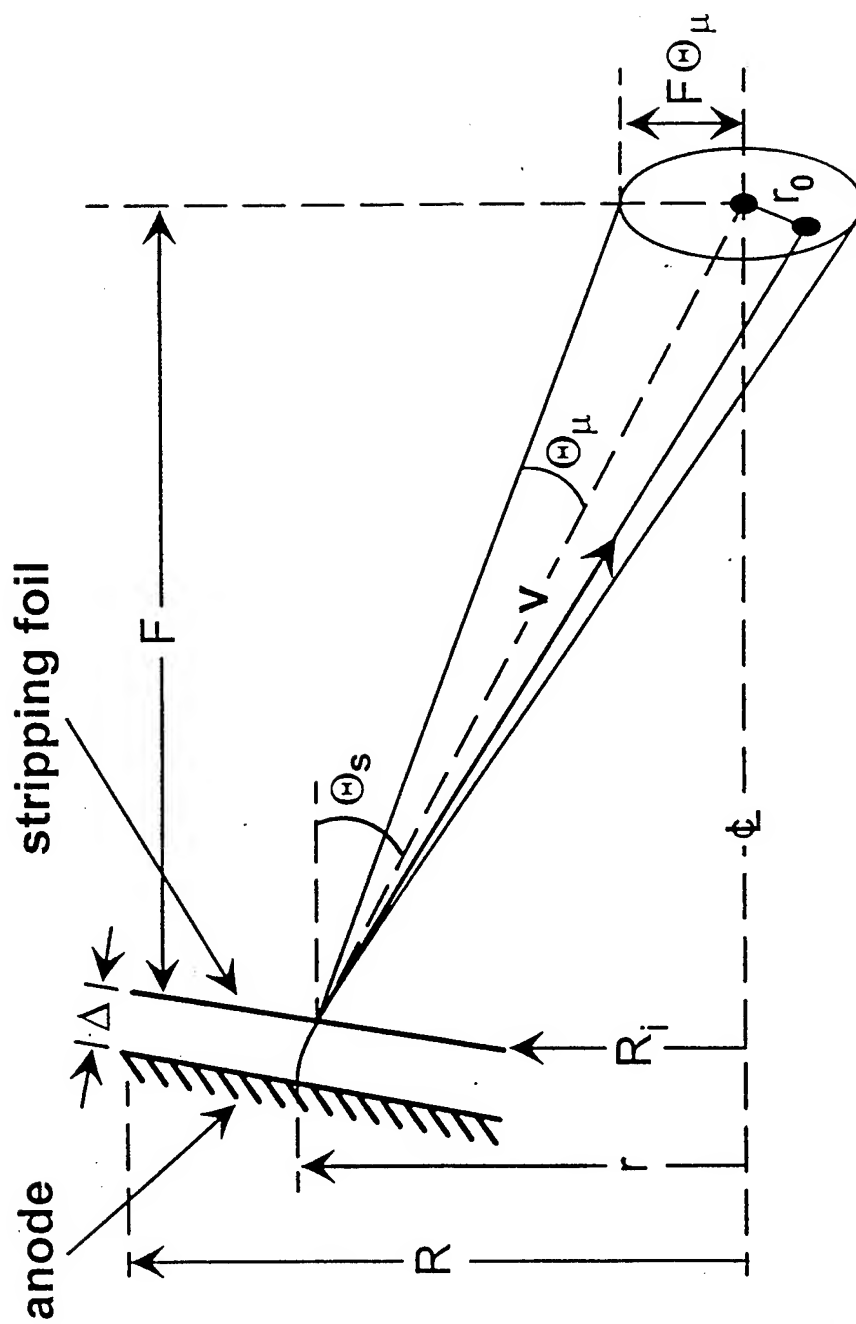


Fig. 5 - Injection geometry for ZDT and WGT.

where T is the arrival time of the beam front at the target, $V_d(0)$ is the initial voltage at time $t = 0$, and α is the bunching factor. The average value of the voltage, V_o , is defined as $(V_d(\tau_d) + V_d(0))/2$, where τ_d is the initial pulse length and I_{do} is the diode ion current when $V_d(t) = V_o$. A power pulse given by Eqs. (1) and (2) will time-of-flight compress to a pulse length of $\tau_b = \tau_d / \alpha$ at a time T after the start of the pulse.

The total path length for the beam from the diode to the target is $D = v_d(0)T$, where $v_d(0) = (2eZ_dV_d(0)/m_i)^{1/2}$, for a non-relativistic beam. Evaluating Eq. (1) at $t = \tau_d$ and substituting the resulting expression for $V_d(\tau_d)$ into the definition of V_o yields

$$V_d(0) = 2V_o - V_d(\tau_d) = \frac{2V_o\xi^2}{(1+\xi^2)}, \quad (3)$$

where

$$\xi = 1 - \left(\frac{\tau_d}{T} \right) \left(\frac{\alpha - 1}{\alpha} \right). \quad (4)$$

Equation (3) relates $V_d(0)$ and $V_d(\tau_d)$ for given values of $\xi(\alpha, \tau_d, T)$. Substituting Eq. (3) into the definition of D yields

$$T^2 = \frac{m_i D^2}{4eZ_d V_o} \left(\frac{1+\xi^2}{\xi^2} \right), \quad (5)$$

which is a transcendental equation for T in terms of given values for m_i , D , V_o , and $\xi(\alpha, \tau_d, T)$. Using Eq. (2) for $I_d(t)$ and setting the total beam energy per module,

$$E_d = \int_0^{\tau_d} I_d(t) V_d(t) dt = \frac{I_{do}}{V_o^k} \int_0^{\tau_d} (V_d(t))^{k+1} dt, \quad (6)$$

equal to E_s/N specifies I_{do} for given values of V_o , E_s , N , k , and $\xi(\alpha, \tau_d, T)$. The system energy, E_s , is the total ion energy available from the N diodes and is related to the energy on target, E_t , by $E_t = \eta_t E_s$. Substituting for $V_d(t)$ from Eq. (1) into Eq. (6) and performing the integration yields

$$I_{do} = \frac{(2k+1)E_s}{2^{k+1}NV_o\tau_d} \left(\frac{1-\xi}{\xi} \right) \frac{(1+\xi^2)^{k+1}}{(1-\xi^{2k+1})}, \quad (7)$$

where ξ is given in Eq. (4).

Using the assumption of uniform current density in the annular diode and the impedance model given in Eq. (2), Θ_b can be written as

$$\Theta_b(r, t) = -\Theta_o \left(\frac{V_d(t)}{V_o} \right)^{k-1/2} \left(\frac{r}{R} - \frac{R}{4r} \right), \quad (8)$$

where

$$\Theta_o = \frac{8I_{do}\Delta}{3c^2R} \left(\frac{eZ_d}{2m_iV_o} \right)^{1/2}. \quad (9)$$

Since Θ_a is assumed fixed in time, Eq. (8) will lead to an inward sweeping of Θ_s over the duration of the pulse.

At the tuning time, $t(V_{tune})$, the steering angle is set equal to $-r/F$, so that the beam is ballistically focused a distance F from the diode for ZDT and WGT. For BTSF, F is set equal to ∞ , so that the beam is extracted parallel to the axis. Combining this condition on the steering angle with Θ_b yields the appropriate anode shape

$$\Theta_a(r) = -\frac{r}{F} + \Theta_o \left(\frac{V_{tune}}{V_o} \right)^{k-1/2} \left(\frac{r}{R} - \frac{R}{4r} \right). \quad (10)$$

The beam ion steering angle defined previously⁹, is now modified to include the voltage tuning parameter, V_{tune} , by combining Eqs. (8) and (10), yielding

$$\Theta_s(r, t) = -\frac{r}{F} + \Theta_o \left(\frac{V_{tune}}{V_o} \right)^{k-\frac{1}{2}} \left(1 - \left(\frac{V_d(t)}{V_{tune}} \right)^{k-\frac{1}{2}} \right) \left(\frac{r}{R} - \frac{R}{4r} \right). \quad (11)$$

This equation combines both geometric anode shaping as well as bending due to self-magnetic field focusing of the beam in the vacuum region of the diode. This form of Eq. (11) is appropriate for ZDT and WGT. For BTSF, where the beam is extracted parallel to the transport symmetry axis (i.e., $F = \infty$) at the time the voltage rises to V_{tune} , the term $-r/F$ in Eq. (11) is set to zero.

For BTSF, the diode and solenoidal lens can be treated as an achromatic lens pair for a particular value of r , assuming small variations about the tuning voltage, V_{tune} . The focal length of the solenoid at the tuning voltage is given by⁵

$$F_{tune} = \frac{4v_{tune}^2}{\omega_c^2 L_s}, \quad (12)$$

where L_s is the axial length of the solenoid, and v_{tune} is the ion velocity associated with the tuning voltage V_{tune} . The lens pair is matched for $r = R$, which maximizes the number of ions chromatically focused because the diode is assumed to have uniform current density. Following the analysis performed in Ref. 9, the matching condition becomes

$$\Theta_o = \frac{4R}{3F_{tune}(k-1/2)} \left(\frac{V_o}{V_{tune}} \right)^{k-1/2}, \quad (13)$$

where Θ_o is given by Eq. (9), resulting in the following expression for Δ ,

$$\Delta = \frac{c^2 R^2}{2(k-1/2)I_{do}F_{tune}} \left(\frac{V_o}{V_{tune}} \right)^{k-1/2} \left(\frac{2m_i V_o}{eZ_d} \right)^{1/2}, \quad (14)$$

where I_{do} is given in Eq. (7).

The source microdivergence for all cases considered in Sec. III and IV of this paper assumes a Gaussian profile, with the half-width, half-maximum, Θ_μ , selected to be 5 mrad. Previous calculations^{5,6,9} assumed a square microdivergence profile with a half-width of Θ_μ . Therefore, additional losses in the "wings" (for $\Theta > \Theta_\mu$) are expected, resulting in a reduction in η_t . Since about 25 % of the ions reside in the wings, additional losses could be significant. A comparison of square and Gaussian profiles for each transport scheme is given in Figs. 6-8. For these calculations, $N = 20$ modules, $E_s = 20$ MJ, $\alpha = 2$, $\Theta_\mu = 5$ mrad, $k = 2$, and $V_{tune} = V_o$. Focus sweep effects⁹ (because $\alpha > 1$) and system design constraints^{5,6,7} will be the predominate mechanisms governing η_t for these results. The BTSF scheme, with Δ matched according to Eq. (14), is shown in Fig. 6. For the cases shown, η_t is reduced by 12 % or less. The potential reduction in η_t due to the use of a Gaussian microdivergence profile is minimized in the BTSF case, because the spot size $F\Theta_\mu$ is smaller than the target radius. For $F = 150$ cm and $\Theta_\mu = 5$ mrad, a spot size of 0.75 cm is obtained while a target radius of 1 cm is used. This situation does not apply to the ZDT (Fig. 7) and WGT (Fig. 8) schemes because the beam is apertured down at the entrance of the transport channel to the spot size $F\Theta_\mu$. For these cases, η_t is reduced by at most 9 % and 20 % for ZDT and WGT respectively. The greater overall reduction in η_t for WGT as seen in Fig. 8 is a result of the Gaussian distributed profile being forward peaked. More low-angular-momentum ions strike the guide wire and are removed from the beam.

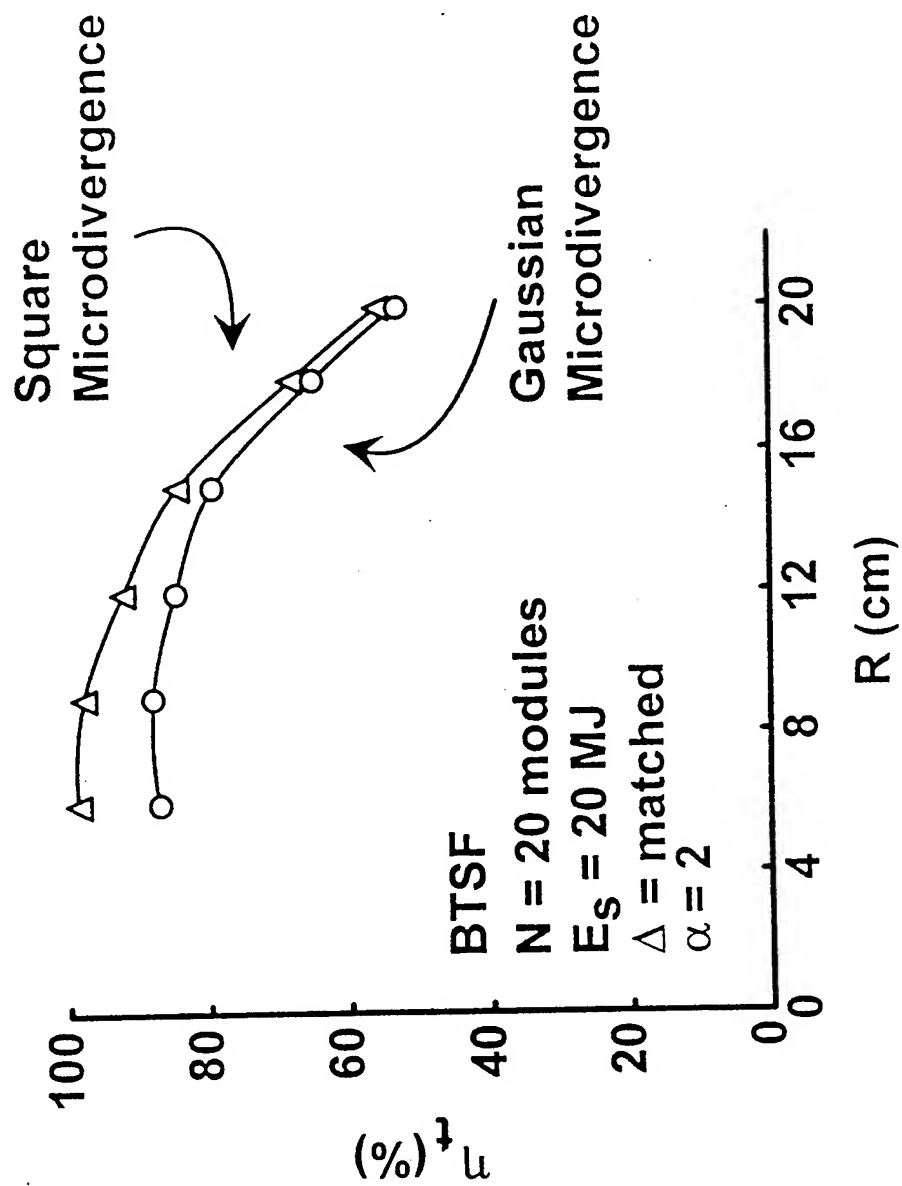


Fig. 6 - Plot of η , vs. R with $\alpha = 2$ for BTSF, comparing square (uniform) and Gaussian microdivergence profiles with $\Theta_\mu = 5$ mrad.

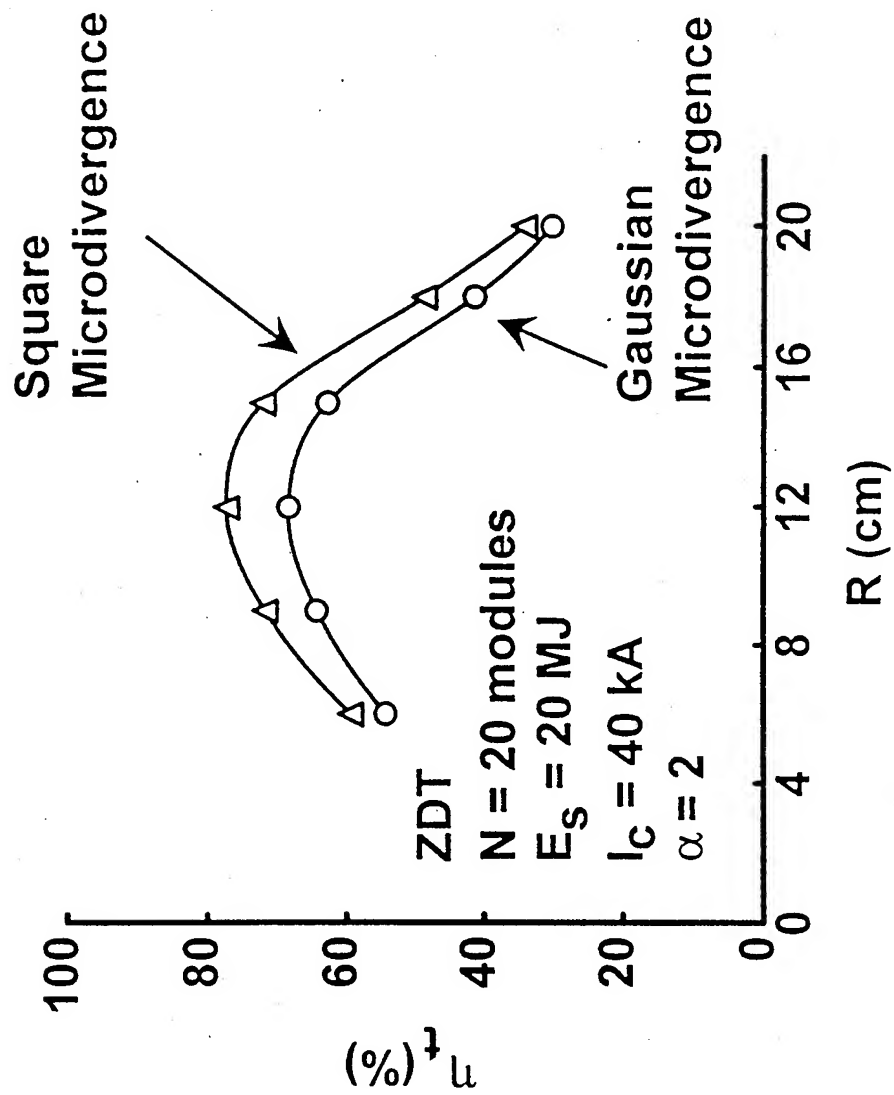


Fig. 7 - Plot of η_u vs. R with $\alpha = 2$ for ZDT, comparing square (uniform) and Gaussian microdivergence profiles with $\Theta_u = 5$ mrad.

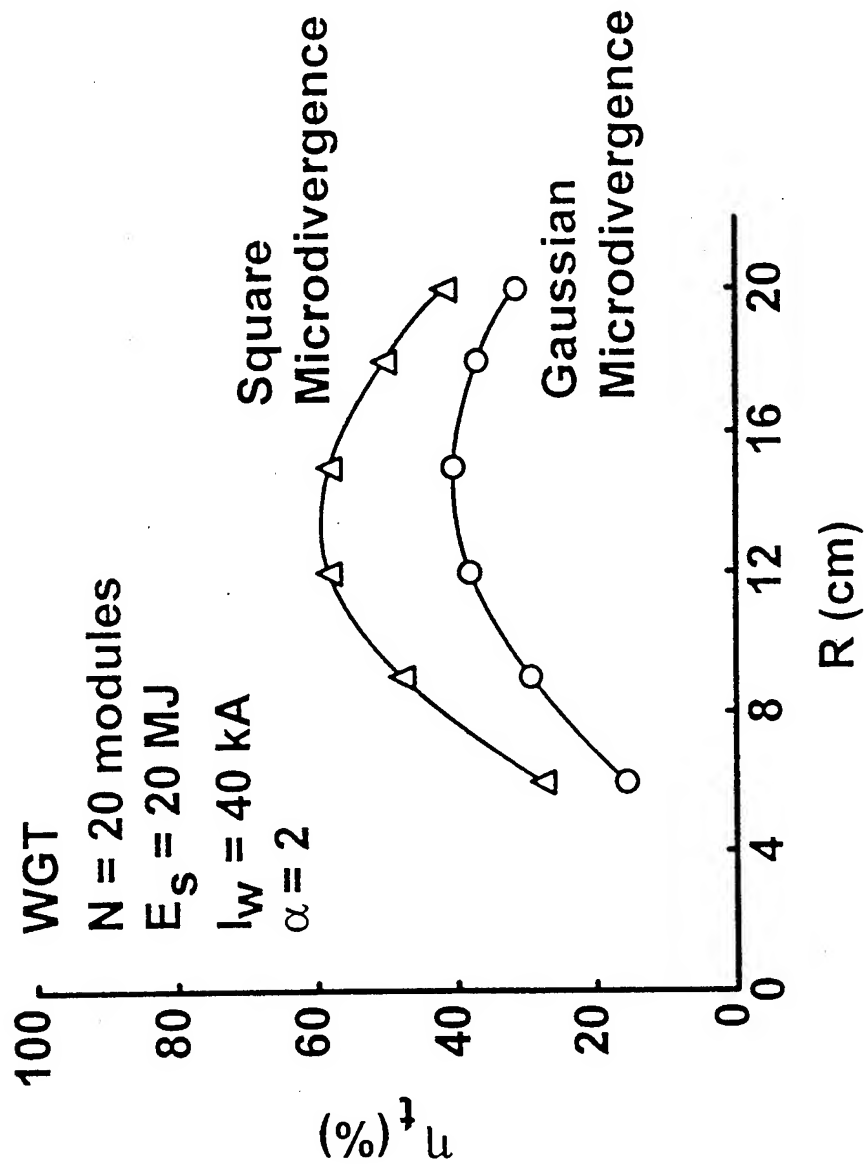


Fig. 8 - Plot of η_u vs. R with $\alpha = 2$ for WGT, comparing square (uniform) and Gaussian microdivergence profiles with $\Theta_u = 5$ mrad.

For the calculations presented here, it is assumed that Li^{+1} ions are accelerated in the diode and are stripped to Li^{+3} as they pass through the foil. A previous analysis⁹ considered a range of values for E_s , N , and α . For this work, these values will be fixed at $E_s = 20$ MJ, $N = 20$, and $\alpha = 2$. In addition, it will be assumed that $V_o = 30$ MV, $D = 400$ cm, and $\tau_b = 15$ ns (so that $\tau_d = 30$ ns). In addition, R will be varied for some calculations between 6 and 20 cm, with $R = 15$ cm used as the baseline diode radius. A centrally located, spherical target of radius $r_t = 1$ cm is assumed at $z = D$ from each of the N diodes.

III. Power Efficiency Tuning

ICF target design considerations indicate that peak power delivered to the target should occur at the end of the driver pulse.¹⁰ This can be accomplished by tuning the voltage for peak power efficiency near the end of the pulse. However, as V_{tune} increases from V_o toward $V(\tau_d)$, η_t decreases. This section examines the impact on η_t of tuning, or moving, the time of peak power later in the pulse.

Allowing the voltage and current waveforms, Eqs. (1) and (2), to evolve in time as the beam is projected ballistically to the target plane at $z = D$, yields

$$V_t(t) = \frac{V_t(T)}{\left(\alpha - t \frac{\alpha - 1}{T}\right)^2}, \quad (15)$$

and

$$I_t(t) = \alpha I_{to} \left(\frac{Z_t V_t(t)}{Z_d V_o} \right)^k, \quad (16)$$

for $T \leq t \leq T + \tau_b$. Here $V_i(T) = Z_d V_d(0) / Z_i$ and $I_{i0} = Z_i I_{d0} / Z_d$ account for the stripping of the beam from Li^{+1} to Li^{+3} in the diode region, before the beam is transported. Equations (15) and (16) ignore path differences in the transverse components of the beam due to microdivergence, focusing, scattering, stopping, etc. and assume 100% transport efficiency. The product of Eqs. (15) and (16) gives the ideal power on target as a function of time. The ratio of the instantaneous power on target to the ideal instantaneous power is Γ_i .

The time at which the voltage pulse rises to the effective voltage $Z_d V_{tune} / Z_i$ at the target (due to stripping of the beam) is $t_i(V_{tune}) = T + t_d(V_{tune}) / \alpha$ or

$$t_i(V_{tune}) = \frac{T}{\alpha - 1} \left(\alpha - \sqrt{\frac{V_d(0)}{V_{tune}}} \right), \quad (17)$$

where $t_d(V_{tune})$ is the time the voltage in the diode rises to V_{tune} which can be obtained from Eq. (1).

For this study, three different voltage tunings were considered at one-half, three-quarters, and the end of the pulse. The voltages corresponding to these tuning times (in the diode) are denoted as $V_{1/2}$, $V_{3/4}$, and $V_{4/4}$, and are given as 29.743 MV, 31.401 MV, and 33.201 MV, respectively for $\alpha = 2$, $k = 2$, $V_o = 30$ MV, $T = 148$ ns, $E_s = 20$ MJ, and $N = 20$ modules. It should be noted that $V_o \neq V_{1/2}$ because the average value of Eq. (1) over the pulse length τ_d does not occur at $\tau_d/2$. Simulations calculating the instantaneous power efficiency at the tuning time, Γ_i^{tune} , the instantaneous power efficiency at the end of the pulse, Γ_i^{end} , and the total transported energy efficiency, η_i , were carried for the BTSF, ZDT, and WGT schemes. A three-dimensional, non-relativistic orbit code was used with 20,000 test particles to give adequate statistics. Full charge and current neutralization is assumed. For the BTSF scheme, the ATHETA code,¹¹ was used to

generate the solenoidal lens magnetic field maps used in the orbit code. For these simulations, a Gaussian microdivergence profile was used with $\Theta_\mu = 5$ mrad.

The impact on η_t of changing the tuning time is qualitatively illustrated for BTSF in Fig. 9 for $R = 15$ cm, $k = 2$, and $\alpha = 2$. This set of plots shows the radius of beam particles arriving at the target position, $z = 400$ cm, as a function of time for three different tunings. About 5 % of the total number of particles used in a typical simulation is represented in these plots. Since each simulation particle is equally weighted in current (but not potential), the increase in power at the tail of the pulse is partially illustrated in Fig. 9 by an increase in the number of particles per time interval. Particles at or below the dashed line at $r = r_t = 1$ cm determine η_t . It is immediately evident that as $t_t(V_{tune})$ is selected to be later in the pulse, more particles do not strike the target, lowering η_t .

For the BTSF scheme, foil placement to achieve achromatic matching is satisfied at only one time in the pulse (the tuning time) and is governed by Eq. (14). For each of the simulations illustrated in Figs. 10-12, different magnetic fields strengths had to be employed in order to optimally focus the ions of velocity v_{tune} onto the target. Figure 10 plots Γ_t^{tune} at the three different tuning voltages. The fall off in Γ_t^{tune} for $R > 15$ cm is due primarily to the packing constraint which limits the maximum solenoidal lens radius. This issue is discussed in detail in Ref. 9. It is evident that the same Γ_t^{tune} can be achieved regardless of which of the three tuning voltages is selected. However, in Fig. 11, the instantaneous power efficiency at the end of the pulse, Γ_t^{end} , does depend on the tuning voltage chosen. Tuning the voltage to the middle of the pulse results in a reduction in Γ_t^{end} by 10 % on average for $R = 9$ to 18 cm compared with tuning the voltage to the end of the pulse. Conversely, the total energy transported to the target for the $V_{4/4}$ case relative to the $V_{1/2}$ case is reduced by an average of 17 % for $R = 9$ to 18 cm as illustrated in Fig. 12. It is evident from this that for BTSF, selecting a tuning time at three-quarters of the pulse length leads to only a slight loss in η_t while maintaining near-optimal power in the tail of the pulse. For the baseline case of $R = 15$ cm, a drop of 6 %

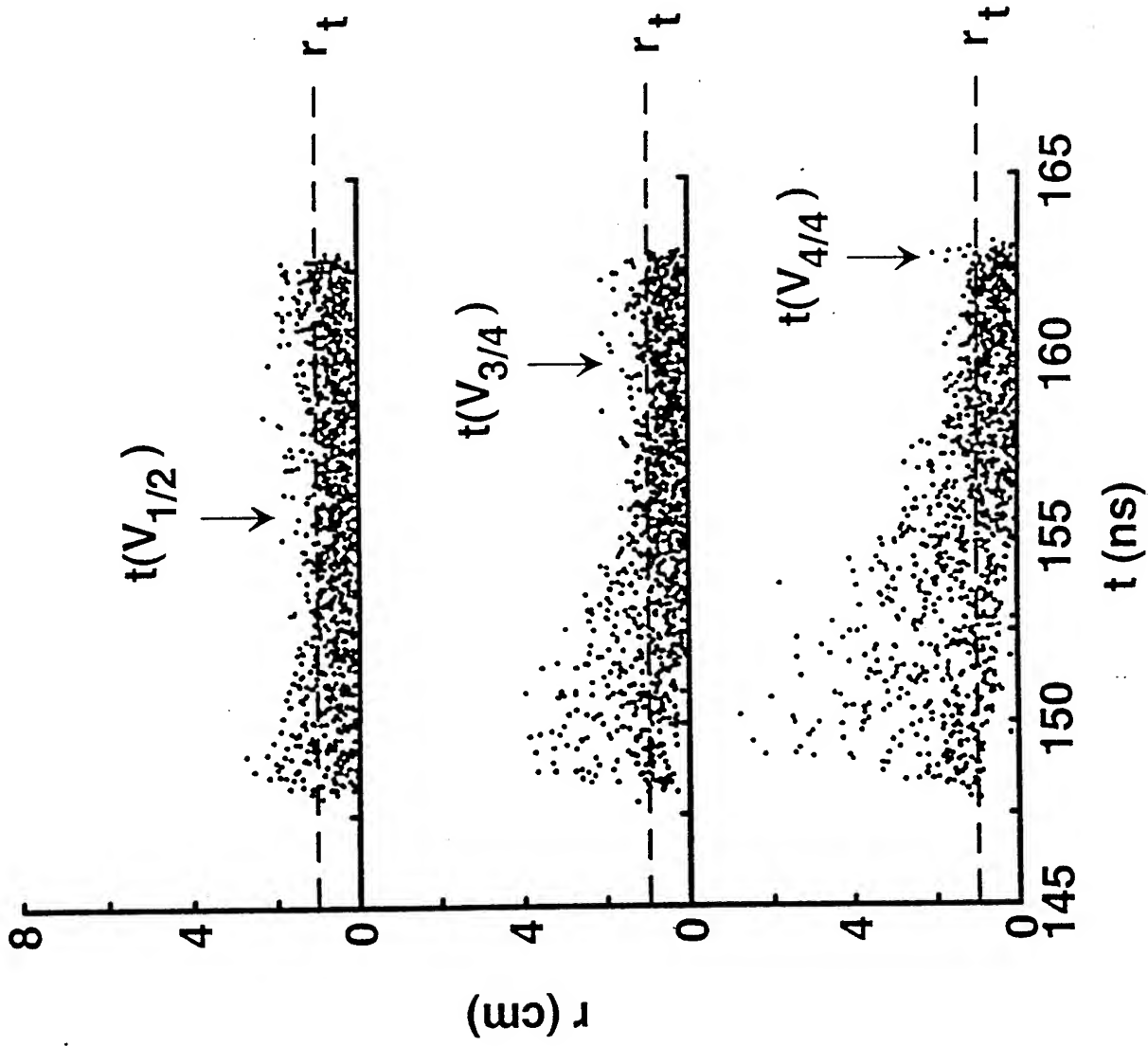


Fig. 9 - Plot of beam particle radius, r , vs. t at the target plane, $z = 400$ cm. Three different tuning times are plotted, $t(V_{1/2})$, $t(V_{3/4})$, and $t(V_{4/4})$. In each plot, 5 % of the total number of particles used in the simulation are represented. For these calculations, $R = 15$ cm, $k = 2$, $\alpha = 2$, $N = 20$, $E_s = 20$ MJ, and $\Theta_\mu = 5$ mrad.

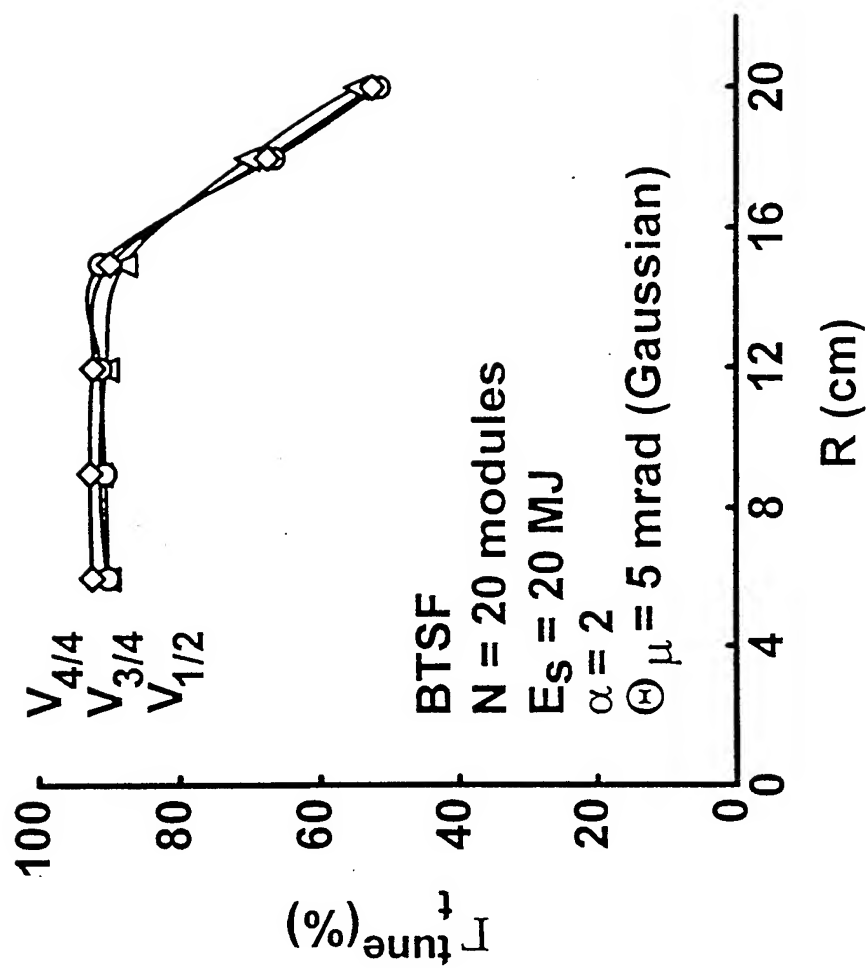


Fig. 10- Plot of Γ_{tune} vs. R for BTSF. The individual curves are for voltage tunings of $V_{1/2}$, $V_{3/4}$, and $V_{4/4}$.

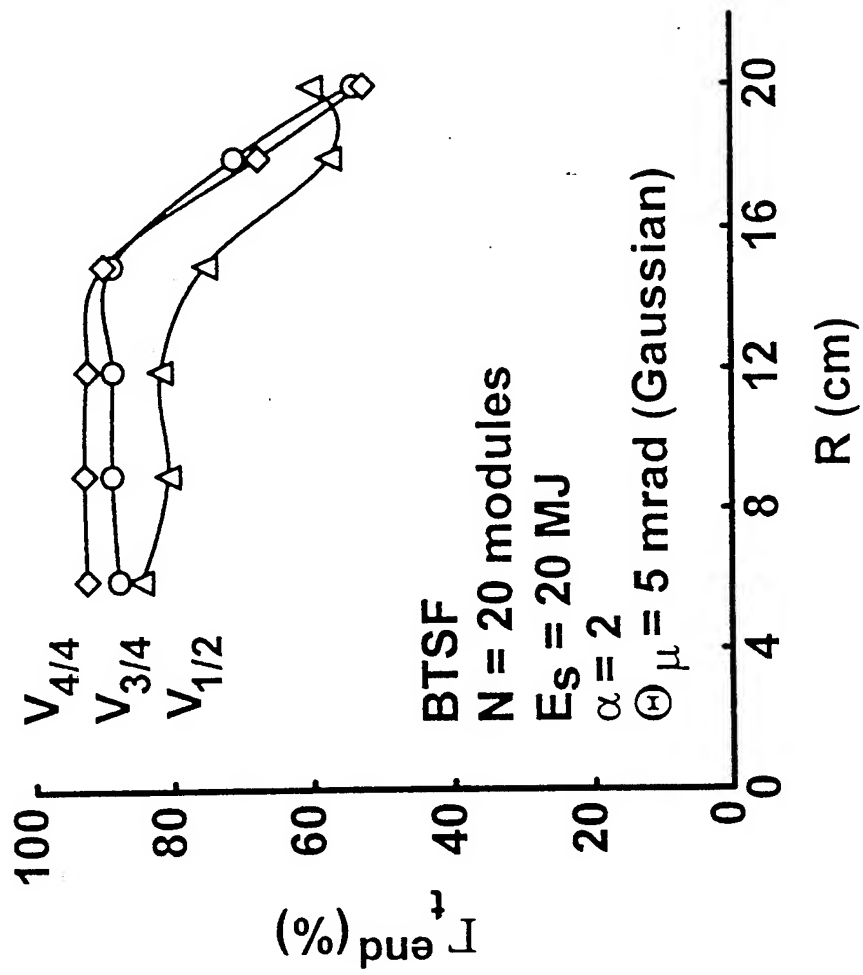


Fig. 11- Plot of Γ_{end}^{end} vs. R for BTSF. The individual curves are for voltage tunings of $V_{1/2}$, $V_{3/4}$, and $V_{4/4}$.

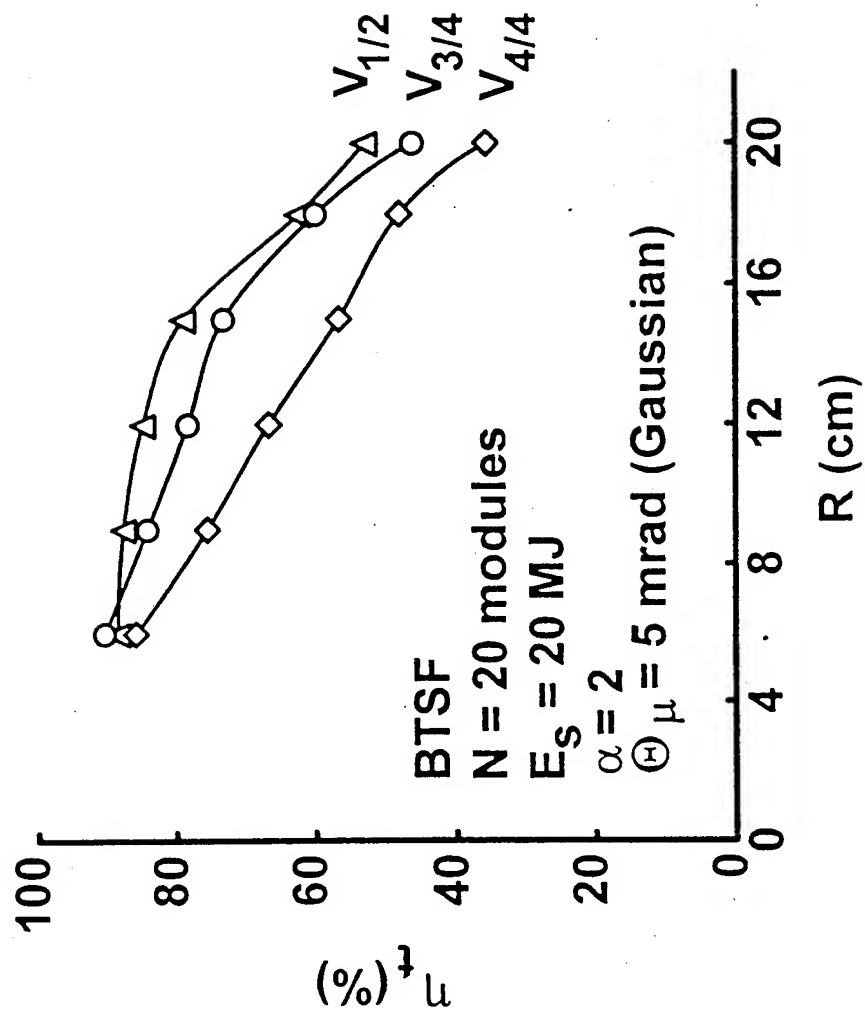


Fig. 12- Plot of η , vs. R for BTSF. The individual curves are for voltage tunings of $V_{1/2}$, $V_{3/4}$, and $V_{4/4}$.

in η_t results in a 14 % gain in Γ_t^{end} when shifting the tuning from the middle to three-quarters through the pulse. For this baseline case with $V_{3/4}$ tuning, $\eta_t = 73$ % and $\Gamma_t^{end} = 89$ %. The maximum Γ_t^{end} is 90 % which occurs for the $V_{4/4}$ tuning.

For ZDT, Δ is held constant at 4 cm. A discharge channel current, I_c , of 40 kA with a channel wall radius of 1 cm was chosen, which confines the entire beam for $\alpha \approx 1$ and $R \leq 10.5$ cm.⁶ For R greater than 10.5 cm, ions are lost to the channel wall. Due to packing constraints, the discharge channels must terminate at a standoff distance⁶ from the target given by $d = r_t(N/2)^{1/2}$. For this study, $d = 3.16$ cm and the length of the transport channel is then $D - F - d$ which is on the order of 250 cm. An aperture of inner radius $F\Theta_\mu = 0.75$ cm is located at the entrance to the discharge system at F .

As found in the BTSF case, simulations for ZDT indicate that Γ_t^{tune} does not change as the tuning time is moved from the middle to the end of the pulse, as shown in Fig. 13. However, Fig. 14 shows that the focus sweep effect dramatically reduces the power in the tail of the pulse for the mid-pulse tuning time for $R = 6$ to 15 cm. For this same range in R , the average drop in η_t that results from moving the tuning from the middle to the end of the pulse is 14 %. Figure 15 illustrates that over the entire range of R , that tuning to the three-quarters time in the pulse results in an almost negligible loss in η_t . In particular, at $R = 15$ cm, η_t was found to be 62 % for both $V_{1/2}$ and $V_{3/4}$. Also Γ_t^{end} gained 12 % to a value of 62 % out of a maximum value of $\Gamma_t^{end} = 69$ % for the $R = 15$ cm case.

For WGT, a wire current, I_w , of 40 kA was chosen. A wire radius, r_w , of 0.035 cm was used throughout and is determined to be the minimum radius required to avoid melting.⁷ Return current wires are placed at radius of about 1.4 times the average beam radius in order to minimize losses due to chaotic orbit effects while maintaining as compact a WGT system as possible for packing.⁷ The standoff distance is about 2.5 times that of the ZDT system,⁹ with a transport distance $D - F - d$ which is on the order of

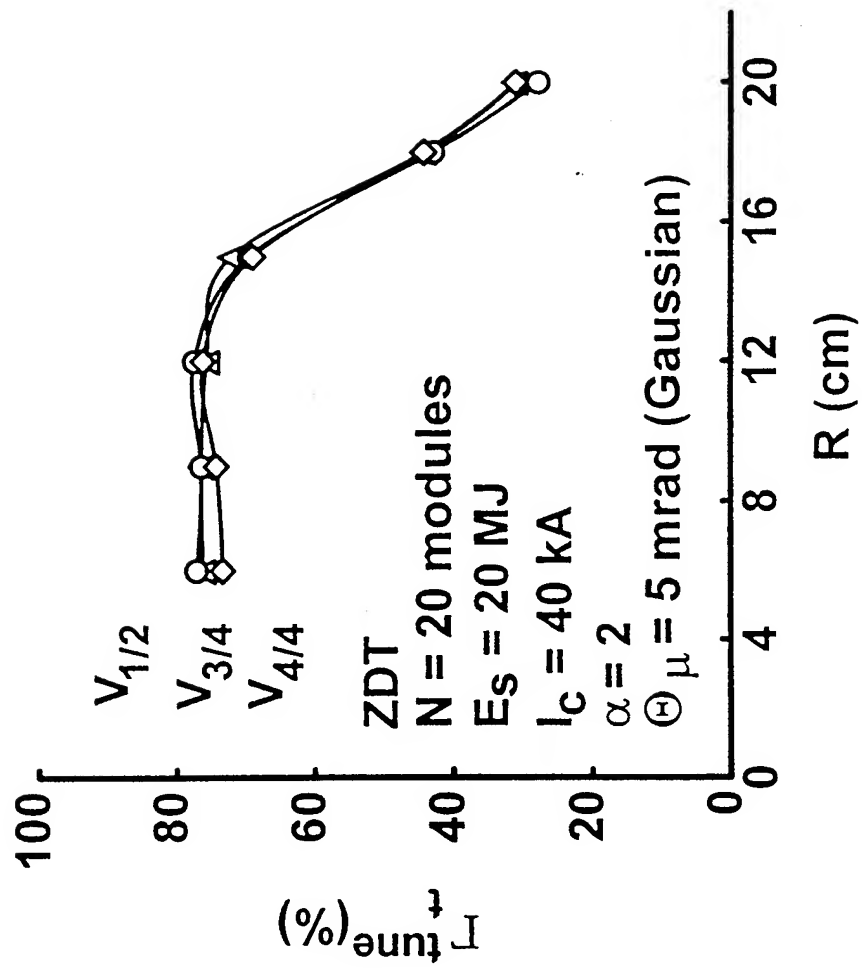


Fig. 13- Plot of Γ_t^{tune} vs. R for ZDT. The individual curves are for voltage tunings of $V_{1/2}$, $V_{3/4}$, and $V_{4/4}$.

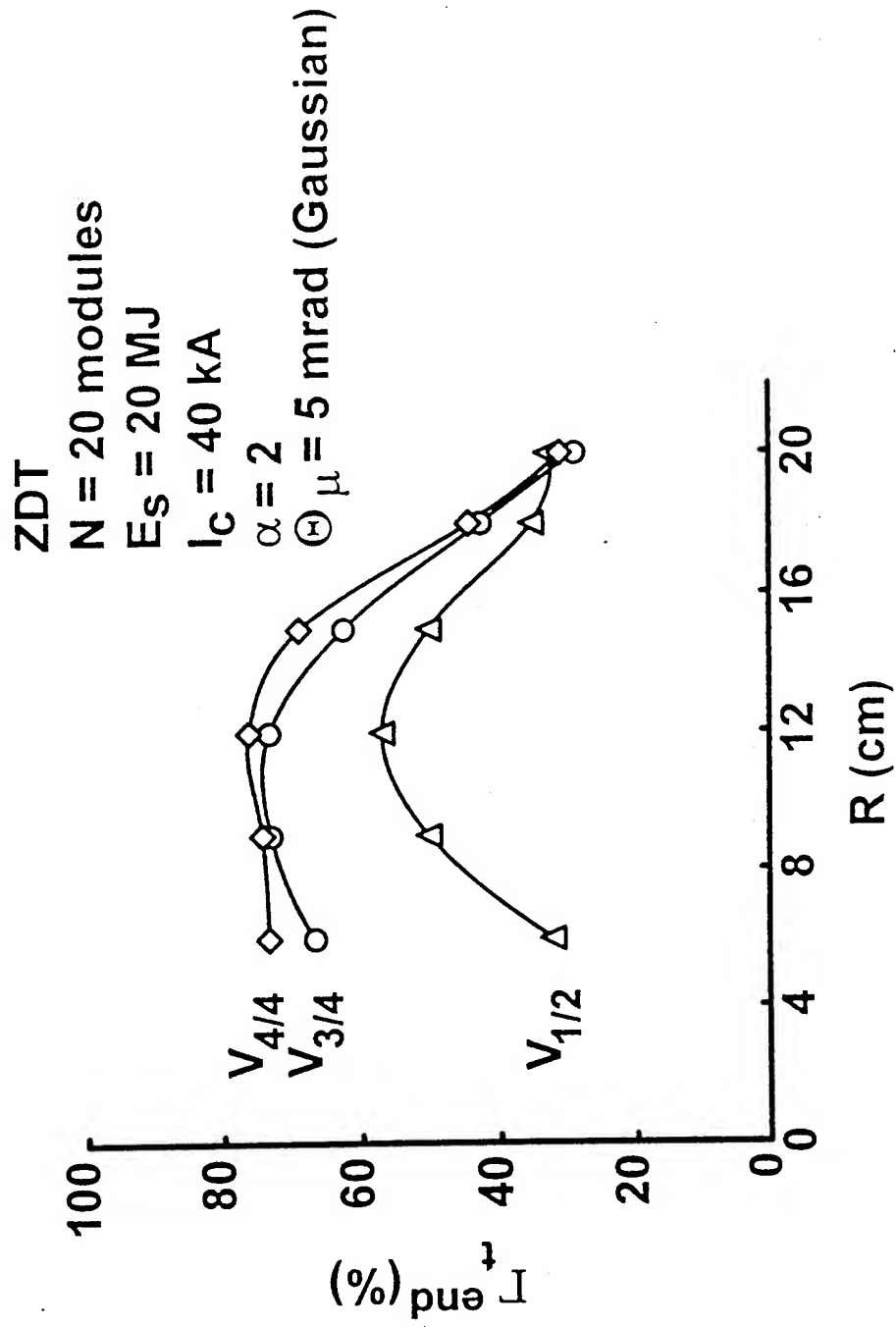


Fig. 14- Plot of Γ_r^{end} vs. R for ZDT. The individual curves are for voltage tunings of $V_{1/2}$, $V_{3/4}$, and $V_{4/4}$.

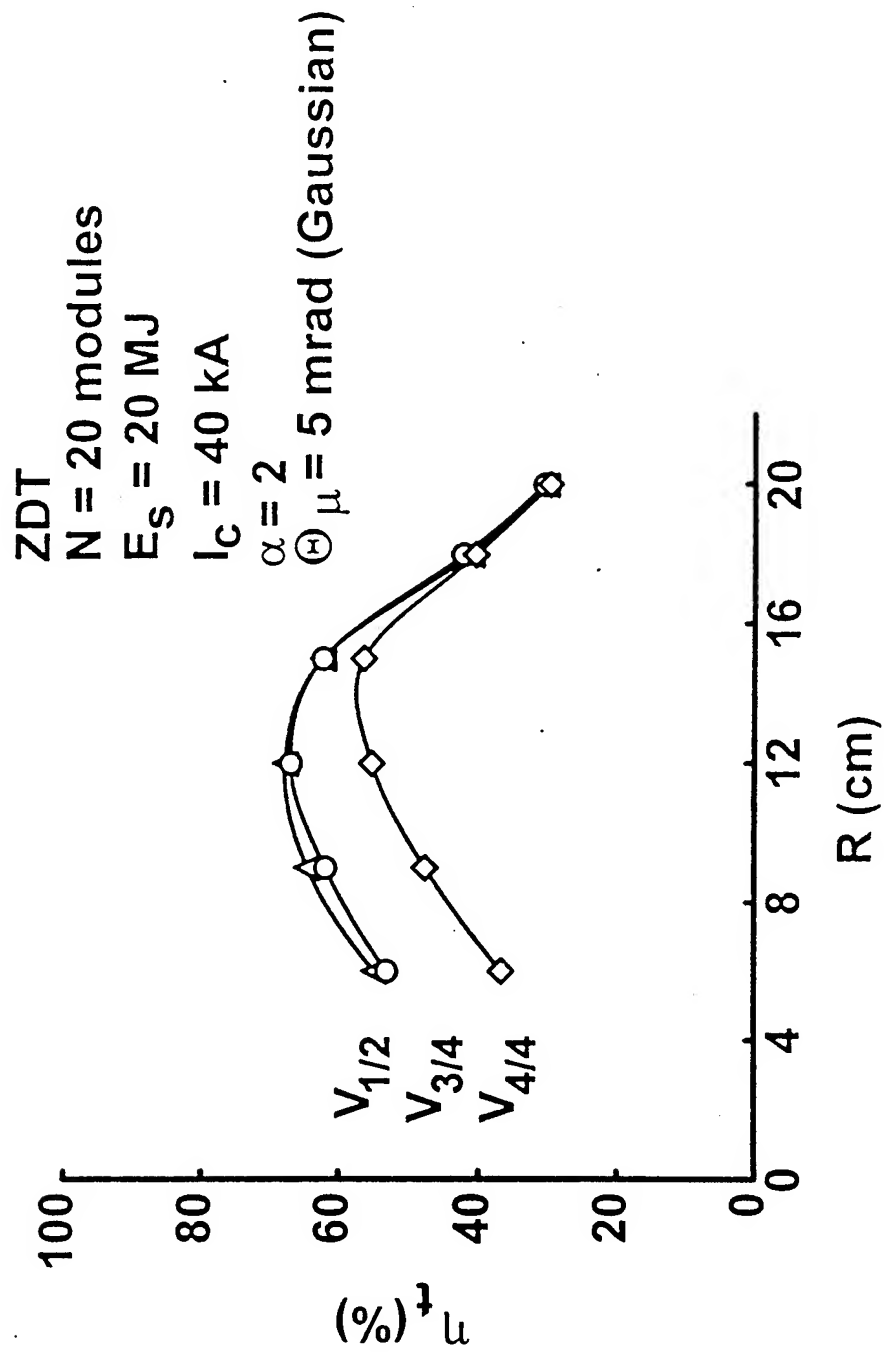


Fig. 15- Plot of η , vs. R for ZDT. The individual curves are for voltage tunings of $V_{1/2}$, $V_{3/4}$, and $V_{4/4}$.

250 cm. An aperture of radius $F\Theta_\mu = 0.75$ cm is located at the entrance to the wire system at F .

As for BTSF and ZDT, simulations for WGT indicate that Γ_t^{tune} does not change as the tuning time is moved from the middle to the end of the pulse, as shown in Fig. 16. In Fig. 17, moving the tuning from the end to the middle of the pulse results in an average drop of 13 % in Γ_t^{end} over the range $R = 6$ to 20 cm. As for the BTSF and ZDT, moving the tuning time from mid-pulse to three-quarters of the pulse length results in only a small average drop in Γ_t^{end} from peak values (about 4 % for tuning at $V_{3/4}$ rather than $V_{4/4}$). In Fig. 18, this choice results in virtually no change in η_t . The optimum case occurs for $R = 15$ cm where $\eta_t = 40$ %, and $\Gamma_t^{end} = 43$ % for $V_{3/4}$ tuning. The maximum Γ_t^{end} of 47 % occurs when $R = 15$ cm with $V_{4/4}$ tuning.

IV. Impedance Model Variations and Non-Ideal Accelerator Wave Forms

The design of the LMF applied- B diode for use in a light-ion LMF system is currently being investigated. One possible design employs a two-stage¹² scheme, whose particular benefits include high beam purity, lower beam microdivergence, control of impedance behavior, reduced accelerating voltage per stage, and commensurately smaller insulating magnetic fields. Since the actual impedance model of such a diode is currently under evaluation, it is desirable to consider the impact of the diode impedance model on the efficiency results presented in Section II. This is achieved by changing the values of k in Eq. (2) over a range of values that seem possible for a two-stage diode design. Figure 19 illustrates the dramatic change in Δ over k in the range 0.75 to 2.5, according to Eq. (14), with $V_{tune} = V_o$, and $R = 15$ cm. Note that Δ scales as R^2 , so that for $R = 10$ cm, Δ increases from 3 cm to 12 cm as k decreases from 2.5 to 1.0. The actual placement of individual foils to relax the requirements on Δ is discussed elsewhere^{9,12} and is beyond the scope of this work.

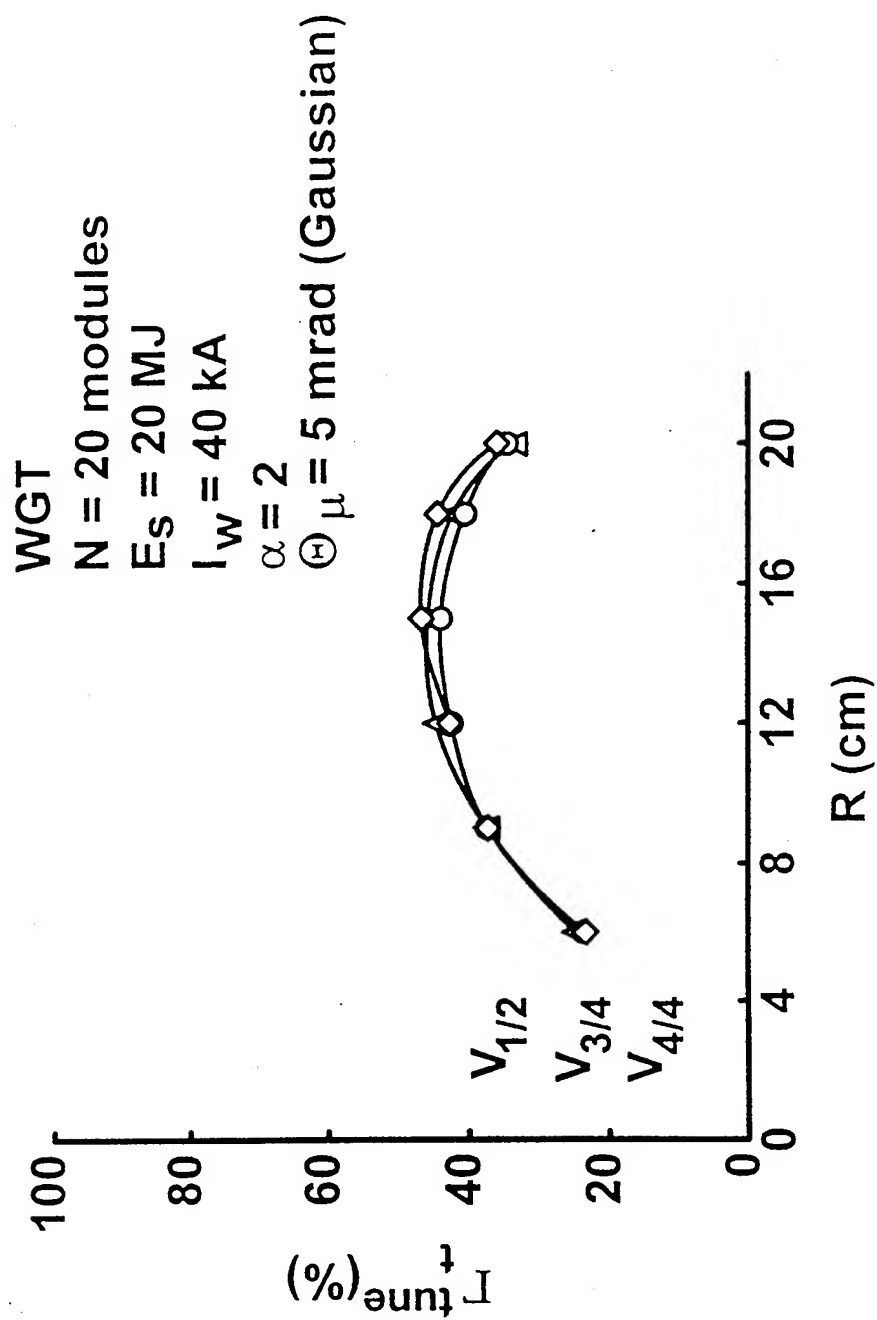


Fig. 16- Plot of Γ_r^{tune} vs. R for WGT. The individual curves are for voltage tunings of $V_{1/2}$, $V_{3/4}$, and $V_{4/4}$

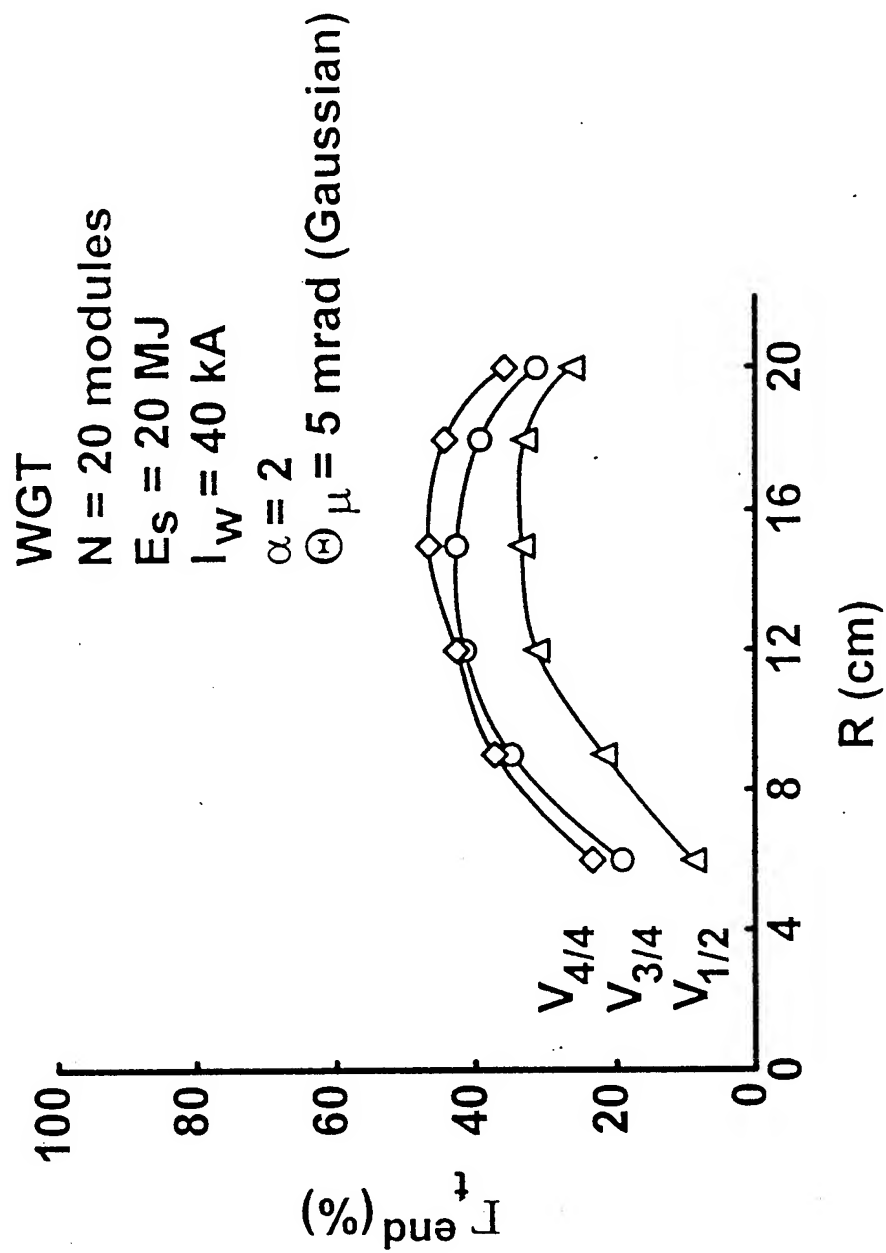


Fig. 17- Plot of Γ_r^{end} vs. R for WGT. The individual curves are for voltage tunings of $V_{1/2}$, $V_{3/4}$, and $V_{4/4}$.

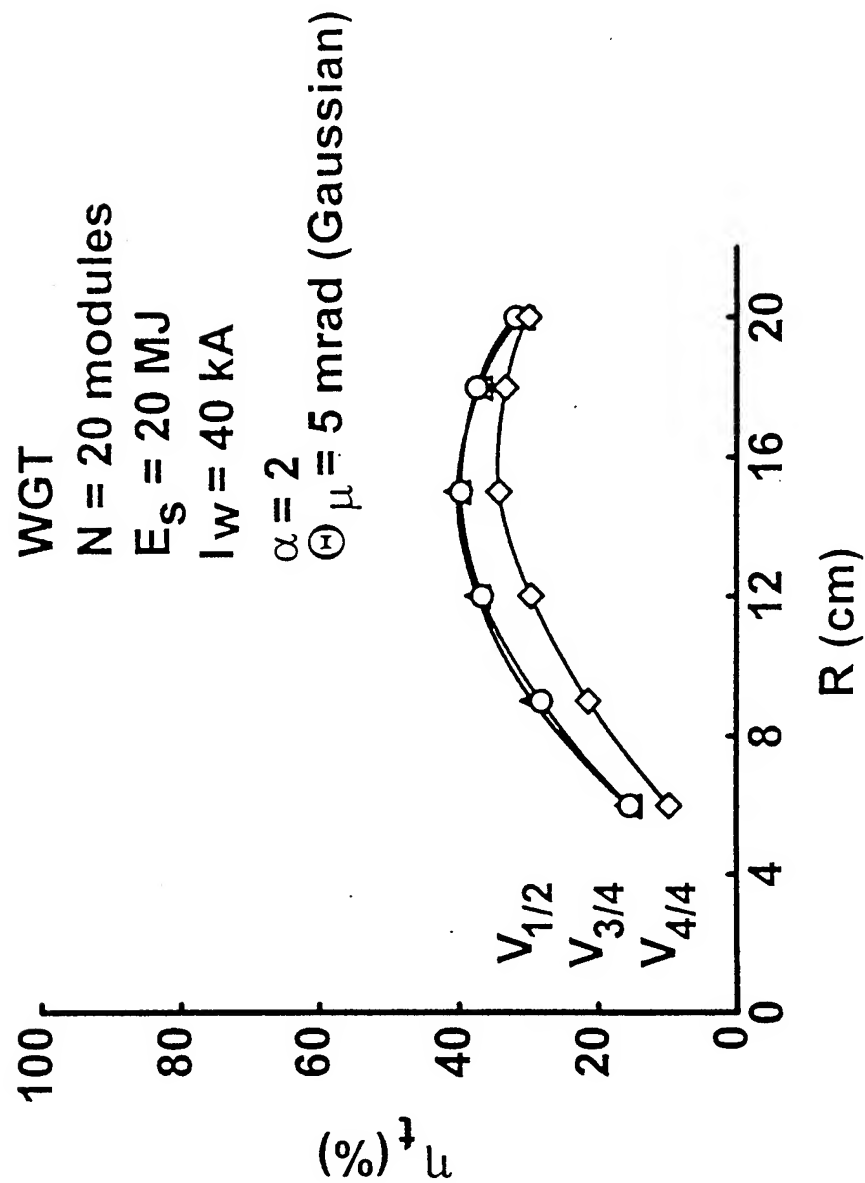


Fig. 18- Plot of η , vs. R for WGT. The individual curves are for voltage tunings of $V_{1/2}$, $V_{3/4}$, and $V_{4/4}$.

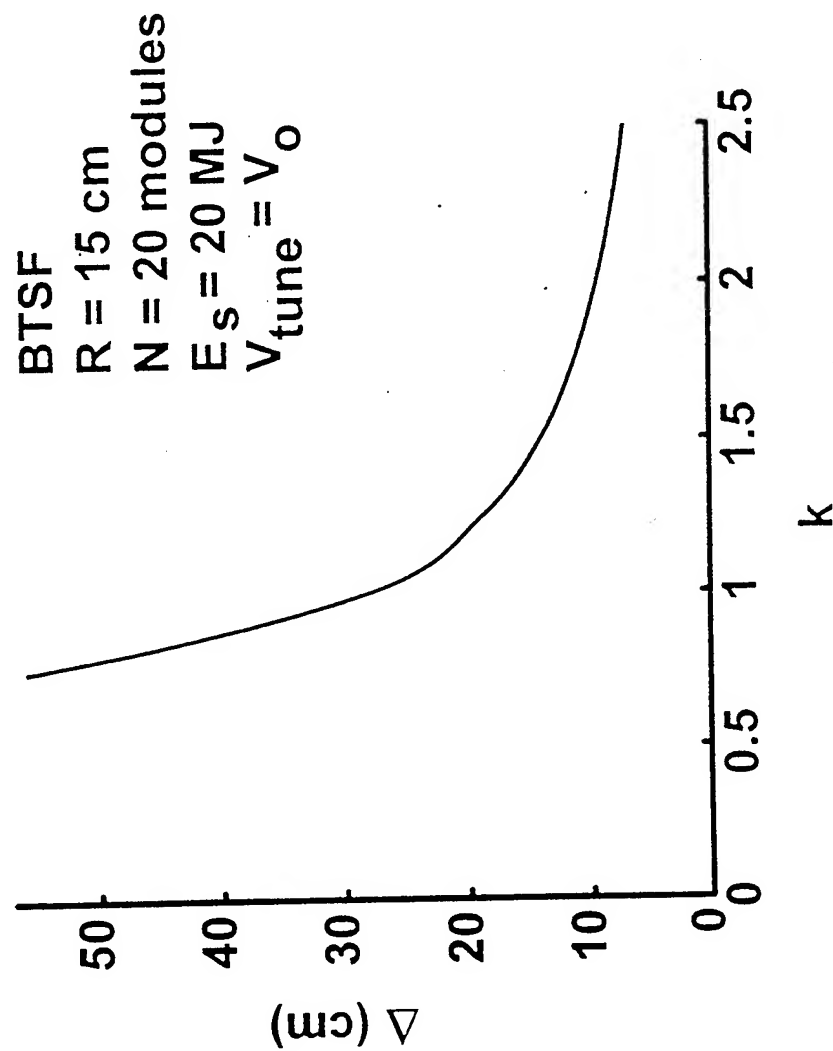


Fig. 19- Plot of Δ vs. k for BTSF matched case.

In Fig. 20, the impact of varying k over the range 0.75 to 2.5 is shown for BTSF, ZDT, and WGT with $R = 15$ cm, $\Theta_\mu = 5$ mrad, $\alpha = 2$, $V_{tune} = V_o = 30$ MV, and $F_{tune} = 150$ cm. For BTSF, virtually no effect of varying k is observed within the range 0.75 and 2.5, indicating that the enhanced focus-sweep effect resulting from larger values of k has little effect on η_i for this nearly achromatic system. The effect of the target size exceeding the spot size contributes to this stability of η_i . For ZDT and WGT, η_i linearly decreases with increasing k for a variation of 11 % and 8 %, respectively over the range of k considered. Therefore, it can be anticipated that the potential benefits of two-stage diodes can be exploited without a significant change in the results presented in Sec. II and III. Since k will most likely decrease for a two-stage diode, η_i would improve slightly for ZDT and WGT.

Another issue of concern to the design of a light-ion ICF system is deviation of the power pulse from the ideal waveform given by the product of Eqs. (1) and (2). Ramped voltage waveforms produced by the accelerator that deviate from the ideal pulse shape prevent the beam from time-of-flight bunching to the optimum pulse length on target. This may result in insufficient energy being delivered to the target in the optimal target drive time, τ_b . To examine this issue, a small sinusoidal oscillation is added to the ideal voltage pulse of Eq. (1), such that the beam is launched as a function of time with voltage

$$V_n(t) = V_d(t) + AV_o \sin(2\pi ft) , \quad (18)$$

where A is the amplitude (expressed as a percentage of the value of V_o) and f is the frequency in units of Hz. For this work, the period of the oscillations are kept large with respect to the time it takes an average ion to cross the typical AK gap. This is done because the model for the diode impedance given in Eq. (2) assumes a slowly varying dependence on voltage. For a gap of 1 cm and typical ion velocities around

$N = 20$ modules
 $E_s = 20$ MJ
 $\alpha = 2, R = 15$ cm
 $\oplus \mu = 5$ mrad (Gaussian)

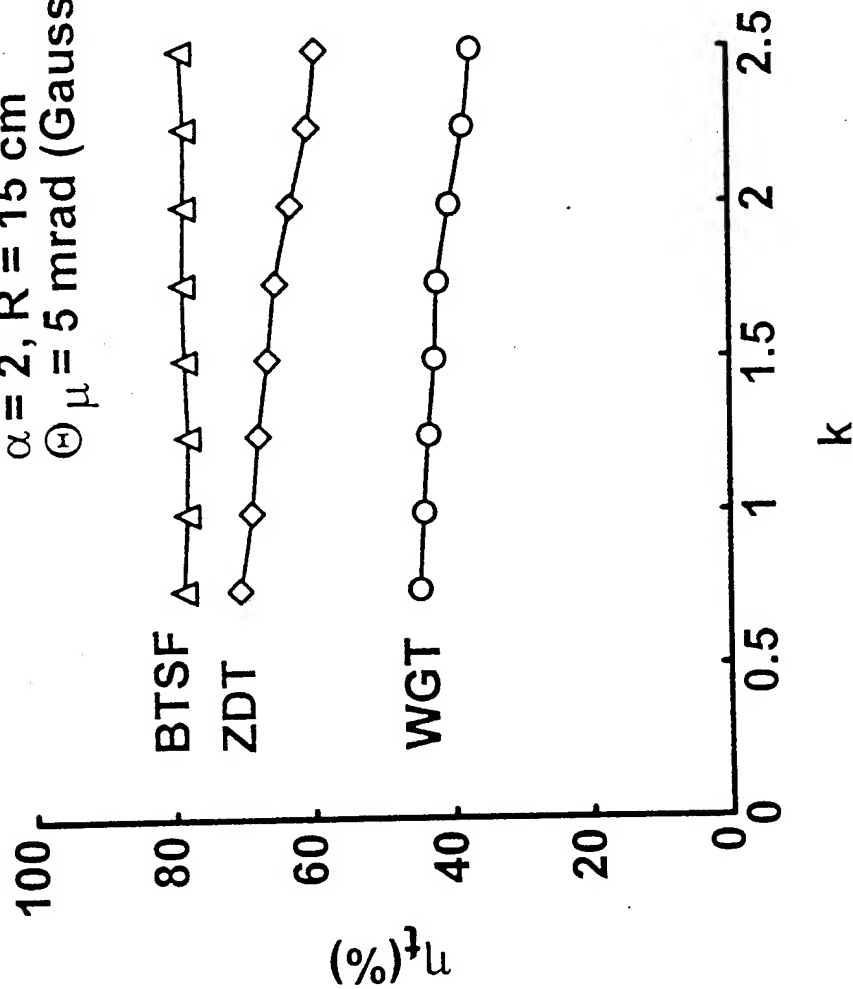


Fig. 20- Plot of η_r vs. k for $R = 15$ cm. Individual curves are for BTSF, ZDT, and WGT.

$v_o = (2eZ_d V_d / m_i)^{1/2} \approx 2.87 \times 10^9$ cm/s, an ion crosses the AK gap in about 1/3 ns. Therefore, only voltage oscillation periods greater than a few ns will be considered here.

Two cases of non-ideal power pulses are considered: (1) the ideal current in the diode is used with the non-ideal voltage waveform [Eqs. (2) and (18) respectively], and (2) both the current and voltage are given a non-ideal shape [Eq. (18) and Eq. (2) with $V_d(t)$ replaced by $V_n(t)$ from Eq. (18)]. For purposes of comparison, the total energy in the non-ideal pulse is normalized to the total energy in the ideal case by scaling the magnitude of the current of the non-ideal to the ideal case. The ratio, γ , of the energy in the ideal to the non-ideal system,

$$\gamma = \left(\int_0^{\tau_d} V_d(t) I_d(t) dt \right) / \left(\int_0^{\tau_d} V_n(t) I_{do} \left[\frac{V_{d,n}(t)}{V_o} \right]^k dt \right), \quad (19)$$

is multiplied by I_{do} giving the current for the non-ideal cases as

$$I_n(t) = I_{no} \left(\frac{V_{d,n}(t)}{V_o} \right)^k, \quad (20)$$

where $I_{no} = \gamma I_{do}$. V_d is used in Eq. (20) for case (1) and V_n is used for case (2). The current scaling is minimal ($0.98 < \gamma < 1.02$) for all cases considered here.

Oscillations of the initial voltage pulse were applied to all three transport schemes for the specific parameters of $R = 15$ cm, $\alpha = 2$, $k = 2$, $V_{rune} = 30$ MV, $N = 20$ modules, and $\Theta_\mu = 5$ mrad (Gaussian). Calculations were performed for $1/f = 10$ ns over a range from $A = 0$ to $A = 0.10$. Two energy transport efficiency numbers were calculated for each run. The first, η_t , is the total energy transport efficiency defined in Section I, calculated over the entire power pulse delivered to the target, and η_t^{15} denotes the energy transport efficiency delivered to the target in the 15 ns centered at the middle of the delivered power pulse. For each transport scheme, η_t and η_t^{15} are plotted against the

range of A , illustrating the impact of non-ideal bunching that is induced from variations in the power pulse. For the BTSF case, an additional investigation into the role of the frequency, f , is analyzed for a given A .

Considering non-ideal waveforms for BTSF, given in Fig. 21, amplitudes $\geq 2\%$ can have a noticeable effect on the energy delivered in the middle 15 ns of the pulse. The combined effect of altered bending in the diode from Eq. (8) (with V_d replaced by V_n), coupled with non-ideal time-of-flight pulse compression, results in additional energy transport losses for $A \geq 2\%$ and $1/f = 10$ ns. η_i^{15} at $A = 2\%$ is 70 %, an 8 % drop from the ideal waveform calculation, and continues to fall off as A increases. The solid markers in Fig. 21 (and Figs. 23, 24) at $A = 5\%$ indicate data points for case (2), while the open data points are for case (1) described above. It can be concluded that the non-ideal voltage waveform drives a temporal spreading of the pulse that reduces η_i^{15} . Small fluctuations in voltage and current do not significantly reduce η_i^{15} by defocusing the beam. Over the range $A = 0$ to 7 %, η_i was essentially constant at 78 %, but falls slightly at $A = 10\%$, to an η_i of 75 %.

Also for BTSF, the role of the frequency of the oscillations in the reduction in η_i was investigated by varying $1/f$ over the range of 5 to 30 ns for A at $\pm 5\%$. Figures 22 and 23 show only a small variation in η_i , while large variations in η_i^{15} are observed. In Fig. 22, a small deviation in η_i of $\pm 2\%$ around the value for the ideal pulse is observed for $1/f < 20$ ns. For larger $1/f$, the deviation in η_i from the ideal pulse begins to increase because the frequency of oscillation is low enough to dominate the waveform characteristics. For example, when $1/f = 30$ ns, exactly one sinusoidal oscillation occurs over the pulse time. The systematic variation seen in Fig. 23 (and to a lesser extent in Fig. 22) results from this dominant effect on the ideal waveforms when the full pulse, $2\pi f\tau_d$, is close to multiples of 2π . When the frequency of the oscillations becomes high enough and many oscillations occur within τ_d , this effect begins to smear out and an average reduction in η_i^{15} is observed, resulting in an 8 % drop in η_i^{15} for $1/f < 10$ ns. In

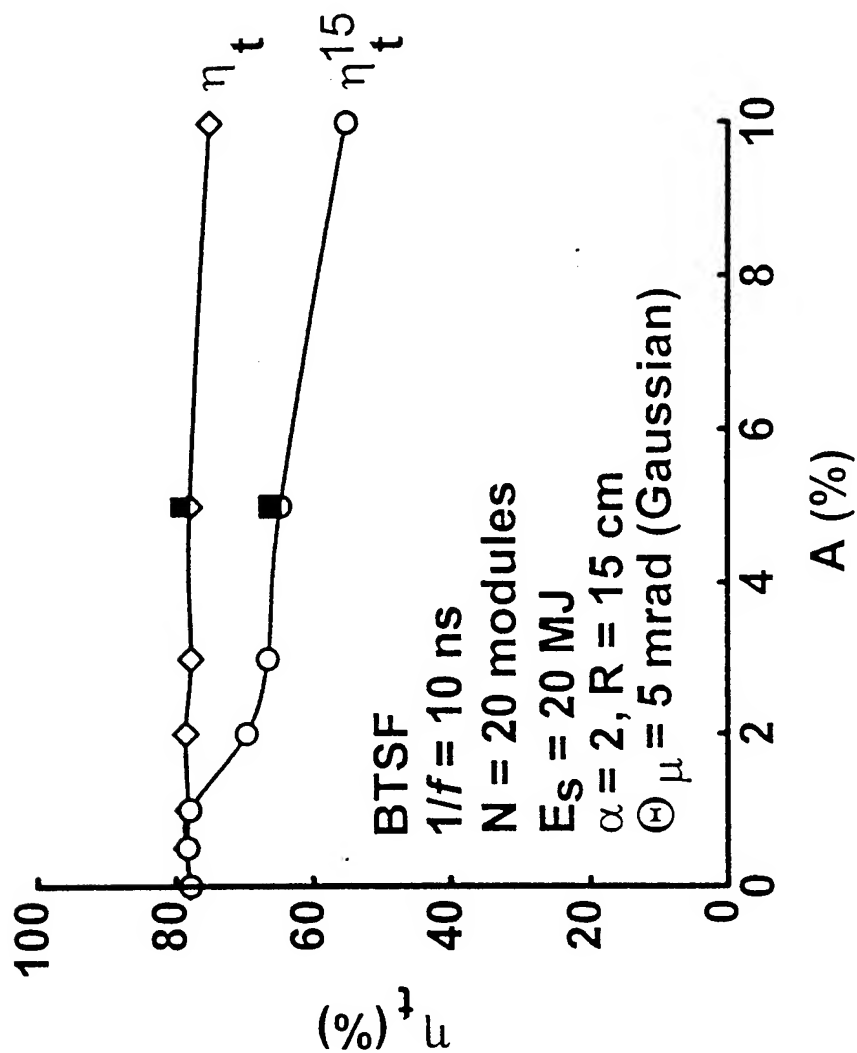


Fig. 21 - Plot of η_t vs. A for BTSF for non-ideally bunched wave forms with $R = 15 \text{ cm}$ and $1/f = 10 \text{ ns}$. Individual curves are for η_t (total energy efficiency on target, full pulse) and η_t^{15} (energy efficiency on target in the middle 15 ns of the pulse). Hollow data points represent calculations for case (1) (non-ideal voltage) and solid data points represent calculations for case (2) (non-ideal voltage and current) as discussed in the text. For these cases $V_{tune} = V_o$.

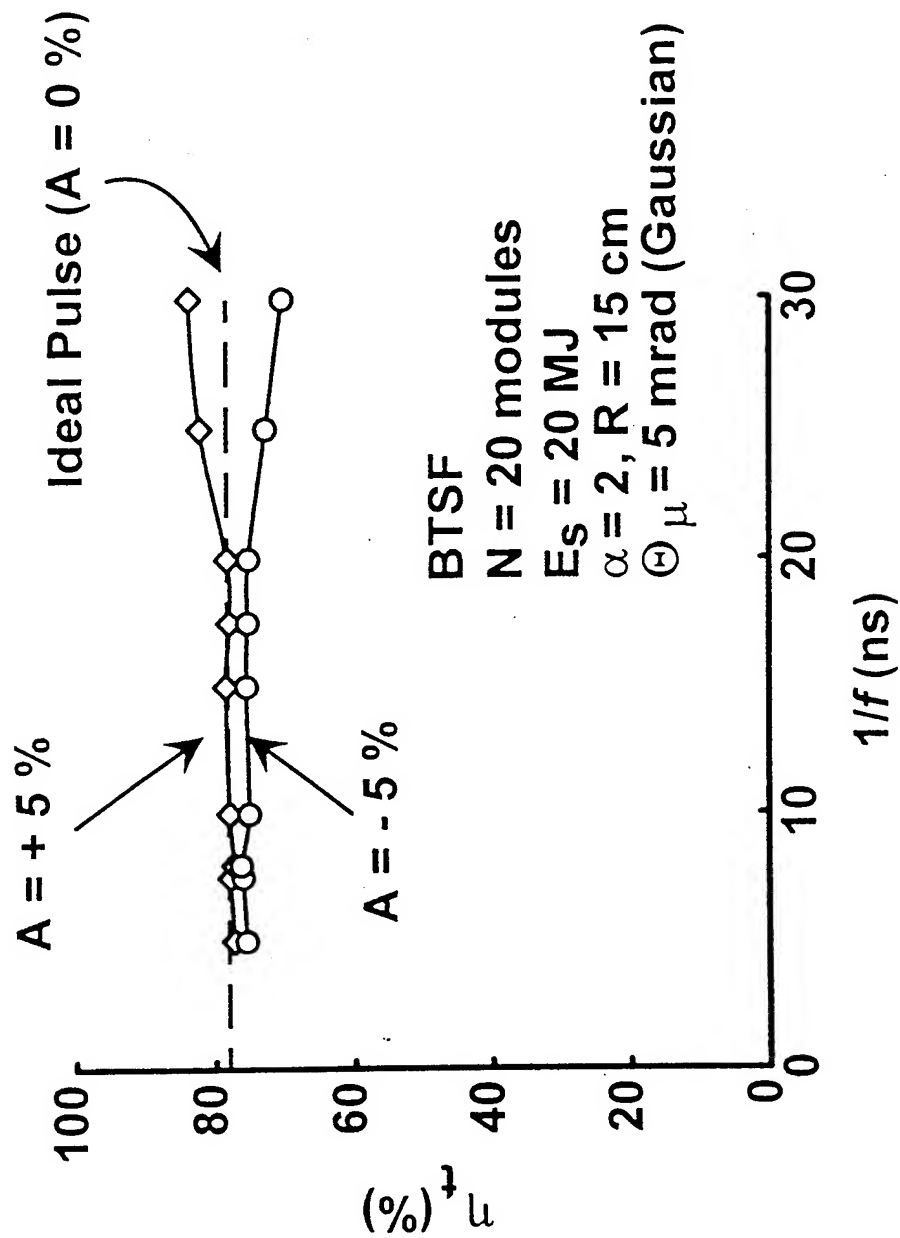


Fig. 22- Plot of η_t vs. $1/f$ for BTSF for non-ideally bunched wave forms with $R = 15$ cm. Individual curves are for $A = 0$ % (ideal pulse), +5 %, and -5 %. For these cases $V_{tune} = V_o$.

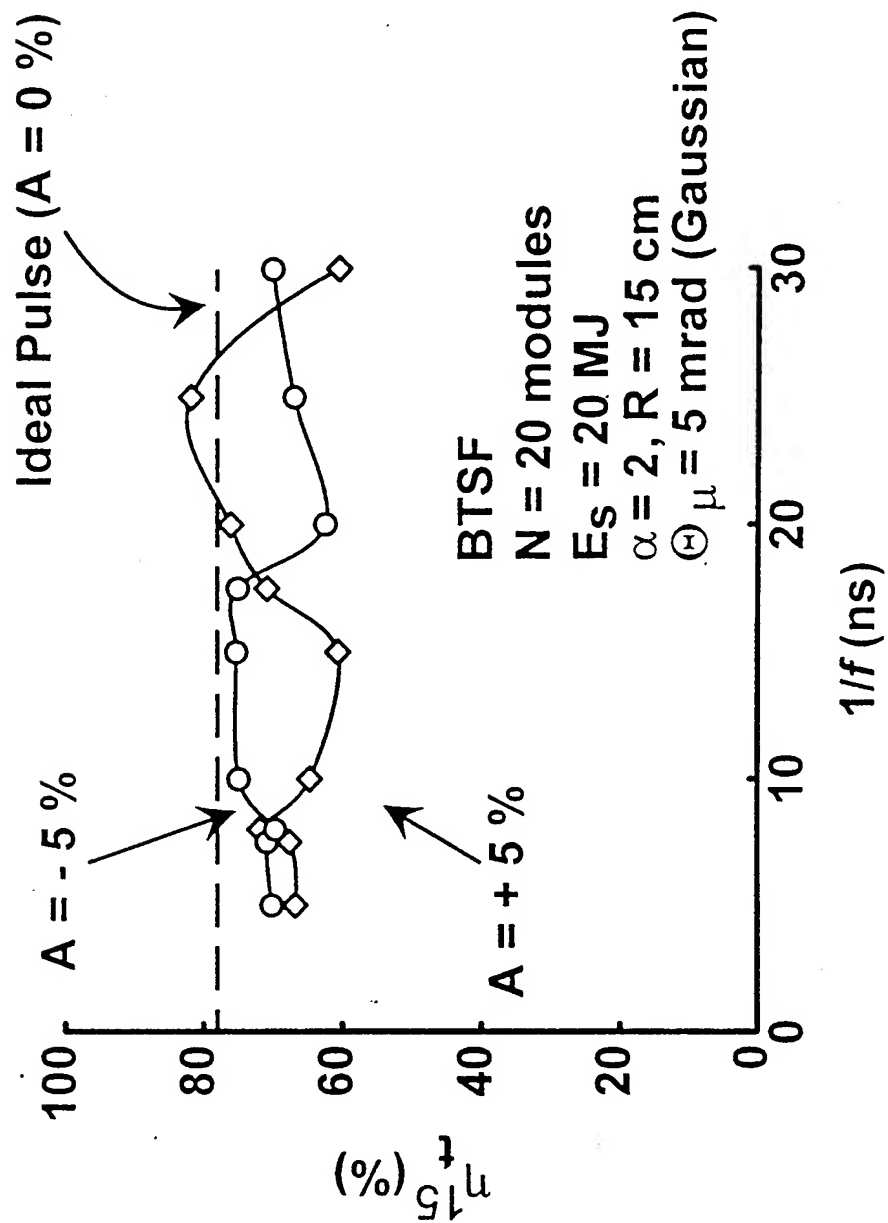


Fig. 23- Plot of η_t^{15} vs. $1/f$ for BTSF for non-ideally bunched wave forms with $R = 15$ cm. Individual curves are for $A = 0 \%$ (ideal pulse), $+5 \%$, and -5% . For these cases $V_{tune} = V_o$.

Fig. 23, the curves for $+A$ and $-A$ are almost symmetric with respect to each other but on average are about 8 % below that of the ideal case ($A = 0$).

For ZDT and WGT, calculations similar to the BTSF case were made, fixing $1/f$ at 10 ns and varying A from 0 to 10 %. Results for these calculations are shown in Figs. 24 (ZDT) and 25 (WGT). Both plots show a trend almost identical to the BTSF case, where significant discrepancies between η_i and η_i^{15} begin at $A = 2$ %. As for the BTSF case, the hollow data points in Figs. 24 and 25 indicate calculations for case (1) and solid data points represent calculations for case (2). For ZDT in Fig. 24, η_i is 63 % on average. At $A = 2$ %, η_i^{15} is 57 %, a drop of 6 % from the ideal case. As A increases, η_i^{15} continues to drop off almost linearly with $\eta_i^{15} = 44$ % at $A = 10$ %. For WGT in Fig. 25, η_i is 40 % on average. Again, at $A = 2$ %, η_i^{15} is 36 %, a drop of only 4 % from the ideal case. As A increases, η_i^{15} continues to drop off almost linearly with $\eta_i^{15} = 28$ % at $A = 10$ %. These results again point to variations in the voltage pulse driving the non-ideal bunching, resulting in a reduction in η_i^{15} . The larger the amplitude of the disturbance, the longer the final pulse duration will be.

V. Summary And Conclusions

In this paper, transported power and energy efficiency studies have been carried for parameters relevant to the design of a light-ion LMF. The square microdivergence profile used in previous studies^{5,6,7,9} has been replaced with a Gaussian profile that has a half-width, half-maximum $\Theta_\mu = 5$ mrad. Losses in η_i of 25 % or less result primarily from ions being in the "wings" of the distribution. A comparison of η_i between square and Gaussian microdivergence profiles over a range of R is presented in Section II for the BTSF, ZDT, and WGT schemes. Results are shown in Figs. 6, 7, and 8. For the Gaussian microdivergence cases shown, η_i is reduced from the square microdivergence case by less than 12 % for BTSF, 9 % for ZDT, and 20 % for WGT. The reduction for

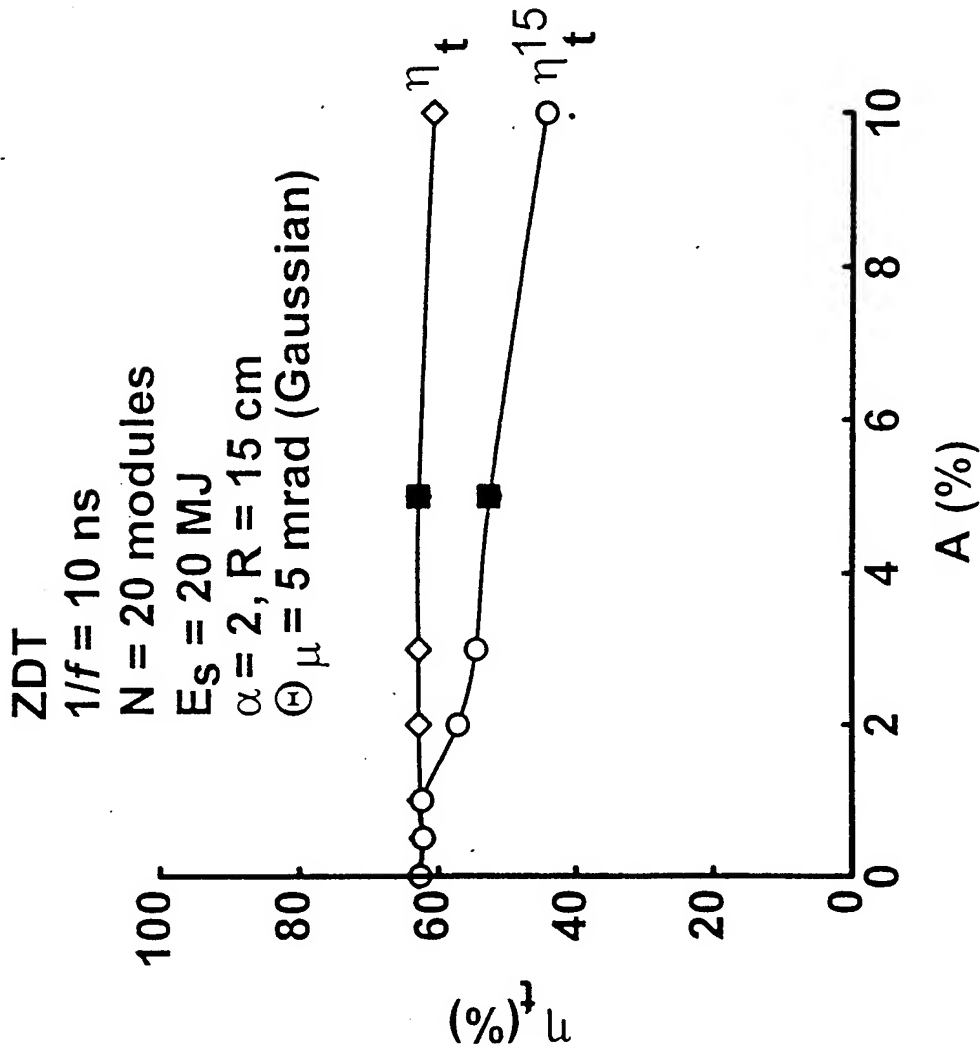


Fig. 24- Plot of η_t vs. A for ZDT for non-ideally bunched wave forms with $R = 15 \text{ cm}$ and $1/f = 10 \text{ ns}$. Individual curves are for η_t (total energy efficiency on target, full pulse) and η_t^{15} (energy efficiency on target in the middle 15 ns of the pulse). Hollow data points represent calculations for case (1) (non-ideal voltage) and solid data points represent calculations for case (2) (non-ideal voltage and current) as discussed in the text. For these cases $V_{tune} = V_o$.

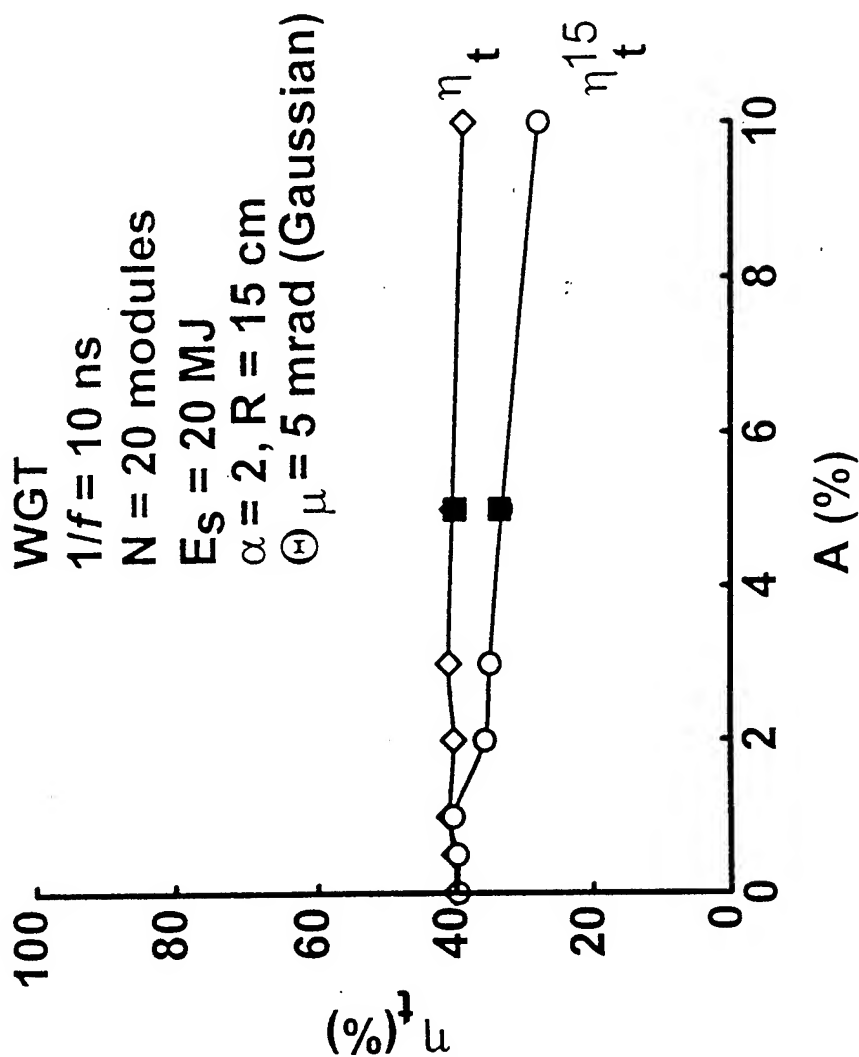


Fig. 25- Plot of η , vs. A for WGT for non-ideally bunched wave forms with $R = 15 \text{ cm}$ and $1/f = 10 \text{ ns}$. Individual curves are for η_t (total energy efficiency on target, full pulse) and η_t^{15} (energy efficiency on target in the middle 15 ns of the pulse). Hollow data points represent calculations for case (1) (non-ideal voltage) and solid data points represent calculations for case (2) (non-ideal voltage and current) as discussed in the text. For these cases $V_{ime} = V_o$.

WGT is the largest because the forward peaked Gaussian distribution produces more low-angular-momentum ions that strike the guide wire and are removed from the beam. The reduction for BTSF is minimized because the spot size $F\Theta_\mu$ is smaller than the target radius.

The impact of power efficiency tuning on η_i has been examined for the BTSF, ZDT, and WGT transport schemes for a range of parameters that are applicable to the design of a light-ion LMF system. Results indicate that moving the point of peak power efficiency to three-quarters of the pulse time results in maintaining a near optimal value for η_i while achieving high Γ_i^{end} at the end of the pulse. For the BTSF baseline case at $R = 15$ cm, tuning the power pulse to maximize Γ_i at three-quarters of the pulse time yields a Γ_i^{end} of 89 % with an η_i of 73 %. This means that only 6 % of overall energy is sacrificed to gain 14 % of instantaneous power at the tail of pulse. By tuning to the end of the pulse, only 1 % more instantaneous power can be obtained at the expense of an additional 17 % of energy loss. Therefore tuning to achieve instantaneous power at the three-quarters point in the power pulse yields the optimum performance for this system. This overall conclusion is the same for the ZDT and WGT systems.

In addition, the diode impedance model has been systematically varied in order to examine the impact of current scaling with voltage on η_i . The value of the scaling constant, k , was varied over a range of values that may result from advanced applied-B diode design, including two-stage diodes. Because BTSF is an achromatic system, virtually no variation in η_i was found for values of k in the range of 0.75 to 2.5, even though higher values of k result in larger manifestations of the focus sweep effect.⁹ It was assumed that the achromatic matching constraint placed on Δ can be met even when Δ becomes large as k approaches 0.5. For the ZDT and WGT schemes, some variation in η_i was found, with η_i becoming larger as k decreases. This results primarily from the increasing focus sweep effect as k increases for these nonachromatic systems. These

calculations were performed for one point design in the LMF parameter regime, namely $R = 15$ cm, $N = 20$ modules, $\alpha = 2$, $E_s = 20$ MJ, $F = 150$ cm, $V_{tune} = V_o$, and $\Theta_\mu = 5$ mrad.

Deviations from the ideal form of the voltage in a programmed power pulse can lead to temporal spreading of the bunched pulse at the target. The effect of non-ideal waveforms on η_t is evaluated by adding a sinusoidally variation to the ideal voltage and current pulses produced at the diode. Results indicate that sinusoidal oscillations with an inverse frequency, $1/f$, of 10 ns and amplitudes greater than 2 % of the average voltage, V_o , reduces η_t delivered to the target in the optimal bunched pulse length, τ_b , denoted as η_t^{15} . For BTSF, this results in an 8 % drop in η_t^{15} , as shown in Fig. 21. As the amplitude of the oscillation is increased, the spread in the pulse increases, further reducing η_t^{15} . For ZDT and WGT, similar results are obtained, as shown in Figs. 24 and 25, respectively. However, Fig. 23 demonstrates that results do depend on the frequency and sign of the amplitude. The results quoted above are close to "worst-case" numbers. Because defocusing does not occur, the ideal pulse efficiency is also recovered if longer pulse durations are acceptable.

This work extends a previous investigation into LMF transport point designs,⁹ examining the impact of the focus sweep effect on transport efficiency. Further issues that need to be considered in order to accurately determine η_t for specific designs include ion-beam species purity, waveform efficiency, and beam energy losses during transport. Details of the ion beam source model, including the radial dependence of Δ and an accurate microdivergence model must be improved in order to further quantify η_t .

VI. Acknowledgments

This work was supported by US DOE through Sandia National Laboratories.

VII. References

1. J.J. Ramirez, R.W. Stinnett, D.L. Johnson, C.L. Olson, T.A. Mehlhorn, J.T. Crow, J.P. Quintenz, K.R. Prestwich, M.P. Desjarlais, R.E. Olson, G.O. Allshouse, T.H. Martin, J.P. VanDevender, D.L. Cook, S.A. Slutz, K.B. Coachman, T.R. Lockner, B.N. Turman, S.A. Goldstein, J.N. Olsen, R.R. Peterson, and R.L. Engelstad, *Fusion Tech.* **15**, 350 (1989).
2. J.J. Ramirez, D.L. Cook, J.K. Rice, M.K. Matzen, D.L. Johnson, J.D. Boyes, C.L. Olson, K.R. Prestwich, M.J. Clauser, T.A. Mehlhorn, R.W. Stinnett, G.O. Allshouse, G.L. Kulcinski, G.A. Moses, R.R. Peterson, and R.L. Engelstad, *Laser and Part. Beams* **11**, 423 (1993).
3. C.L. Olson, in the Proceedings of the 1989 Particle Accelerator Conference, F. Bennett and J. Kaptan, eds. (Chicago, IL, March 20-23, 1989), p. 1011.
4. D. Mosher, D.D. Hinshelwood, J.M. Neri, P.F. Ottinger, J.J. Watrous, C.L. Olson, and T.A. Mehlhorn, in the Proceedings of the 8th International Conference on High-Power Particle Beams, B.N. Breizman and B.A. Knyazev, eds. (Novosibirsk, USSR, July 2-5, 1990), p. 26.
5. P.F. Ottinger, D.V. Rose, J.M. Neri, and C.L. Olson, *J. Appl. Phys.* **72**, 395 (1992).
6. P.F. Ottinger, D.V. Rose, D. Mosher, and J.M. Neri, *J. Appl. Phys.* **70**, 5292 (1991).
7. J.J. Watrous, D. Mosher, J.M. Neri, P.F. Ottinger, C.L. Olson, J.T. Crow, and R.R. Peterson, *J. Appl. Phys.* **69**, 639 (1991).
8. R.F. Hubbard, M. Lampe, G. Joyce, S.P. Slinker, I. Haber, and R.F. Fernsler, *Part. Accel.* **37-38**, 161 (1992).
9. P.F. Ottinger, D.V. Rose, and C.L. Olson, *J. Appl. Phys.* **75**, 4402 (1994).

10. R.E. Olson, G.O. Allshouse, D.L. Cook, T.R. Lockner, M.G. Mazarakis, C.L. Olson, D.L. Smith, in the Proceedings of the 15th IEEE Symp. on Fusion Engineering (Hyannis, MA, October 11-15, 1993), to be published.
11. J.P. Quintenz and D.B. Seidel, Sandia Nat. Lab. Report SAND84-1336 (June 1984).
12. S.A. Slutz, and M.P. Desjarlais, J. Appl. Phys. 67, 6705 (1990).

VIII. List Of Variables

η_t	Energy transport efficiency
η_t^{15}	Energy transport efficiency for the middle 15 ns of the power pulse
V_o	Average diode voltage
Z_d	Beam charge state in the diode
Z_t	Beam charge state after stripping
E_t	Energy on target
E_s	Energy of the system
α	Bunching factor
N	Number of modules
τ_d	beam pulse duration in the diode
τ_b	beam pulse duration at target
I_{do}	Ion current in the diode at time when $V_d(t) = V_o$
I_{no}	Ion current in the diode at time when $V_d(t) = V_o$ for case (2) in text ($V_n(t)$ is a function of V_d and t)
I_{to}	Average ion current at the target
R	Diode outer radius
R_i	Diode inner radius
$V_d(t)$	Voltage wave form at the diode
$V_n(t)$	Non-ideal voltage wave form at the diode
$V_t(t)$	Voltage wave form at the target
V_{tune}	Tuning voltage
Δ	Diode vacuum gap spacing
c	Speed of light
e	Electron charge
m_i	Beam ion mass
F	Focal distance
D	Total transport distance
L	Transport distance (~ 250 cm)
k	Ion current scaling constant
T	Arrival time of beam front on target
f	Frequency of non-ideal pulse oscillations
γ	Energy correction factor
$I_d(t)$	Beam current at the diode
$I_n(t)$	Beam current at the diode, non-ideal wave form case
$I_t(t)$	Beam current at the target
Θ_μ	Microdivergence
Γ_t	Instantaneous power efficiency on target
Γ_t^{tune}	Instantaneous power efficiency on target at the tuning time
Γ_t^{end}	Instantaneous power efficiency on target at end of pulse
$\Theta_a(r)$	Anode surface shaping function in the diode

$\Theta_b(r, t)$	Self-magnetic bending angle function for beam at diode
$\Theta_s(r, t)$	Beam steering function at diode
Θ_0	Steering angle coefficient
$v_d(0)$	Ion velocity at beginning of beam pulse
R_s	Solenoid inner radius
L_s	Solenoid axial length
r_a	Transport channel entrance aperture radius
r_c	Discharge channel radius
r_w	Wire radius
ω_c	Ion cyclotron frequency
I_c	Discharge channel current
I_w	Central guide wire current
d	Standoff distance
r_t	Target radius

Transport Efficiency Studies for Light-Ion Inertial Confinement Fusion Systems Using Ballistic Transport with Solenoidal Lens Focusing

D. V. Rose, P. F. Ottinger, *Member, IEEE*, and C. L. Olson

Abstract— The proposed Laboratory Microfusion Facility (LMF) will require ≥ 10 MJ of 30 MeV lithium ions to be transported and focused onto high-gain, high-yield inertial confinement fusion targets. The light-ion LMF approach uses a multimodular system with individual ion extraction diodes as beam sources. Previous work examined the effect of time-of-flight bunching on energy transport efficiency, η_t , under realistic constraints on diode operation, beam transport, and packing. Target design considerations suggest that the instantaneous power efficiency, Γ_t , be maximized near peak power. Because of time-of-flight bunching, peak power occurs at the end of the power pulse for LMF designs. This work examines the effect of power efficiency tuning on η_t for an LMF design using ballistic transport with solenoidal lens focusing. Results indicate that tuning the power pulse to maximize Γ_t at about three-quarters through the pulse provides high power efficiency at the end of the pulse while still maintaining high η_t . In addition to power efficiency tuning, effects on η_t from variations of the diode impedance model and the diode voltage waveform are also examined.

I. INTRODUCTION

THE Laboratory Microfusion Facility (LMF) has been proposed for the study of high-gain, high-yield inertial confinement fusion (ICF) targets [1]. A multimodular light-ion approach, based on Hermes-III technology, is under investigation [1], [2]. This approach requires the transport and focusing of a number of intense ion beams over distances of several meters to a centrally located, high-gain, high-yield ICF target. The distance between the target and beam generators provides for packing of the beam generators around the target chamber, and isolation of the diode hardware from the target blast. In addition, the transport distance allows for time-of-flight (TOF) bunching of the beams to achieve power multiplication. Several beam transport and focusing schemes are being evaluated for LMF [3], [4], including ballistic transport with solenoidal lens focusing (BTSF) [5], and ballistic focusing with z-discharge transport [6], wire-guided transport [7], or self-pinch transport [8]. The baseline approach for LMF utilizes the BTSF scheme.

A previous analysis [9] examined the effect of time-of-flight bunching on energy transport efficiency, η_t , under realistic constraints on diode operation, beam transport, and packing. The energy transport efficiency η_t is defined here as the ratio of total ion energy delivered to the target to the total ion energy produced in the diodes. This effort extends the previous analysis to examine the impact of systematic variations in several key aspects of the model. These aspects include changing the time of peak power coupling between the beam and the target, current scaling for the diode impedance model, and diode voltage variations about the ideal voltage ramp for TOF bunching. The square microdivergence profile for the ion source model, used in the previous studies [5]–[7], [9], has also been replaced with a Gaussian microdivergence profile. This paper presents an analysis based on the BTSF system only. A similar analysis for the z-discharge and wire-guided transport systems is presented elsewhere [10]. Results for self-pinch transport should be similar to those for z-discharge transport.

Power efficiency Γ_t is defined as the ratio of the instantaneous transported ion power on target to the power at that same instant of an ideal bunched beam pulse at the target location. For BTSF, the diode and solenoidal lens form an achromatic lens pair (to first order in small variations of the voltage) by applying a matching condition [5]. Since the beam is annular rather than solid, this achromatic matching condition only strictly applies to ions born at one radius in the diode [5]. Because of the residual chromatic focusing effects, Γ_t changes in time as the voltage changes. Typically, the achromatic matching condition for BTSF is fixed at mid-pulse to optimize η_t . In this case Γ_t peaks near mid-pulse. However, Γ_t can be tuned to peak at other times at the expense of lower η_t . Previous work [9] examined chromatic effects on η_t with power efficiency tuned to peak at mid-pulse. Target design considerations indicate that peak power should be delivered at the end of the pulse [11]. In this paper, the time of peak power efficiency is varied between the mid-point and the end of the voltage pulse to determine the effect on η_t . Results indicate that tuning the power pulse to maximize Γ_t at about three-quarters through the pulse provides high power efficiency at the end of the pulse while still maintaining high η_t . For BTSF, this yields 89% instantaneous power efficiency at the tail of the pulse with η_t of 73% for parameters of interest (a ballistic transport distance of 250 cm, a solenoidal lens focusing distance of 150 cm, a diode radius of 15 cm, and a microdivergence of 5 mrad) for a system

Manuscript received September 6, 1994. This work was supported by US DOE through Sandia National Laboratories.

D. V. Rose is with JAYCOR, Inc., Vienna, VA 22182 USA.

P. F. Ottinger is with the Plasma Physics Division, Naval Research Laboratory, Washington, DC 20375 USA.

C. L. Olson is with the Sandia National Laboratories, Albuquerque, NM 87185 USA.

IEEE Log Number 9409796.

with 20 modules and 20 MJ of ion energy available at the diodes.

Applied- B diode designs are currently being investigated for LMF. Thus, the actual impedance characteristics of the diode are not yet determined. In order to examine the impact of current scaling with voltage on η_t , the diode impedance model presented previously [9] is systematically varied over a range of values that may result from advanced applied- B diode design. Because BTSF is an achromatic system, little change in η_t was found for this variation. However, the achromatic matching condition can change significantly as the diode impedance model is varied.

Deviations from the ideal voltage waveform for TOF bunching can lead to temporal spreading of the bunched beam pulse at the target. The effect of non-ideal waveforms on η_t is evaluated by adding a sinusoidal variation to the ideal voltage and current pulses produced at the diode. Results indicate that oscillations with an inverse frequency, $1/f$, of 10 ns and an amplitude A greater than 2% of the average voltage, V_o , reduces η_t^{15} . Here, η_t^{15} is the energy transport efficiency delivered to the target in the 15 ns centered about the middle of the delivered power pulse. This results in an 8% drop in η_t^{15} at $A = 2\%$. As the amplitude of the oscillation is increased, the spreading in the pulse increases, further reducing η_t^{15} . However, the results do depend on the frequency and sign of the amplitude, and, thus, the results quoted above are close to "worst-case" numbers. Because defocusing does not occur, the ideal transport efficiency is recovered if longer pulse durations on target are acceptable.

Note that when comparing two efficiency numbers in this paper, absolute differences (in %) are quoted rather than percentage changes.

Section II of this paper reviews the ion source model used in this work and highlights changes from [9]. In Section III, the effect of power efficiency tuning on η_t is examined. Section IV of this paper examines the impact on η_t due to variations in the diode impedance model and the diode voltage waveform. A summary is given in Section V.

II. ION SOURCE MODEL

The LMF system is schematically illustrated for BTSF in Fig. 1. Here it is assumed that the ballistic transport distance L (diode to lens) is 250 cm and the focal distance F (lens to target) is 150 cm. The total distance from the diode to the target, $D = L + F$, will be used to define the voltage pulse shape for TOF bunching. The ion source model is based on the extraction applied- B diode [12] with an annular emitting surface extending from an inner radius $R_i = R/2$ to an outer radius R . Ions accelerated across the vacuum region in the diode are bent toward the axis by the self-magnetic field of the beam. For small angles, this bending angle $\Theta_b(r, t)$ is $\omega_c \Delta / v$, where Δ is the width of the vacuum region, $v(t)$ is the ion speed, and ω_c is the beam ion cyclotron frequency associated with the self-magnetic field in the diode region so that $\omega_c = 2eZ_d I_d / r m_i c^2$. Here, $I_d(t)$ is the ion current in the diode, eZ_d and m_i are the beam ion charge in the diode and the ion mass, and c is the speed of light. Uniform current density is assumed in the annular emitting region of the diode.

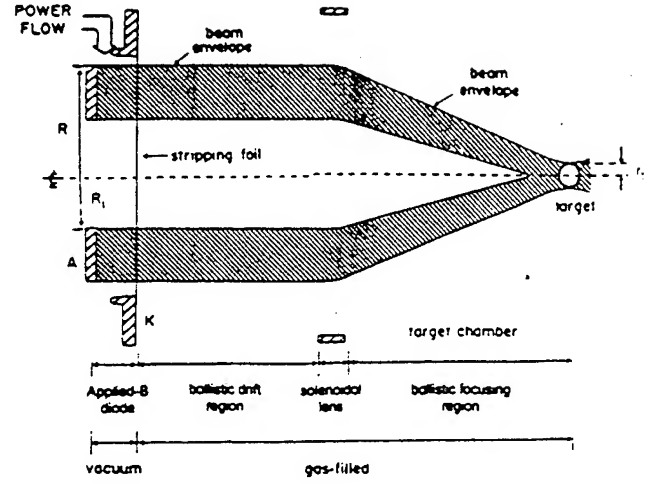


Fig. 1. Schematic of BTSF system.

A stripping foil separates the diode vacuum region from the gas-filled transport region. Singly charged lithium ions accelerated across the vacuum gap are stripped to Li^{+3} as they enter the gas-filled region. For applied- B extraction diodes, the position and shape of this stripping foil are determined by ion beam angular momentum considerations. This topic is addressed in detail in [9]. For the purposes of this work, Δ is determined solely from the achromatic matching condition [5] and it will be assumed that both achromatic and angular momentum conditions have been satisfied [9].

As illustrated in Fig. 2, ions are assumed to leave the diode region distributed in a cone of half-angle Θ_μ about a steering angle $\Theta_s = \Theta_b(r, t) + \Theta_a(r)$, where Θ_μ is the source microdivergence, and $\Theta_a(r)$ is due to the anode surface shape (assuming no anode plasma motion). It is assumed that Θ_μ is independent of radius and time, and, unlike the previous analysis [9], that Θ_μ has a Gaussian profile in velocity space. The impact of this change is discussed at the end of this section. Fig. 2 shows the beam extracted parallel to the axis. Since Θ_b varies as $V_d^{k-1/2}$, where $V_d(t)$ is the diode accelerating voltage and diode current scales as V_d^k (typically k is assumed to be 2.0), Θ_a can compensate for Θ_b at only one point in time. At this time, referred to as the tuning time, the instantaneous power transport efficiency is optimized. The previous analysis [9] used a tuning time near mid-pulse, when the average voltage V_o is reached, optimizing η_t . For this analysis, the tuning time, expressed in terms of the tuned diode voltage V_{tune} , is varied between the middle and the end of the pulse in order to study the impact of changing the time of optimal power efficiency (delivered to the target) on η_t .

The ideal ramped voltage and current pulses produced by the diode are

$$V_d(t) = \frac{V_d(0)}{\left(1 - \frac{t}{T} \frac{\alpha - 1}{\alpha}\right)^2} \quad (1)$$

and

$$I_d(t) = I_{d0} \left(\frac{V_d(t)}{V_o} \right)^k \quad (2)$$

where T is the arrival time of the beam front at the target, $V_d(0)$ is the initial voltage at time $t = 0$, and α is the bunching

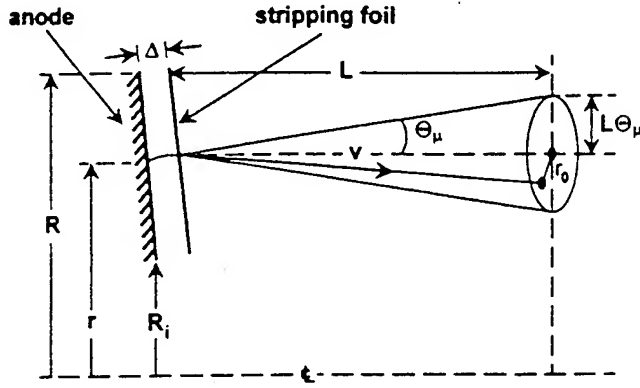


Fig. 2. Injection geometry for BTSF.

factor. The average value of the voltage, V_o , is defined as $(V_d(\tau_d) + V_d(0))/2$, where τ_d is the initial pulse duration and I_{do} is the diode ion current when $V_d(t) = V_o$. A power pulse given by (1) and (2) will time-of-flight compress to a pulse length of $\tau_b = \tau_d/\alpha$ at a time T after the start of the pulse.

The total path length for the beam from the diode to the target is $D = v_d(0)T$, where $v_d(0) = \sqrt{2eZ_d V_d(0)/m_i}$. Evaluating (1) at $t = \tau_d$ and substituting the resulting expression for $V_d(\tau_d)$ into the definition of V_o yields

$$V_d(0) = 2V_o - V_d(\tau_d) = \frac{2V_o \xi^2}{(1 + \xi^2)} \quad (3)$$

where

$$\xi = 1 - \left(\frac{\tau_d}{T}\right) \left(\frac{\alpha - 1}{\alpha}\right). \quad (4)$$

Equation (3) relates $V_d(0)$ and $V_d(\tau_d)$ for given values of $\xi(\alpha, \tau_d, T)$. Substituting (3) into the definition of D yields

$$T^2 = \frac{m_i D^2}{4eZ_d V_o} \left(\frac{1 + \xi^2}{\xi^2}\right) \quad (5)$$

which is a transcendental equation for T in terms of given values for m_i , D , Z_d , V_o , and $\xi(\alpha, \tau_d, T)$. Using (2) for $I_d(t)$ and setting the total beam energy per module,

$$E_d = \int_0^{\tau_d} I_d(t) V_d(t) dt = \frac{I_{do}}{V_o^k} \int_0^{\tau_d} (V_d(t))^{k+1} dt \quad (6)$$

equal to E_s/N specifies I_{do} for given values of V_o , E_s , N , k , and $\xi(\alpha, \tau_d, T)$. The system energy, E_s , is the total ion energy available from the N diodes and is related to the energy on target, E_t , by $E_t = \eta_t E_s$. Substituting for $V_d(t)$ from (1) into (6) and performing the integration yields

$$I_{do} = \frac{(2k+1)E_s}{2^{k+1}NV_o\tau_d} \left(\frac{1-\xi}{\xi}\right) \frac{(1+\xi^2)^{k+1}}{(1-\xi^{2k+1})} \quad (7)$$

where ξ is given in (4).

Using the assumption of uniform current density in the annular diode and the impedance model given in (2), Θ_b can be written as

$$\Theta_b(r, t) = -\Theta_o \left(\frac{V_d(t)}{V_o}\right)^{k-1/2} \left(\frac{r}{R} - \frac{R}{4r}\right) \quad (8)$$

where

$$\Theta_o = \frac{8I_{do}\Delta}{3c^2 R} \left(\frac{eZ_d}{2m_i V_o}\right)^{1/2}. \quad (9)$$

Since Θ_o is assumed fixed in time, (8) will lead to an inward sweeping of Θ_b over the duration of the pulse.

At the tuning time, $t(V_{tune})$, the steering angle is set equal to zero, so that the beam is extracted parallel to the axis. Combining this condition on the steering angle with Θ_b yields the appropriate anode shape

$$\Theta_a(r) = \Theta_o \left(\frac{V_{tune}}{V_o}\right)^{k-1/2} \left(\frac{r}{R} - \frac{R}{4r}\right). \quad (10)$$

The beam ion steering angle defined previously [9], is now modified to include the voltage tuning parameter, V_{tune} , by combining (8) and (10), yielding

$$\Theta_s(r, t) = \Theta_o \left(\frac{V_{tune}}{V_o}\right)^{k-1/2} \left(1 - \left(\frac{V_d(t)}{V_{tune}}\right)^{k-1/2}\right) \cdot \left(\frac{r}{R} - \frac{R}{4r}\right). \quad (11)$$

This equation combines both geometric anode shaping as well as self-magnetic-field orbit bending of the ions in the vacuum region of the diode.

The diode and solenoidal lens can be treated as an achromatic lens pair for a particular value of r , assuming small variations about the tuning voltage, V_{tune} . The focal length of the solenoid at the tuning voltage is given by [5]

$$F = \frac{4v_{tune}^2}{\omega_c^2 L_s} \quad (12)$$

where L_s is the axial length of the solenoid, and v_{tune} is the ion velocity associated with the tuning voltage V_{tune} . The lens pair is matched for $r = R$, which maximizes the number of ions achromatically focused because the diode is assumed to have uniform current density. Following the analysis performed in [9], the matching condition becomes

$$\Theta_o = \frac{4R}{3F(k-1/2)} \left(\frac{V_o}{V_{tune}}\right)^{k-1/2} \quad (13)$$

where Θ_o is given by (9), resulting in the following expression for Δ ,

$$\Delta = \frac{c^2 R^2}{2(k-1/2)I_{do}F} \left(\frac{V_o}{V_{tune}}\right)^{k-1/2} \left(\frac{2m_i V_o}{eZ_d}\right)^{1/2} \quad (14)$$

where I_{do} is given in (7).

The source microdivergence for all cases considered in Sections III and IV of this paper assumes a Gaussian profile, with the half-width, half-maximum, Θ_μ , selected to be 5 mrad. Previous calculations [5]–[7], [9] assumed a square microdivergence profile. A detailed comparison of transport efficiency for square and Gaussian profiles is given in [10] for the various LMF transport schemes. For the BTSF scheme, with Δ matched according to (14), η_t is reduced by 12% or less when a Gaussian rather than a square microdivergence profile is used.

For the calculations presented here, a fixed set of LMF system parameters are chosen. It is assumed that Li^{+1} ions are accelerated in the diode and are stripped to Li^{+3} as they pass through the foil. A previous analysis [9] considered a range of values for E_s , N , and α . For this work, these values will be fixed at $E_s = 20$ MJ, $N = 20$, and $\alpha = 2$. In addition, it will be assumed that $F = 150$ cm, $\Theta_\mu = 5$ mrad, $V_o =$

30 MV, $D = 400$ cm, and $\tau_b = 15$ ns (so that $\tau_d = 30$ ns). For this case $T = 148$ ns, $V_d(0) = 26.8$ MV, $V_d(\tau_d) = 33.2$ MV, and $I_{do} = 1.12$ MA. For some calculations R will be varied between 6 and 20 cm, with $R = 15$ cm used as the baseline diode radius. A centrally located, spherical target of radius $r_t = 1$ cm is assumed at $z = D$ from each of the N diodes.

III. POWER EFFICIENCY TUNING

ICF target design considerations indicate that peak power delivered to the target should occur at the end of the driver pulse [11]. This can be accomplished by tuning the voltage for peak power efficiency near the end of the pulse. However, as V_{tune} increases from V_o toward $V(\tau_d)$, η_t decreases. This section examines the impact on η_t from tuning, or moving, the time of peak power efficiency later in the pulse.

Allowing the voltage and current waveforms, (1) and (2), to evolve in time as the beam is projected ballistically to the target plane at $z = D$, yields

$$V_t(t) = \frac{V_t(T)}{\left(\alpha - t \frac{\alpha - 1}{T}\right)^2} \quad (15)$$

and

$$I_t(t) = \alpha I_{to} \left(\frac{Z_t V_t(t)}{Z_d V_o} \right)^k \quad (16)$$

for $T \leq t \leq T + \tau_b$. Here $V_t(T) = Z_d V_d(0)/Z_t$ and $I_{to} = Z_t I_{do}/Z_d$ account for the stripping of the beam from Li^{+1} to Li^{+3} in the diode region, before the beam is transported. Equations (15) and (16) ignore beam dispersion due to microdivergence, focusing, scattering, etc. and assume 100% transport efficiency. The product of (15) and (16) gives the ideal power on target, P_t , as a function of time. The ratio of the instantaneous power on target to the ideal instantaneous power is Γ_t . The time at which the voltage pulse rises to the effective voltage $Z_d V_{\text{tune}}/Z_t$ at the target is $t_t(V_{\text{tune}}) = T + t_d(V_{\text{tune}})/\alpha$, where $t_d(V_{\text{tune}})$ is the time it takes for the diode voltage to rise to V_{tune} [see (1)].

For this study, three different tuning times were considered, namely mid-pulse, three-quarters through the pulse, and the end of the pulse. The voltages corresponding to these tuning times are denoted as $V_{1/2}$, $V_{3/4}$, and $V_{4/4}$, and are given as 29.743, 31.401, and 33.201 MV, respectively for the parameters considered here with $k = 2$. It should be noted that $V_o \neq V_{1/2}$ because the average value of (1) over the pulse length τ_d does not occur at $\tau_d/2$. Simulations calculating the instantaneous power efficiency at the tuning time, Γ_t^{tune} , the instantaneous power efficiency at the end of the pulse, Γ_t^{end} , and the total transported energy efficiency, η_t , were carried out. A three-dimensional, non-relativistic orbit code was used with 20 000 test particles to give adequate statistics. Full charge and current neutralization is assumed. The ATHETA code [13], was used to generate the solenoidal lens magnetic field maps used in the orbit code. For each of the simulations carried out for this work, different solenoidal magnetic field strengths had to

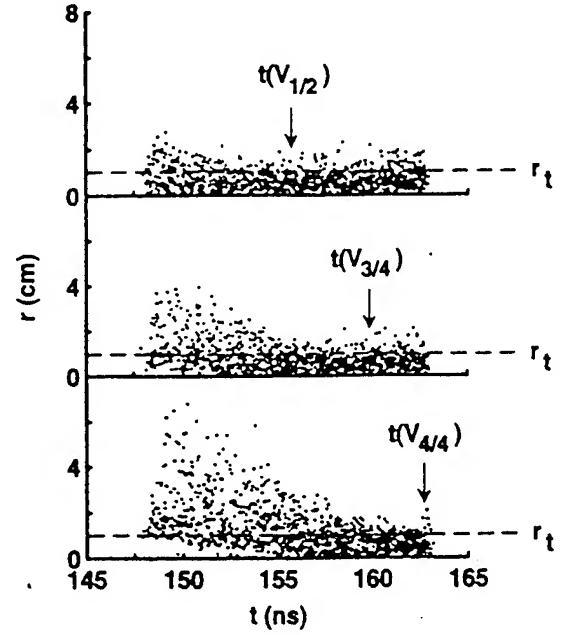


Fig. 3. Plot of beam particle radius, r , versus t at the target plane, $z = 400$ cm. Cases for three different tuning times are plotted, $t(V_{1/2})$, $t(V_{3/4})$, and $t(V_{4/4})$. In each plot, 5% of the total number of particles used in the simulation are represented. For these calculations, $R = 15$ cm, $k = 2$, $\alpha = 2$, $N = 20$, $E_s = 20$ MJ, and $\Theta_\mu = 5$ mrad.

be employed in order to optimally focus the ions of velocity v_{tune} onto the target [5].

The impact on η_t of changing the tuning time is qualitatively illustrated in Fig. 3 for $R = 15$ cm, and $k = 2$. This set of plots shows the radius of beam particles arriving at the target position, $z = 400$ cm, as a function of time for three different tunings. The head of the bunched beam arrives at the target at $T \approx 148$ ns and the tail arrives 15 ns later at $T + \tau_b = 163$ ns. About 5% of the total number of particles used in a typical simulation is represented in these plots. Each simulation particle is equally weighted in current. Particles at or below the dashed line at $r = r_t = 1$ cm strike the target and determine η_t . It is evident that as $t_t(V_{\text{tune}})$ is moved later in the pulse, less particles strike the target, lowering η_t . In particular, note that most ions in the head of the beam miss the target for $V_{\text{tune}} = V_{4/4}$.

The power on target, $P_t(t)$, is shown for three different tunings in Fig. 4 for the baseline case ($R = 15$ cm and $k = 2$). These curves qualitatively illustrate the effect that changing the tuning time at the diode has on the time of peak power efficiency at the target. The impact on η_t due to moving the tuning time later in the pulse is observed by noting the total area under each of the power curves. Also, as the tuning time is selected to be later in the pulse, the half-width of P_t becomes smaller. These results are typical for P_t over the range of R considered in this work. The curves presented in Fig. 4 have been smoothed in order to make the comparison between them easier.

Fig. 5 plots Γ_t^{tune} at the three different tuning voltages. The fall off in Γ_t^{tune} for $R > 15$ cm is due primarily to the packing constraint which limits the maximum solenoidal lens

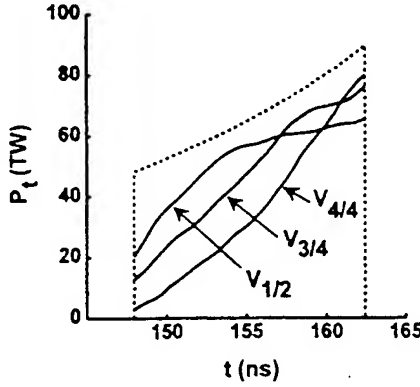


Fig. 4. Plot of P_t versus t at the target plane, $z = 400$ cm. Cases for three different tuning times are plotted, $t(V_{1/2})$, $t(V_{3/4})$, and $t(V_{4/4})$. The dashed line shows the bunched power pulse on target assuming no losses during transport. For these calculations, $R = 15$ cm, $k = 2$, $\alpha = 2$, $N = 20$, $E = 20$ MJ, and $\Theta_\mu = 5$ mrad.

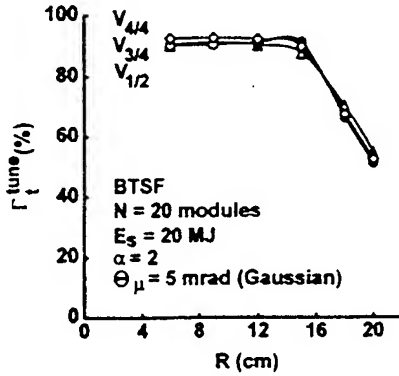


Fig. 5. Plot of Γ_t^{tune} versus R for BTSF. The individual curves are for voltage tunings of $V_{1/2}$, $V_{3/4}$, and $V_{4/4}$.

radius [9]. It is evident that the same Γ_t^{tune} can be achieved regardless of which of the three tuning voltages is selected. However, in Fig. 6, the instantaneous power efficiency at the end of the pulse, Γ_t^{end} , does depend on the tuning voltage chosen. Tuning the voltage to the middle of the pulse results in a reduction in Γ_t^{end} by 10% on average for $R = 9$ to 18 cm compared with tuning the voltage to the end of the pulse. Conversely, the total energy transported to the target for the $V_{4/4}$ case relative to the $V_{1/2}$ case is reduced by an average of 17% for $R = 9$ to 18 cm as illustrated in Fig. 7. Thus, selecting a tuning time at three-quarters of the pulse length leads to only a slight loss in η_t while achieving near-optimal power efficiency at the tail of the pulse. For the baseline case of $R = 15$ cm, a drop of 6% in η_t results in a 14% gain in Γ_t^{end} when shifting the tuning from the middle to three-quarters through the pulse. For this case with tuning at $V_{3/4}$, $\eta_t = 73\%$ and $\Gamma_t^{end} = 89\%$. The maximum Γ_t^{end} is 90%, which occurs for tuning at $V_{4/4}$.

IV. IMPEDANCE MODEL VARIATIONS AND NON-IDEAL ACCELERATOR WAVEFORMS

The design of the LMF applied- B diode for use in a light-ion LMF system is currently being investigated. One possible design employs a two-stage scheme [14], whose

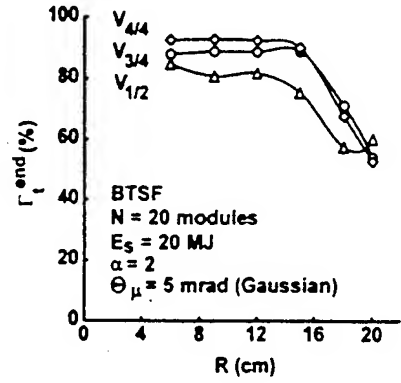


Fig. 6. Plot of Γ_t^{end} versus R for BTSF. The individual curves are for voltage tunings of $V_{1/2}$, $V_{3/4}$, and $V_{4/4}$.

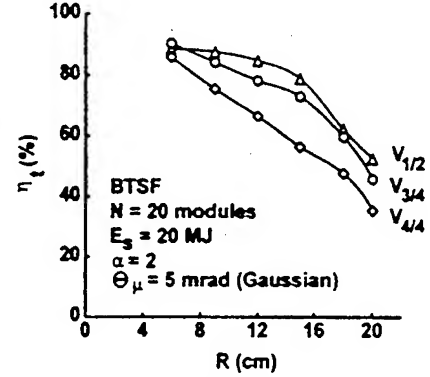


Fig. 7. Plot of η_t versus R for BTSF. The individual curves are for voltage tunings of $V_{1/2}$, $V_{3/4}$, and $V_{4/4}$.

possible benefits include higher beam purity, lower beam microdivergence, better control of impedance behavior, reduced accelerating voltage per stage, and commensurately smaller insulating magnetic fields. Since the actual impedance model of such a diode is currently under evaluation, it is desirable to consider the impact of the diode impedance model on the efficiency results presented in Section II. This is achieved by changing the values of k in (2) over a range of values that seem possible for a two-stage diode design. However, varying k also affects the achromatic matching condition for BTSF. According to (14), Δ increases rapidly as k approaches 0.5. For example, Δ increases from 7 to 28 cm as k decreases from 2.5 to 1.0 for the LMF system parameters considered here with $V_{tune} = V_o$, and $R = 15$ cm. Note that Δ scales as R^2 , so that for $R = 10$ cm, Δ increases from 3 to 12 cm as k decreases from 2.5 to 1.0. Foil placement issues are discussed elsewhere [9], [14], and are beyond the scope of this work.

Simulations were performed varying k over the range of 0.75 to 2.5 for the LMF system parameters considered here with $R = 15$ cm, and $V_{tune} = V_o = 30$ MV. No significant change in η_t is observed for k within the range 0.75 and 2.5, indicating that the enhanced focus-sweep effect resulting from larger values of k has little effect on η_t for this nearly achromatic system. Therefore, it can be anticipated that the potential benefits of two-stage diodes can be exploited without a significant change in the results presented in Sections II and III as long as the effect on Δ can be accommodated.

Another issue of concern to the design of a light-ion ICF system is deviation of the power pulse from the ideal wave-

form. Ramped voltage waveforms produced by the accelerator that deviate from the ideal pulse shape prevent the beam from time-of-flight bunching to the optimum pulse length on target. This may result in insufficient energy being delivered to the target in the optimal target drive time, τ_b . To examine this issue, a small sinusoidal oscillation is added to the ideal voltage pulse of (1), such that the beam is launched as a function of time with voltage

$$V_n(t) = V_d(t) + AV_o \sin(2\pi ft) \quad (17)$$

where A is the amplitude (expressed as a percentage of the value of V_o) and f is the frequency in units of Hz. For this work, the period of the oscillations are kept large with respect to the time it takes an average ion to cross the typical AK gap so that the diode can be assumed to be in quasi-equilibrium at all times. For a gap of 1 cm and typical ion velocities around $v_o = \sqrt{2eZ_d V_o / m_i} \approx 2.87 \times 10^9$ cm/s, an ion crosses the AK gap in about 1/3 ns. Therefore, only voltage oscillation periods greater than a few ns will be considered here.

Two cases of non-ideal power pulses are considered: i) the ideal current in the diode is used with the non-ideal voltage waveform ((2) and (17), respectively), and ii) both the current and voltage are given a non-ideal shape ((17) and (2) with $V_d(t)$ replaced by $V_n(t)$ from (17)). For purposes of comparison, the total energy in the non-ideal pulse is normalized to the total energy in the ideal case by scaling the magnitude of the current of the non-ideal case. The ratio, γ , of the energy in the ideal to the non-ideal system,

$$\gamma = \left(\int_0^{\tau_d} V_d(t) I_d(t) dt \right) / \left(\int_0^{\tau_d} V_n(t) I_{do} \left[\frac{V_{d,n}(t)}{V_o} \right]^k dt \right) \quad (18)$$

is multiplied by I_{do} giving the current for the non-ideal cases as

$$I_n(T) = I_{no} \left(\frac{V_{d,n}(t)}{V_o} \right)^k \quad (19)$$

where $I_{no} = \gamma I_{do}$. V_d is used in (19) for case i) and V_n is used for case ii). The current scaling is minimal ($0.98 < \gamma < 1.02$) for all cases considered here.

Oscillations of the initial voltage pulse were applied to the LMF system for the parameters considered here with $R = 15$ cm, $k = 2$, and $V_{tune} = 30$ MV. Calculations were performed for $1/f = 10$ ns over a range from $A = 0$ to 0.10. Two energy transport efficiency numbers were calculated for each run. The first, η_t , is the total energy transport efficiency defined in Section I, calculated over the entire power pulse delivered to the target, and η_t^{15} denotes the energy transport efficiency delivered to the target in the 15 ns centered about the middle of the delivered power pulse. For each transport scheme, η_t and η_t^{15} are plotted against the range of A , illustrating the impact of temporal spreading of the beam that is induced from variations in the power pulse.

The role of the frequency, f , is also analyzed for a fixed value of A . The result of varying A is shown in Fig. 8 for $1/f = 10$ ns. Over the range $A = 0$ to 7%, η_t was essentially constant at 78%, but falls slightly at $A = 10\%$, to an η_t 75%. However, non-ideal waveform amplitudes of $\geq 2\%$ do have a noticeable effect on the energy delivered in the middle 15

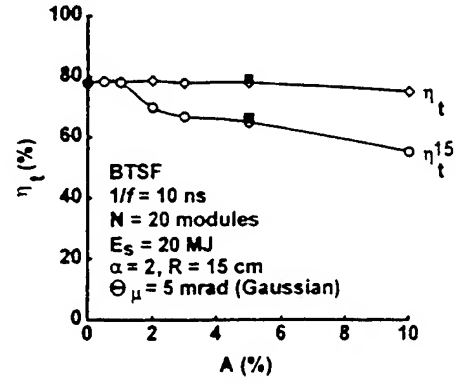


Fig. 8. Plot of η_t versus A for BTSF for non-ideal waveform with $R = 15$ cm and $1/f = 10$ ns. Individual curves are for η_t (total energy efficiency on target, full pulse) and η_t^{15} (energy efficiency on target in the middle 15 ns of the pulse). Hollow data points represent calculations for case (i) (non-ideal voltage), and solid data points represent calculations for case (ii) (non-ideal voltage and current) as discussed in the text. For these cases $V_{tune} = V_o$.

ns of the pulse. The combined effect of altered bending in the diode from (8) (with V_d replaced by V_n), coupled with non-ideal time-of-flight pulse compression, results in a reduction of η_t^{15} for $A \geq 2\%$. At $A = 2\%$, η_t^{15} is 70%, an 8% drop from the ideal waveform calculation; η_t^{15} continues to fall off as A increases. The solid markers in Fig. 8 at $A = 5\%$ indicate data points for case (ii), while the open data points are for case (i) described above. Small fluctuations in voltage and current do not significantly reduce η_t by defocusing the beam. Thus, it can be concluded that the non-ideal voltage waveform drives a temporal spreading of the pulse that reduces the ideal η_t to η_t^{15} .

The role of the frequency of the oscillations in the reduction in η_t was investigated by varying $1/f$ over the range of 5 to 30 ns for A at $\pm 5\%$. Figs. 9 and 10 show only a small variation in η_t while larger variations in η_t^{15} are observed. In Fig. 9, a small deviation in η_t of $\pm 2\%$ around the value for the ideal pulse is observed for $1/f < 20$ ns. For larger $1/f$, the deviation in η_t from the ideal pulse begins to increase because the frequency of oscillation is low enough to dominate the waveform characteristics. For example, when $1/f = 30$ ns, exactly one sinusoidal oscillation occurs over the pulse time. The systematic variation seen in Fig. 10 (and to a lesser extent in Fig. 9) results from the full phase of the voltage variations, $2\pi f \tau_d$, passing through multiples of 2π . When the frequency of the oscillations becomes high enough and many oscillations occur within τ_d , this effect begins to smear out and an average reduction in η_t^{15} is observed, resulting in an 8% drop in η_t^{15} for $1/f < 10$ ns. In Fig. 10, the curves for $+A$ and $-A$ are almost symmetric with respect to each other but on average are about 8% below that of the ideal case ($A = 0$). However, the exact effect on η_t^{15} depends on all of the details of the voltage variations, f , A , and the sign of A .

V. SUMMARY AND CONCLUSIONS

In this paper, transport efficiency studies have been carried for parameters relevant to the design of a light-ion LMF. This work extends a previous investigation into LMF transport point designs [9], examining the impact of the focus sweep effect on transport efficiency. The impact of power efficiency tuning on η_t has been examined for the BTSF scheme for a range

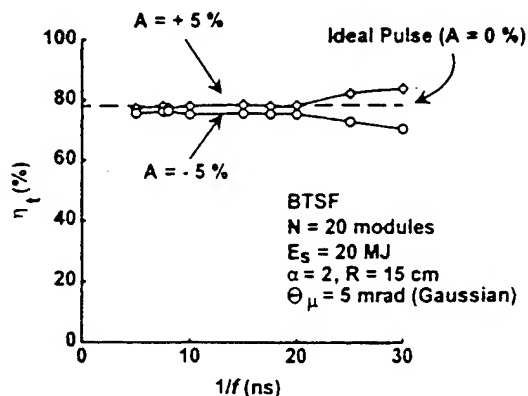


Fig. 9. Plot of η_t versus $1/f$ for BTSF for non-ideal waveform with $R = 15$ cm. Individual curves are for $A = 0\%$ (ideal pulse), $+5\%$, and -5% . For these cases $V_{\text{tune}} = V_0$.

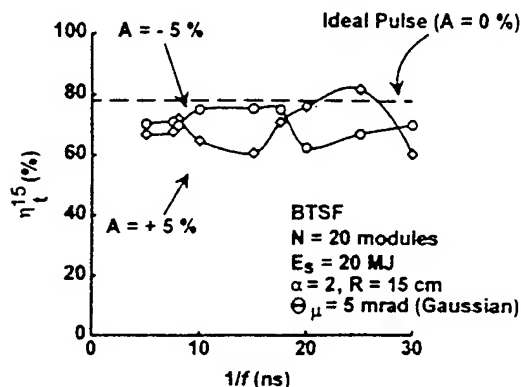


Fig. 10. Plot of η_t^{15} versus $1/f$ for BTSF for non-ideal waveform with $R = 15$ cm. Individual curves are for $A = 0\%$ (ideal pulse), $+5\%$, and -5% . For these cases $V_{\text{tune}} = V_0$.

of parameters that are applicable to the design of a light-ion LMF system. Results indicate that moving the point of peak power efficiency to three-quarters of the pulse time results in maintaining a near optimal value for η_t while achieving high Γ_t^{end} . For $R = 15$ cm, tuning the power pulse to maximize Γ_t at three-quarters of the pulse time yields a Γ_t^{end} of 89% with an η_t of 73%. This means that only 6% of overall energy is sacrificed to gain 14% in power at the tail of pulse. By tuning to the end of the pulse, only 1% more in instantaneous power can be obtained at the expense of an additional 17% reduction in energy. Therefore, tuning to achieve maximum instantaneous power at the three-quarters point in the power pulse yields near optimum performance for this system.

In addition, the diode impedance model has been systematically varied in order to examine the impact of current scaling with voltage on η_t . The value of the scaling constant, k , was varied over a range of values that may result from advanced applied- B diode design, including two-stage diodes. Because BTSF is an achromatic system, virtually no variation in η_t was found for values of k in the range of 0.75 to 2.5, even though higher values of k result in larger manifestations of the focus sweep effect [9]. It was assumed that the achromatic matching constraint placed on Δ can be met even when Δ becomes large.

Deviations from the ideal voltage waveform for TOF bunching can lead to temporal spreading of the bunched pulse at

the target. The effect of non-ideal waveforms on η_t has been evaluated by adding a sinusoidal variation to the ideal voltage and current pulses produced at the diode. Results indicate that oscillations with an inverse frequency, $1/f$, of 10 ns and amplitudes greater than 2% of the average voltage, V_0 , reduces η_t^{15} . This results in an 8% drop in η_t^{15} at $A = 2\%$. As the amplitude of the oscillation is increased, the spreading in the pulse increases, further reducing η_t^{15} . However, Fig. 10 demonstrates that results do depend on the frequency and sign of the amplitude, and thus, the results quoted above are close to "worst-case" numbers. Because significant defocusing does not occur, the ideal transport efficiency is recovered if longer pulse durations on target are acceptable.

The analysis presented in this paper has also been carried out for the z-discharge and wire-guided transport schemes and is reported elsewhere [10]. Further issues that need to be considered in order to accurately determine η_t for specific designs include ion-beam species purity, waveform efficiency, and beam energy losses during transport. Details of the ion beam source model, including the radial dependence of Δ and an accurate microdivergence model must be improved in order to further quantify η_t . Work is presently under way to evaluate beam current neutralization for transport in field-free space [15] and in the presence of a solenoidal magnetic field [16].

REFERENCES

- [1] J. J. Ramirez, R. W. Stinnett, D. L. Johnson, C. L. Olson, T. A. Mehlhorn *et al.*, "Design issues for a light ion beam LMF driver," *Fusion Technol.*, vol. 15, pp. 350-356, 1989.
- [2] J. J. Ramirez, D. L. Cook, J. K. Rice, M. K. Matzen, D. L. Johnson *et al.*, "Intense light-ion beams provide a robust, common-driver path toward ignition, gain, and commercial fusion energy," *Laser and Part. Beams*, vol. 11, pp. 423-430, 1993.
- [3] C. L. Olson, "Phase space acceptance of LMF transport schemes," in *Proc. 1989 Particle Accelerator Conf.*, Chicago, IL, Mar. 20-23, 1989, pp. 1011-1013.
- [4] D. Mosher, D. D. Hinshelwood, J. M. Neri, P. F. Ottinger, J. J. Watrous, C. L. Olson, and T. A. Mehlhorn, "Ion transport for LMF," in *Proc. 8th Int. Conf. High-Power Particle Beams*, Novosibirsk, USSR, July 2-5, 1990, pp. 26-38.
- [5] P. F. Ottinger, D. V. Rose, J. M. Neri, and C. L. Olson, "Ballistic transport and solenoidal focusing of intense ion beams for inertial confinement fusion," *J. Appl. Phys.*, vol. 72, pp. 395-404, 1992.
- [6] P. F. Ottinger, D. V. Rose, D. Mosher, and J. M. Neri, "Z-discharge transport of intense ion beams for inertial confinement fusion," *J. Appl. Phys.*, vol. 70, pp. 5292-5305, 1991.
- [7] J. J. Watrous, D. Mosher, J. M. Neri, P. F. Ottinger, C. L. Olson, *et al.*, "Wire-guided transport of intense ion beams," *J. Appl. Phys.*, vol. 69, pp. 639-655, 1991.
- [8] R. F. Hubbard, M. Lampe, G. Joyce, S. P. Slinker, I. Haber, and R. F. Fernsler, "Target chamber propagation of heavy ion beams in the pressure regime above 10^{-3} torr," *Part. Accel.*, vol. 37-38, pp. 161-165, 1992.
- [9] P. F. Ottinger, D. V. Rose, and C. L. Olson, "Effect of time-of-flight bunching on efficiency of light-ion-beam inertial-confinement-fusion transport schemes," *J. Appl. Phys.*, vol. 75, pp. 4402-4414, 1994.
- [10] D. V. Rose, P. F. Ottinger, and C. L. Olson, "Transport efficiency studies for light-ion inertial confinement fusion," Naval Research Laboratory Memo. Rep. #7609, 1994.
- [11] R. E. Olson, G. O. Allshouse, D. L. Cook, T. R. Lockner, M. G. Mazarakis, *et al.*, "The light ion LMF and its relevance to IFE," in *Proc. 15th IEEE Symp. Fusion Eng.*, Hyannis, MA, Oct. 11-15, 1993, pp. 189-193.
- [12] S. A. Slutz and D. B. Seidel, "Magnetic insulation of extraction applied-B ion diodes," *J. Appl. Phys.*, vol. 59, pp. 2685-2688, 1986.
- [13] J. P. Quintenz and D. B. Seidel, "ATHETA—A quick magnetic-field solver for general boundary conditions," *Particle Beam Fusion Progress Report, January-June 1984*, SAND84-1336. Albuquerque, NM: Sandia National Laboratories, 1985.

- [14] S. A. Slutz and M. P. Desjarlais, "Theory of multistage intense ion-beam acceleration," *J. Appl. Phys.*, vol. 67, pp. 6705-6717, 1990.
- [15] F. C. Young, R. F. Hubbard, M. Lampe, J. M. Neri, P. F. Ottinger, *et al.*, "Interaction of intense, MeV light-ion beams with low-pressure gases," *Phys. Plasmas*, vol. 1, pp. 1700-1707, 1994.
- [16] B. V. Oliver and R. N. Sudan, "Self-field generation in solenoidal focussing of light ion beams," in *Proc. 10th Int. Conf. High-Power Particle Beams*, San Diego, CA, June 20-24, 1994, pp. 678-682.

D. V. Rose was born in Harrisburg, PA. He received the B.A. in physics in 1986 from Temple University, Philadelphia, PA, and the M.S. degree in applied physics in 1991 from Johns Hopkins University, Baltimore, MD. He is currently pursuing a Ph.D. degree in computational physics at George Mason University, Fairfax, VA.

From 1987 to the present he has worked for JAYCOR, Vienna, VA, as a Computer Scientist and Research Physicist. His research has included ion beam transport/focusing and high power diode physics.

P. F. Ottinger (M'91) was born in Philadelphia, PA. He received the B. A. degree in physics from the University of Pennsylvania, Philadelphia, in 1970 and the M.S. and Ph.D. degrees in theoretical plasma physics from the University of Maryland, College Park, in 1974 and 1977, respectively.

Since 1985 he has been with the Naval Research Laboratory as the Head of the Theory and Analysis Section in the Pulsed Power Physics Branch. Before joining NRL, he was a National Research Council Associate at NRL and worked as a Senior Research Scientist in private industry for JAYCOR, Inc. During his career he has developed expertise in the specialized areas of intense particle beams, fast opening plasma switches, and plasma radiation sources. In particular, his research has concentrated on the areas of ion beam generation, transport and stability.

Dr. Ottinger is a fellow of the American Physical Society (APS) and a member of IEEE Nuclear and Plasma Science Society.

C. L. Olson, photograph and biography not available at the time of publication.

BEAM TRANSPORT*

C.L. Olson,¹ M.E. Cunico,¹ M.P. Desjarlais,¹ D.L. Hanson,¹ D.D. Hinshelwood,² R.F. Hubbard,³ G.L. Kulcinski,⁶ M. Lampe,³ T.R. Lockner,¹ J.E. Macnchen,¹ M.G. Mazarakis,¹ J.M. Neri,³ B.V. Oliver,⁵ J.C. Olson,⁵ R.E. Olson,¹ P.F. Ottinger,³ R.R. Peterson,⁶ T.D. Pointon,¹ J.W. Poukey,¹ D.V. Rose,² T.W.L. Sanford,¹ S.P. Slinker,³ S.A. Slutz,¹ S.J. Stephankis,³ D.R. Welch,⁴ and F.C. Young³

¹Sandia National Laboratories, Albuquerque, NM 87185

²JAYCOR, Inc., Vienna, VA 22182

³Naval Research Laboratory, Washington, DC 20375

⁴Mission Research Corporation, Albuquerque, NM 87106

⁵Cornell University, Ithaca, NY 14853

⁶U. Wisconsin, Madison, WI 53706

ABSTRACT

Transport and focusing of light ion beams for inertial confinement fusion is discussed, including transport schemes, gas breakdown research, and a strategy for divergence reduction.

1. INTRODUCTION

Transport and focusing of extracted light ion beams¹ over distances of several meters is required for high yield applications such as the Laboratory Microfusion Facility (LMF),² and for energy applications such as the light ion fusion reactor concept LIBRA-LiTE.³ Transport schemes for LMF and LIBRA-LiTE are discussed in Sec. 2. Gas breakdown research, which is fundamental to understanding ballistic transport and self-pinch transport, is summarized in Sec. 3. Lastly, a strategy for achieving the required beam microdivergence is presented in Sec. 4.

2. TRANSPORT FOR HIGH YIELD (LMF) AND ENERGY (LIBRA)

LMF has specific beam requirements based on the LMF target design. In all cases, beams will be produced in extraction diodes, which are voltage ramped (26-35 MeV Li) to produce axial time-of-flight bunching by a factor of about 2. The diode-to-target transport length will be 400 cm, and any final focusing element must be at least 100 cm from the target. The transport method must accommodate the energy spread produced by the ramped voltage, the diode must be protected from the blast, and minimal transport apparatus is allowed inside the containment chamber.

*Supported under DOE contract number DE-AC04-94AL85000.

The baseline LMF transport method, which satisfies all of the above LMF requirements, is an achromatic lens system.^{4,5} This system consists of the high current extraction diode (which acts as a self-field lens) and a solenoidal lens. As shown in Fig. 1, the beam is transported ballistically in gas from the diode to the lens over a distance L , is focused by the lens, and then transported ballistically in gas from the lens to the target over a distance F . For LMF, $L = 300$ cm and $F = 100$ cm. The gas is assumed to provide complete charge and current neutralization. The diode lens and solenoidal lens act together to form a system that is achromatic to lowest order in the diode voltage ramp variation. The main features are that the spot size is determined by $\theta_\mu F$ [and not $\theta_\mu(F+L)$], there is no apparatus inside the chamber, and the diode is shielded from debris by a center plug which fits inside the annular beam. The basic elements of this system (diode lens effect, gas neutralization, and solenoidal lens effect) are all routinely observed on PBFA II, although a complete extracted beam, achromatic system has not been demonstrated.

Backup transport methods for LMF include wall-confined channel transport,⁶ wire-guided transport,⁷ and self-pinched transport. For each of these "channel-like" schemes, the beam from the diode is first focused down to a small radius (< 1 cm) and then transported at small radius over several meters to the target. For LMF parameters (26-35 MeV Li, microdivergence $\theta_\mu \sim 6$ mrad), all channel-like schemes require a channel current $I_c \sim 50$ kA. The current I_c can be from a preformed discharge (wall-confined transport), a wire (wire-guided transport), or from the net current resulting from gas breakdown (self-pinched transport).

Both, channel transport and wire-guided transport have been thoroughly demonstrated at low energy (1 MeV p) and are expected to work at LMF energies (35 MeV Li), but require some transport apparatus (low mass tubes or wires) inside the containment chamber; these schemes could be used for LMF. The achromatic lens system and self-pinched transport are attractive because no apparatus is required inside the containment chamber; these schemes can be used for LMF and LIBRA.

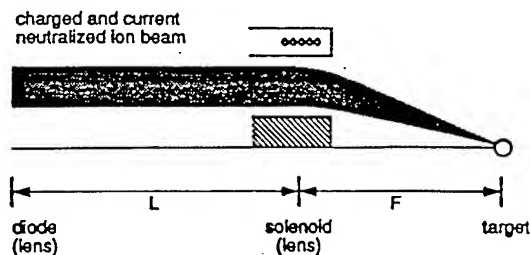


Figure 1. Achromatic lens system for LMF and LIBRA.

3. GAS BREAKDOWN RESEARCH

All light ion transport schemes involve ion beam interactions with neutral gas, plasma, or electrons to provide charge neutralization and some current neutralization. Present transport research is developing a thorough physics understanding of gas breakdown, which is needed for both the achromatic lens system and self-pinched transport, as well as the ballistic transport input section of all channel-like schemes. Specifically, we intend to understand current neutralization so that by varying certain parameters (e.g., gas type, gas pressure, beam current risetime, beam radius, etc.) we can achieve either essentially complete current neutralization (for ballistic transport) or partial current neutralization (for self-pinched transport).

The physical processes involved in gas breakdown and the growth of the electrical conductivity include ion impact ionization, secondary electron impact ionization, electron avalanching, and late time Ohmic heating. Energetic electrons can be created in ionizing collisions between beam ions and neutral gas atoms (ion impact ionization), in momentum-changing collisions between beam ions and free electrons (knock-on collisions), and from free electron acceleration in electric fields (avalanching). In the 1 Torr pressure regime, the mean free path between collisions can be of the order of the beam radius; then the gas breakdown processes are "non-local" and they must be followed accurately in space and time.

The first experiments designed to study ion beam-induced gas breakdown and conductivity growth have been performed on the GAMBLE II accelerator at NRL.⁸ In these experiments, a 1 MeV proton beam produced in a pinch reflex diode is injected through a collimator section into an experimental section. A ~ 6 kA, 1 kA/cm^2 proton beam enters the experimental section which is filled with helium, air, or neon at pressures in the range of 0.25–4.0 Torr. Extensive diagnostics are used. Net current fractions range from 2.3% to 8% and peak electron densities are of order 10^{15} cm^{-3} corresponding to ionization fractions of 0.6% to 4.6%.

IPROP and DYNAPROP simulations were performed to evaluate net currents and electron densities. IPROP is a 3-D EM hybrid code with a full tensor conductivity.⁹ Beam ions are treated as particles, and fast electrons ($> 100 \text{ eV}$) are also treated as particles. Slow electrons ($< 100 \text{ eV}$) are treated as a fluid, while plasma ions are treated as a stationary background. The important unique feature is that the fast electrons are followed explicitly, and that these are the particles responsible for non-local breakdown effects. DYNAPROP is a 1-D code based on a resistive plasma model in which the beam dynamics are described by an envelope equation.¹⁰ The plasma properties (density, temperature) are determined by rate equations, and the net current is calculated from a circuit equation.

Figure 2 shows a comparison of the net current in the GAMBLE II experiments with IPROP and DYNAPROP results. Many such comparisons have been made; this example illustrates the main effects. If fast electrons are not included, note that both IPROP and DYNAPROP predict a net current much higher than that observed in the experiment by the

B-dot monitor at $r = 4$ cm. By including fast electrons in IPROP, good agreement is obtained with the experiments. Note that fast electrons outside the beam radius contribute significantly to the return current.

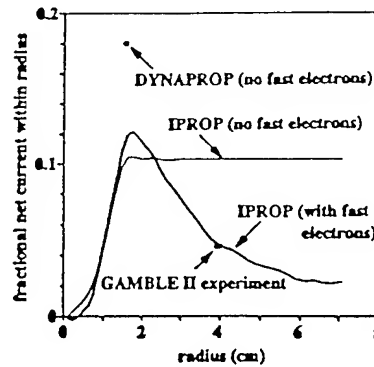


Figure 2. Net current fraction contained within a given radius for the GAMBLE II experiments, IPROP simulations, and DYNAPROP simulations (1 MeV p, ~ 6 kA, ~ 1 kA/cm², $r_0 = 1.5$ cm, B-dot at $r = 4$ cm, 1 Torr He).

IPROP has also been used to compare with net current measurements for the barrel diode geometry of PBFA II, including applied magnetic field effects. IPROP predicts $\geq 99.8\%$ neutralization for 6 MeV Li ions in 4 Torr argon on PBFA II. It is important to note that the net current fraction here is even smaller than in the GAMBLE II experiments because the total current is higher (~ 1 MA instead of ~ 6 kA), the ions are Li^{+3} which ionize faster than protons, and the gas is argon which is easier to ionize than helium.

Self-pinch transport requires higher net current fractions ($\geq 2\%$) and preliminary IPROP code results indicate that these appear achievable for small-radius intense beams in lower pressure gases (≤ 1 Torr). Several self-pinch transport concepts look promising.

4. DIVERGENCE REDUCTION STRATEGY

All transport modes require microdivergences of ~ 6 mrad for 35 MeV Li for LMF. In Table 1, a summary of achieved and proposed divergence values is given. For each case, the accelerator, ion species, diode type, ion energy, and beam microdivergence (θ_μ) is shown. Also shown is the equivalent θ_μ for LMF. This is defined by assuming the ion transverse temperature is fixed and the ion axial velocity, v_z , is increased to $\beta = v_z/c = 0.1$. This concept of divergence reduction has already been demonstrated in two-stage diode experiments on ALIAS.¹¹ Note that a 5 MeV proton and a 35 MeV Li ion have the same value of β . Most importantly, note that LMF equivalent values of $\theta_\mu < 9$ mrad have already been achieved on ALIAS, KALIF,¹² and PBFA II.

The concept of a fixed ion transverse source temperature has a strong foundation in the high energy accelerator physics community. In a typical high energy accelerator, the ion source sets the initial beam emittance, and there is almost negligible emittance growth during acceleration over long distances to high energies. For high current pulsed power diode accelerators, increasing the voltage in a single-stage diode may self-consistently raise the transverse ion temperature. This divergence issue has been, and is being, studied extensively. However, for two-stage diodes, it has already been demonstrated on ALIAS that there is negligible growth of the transverse ion temperature in the second stage. Thus, the concept of fixed source temperature holds well for two-stage diodes, as presently tested.

The last four lines in Table 1 outline our strategy for achieving 6 mrad for LMF. The first goal is to achieve 12 mrad for 5 MeV protons in a single-stage diode on SABRE. This represents a substantial improvement over the current value of 17 mrad. The second goal is to achieve 9 mrad for 5 MeV protons in a two-stage diode on SABRE. This is exactly equivalent to the KALIF results that have already been achieved. By this we mean that if the KALIF results are reproduced in the first stage (at 1.7 MeV) of a two-stage diode on SABRE, and there is negligible transverse temperature growth in the second stage (to a total of 5 MeV), then the final divergence will be < 9 mrad. Similarly, if a 5 MV single-stage diode on SABRE could operate with the same transverse temperature as the KALIF diode, then the divergence would also be < 9 mrad. The third goal is to achieve 9 mrad Li ions at 14 MeV in a two-stage diode on Hermes III. Note that in terms of LMF equivalent values of θ_μ , this requires only a reduction from the PBFA II equivalent LMF value of 8.6 mrad to 6 mrad. The fourth goal is to achieve 6 mrad for LMF. Having achieved 9 mrad on HERMES III at 14 MeV means that by simply increasing the diode voltage to the full LMF value will produce 35 MeV Li ions at the desired 6 mrad.

Table 1. Microdivergence (θ_μ): Achieved and Proposed.

Accelerator	Ion	Diode	e_i (MeV)	θ_μ (mrad)	Status	Equivalent θ_μ (mrad) for LMF ($\beta=0.1$; 5 MeV p or 35 MeV Li)
ALIAS	p	1-stage	< 0.6	19	achieved	< 6.6
ALIAS	p	2-stage	> 1	10	achieved	> 4.5
KALIF	p	1-stage	1.7	15	achieved	8.7
PBFA II	Li	1-stage*	9	17	achieved	8.6
SABRE	p	1-stage	5	17	achieved	17
SABRE	p	1-stage	5	12	proposed	12
SABRE	p	2-stage	5	9	proposed	9
Hermes III	Li	2-stage	14	9	proposed	6
LMF	Li	2-stage	35	6	proposed	6

*barrel diode; all other cases are extraction diodes.

REFERENCES

1. C. L. Olson, "Ion Beam Propagation and Focusing," *J. Fusion Energy* **1**, 309 (1982).
2. R. E. Olson, G. O. Allshouse, D. L. Cook, T. R. Lockner, M. G. Mazarakis, C. L. Olson, and D. L. Smith, "The Light Ion LMF and Its Relevance to IFE," *Proc. 15th IEEE Symp. Fusion Eng.*, (Oct. 11-15, 1993), to be published.
3. G. Kulcinski et al., "LIBRA-LiTE: A 1000 MWe Reactor," *J. Fusion Energy* **10**, 339 (1991).
4. C. L. Olson, "Achromatic Magnetic Lens Systems for High Current Ion Beams," *Proc. 1988 Linear Accel. Conf.*, Newport News, VA, CEBAF-89-001, 34 (1989).
5. P. F. Ottinger, D. V. Rose, J. M. Neri, and C. L. Olson, "Ballistic Transport and Solenoidal Focusing of Intense Ion Beams for Inertial Confinement Fusion," *J. Appl. Phys.* **72**, 395 (1992).
6. J. M. Neri, P. F. Ottinger, D. V. Rose, P. J. Goodrich, D. D. Hinshelwood, D. Mosher, S. J. Stephanakis, and F. C. Young, "Intense Ion Beam Transport Experiments Using a Z-Discharge Plasma Channel," *Phys. Fluids B* **5**, 176 (1993).
7. J. J. Watrous, D. Mosher, J. M. Neri, P. F. Ottinger, C. L. Olson, J. T. Crow, and R. R. Peterson, "Wire-Guided Transport of Intense Ion Beams," *J. Appl. Phys.* **69**, 639 (1991).
8. F. C. Young, D. D. Hinshelwood, R. F. Hubbard, M. Lampe, J. M. Neri, C. L. Olson, P. F. Ottinger, D. V. Rose, S. P. Slinker, S. J. Stephanakis, and D. R. Welch, "Current Neutralization of Intense MeV Proton Beams Transported in Low-Pressure Gas," *Phys. Rev. Lett.* **70**, 2573 (1993).
9. D. R. Welch, C. L. Olson, and T. W. L. Sanford, "Simulation of Charged Particle Beam Transport in a Gas Using a Hybrid Particle Fluid Plasma Model," *Phys. Plasmas* **1**, 764 (1994).
10. R. F. Hubbard, S. P. Slinker, M. Lampe, G. Joyce, and P. F. Ottinger, "Current Neutralization in Ballistic Transport of Light Ion Beams," *NRL Memorandum Report No. 7112* (Oct. 1992).
11. T. Lockner, S. A. Slutz, J. W. Poukey, and W. A. Stygar, "Theoretical and Experimental Studies of the 2-Stage Ion Diode," *Proc. IEEE 9th Int. Pulsed Power Conference*, Albuquerque, NM, (1993), to be published.
12. H. Bluhm, P. J. W. Hoppe, H. P. Laqua, and D. Rusch, "Production and Investigation of TW Proton Beams from an Annular Diode Using Strong Radial Magnetic Insulation Fields and a Preformed Anode Plasma Source," *Proc. IEEE* **80**, 995 (1992).

AIP CONFERENCE PROCEEDINGS 318

LASER INTERACTION AND RELATED PLASMA PHENOMENA

11th INTERNATIONAL WORKSHOP
MONTEREY, CA OCTOBER 1993

EDITOR: GEORGE H. MILEY
UNIVERSITY OF ILLINOIS

AIP
PRESS

American Institute of Physics

New York

Authorization to photocopy items for internal or personal use, beyond the free copying permitted under the 1978 U.S. Copyright Law (see statement below), is granted by the American Institute of Physics for users registered with the Copyright Clearance Center (CCC) Transactional Reporting Service, provided that the base fee of \$2.00 per copy is paid directly to CCC, 27 Congress St., Salem, MA 01970. For those organizations that have been granted a photocopy license by CCC, a separate system of payment has been arranged. The fee code for users of the Transactional Reporting Service is: 0094-243X/87 \$2.00.

© 1994 American Institute of Physics.

Individual readers of this volume and nonprofit libraries, acting for them, are permitted to make fair use of the material in it, such as copying an article for use in teaching or research. Permission is granted to quote from this volume in scientific work with the customary acknowledgment of the source. To reprint a figure, table, or other excerpt requires the consent of one of the original authors and notification to AIP. Republication or systematic or multiple reproduction of any material in this volume is permitted only under license from AIP. Address inquiries to Series Editor, AIP Conference Proceedings, AIP Press, American Institute of Physics, 500 Sunnyside Boulevard, Woodbury, NY 11797-2999.

L.C. Catalog Card No. 94-78097
ISBN 1-56396-324-8
DOE CONF-931048

Printed in the United States of America.

Light-Ion-Beam Transport Research at NRL*

P.F. Ottinger¹, D.D. Hinshelwood², R.F. Hubbard¹, M. Lampe¹, D. Mosher¹,
J.M. Neri¹, W. Noonan⁺, C.L. Olson³, D.V. Rose², S.P. Slinker¹,
S.J. Stephanakis¹, D.R. Welch⁴, and F.C. Young¹

¹ Plasma Physics Division, Naval Research Laboratory, Washington, DC 20375

² JAYCOR, Inc., Vienna, VA 22182

³ Sandia National Laboratories, Albuquerque, New Mexico 87185

⁴ Mission Research Corporation, Albuquerque, New Mexico 87106

Abstract

Ion-driven inertial confinement fusion requires transport of intense beams over several meters to isolate the ion source from the target explosion and allow for focusing and time-of-flight bunching. Transport in a low pressure background gas is possible only if rapid beam-induced gas ionization leads to formation of a plasma with electrical conductivity sufficient to charge- and current-neutralize the beam. In order to minimize collisional energy loss and scattering of the beam, helium at 1-Torr pressure is proposed for the background gas. Transport in the 1-Torr regime is not well understood because this pressure falls between the high-density regime treated by resistive models, and the low-density regime treated by collisionless models. Experiments and theoretical analyses are being carried out to study beam-induced gas ionization in this pressure regime in order to evaluate its impact on the various transport schemes including ballistic transport with solenoidal lens focusing, self-pinched transport, z-discharge transport, and wire-guided transport. Work in this area is reviewed along with other transport considerations including beam transport efficiency, beam-driven instabilities, and beam energy losses.

I. Introduction

The Laboratory Microfusion Facility (LMF) has been proposed for the study of high-gain, high-yield ICF targets.¹ A number of transport and focusing schemes are being considered for LMF.² The baseline approach is ballistic transport with solenoidal lens focusing^{3,4} (BTSF), and back-up approaches include z-discharge transport⁵ (ZDT), wire-guided transport⁶ (WGT), and self-pinched transport⁷ (SPT). Work at the Naval Research Laboratory (NRL) is concentrating on the important physics issues associated with beam transport and on evaluating these transport schemes for LMF.

II. Beam-Induced Gas Ionization

Experiments and theoretical analyses are being carried out to study beam-induced ionization of gases in the 1-Torr pressure regime in order to evaluate its impact on the various transport schemes. This pressure regime falls between the high-density collisional regime and the low-density collisionless regime. Fast electrons, produced by beam-ion impact, knock-on collisions, and runaway processes, can have mean-free-paths on the order of the beam radius leading to nonlocal secondary ionization. In initial experiments to study this physics, 1-MeV, 1-kA/cm² proton beams were produced on Gamble II by collimating the beam from a pinch-reflex ion

Table I - Comparisons of Data with Theory for Helium

Pressure (Torr)	Net Currents (kA)				Electron Densities (10^{15} cm^{-3})			
	Measured ($r = 4 \text{ cm}$)	IPROP ($r = 4 \text{ cm}$)	IPROP ($r = 1.5 \text{ cm}$)	DYNAPROP ($r = 1.5 \text{ cm}$)	Measured (line average)	IPROP ($r = 0$)	IPROP ($r = 1.5 \text{ cm}$)	DYNAPROP ($r = 0$)
0.25	0.31	0.31	0.9	1.3	-	0.2	0.2	0.2
1.0	0.32	0.39	1.0	1.5	0.7	1.0	0.6	0.7
4.0	0.47	0.63	1.6	2.1	1.5	3.2	1.8	1.9

diode. The beam from the collimator was 1.5 cm in radius and limited to a divergence of about 50 mrad. Beams were transported through helium, neon, argon, and air at pressures in the range of 0.25 to 4 Torr. Details of this experiment are described in Ref. 8. Small net currents (2%-8%) were measured outside the beam channel with a dB/dt monitor located at a radius of 4 cm. Net current fractions are smaller for neon and air and larger for helium and argon. They also tend to increase with pressure. Interferometric measurements across the channel indicated that these gases are only weakly ionized (0.6%-5%) and that the ionization is confined predominantly to the beam channel. Measured net currents and electron densities for helium are shown in Table I. Transported beam currents for these shots were about 6 kA.

The DYNAPROP⁹ and IPROP¹⁰ codes were used to analyze these experiments. DYNAPROP is a 1-D code which uses a resistive model to treat plasmas created by beam interactions with high-density, collisional gases. Fast electrons are not treated. IPROP is a 3-D hybrid code which treats beam ions and fast electrons ($>100 \text{ eV}$) as particles. The remaining electrons are treated as a resistive medium, and plasma ions form a stationary background. Results from the simulations are compared with the measurements for 1-Torr helium in Table I. Both codes predict net currents at the beam radius (1.5 cm) that are substantially larger than net currents measured outside the beam. As shown in Fig. 1, an IPROP simulation (with fast electrons)

predicts net currents outside the beam at the dB/dt monitor location which agree with experiment. In this simulation, fast electrons carry a significant fraction of the return current at the beam edge. An IPROP simulation without fast electrons does not agree with the experiment. Measurements of ion energies after transport show energy losses that are consistent with beam slowing in an induced electric field due to an effective net current within the beam channel that is larger than the net current measured outside the beam. These results imply that fast electrons and nonlocal ionization play an important role in this pressure regime.

Electron densities predicted by both codes are consistent with the measured densities for helium as indicated in Table I. The

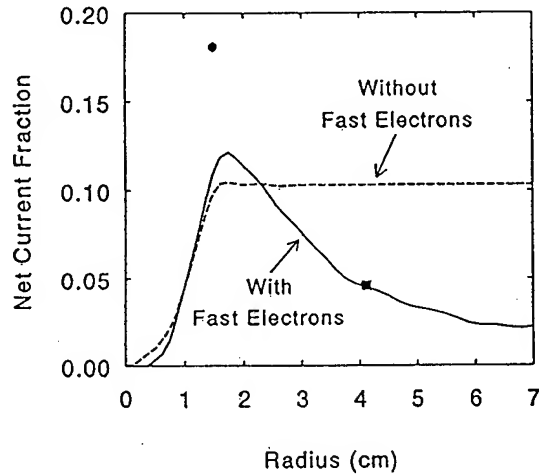


Fig. 1. Net current fraction enclosed within a given radius. Solid (dashed) curve is from IPROP simulation with (without) fast electrons. Square point is experimental measurement and circular point is from DYNAPROP simulation.

magnitude of the density is consistent with ion impact ionization being the predominant electron-production mechanism. At higher LMF-level currents, electron avalanche is expected to be the dominant mechanism.

Results from these and future experiments will be used to benchmark IPROP in order to extrapolate to LMF transport parameters. For BTSF, current neutralization must be evaluated both in the ballistic-transport regions and in the solenoidal-lens region. Net-current fractions of $\leq 0.1\%$ are required. Larger net currents will act as a distributed lens which must be taken into account. For SPT, net currents of $\geq 2\%$ are required in the pinch region. Current neutralization must also be evaluated in the ballistic focusing region for ZDT, WGT and SPT in order to determine the location of the beam focus.

III. LMF Transport Efficiency

The light-ion LMF approach uses a multimodular system with applied-B extraction diodes as ion sources. The number of modules N is expected to be between 10 and 30. Beams are extracted from these diodes and transported to the target. The transport efficiency η_t is defined as the ratio of the ion energy produced in all N diodes to the total

ion energy which hits the target. η_t has been calculated as a function of various parameters so that LMF point designs can be developed for BTSF, ZDT, and WGT. Results for SPT should be similar to ZDT results.

Focus sweeping due to a voltage ramp for time-of-flight (TOF) bunching has recently been considered.¹¹ This voltage ramp will decrease η_t . Because BTSF is nearly achromatic^{3,11}, the focus sweep effect reduces η_t the least for this scheme. Results for all three transport schemes are shown in Figs. 2-4 as a function of the diode radius R and the bunching factor α . The parameter Δ is the distance between the anode and the foil which separates the diode vacuum region from the gas-filled transport region. For BTSF, Δ is varied to achromatically match the diode lens with the solenoidal lens. For the cases shown in Figs. 2-4, the beam microdivergence is 5 mrad, the focal length F is 150 cm, the total ion energy at the diode sources E_s is 20 MJ, the number of modules N is 20, the target radius is 1 cm, and the beam pulse duration at the target is 15 ns. Here, F refers to the solenoidal lens focusing length for BTSF, and the ballistic focusing distance between the diode and the channel entrance for ZDT, WGT, and SPT. The achromatic matching

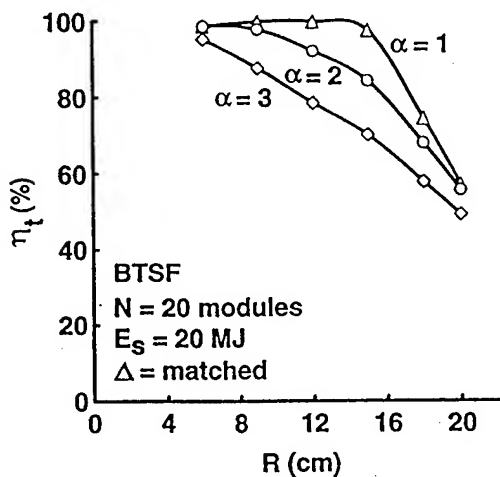


Fig. 2. Transport efficiency as a function of diode radius for a BTSF system.

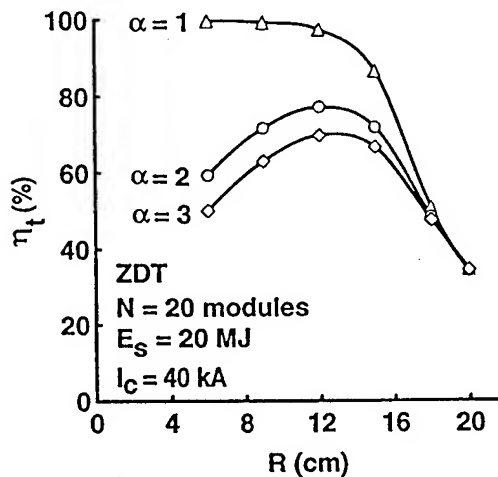


Fig. 3. Transport efficiency as a function of diode radius for a ZDT system.

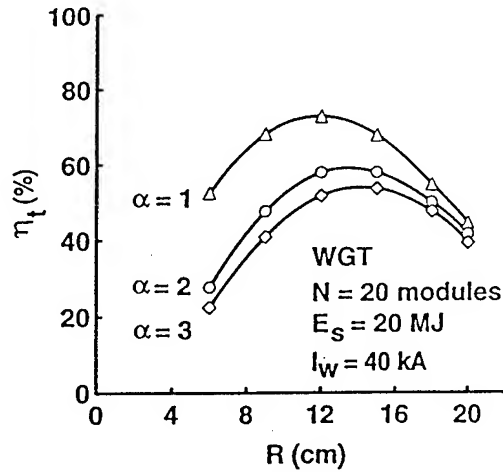


Fig. 4. Transport efficiency as a function of diode radius for a WGT system.

condition has been applied in the case of BTSF, while the channel current I_c and the wire current I_w are set equal to 40 kA for ZDT and WGT. These results also assume a square profile for the beam microdivergence and that the ion current from the diode scales as the square of the diode voltage.

Results indicate that reasonably high transport efficiency ($> 50\%$) can be obtained for all three systems for bunching factors as large as $\alpha = 3$ with $R \leq 15$ cm. In particular, the point design for LMF using the baseline BTSF system with $R = 15$ cm and $\alpha = 2$ is calculated to have $\eta_t = 84\%$. At the same values of R and α , the ZDT system has $\eta_t = 72\%$ and the WGT system has $\eta_t = 60\%$.

The results assume that the system is tuned to obtain optimum power efficiency on target at midpulse. This maximizes η_t for a given set of system parameters. However, target considerations suggest that optimum power efficiency should occur near peak power (i.e., at the end of the pulse for a TOF ramped voltage pulse). It has been found¹² that tuning the system for optimum power efficiency at the end of the pulse can significantly reduce η_t . A compromise is obtained by tuning the system to optimize power efficiency three-quarters of the way through

the pulse. In this case, η_t is only slightly reduced and the power efficiency at the end of the pulse is on the order of 95% for all three transport schemes.

IV. Summary

Beam-induced gas ionization experiments for evaluating beam transport schemes for LMF have begun. Future experiments on Gamble II will use an applied-B extraction ion diode. Presently, an exploding metal foil anode plasma source (EMFAPS) is being developed for this diode. Gas ionization induced by the annular ion beam from this diode will be studied both in field-free space and in the transverse magnetic field of a solenoidal lens. In addition, consideration of beam energy losses during transport, thresholds for beam-driven instabilities and background plasma magnetohydrodynamics will be combined with transport efficiency calculations to define an operational window for each LMF transport scheme.

V. References

- * Work supported by the U.S. Department of Energy through Sandia National Laboratories.
- + National Research Council Research Associate at the Naval Research Laboratory.
- 1. J.J. Ramirez, *et al.*, Fusion Tech. 15, 350 (1989).
- 2. D. Mosher, *et al.*, Proc. of the 8th Inter. Conf. on High-Power Particle Beams, (Novosibirsk, USSR, July 1990), p. 26.
- 3. C.L. Olson, Proc. of the 1988 Linear Accel. Conf., (Newport News, VA, Oct. 1988), p. 34.
- 4. P.F. Ottinger, *et al.*, J. Appl. Phys. 72, 395 (1992).
- 5. P.F. Ottinger, *et al.*, J. Appl. Phys. 70, 5292 (1991).
- 6. J.J. Watrous, *et al.*, J. Appl. Phys. 69, 639 (1991).
- 7. R.F. Hubbard, *et al.*, Part. Accel. 37-38, 161 (1992).
- 8. F.C. Young, *et al.*, Phys. Plasmas 1, 1700 (1994).
- 9. R.F. Hubbard, *et al.*, NRL Memorandum Report No. 7112, 1992.
- 10. D.R. Welch, C.L. Olson and T.W.L. Sanford, Phys. Plasmas 1, 764 (1994).
- 11. P.F. Ottinger, D.V. Rose, C.L. Olson, J. Appl. Phys. 75, 4402 (1994).
- 12. D.V. Rose, P.F. Ottinger and C.L. Olson, to be published.

10th International Conference on High-Power
Particle Beams (San Diego, CA, June 1994)

(P)196

LIF Standoff Research*

C.L. Olson,¹ M.E. Cuneo,¹ M.P. Desjarlais,¹ A. B. Filuk,¹ J. B. Greenly,⁶ D.L. Hanson,¹ D.D. Hinshelwood,² R.F. Hubbard,³ M. Lampe,³ T.R. Lockner,¹ J.E. Maenchen,¹ M.G. Mazarakis,¹ C. W. Mendel, Jr.,¹ P. R. Menge,¹ D. Mosher,³ T. J. Nash,¹ J.M. Neri,³ W. Noonan,³ B.V. Oliver,⁶ J.C. Olson,⁶ R.E. Olson,¹ P.F. Ottinger,³ R.R. Peterson,⁷ T.D. Pointon,¹ J.W. Poukey,¹ J. P. Quintenz,¹ D.V. Rose,² T.W.L. Sanford,¹ S.P. Slinker,³ S.A. Slutz,¹ J. R. Smith,⁵ S.J. Stephankis,³ D.R. Welch,⁴ and F.C. Young³

¹Sandia National Laboratories, Albuquerque, NM 87185

²JAYCOR, Inc., Vienna, VA 22182

³Naval Research Laboratory, Washington, DC 20375

⁴Mission Research Corporation, Albuquerque, NM 87106

⁵Titan Corporation, Albuquerque, NM 87106

⁶Cornell University, Ithaca, NY 14853

⁷University of Wisconsin, Madison, WI 53706

Abstract

Present LIF target experiments on PBFA II use a barrel diode in which the total transport length from the anode to the target is ≤ 15 cm. Future LIF development includes high yield applications (LMF) and energy production (ETF and LIBRA power plants) that require standoff - the generation of extracted ion beams and transport of these beams over distances of several meters. Standoff research includes the development of high efficiency extraction diodes (single stage and two-stage), improvements in beam quality (divergence, purity, uniformity, etc.), and the efficient transport and focusing of these beams over distances of several meters to a fusion target. Progress in all of these areas is discussed, as well as a strategy to reduce the divergence from the present 17 mrad for 5 MeV protons on SABRE to the required 6 mrad for 35 MeV Li ions for LMF. The status of experiments is summarized, and future directions are indicated.

Introduction

The Light Ion Fusion (LIF) program at Sandia National Laboratories (SNL) is developing light ion drivers for the long range goals of high-yield applications and energy production. The high yield applications require development of a laboratory microfusion facility (LMF) with a fusion yield of 200-1000 MJ for an input beam energy of the order of 10 MJ, on a single shot basis. Energy production requires fusion yields of the order of 200-600 MJ for an input beam energy of several MJ and a repetition rate of several Hz. Present LIF target experiments on PBFA II use a barrel diode in which the total transport length from the barrel-shaped anode to the

centrally-located target is ≤ 15 cm. Future LIF development will require standoff - the generation of extracted beams and the transport of these beams over distances of several meters from the diode to the target. In this paper, recent results and the status of research on standoff are summarized, including future development options.

Generation of Extracted Beams

Extraction diodes are required for all high yield and energy applications. Barrel diodes and extraction diodes are compared in Fig. 1. Barrel diodes are used on PBFA II and have been the foundation of the LIF program. Extraction diodes have been used on

p. 104

The ion beam microdivergence θ_μ is being examined in 3D QUICKSILVER simulations of the SABRE diode⁹. Earlier work indicated divergences in extraction diodes were typically lower than in barrel diodes. The present simulations use a geometry closer to the SABRE diode, and actual values of experimental applied B fields and driver voltages. The instability evolution¹⁰ still shows a diocotron instability (with $\theta_\mu \sim 10$ mrad) followed by a transition to the ion mode (with $\theta_\mu \gtrsim 30$ mrad).⁹ VUV and visible spectroscopy diagnostics are now used to view the SABRE A-K gap and should help lead to a detailed understanding of $\theta_\mu(t)$.¹¹

A divergence reduction strategy has been developed to reach the goal of $\theta_\mu = 6$ mrad for 35 MeV Li for LMF, which is required for all transport modes. In Table 1, a summary of

achieved and proposed divergence values is given. For each case, the accelerator, ion species, diode type, ion energy, and θ_μ are shown. Also shown is the equivalent θ_μ for LMF. This is defined by assuming the ion transverse temperature is fixed and the ion axial velocity, v_i , is increased to $\beta = v_i/c = 0.1$. This concept of divergence reduction has already been demonstrated in two-stage diode experiments on ALIAS.¹² Note that a 5 MeV proton and a 35 MeV Li ion have the same value of β . Most importantly, note that LMF equivalent values of $\theta_\mu < 9$ mrad have already been achieved on ALIAS, KALIF, PBFA II, LION, and GAMBLE II.

The last three lines in Table 1 outline our strategy for achieving 6 mrad for LMF. The first goal is to achieve 12 mrad for 5 MeV protons in a single-stage diode on SABRE. This represents a substantial improvement

Table 1. Microdivergence (θ_μ): Achieved and Proposed.

Accelerator	Ion	Diode	e_i (MeV)	θ_μ (mrad)	Status	Equivalent θ_μ (mrad) for LMF ($\beta = 0.1$; 5 MeV p or 35 MeV Li)
ALIAS	p	1-stage	<0.6	19	achieved	<6.6
ALIAS	p	2-stage	>1	10	achieved	>4.5
KALIF	p	1-stage	1.7	15	achieved	8.7
PBFA II	Li	1-stage*	9	17	achieved	8.6
SABRE	p	1-stage	5	17	achieved	17
LION	p	1-stage	1	19	achieved	8.5
GAMBLE II	p	1-stage	1	17	achieved	7.6
SABRE	p	1-stage	5	12	proposed	12
Hermes III	Li	2-stage	14	9	proposed	6
LMF	Li	2-stage	35	6	proposed	6

*barrel diode; all other cases are extraction diodes.

schemes require a channel current $I_c \sim 50$ kA. The current I_c can be from a preformed discharge (wall-confined transport), a wire (wire-guided transport), or from the net current resulting from gas breakdown (self-pinched transport).

Self-pinched transport, as shown in Fig. 3, should be particularly attractive for high yield and energy; here it is proposed to first transport the beam in the self-pinched mode in a guide tube over a sizeable distance (≥ 1 meter) to establish a propagation axis and a quasi-equilibrium radial distribution function. The aimed beam then continues directly into the chamber in the pinched mode. Self-pinched transport is attractive because it requires only small holes in the chamber wall, needs no apparatus inside the chamber, permits gas in the chamber, and allows the diode to be shielded from x-rays and debris. Self-pinched transport has not been demonstrated yet.

Both channel transport and wire-guided transport have been thoroughly demonstrated at low energy (1 MeV p) and are expected to work at LMF energies (35 MeV Li), but require some transport apparatus (low mass tubes or wires) inside the containment chamber; these schemes could be used for LMF. The achromatic lens system and self-

-pinched transport are attractive because no apparatus is required inside the containment chamber; these schemes can be used for LMF and LIBRA.

All light ion transport schemes involve ion beam interactions with neutral gas, plasma, or electrons to provide charge neutralization and some current neutralization. Present transport research is developing a thorough physics understanding of gas breakdown, which is needed for both the achromatic lens system and self-pinched transport, as well as the ballistic transport input section of all channel-like schemes. Specifically, very high current neutralization ($\geq 99.9\%$) is needed for the achromatic lens system, and moderate current neutralization ($\sim 90-98\%$) is needed for self-pinched transport.

Detailed gas breakdown experiments^{25,26} are being performed on GAMBLE II at NRL at the 10 kA proton level; the results are in good agreement with IPROP computer code²⁷ results (see following paper).²⁸ A unique result is that fast electrons can create a halo conductivity region outside the beam. IPROP treats fast electrons (> 100 eV) as particles, and is thus able to predict non-local breakdown effects.

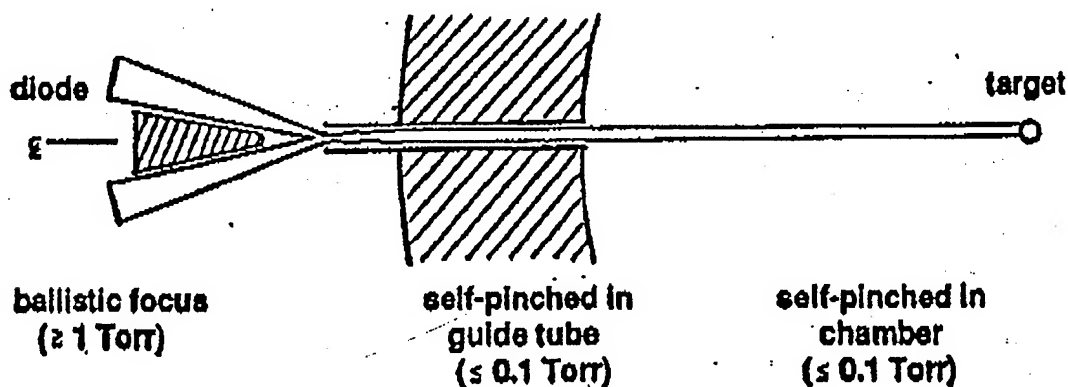


Fig. 3 Self-pinched transport for high yield and energy.

Table II. Development of pulsed power/extraction diodes/transport for high yield and energy

	ion	E_i (MeV)	I_i (kA)	τ (ns)	θ_{μ} (mrad)
<u>Present Facilities</u>					
SABRE (SNL)	p	5	75	~ 40	17
GAMBLE II (NRL)	p	1	150	~ 50	17
LION (Cornell)	p	1	150	~ 40	19
<u>Current Options at SNL</u>					
Hermes III	Li	14	400	~ 25	9
PBFA II Voltage Adder	Li	20	2,500	~ 50	9
PBFA II Extractor	Li	17	800	~ 50	12
<u>Future Directions</u>					
LMF (B module)	Li	26-35	850-1,062	40	6
ETF (B module)	Li	37	294	40	6
LIBRA-LITE	Li	25-35	313	40	4

References

*This research was supported by Martin Marietta/U.S. Dept. of Energy under contract DE-AC04-94AL85000.

1. M. E. Cuneo et al., this Conference; also see M. E. Cuneo et al., Proc. 9th Int. Pulsed Power Conf., 1993, p. 423.
2. D. L. Hanson et al., this Conference.
3. J. W. Poukey et al., this Conference.
4. R. E. Rosenthal et al., private communication (1994).
5. M. E. Cuneo, private communication (1994).
6. J. B. Greenly et al., this Conference.
7. J. M. Neri et al., this Conference.
8. J. R. Smith et al., this Conference.
9. T. D. Pointon and M. P. Desjarlais, private communication (1994).
10. S. A. Slutz et al., this Conference.
11. A. B. Filuk et al., this Conference.
12. T. R. Lockner, private communication (1993); also see M. P. Desjarlais, this Conference, and T. R. Lockner et al., this Conference.
13. C. L. Olson, J. Fusion Energy 1, 309 (1982).
14. D. Mosher et al., Proc. Eighth Int. Conf. High Power Beams (World Scientific, Singapore, 1991), p. 26.
15. P. F. Ottinger et al., Proc. IEEE 80, 1010 (1992).
16. C. L. Olson, Proc. 1988 LINAC Conf., CEBAF-89-001, p. 34 (1989).
17. P. F. Ottinger et al., J. Appl. Phys. 72, 395 (1992).
18. P. F. Ottinger et al., J. Appl. Phys. 75, 4402 (1994).

TITLE: **DEVELOPMENT OF RUTHERFORD SCATTERING
TO DIAGNOSE PROTON BEAMS FROM GAMBLE II**

AUTHOR(S): F.C. Young, D.D. Hinshelwood, W.A. Noonan, and
 S. J. Stephanakis

DATE: 7 July 1994

ABSTRACT: Rutherford scattering measurements of pulsed proton beams on Gamble II are carried out and analyzed to evaluate the usefulness of this technique as a proton-fluence diagnostic in low-pressure background gases. Scattered protons are recorded with a silicon PIN detector. The target must be thin, and a thin filter must be used on the detector to make reliable measurements. Also, the proton energy spectrum must be sufficiently well known to estimate the mean proton energy and to correct for proton energy losses in the target and in the filter on the detector.

For the "backless" pinched-beam diode, reduced proton energies are inferred from two different measurements. Proton energy losses in different thickness filters on the PIN diode are larger than expected. Also, proton flight times from the anode to the detector are longer than expected. Both of these measurements are consistent with proton energies that are smaller than expected from the measured diode voltage. Bunching of the beam pulse is observed as the flight path is increased, consistent with reduced proton energy at the head of the beam. Protons at the beam head may be reduced in energy due to electric fields induced at the head of the beam. When the beam is injected into vacuum, a burst of energetic electrons, possibly driven by such fields, is observed during the onset of the ion pulse. Time-resolved magnetic spectrometer measurements close to the ion diode are proposed to localize and possibly identify where this energy loss occurs.

THIS REPORT REPRESENTS UNPUBLISHED
INTERNAL WORKING DOCUMENTS AND SHOULD NOT
BE REFERENCED OR DISTRIBUTED

DEVELOPMENT OF RUTHERFORD SCATTERING TO DIAGNOSE PROTON BEAMS FROM GAMBLE II

I. Introduction

Measurements of elastically scattered ions can potentially provide a simple time-resolved diagnostic for intense pulsed ion-beam fluences in low pressure background gases as envisioned for light-ion ICF transport schemes. Direct measurements of ion currents with charge collecting diagnostics have failed to provide a reliable time-resolved measure of the kA/cm^2 beams in low pressure background gases (~ 1 Torr) required to current neutralize these beams for efficient transport over several meters to the pellet target.¹ Silicon PIN diode charged-particle detectors have been operated successfully in 1-Torr air, and elastic scattering provides a convenient and simple way to reduce the ion beam fluence to a level appropriate for such detectors.

The cross section for elastic scattering of MeV protons depends on the incident proton energy, the target atomic number and the angle of the scattered protons relative to the direction of the incident protons. This Rutherford scattering cross section in mb/sr may be written:

$$\sigma = 1.3 (Z/E)^2 / \sin^4(\alpha/2) \quad (1)$$

where E is the incident proton energy in MeV, Z is the atomic number of the target nucleus, and α is the laboratory scattering angle.² In the present experiments, all of the measurements are made at $\alpha = 90^\circ$. For this case, Eq. 1 becomes:

$$\sigma = 5.2 (Z/E)^2 \quad (2)$$

This cross section is appropriate for targets of sufficiently high atomic number so that the incident proton energy is well below the Coulomb barrier, and contributions from nuclear resonances are negligible. For protons on aluminum, the Coulomb barrier is ~ 4 MeV, well above the 1-MeV energies used in this experiment.

For a finite thickness target, the number of scattered protons is given by

$$N_s = n N \Delta x \sigma \Omega = 5.2 \times 10^{-27} n N \Delta x (Z/E)^2 \Omega \quad (3)$$

where n is the number of incident protons, N is the number of target nuclei/ cm^3 , Δx

is the target thickness in cm, and Ω is the solid angle of the detector in sr. If the target is sufficiently thick, it is necessary to integrate over the target thickness. Then Eq. 3 becomes:

$$N_s = 5.2 \times 10^{-27} n Z^2 \Omega \int 1/(\epsilon E^2) dE \quad (4)$$

where $\epsilon = (1/N)(dE/dx)$ is the proton stopping cross section. If the target is sufficiently thin, this integration may not be necessary. Most of the measurements in this Technote were made with thin aluminum targets (0.8- μ m thick) for which the energy loss of 1-MeV protons is only 40 keV.

In pulsed power experiments, n , E and N_s are time dependent. At each instant in time, it is assumed that there is a unique incident number of protons $n(t)$ of energy $E(t)$. Then the number of scattered protons at time t_s is given by

$$N_s(t_s) = 5.2 \times 10^{-27} n(t) Z^2 \Omega \int 1/(\epsilon E^2(t)) dE \quad (5)$$

where $t_s = t + v/l$. The time shift (v/l) is the flight time for ions of velocity v ($E = mv^2/2$) over a distance l from the location where the proton fluence is to be determined to the detector.

In these experiments a silicon PIN detector is used to measure the scattered protons. The output of this detector is proportional to the product of the number of protons incident on the detector and their energy after the protons have been scattered from the target and transmitted through a thin filter on the front of the detector. For 90° scattering by an ion of mass M_1 from a target nucleus of mass M_2 , the scattered ion energy is given by:

$$E_s = (M_2^2 - M_1^2)/(M_1 + M_2)^2 E \quad (6)$$

which reduces to $E_s = 0.93 E$ for protons on aluminum. For a thin aluminum target, the energy on the PIN diode after traversing the filter is:

$$E_d = N_s E_s (1 - f) = 0.049 (n E) \Delta x \Omega (1 - f) / E^2 \quad (7)$$

where f is the fraction of energy lost in the filter on the front of the detector. Equation 6 has been used for E_s , and Eq. 3 has been used for N_s with $Z = 13$ and

$N = 6.03 \times 10^{22}/\text{cm}^3$. The thickness of the filter on the front of the detector is varied in the experiments in this Technote in order to estimate scattered proton energies.

The time-integrated signal recorded by a PIN diode is proportional to the energy E_d and can be used to determine the total incident ion beam energy represented by $(n E)$ in Eq. 7. Charge from the PIN detector is integrated with 50Ω to record the signal in Volts. Then, the time-integrated signal in Volt-s is given by

$$S_I = \int V(t) dt = (50 \Omega / 3.62 \text{ eV}) E_d \quad (8)$$

for E_d in Joules. The denominator is the average ion energy lost per ion pair produced in silicon. The incident fluence is determined from the measured value of S_I by combining Eqs. 7 and 8. The fluence is given by:

$$F = (n E)/A = 1.48 S_I E^2 / [A \Delta x \Omega (1 - f)] \quad (9)$$

where A is the beam area exposed to the scattering foil. Knowledge of the ion energy spectrum is required to evaluate the quantities E^2 and f in Eq. 9. In this Technote, ion beam fluences determined from Eq. 9 are compared with fluences measured with calorimeters.

During February-March 1994, measurements were carried out on Gamble II to evaluate the validity and reliability of Rutherford scattering as an ion-fluence diagnostic for ion beams transported in low pressure gases. This Technote presents the results of those measurements. The experimental procedure is described in Sect. II. The results of time-integrated measurements are presented in Sect. III and time-resolved measurements in Sect IV. The implications of these results are discussed in Sect. V.

II. Experimental Procedure

An ion beam produced with the "backless" pinched-beam diode³ on Gamble II is injected through a $1.8\text{-}\mu\text{m}$ thick Kimfol into 1-Torr air. The beam is transported in 1-Torr air to scattering foils initially located at 173 cm from the anode [Fig. 1(a)] and later at 23 cm from the anode [Fig. 1(b)]. At 173 cm, the beam has expanded to fill a 50-cm diam tank, and an array of up to four scattering foils is fielded on a 5-cm radius. Each foil is exposed to the ion beam through a 1.27-cm diam aperture, as illustrated in Fig. 1(a). The foils are located 2.5 cm behind the apertures and are

mounted at 45° to the incident beam. Each foil is 2.5 cm in diameter in order to intercept all of the beam transmitted through the aperture. Silicon PIN diode detectors located at 90° to the incident beam and at 8 to 20 cm from each scattering foil (i.e., target) are used to record scattered ions. Scattered ions may be recorded either in transmission or in reflection; however, reflection must be used for thick targets. Carbon calorimeters of 2.3-cm diameter located adjacent to the target apertures are used to measure incident ion beam fluences.

When proton scattering is measured at 23 cm from the anode, the beam has not expanded much so a single target can be used to sample a majority of the ion beam, as shown in Fig. 1(b). At this distance, a 7.5-cm diam, 0.8- μm thick aluminum scattering foil is mounted at 45° to the incident proton beam direction. The incident beam on this target is restricted by a 5-cm diam aperture located 17 cm from the anode. Scattered ions are recorded by PIN diodes located at distances of 68.5, 46, or 22 cm from the target and at 90° to the incident beam direction. Measurements are made in both reflection and transmission on most shots.

Two types of PIN diodes⁴ are used in these experiments. A large-area diode (25 mm²) of 125- μm depletion depth is compared with a small-area diode (3 mm² apertured to 1-mm diam) of 35- μm depletion depth. Both detectors are expected to have subnanosecond time response, and silicon dead-layer entrance windows on these detectors are typically 0.75 μm . Initially, a 2.5- μm thick titanium filter was used on each diode to prevent exposure to visible and UV radiation. The energy loss of 1-MeV protons in this filter is 160 keV. Later, aluminum filters of 0.8, 1.8, 4.0 or 7.0- μm thickness were used. For most of the measurements in this Technote, a 0.8- μm aluminum filter is used. The energy loss of 1-MeV protons in this filter is only 40 keV.

Measurements with these two PIN diodes on Shots 5938 and 5940 are compared in Fig. 2. The diode voltage V_d and the ion current I_i are also presented for these two shots. To compare the PIN diodes, the sensitivity of the large-area diode is reduced with a 1-mm diam pinhole for comparison with the small-area diode. For the measurement in Fig. 2(a), this pinhole is located close to the PIN diode so that only the central portion of the sensitive area of the diode is exposed to scattered ions. In this case, the signal exhibits a long tail relative to the signal from the small-area diode. This behaviour is attributed to local space-charge buildup in the PIN diode which reduces the electric field and increases the charge-collection time. Relocating the pinhole to expose the full sensitive area of the detector to scattered ions gives the result in Fig. 2(b). Now the full electric field is restored and

rapid charge collection is observed. In this case, signals of similar shape are recorded by both detectors. The signal from the large-area detector in Fig. 2(b) is delayed because this detector is now 10 cm farther from the target. It is also noted in Fig. 2 that the larger-volume detector is more sensitive to diode bremsstrahlung. For another shot where both detectors view the same 0.8- μm aluminum target, one in transmission and one in reflection, the ratio of the time-integrated signals agrees with the ratio of the detector solid angles to within 5%. Reliable time-resolved measurements can be made with either detector; however, the large-area detector must be properly apertured. Small-area PIN diodes are used for the remaining measurements in this report because multiple detectors could be fielded easily on a single shot; signals of several volts are obtained even with thin aluminum targets; and the bremsstrahlung contribution is minimized even when the detectors are located close to the ion diode. Operating both PIN diodes in 1-Torr air has produced some failures. Fielding four diodes per shot for 17 shots resulted in three diodes with unacceptably large leakage current ($> 30 \mu\text{A}$).

The variations of scattered-ion intensity with target atomic number and with different thickness targets in Fig. 2 give an indication of some of the difficulties encountered with this diagnostic. All of the measurements in Fig. 2 are made with 2.5- μm titanium filters on the PIN diodes. When an aluminum target is used instead of gold, the small-area-diode scattered-ion signal decreases by a factor of ten. However, a reduction of forty is expected based on the Z -dependence of the Rutherford scattering cross section. When the aluminum target thickness is reduced from a thick target (i.e., thickness greater than the proton range) to 0.8 μm , the scattered-ion intensity decreases by a factor of four. This decrease is less than expected from the linear dependence on target thickness in Eq. 7. Interpreting these scattered-ion measurements is complicated by ion energy losses in the target and in the filter on the detector. These issues are addressed in the following experiments.

III. Time-Integrated Measurements.

A. Scaling with Target Thickness

The dependence of the scattered-ion intensity on the thickness of the target is determined on a single shot by using an array of four PIN diodes to record scattered ions from aluminum targets of 0.8-, 1.8-, 4.0-, and 7.0- μm thickness. The results are presented in Fig. 3. The relative sensitivity of each detector was measured on a

separate shot with all four detectors viewing 2.5- μm thick titanium targets. The standard deviation for the average of these four measurements is $\pm 9\%$. This uncertainty is assigned to the measurements in Fig. 3. The curve is a fit to the data points.

The scaling of scattered-ion intensity with target thickness in this figure is consistent with expectations. For thin targets with little energy loss in the target or in the filter on the detector, the PIN signal increases linearly with target thickness up to 1.8 μm . This is the expected behavior according to Eq. 7. For thicker targets, ions scattered deeper in the target emerge with reduced energy and lose a significant fraction of their energy in the filter on the PIN diode. The PIN signal ceases to increase when all the ions are completely stopped by the filter corresponding to $f = 1$ in Eq. 7. This saturation of the scattered ion intensity for thicker targets is observed in Fig. 3. The level of this saturation depends on the ion energy spectrum. Saturation will occur at smaller target thickness as the energy spectrum is softened. Thin targets should be used to minimize the sensitivity of the scattered-proton intensity to the ion energy spectrum. In the remainder of this Technote, 0.8- μm thick aluminum targets are used because this thin foil is readily available in our laboratory and is easily mounted on the target holders used in this experiment. Even thinner targets of higher atomic number materials could be used to reduce the spectral sensitivity and increase the scattered intensity, but these foils would be more fragile and are more expensive.

B. Comparison of Scattered-Ion and Calorimeter Fluences

Time-integrated scattered-ion intensities are combined with the 1.27- cm^2 area aperture in front of each scattering foil to determine the ion beam fluence according to Eq. 9. The ion energy spectrum determined from the measured diode voltage and ion current at the Kimfol are used to evaluate the quantities f and E in Eq. 9. The diode voltage is corrected for proton energy loss in the 1.8- μm thick Kimfol, in the aluminum target, and in 1-Torr air between the Kimfol and the PIN diode. Then, this energy spectrum is used to determine the fraction of energy lost by protons in the 0.8- μm aluminum filter and the 0.75- μm silicon dead-layer on the front of the PIN diode. The fraction f is given by the ratio of the total energies in these two spectra. The power-weighted mean energy of the spectrum after transmission through the filters is used for the energy E in Eq. 9. The power-weighted mean is

used because the PIN detector output is proportional to the product of the number of scattered ions N_s and their energy E_s as indicated in Eq. 7.

The fluence determined in this way is compared with the fluence from nearby calorimeters in Fig. 4. Fluence variations in this figure are a combination of shot-to-shot variations and positioning the detectors at different radial locations. An uncertainty of $\pm 5\%$ is assigned to the calorimeter fluence based on variations observed on a few shots between two calorimeters at the same radius. An uncertainty of $\pm 10\%$ is assigned to the scattered-ion fluence primarily due to using a spectrally averaged energy in Eq. 9. A more accurate analysis using time-resolved current and voltage waveforms, as indicated by Eq. 5, is not merited. The reason will become clear in Sect. III.C. The scattered-ion fluence in Fig. 4 scales linearly with the calorimeter fluence as indicated by the solid-line fit to the data. However, the scattered-ion fluence is 11% larger than the calorimeter fluence. The dashed line is the expected result for identical fluences. This discrepancy is probably associated with using an incorrect energy spectrum. For the shots in Fig. 3, the power-weighted mean energies range from 0.95 to 1.16 MeV, and the fraction f ranges from 0.22 to 0.27 for the 0.8- μm aluminum filter except, for the lowest-fluence data point where $f = 0.5$. For this point, the output switch on Gamble II was tracked; and the mean energy is only 0.56 MeV.

A few measurements with thicker filters are also presented in Fig. 4. For a 1.8- μm aluminum filter, scattered-ion fluences determined from Eq. 9 are also consistent with the calorimeter fluences. For this filter, $f \approx 0.3$ and the mean proton energy is reduced by only $\approx 10\%$. For the 0.8- and 1.8- μm aluminum filters, the mean proton energy is reduced relatively little by the filter. For a 2.5- μm titanium filter, the scattered-ion fluences in Fig. 3 are only two-thirds to one-half of the calorimeter fluences. For this filter, $f \approx 0.4$ and the mean proton energy after transmission through this filter is reduced by 25%. For a modestly softer energy spectrum, this fraction will increase dramatically and may account for the discrepancy between the fluences in Fig. 3 with this filter. Measurements in the next section indicate that the spectrum is softer than expected from the ion-diode voltage and current.

Scattered-proton measurements at 23 cm from the anode can be used to measure large fluences close to the diode where calorimeter measurements are complicated by material ablation and rapid variation of the radial distribution of the ion beam. Calibration of the scattered-ion intensity in terms of the calorimeter fluence at 173 cm from the diode is used to determine the fluence at 23 cm from the diode. The same thickness aluminum target and PIN diode filter are used at both distances.

Corrections are made for different-area targets and different detector solid angles. With the target 23 cm from the anode, the area of the target viewed by the detector is restricted to a diameter of 4.8 cm by the extension tube in which the PIN diode is mounted.[see Fig. 1(b)] Then, the average on-axis fluence over a 4.8-cm diam area measured for three shots is $48 \pm 2 \text{ cal/cm}^2$. For comparison, measurements at 35 cm from the anode with a calorimeter mounted on a salt shaker to attenuate the beam intensity give an average on-axis fluence for three shots of $47 \pm 4 \text{ cal/cm}^2$ over a 1.8-cm diam area.⁵ These results are consistent with each other if account is taken of the different areas and axial positions of the measurements. Near the diode, the radial distribution of the beam is strongly peaked on axis with a radial width which decreases as the distance from the anode is reduced.⁶ Consequently, the fluence over a small area at 35 cm from the diode can be comparable to the fluence over a larger area at 23 cm from the diode.

C. Spectral Comparisons

Proton energy spectra determined from Gamble II diode voltage and current measurements are compared with spectral measurements of scattered ions. Ion energies transmitted through aluminum filters of 0.8-, 1.8-, 4.0- and 7.0- μm thickness are measured on a single shot with an array of four PIN diodes. The 0.8- μm aluminum targets are located 173 cm from the anode. Measured transmissions are compared with calculated energies using proton energy spectra given by the measured ion-diode voltage and current. These energy spectra are corrected for proton energy losses in four different materials: (1) the 1.8- μm thick Kimfol, (2) the 0.8- μm thick aluminum target, (3) the 1-Torr air between the Kimfol and the PIN diode, and (4) the 0.75- μm silicon dead-layer and different thickness aluminum filters on the PIN diodes. The integral of each energy spectrum should be proportional to the energy absorbed by each PIN diode. This absorbed energy in kJ is not corrected for the beam fraction on target or for the fraction scattered into the detector.

Time-integrated PIN diode signals, normalized to the calculated energy absorbed in each detector, are presented in Fig. 5 as a function of aluminum filter thickness. Results for four shots are displayed along with linear fits to the data. For Shots 5945 and 5946, each detector views a different aluminum target. For Shot 5945, the measurement with a 4- μm aluminum filter is a lower limit because the recording instrument saturated. For Shots 5949 and 5951, all four detectors view

the same target. In addition, for Shot 5951, an additional 0.8- μm aluminum target is located 23 cm from the anode, and protons are transmitted through this foil to the target at 173 cm. Energy loss in this target is also included in calculating the absorbed energies for this shot. For all four shots, the normalized PIN intensities decrease with increasing filter thickness more rapidly than expected from the ion-diode voltage and current. If the proton energy spectrum were given by the ion-diode voltage and current, these normalized intensities should remain constant as the filter thickness is increased. The decrease with increasing filter thickness indicates that the energy spectrum is softer than expected. For Shot 5951, the measurements are nearly constant within a $\pm 20\%$ variation. The presence of the target at 23 cm may account for the nearly constant ratio on this shot, but no physical reason for this behavior is known at this time.

IV. Time-Resolved Measurements

A. Measurements at 173 cm from the Anode

Scattered-ion signals with the target located 173 cm from anode consistently start later in time and are of shorter duration than expected from measured diode voltages and currents. This situation is illustrated in Fig. 6 where the scattered-ion signal is compared with the ion power transported to the detector using the ion voltage V_i and ion current I_i measured at the diode. This voltage has been corrected for proton energy loss in the 1.8- μm Kimfol and in the 0.8- μm aluminum target at 23 cm from the anode. The transported power is the product $V_i \times I_i$ time-of-flight shifted to the detector location with the velocity at each instant in time determined from the proton energy. The scattered-ion signal is compared with transported power because the PIN diode signal is proportional to the product of the number and energy of the scattered ions. The transported power does not include the energy dependence of the Rutherford cross section, as given in Eq. 7, which tends to increase the relative contribution of lower energy ions late in time, and does not correct for energy losses in the filter on the detector which tends to decrease their contribution. However, this calculation can be independently checked at discrete times as shown in Fig 6. The time of arrival of transported power is indicated in Fig. 6 for voltages at two different instants corresponding to 1.2 and 1.4 MV on the rising portion of the voltage pulse. The transported power at these instants precedes the measured scattered-ion signal by about 30 ns. Also, the duration of the

transported power is substantially longer than the duration of the measured signal. The transported power does not include time-of-flight corrections for energy losses in 1-Torr air or in the aluminum target at 173 cm. These corrections are negligible. For example, if all the proton energy loss in 1-Torr air occurs at the beginning of the flight path, the additional time delay of 1-MeV protons is only 2 ns. After scattering from the aluminum target, the proton flight path to the detector is only 8 cm compared with a flight path of 172 cm from the Kimfol to the target. Consequently, for 1-MeV protons the energy loss due to scattering adds only 0.3 ns to the flight time.

Could the short ion-pulse duration at 173 cm simply result from sweeping the ion beam across the small area of the scattered-ion detector as the beam undergoes focusing and defocusing during the diode discharge? To address this issue, four identical scattered-ion detectors were located 173 cm from the anode at radii of 5.1, 10.2, 15.2 and 20.3 cm on a single shot. If the beam is sweeping, variations in the start time and duration of these scattered-ion signals is expected. No significant differences in pulse duration or start time are observed. All four detectors have similar pulse shapes with a FWHM of 15 ± 1 ns. The start times are the same within ± 1 ns for the detectors at 5-, 10-, and 15-cm radius, while the detector at 20 cm starts only 5 ns later. No evidence for radial sweeping of the beam to account for the short pulse duration is observed. This result is consistent with the beam microdivergence and beam expansion after focusing expected for the "backless" diode.⁷

The radial distribution of the scattered ion intensity can be compared with the fluence determined from nearby calorimeters. Scattered-ion intensities, normalized to calorimeter fluence, are presented in Fig. 7 along with the radial distribution measured with the calorimeters. An uncertainty of $\pm 5\%$ is assigned to the calorimeter fluences and $\pm 9\%$ to the integrated PIN diode intensities. The calorimeter fluence decreases by about a factor of two as the radius increases from 5 to 20 cm. These two distributions are in good agreement except at large radius where the ratio of the scattered-ion signal to the calorimeter fluence is 50% larger. This increase in scattered-ion signal at 20 cm may be attributed to a small fraction of ions scattering from the edge of the brass target holder. For these measurements, the targets were not repositioned to correct for a small transverse displacement of the beam in traveling 2.5 cm from the aperture to the target. At 20-cm radius, this displacement is sufficient to move a very small portion of the beam onto the edge of the target holder. The thick brass holder can produce a substantial scattered-ion

signal. For the detectors at smaller radii, this displacement is less and no beam hits the target holder.

B. Measurements at 23 cm from the Anode

In an effort to sample a larger fraction of the ion beam and to reduce uncertainties due to ion time-of-flight, measurements were carried out with the target at 23 cm from the anode. This is as close as the target could be located to the anode with the PIN diodes mounted on extension tubes at 90° to the incident beam direction. The distance of the PIN diodes from the target was increased to avoid saturating the detectors. Results of measurements at three different distances are presented in Fig. 8 along with a measurement with the target at 173 cm from the anode. As the ion flight path is decreased, the duration of the scattered-ion pulse increases from 13 to 44 ns. This behavior of the pulse duration with distance is suggestive of beam bunching due to an ion voltage which ramps up during the pulse.

The timing of the scattered-ion signals is still not consistent with the ion voltage and current. The scattered-ion signal for a 91.5-cm total ion flight path is compared with the transported ion power in Fig. 9. The measured signal starts later in time and is shorter in duration than expected from the measured voltage and current. The time of arrival of transported power is indicated at two instants corresponding to 1.2 and 1.4 MV on the rise of the voltage pulse. In this case, the transported power precedes the scattered-ion signal by about 20 ns. This time difference is less than the 30-ns time difference obtained with a 181-cm total flight path. The scaling of this time difference with distance is consistent with ions propagating from the diode at a lower velocity than expected from the ion voltage so that the time difference simply increases as the distance from the diode increases.

C. Beam Injection through Kimfol into Vacuum.

It is clear from the previous results that the proton energy spectrum is softer than expected from the diode voltage. The reason for this energy reduction is not known. Three shots were taken without 1-Torr air behind the Kimfol to examine the dependence of the ion energy on the ion-beam-neutralization conditions. Without a background gas, the ion beam can still be charge and current neutralized by drawing electrons from the plasma created by beam ionization of the Kimfol. However, ionization of the background gas by the front of the ion beam to provide a source of

electrons for neutralization is not possible if the gas is removed. The vacuum behind the Kimfol was 3.5 to 7.0×10^{-4} Torr. Scattered-ion measurements were made with the target at 23 cm from the anode for three different ion flight paths.

The results of spectral measurements with vacuum behind the Kimfol are similar to the results with 1-Torr air. Measurements of spectral hardness determined with different thickness aluminum filters on the PIN diodes are presented in Fig. 10. Time-integrated PIN diode signals, normalized to the calculated energy absorbed in each detector, are presented as a function of aluminum filter thickness. In this figure, the vacuum measurements are compared with similar measurements with 1-Torr air behind the Kimfol. Initially, only two detectors were used; one in reflection and one in transmission, with ion flight paths of 69 cm. Later four detectors were used in transmission with a flight path of 45 cm. The vacuum measurement for the 7.0- μ m aluminum filter was lost because the leakage current on this PIN diode was too large. The results in Fig. 10 are similar to the results in Fig. 5. With or without 1-Torr air, the normalized scattered-ion intensities tend to decrease as the filter thickness is increased indicating that the spectrum is softer than expected.

The temporal behavior of the scattered-ion signals with vacuum behind the Kimfol is also similar to the results with 1-Torr air behind the Kimfol. Scattered-ion signals in vacuum are presented in Fig. 11 for three different flight paths. These measurements are similar to the measurements in Fig. 8 for 1-Torr air. Again, the duration of the scattered-ion pulse decreases as the flight path increases, suggestive of ion-beam bunching. These scattered-ion signals are also delayed relative to the transported power calculated from measured ion-voltage and current traces. No significant differences in the scattered-ion signals are observed with 1-Torr air or with vacuum behind the Kimfol.

With vacuum behind the Kimfol, an intense burst of fast electrons is recorded by the PIN diodes when the ion beam is injected through the Kimfol. The peak near 60 ns in Fig. 11 is attributed to fast electrons. This peak is not observed if a permanent magnet is located between the target and the diode to deflect electrons away from the detector. For example, the signals in Fig. 11 for 45- and 69-cm flight paths were obtained on the same shot in transmission and in reflection respectively, but a magnet was used to remove fast electrons on the 69-cm detector. The remaining foot on this signal arises from diode bremsstrahlung. The relative transmission of these electrons through 0.8- and 4.0- μ m aluminum filters indicates that these electrons have energies of 20 to 40 keV. These electrons may be

associated with the injection of the ion beam through the Kimfol because the onset of this signal is about 20 ns after the start of the ion current as measured by the ion-current monitor at the Kimfol and lasts for no more than 20 ns. These electrons are not observed with 1-Torr air behind the Kimfol.

The timing of this burst of electrons suggests that these electrons originate at the Kimfol and are accelerated toward the aluminum target by space charge developed at the front of the ion beam in the vacuum between the Kimfol and the target. After correcting for the 10-ns electron flight time from the Kimfol to the detector at 91.5 cm, the onset of the electron burst at the Kimfol occurs only 10 ns after the start of the ion current. Also, the duration of the electron burst is comparable to the ion flight time from the Kimfol to the target (16 ns for 1-MeV protons). Once electrical conductivity between the Kimfol and the target is established through the charge and current neutralized ion beam, this space charge can be dissipated and the fast electrons disappear.

V. Summary and Discussion

Time-integrated measurements of scattered-ion intensities suggest that this diagnostic can be used as a reliable proton-fluence diagnostic in low-pressure background gases only if a thin filter on the detector and a thin target are used. In addition, the proton energy spectrum must be sufficiently well known to estimate the mean proton energy and to correct for proton energy losses in the filter on the detector and in the target. Measurements with different thickness filters indicate that the proton energy spectrum from the "backless" pinched-beam diode on Gamble II is softer than expected from ion voltage and current measurements. This is a real problem! Time-resolved measurements of scattered ions are also not consistent with the temporal profile expected from the ion voltage and current. The scattered ions consistently arrive at the detector later than expected. Also, bunching of the beam as the ions travel away from the diode is inconsistent with the ion-voltage waveform.

Beam bunching is observed for measurements with either 1-Torr air or vacuum behind the Kimfol. Values of the full-width at half-maximum (FWHM) for the scattered-ion signals in Figs. 8 and 11 are summarized in Fig. 12. The FWHM are assigned uncertainties of $\pm 10\%$. The FWHM decrease from about 50 ns at 45 cm from the diode to less than 15 ns at 181 cm. The FWHM near the diode should be

about 60 ns based on the ion voltage and current at the diode. The measurements in Fig. 12 approach this value.

A variety of diagnostics have been used in the past to evaluate ion energies from the pinch reflex diode (PRD) on Gamble II in different experiments. Results from four different diagnostics are summarized in Table I. Stacked-foil activations with the $^{12}\text{C}(p,\gamma)^{13}\text{N}$ reaction have been used in beam transport experiments with a collimated beam and in thermostructural response (TSR) testing with uncollimated beams. At the low ion currents used for TSR testing the energy spectrum is consistent with diode electrical measurements.⁸ However, for the higher currents used in transport experiments, the mean energy is about 10% less than expected, and the highest portion of the spectrum is downshifted by 200 to 300 keV.⁹ Measurements with $d(d,n)$ neutron time-of-flight in the same experiment indicate a 400-keV downshift in energy by the time the beam travels 2.4 meters.¹ With the target located at the Kimfol position, a 25% reduction in ion energy has also been observed using $d(d,n)$ neutron time-of-flight.¹⁰ Prompt γ -rays from the $^{19}\text{F}(p,\alpha\gamma)^{16}\text{O}$ reaction have been used to measure proton energies in z-discharge transport experiments. Two Teflon targets, separated by one meter in the transport channel, are used. Energy losses of 100 to 400 keV are deduced from experiments¹¹ with the PRD, while no losses are reported in similar experiments⁷ with the "backless" or modified PRD. It is of interest to note that energy losses are observed with the modified PRD only using the scattered-ion diagnostic. Perhaps the energy losses are less severe with the modified PRD and are only apparent with the time resolution of this diagnostic.

Where do these energy losses occur? Most of the diagnostics in Table I are fielded at 1 to 2 meters from the diode in order to reduce the ion beam intensity on target or to provide a measurable ion flight time. In this case, it is difficult to pin down the region of energy loss. Note, however, that measurement #4 in Table I indicates energy loss in the diode. The scattered-ion measurements are made closer to the diode than most of the other measurements in Table I, and they are time resolved. Consequently, these measurements can be used to evaluate the onset of ion emission at the diode and possibly to localize the energy loss.

Two different analyses of the scattered-ion measurements are made to assess the onset of ion emission from the diode. First, the scaling of ion flight time with distance from the diode is extrapolated to small distance. In Fig. 13, measured ion flight times are presented for four different total flight paths from the anode to the PIN detector. The flight time is measured from the start of the voltage pulse to the

Table I

Summary of Ion Energy Measurements for Pinch-Reflex Diodes on Gamble II.

#	Diagnostic (anode-to-target distance)	Diode	Transport Geometry	Ion Current at Peak Power (kA)	Comparison with Ion Voltage and Current
1.	Stacked-Foil Activation (2.2 m)	PRD	Collimated Beam	400	Highest energy ions are downshifted 200 to 300 keV.
2.	Stacked-Foil Activation (2.2 m)	Backless PRD	No collimation	60	No measurable energy loss ($<10\%$).
3.	Neutron Time- of-Flight (0.46, 2.4 m)	PRD	Collimated Beam	400	Highest energy ions lose 400 keV in 2.4 meters.
4.	Neutron Time- of-Flight (0.01 m)	PRD	CD ₂ Target at Kimfol	250	25% energy loss for highest energy ions.
5.	Prompt γ -Rays (0.3, 1.3 m)	PRD	Z-discharge Channel	500	Highest energy ions lose 100 to 400 keV.
6.	Prompt γ -Rays (1.5 m)	Backless PRD	Z-discharge Channel	400	Reasonable agreement.
7.	Scattered Ions (0.23, 1.73 m)	Backless PRD	No Collimation	400	Spectrum is softer and beam bunches.

start of the scattered-ion signal. The precision of these measurements is ± 3 ns. The scatter of the measurements for each flight path represents shot-to-shot variations. A linear fit to these measurements corresponds to an average proton energy of 0.90 ± 0.08 MeV, and extrapolation of this fit to zero distance indicates a start time of 32 ± 5 ns. This start time is consistent with the timing of the ion-current relative to the voltage for this diode (see Figs. 2 and 6). Second, to avoid uncertainties due to shot-to-shot variations, simultaneous scattered-ion measurements with targets at 22 and 171 cm from the Kimfol are extrapolated to the Kimfol location where the ion current is measured. These measurements are presented in Fig. 14 along with the ion voltage and current. The average proton energy, determined from the time interval between the onset of these two scattered-ion signals, is 0.92 MeV. The time shift of these signals to correct for ion flight time from the Kimfol to the PIN diodes is indicated in Fig. 14. This shift suggests that these ions leave the diode 37 ns after the start of the voltage. At this time, the ion current has increased to 150 kA and the ion voltage is 1.3 MV. Apparently, these ions leave the diode with less energy than expected from this voltage. Both analyses are consistent with ions at the leading edge of the scattered-ion signal originating 30 to 40 ns after the start of the voltage, but with less kinetic energy than expected from the voltage at that time.

Several possibilities are contemplated to explain the apparent reduced ion energies in these experiments. The simplest explanation is that the diode voltage is incorrect. Periodic calibrations of the capacitive voltage monitor on Gamble II indicate that this monitor is reproducible to within $\pm 1\%$.¹² However, substantial inductive corrections are made to the voltage measured with this monitor in order to determine the voltage across the anode-cathode gap where the ions are generated. This magnitude of this correction is up to a factor-of-two during the voltage risetime and decreases to 30% at the peak of the corrected voltage. This inductively corrected voltage has been compared with a direct measurement of the voltage across the anode-cathode gap obtained with an inductive voltmeter. The shapes of these two voltages are similar, however, the maximum voltage from the inductive voltmeter is 20% less than the inductively corrected voltage and is in agreement with the results of neutron time-of-flight measurements (# 4 in Table I).¹⁰ No explanation has been presented to account for this difference between these two voltages.

It has been suggested that ions from the PRD may be reduced in energy due to processes in the anode plasma where the ions are born.¹³ Charge exchange

collisions in the anode plasma may generate a distribution of ions with lower energies.¹⁴ Also, a radial resistive voltage drop across the anode may produce lower energy ions. Evidence for these effects was not observed in previous experiments.¹³

Once the beam leaves the diode and passes through the Kimfol, it is speculated that a portion of the beam may be slowed by electric fields induced at the head of the beam.¹ This process was used to account for the energy loss indicated in #3 of Table I. The presence of strong fields at the head of the beam is also implied by the energetic electron observations reported in Sect. IV.C. Modification of the ion energy by fields at the front of the beam is expected to produce a ramped-up voltage that can account for beam bunching. Calculations with a ramped voltage profile are presented in Fig. 15 to demonstrate how such a voltage pulse may account for the narrow scattered-ion signals observed in these experiments. For this calculation, the voltage from Shot 5951 (Fig. 6) was modified by replacing the voltage rise with a linear ramp. This modification was easily implemented with the software used to analyze data from Gamble II. The ion voltage V_{ramp} and ion current I_i in Fig. 15 are used to calculate the transported ion powers in this figure for comparison with experiment. The transported ion powers have been normalized to the peaks of the measured signals for this comparison. Start times for the measured signals and the transported powers are in agreement for targets at 23 and 173 cm from the anode. Also, the widths of the transported powers are much closer to the measurements than the widths of transported powers calculated using measured ion voltages (see Figs. 6 and 9). Clearly, bunching of the ion beam, similar to the observed bunching, can be produced with a ramped ion voltage.

No explanation has been identified to account for such a voltage in these experiments. The voltage V_{ramp} in Fig. 15 is just an artificial modification to indicate what kind of change in voltage is required to account for the observed beam bunching. However, it may be possible to determine the time-resolved ion energy pulse at the diode with time-resolved magnetic-spectrometer measurements.¹⁵ The magnetic spectrometer can be used to select specific scattered-ion energies and to measure time-resolved ion intensities at those energies. These measurements should be made as close to the diode as feasible in order to minimize uncertainties arising from unknown energy losses during flight from the diode to the spectrometer. If these signals can be accurately time shifted to the diode, then the ion energy can be determined as a function of time during the period that ions are emitted from the diode.

REFERENCES

1. F.C. Young, *et al.*, Phys. Plasmas 1, 1700 (1994).
2. J.B. Marion and F.C. Young, *Nuclear Reaction Analysis* (North Holland, Amsterdam, 1968) p. 154.
3. S.J. Stephanakis, J.R. Boller, G. Cooperstein, B.V. Weber and F.C. Young, in *Proceedings of the Ninth International Conference on High-power Particle Beams*, edited by D. Mosher and G. Cooperstein (National Technical Information Service Document No PB92-206168) Copies may be ordered from National Technical Information Service, Springfield, VA 22161.
4. Available from Quantrad Sensors, 2360 Owens St. Santa Clara, CA 95054.
5. S.J. Stephanakis, private communication.
6. S.H. Richter, L.M. Lee, D.V. Keller, D. Mosher, S.J. Stephanakis and F.C. Young, J. Rad. Effects 9, 252 (1990).
7. J.M. Neri, *et al.*, Phys. Fluids B 5, 176 (1993).
8. D. Mosher, *et al.*, Thermostructural Response Testing with Ion Beams, Proceedings of the 11th Hardened Electronics and Radiation Technology (HEART) Conference, Orlando, FL, February, 1993.
9. F.C. Young, *et al.*, Phys. Rev. Lett. 70, 2573 (1993).
10. F.C. Young, S.J. Stephanakis, J.R. Boller and S.A. Goldstein, 1993 IEEE International Conference on Plasma Science, IEEE Cat. No. 83Ch1847-3, p. 33.
11. F.C. Young, *et al.*, Analysis of Proton Transport Experiments, NRL Memorandum Report 4322, September, 1980.
12. J.R. Boller, private communication.
13. F.C. Young, S.J. Stephanakis and S.A. Goldstein, Bull. Am. Phys. Soc. 27, 1121 (1982).
14. D.S. Prono, H. Ishizuka, E.P. Lee, B.W. Stallard, and W.C. Turner, J. Appl. Phys. 52, 3004 (1981).
15. W.A. Noonan, F.C. Young, and E.P. Donovan, Rev. Sci. Instrum. (accepted for publication).

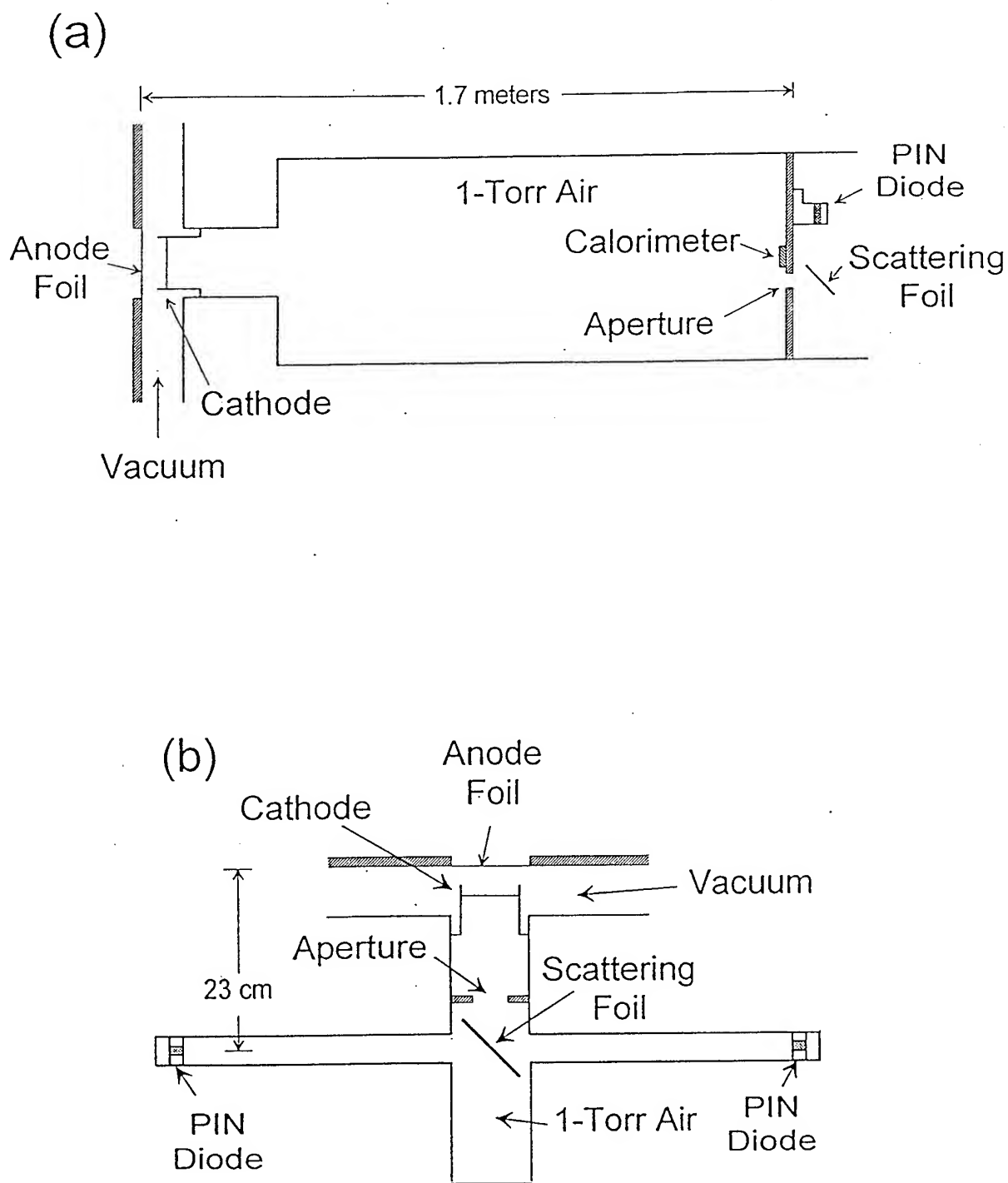


Fig. 1 Experimental arrangement for scattered-ion measurements with the target located (a) at 173 cm from the anode and (b) at 23 cm from the anode.

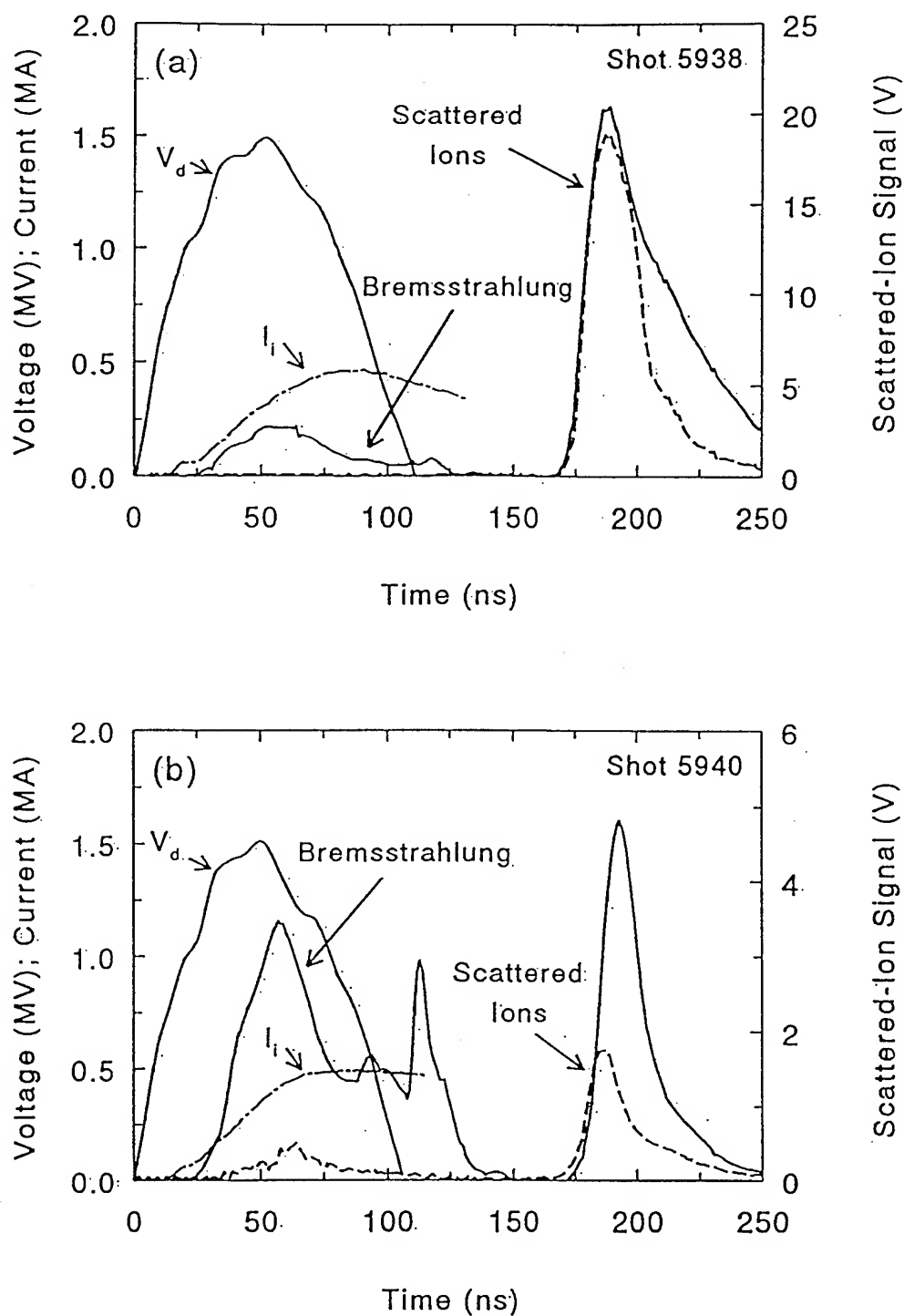


Fig. 2. Scattered-ion signals for the large-area PIN diode (solid line) and for the small-area PIN diode (dashed line) for (a) Shot 5938 and (b) Shot 5940. The diode voltage V_d and ion current I_i for each shot are also shown. In (a), the targets are thick tantalum (large-area diode) and thick gold (small-area diode). In (b), the targets are 0.8- μm aluminum (large-area diode) and thick aluminum (small-area diode).

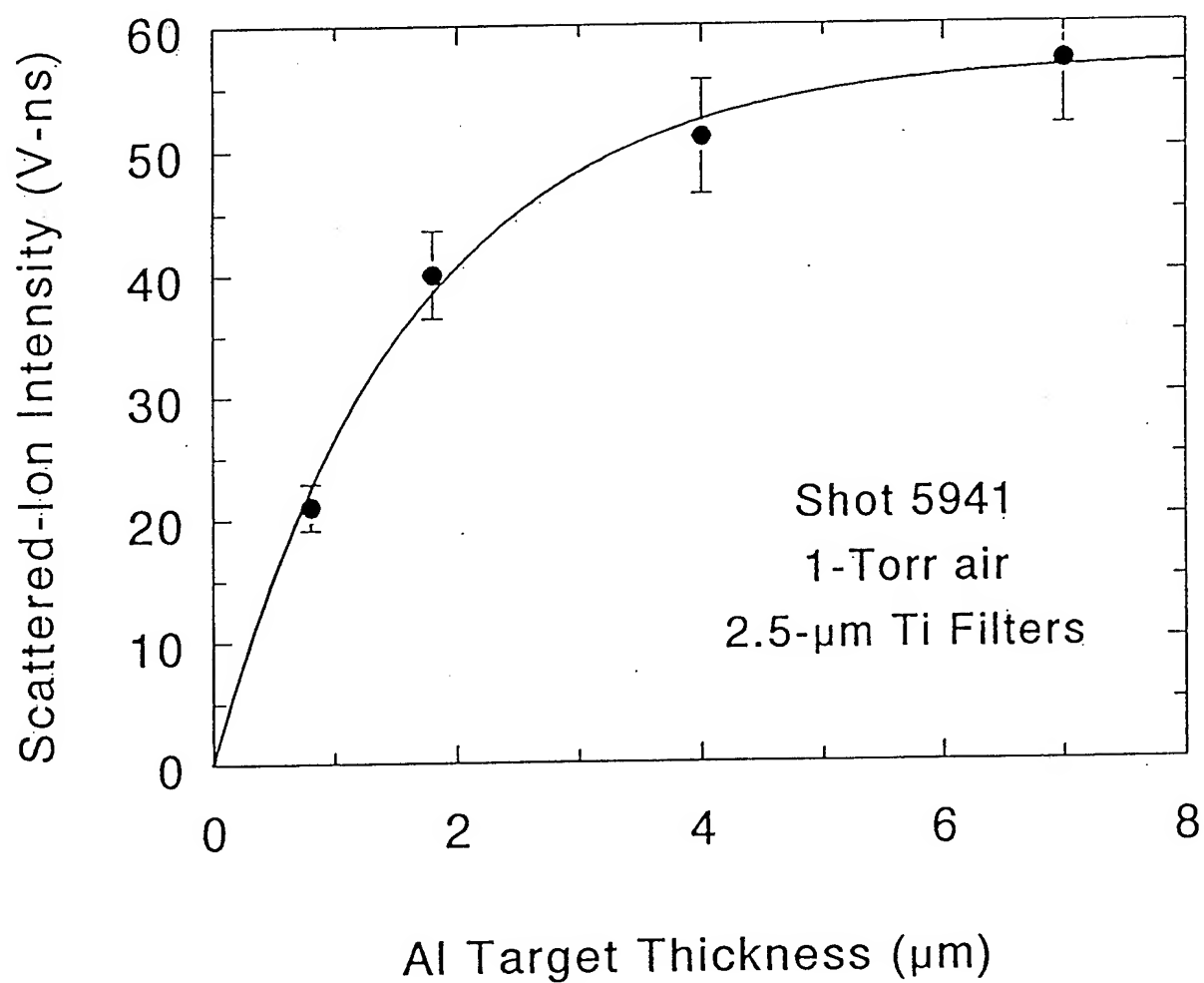


Fig. 3. Measurements of the time-integrated scattered-ion intensity as a function of aluminum target thickness.

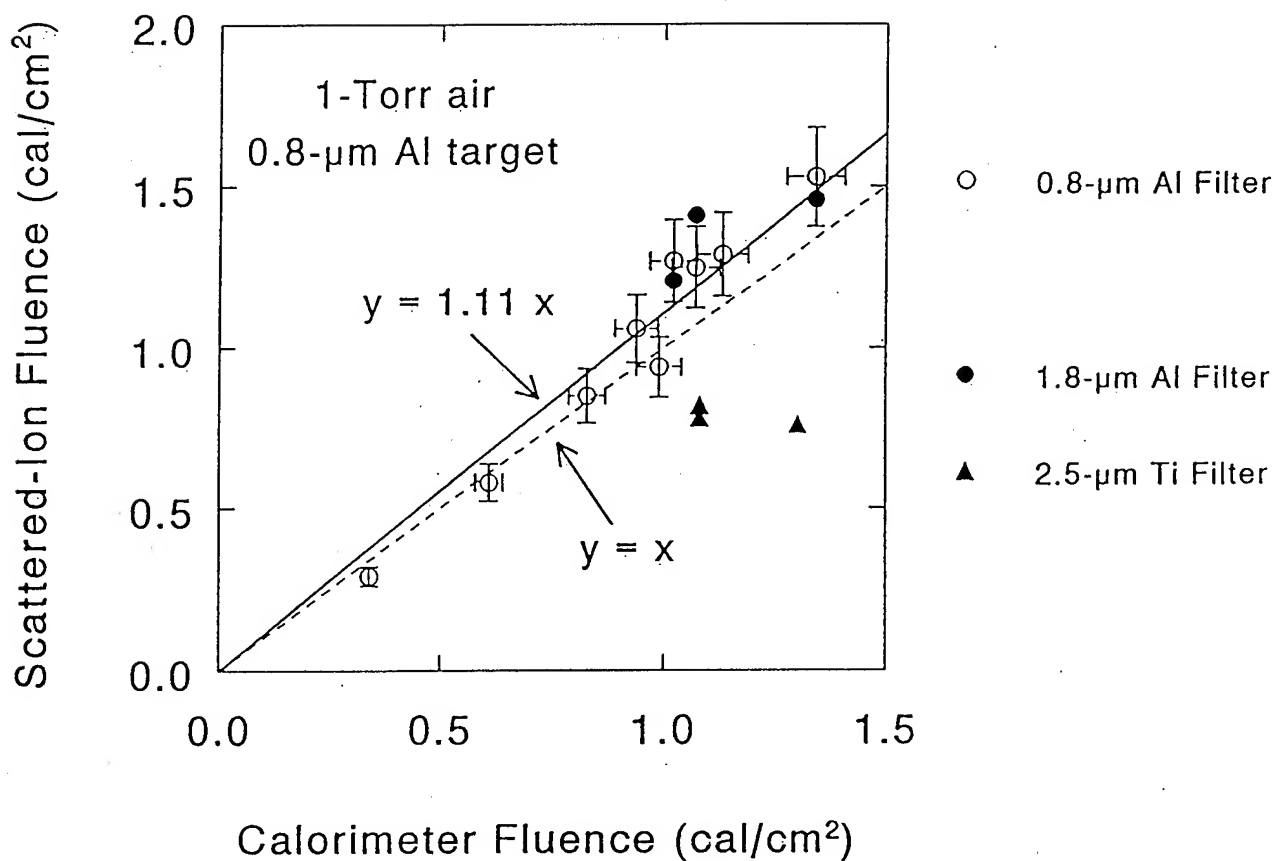


Fig. 4. Comparisons of the scattered-ion fluence with the fluence determined from calorimeters. The solid line is a linear fit to the data for a 0.8- μm aluminum filter on the PIN diode. The dashed line is for identical scattered-ion and calorimeter fluences.

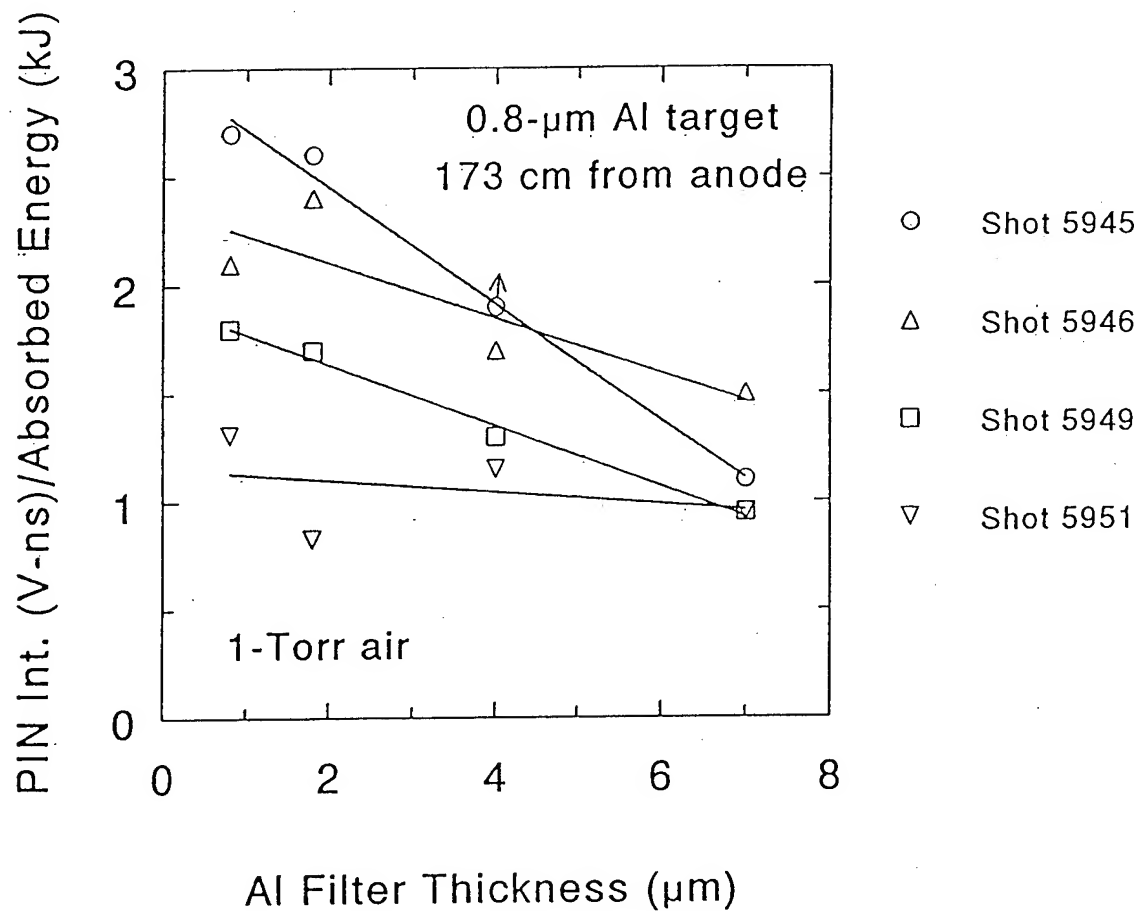


Fig. 5. Scattered-ion intensities as a function of filter thickness on each PIN diode. The intensities are normalized to calculated energies absorbed by each PIN diode based on ion-voltage and current measurements.

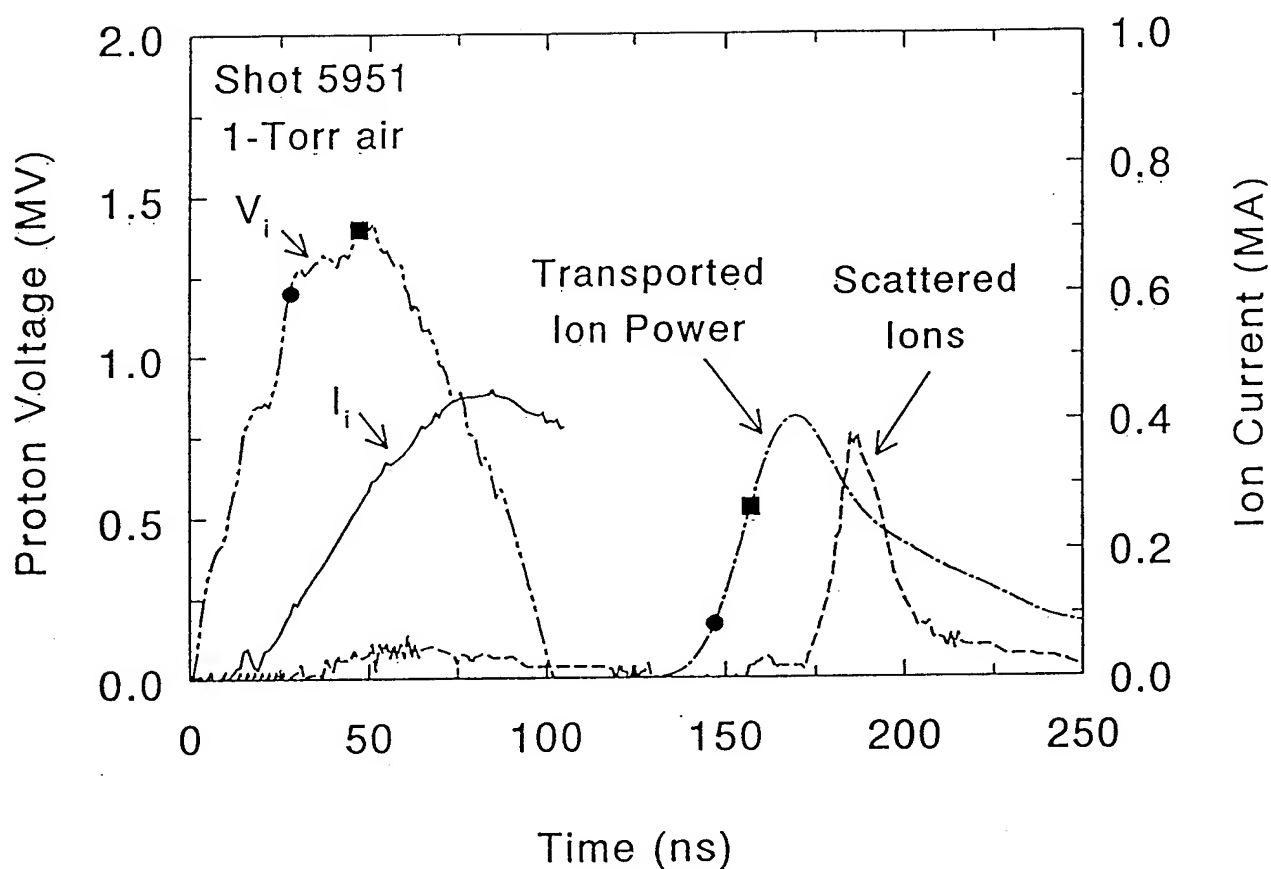


Fig. 6. Comparison of the measured scattered-ion signal for the target at 173 cm from the anode with the transported ion power calculated using the ion voltage V_i and the ion current I_i for Shot 5951. Time-of-flight shifting of the points at 1.2 and 1.4 MeV on V_i gives the corresponding points indicated on transported ion power.

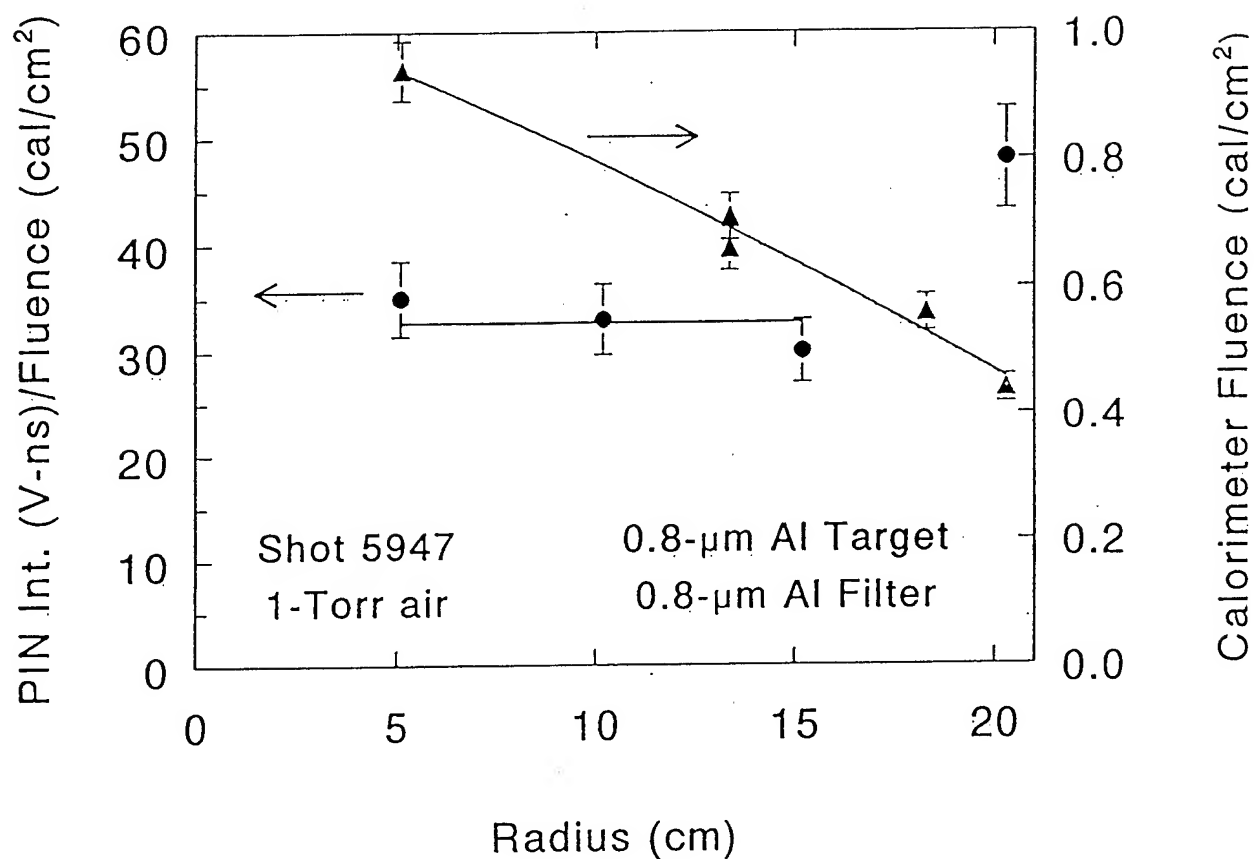


Fig. 7. Radial distribution of the scattered-ion intensity at 173 cm from the anode (circles), normalized to the calorimeter fluence. The measurements at 5, 10, and 15 cm are constant as indicated by the horizontal line. The radial distribution of the calorimeter fluence is also shown (triangles). The curve is a fit to the data.

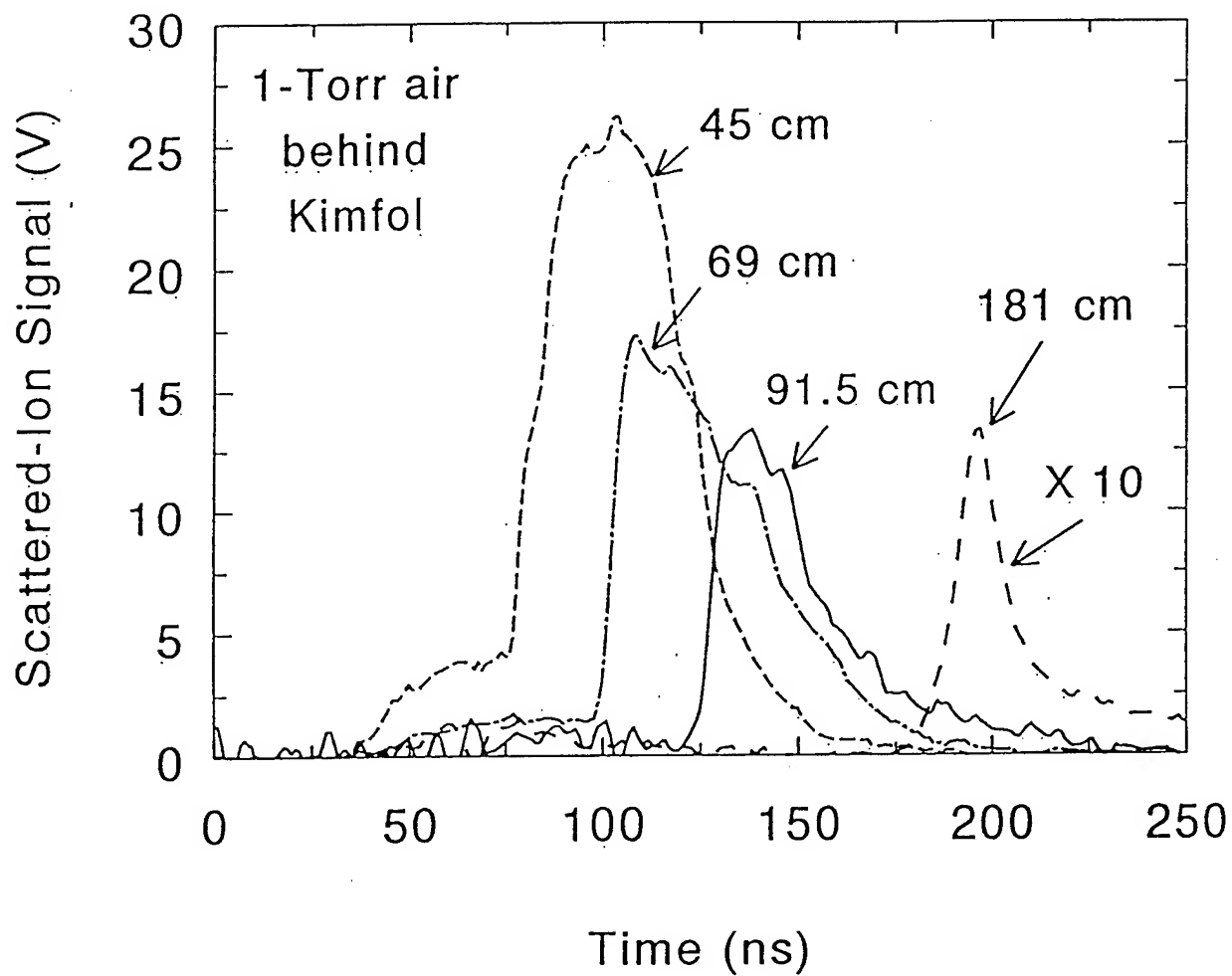


Fig. 8. Scattered-ion signals measured for different ion flight paths. The target is 23 cm from the anode for the 45-, 69- or 91.5-cm flight paths and 173 cm from the anode for the 181-cm flight path.

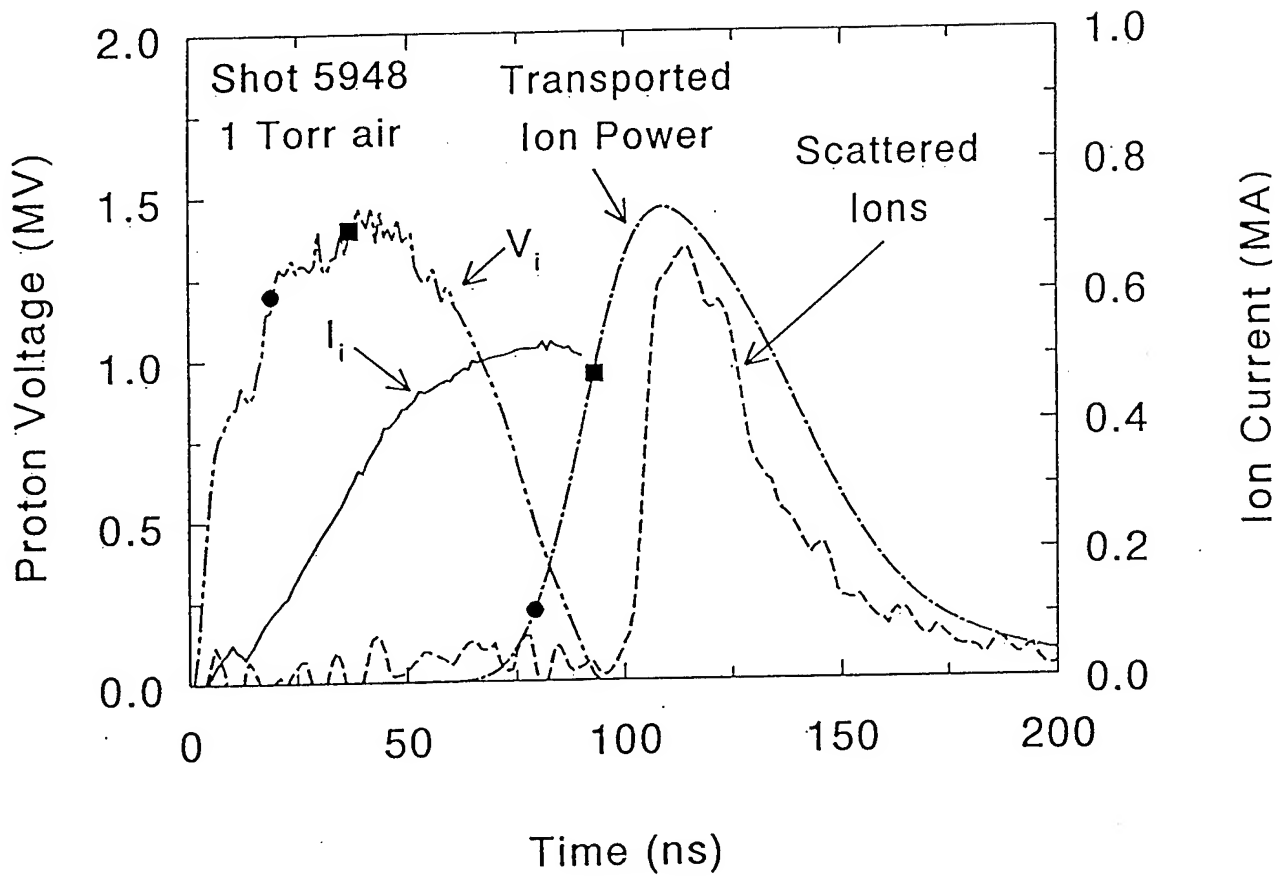


Fig. 9. Comparison of the scattered-ion signal measured for the target at 23-cm from the anode with the transported ion power calculated using the ion voltage V_i and the ion current I_i for Shot 5948. Time-of-flight shifting of the points at 1.2 and 1.4 MV on V_i gives the corresponding points indicated on transported ion power.

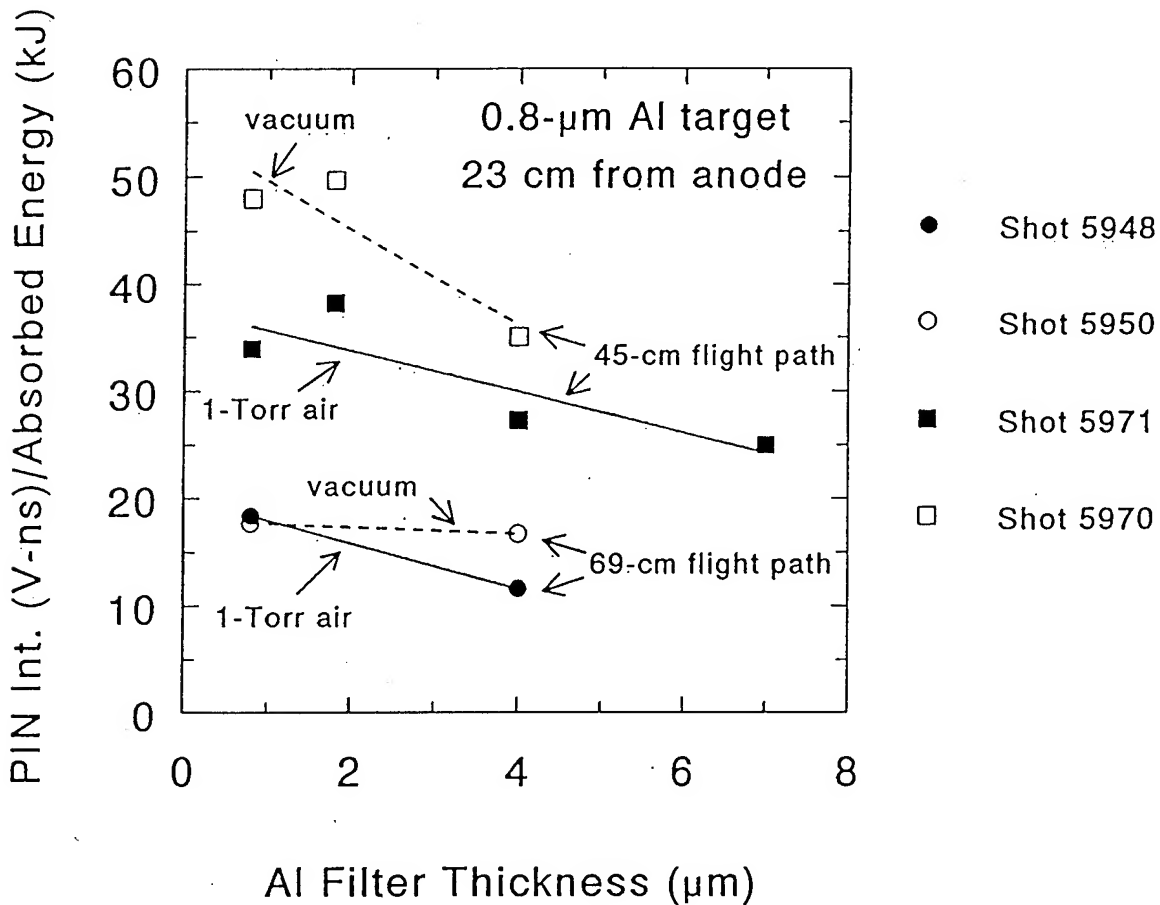


Fig. 10. Scattered-ion intensities as a function of aluminum filter thickness on each PIN diode for shots with vacuum behind the Kimfol and for shots with 1-Torr air behind the Kimfol. The intensities are normalized to calculated energies absorbed by each PIN diode based on ion-voltage and current measurements. Results are presented for ion flight paths of 45 and 69 cm from the anode to the PIN diode.

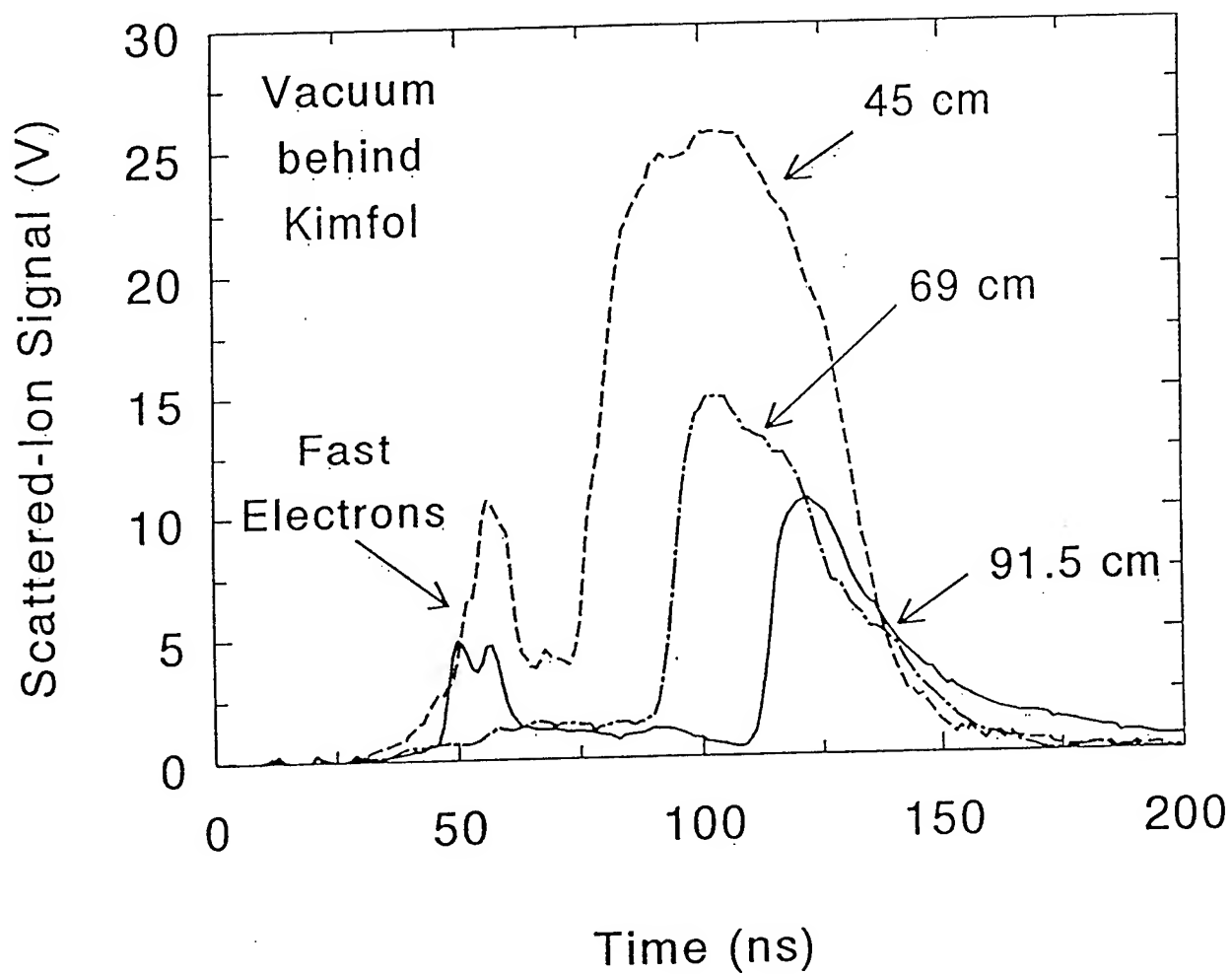


Fig. 11. Scattered-ion signals measured for ion flight paths of 45, 69 and 91.5 cm with vacuum behind the Kimfol. The target is 23 cm from the anode.

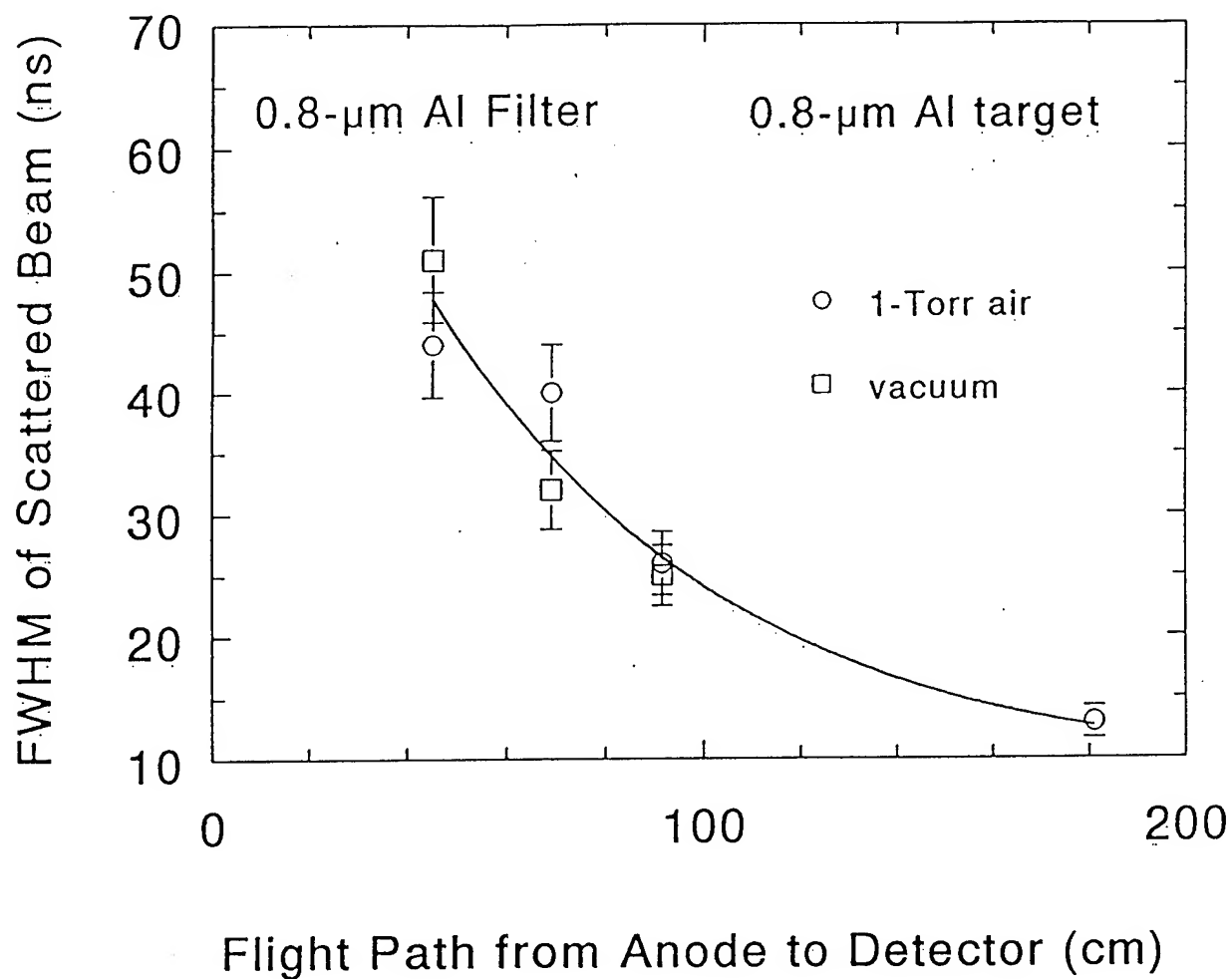


Fig. 12. Measured values of the full-width at half-maximum (FWHM) of scattered-ion signals for different flight paths from the anode to the PIN diode. The curve is a quadratic fit to the measurements.

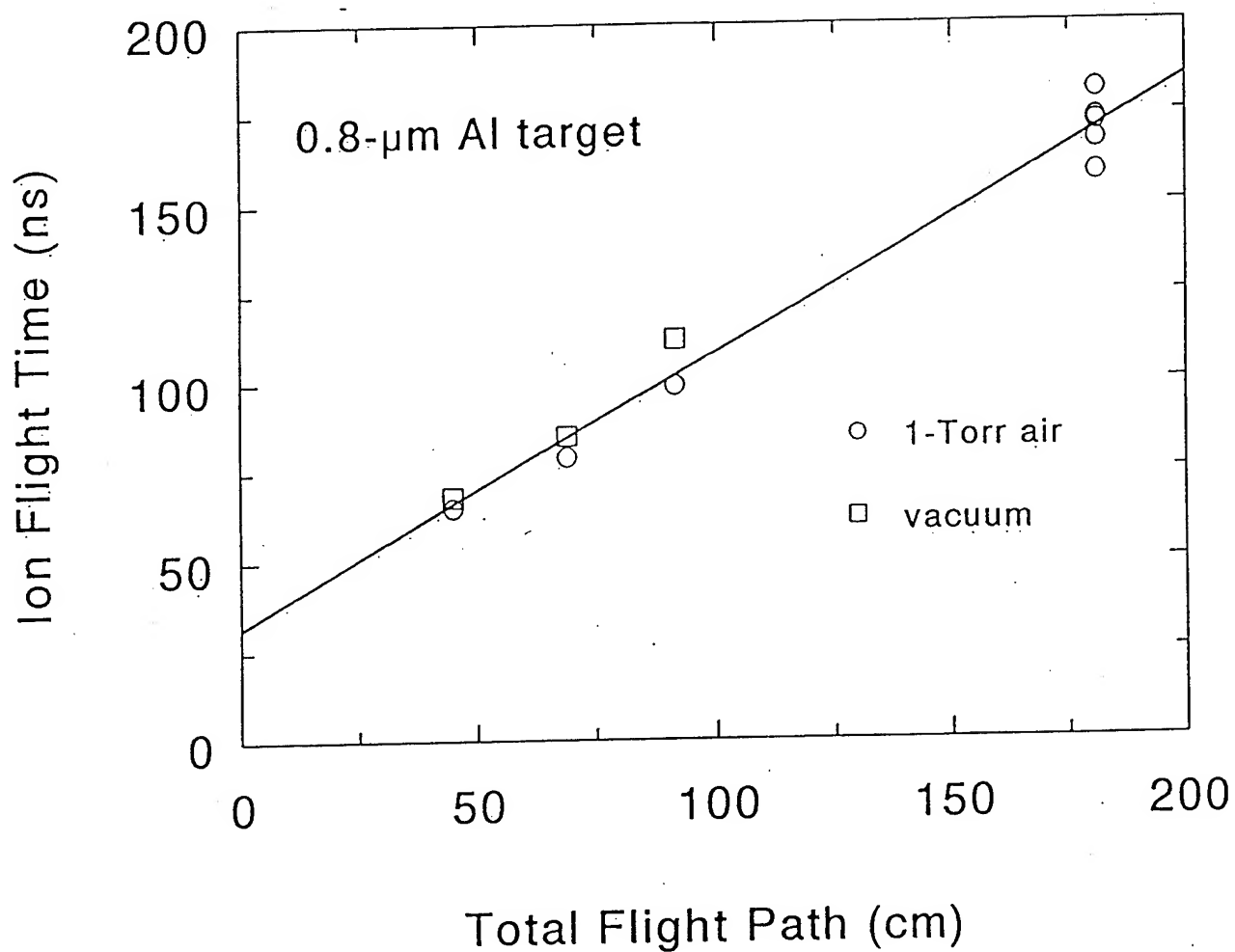


Fig. 13. Ion flight times from scattered-ion measurements as a function of the total flight path from the anode to the PIN diode. The target is 23 cm from the anode for flight paths less than 100 cm and 173 cm from the anode for the longer flight path. The line is a linear fit to the data.

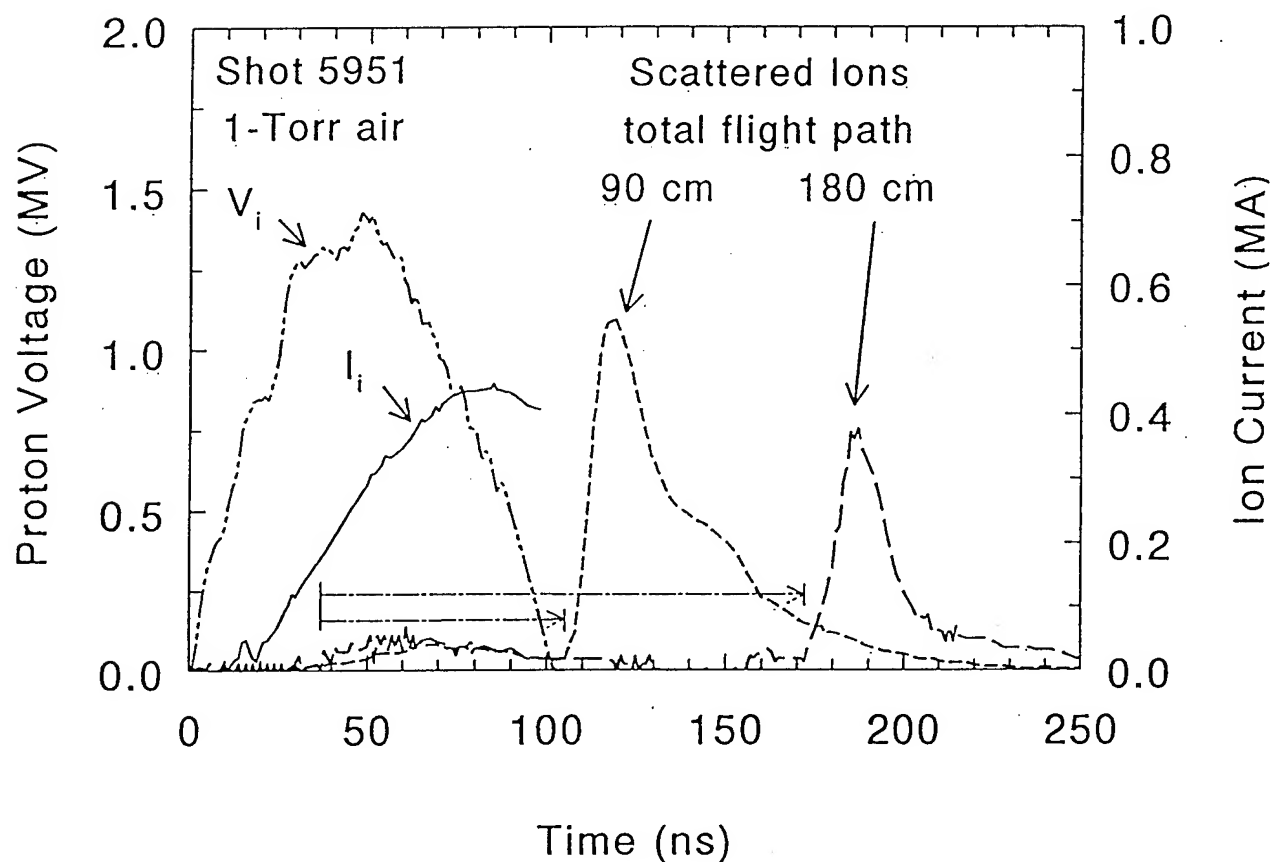


Fig. 14. Scattered-ion signals for Shot 5951 with 0.8- μm aluminum targets located at 23 and 173 cm from the anode. The ion voltage V_i and ion current I_i at the exit of the Kimfol are also shown. The flight times for ions at the onset of the scattered-ion signals correspond to a start time of 37 ns at the Kimfol.

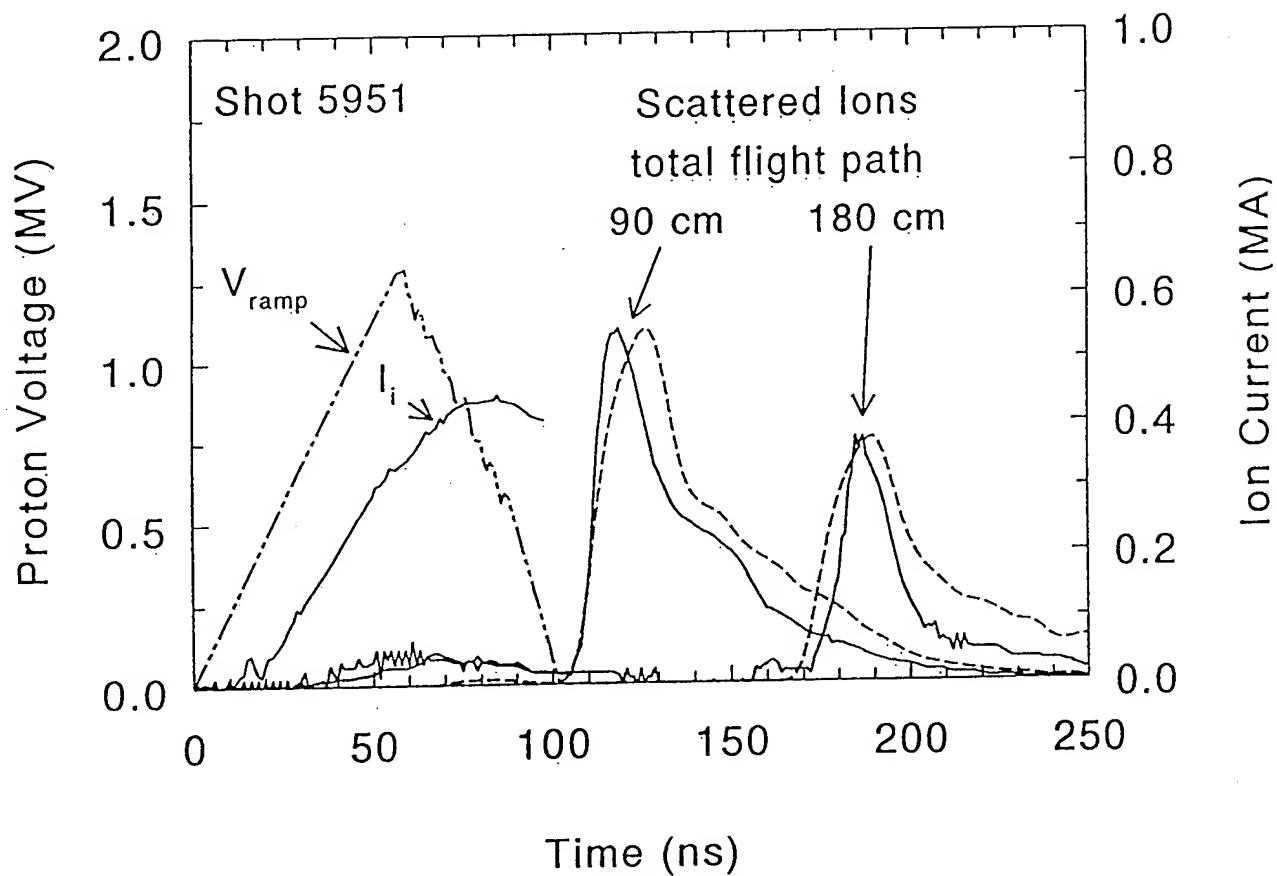


Fig. 15. Comparison of scattered-ion signals for Shot 5951 with transported ion powers calculated using the voltage V_{ramp} and the ion current I_i . The solid curves are scattered-ion signals and the dashed curves are transported ion powers.

PULSED POWER PHYSICS TECHNOTE 94-17

Title: INCORPORATION OF TRIM ION ENERGY LOSS CALCULATIONS
INTO ANALYSIS ROUTINES

Author: D. Hinshelwood

Date: August 26, 1994

Abstract: The ion energy loss routine used in our ANALYSIS program has been updated by incorporating the stopping calculations of Ziegler and coworkers. The stopping routine used in their TRIM program has been adapted, in VMS FORTRAN, to our program. This routine calculates the stopping of any ion in any elemental target. This routine has also been written as a stand-alone program DTEST, in VMS FORTRAN, which can be incorporated into other users' programs.

INTRODUCTION

The ion energy loss routine used in our ANALYSIS program has been updated by incorporating the stopping calculations of Ziegler and coworkers. The stopping routine used in their TRIM program has been adapted, in VMS FORTRAN, to our program. This routine calculates the stopping of any ion in any elemental target. This routine has also been written as a stand-alone program DTEST, in VMS FORTRAN, which can be incorporated into other users' programs. DTEST is available on 3.5 in floppy disk to anyone who is interested. This note summarizes briefly the work of Ziegler and then describes the routine and our adaption.

REFERENCES

The present work is derived from three references:

- (1) J. F. Ziegler, J. P. Biersack, and U. Littmark, "The Stopping and Range of Ions in Solids," Pergamon Press, 1985 (Vol 1 of "The Stopping and Ranges of Ions in Matter").

This is the final volume in the series which includes the well-known volumes on proton and helium stopping by Anderson and Ziegler (The "volume 1" is misleading). The calculations presented in this book are considered to be more accurate than those in the prior volumes. This book presents a detailed, tutorial discussion of ion stopping, including range calculations. The results are said to be accurate to within ten percent or better. The stopping of protons is modeled by an eight parameter fit for each elemental target. These fits supersede the fits given in Anderson and Ziegler. Stopping of heavy ions is calculated by assuming that the stopping of a heavy ion is the same as that of a proton at the same velocity, times the ion charge squared. Calculation of the (partially stripped) heavy ion charge makes up the bulk of the routine. The book then discusses range calculations, including all of the relevant physics. These calculations are used in the program TRIM, which performs a Monte Carlo calculation of range distributions. John Maenchen has told me that this book is out of print, so I have photocopied it and will make a copy for any interested party.

- (2) J. F. Ziegler and J. M. Manoyan, "The Stopping of Ions in Compounds," NIM B35, 215 (1988).

This paper discusses deviations from the Bragg rule in the stopping of compounds. Such deviations are observed for hydrocarbon compounds, including the plastics we use. They arise because of differences in atomic structure between compounds and their individual constituents. These deviations are on the order of 5-10 percent, peaking at ion energies around 25 keV/amu, and dropping off at higher energies. Deviations for compounds containing heavy ions, such as metallic oxides, are said to be negligible.

(3) TRIM 9107

This program was given to me on a floppy disk by Chris Meli in code 6670, and is installed on the PC in my office. The files include the full TRIM program, stopping and range routines, and some, but not all, of the source code in BASIC. The full TRIM program is more relevant to ion implantation, and calculates many phenomena of no interest to us. However, the stopping and range routines are very useful. I have included a sample of the output from the routine SR, which is apparently based on RSTOP in Ref. 1. The program also calculates stopping for a large library of compounds, incorporating, where necessary, deviations from the Bragg rule.

STOPPING ROUTINE

Total (electronic plus nuclear) stopping is calculated in ANALYSIS by the subroutine DEDXC(DEDX,RZ,ZT,I). Many of our ANALYSIS routines involve transport of the ion beam through several foils and gas regions. To calculate the energy loss for each increment of material, at each timestep of the ion current an voltage, would be too time-consuming. Instead, an array DEDX(12,410) is calculated once at the start of the particular ANALYSIS routine. The (up to) 12 columns in DEDX correspond to each ion-target combination needed for that particular routine (we may have to allow more combinations when we start modeling deposition in multilayer targets). Rows 1-400 in DEDX contain the value of dE/dx , in kV/micron for solids and kV/Torr-meter for gases, at voltages from 25 kV-10 MV, in 25 kV increments. By dealing with voltage rather than energy, the energy range is extended for multiply charged ions. The argument RZ is the incident ion atomic number Z1 and charge Q, entered as the real number Z1.Q. The ion is assumed to be the most common isotope, except for deuterons which are imported as Z1=0. The target is identified by ZT. Values from 1-92 refer to pure elements and 92-120 refer to compounds. So far, we have several plastics, air, and two solids used in PIBE work. Others will be added as needed. It is trivial to add compounds since stopping is calculated using the Bragg rule (with a correction for plastics). Various element and compound parameters needed for this and other calculations (e.g., Rutherford scattering) are contained in the include file DMCOEF.FOR. The slight correction necessary for plastics is also included in DEDXC. I use a different functional fit because the one in Ref. 3 makes no sense to me, but the peak values are taken from the TRIM program. For each element in the target, DEDX calls the function DSTOP.

The function DSTOP(ENERGY,Z1,ZT) calculates the stopping of an ion with atomic number Z1 and ENERGY in kV in an elemental target of atomic number ZT. This function includes both electronic and nuclear stopping. The latter is insignificant for protons at energies of interest but not necessarily so for heavier ions. This function is essentially copied from the code in Ref. 1, with minor changes in variables and data storage. Here, two INCLUDE files store the necessary coefficients for protonic stopping (DPCOE.FOR) and for heavy ion stopping (DECOEF.FOR). The code differs slightly from the procedure discussed in Ref. 3 in the addition of the inner shell correction to the screening factor calculation.

I am sure that the calculation of heavy ion effective charge could be made simpler with minimal error, but as the program length is dominated by the proton coefficients, there is no reason to do so.

Finally, the program DTEST contains a shell that uses DEDXC to calculate the range by integrating the inverse of dE/dx . This shell was used to check my coding by comparing the outputs with TRIM results. For a variety of ion/target combinations and energies, the two yield dE/dx values that are in agreement.

LIMITATIONS

Simply integrating $1/dE/dx$ to get the range, as is essentially done in our ANALYSIS routines, leaves out two effects that TRIM includes. These are: (1) range shortening, which occurs because nuclear stopping at the end of the ion range causes deviations of the ion trajectories from a straight line, thus reducing the projected range; and (2) range straggling, resulting from a statistical variation in collisions. John Maenchen and I thought about trying to model these (one such unsuccessful attempt is commented out at the end of DSTOP) before concluding, along with Frank Young, that this was unnecessary. The reason for this is shown schematically in Figure 1. Both straggling and shortening introduce some uncertainty in the depth-dose profile of each ion at the very end of its range. However, for all but the highest-energy ions, this contribution to the total profile is negligible compared to that provided by higher-energy ions. The tail of the highest energy ions, in turn, makes up a negligible fraction of the total energy.

Actually, the ranges calculated by DTEST agree quite well with those calculated by TRIM, for proton energies above 100 kV and heavy particle energies above about 10-50 kV/amu. Even at lower energies, where the percentage error in the range calculation is large, the absolute error is less than 0.1 microns. Detailed calculations of straggling and shortening would only be warranted, if at all, for modeling deposition by very low E/A beams, e.g., 100-kV C or 10-kV proton beams.

Non-local effects, such as secondary electron emission or ion recoils, are another conceivable concern, but these are also unimportant for our applications. Since ion recoils occur only toward the end of the range, the argument in the previous paragraph is applicable. Secondary electrons are produced with energies too low to travel a significant distance within the target. Simple kinematics dictates that target electrons have at most $4m/M$ times the ion energy. Thus, 1-MV protons will produce at most 2.2-kV secondary electrons, which have a range of about 0.02 microns in aluminum (Marion and Young, p10). Even 5-MV protons will produce at most only 11-keV secondaries, having a range of about 0.75 microns, which is insignificant compared with the proton range of almost 200 microns.

Note also that any errors introduced by the above approximations are also negligible compared with the fundamental (~5 percent) uncertainties in the beam voltage, possible voltage spread, trajectory angle, foil thicknesses, etc.

USE OF ANALYSIS ROUTINES

Our routines for energy loss, deposition profiles, and Rutherford scattering have been modified to use the updated stopping calculations and to accept arbitrary incident ions. Use should be self-explanatory; just remember that multiply charged ions are entered as Z.Q (ions entered as Z are given a default charge of 1) and deuterons are entered as 0. I will modify the deposition profile routine to accept multilayer targets in the near future.

The effect of these changes on proton stopping calculations is small. For example, Figure 2 shows the stopping of 7 layers of 1.8-micron Kimfol, as calculated by the new and old programs. The slight difference is mainly a result of the inclusion of deviations from the Bragg rule.

==> Version - 91.08 <==

Ion = H (Mass = 1)

Target = Ti(100 %)

Density = 4.5190E+00 g/cm3

Disk File Name = HTi

Stopping Units = keV / micron

Ion Energy	dE/dx Elec.	dE/dx Nuclear	Projected Range	Longitudinal Straggling	Lateral Straggling
50.00 keV	1.604E+02	4.833E-01	3534 A	839 A	1284 A
55.00 keV	1.639E+02	4.523E-01	3817 A	861 A	1336 A
60.00 keV	1.668E+02	4.255E-01	4097 A	882 A	1386 A
65.00 keV	1.692E+02	4.020E-01	4374 A	902 A	1433 A
70.00 keV	1.712E+02	3.813E-01	4649 A	920 A	1479 A
80.00 keV	1.739E+02	3.463E-01	5195 A	955 A	1564 A
90.00 keV	1.753E+02	3.177E-01	5738 A	987 A	1645 A
100.00 keV	1.757E+02	2.940E-01	6280 A	1017 A	1722 A
110.00 keV	1.753E+02	2.738E-01	6826 A	1045 A	1795 A
120.00 keV	1.742E+02	2.565E-01	7375 A	1072 A	1867 A
130.00 keV	1.727E+02	2.415E-01	7930 A	1098 A	1937 A
140.00 keV	1.708E+02	2.283E-01	8492 A	1123 A	2006 A
150.00 keV	1.686E+02	2.166E-01	9061 A	1148 A	2075 A
160.00 keV	1.662E+02	2.062E-01	9640 A	1172 A	2143 A
170.00 keV	1.637E+02	1.968E-01	1.02 um	1196 A	2210 A
180.00 keV	1.611E+02	1.883E-01	1.08 um	1220 A	2278 A
200.00 keV	1.558E+02	1.735E-01	1.21 um	1273 A	2414 A
220.00 keV	1.505E+02	1.610E-01	1.33 um	1327 A	2551 A
240.00 keV	1.454E+02	1.504E-01	1.46 um	1380 A	2691 A
260.00 keV	1.405E+02	1.412E-01	1.60 um	1435 A	2834 A
280.00 keV	1.358E+02	1.331E-01	1.74 um	1490 A	2980 A
300.00 keV	1.315E+02	1.260E-01	1.89 um	1546 A	3129 A
330.00 keV	1.254E+02	1.168E-01	2.12 um	1643 A	3360 A
360.00 keV	1.199E+02	1.089E-01	2.36 um	1742 A	3600 A
400.00 keV	1.135E+02	1.000E-01	2.70 um	1894 A	3933 A
450.00 keV	1.064E+02	9.094E-02	3.14 um	2107 A	4371 A
500.00 keV	1.004E+02	8.347E-02	3.62 um	2325 A	4834 A
550.00 keV	9.515E+01	7.721E-02	4.13 um	2549 A	5320 A
600.00 keV	9.054E+01	7.189E-02	4.66 um	2778 A	5829 A
650.00 keV	8.646E+01	6.730E-02	5.21 um	3012 A	6360 A
700.00 keV	8.281E+01	6.331E-02	5.80 um	3251 A	6913 A
800.00 keV	7.653E+01	5.668E-02	7.04 um	3940 A	8080 A
900.00 keV	7.131E+01	5.138E-02	8.38 um	4623 A	9327 A
1.00 MeV	6.687E+01	4.705E-02	9.81 um	5308 A	1.06 um
1.10 MeV	6.305E+01	4.344E-02	11.33 um	6000 A	1.20 um
1.20 MeV	5.970E+01	4.038E-02	12.94 um	6701 A	1.35 um
1.30 MeV	5.675E+01	3.774E-02	14.64 um	7414 A	1.50 um
1.40 MeV	5.412E+01	3.545E-02	16.43 um	8140 A	1.66 um
1.50 MeV	5.176E+01	3.344E-02	18.30 um	8878 A	1.83 um
1.60 MeV	4.962E+01	3.166E-02	20.25 um	9630 A	2.00 um
1.70 MeV	4.768E+01	3.007E-02	22.29 um	1.04 um	2.18 um
1.80 MeV	4.590E+01	2.864E-02	24.40 um	1.12 um	2.37 um
2.00 MeV	4.277E+01	2.618E-02	28.88 um	1.35 um	2.76 um
2.20 MeV	4.009E+01	2.413E-02	33.66 um	1.58 um	3.17 um
2.40 MeV	3.776E+01	2.240E-02	38.76 um	1.81 um	3.60 um
2.60 MeV	3.572E+01	2.091E-02	44.15 um	2.04 um	4.06 um
2.80 MeV	3.392E+01	1.962E-02	49.85 um	2.27 um	4.54 um
3.00 MeV	3.231E+01	1.849E-02	55.84 um	2.51 um	5.04 um
3.30 MeV	3.019E+01	1.703E-02	65.37 um	2.97 um	5.84 um

3.60 MeV	2.837E+01	1.579E-02	75.53 um	3.43 um	6.68 um
4.00 MeV	2.629E+01	1.441E-02	90.06 um	4.17 um	7.87 um
4.50 MeV	2.413E+01	1.301E-02	109.76 um	5.23 um	9.47 um
5.00 MeV	2.233E+01	1.187E-02	131.15 um	6.26 um	11.20 um
5.50 MeV	2.080E+01	1.092E-02	154.17 um	7.30 um	13.04 um
6.00 MeV	1.950E+01	1.013E-02	178.82 um	8.34 um	15.01 um
6.50 MeV	1.836E+01	9.440E-03	205.05 um	9.40 um	17.09 um
7.00 MeV	1.736E+01	8.846E-03	232.86 um	10.48 um	19.28 um
8.00 MeV	1.569E+01	7.868E-03	293.02 um	14.03 um	23.99 um
9.00 MeV	1.434E+01	7.093E-03	359.23 um	17.43 um	29.14 um
10.00 MeV	1.323E+01	6.464E-03	431.35 um	20.80 um	34.70 um

 Multiply Stopping by

for Stopping Units

1.0000E-01	eV / Angstrom
1.0000E+00	keV / micron
1.0000E+00	MeV / mm
2.2130E-03	keV / (ug/cm2)
2.2130E-03	MeV / (mg/cm2)
2.2130E+00	keV / (mg/cm2)
1.7602E-01	eV / (1E15 atoms/cm2)
1.3652E-01	L.S.S. reduced units

```

*****
THIS IS JUST A SHELL TO TEST THE STOPPING CALCULATIONS

PROGRAM DTEST
REAL ENERGY,RANGE,DEDX(12,410),RZ,DEX,EI,DE,DI
INTEGER ZT,II
TYPE *, 'ENTER RZ,ZT'
ACCEPT *,RZ,ZT
CALL DEDXC(DEDX,RZ,ZT,1)
TYPE *, 'ENTER ENERGY'
ACCEPT *, ENERGY
II=INT(ENERGY/25)
DEX=DEDX(1,II)
RANGE=0
DO 99 DI=ENERGY/1000,ENERGY, ENERGY/1000
EN=MAX(25.,DI)
II=INT(EN/25)
EI=EN/25-II
DE=DEDX(1,II)*(1-EI)+DEDX(1,II+1)*EI
RANGE=RANGE+1/DE*ENERGY/1000
CONTINUE
TYPE *, DEX,RANGE
GOTO 10

99
END

*****
SUBROUTINE DEDXC(DEDX,RZ,ZT,I)

THIS SUBROUTINE FILLS THE ARRAY DEDX WITH STOPPING AND OTHER DATA
FOR SINGLE ELEMENTS AND SELECTED COMPOUNDS, UP TO 10 MV DIODE VOLTAGE.
IT IS TO BE CALLED ONCE DURING ROUTINE EXECUTION FOR EACH MATERIAL
THEN, DATA WILL BE PULLED FROM DEDX RATHER THAN RE-CALCULATED TO
SAVE TIME. I IS THE INDEX IN DEDX (12,410)
DEDX(I,1-400) IS STOPPING IN 25-KV INCREMENTS. (1,401) IS THE DENSITY.
OTHER INDICES RESERVED FOR FUTURE CALCS OF MATERIAL PROPERTIES
DE/DX IS GIVEN IN KV/MICRON FOR SOLIDS AND KV/TORR-METER FOR GASES
ENERGY IS IN KV, DENSITY IS IN MOLECULES/CM3 FOR SOLIDS
NOTE THAT SINGLE-ELEMENT GASES ARE ASSUMED TO BE ATOMIC
(I.E., USE TWICE ACTUAL PRESSURE FOR N2, O2, H2)
ZT'S FOR COMPOUNDS: 93-AIR, 100-KIMFOL, 101-POLY, 102-MYLAR,
105-Mn0.5Zn0.5Fe204, 106-YBa2Cu307

THE BRAGG RULE IS USED FOR COMPOUNDS EXCEPT PLASTICS,
WHERE ZIEGLER'S FORAMLISM IS USED (NIM B35, p215, 1988)
Z IS THE ION ATOMIC NUMBER AND Q IS THE CHARGE STATE OF THE ION
THE CHARGE IS IMPORTED HERE SO THAT THE VOLTAGE RANGE CAN BE EXTENDED FOR
HEAVIER IONS. Z AND Q ARE IMPORTED AS RZ=Z.Q, TO SIMPLIFY INPUT.
DEUTERONS ARE IMPORTED AS Z=0
THEREFORE, BOTH THE INDEX AND VALUE OF DEDX REFER TO VOLTAGE, NOT ENERGY.

REAL DEDX(12,410), DENSITY, ENERGY, MCOEF(10,120), DSTOP, RZ
REAL COMFACT, VREL, AMU
INTEGER Z,ZT,Q,I,J
INCLUDE 'DMCOEF.FOR'
DENSITY=MCOEF(2,ZT)
DEDX(I,401)=DENSITY
GET CHARGE AND MASS

```

```

C      Z=INT(RZ)
C      Q=MAX(INT((RZ-Z)*10+.1),1)
C
C      DO 1501 J=1,400
C      ENERGY=25*J*Q
C
C      GOTO (92,93,1500,1500,1500,1500,1500,1500,1500,1500,101,
C      +102,1500,1500,105,106,1500), ZT-91
C
C      92 DEDX(I,J)=DSTOP(ENERGY,Z,ZT)*DENSITY
C      GOTO 1500
C      93 DEDX(I,J)=(0.8*DSTOP(ENERGY,Z,7)+0.2*DSTOP(ENERGY,Z,8))*
C      +DENSITY
C      GOTO 1500
C      100 DEDX(I,J)=(16*DSTOP(ENERGY,Z,6)+14*DSTOP(ENERGY,Z,1)+
C      +3*DSTOP(ENERGY,Z,8))*DENSITY
C      COMFACT=0.044
C      GOTO 1400
C      101 DEDX(I,J)=(DSTOP(ENERGY,Z,6)+2*DSTOP(ENERGY,Z,1))*
C      +DENSITY
C      COMFACT=0.06
C      GOTO 1400
C      102 DEDX(I,J)=(10*DSTOP(ENERGY,Z,8)+8*DSTOP(ENERGY,Z,1)
C      +4*DSTOP(ENERGY,Z,8))*DENSITY
C      COMFACT=0.02
C      GOTO 1400
C
C      CORRECTION FOR PLASTICS
C      THIS USES A DIFFERENT FUNCTION THAN ZIEGLER BECAUSE I DONT
C      UNDERSTAND HIS. ANYWAY, THE TOTAL CORRECTION IS SO SMALL THAT
C      THIS WHOLE EXERCISE MAY BE UNNECESSARY
C      1400 AMU=MCDEF(1,Z)
C      IF (Z.EQ.0) AMU=2.01
C      VREL=ENERGY/25/AMU
C      COMFACT=1+MAX(0.,COMFACT*(1-(VREL-2.5)**2/50))
C      DEDX(I,J)=DEX(I,J)*COMFACT
C      GOTO 1500
C
C      105 DEDX(I,J)=(DSTOP(ENERGY,Z,28)*.76*DSTOP(ENERGY,Z,30)/4
C      +2*DSTOP(ENERGY,Z,26)+4*DSTOP(ENERGY,Z,8))*DENSITY
C      106 DEDX(I,J)=(DSTOP(ENERGY,Z,39)+2*DSTOP(ENERGY,Z,56)+
C      +3*DSTOP(ENERGY,Z,29)+7*DSTOP(ENERGY,Z,8))*DENSITY
C
C      1500 DEDX(I,J)=DEX(I,J)/Q
C      1501 CONTINUE
C
C      RETURN
C      END
C
C      *****
C      REAL FUNCTION DSTOP (ENERGY,Z1,ZT)
C
C      THIS CALCULATES ION STOPPING ACCORDING TO ZIEGLER, ET AL
C      REF: THE STOPPING AND RANGE OF IONS IN SOLIDS - ZIEGLER, BIRSACK,
C      AND LITTMARK, PERGAMON, 1985
C      Z IS ION Z, ZT IS TARGET Z
C      THIS CALCULATES DE/DX IN keV-cm2/10**18 ATOMS FOR SINGLE ELEMENTS
C      NOTE - DEUTERONS ARE IMPORTED AS Z=0

```

```

REAL ENERGY,E,E1,EMIN,SL,SH,RATIO,EPSIL,NSTOP
REAL PCOEF(8,92),ECOEF(3,92),AMU,AMUT,VFERMI,LFCTR
REAL V,VR,YR,Q,Q1,L,L0,L1,L2,ZETA,ZETA1,VELPWR,PVELPWR
REAL VMIN,VRMIN
INTEGER Z,Z1,ZT,I,J
INCLUDE 'DPCOEF.FOR'
INCLUDE 'DECOEF.FOR'

C
C
C GET NECESSARY CONSTANTS
Z=Z1
AMU=ECOEF(1,Z)
AMUT=ECOEF(1,ZT)
IF (Z1.EQ.0) THEN
  AMU=2.01
  Z=1
END IF
E=ENERGY/AMU
VFERMI=ECOEF(2,ZT)
LFCTR=ECOEF(3,Z)
RATIO=1

C
C
C NUCLEAR STOPPING
EPSIL=32.53*AMUT*ENERGY/(Z*ZT*(AMU+AMUT)*(Z**.23+ZT**.23))
IF (EPSIL.GE.30)GOTO 141
E1=(.01321*EPSIL**.21226)+(.19593*EPSIL**.5)
NSTOP=.5*ALOG(1+1.1383*EPSIL)/(EPSIL+E1)
GOTO 142

141 NSTOP=ALOG(EPSIL)/(2*EPSIL)
142 NSTOP=NSTOP*Z*ZT*AMU*.462/((AMU+AMUT)*(Z**.23+ZT**.23))

C
C
C BRANCH DEPENDING ON ION
IF (Z.EQ.1) GOTO 99
IF (Z.EQ.2) GOTO 88

C
C
C HEAVY ION STOPPING

C
C
C GET REDUCED VELOCITY, HERE IN UNITS OF BOHR VEL
V=SQRT(E/25)/VFERMI
VR=V*VFERMI*(1+.1/(5.*V*V))
IF (V.LT.1)VR=(3*VFERMI/4)*(1+(2*V*V/3)-V**4/15)

C
C
C THEN, GET YR SUBJECT TO CONDITIONS
YR=MAX(.13,VR/Z**.6667)
YR=MAX(YR,1./Z**.6667)

C
C
C NEXT, CALCULATE IONIZATION LEVEL
Q1=-.803*YR**.3+1.3167*YR**.6+.38157*YR+.008983*YR*YR
Q=MIN(1.,MAX(0.,1.-EXP(-MIN(Q1,50.))))

C
C
C NOW, CALCULATE SCREENING FACTOR
L0=(.8-Q*MIN(1.2,.8+Z/30.))/Z**.3333
L1 IS INNER SHELL CORRECTION, STRAIGHT LINE FIT WITH MAX OF L2
L2=(MIN(.43,MAX(.32,.12+.025*Z)))/Z**.3333
IF (Q.LT.0.2) THEN
  L1=0
ELSE IF (Q.LT.(MAX(0.,.9-.025*Z))) THEN
  L1=L2*(Q-.2)/ABS(MAX(0.,.9-.025*Z)-.2000001)
ELSE IF (Q.LT.MAX(0.,1.-.025*MIN(16.,1.*Z))) THEN
  L1=L2
ELSE

```

```

      L1=L2*(1.-Q)/(.025*MIN(16.,1.*Z))
END IF
170 L=MAX (L1,L0*LFCTR)
C
C GET CHARGE FROM SCREENING FACTOR
ZETA=Q*(1./(2.*VFERMI**2))*(1.-Q)*ALOG(1+(4.*L*VFERMI/1.919)**2)
C
C ADD Z**3 EFFECT
ZETA1=- (7.6-MAX(0.,ALOG(E)))**2
ZETA=ZETA*(1.+(1./Z**2)*(.18+.0015*ZT)*EXP(ZETA1))
C
C RATIO=(ZETA*Z)**2
C
C CHECK FOR VEL DEP CRITERION
IF (YR.LE.MAX(.13,1./Z**8687)) THEN
  VRMIN=MAX(1.,.13*Z**8687)
  VMIN=.5*(VRMIN+SQRT(MAX(0.,1-.8*VFERMI**2)))
  EMIN=25*VMIN**2
  VELPWR=.5
  IF ((ZT.EQ.6).OR.((ZT.EQ.14).OR.(ZT.EQ.32)).AND.(Z.LE.19)))
    + VELPWR=.375
    RATIO=RATIO*(E/EMIN)**VELPWR
    E=EMIN
  END IF
  GOTO 99
C
C 88 CONTINUE
C
C HELIUM STOPPING
C
E1=ALOG(E)
L0=.2865+.1266*E1-.01429*E1*E1+.02402*E1*E1*E1-.01135*E1**4
+.001475*E1**5
L1=1-EXP(-MIN(30.,L0))
C
C ADD Z**3 EFFECT
L2=(1.+(.007+.0005*ZT)*EXP(-(7.6-MAX(0.,E1))**2))
L1=L1*L2*L2
C
RATIO=L1*Z*Z
C
C 99 CONTINUE
C
C PROTON STOPPING
C THE FOLLOWING CALCULATES THE STOPPING OF A PROTON OF GIVEN ENERGY
C IN MATERIAL OF ATOMIC NUMBER ZT, USING FITS OF ZIEGLER, ET AL
C ENERGY IS IN keV AND STOPPING IS IN keV-cm2/10**18 ATOMS
C
C FORCE NONZERO ENERGY TO AVOID INFINITE LOOP FROM ROUNDOFF ERROR
E=MAX(E,0.1)
NOTE LOGICAL TRUE HAS VALUE -1
VELPWR=.25-.2*(ZT.GT.6)
IF (E.LT.26.0) RATIO=RATIO*(E/25.0)**VELPWR
E=MAX(E,25.0)
SL=PCOE(1,ZT)*E**PCOE(2,ZT)+PCOE(3,ZT)*E**PCOE(4,ZT)
SH=PCOE(5,ZT)/E**PCOE(6,ZT)*
+ALOG(PCOE(7,ZT)/E+PCOE(8,ZT)*E)
DSTOP=SL*SH/(SL*SH)
C
C FOR NOW, DON'T WORRY ABOUT HIGH ENERGY STOPPING, E>10 MEV/AMU

```



```
C
C THE FOLLOWING IS AN EMPIRICAL FIT TO THE DECREASE IN PROJECTED RANGE
C THE SCALING OF ZT**1.33/EN IS MOTIVATED BY THOMAS-FERMI ENERGY UNITS
C THE FACTOR OF 2.5 AND POWER OF 1.25 COME FROM TRIAL AND ERROR
C THIS FIT IS NOT USED FOR NOW - A BETTER FIT SHOULD BE USED
C DSTOP=DSTOP*2.5*(ZT**1.3333/E)**1.25
C
C DSTOP=DSTOP*RATIO
C DSTOP=DSTOP*NSTOP
C
C RETURN
C END
C *****
```

+7.137,0.004313,9.425,0.2794,2726.,0.916,3166.1,0.025,
+4.898,0.004294,3.779,0.5,2824.,0.9103,1282.4,0.0171,
+1.368,0.004302,2.568,0.6082,6908.,0.9817,828.0.0068,
+2.235,0.00431,4.886,0.4788,4372.,0.9515,1185.2,0.0032,
+0.421,0.004117,0.017,2.3618,2263.,0.8919,39.8,0.0278,
+30.78,0.003774,0.558,0.7682,7113.,0.977,1604.4,0.0065,
+11.576,0.004212,7.024,0.3776,4714.,0.9426,2493.2,0.0113,
+6.241,0.004192,5.27,0.4945,4235.,0.9323,2063.9,0.0118,
+0.331,0.004124,1.725,1.1062,1930.,0.8691,27.4,0.0382,
+0.018,0.004172,0.146,1.7305,1804.,0.8632,29.7,0.0321,
+3.723,0.004177,4.629,0.5677,1678.,0.862,3094.0.0624,
+0.14,0.004133,0.256,1.4241,1919.,0.8633,72.8,0.0322,
+0.286,0.004139,0.313,1.3424,1956.,0.8618,115.2,0.0293,
+0.76,0.004218,3.386,0.7628,1967.,0.8581,70.0.0364,
+6.398,0.004193,5.469,0.4138,1713.,0.854,18493.0.0565,
+3.472,0.004134,3.234,0.6379,1116.,0.8196,4766.0.1179,
+2.527,0.004228,4.532,0.5366,1031.,0.8165,16252.2,0.1972,

+7.368,0.004101,4.879,0.5143,1100.,0.8245,17964.8,0.1332,
+7.72,0.004388,3.242,0.6843,1428.,0.834,1786.7,0.0665,
+16.78,0.004192,9.32,0.2957,3371.,0.9029,7431.7,0.0262,
+4.213,0.00421,4.675,0.5795,3504.,0.8928,1468.9,0.0144,
+4.619,0.00422,5.816,0.5218,3961.,0.9041,1473.3,0.0142,
+0.185,0.003621,0.001,3.5315,2931.,0.8894,26.2,0.0264,
+4.825,0.004146,8.093,0.5703,2300.,0.8636,2980.7,0.0387,
+0.499,0.004105,1.978,0.9588,787.,0.7851,806.6,0.4088,
+3.275,0.004218,5.768,0.5405,6631.,0.9428,744.1,0.0083,
+2.998,0.00409,4.53,0.6202,2161.,0.8567,1268.6,0.043,
+2.87,0.004090,4.257,0.6138,2130.,0.8523,1704.1,0.0394,
+10.853,0.004115,5.891,0.4683,2857.,0.8755,3654.2,0.03,
+3.841,0.004178,4.874,0.5786,1268.,0.8221,3508.2,0.2417/

C

DATA ((PCOEF(I,J),I=1,8),J=63,92)/

C

+17.845,0.004099,6.586,0.3273,393.1,0.9075,5156.7,0.0363,
+7.531,0.004081,4.939,0.5068,2520.,0.8582,3314.6,0.0305,
+5.474,0.004083,4.897,0.5111,2340.,0.853,2342.7,0.0357,
+4.266,0.004067,4.503,0.5526,2076.,0.8415,1666.6,0.0408,
+6.831,0.004049,4.399,0.5167,2003.,0.8344,1410.4,0.0348,
+1.271,0.004055,4.629,0.5743,1628.,0.8186,995.7,0.0553,
+5.756,0.004049,4.357,0.525,2207.,0.838,1579.5,0.0272,
+14.127,0.00406,5.83,0.3775,3646.,0.8782,3411.8,0.0164,
+6.895,0.00406,4.936,0.4796,2719.,0.8525,1885.8,0.0197,
+3.062,0.004051,3.58,0.5908,2346.,0.8371,1222,0.0201,
+10.811,0.003301,1.377,0.7651,2004.,0.8227,1110.6,0.025,
+2.71,0.004096,1.229,0.986,1232.,0.7907,165.4,0.0473,
+0.523,0.004024,1.404,0.8551,1461.,0.7968,503.3,0.0368,
+0.462,0.00402,1.301,0.8704,1474.,0.7969,443.1,0.0363,
+0.978,0.004037,2.013,0.7225,1891.,0.8175,930.7,0.0277,
+3.209,0.004051,3.666,0.5362,3091.,0.856,1508.1,0.0154,
+2.004,0.004043,7.488,0.3561,4464.,0.8884,3966.5,0.0128,
+15.43,0.003943,1.124,0.707,4596.,0.8844,1576.5,0.0089,
+3.151,0.004052,4.1,0.5425,3246.,0.8577,1691.8,0.0151,
+7.19,0.004059,8.693,0.3584,4761.,0.8883,2888.3,0.011,
+9.321,0.004054,11.543,0.3203,4866.,0.8912,3213.4,0.0119,
+29.242,0.003619,0.169,1.1228,5688.,0.8981,1033.3,0.0071,
+1.852,0.003997,3.156,0.651,3755.,0.8638,1602,0.012,
+3.222,0.004004,5.902,0.5268,4040.,0.868,1658.4,0.0117,
+9.341,0.003966,7.921,0.4298,5181.,0.8877,2173.2,0.0092,
+36.183,0.0036,0.583,0.8675,5990.,0.9108,1417.1,0.0062,
+5.928,0.003969,6.408,0.5212,4620.,0.8808,2323.5,0.0116,
+5.246,0.003974,6.797,0.4854,4586.,0.8779,2481.5,0.0113,
+33.702,0.00369,0.473,0.8924,5296.,0.8893,2053.3,0.0092,
+2.759,0.003981,3.209,0.6612,2505.,0.8286,2065.1,0.0228/

C

END COEFFICIENT INCLUDE FILE DPCOEF.FOR

C

U U U U U U U U U U

U U U U U U U U

U U

U U

```

+112.40,0.90,0.88,
+114.82,0.74,0.9,
+118.69,0.86,0.9,
+121.75,0.93,0.9,
+127.60,1.00,0.9,
+126.90,0.55,0.96,
+131.30,0.43,1.2,
+132.91,0.33,0.9,
+137.34,0.51,0.88,
+138.91,0.70,0.88,
+140.12,0.73,0.85,
+140.91,0.71,0.9,
+144.24,0.67,0.9,
+147.00,0.71,0.92,
+150.35,0.71,0.95/
C DATA ((ECOEF(I,J), I=1,3), J=63,92) /
C
+151.98,0.59,0.99,
+157.25,0.70,1.03,
+158.92,0.68,1.05,
+162.50,0.68,1.07,
+164.93,0.68,1.08,
+167.26,0.69,1.1,
+168.93,0.69,1.08,
+173.04,0.62,1.08,
+174.97,0.72,1.08,
+178.49,0.83,1.08,
+180.95,1.12,1.09,
+183.85,1.24,1.09,
+186.20,1.05,1.1,
+190.20,1.07,1.11,
+192.20,1.10,1.12,
+195.09,1.24,1.13,
+198.97,1.29,1.14,
+200.59,0.79,1.15,
+204.37,0.86,1.17,
+207.19,0.85,1.2,
+208.98,0.88,1.18,
+210.00,0.81,1.17,
+210.00,0.43,1.17,
+222.00,0.42,1.16,
+223.00,0.44,1.16,
+226.00,0.51,1.16,
+227.00,0.73,1.16,
+232.00,0.81,1.16,
+231.00,1.98,1.16,
+238.04,1.03,1.16/
C
C END OF COEF INCLUDE FILE DECOEF.FOR

```

COEFFICIENT INCLUDE FILE DMCOEF.FOR

THIS FILE CONTAINS MATERIAL QUANTITIES FOR ELEMENTS AND
COMPOUNDS USED IN THE ANALYSIS PROGRAM
ROWS 1-92 CORRESPOND TO ELEMENTS, ROWS 93-120 CORRESPOND TO
COMPOUNDS. SO FAR, ONLY THREE QUANTITIES ARE STORED:
COLUMN 1 IS THE AVERAGE AMU (USED WEAKLY IN RUTH SCATT)
COLUMN 2 IS THE DENSITY IN 10**22 MOL/CM3, 10**16 MOL/CM3/TORR FOR GASES
COLUMN 3 IS THE SUM OF Z**2/MOLECULE (USED IN RUTH SCATT)
OTHER COLUMNS CAN BE ADDED AS NEEDED, FOR EXAMPLE TO MODEL HEAT
TRANSPORT OR PHASE CHANGES

DATA ((MCOEF(I,J),I=1,3),J=1,40)/

+1.01,4.27,1,
+4,1.89,4,
+6.94,4.6,8,
+9.01,12.05,16,
+10.81,13.09,25,
+12.01,11.36,36,
+14.01,3.48,49,
+16,4.3,64,
+19,3.52,81,
+20.18,3.59,100,
+22.99,2.54,121,
+24.31,4.3,144,
+26.98,6.02,169,
+28.09,4.98,196,
+30.97,3.54,225,
+32.06,3.89,256,
+35.45,3.22,289,
+39.96,2.49,324,
+39.1,1.33,361,
+40.08,2.01,400,
+44.96,4.02,441,
+47.9,5.68,484,
+50.94,7.21,529,
+52,8.33,576,
+54.94,8.15,625,
+55.85,8.48,676,
+58.93,8.99,729,
+58.71,9.13,784,
+63.54,8.48,841,
+65.37,6.55,900,
+69.72,5.1,961,
+72.59,4.43,1024,
+74.92,4.6,1089,
+78.98,3.85,1156,
+79.91,2.56,1225,
+83.8,1.87,1296,
+85.47,1.08,1369,
+87.82,1.79,1444,
+88.91,3.04,1521,
+91.22,4.27,1600/
DATA ((MCOEF(I,J),I=1,3),J=41,80)/
+92.91,5.58,1681,
+95.94,6.41,1764,
+99.0,1849,
+101.07,7.26,1936,
+102.91,7.26,2025,
+108.4,6.77,2116,
+107.87,5.85,2209,

+112.4,4.6,2304,	
+114.82,3.84,2401,	
+118.69,3.7,2500,	
+121.75,3.27,2601,	
+127.6,2.94,2704,	
+126.9,2.34,2809,	
+131.3,1.4,2916,	
+132.91,0.86,3025,	
+137.34,1.54,3136,	
+138.91,2.68,3249,	
+140.12,2.87,3364,	
+140.91,2.9,3481,	
+144.24,2.92,3600,	
+147.0,3721,	
+150.35,3.03,3844,	
+151.96,2.08,3969,	
+157.26,3.03,4096,	
+158.92,3.14,4225,	
+162.5,3.17,4356,	
+164.93,3.22,4489,	
+167.26,3.27,4624,	
+168.93,3.33,4761,	
+173.04,2.43,4900,	
+174.97,3.38,5041,	
+178.49,4.43,5184,	
+180.95,5.53,5329,	
+183.85,6.32,5476,	
+186.2,6.81,5625,	
+190.2,7.14,5776,	
+192.2,7.05,5929,	
+195.09,6.82,6084,	
+196.97,5.9,6241,	
+200.59,4.07,6400/	
DATA (MCOEF(I,J),I=1,3),J=81,120)/	
+204.37,3.5,6561,	
+207.19,3.29,6724,	
+208.98,2.83,6889,	
+210.2,6.5,7056,	
+210.0,7225,	
+222.0,7396,	
+223.0,7569,	
+226.1,34,7744,	
+227.0,7921,	
+232.3,03,8100,	
+231.4,02,8281,	
+238.04,4.82,8464,	
+7.06,14.4,0,	!air
+0,0,0,	
+0,0,0,	
+0,0,0,	
+0,0,0,	
+0,0,0,	
+0,0,0,	
+0,0,0,	
+4.6,0.329,782,	!kimfol, 1.39 g/cm3
+7.7,4.09,38,.95,	!polyethylene, .95 g/cm3
+7.2,0.528,624,	!mylar, 1.4 g/cm3
+0,0,0,	
+0,0,0,	
+35,1.3,2421,	!ferrite, guess at 5 g/cm3
+51,.578,10764	!YBCO, 6.40 g/cm3
+0,0,0,	

Fig 1

STRAGGLING AND RANGE SHORTENING
ARE INSIGNIFICANT BEFORE THE END OF
THE TOTAL BEAM DEPTH-DOSE PROFILE

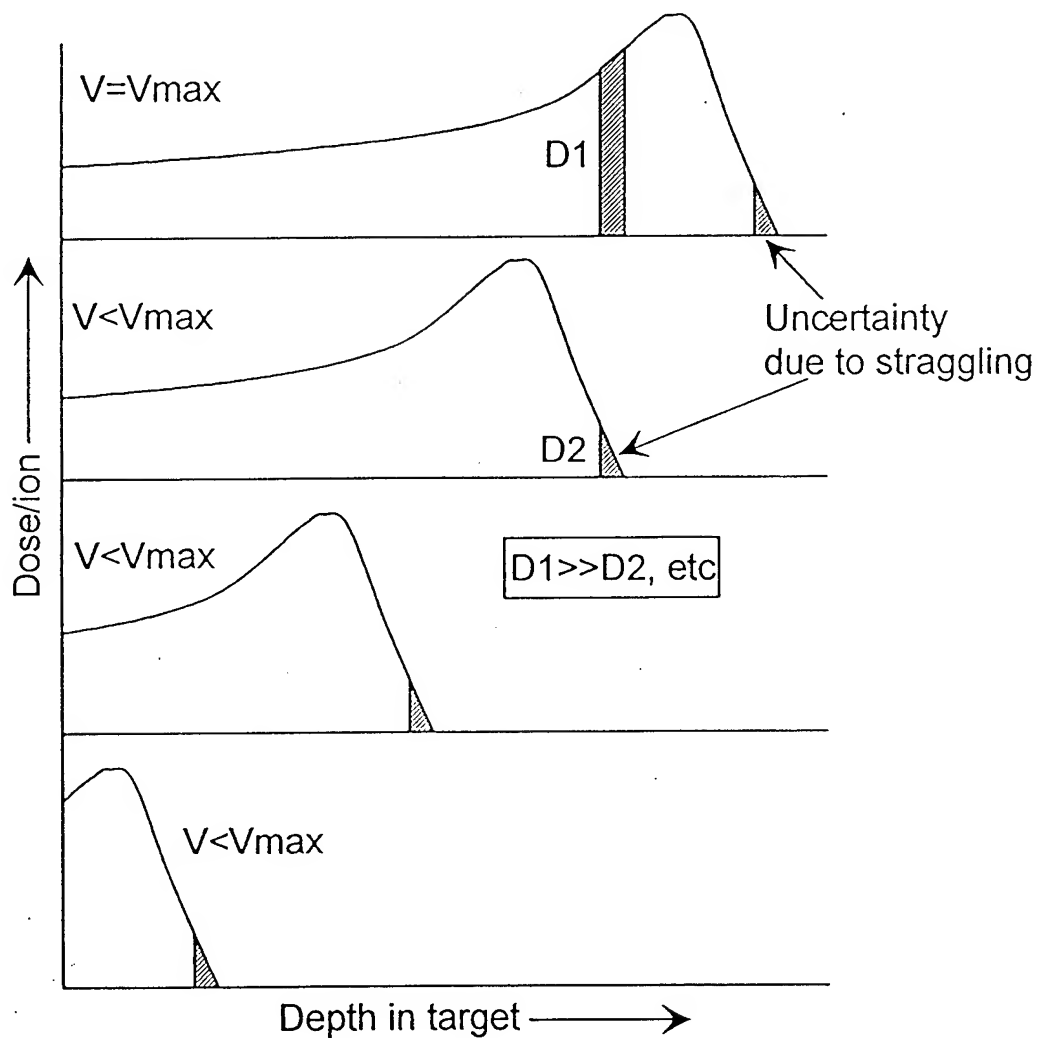


Fig 2

Shot 5960

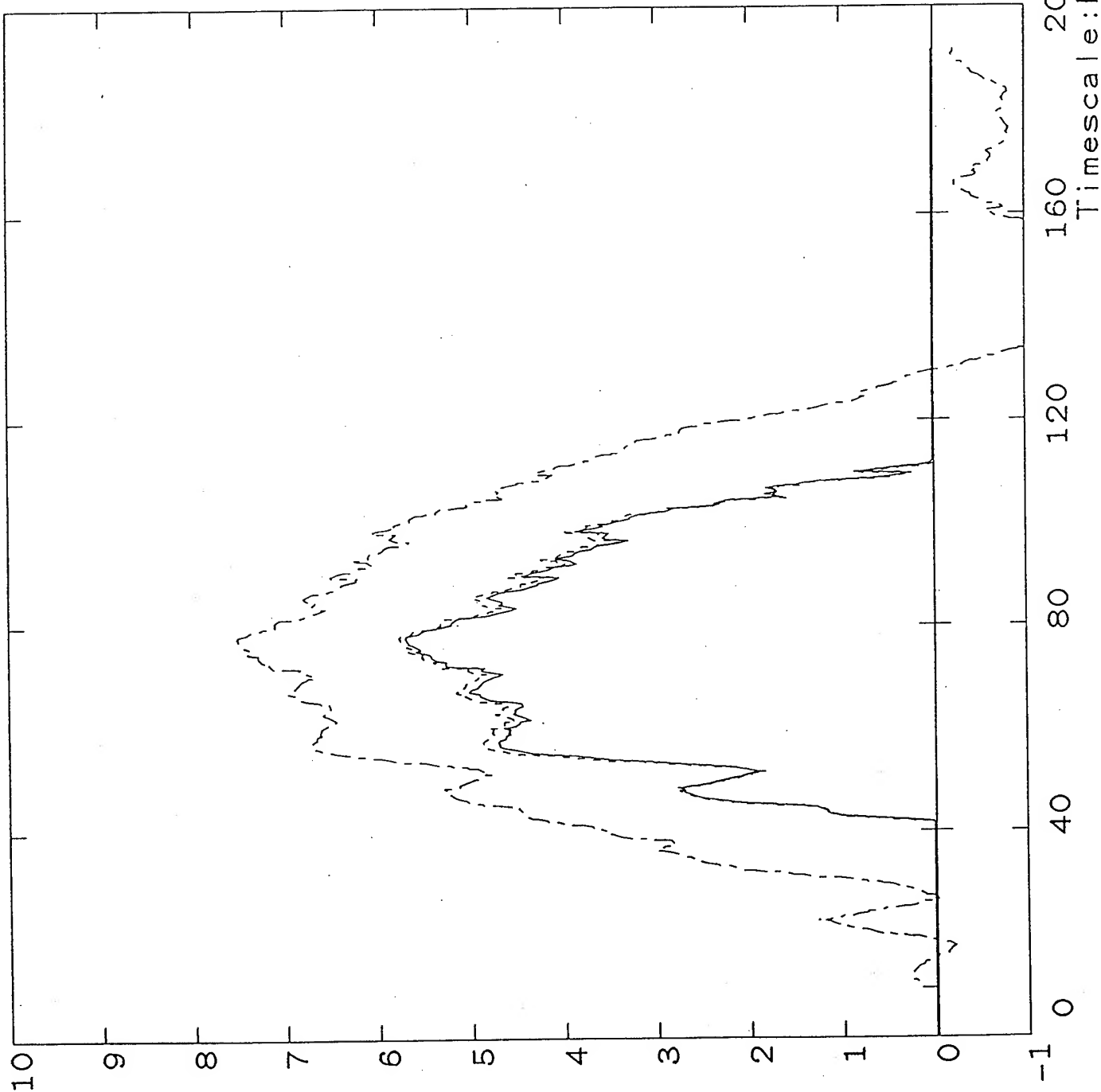
----- VTK1 Volts
Units: 2.00E+05
Max: 1.14E+06
Ts(ns): 0.00E+00
new

7 layers 1.8 μ
Kinfol

----- VTK2 Volts
Units: 2.00E+05
Max: 1.15E+06
Ts(ns): 0.00E+00

7 layers Kinfol
option 121
(018)

----- VCOR Volts
Units: 2.00E+05
Max: 1.50E+06
Ts(ns): 0.00E+00



Timescale: Nanoseconds

RADIOACTIVITIES PRODUCED BY
PROTON AND DEUTERON BEAMS UP TO 10 MeV*

Frank C. Young
Plasma Physics Division
Naval Research Laboratory
Washington, DC 20375-5320

and

David V. Rose
JAYCOR
Vienna, VA 22180-2270

Abstract: Proton and deuteron induced nuclear reactions which produce radioactivities are surveyed. Reactions with up to 10-MeV protons or deuterons on carbon, aluminum, titanium-alloy, steel, and brass targets are identified. For each target material, the nuclear reaction, associated radioactivity, half-life and decay products are tabulated. Measured cross sections from the published literature are used to identify reaction yields. For protons, thick-target yields are evaluated for (p,n) reactions on these targets. For deuterons, thick-target yields are evaluated for (d,n) , (d,p) and (d,α) reactions on these targets where cross sections are reported in the literature. Graphs of thick-target yield as a function of incident ion energy are presented for the elements in these targets

* Work supported by the Department of Energy through Sandia National Laboratories.

TABLE OF CONTENTS

I. Introduction	3
II. Explanation of Tables	6
III. Carbon Target	7
IV. Aluminum Target	9
V. Proton Induced Radioactivities in the Alloy Targets	11
VI. Deuteron Induced Radioactivities in the Alloy Targets	17
References	29

I. Introduction

Proton and deuteron induced nuclear reactions which produce radioactivity in commonly used materials are surveyed. The primary motivation for this survey is to provide sufficient nuclear data to evaluate the radiological hazard associated with ion induced radioactivities. Intense ion beam generators can produce MA level ion beams with particle energies of several MeV. Radioactivities induced in carbon, aluminum, steel, and brass exposed to such beams may pose a radiological hazard depending on the energy and intensity of the ion beam and on properties of the induced radioactivity. In addition, radioactivity induced by reactions in a titanium alloy is considered because this alloy is used in intense beam diodes.¹ The nuclear data tabulated in this report may be relevant to other technical areas, including radioisotope production, materials modification by ion implantation, and techniques to diagnose intense pulsed ion beams.

In this report, radioactivities produced by proton and deuteron beams incident on carbon, aluminum, titanium-alloy, steel, and brass targets are identified. For these singly-charged ion beams, incident energies of up to 10 MeV are considered. Proton and deuteron induced reactions leading to the following products are considered: neutrons, protons, deuterons, tritons, ^3He , and α particles. Both positive and negative Q-value reactions are included. The tabulation of Keller et al.² is used as a guide to identify the more energetically favorable reactions. Tabulated Q-values are based on mass excesses from Ref. 3. Positive Q-value reactions are allowed by kinematics for any bombarding energy. Negative Q-value reactions have a threshold energy given by $(M_1 + M_2)(-Q)/M_2$ where M_1 is the incident projectile mass and M_2 is the target mass.

For each reaction, the residual radioactive nucleus and its decay properties are tabulated. Reactions which produce the long-lived isotopes ^{53}Mn ($T_{1/2} = 3.7 \times 10^6$ yr), ^{59}Ni ($T_{1/2} = 8 \times 10^4$ yr), and ^{63}Ni ($T_{1/2} = 10^2$ yr) are not included in this survey. Unrealistically large ion beam fluences would be required to

produce significant activities of these long-lived isotopes. Decay modes, halflives, end-point energies and γ -ray energies for each radioisotope are taken from Ref. 4. The most intense γ -decays are identified from Ref. 5.

Measured cross sections for some of these reactions were found in the published literature. Compilations in Ref. 6 were used to locate published sources prior to 1976. Compilations in Ref. 7 were used to locate additional sources. The computerized catalog DIALOG⁸ was used for the period from 1976 to 1992. Since DIALOG does not include all the journals of interest in this time period, Physics Abstracts was used to supplement this survey. No attempt was made to incorporate cross sections from unpublished technical reports. Cross sections determined from residual activities, rather than prompt particle emissions, are the desired quantities. In many cases, excitation functions (cross sections as a function of incident proton energy) are determined by measuring delayed radioactivities induced in stacked foils. For reactions where sufficient excitation functions are available, the cross sections are combined with known stopping cross sections⁹ to determine thick-target yields. Graphs of thick-target yields versus incident ion energy are included in this report.

Reactions on carbon are discussed in Sec. III. Reactions on aluminum are discussed in Sec. IV. Proton induced reactions on titanium alloy, steel, and brass are discussed in Sec. V. Deuteron induced reactions on these alloy targets are discussed in Sec. VI. For the alloy targets, only isotopes for which the product of the isotopic abundance and the alloy proportion exceeds 1% are included because these isotopes are expected to be the primary sources of radioactivity.

For the proton induced reactions, radioactivities are produced primarily by (p,n) reactions. Yields for these reactions increase rapidly from threshold. Thresholds are less than 4 MeV for the carbon, titanium-alloy, steel, and brass targets and 5.8 MeV for an aluminum target. At 10 MeV, the $^{51}\text{V}(p,n)$ and $^{65}\text{Cu}(p,n)$ reactions have the largest thick-target yields ($\sim 10^{-3}$ reactions/proton); these two reactions also have

the smallest thresholds. Residual activities with hour-to-day halflives resulting from proton bombardment of aluminum, titanium, steel and brass have been measured and specific radioisotopes identified.¹⁰ The observed activities are consistent with the results of this survey.

For the deuteron induced reactions, radioactivities are produced primarily by the (d,n), (d,p), and (d, α) reactions. The (d, α) yields are smaller than the (d,n) or (d,p) yields. Thick-target yields for the (d,n) and (d,p) reactions increase rapidly at low energy and approach 5×10^{-4} reactions/deuteron at 10 MeV. At low energy, the (d,n) yield for carbon is larger than for the other targets presumably due to the smaller Coulomb barrier. In the energy range from 8 to 10 MeV, thick-target yields for the (d,n) and (d,p) reactions are similar so differences in the yields for different targets are due primarily to the different target abundances. For some of these reactions, significant differences are found in the literature for the same reaction cross section measured in different experiments by different researchers. In some cases, additional measurements have been reported in order to sort out these differences. However, large differences remain for the $^{27}\text{Al}(d,p)^{28}\text{Al}$ reaction, as indicated in Fig. 4. Additional measurements are needed to provide reliable cross sections for this reaction.

The radioactivity produced by a single intense pulse of ions can be evaluated from the thick-target yield. For a 100-kA, 100-ns duration pulse of protons or deuterons, the initial activity in Curies is given by $1.2 \times 10^6 f Y(E) / T_{1/2}$ where f is the fractional abundance of the target element in the alloy target; $Y(E)$ is the thick-target yield at energy E ; and $T_{1/2}$ is the halflife of the induced radioactivity in seconds. To illustrate this evaluation, activities are determined for two reactions which have large yields. For 10-MeV protons on brass, the ^{65}Zn activity from the $^{65}\text{Cu}(p,n)$ reaction is 34 μCurie , while the ^{63}Zn activity from the $^{63}\text{Cu}(p,n)$ reaction is 0.16 Curie. The large difference in these activities is due to the shorter ^{63}Zn halflife (38 min) compared with the ^{65}Zn halflife (244 da). For 10-MeV deuterons on carbon, the ^{13}N activity from the $^{12}\text{C}(d,n)$

reaction is 0.96 Curie. These examples indicate that relatively large radioactivities can be produced by intense proton or deuteron beams under some conditions. Much smaller activities are obtained for targets which have smaller yields and produce longer half-life activities. For example, for 10-MeV protons on the titanium-alloy target, the ^{47}V and ^{48}V activities from the $^{47}\text{Ti}(p,n)$ and $^{48}\text{Ti}(p,n)$ reactions are only 13 mCurie and 0.31 mCurie, respectively. These activities are even less for lower energy protons.

Radioactivities induced by ^7Li ions of up to 15 MeV on the same target materials have also been surveyed,¹¹ and some measurements of lithium induced radioactivities have been reported.¹⁰

Acknowledgements

Appreciation is expressed to Dr. Richard Peacock and Ms. Harriet Oxley of the Naval Research Laboratory Library Staff for their assistance with the DIALOG literature search. The encouragement of John Maenchen (Sandia National Laboratories) to carry out this work is appreciated.

II. Explanation of Tables

<u>Symbol</u>	<u>Explanation</u>
β^-	Decay by electron emission
β^+	Decay by positron emission
ϵ	Decay by electron capture
E_β	End-point energy for the β -spectrum
E_γ	Energy of the most intense γ -ray associated with the decay.
IT	Isomeric transition

Both β^+ and ϵ are listed when these two decay modes are of comparable intensity. Two values are listed for E_γ when these two γ -rays are of comparable intensity.

III. Carbon Target

Nuclear reactions on carbon leading to radioactive products are listed in Table I. A natural carbon target consists of two isotopes, ^{12}C and ^{13}C , with the abundances given in Table I. For thick-target calculations, the target is assumed to be natural-abundance carbon. Each reaction listed in Table I is discussed below, and thick-target yields are given in Figs. 1 and 2.

$^{12}\text{C}(p,\gamma)^{13}\text{N}$: The thick-target yield for this reaction below 3 MeV is determined by resonances at 457 keV and 1.70 MeV.¹² Above 3 MeV, the ^{13}N activity from the $^{13}\text{C}(p,n)$ reaction exceeds the $^{12}\text{C}(p,\gamma)$ activity even though the isotopic abundance of ^{13}C in natural carbon is only 1.1%.

$^{13}\text{C}(p,n)^{13}\text{N}$: The threshold for this reaction is 3.25 MeV. The thick-target yield is based on measured cross sections from Ref. 13. It should be noted that the ^{13}N activity can also be produced by the $^{16}\text{O}(p,\alpha)^{13}\text{N}$ reaction with comparable cross sections¹³ for proton energies above 7 MeV.

$^{12}\text{C}(d,n)^{13}\text{N}$: The threshold for this reaction is 0.33 MeV.¹⁵ The thick-target yield from 2 to 5 MeV has been reported for a natural carbon target,¹⁶ and this yield has been extended to lower energies using measured relative cross sections.¹² The measured cross sections of Wilkinson¹⁷ were used to extend the thick-target yield to 10 MeV. This reaction is the most prolific source of radioactivity for a carbon target over the energy range of interest.

$^{13}\text{C}(d,p)^{14}\text{C}$: This reaction was not seriously considered in this survey for three reasons. First, the small natural abundance of ^{13}C reduces the radioactivity from this reaction by two orders of magnitude for a natural carbon target. Second, the activity will be small because the ^{14}C half-life is long, e.g., it takes more radioactive nuclei to produce a given activity for a longer half-life. Third, the ^{14}C decay produces only a low energy β -particle which is easily shielded.

Table I

Radioactivities Induced by Protons or Deuterons
on Carbon

Target		Nuclear Reaction		Residual Nucleus			
Iso- tope	Abun- dance	Reaction	Q-Value (MeV)	Decay Mode	Half Life	E_{β} (MeV)	E_{γ} (MeV)
^{12}C	98.9%	$^{12}\text{C}(\text{p}, \gamma) ^{13}\text{N}$	+1.94	β^+	10 min	1.20	0.51
		$^{12}\text{C}(\text{d}, \text{n}) ^{13}\text{N}$	-0.28	β^+	10 min	1.20	0.51
^{13}C	1.1%	$^{13}\text{C}(\text{p}, \text{n}) ^{13}\text{N}$	-3.00	β^+	10 min	1.20	0.51
		$^{13}\text{C}(\text{d}, \text{p}) ^{14}\text{C}$	+5.95	β^-	5.7 yr	0.16	-

IV. Aluminum Target

Nuclear reactions on aluminum leading to radioactive products are listed in Table II. Aluminum consists of a single isotope, ^{27}Al . The target is assumed to be 100% aluminum for thick-target calculations. Each reaction listed in Table II is discussed below, and thick-target yields are given in Fig. 3.

$^{27}\text{Al}(p,n)^{27}\text{Si}$: The reaction threshold is 5.8 MeV. The thick-target yield is based on measured cross sections from Ref. 18.

$^{27}\text{Al}(p,d)^{26}\text{Al}$: The threshold for this reaction is 11.6 MeV. No activity is possible for proton energies below 10 MeV.

$^{27}\text{Al}(d,p)^{28}\text{Al}$: The cross section for this reaction is not well known. A best fit to cross sections measured in three different experiments (Refs. 19, 20 and 21) was used to generate a thick-target yield to 5 MeV for this reaction.²² This best-fit cross section curve is shown in Fig. 4, and the thick-target yield is given in Fig. 3. Cross sections from Ref. 21 were used to extend this yield curve to 10 MeV. Two more recent cross section measurements^{23,24} are much larger than the best fit from Ref. 22, as shown in Fig. 4. The reason for the large differences ($\times 160$ at 3 MeV and $\times 4$ at 6.8 MeV) is not known. The values in Ref. 23 (0.6 to 3.2 MeV) are based on thick-target measurements and are much larger than (d,p) cross sections on other nuclei in this mass range.⁷ In a thick target, additional ^{28}Al activity may be produced by the $^{27}\text{Al}(n,\gamma)^{28}\text{Al}$ reaction induced by neutrons from the $^{27}\text{Al}(d,n)^{28}\text{Si}$ reaction in the same target. This process may account for the large cross sections in Refs. 23 and 24. This process was shown to be negligible for the measurements in Ref. 21.

$^{27}\text{Al}(d,\alpha p)^{24}\text{Na}$: The kinematic threshold for this reaction is 5.8 MeV, but measured excitation functions^{24,25} for this reaction indicate that the cross section is small below 10 MeV. Therefore no significant activity is expected from this reaction.

$^{27}\text{Al}(d,2p)^{27}\text{Mg}$: The kinematic threshold for this reaction is 4.4 MeV, but measured cross sections^{24,26} indicate that the yield is small below 10 MeV. Therefore, no thick-target yield was evaluated for this reaction.

Table II

Radioactivities Induced by Protons or Deuterons
on Aluminum

Target		Nuclear Reaction		Residual Nucleus			
Iso- tope	Abun- dance	Reaction	Q-Value (MeV)	Decay Mode	Half Life	E_{β} (MeV)	E_{γ} (MeV)
^{27}Al	100%	$^{27}\text{Al}(\text{p}, \text{n})^{27}\text{Si}$	-5.59	β^+	4.2 s	3.8	0.51
		$^{27}\text{Al}(\text{p}, \text{d})^{26}\text{Al}$	-10.8	β^+, ϵ	6.4 s	3.21	0.51
		$^{27}\text{Al}(\text{d}, \text{p})^{28}\text{Al}$	+5.51	β^-	2.24 min	2.86	1.78
		$^{27}\text{Al}(\text{d}, \alpha\text{p})^{24}\text{Na}$	-5.36	β^-	15.0 hr	1.39	2.75 1.37
		$^{27}\text{Al}(\text{d}, 2\text{p})^{27}\text{Mg}$	-4.06	β^-	9.45 min	1.77	0.844

V. Proton Induced Radioactivities in the Alloy Targets

For the medium-weight nuclei in titanium-alloy, steel, and brass targets, radioactivities are produced typically by either (p,n) or (p, α) reactions. Radioactivities produced by these reactions are identified, and reaction yields are briefly discussed for the constituent elements of these alloys. Thick-target yields for these targets have not been reduced by the alloy composition since these may change from one material to another.

A. Titanium-Alloy Target

The titanium 6-4 alloy consists of 90% titanium, 6% aluminum and 4% vanadium. Titanium consists of five stable isotopes with abundances ranging from 5% to 74%, while vanadium is 99.8% ^{51}V . Radioactivity produced by irradiation of the aluminum in this alloy was discussed in Sec. IV. Proton induced reactions on titanium and vanadium leading to radioactive products are listed in Table III. The (p,n) and (p, α) reactions are discussed below, and (p,n) thick-target yields are given in Figs. 5 and 6.

(p,n) Reactions: The threshold for the (p,n) reaction on ^{46}Ti is 8.0 MeV. Immediately above threshold, ^{46}V activity has been measured,²⁷ but the cross section was not reported. The (p,n) reactions on ^{47}Ti and ^{48}Ti have lower thresholds of 3.78 and 4.90 MeV, respectively, and their cross sections have been measured.²⁸ Smooth fits were made to these cross sections to determine thick-target yields for a natural-abundance titanium target. These reactions are primary sources of radioactivity from the proton bombardment of titanium. To produce significant activation of the long-lived ^{49}V isotope by the $^{49}\text{Ti}(p,n)$ reaction, extremely large proton fluences would be required. Furthermore, ^{49}V decays only by electron capture so its radiation hazard is minimal. For vanadium, the threshold for the (p,n) reaction is 1.56 MeV, and cross sections for this reaction have been determined from 3.1 to 10.4 MeV by measuring ^{51}Cr activity²⁹ and from 1.6 to 4.5 MeV by measuring neutron emission.³⁰ Independent measurements with these two techniques³¹ are

Table III

Radioactivities Induced by Protons on Titanium and Vanadium

Target		Nuclear Reaction		Residual Nucleus			
Iso- tope	Abun- dance	Reaction	Q-Value (MeV)	Decay Mode	Half Life	E_{β} (MeV)	E_{γ} (MeV)
^{46}Ti	8.0%	$^{46}\text{Ti}(p,n)^{46}\text{V}$	-7.85	β^+	0.43 s	6.04	0.51
		$^{46}\text{Ti}(p,\alpha)^{43}\text{Sc}$	-3.09	β^+	3.89 hr	1.20	0.51
^{47}Ti	7.5%	$^{47}\text{Ti}(p,n)^{47}\text{V}$	-3.70	β^+	31 min	1.90	0.51
		$^{47}\text{Ti}(p,\alpha)^{44}\text{Sc}$	-2.25	β^+	3.93 hr	1.47	1.16
^{48}Ti	73.7%	$^{48}\text{Ti}(p,n)^{48}\text{V}$	-4.80	β^+, ϵ	16.0 da	0.70	1.31 0.98
^{49}Ti	5.5%	$^{49}\text{Ti}(p,n)^{49}\text{V}$	-1.39	ϵ	331 da	-	-
		$^{49}\text{Ti}(p,\alpha)^{46}\text{Sc}$	-1.94	β^-	83.8 da	0.36	1.12 0.89
^{50}Ti	5.3%	$^{50}\text{Ti}(p,\alpha)^{47}\text{Sc}$	-2.24	β^-	3.41 da	0.44	0.16
^{51}V	99.8%	$^{51}\text{V}(p,n)^{51}\text{Cr}$	-1.53	ϵ	27.7 da	-	0.32

consistent and are in agreement with the measurements in Ref. 30. Therefore, the cross sections from Ref. 29 are scaled to values in Ref. 30 to provide cross sections from 1.6 to 10.5 MeV. A smooth fit to these cross sections was used to calculate the thick-target yield.

(p, α) Reactions: Thresholds for the (p, α) reactions on ^{46}Ti , ^{47}Ti , ^{49}Ti and ^{50}Ti range from 2.0 to 3.2 MeV. The (p, α) reaction on ^{48}Ti , the most abundant isotope, produces no radioactivity. These reactions tend to have small cross sections as described in Sec. VB. The reactions on ^{46}Ti and ^{50}Ti have been measured by detecting α -emission, and ground-state differential cross sections of only 0.03 to 0.4 mb/sr for 9- to 10-MeV protons have been reported.³² For 14-MeV protons, total cross sections of 30 mb for ^{48}Ti and 25 mb for ^{51}V have been measured.³³ Because cross sections below 10 MeV are expected to be small and measured excitation functions are not available in the literature, no thick-target yields were evaluated for these reactions.

B. Steel and Brass Targets

These alloy targets contain several elements in different proportions. For this survey, a 70% iron, 20% chromium, 10% nickel composition is assumed for #304 stainless steel. The brass composition is 67% copper and 33% zinc. Each of these elements consists of several stable isotopes with significant fractional abundances. Proton induced reactions leading to radioactive products are listed in Table IV for a steel target and in Table V for a brass target. Reactions listed in these two Tables are discussed below. Thick-target yields for the elements in the steel target are given in Figs. 7, 8, and 9. Thick-target yields for copper and zinc, the elements in brass, are given in Figs. 10 and 11.

(p,n) Reactions: Thresholds for the (p,n) reactions range from 1.65 MeV for ^{57}Fe to 9.51 MeV for ^{58}Ni . These reactions have been studied extensively and their cross sections increase rapidly from zero at threshold to relatively large values (10^2 - 10^3 mb) a few MeV above threshold. For chromium, two activities

Table IV

Radioactivities Induced by Protons on Chromium, Iron and Nickel

Target		Nuclear Reaction		Residual Nucleus			
Iso- tope	Abun- dance	Reaction	Q-Value (MeV)	Decay Mode	Half Life	E_{β} (MeV)	E_{γ} (MeV)
^{52}Cr	83.8%	$^{52}\text{Cr}(p,n)^{52}\text{Mn}$	-5.49	ϵ, β^+	5.6 da	0.57	1.434 0.94 0.74
		$^{52}\text{Cr}(p,n)^{52m}\text{Mn}$	-5.87	β^+	21 min	2.63	1.434
		$^{52}\text{Cr}(p,\alpha)^{49}\text{V}$	-2.60	ϵ	331 da	-	-
^{54}Fe	5.8%	$^{54}\text{Fe}(p,n)^{54}\text{Co}$	-9.03	β^+	1.5 min	4.3	0.51
		$^{54}\text{Fe}(p,\alpha)^{51}\text{Mn}$	-3.12	β^+	46 min	2.2	0.51
^{56}Fe	91.7%	$^{56}\text{Fe}(p,n)^{56}\text{Co}$	-5.36	ϵ, β^+	78 da	1.46	0.847
^{57}Fe	2.1%	$^{57}\text{Fe}(p,n)^{57}\text{Co}$	-1.62	ϵ	271 da	-	0.122
		$^{57}\text{Fe}(p,\alpha)^{54}\text{Mn}$	+0.24	ϵ	312 da	-	0.835
^{58}Ni	68.3%	$^{58}\text{Ni}(p,n)^{58}\text{Cu}$	-9.35	β^+	3.2 s	7.5	1.45
		$^{58}\text{Ni}(p,\alpha)^{55}\text{Co}$	-1.35	β^+, ϵ	17.9 hr	1.5	0.51
^{60}Ni	26.1%	$^{60}\text{Ni}(p,n)^{60}\text{Cu}$	-6.91	β^+	23 min	3.77	1.76 1.33
		$^{60}\text{Ni}(p,\alpha)^{57}\text{Co}$	-0.27	ϵ	271 da	-	0.122

Table V

Radioactivities Induced by Protons on Copper and Zinc

Target		Nuclear Reaction		Residual Nucleus			
Iso- tope	Abun- dance	Reaction	Q-Value (MeV)	Decay Mode	Half Life	E_{β} (MeV)	E_{γ} (MeV)
^{63}Cu	69.1%	$^{63}\text{Cu}(p,n)^{63}\text{Zn}$	-4.15	β^+	38 min	2.34	0.51
		$^{63}\text{Cu}(p,d)^{62}\text{Cu}$	-8.62	β^+	9.8 min	2.93	0.51
^{65}Cu	30.9%	$^{65}\text{Cu}(p,n)^{65}\text{Zn}$	-2.13	ϵ	244 da	-	1.115
		$^{65}\text{Cu}(p,d)^{64}\text{Cu}$	-7.69	β^-	12.8 hr	0.575	-
				ϵ, β^+	12.8 hr	0.656	0.51
		$^{65}\text{Cu}(p,\alpha d)^{61}\text{Co}$	-6.76	β^-	1.65 hr	1.24	0.068
		$^{65}\text{Cu}(p,\alpha\alpha)^{57}\text{Mn}$	-7.35	β^-	1.6 min	2.56	0.122
^{64}Zn	48.9%	$^{64}\text{Zn}(p,n)^{64}\text{Ga}$	-7.85	β^+	2.6 min	6.05	0.51
		$^{64}\text{Zn}(p,\alpha)^{61}\text{Cu}$	+0.85	β^+, ϵ	3.4 hr	1.22	0.51
^{66}Zn	27.8%	$^{66}\text{Zn}(p,n)^{66}\text{Ga}$	-5.96	β^+, ϵ	9.5 hr	4.15	0.51
		$^{66}\text{Zn}(p,d)^{65}\text{Zn}$	-8.81	ϵ	244 da	-	1.115
^{68}Zn	18.6%	$^{68}\text{Zn}(p,n)^{68}\text{Ga}$	-3.70	β^+	68 min	1.90	0.51

are produced: the 5.6-da ground state and a 21-min isomer. The symbol ^{52m}Mn in Tables IV and V refers to an isomeric state where ^{52}Mn is the ground state. Thick-target yields for the (p,n) reaction on ^{52}Cr were calculated using cross sections from Refs. 29, 34, and 35. For iron, (p,n) cross sections are taken from Ref. 27 for ^{57}Fe and from Ref. 36 for ^{56}Fe . The cross sections from Ref. 36 below 10 MeV fit smoothly onto the cross sections from Ref. 37 above 10 MeV. A precise threshold measurement has been reported for the (p,n) reaction on ^{54}Fe , (Ref. 38) but no cross sections were found in the literature. The 9.20-MeV threshold for this reaction suggests that little activity can be expected below 10 MeV. For nickel, little activation is expected below 10 MeV. Activity from the (p,n) reaction on Ni^{58} is limited by the 9.51-MeV threshold. The thick-target yield for the (p,n) reaction on ^{60}Ni is calculated from cross sections in Ref. 39. For copper, the (p,n) thick-target yields for ^{63}Cu and ^{65}Cu are based on cross sections found in Ref. 40. For zinc, (p,n) cross sections were taken from Ref. 41 for ^{64}Zn , and from Refs. 41-43 for ^{66}Zn and ^{68}Zn . Smooth fits were made to these cross sections to evaluate the thick-target yields.

(p, α) reactions: No excitation functions were found in the literature for chromium, iron, or copper targets for proton energies below 9 MeV. Above 9 MeV, excitation functions have been determined for a variety of targets by measuring emitted α -particles,⁴⁴⁻⁴⁶ rather than residual radioactivities. These (p, α) studies indicate that this reaction proceeds by a compound-nucleus process where the incident proton penetrates the Coulomb barrier of the target nucleus and excites the target. The density of nuclear excited states is large for these medium weight nuclei so that a statistical treatment of the compound nucleus is appropriate. The α -particle emission is described by an α -particle preformation coefficient in the nucleus and by Coulomb barrier transmission to exit the nucleus. Since the Coulomb barrier in this mass range is about 6.5 MeV for protons and about 13 MeV for α -particles, (p, α) cross sections should be small below 10 MeV. At 10 MeV, modest cross sections (31 mb for copper, 29 mb for zinc, 9 mb for iron, and 5 mb for chromium)

have been reported.^{44,45} The $^{64}\text{Zn}(p,\alpha)$ cross section has been determined from 8 to 22 MeV by measuring residual radioactivity.⁴⁷ Despite the positive Q-value of this reaction, the cross section is only 17 mb at 8 MeV and increases to a maximum of 80 mb at 15 MeV. For nickel, thick-target yields to produce ^{55}Co and ^{57}Co activities were calculated using cross sections from Ref. 48. For all these (p,α) reactions, the excitation functions decrease rapidly with decreasing energy as expected from Coulomb-barrier-penetration considerations. A similar argument applies to the $^{65}\text{Cu}(p,\alpha\alpha)$ and $^{65}\text{Cu}(p,\alpha d)$ reactions.

(p,d) reactions: These reactions on copper and zinc have large negative Q-values. Experiments indicate that these reactions are not common for medium-weight elements.⁴⁹ On the other hand, (p,pn) reactions are commonly observed. These reactions require an additional 2.22 MeV which corresponds to thresholds greater than 10 MeV for the (p,pn) reactions on ^{65}Cu and ^{66}Zn .

VI. Deuteron Induced Radioactivities in the Alloy Targets

For the medium-weight elements in the titanium-alloy, steel, and brass targets, a specific radioactivity may be produced by several different deuteron induced reactions. Therefore, it is difficult to associate a measured radioactivity with one nuclear reaction. Consequently, only a limited number of excitation functions for deuteron induced reactions have been measured for these elements. Furthermore, the (d,n) , (d,p) and (d,α) reactions all have positive Q-values and cross sections on the order of 100 mb above the Coulomb barrier. For deuterons in the few MeV range (below the Coulomb barrier), the (d,α) reactions have appreciably smaller cross sections than the (d,n) and (d,α) reactions.⁵⁰ Substantial radioactivities can be expected from these reactions, and the following discussion will focus on these reactions. Deuteron-induced reactions leading to radioactivities are identified, and activation yields are briefly discussed for these alloy targets.

A. Titanium-Alloy Target

Deuteron induced reactions on titanium and vanadium in the titanium alloy target which lead to radioactive products are listed in Table V. For titanium, there are four isotopes with abundances of 5% to 8%, while ^{48}Ti is 74% abundant. Cross sections for the $^{47}\text{Ti}(\text{d},\text{n})$ reaction and for the (d,α) reactions on ^{46}Ti , ^{48}Ti and ^{49}Ti have been determined in the range from 5.5 to 10 MeV,⁵¹ but these measurements are insufficient to evaluate thick-target yields. These cross sections increase monotonically up to 10 MeV with values at 10 MeV of 130 mb for the (d,n) reaction and 40 to 80 mb for the (d,α) reactions. For the bombardment of a natural titanium target with 6.5-MeV deuterons, a thick-target yield of 8.3×10^{-5} ^{48}V /deuteron has been reported for producing ^{48}V activity.⁵² This activity includes both the $^{47}\text{Ti}(\text{d},\text{n})^{48}\text{V}$ and $^{48}\text{Ti}(\text{d},2\text{n})^{48}\text{V}$ reactions. Cross sections for several of the negative Q-value reactions on titanium are negligible below 5 MeV and increase rapidly with energy from 5 and 10 MeV. For example, the $^{47}\text{Ti}(\text{d},2\text{n})^{47}\text{V}$ reaction cross section is negligible at 5.5 MeV, but approaches 200 mb at 10 MeV.⁵¹ A similar behavior is observed for the $^{48}\text{Ti}(\text{d},2\text{n})^{48}\text{V}$ reaction.⁵³ The (d,n) and (d,α) reactions on the most abundant ^{48}Ti isotope lead to rather long-lived isotopes so large activities are not expected for these reactions. Shorter half-life activities are produced by these reactions on the other isotopes, however these activities are reduced by the smaller isotopic abundances. Consequently, the activation of titanium by deuterons is not as large as for some other target materials.

For vanadium, the most likely source of radioactivity is the positive Q-value $^{51}\text{V}(\text{d},\text{p})^{52}\text{V}$ reaction. Cross sections for this reaction, based on proton measurements, are 11 mb at 3.8 MeV and 17 mb at 4.5 MeV.⁵⁴ Even larger cross sections can be expected for the activation of ^{52}V because these proton measurements include only higher-energy emitted protons. Thick-target yields for producing ^{51}Cr by deuteron bombardment of vanadium has been reported.⁵⁵ This yield is nearly zero at 5 MeV and increases monotonically to 2.3×10^{-4} ^{51}Cr /deuteron at 10 MeV. This activity is attributed to the $^{51}\text{V}(\text{d},2\text{n})^{51}\text{Cr}$ reaction. No other

Table V

Radioactivities Induced by Deuterons on Titanium and Vanadium

Target		Nuclear Reaction		Residual Nucleus			
Iso- tope	Abun- dance	Reaction	Q-Value (MeV)	Decay Mode	Half Life	E_{β} (MeV)	E_{γ} (MeV)
^{46}Ti	8.0%	$^{46}\text{Ti}(d,n)^{47}\text{V}$	+2.95	β^+	31 min	1.90	0.51
		$^{46}\text{Ti}(d,t)^{45}\text{Ti}$	-6.94	β^+	3.08 hr	1.04	0.51
		$^{46}\text{Ti}(d,\alpha)^{44}\text{Sc}$	+4.40	β^+	3.93 hr	1.47	1.16
		$^{46}\text{Ti}(d,2p)^{46}\text{Sc}$	-3.81	β^-	83.8 da	0.36	1.12 0.89
		$^{46}\text{Ti}(d,\alpha n)^{43}\text{Sc}$	-5.31	β^+	3.89 hr	1.20	0.51
^{47}Ti	7.5%	$^{47}\text{Ti}(d,n)^{48}\text{V}$	+4.61	β^+, ϵ	16.0 da	0.70	1.31 0.98
		$^{47}\text{Ti}(d,^3\text{He})^{46}\text{Sc}$	-4.97	β^-	83.8 da	0.36	1.12 0.89
		$^{47}\text{Ti}(d,2p)^{47}\text{Sc}$	-2.04	β^-	3.41 da	0.44	0.16
		$^{47}\text{Ti}(d,2n)^{47}\text{V}$	-5.92	β^+	31 min	1.90	0.51
		$^{47}\text{Ti}(d,\alpha n)^{44}\text{Sc}$	-4.47	β^+	3.93 hr	1.47	1.16
^{48}Ti	73.7%	$^{48}\text{Ti}(d,n)^{49}\text{V}$	+4.52	ϵ	331 da	-	-
		$^{48}\text{Ti}(d,^3\text{He})^{47}\text{Sc}$	-5.95	β^-	3.41 da	0.44	0.16
		$^{48}\text{Ti}(d,\alpha)^{46}\text{Sc}$	+3.98	β^-	83.8 da	0.36	1.12 0.89
		$^{48}\text{Ti}(d,2p)^{48}\text{Sc}$	-5.42	β^-	43.7 hr	0.65	1.31 1.04 0.98
		$^{48}\text{Ti}(d,2n)^{48}\text{V}$	-7.02	β^+, ϵ	16.0 da	0.70	1.31 0.98
		$^{48}\text{Ti}(d,\alpha p)^{45}\text{Ca}$	-4.25	β^-	163 da	0.26	-
		$^{48}\text{Ti}(d,2\alpha)^{42}\text{K}$	-5.18	β^-	12.4 hr	3.52	1.53

Continued on next page.

Table V Continued

Radioactivities Induced by Deuterons on Titanium and Vanadium

Target		Nuclear Reaction		Residual Nucleus			
Iso- tope	Abun- dance	Reaction	Q-Value (MeV)	Decay Mode	Half Life	E_β (MeV)	E_γ (MeV)
^{49}Ti	5.5%	$^{49}\text{Ti}(d, ^3\text{He})^{48}\text{Sc}$	-5.85	β^-	43.7 hr	0.65	1.31 1.04 0.98
		$^{49}\text{Ti}(d, \alpha)^{47}\text{Sc}$	+6.48	β^-	3.41 da	0.44	0.16
		$^{49}\text{Ti}(d, 2p)^{49}\text{Sc}$	-3.45	β^-	57 min	2.00	-
		$^{49}\text{Ti}(d, \alpha n)^{46}\text{Sc}$	-4.16	β^-	83.8 da	0.36	1.12 0.89
		$^{49}\text{Ti}(d, 2\alpha)^{43}\text{K}$	-3.69	β^-	22.2 hr	0.83	0.62 0.37
^{50}Ti	5.3%	$^{50}\text{Ti}(d, p)^{51}\text{Ti}$	+4.16	β^-	5.8 min	2.14	0.32
		$^{50}\text{Ti}(d, ^3\text{He})^{49}\text{Sc}$	-6.68	β^-	57 min	2.00	-
		$^{50}\text{Ti}(d, \alpha)^{48}\text{Sc}$	+3.79	β^-	43.7 hr	0.65	1.31 1.04 0.98
		$^{50}\text{Ti}(d, 2p)^{50}\text{Sc}$	-7.91	β^-	1.7 min	3.7	1.55
		$^{50}\text{Ti}(d, \alpha n)^{47}\text{Sc}$	-4.47	β^-	3.41 da	0.44	0.16
		$^{50}\text{Ti}(d, \alpha p)^{47}\text{Ca}$	-5.66	β^-	4.54 da	0.69	1.30
		$^{50}\text{Ti}(d, 2\alpha)^{44}\text{K}$	-7.79	β^-	22 min	5.66	1.16
^{51}V	99.8%	$^{51}\text{V}(d, p)^{52}\text{V}$	+5.08	β^-	3.8 min	2.5	1.43
		$^{51}\text{V}(d, 2p)^{51}\text{Ti}$	-3.90	β^-	5.8 min	2.14	0.32
		$^{51}\text{V}(d, 2n)^{51}\text{Cr}$	-3.76	ϵ	27.7 da	-	0.32
		$^{51}\text{V}(d, \alpha p)^{48}\text{Sc}$	-4.27	β^-	43.7 hr	0.65	1.31 1.04 0.98
		$^{51}\text{V}(d, 2\alpha)^{45}\text{Ca}$	-3.10	β^-	163 da	0.26	-

activation cross sections have been published for deuterons on vanadium.

B. Steel Target

Deuteron induced reactions leading to radioactive products are listed in Table VI for a steel target. For the 20% chromium component of this target, only ^{52}Cr and ^{53}Cr have significant abundances. For natural-abundance chromium, the thick-target yield (reactions/deuteron) at 8 MeV for activating ^{52}Mn by the $^{52}\text{Cr}(d,2n)^{52}\text{Mn}$ reaction is $7\times$ less than the thick-target yield for activating ^{51}Cr by the $^{50}\text{Cr}(d,n)^{51}\text{Mn}(\beta^-)^{51}\text{Cr}$ and $^{50}\text{Cr}(d,p)^{51}\text{Cr}$ reactions.⁵⁶ The isotopic abundance of ^{50}Cr is only 4.4%. Reactions on ^{50}Cr are not included in Table VI because the abundance of this isotope in a steel target is less than 1%, and ^{51}Cr is not expected to be a primary source of radioactivity. Above 8 MeV, the activation of ^{52}Mn increases rapidly with energy, and calculated thick-target yields for Mn^{52} and the isomer Mn^{52m} , evaluated using cross sections from Ref. 57, are presented in Fig. 12. The thick-target yield for producing ^{54}Mn by deuteron bombardment of chromium has been determined.⁵⁶ This yield increases monotonically from nearly zero at 1 MeV to 5.8×10^{-5} ^{54}Mn /deuteron at 10 MeV.

Radioactivities produced by deuteron induced reactions on natural iron have been identified and excitation functions have been measured for deuterons above 5 MeV.⁵⁸ In the range from 5 to 10 MeV, the largest activation cross sections are for ^{55}Co , ^{57}Co , and ^{54}Mn . The cobalt activities are induced principally by the $^{54}\text{Fe}(d,n)^{55}\text{Co}$ and $^{56}\text{Fe}(d,n)^{57}\text{Co}$ reactions. Below 5 MeV, ^{55}Co activation cross sections,⁵⁹ measured over the energy range from 2.44 to 5.5 MeV, are a factor-of-two smaller than the cross sections in Ref. 58. The cross sections in Ref. 59 were used to evaluate thick-target yields because the initial deuteron energy for the stacked-foil measurements in this experiment is 5.5 MeV, compared with 40 MeV in Ref. 58. The excitation function for ^{55}Co in Ref. 58 is scaled to cross sections in Ref. 59 to give activation cross sections for ^{55}Co and ^{57}Co up to 10 MeV. The ^{54}Mn activity is produced principally by the $^{56}\text{Fe}(d,\alpha)^{54}\text{Mn}$ and

Table VI

Radioactivities Induced by Deuterons on Chromium,
Iron and Nickel

Target		Nuclear Reaction		Residual Nucleus			
Iso- tope	Abun- dance	Reaction	Q-Value (MeV)	Decay Mode	Half Life	E_{β} (MeV)	E_{γ} (MeV)
^{52}Cr	83.8%	$^{52}\text{Cr}(d, t)^{51}\text{Cr}$	-5.78	ϵ	27.7 da	-	-
		$^{52}\text{Cr}(d, 2n)^{52}\text{Mn}$	-7.78	ϵ, β^+	5.6 da	0.57	1.434 0.94 0.74
		$^{52}\text{Cr}(d, 2n)^{52m}\text{Mn}$	-8.10	β^+	21 min	2.63	1.43
		$^{52}\text{Cr}(d, 2p)^{52}\text{V}$	-3.98	β^-	3.8 min	2.5	1.43
		$^{53}\text{Cr}(d, n)^{54}\text{Mn}$	5.34	ϵ	312 da	-	0.835
^{53}Cr	9.5%	$^{53}\text{Cr}(d, ^3\text{He})^{52}\text{V}$	-5.64	β^-	3.8 min	2.5	1.43
		$^{53}\text{Cr}(d, 2p)^{53}\text{V}$	-4.5	β^-	1.6 min	2.4	1.00
		$^{54}\text{Fe}(d, n)^{55}\text{Co}$	2.83	β^+, ϵ	17.9 hr	1.5	0.51
^{54}Fe	5.8%	$^{54}\text{Fe}(d, p)^{55}\text{Fe}$	7.08	ϵ	2.7 yr	-	-
		$^{54}\text{Fe}(d, t)^{53}\text{Fe}$	-7.36	β^+	8.5 min	2.8	0.51
		$^{54}\text{Fe}(d, \alpha)^{52}\text{Mn}$	5.17	ϵ, β^+	5.6 da	0.57	1.434 0.94 0.74
		$^{54}\text{Fe}(d, \alpha)^{52m}\text{Mn}$	4.79	β^+	21 min	2.63	1.43
		$^{54}\text{Fe}(d, 2p)^{54}\text{Mn}$	-2.14	ϵ	312 da	-	0.835
		$^{56}\text{Fe}(d, n)^{57}\text{Co}$	3.80	ϵ	271 da	-	0.122
		$^{56}\text{Fe}(d, t)^{55}\text{Fe}$	-4.95	ϵ	2.7 yr	-	-
^{56}Fe	91.7%	$^{56}\text{Fe}(d, \alpha)^{54}\text{Mn}$	5.66	ϵ	312 da	-	0.835
		$^{56}\text{Fe}(d, 2n)^{56}\text{Co}$	-7.58	ϵ, β^+	78 da	1.46	0.847
		$^{56}\text{Fe}(d, 2p)^{56}\text{Mn}$	-5.14	β^-	2.58 hr	2.85	0.847

Continued on next page

Table VI Continued

Radioactivities Induced by Deuterons on Chromium,
Iron and Nickel

Target		Nuclear Reaction		Residual Nucleus			
Iso- tope	Abun- dance	Reaction	Q-Value (MeV)	Decay Mode	Half Life	E_{β} (MeV)	E_{γ} (MeV)
^{57}Fe	2.1%	$^{57}\text{Fe}(\text{d}, \text{n})^{58}\text{Co}$	4.73	ϵ, β^+	71 da	0.47	0.81
		$^{57}\text{Fe}(\text{d}, ^3\text{He})^{56}\text{Mn}$	-5.07	β^-	2.58 hr	2.85	0.847
		$^{57}\text{Fe}(\text{d}, 2\text{n})^{57}\text{Co}$	-3.84	ϵ	271 da	-	0.122
		$^{57}\text{Fe}(\text{d}, 2\text{p})^{57}\text{Mn}$	-4.14	β^-	1.6 min	2.56	0.122
^{58}Ni	68.3%	$^{58}\text{Ni}(\text{d}, \text{n})^{59}\text{Cu}$	1.20	β^+	82 s	3.78	0.51
		$^{58}\text{Ni}(\text{d}, \alpha)^{56}\text{Co}$	6.51	ϵ, β^+	78 da	1.46	0.847
		$^{58}\text{Ni}(\text{d}, \text{t})^{57}\text{Ni}$	-5.94	ϵ, β^+	36 hr	0.84	1.37
		$^{58}\text{Ni}(\text{d}, ^3\text{He})^{57}\text{Co}$	-2.68	ϵ	271 da	-	0.122
		$^{58}\text{Ni}(\text{d}, 2\text{p})^{58}\text{Co}$	-1.83	ϵ, β^+	71 da	0.47	0.81
		$^{58}\text{Ni}(\text{d}, \alpha\text{n})^{55}\text{Co}$	-3.57	β^+, ϵ	17.9 hr	1.5	0.51
		$^{58}\text{Ni}(\text{d}, \alpha\text{p})^{55}\text{Fe}$	0.67	ϵ	2.7 yr	-	-
		$^{58}\text{Ni}(\text{d}, 2\alpha)^{54}\text{Mn}$	3.61	ϵ	312 da	-	0.835
^{60}Ni	26.1%	$^{60}\text{Ni}(\text{d}, \text{n})^{61}\text{Cu}$	2.58	β^+, ϵ	3.4 hr	1.22	0.51
		$^{60}\text{Ni}(\text{d}, \alpha)^{58}\text{Co}$	6.08	ϵ, β^+	71 da	0.47	0.81
		$^{60}\text{Ni}(\text{d}, 2\text{n})^{60}\text{Cu}$	-9.13	β^+	23 min	3.77	1.33
		$^{60}\text{Ni}(\text{d}, 2\text{p})^{60}\text{Co}$	-4.26	β^-	5.27 yr	0.32	1.17 1.33
		$^{60}\text{Ni}(\text{d}, \alpha\text{n})^{57}\text{Co}$	-2.49	ϵ	271 da	-	0.122

$^{54}\text{Fe}(d,2p)^{54}\text{Mn}$ reactions, and cross sections for ^{54}Mn are taken from Ref. 58. Thick-target yields for a natural iron target, calculated using these cross sections, are presented in Fig. 13.

For the 10% nickel component in the steel target, only ^{58}Ni and ^{60}Ni have significant abundances. Excitation functions for (d,n) reactions on these nuclei have been measured over the energy range from 2 to 12 MeV.⁶⁰ These cross sections increase rapidly with energy up to peaks of 200 mb at 8 MeV for ^{58}Ni and 470 mb at 8 MeV for ^{60}Ni . Above these peaks, the cross sections decrease slowly with increasing energy. These activation cross sections are smaller than the cross sections for ^{58}Ni at 3.0, 3.5 and 4.0 MeV in Ref. 61 and larger than the cross sections for ^{60}Ni at 7.2 and 9.4 MeV in Ref. 62. Thick-target yields were evaluated using the cross sections in Ref. 60 because they encompass a broad energy range. These yields are presented in Fig. 14. Activation cross sections for the (d,α) reactions on ^{58}Ni and ^{60}Ni are smaller than the (d,n) cross sections.^{62,63} The (d,α) cross sections increase monotonically with increasing deuteron energy from 5 to 10 MeV. The thick-target yield for the reaction $^{58}\text{Ni}(d,\alpha)^{56}\text{Co}$, calculated using cross sections in Refs. 62 and 63, is displayed in Fig. 14. For a natural nickel target, ^{58}Co activation may be produced by both the $^{60}\text{Ni}(d,\alpha)^{58}\text{Co}$ and $^{58}\text{Ni}(d,2p)^{58}\text{Co}$ reactions. The ^{58}Co activation in Fig. 2 of Ref. 64 is presumably due to both reactions rather than just the $^{58}\text{Ni}(d,2p)^{58}\text{Co}$ reaction. The thick-target yield for ^{58}Co activation, calculated from cross sections in Refs. 62 and 64 is presented in Fig. 14. Cross sections for the (d,t) , $(d,^3\text{He})$, $(d,\alpha n)$, $(d,\alpha p)$ and $(d,2\alpha)$ reactions on ^{58}Ni and the $(d,2n)$ and $(d,\alpha n)$ reactions on ^{60}Ni have been measured,⁶²⁻⁶⁵ and activities induced by these reactions are extremely small below 10 MeV.

C. Brass Target

Deuteron induced reactions leading to radioactive products are listed in Table VII for the 67% copper component in this target. The (d,p) and $(d,2n)$ reactions on ^{63}Cu and ^{65}Cu are prolific sources of radioactivity for deuterons below 10 MeV. A seminal study of activations for these reactions may be found in

Table VII

Radioactivities Induced by Deuterons on Copper

Target		Nuclear Reaction		Residual Nucleus			
Iso- tope	Abun- dance	Reaction	Q-Value (MeV)	Decay Mode	Half Life	E_{β} (MeV)	E_{γ} (MeV)
^{63}Cu	69.1%	$^{63}\text{Cu}(\text{d}, \text{p})^{64}\text{Cu}$	5.69	β^- ϵ, β^+	12.8 hr 12.8 hr	0.575 0.656	- 0.51
		$^{63}\text{Cu}(\text{d}, \text{t})^{62}\text{Cu}$	-4.58	β^+	9.8 min	2.93	0.51
		$^{63}\text{Cu}(\text{d}, 2\text{n})^{63}\text{Zn}$	-6.37	β^+	38 min	2.34	0.51
		$^{63}\text{Cu}(\text{d}, \alpha\text{p})^{60}\text{Co}$	-0.51	β^-	5.27 yr	0.318	1.17 1.33
^{65}Cu	30.9%	$^{65}\text{Cu}(\text{d}, \text{p})^{66}\text{Cu}$	4.84	β^-	5.1 min	2.63	1.04
		$^{65}\text{Cu}(\text{d}, \text{t})^{64}\text{Cu}$	-3.65	β^- ϵ, β^+	12.8 hr 12.8 hr	0.575 0.656	- 0.51
		$^{65}\text{Cu}(\text{d}, 2\text{n})^{65}\text{Zn}$	-4.36	ϵ	244 da	-	1.115
		$^{65}\text{Cu}(\text{d}, 2\text{p})^{65}\text{Ni}$	-3.57	β^-	2.52 hr	2.13	1.48
		$^{65}\text{Cu}(\text{d}, \alpha\text{p})^{62}\text{Co}$	-2.32	β^-	14 min	2.88	1.17

Ref. 66. For the (d,p) reactions, significant disagreements in the magnitude and shape of the excitation functions are observed between three independent cross-section measurements. For the (d,2n) reactions, there is good agreement between the same three experiments. Thick-target yields, based on cross sections from Ref. 66, are presented in Fig. 15. Measurements^{67,68} of the $^{63}\text{Cu}(d,t)^{62}\text{Cu}$ and $^{65}\text{Cu}(d,2p)^{65}\text{Ni}$ reactions indicate that the activation cross sections for these reactions are much less than for the (d,p) and (d,2n) reactions.

For the zinc in this target, deuteron induced reactions leading to radioactive products are listed in Table VIII. The ^{64}Zn , ^{66}Zn , and ^{68}Zn isotopes have significant abundances for the 33% zinc component of the target. Excitation functions have been measured for the (d,p) and (d,n) reactions in Table VIII. Activation cross sections for the $^{64}\text{Zn}(d,p)^{65}\text{Zn}$ reaction include the $^{64}\text{Zn}(d,n)^{65}\text{Ga}$ reaction because the 15-min ^{65}Ga isotope decays to the 244-da ^{65}Zn isotope.^{69,70} This short-lived precursor is included in delayed activation measurements of ^{65}Zn . For ^{66}Zn , cross sections⁷¹ for the $^{66}\text{Zn}(d,n)^{67}\text{Ga}$ reaction include a small contribution from the $^{67}\text{Zn}(d,2n)^{67}\text{Ga}$ reaction at higher deuteron energy. The natural abundance of ^{67}Zn is only 4.1%. For ^{68}Zn , the (d,p) reaction produces either ^{69}Zn or the isomer, ^{69m}Zn . The isomer decays by an isomeric transition (IT) with the emission of a 0.44-MeV γ -ray to ^{69}Zn . Separate cross sections have been measured for these two activities.⁷² Thick-target yields, based on cross sections from Refs. 69-72, are presented in Fig. 16.

For the (d, α) reactions in Table VIII, only the cross section for activating ^{64}Cu has been published.⁷³ Isotopically enriched targets were required to extract the excitation function for this activity. The more intense (d,p) and (d,n) reactions which induce competing short-lived activities make measurements of the smaller (d, α) cross sections difficult. No excitation functions have been reported for the 10-min ^{62}Cu or 5-min ^{66}Cu activities. The thick-target yield for ^{64}Cu activity, based on the cross sections in Ref. 73, is presented in Fig. 16.

Table VIII

Radioactivities Induced by Deuterons on Zinc

Target		Nuclear Reaction		Residual Nucleus			
Iso- tope	Abun- dance	Reaction	Q-Value (MeV)	Decay Mode	Half Life	E_β (MeV)	E_γ (MeV)
^{64}Zn	48.9%	$^{64}\text{Zn}(d,n)^{65}\text{Ga}$	1.72	β^+	15 min	2.24	0.51
		$^{64}\text{Zn}(d,p)^{65}\text{Zn}$	5.76	ϵ	244 da	-	1.115
		$^{64}\text{Zn}(d,t)^{63}\text{Zn}$	-5.60	β^+	38 min	2.34	0.51
		$^{64}\text{Zn}(d,\alpha)^{62}\text{Cu}$	7.52	β^+	9.8 min	2.93	0.51
		$^{64}\text{Zn}(d,2p)^{64}\text{Cu}$	-2.01	β^- ϵ, β^+	12.8 hr 12.8 hr	0.575 0.656	- 0.51
^{66}Zn	27.8%	$^{66}\text{Zn}(d,n)^{67}\text{Ga}$	3.05	ϵ	78 hr	-	0.093
		$^{66}\text{Zn}(d,t)^{65}\text{Zn}$	-4.78	ϵ	244 da	-	1.115
		$^{66}\text{Zn}(d,\alpha)^{64}\text{Cu}$	7.26	β^- ϵ, β^+	12.8 hr 12.8 hr	0.575 0.656	- 0.51
		$^{66}\text{Zn}(d,2p)^{66}\text{Cu}$	-4.07	β^-	5.1 min	2.63	1.04
		$^{66}\text{Zn}(d,2n)^{66}\text{Ga}$	-8.18	β^+, ϵ	9.5 hr	4.15	0.51
^{68}Zn	18.6%	$^{68}\text{Zn}(d,p)^{69}\text{Zn}$	4.28	β^-	57 min	0.91	-
		$^{68}\text{Zn}(d,p)^{69m}\text{Zn}$	3.84	IT	13.9 hr	-	0.44
		$^{68}\text{Zn}(d,^3\text{He})^{67}\text{Cu}$	-4.50	β^-	62 hr	0.57	0.185
		$^{68}\text{Zn}(d,\alpha)^{66}\text{Cu}$	6.97	β^-	5.1 min	2.63	1.04
		$^{68}\text{Zn}(d,2n)^{68}\text{Ga}$	-5.93	β^+	68 min	1.90	0.51
		$^{68}\text{Zn}(d,2p)^{68}\text{Cu}$	-6.03	β^-	31 sec	3.51	1.08

Excitation functions have been measured for several of the negative Q-value reactions in Table VIII. For the $^{64}\text{Zn}(d,2p)$ reaction, the cross section is small (5 mb) at 10 MeV and negligible below 8 MeV.⁷³ For the $^{66}\text{Zn}(d,2n)^{66}\text{Ga}$ reaction, the cross section increases from zero at the 8.4-MeV threshold to 150 mb at 10 MeV.⁷² For the $^{68}\text{Zn}(d,2n)^{68}\text{Ga}$ reaction the threshold is 6.1 MeV, but some ^{68}Ga activity is produced at lower energy from the $^{67}\text{Zn}(d,n)^{68}\text{Ga}$ reaction. The thick-target yield for ^{68}Ga activity, based on the cross sections in Ref. 72, is presented in Fig. 16.

REFERENCES

1. J. Golden, C.A. Kapetanacos, J.A. Pasour and R.A. Mahaffey, American Scientist 69, 173 (1981).
2. K.A. Keller, J. Lange and H. Münzel, in Landolt-Bornstein Numerical Data and Functional Relationships in Science and Technology Vol. 5, Part a, Q-Values, edited by H. Schopper (Springer-Verlag, New York, 1973).
3. J.B. Marion and F.C. Young, Nuclear Reaction Analysis (North-Holland, Amsterdam, 1968) p. 157.
4. Chart of the Nuclides, Knolls Atomic Power Laboratory, 11th Edition, April, 1972.
5. C.M. Lederer, J.M. Hollander and I. Perlman, Table of Isotopes, 6th Edition (John Wiley, New York, 1967).
6. F.K. McGowan, W.T. Milner, H.J. Kim and Wanda Hyatt, Nuclear Data Tables A6, 353 (1969); A7, 1 (1969); F.K. McGowan and W.T. Milner, Nuclear Data Tables A8, 199 (1970); 9, 469 (1971); 11, 1 (1972); Atomic Data and Nuclear Data Tables 12, 499 (1973); 15, 189 (1975); 18, 1 (1976).
7. K.A. Keller, J. Lange, H. Münzel and G. Pfennig, in Landolt-Bornstein Numerical Data and Functional Relationships in Science and Technology Vol. 5, Part b, Excitation Functions for Charged-Particle Induced Nuclear Reactions, edited by H. Schopper (Springer-Verlag, New York, 1973).
8. DIALOG Information Services, Inc., 3460 Hillview Ave., Palo Alto, CA 94304.
9. H.H. Andersen and J.F. Ziegler, The Stopping and Ranges of Ions in Matter, Vol. 3, Hydrogen (Pergamon Press, New York, 1977).
10. S.K. Vosburg, C.L. Ruiz, G.W. Cooper and F.A. Schmidlapp, An Experimental Investigation of Radioactivity Induced by Ions Associated with the Operation of Pulsed-Power Generators, Sandia Report SAND92-2075, March, 1993.
11. F.C. Young and D.V. Rose, Survey of Radioactivities Induced by Lithium Ions, Naval Research Laboratory Memorandum Report No. 6974, June, 1992.
12. F.C. Young, J. Golden and C.A. Kapetanacos, Rev. Sci. Instrum. 48, 432 (1977).
13. P. Dagley, W. Haeberli and J.X. Saladin, Nucl. Phys. 24, 353 (1961).
14. A.B. Whitehead and J.S. Foster, Can. J. Phys. 36, 1276 (1958).

15. T.W. Bonner, J.E. Evans and J.E. Hill, Phys. Rev. 75, 1398 (1949).
16. R.J. Jaszczak, R.L. Macklin and J.H. Gibbons, Phys. Rev. 181, 1428 (1969).
17. D.H. Wilkinson, Phys. Rev. 100, 32 (1955).
18. I.F. Bubb, J.M. Poate and R.H. Spear, Nucl. Phys. 65, 655 (1965).
19. E. McMillan and E.O. Lawrence, Phys. Rev. 47, 343 (1935).
20. C.S. Lin and E.K. Lin, Nuovo Cimento A 66, 336 (1970).
21. J.M. Flores, Phys. Rev. 127, 1246 (1962).
22. F.C. Young and M. Friedman, J. Appl. Phys. 46, 2001 (1975).
23. E. Schuster and K. Wohlleben, J. Appl. Rad. Isotopes 19, 471 (1968).
24. R.L. Wilson, D.J. Frantsvog and A.R. Kunselman, C. Détraz and C.S. Zaidins, Phys. Rev. C 13, 976 (1976).
25. H.F. Röhm, C.J. Verwey, J. Steyn and W.L. Rautenbach, J. Inorg. Nucl. Chem. 31, 3345 (1969).
26. R. Radicella, J. Rodriguez, G.B. Baró and O. Hittmair, Z. Physik 150, 653 (1958).
27. J. Jänecke, Phys. Lett. 6, 69 (1963).
28. S. Tanaka and M. Furukawa, J. Phys. Soc. Japan 14, 1269 (1959).
29. J. Wing and J.R. Huizenga, Phys. Rev. 128, 280 (1962).
30. J.L. Zyskind, C.A. Barnes, J.M. Davidson, W.A. Fowler, R.E. Marrs and M.H. Shapiro, Nucl. Phys. A343, 295 (1980).
31. S. Kailas, S.K. Gupta, S.S. Kerekatte and C.V. Fernandes, Pramana 24, 629 (1985).
32. H.S. Plendl, L.J. Defelice and R.K. Sheline, Nucl. Phys. 73, 131 (1965).
33. N.T. Porile, C.R. Lux, J.C. Pacer and J. Wiley, Nucl. Phys. A240, 77 (1975).
34. F. Boehm, P. Marmier and P. Preiswerk, Helv. Phys. Acta 25, 599 (1952).
35. H. Taketani and W. Parker Alford, Phys. Rev. 125, 291 (1962).

36. I.L. Jenkins and A.G. Wain, J. Inorg. Nucl. Chem. 32, 1419 (1970).
37. E. Gadioli, A.M. Grassi Strini, G. Lo Bianco, G. Strini and G. Tagliaferri, Nuovo Cimento 22A, 547 (1974).
38. S.D. Hoath, R.J. Petty, J.M. Freeman, G.T.A. Squier and W.E. Burcham, Phys. Lett. 51B, 345 (1974).
39. S. Tanaka, M. Furukawa and M. Chiba, J. Inorg. Nucl. Chem. 34, 2419 (1972).
40. R. Collé, R. Kishore and J.B. Cumming, Phys. Rev. C 9, 1819 (1974).
41. H.A. Howe, Phys. Rev. 109, 2083 (1958).
42. J.-P. Blaser, F. Boehm, P. Marmier and D.C. Peaslee, Helv. Phys. Acta 24, 3 (1951).
43. M. Hille, P. Hille, M. Uhl and W. Weisz, Nucl. Phys. A198, 625 (1972).
44. C.B. Fulmer and C.D. Goodman, Phys. Rev. 117, 1339 (1960).
45. I. Kumabe, C.L. Wang, M. Kawashima, M. Yada and H. Ogata, J. Phys. Soc. Japan 14, 713 (1959).
46. L. Milazzo Colli, G.M. Braga Marcazzan, R. Bonetti, M. Milazzo and J.W. Smits, Nuovo Cimento 39, 171 (1977).
47. B.L. Cohen, E. Newman, R.A. Charpie and T.H. Handley, Phys. Rev. 94, 620 (1954).
48. F. Tárkányi, F. Szelecsényi and P. Kopecky, Appl. Radiat. Isot. 42, 513 (1991).
49. B.L. Cohen and E. Newman, Phys. Rev. 99, 718 (1955).
50. J.H. Bjerregaard, P.F. Dahl, O. Hansen and G. Sidenius, Nucl. Phys. 51, 641 (1964).
51. K.L. Chen and J.M. Miller, Phys. Rev. 134, B1269 (1964).
52. P.P. Dmitriev, I.O. Konstantinov and N.N. Krasnov, Soviet Atomic Energy, 29, 916 (1970).
53. W.H. Burgess, G.A. Cowan, J.W. Hadley, W. Hess, T. Shull, M.L. Stevenson and H.F. York, Phys. Rev. 95, 750 (1954).
54. J.P. Schiffer and L.L. Lee, Jr., Phys. Rev. 115, 1705 (1959).
55. C.P. Dmitriev, I.O. Konstantinov and N.N. Krasnov, Soviet Atomic Energy, 29, 917 (1970).

56. P. Kafalas and J.W. Irvine, Jr., Phys. Rev. 104, 703 (1956).
57. H.I. West, Jr., R.G. Lanier and M.G. Mustafa, Phys. Rev. C 35, 2067 (1987).
58. J.W. Clark, C.B. Fulmer and I.R. Williams, Phys. Rev. 179, 1104 (1969).
59. P.P. Coetzee and M. Peisach, Radiochim. Acta 17, 1 (1972).
60. M. Cogneau, L.J. Lilly and J. Cara, Nucl. Phys. A99, 686 (1967).
61. J.H. Carver and G.A. Jones, Nucl. Phys. 24, 607 (1961).
62. J. Zweit, A.M. Smith, S. Downey and H.L. Sharma, Appl. Radiat. Isot. 42, 193 (1991).
63. M. Blann and G. Merkel, Phys. Rev. 131, 764 (1963).
64. C.K. Cline, Nucl. Phys. A174, 73 (1971).
65. R. Radicella, J. Rodriguez, G.B. Baró and O. Hittmair, Z. Physik 153, 314 (1958).
66. H. Okamura and S. Tamagawa, Nucl. Phys. A169, 401 (1971).
67. C.B. Fulmer and I.R. Williams, Nucl. Phys. A155, 40 (1970).
68. J.W. Irvine, Jr., J. Chem. Soc. (London) Suppl. S356 (1949).
69. S.J. Nassiff and H. Münzel, Radiochem. Radioanal. Lett. 12, 353 (1972).
70. J.H. Carver and G.A. Jones, Nucl. Phys. 11, 400 (1959).
71. S.J. Nassiff and H. Münzel, Radiochim. Acta 19, 97 (1973).
72. L.J. Gilly, G.A. Henriët, M. Preciosa Alves and P.C. Capron, Phys. Rev. 131, 1727 (1963).
73. D.C. Williams and J.W. Irvine, Jr., Phys. Rev. 130, 265 (1963).

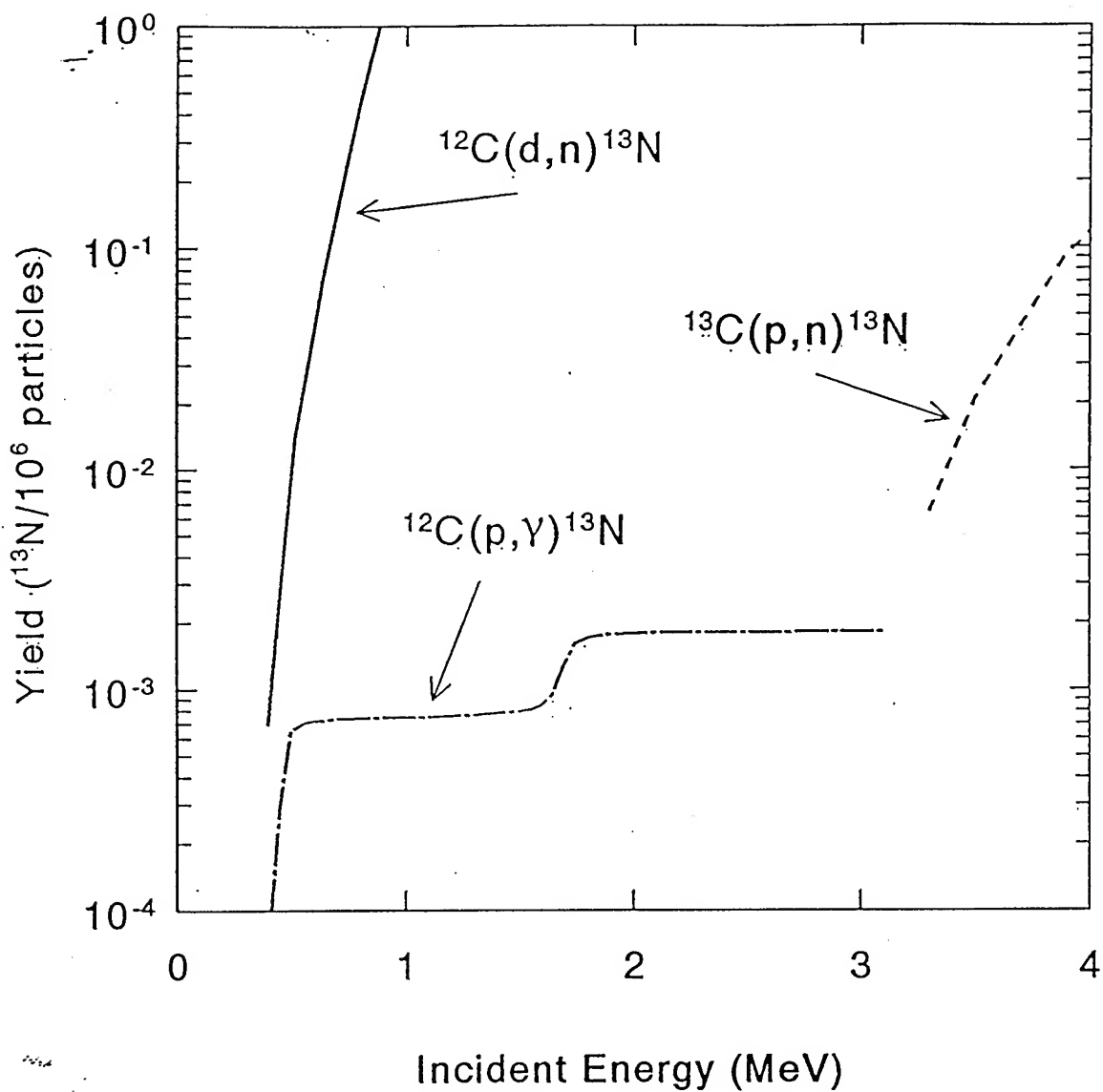


Fig. 1. Thick-target yields for the $^{12}\text{C}(\text{p},\gamma)^{13}\text{N}$, $^{13}\text{C}(\text{p},\text{n})^{13}\text{N}$ and $^{12}\text{C}(\text{d},\text{n})^{13}\text{N}$ reactions below 4 MeV in a natural carbon target.

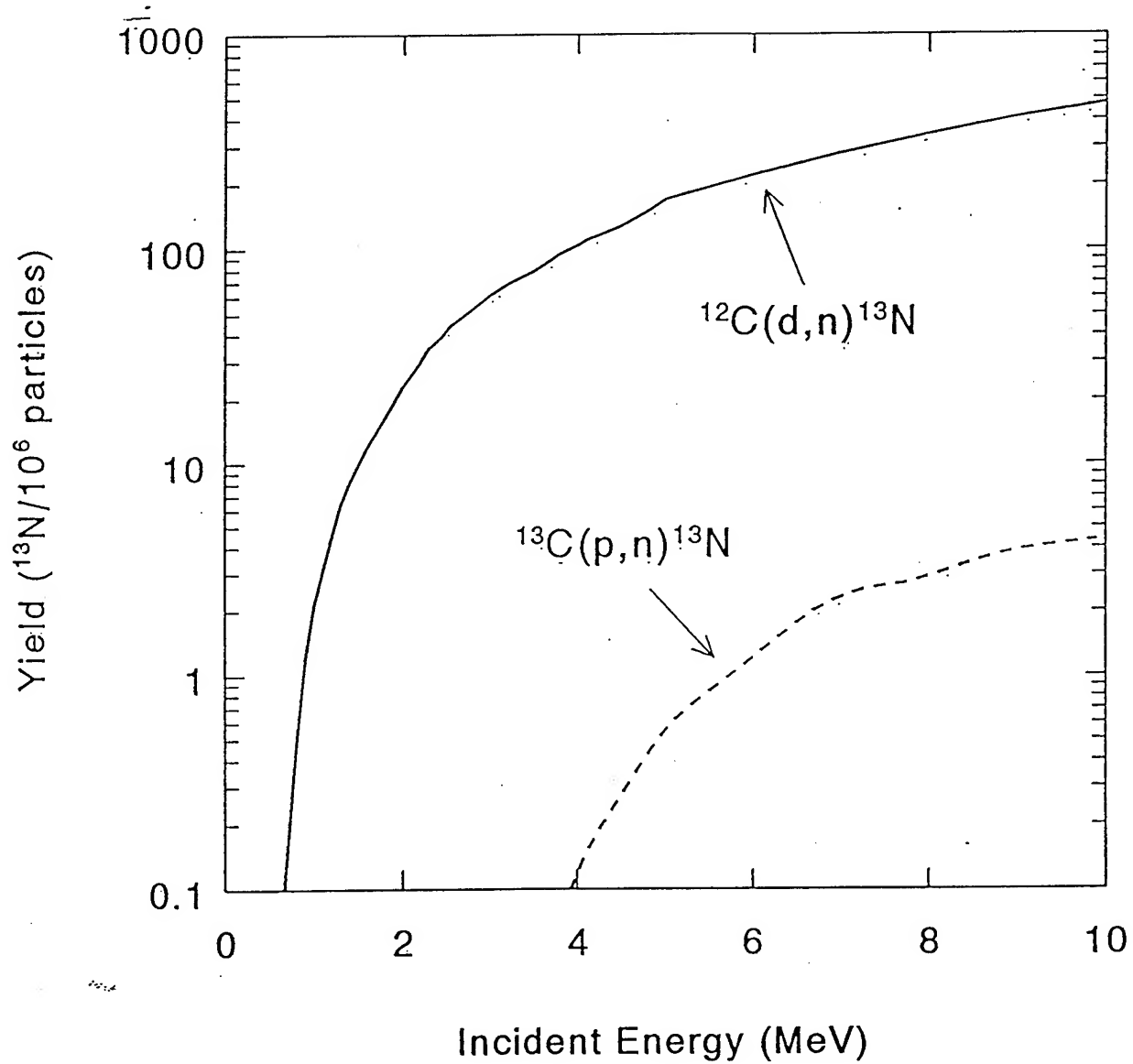


Fig. 2. Thick-target yields for the $^{13}\text{C}(\text{p},\text{n})^{13}\text{N}$ and $^{12}\text{C}(\text{d},\text{n})^{13}\text{N}$ reactions up to 10 MeV in a natural carbon target.

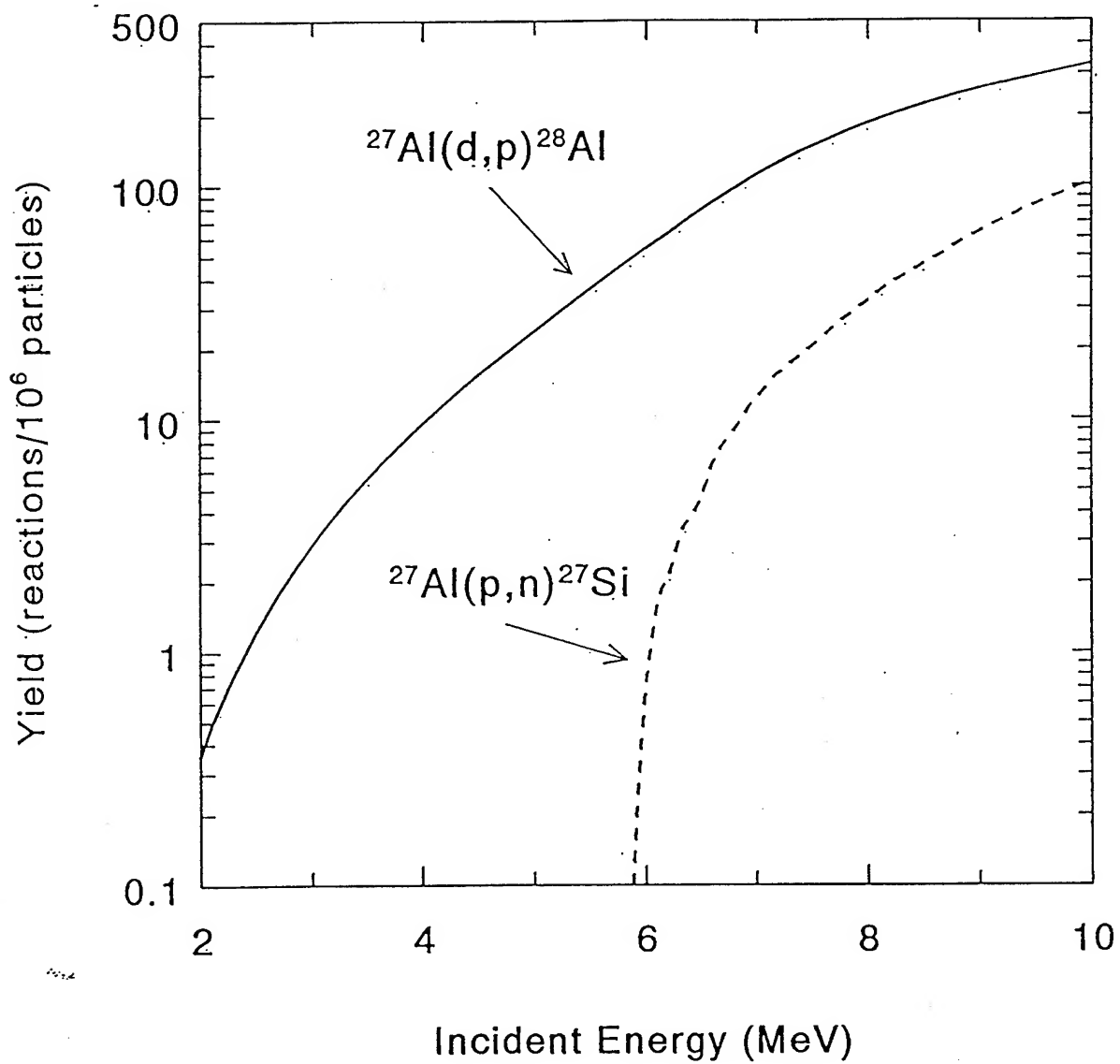


Fig. 3. Thick-target yields for the $^{27}\text{Al}(p,n)^{27}\text{Si}$ and $^{27}\text{Al}(d,p)^{28}\text{Al}$ reactions in an aluminum target.

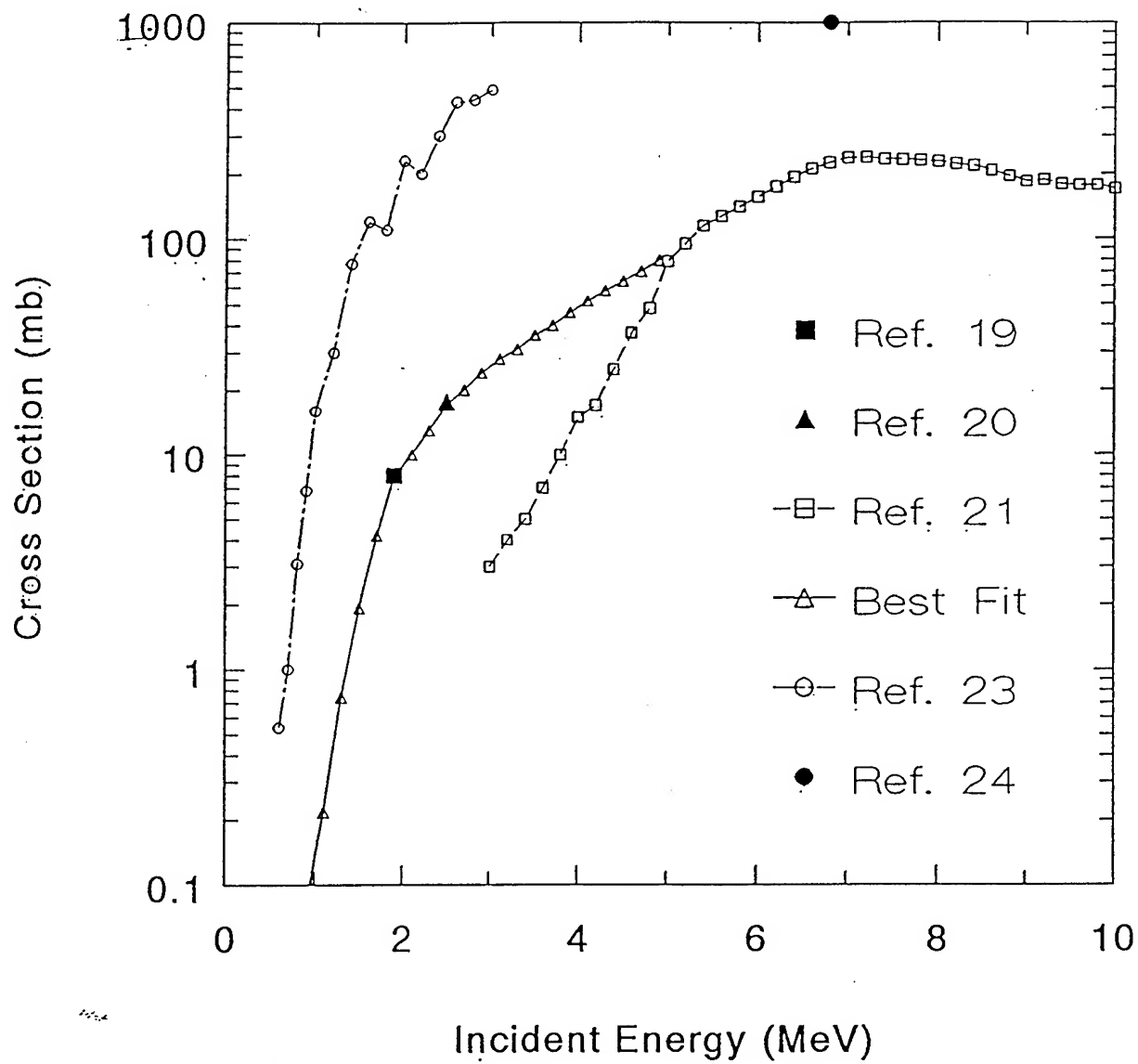


Fig. 4. Measured cross sections for the $^{27}\text{Al}(d,p)^{28}\text{Al}$ reaction. The best fit is for cross sections from References 19, 20 and 21.

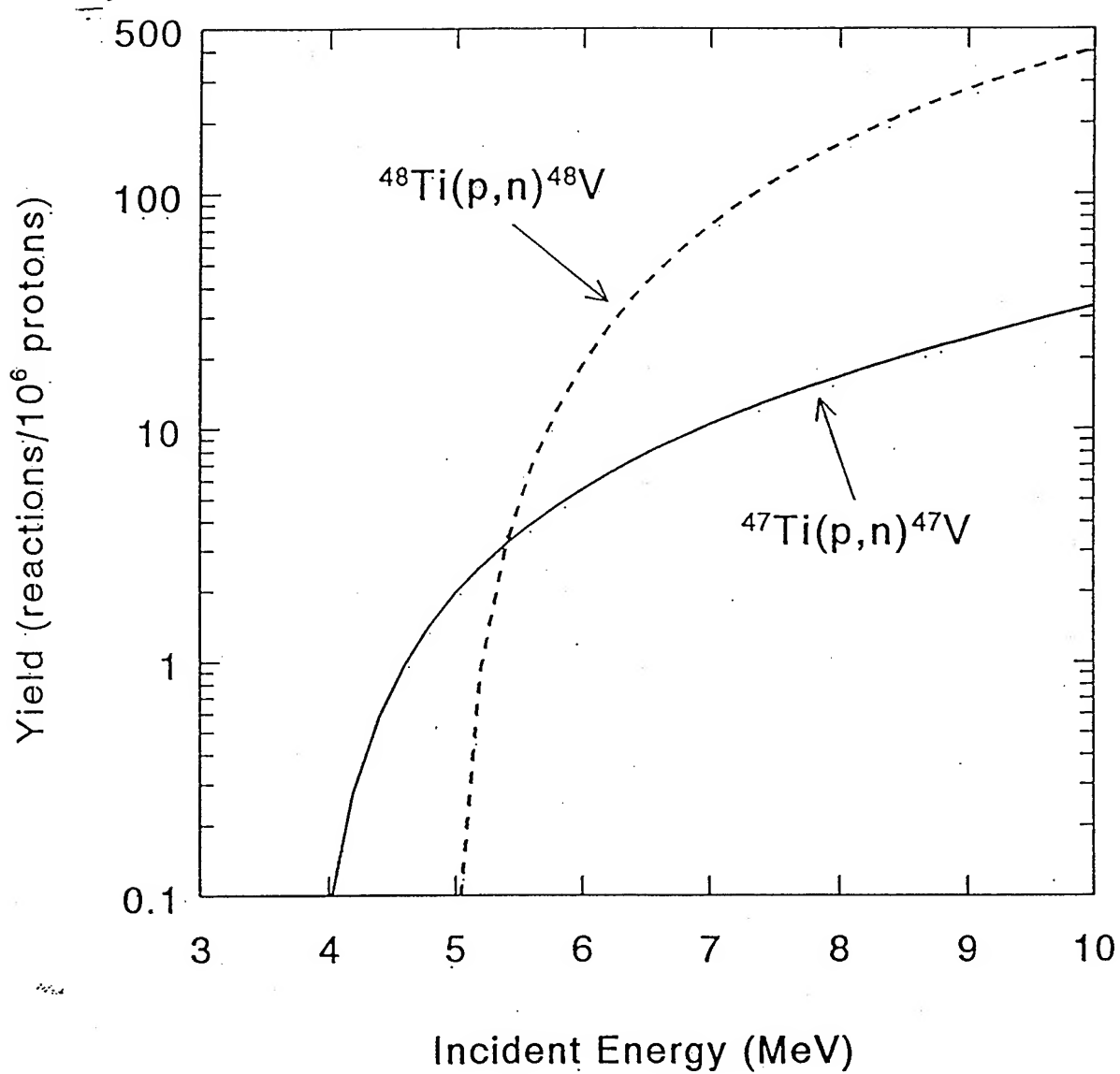


Fig. 5. Thick-target yields for the $^{47}\text{Ti}(p,n)^{47}\text{V}$ and $^{48}\text{Ti}(p,n)^{48}\text{V}$ reactions in a natural titanium target.

Table V
Thick-target yields for a natural titanium target

Incident Energy (MeV)	Yield (reactions/10 ⁶ protons)	
	⁴⁷ Ti(p,n) ⁴⁷ V	⁴⁸ Ti(p,n) ⁴⁸ V
3.8	0.005097	
3.8	0.005344	
4.0	0.07977	
4.2	0.2763	
4.4	0.5769	
4.6	0.9673	
4.8	1.436	
4.9		0
5.0	1.975	0.04961
5.2	2.578	0.931
5.4	3.24	3.203
5.6	3.959	6.909
5.8	4.732	12.08
6.0	5.56	18.73
6.2	6.44	26.86
6.4	7.374	36.48
6.6	8.361	47.55
6.8	9.401	60.06
7.0	10.49	73.96
7.2	11.64	89.22
7.4	12.84	105.8
7.6	14.09	123.6
7.8	15.4	142.5
8.0	16.76	162.6
8.2	18.17	183.7
8.4	19.64	205.8
8.6	21.17	228.9
8.8	22.76	252.8
9.0	24.41	277.6
9.2	26.13	303.1
9.4	27.92	329.4
9.6	29.77	356.6
9.8	31.68	384.5
10.0	33.65	413.2

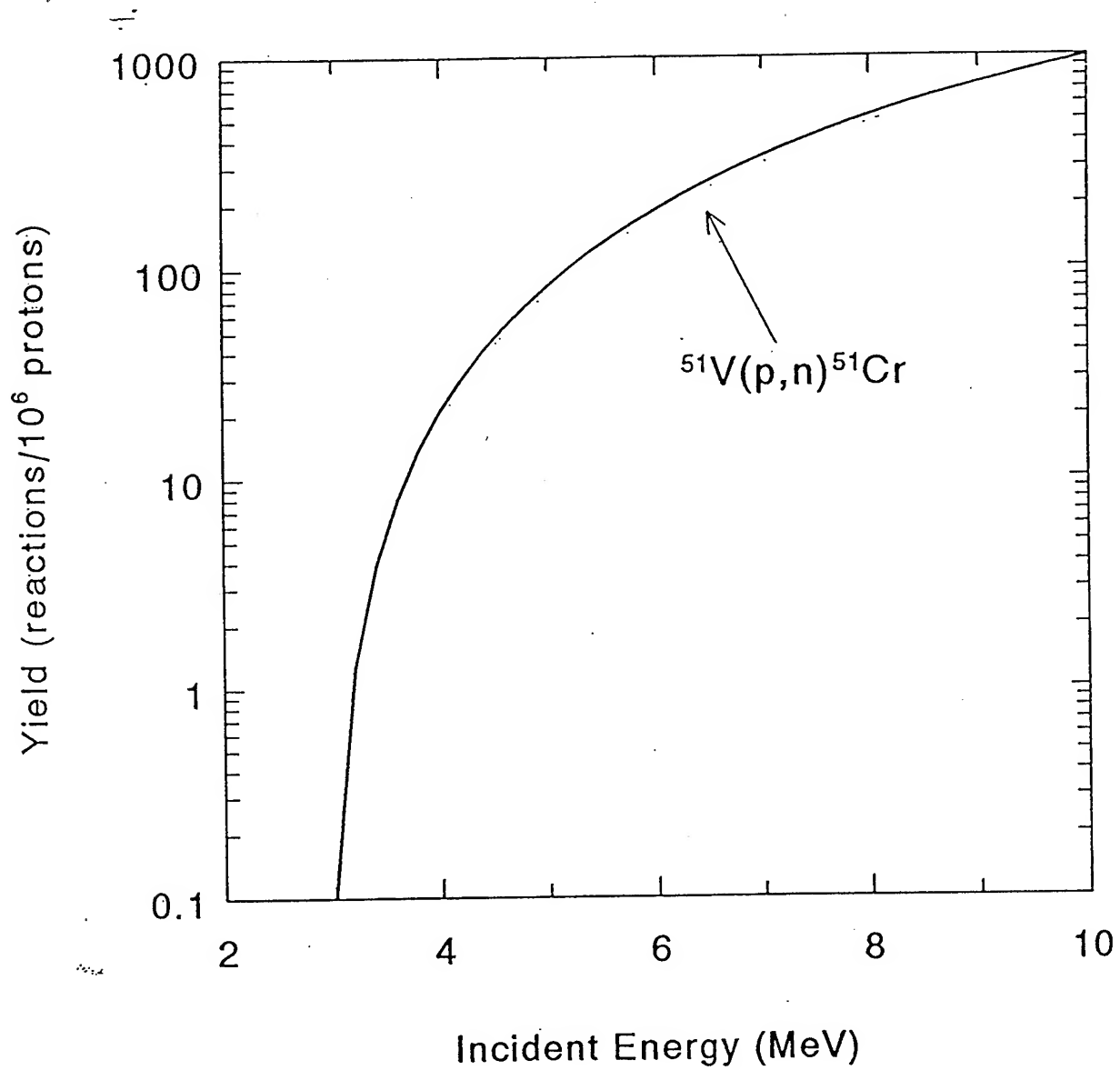


Fig. 6. Thick-target yield for the $^{51}\text{V}(p,n)^{51}\text{Cr}$ reaction in a natural vanadium target.

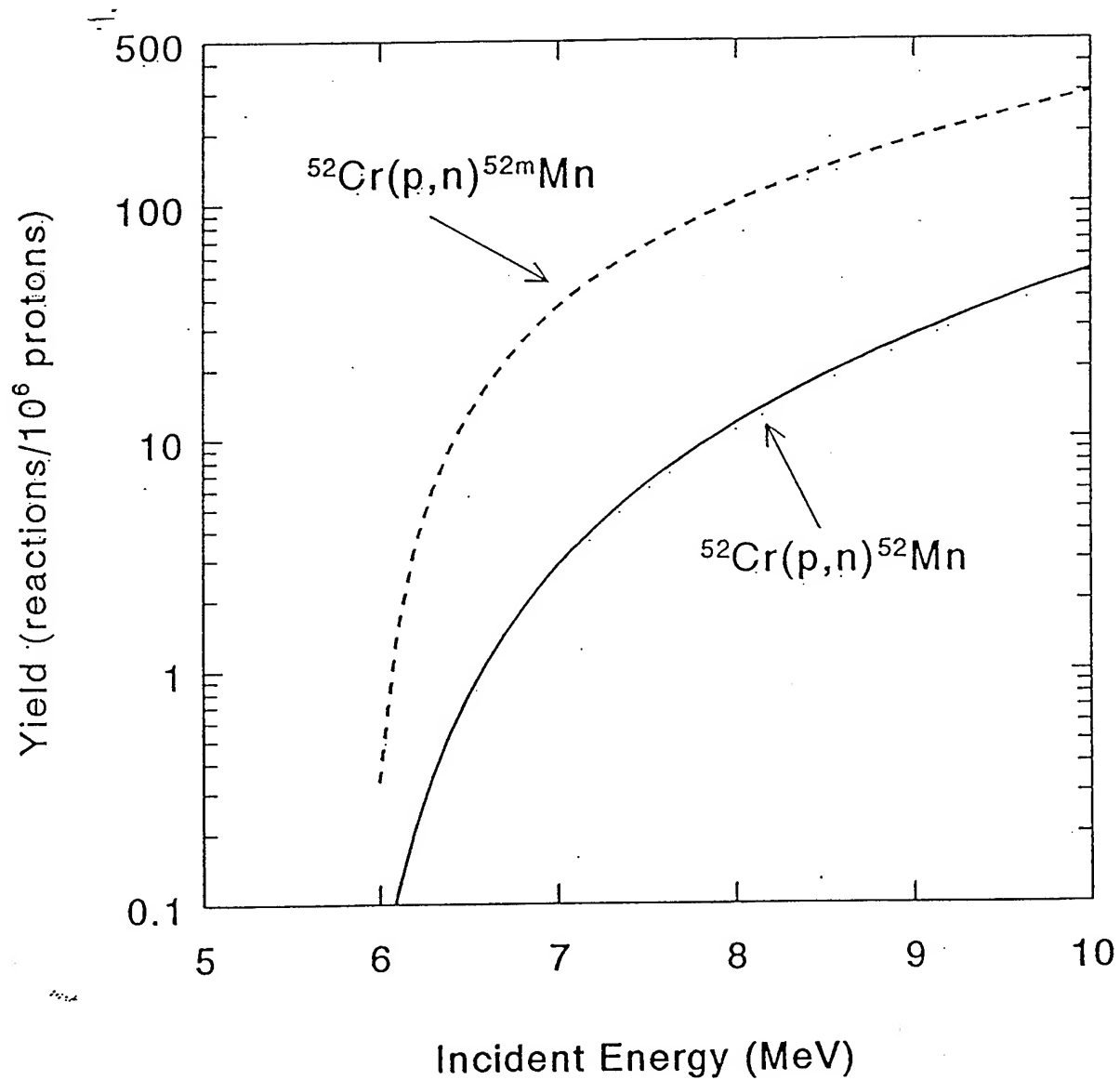


Fig. 7. Thick-target yields for the $^{52}\text{Cr}(p,n)^{52}\text{Mn}$ and $^{52}\text{Cr}(p,n)^{52\text{m}}\text{Mn}$ reactions in a natural chromium target.

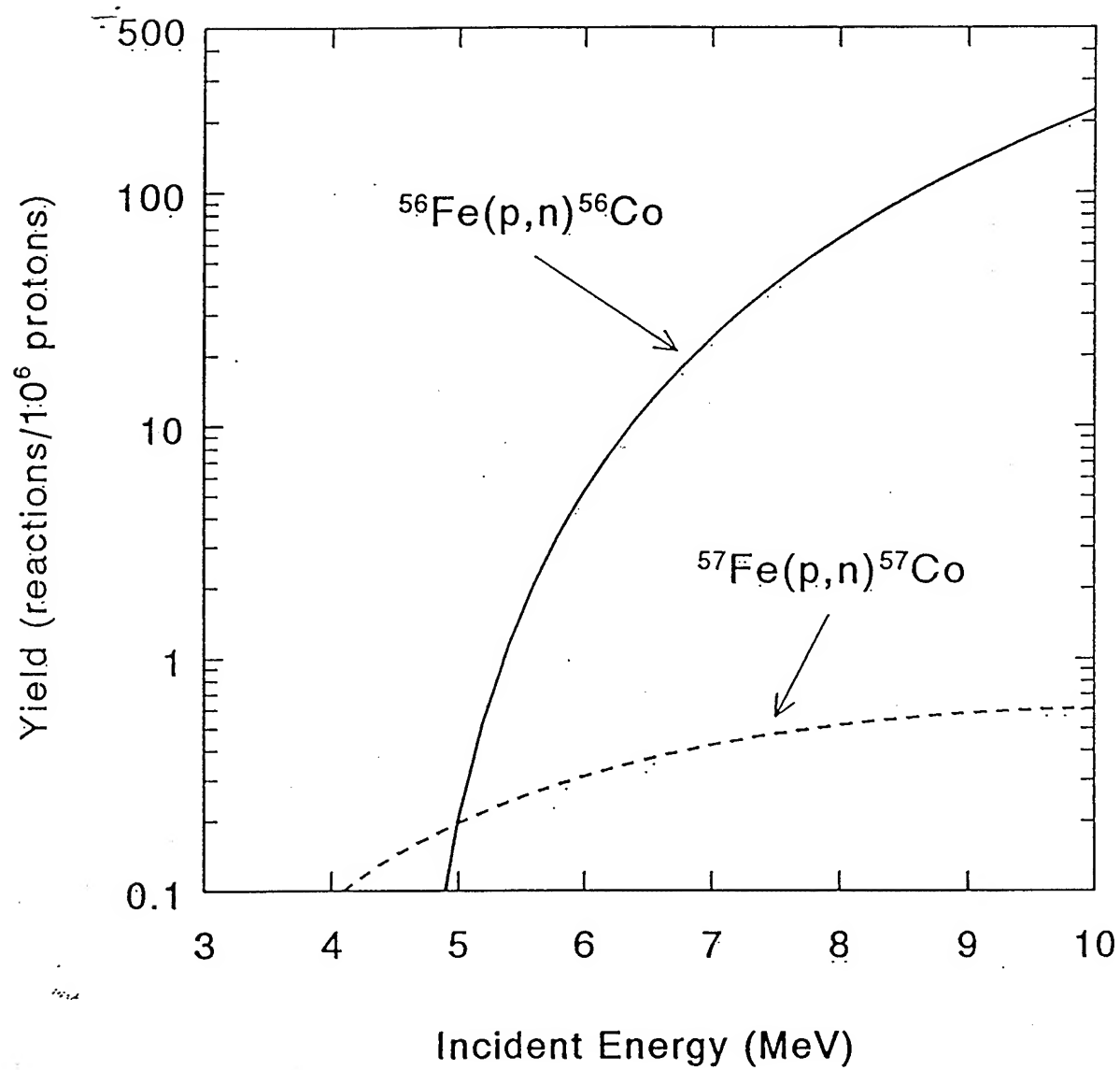


Fig. 8. Thick-target yields for the $^{56}\text{Fe}(p,n)^{56}\text{Co}$ and $^{57}\text{Fe}(p,n)^{57}\text{Co}$ reactions in a natural iron target.

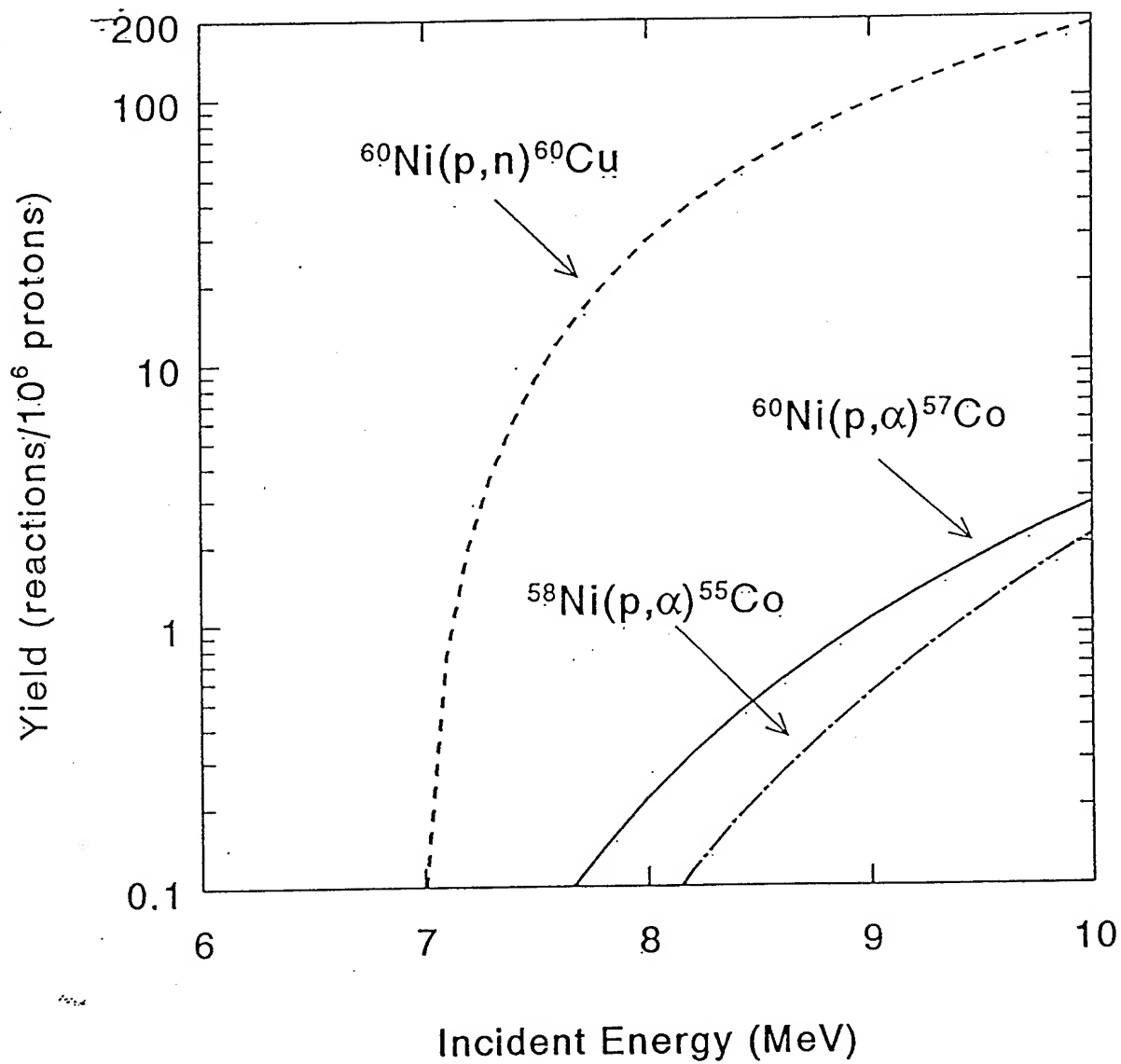


Fig. 9. Thick-target yields for the $^{60}\text{Ni}(p,n)^{60}\text{Cu}$, $^{60}\text{Ni}(p,\alpha)^{57}\text{Co}$, and $^{58}\text{Ni}(p,\alpha)^{55}\text{Co}$ reactions in a natural nickel target.

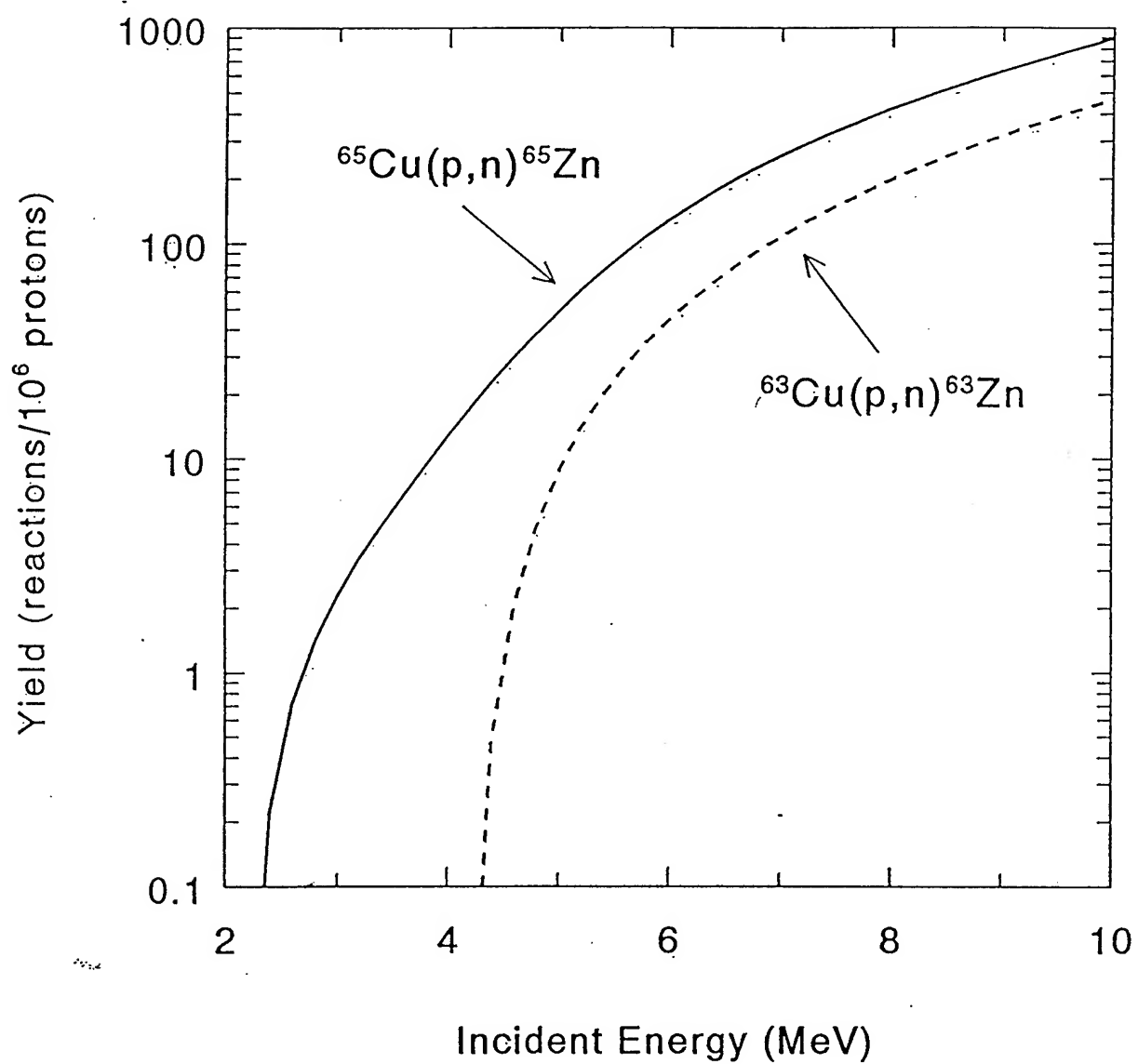


Fig. 10. Thick-target yields for the $^{65}\text{Cu}(p,n)^{65}\text{Zn}$ and $^{63}\text{Cu}(p,n)^{63}\text{Zn}$ reactions in a natural copper target.

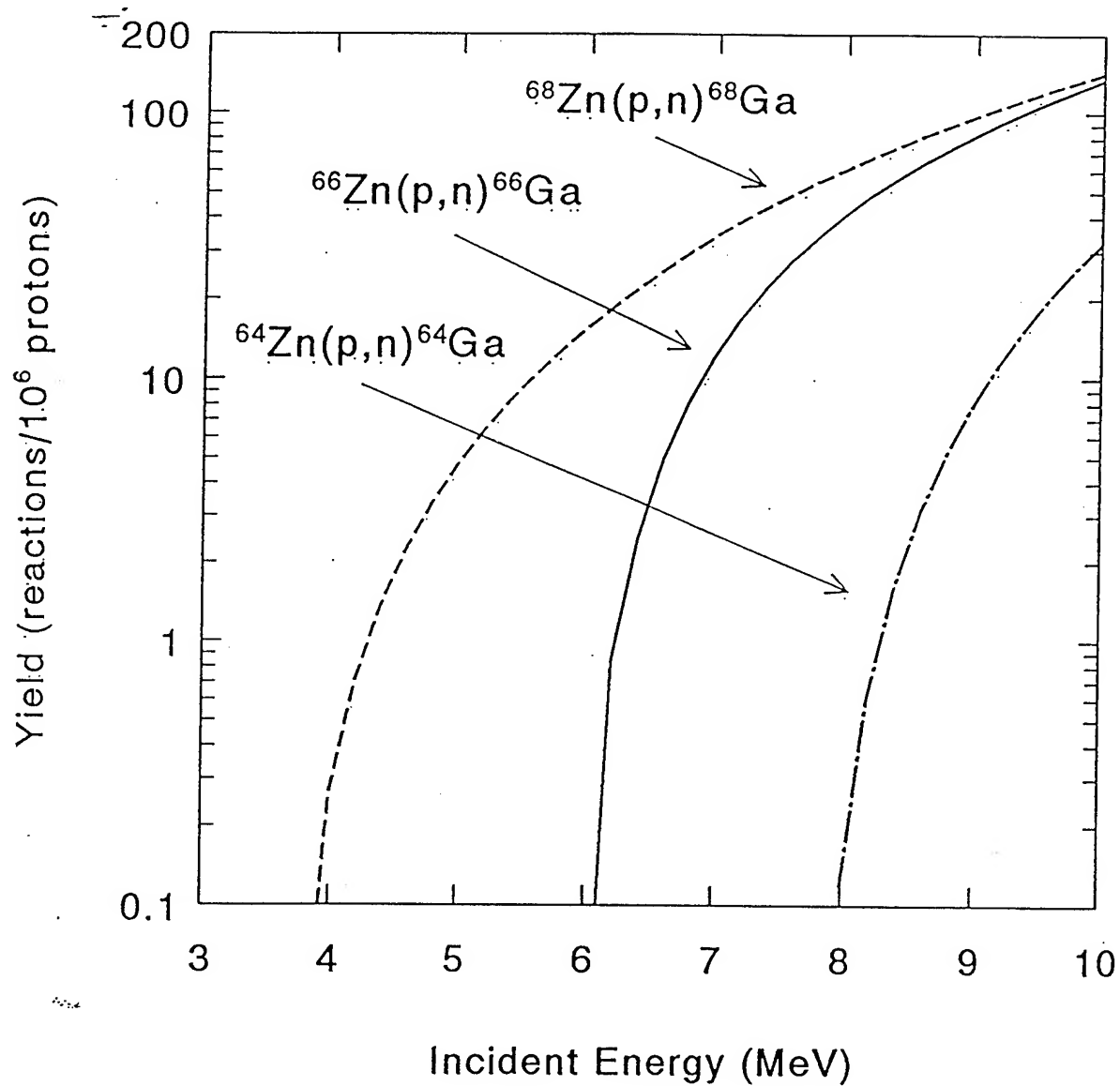


Fig. 11. Thick-target yields for the $^{64}\text{Zn}(p,n)^{64}\text{Ga}$, $^{66}\text{Zn}(p,n)^{66}\text{Ga}$, and $^{68}\text{Zn}(p,n)^{68}\text{Ga}$ reactions in a natural zinc target.

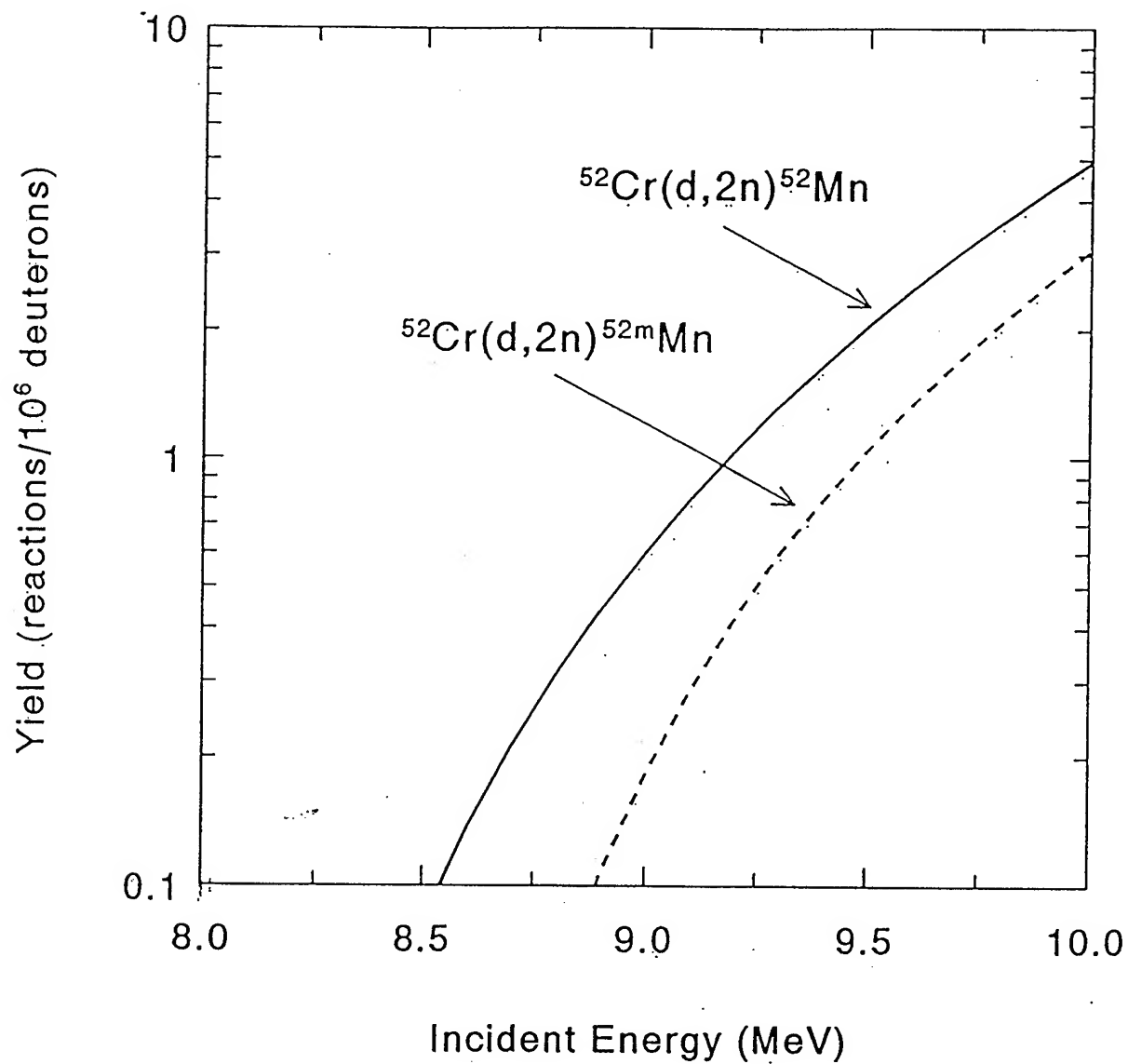


Fig. 12. Thick-target yields for the $^{52}\text{Cr}(d,2n)^{52}\text{Mn}$ and $^{52}\text{Cr}(d,2n)^{52m}\text{Mn}$ reactions in a natural chromium target.

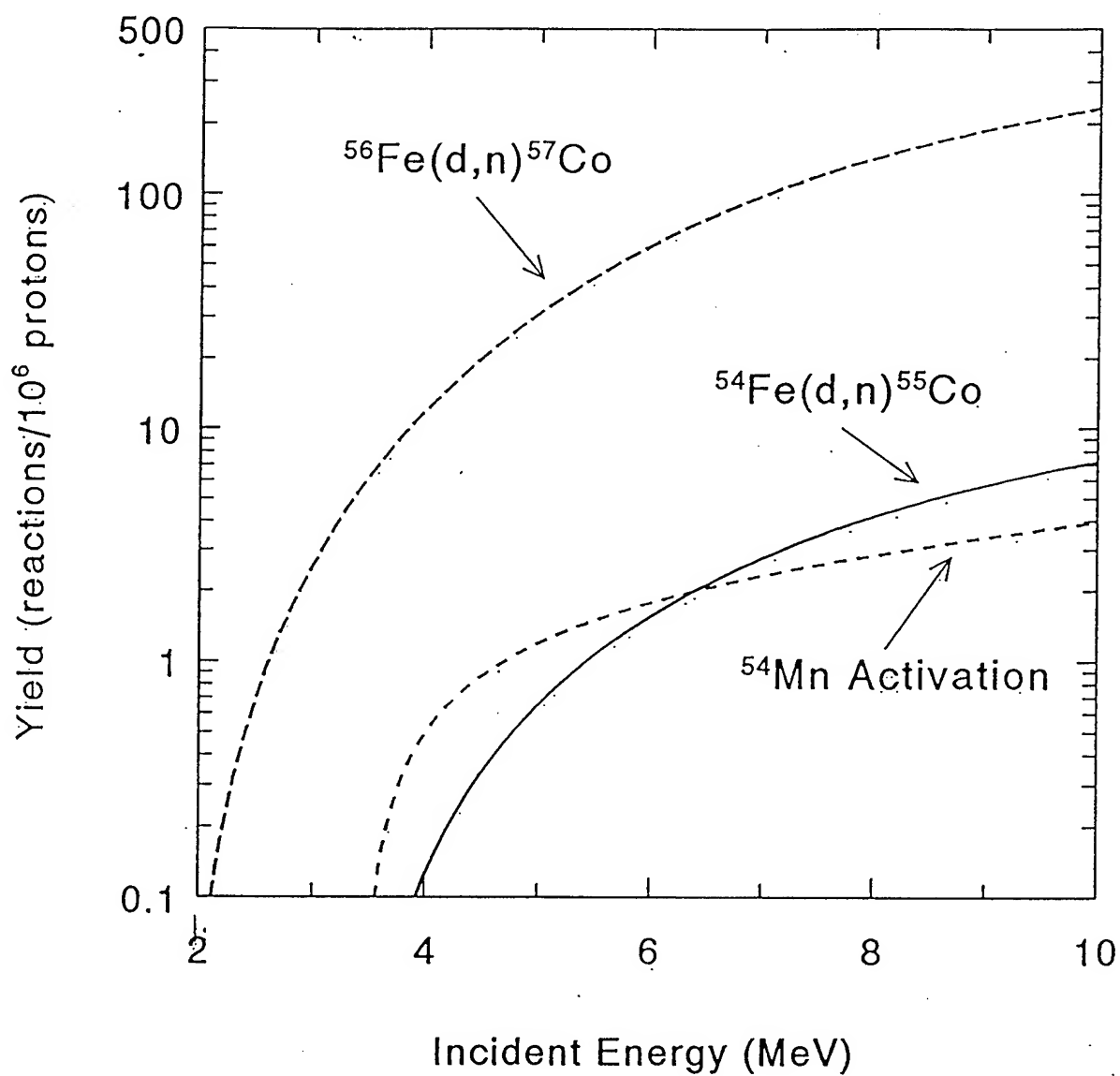


Fig. 13. Thick-target yields for the $^{56}\text{Fe}(d,n)^{57}\text{Co}$ and $^{54}\text{Fe}(d,n)^{55}\text{Co}$ reactions and for the activation of ^{54}Mn by deuterons on a natural iron target.

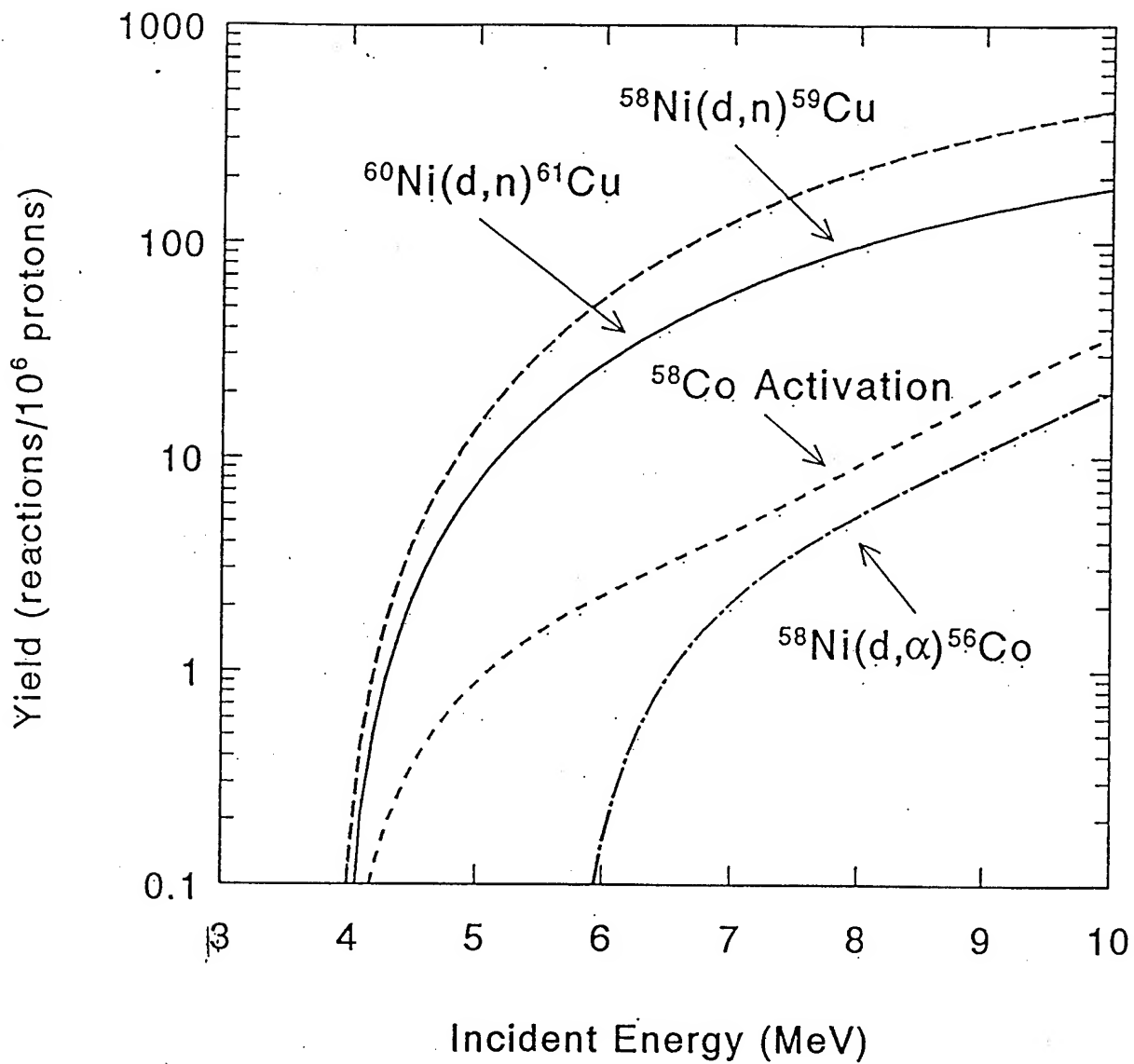


Fig. 14. Thick-target yields for the $^{58}\text{Ni}(d,n)^{59}\text{Cu}$, $^{60}\text{Ni}(d,n)^{61}\text{Cu}$, and $^{58}\text{Ni}(d,\alpha)^{56}\text{Co}$ reactions and for the activation of ^{58}Co by deuterons on a natural nickel target.

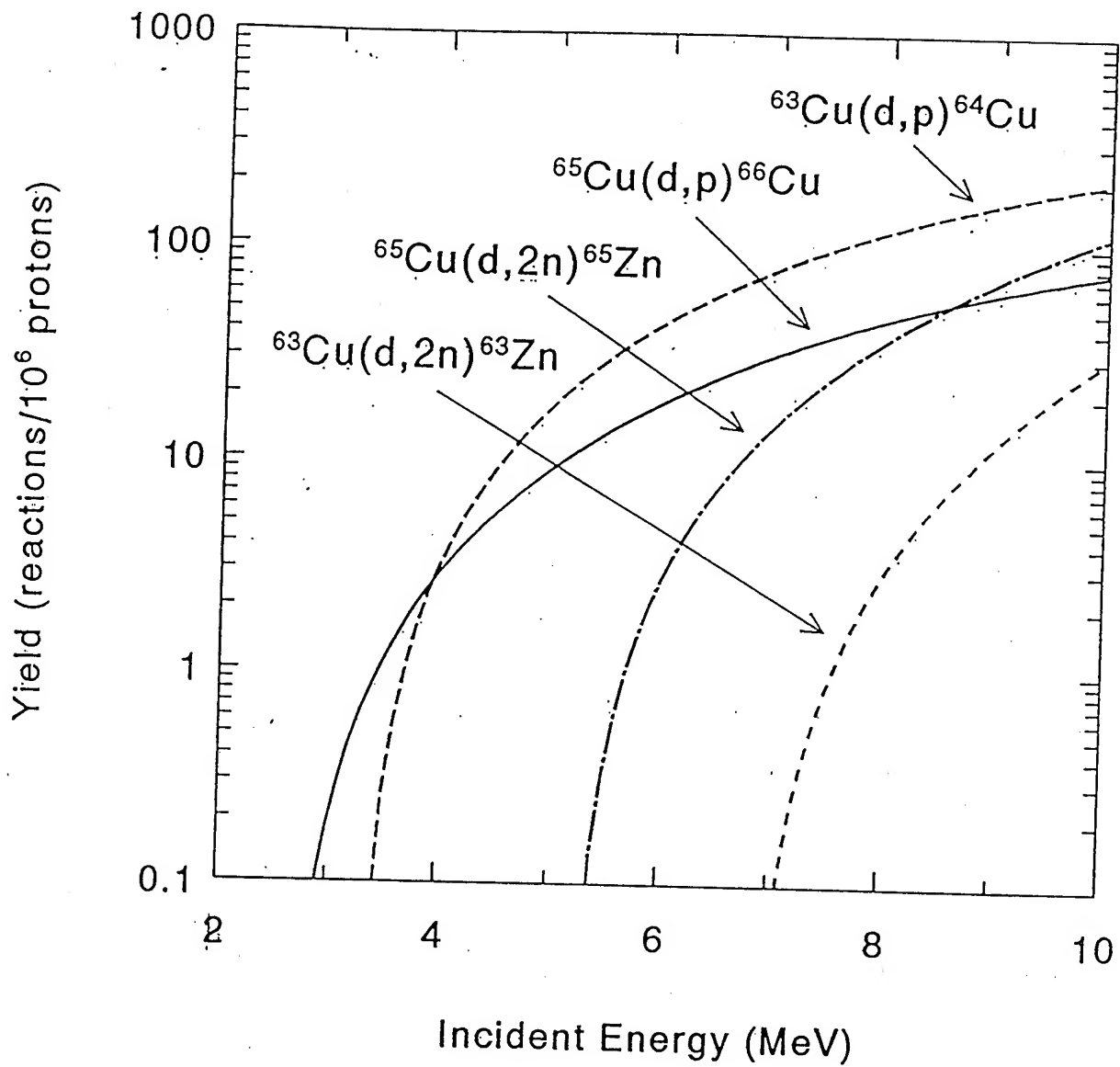


Fig. 15. Thick-target yields for the $^{63}\text{Cu}(d,p)^{64}\text{Cu}$, $^{65}\text{Cu}(d,p)^{66}\text{Cu}$, $^{63}\text{Cu}(d,2n)^{63}\text{Zn}$, and $^{65}\text{Cu}(d,2n)^{65}\text{Zn}$ reactions in a natural copper target.

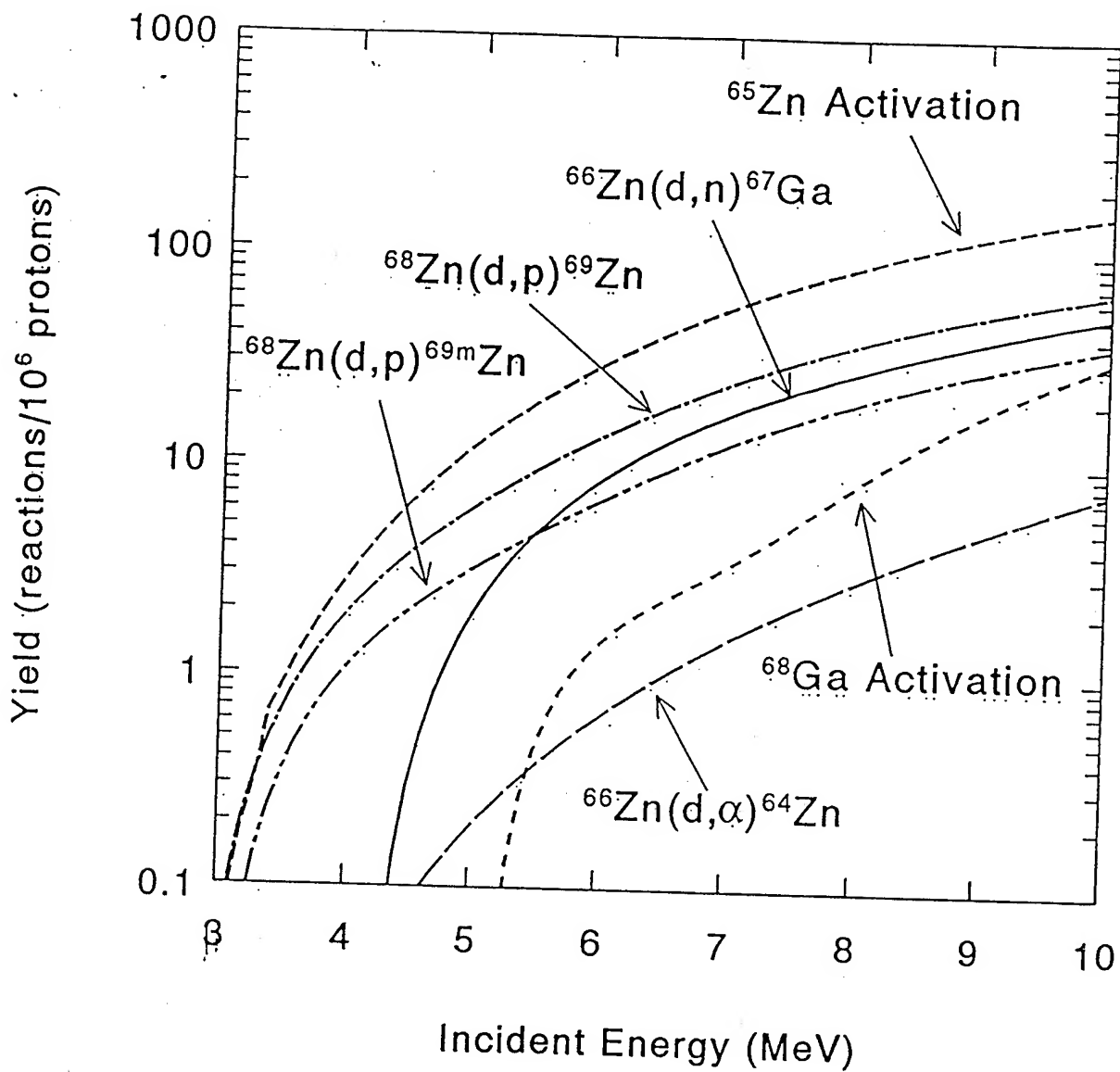


Fig. 16. Thick-target yields for the activation of ^{65}Zn by deuterons and for the $^{66}\text{Zn}(d,n)^{67}\text{Ga}$, $^{68}\text{Zn}(d,p)^{69}\text{Zn}$, $^{68}\text{Zn}(d,p)^{69m}\text{Zn}$, $^{66}\text{Zn}(d,\alpha)^{64}\text{Cu}$, and $^{68}\text{Zn}(d,2n)^{68}\text{Ga}$ reactions in a natural zinc target.



OAK RIDGE NATIONAL LABORATORY

(P)207

International Conference on

Nuclear Data for Science and Technology

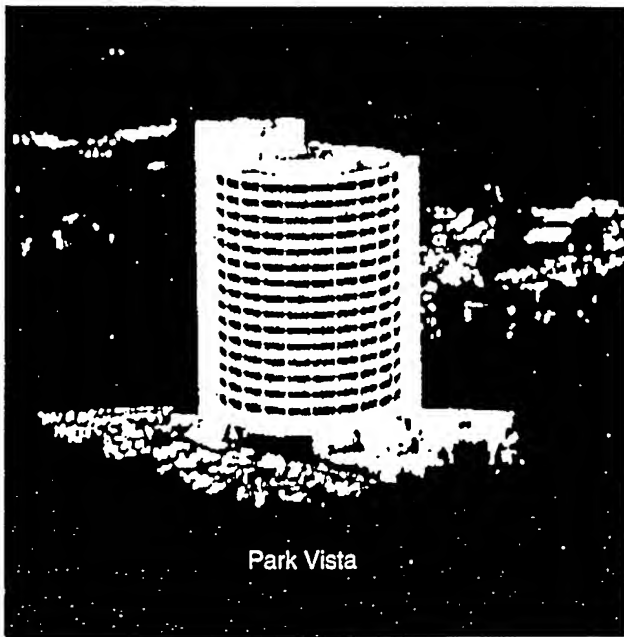
Nuclear Data for the Twenty-first Century

May 9-13, 1994

Gatlinburg, Tennessee USA

"Where the gods enjoy the springtime"

R. W. Peelle



SURVEY OF RADIOACTIVITIES INDUCED BY INTENSE PULSED ION BEAMS

Frank C. Young
Plasma Physics Division
Naval Research Laboratory
Washington, DC 20375-5346
Ph (202) 767-3066

David V. Rose
JAYCOR
1608 Springhill Road
Vienna, VA 22182
Ph (202) 404-7567

ABSTRACT

Proton, deuteron and ^7Li induced nuclear reactions which produce radioactivities are surveyed for application to experiments with intense ion beams from pulsed power generators. Reactions with up to 10-MeV protons or deuterons and up to 15-MeV ^7Li ions bombarding carbon, aluminum, titanium-alloy, steel and brass targets are considered. Measured cross sections from the published literature are used to calculate thick-target yields and evaluate radioactivities induced by protons or deuterons. The ^7Li induced reactions are dominated by Coulomb barrier penetration.

I. INTRODUCTION

Intense pulsed ion beams are being developed for use in a variety of applications including material modification studies and inertial confinement fusion (ICF) with light-ion beams.¹ Beam currents in the kiloampere to megampere range and ion energies of up to 20 MeV can be generated with modern pulsed power generators. Proton and deuteron beams are commonly used for these applications. For light-ion ICF, lithium beams of up to 15 MeV have been generated and an energy of about 30 MeV is ultimately required.² Residual radioactivities can be induced in target materials by these intense beams. These radioactivities can be used to diagnose the intensity and energy of the incident beam.³ Also, for some materials the induced radioactivities can pose a radiological hazard.

Surveys have been carried out to identify radioactivities produced by protons and deuterons of up to 10 MeV (Ref. 4) and by ^7Li beams of up to 15 MeV (Ref. 5). Commonly used target materials: carbon, aluminum, steel and brass were considered, as well as a titanium-aluminum alloy. For protons and deuterons, reactions leading to the following products were included: n, p, d, t, ^3He and α . For ^7Li beams, reactions leading to n, p, d, t, ^3He , α , ^6He and ^6Li were included. For each reaction, the radioactive residual nucleus is identified and its primary decay mode is tabulated. Long lived isotopes are not included because unrealistically large ion-beam fluences would be required to produce significant radioactivities.

For the alloy targets, only isotopes for which the product of the isotopic abundance and the alloy proportion exceeds 1% are considered because these isotopes are expected to be the primary sources of radioactivity. Compositions of the targets included in these surveys are listed in Table I.

Measured cross sections for some of these reactions were found in the published literature. The compilations of McGowan *et al.*⁶ were used to locate published sources prior to 1976. Additional sources were found in the

Table I. Composition of Target Materials

Material	Elemental Abundance	Isotope	Isotopic Abundance
Carbon	100% C	^{12}C	98.9%
		^{13}C	1.1%
Aluminum	100% Al	^{27}Al	100.0%
Titanium 6-4 alloy	90% Ti	^{46}Ti	8.0%
		^{47}Ti	7.5%
		^{48}Ti	73.7%
		^{49}Ti	5.5%
		^{50}Ti	5.3%
	6% Al	^{28}Al	100.0%
	4% V	^{51}V	99.8%
Stainless Steel (#304)	70% Fe	^{54}Fe	5.8%
		^{56}Fe	91.7%
		^{57}Fe	2.1%
	20% Cr	^{52}Cr	83.4%
	10% Ni	^{58}Ni	68.3%
		^{60}Ni	26.1%
Brass	67% Cu	^{63}Cu	69.1%
		^{65}Cu	30.9%
	33% Zn	^{64}Zn	48.9%
		^{66}Zn	27.8%
		^{68}Zn	18.6%

compilation of Keller *et al.*⁷ The information service DIALOG⁸ was used for the period from 1976 to 1992. In addition, *Physics Abstracts* was used to supplement this later period. No attempt was made to incorporate cross sections from unpublished reports.

Cross sections determined from residual radioactivities, rather than from prompt particle emissions, are the desired quantities. In many cases, excitation functions are determined by measuring residual radioactivities induced in stacked foils. For reactions where sufficient excitation functions are available, the cross sections are combined with known stopping cross sections⁹ to determine thick-target yields. Graphs of thick-target yield versus incident ion energy may be found in Refs. 4 and 5. Results from these surveys are summarized in this report. For protons and deuterons, some cross sections are well documented in the literature, while others have substantial discrepancies. For lithium-7 ions, there is a real need for additional measurements in the energy range of interest.

II. PROTON-INDUCED RADIOACTIVITIES

For proton-induced reactions, the radioactivities are produced primarily by (p,n) reactions. Threshold energies for these reactions on the targets in Table I are listed in

Table II along with the primary decay modes of the residual nucleus (β^+ for positron decay and ϵ for electron capture). The decay modes, half lives, β -decay end-point energies (E_β), and most intense γ -ray energies (E_γ) are taken from Ref. 10. The most intense γ -decays are identified from Ref. 11. Most of these reactions are well studied, and thick-target yields were evaluated using published cross sections.⁴ The thick-target yields increase rapidly from threshold. At 10 MeV, the yields are largest ($\approx 10^{-3}$ reactions/proton) for the $^{51}\text{V}(\text{p},\text{n})$ and $^{65}\text{Cu}(\text{p},\text{n})$ reactions. These two reactions also have the lowest threshold energies.

Residual activities induced in each elemental target by a pulse of 10^{16} protons at 10 MeV are also listed in Table II. These activities range from several Curies to negligible quantities. The (p,n) reactions on ^{49}Ti and ^{57}Fe are not included in Table II because extremely large fluences would be required to produce significant activities of the longer lived ^{49}V ($T_{1/2} = 331$ da) and ^{57}Co ($T_{1/2} = 271$ da) isotopes. A single intense proton pulse may contain more than 10^{16} protons (30 kA for 60 ns) and produce substantial radioactivity depending on the target composition.

Table II. Radioactivities from (p,n) Reactions

Reaction	Threshold Energy (MeV)	Residual Nucleus			Activity induced by 10^{16} protons at 10 MeV (mCuries)	
		Decay Mode	Half Life	E_β (MeV)	E_γ (MeV)	
$^{13}\text{C}(\text{p},\text{n})^{13}\text{N}$	3.25	β^+	10 min	1.20	0.51	1.4
$^{27}\text{Al}(\text{p},\text{n})^{27}\text{Si}$	5.8	β^+	4.2 s	3.8	0.51	4500.
$^{47}\text{Ti}(\text{p},\text{n})^{47}\text{V}$	3.8	β^+	31 min	1.90	0.51	3.3
$^{48}\text{Ti}(\text{p},\text{n})^{48}\text{V}$	4.9	β^+, ϵ	16.0 da	0.70	1.31	0.054
$^{51}\text{V}(\text{p},\text{n})^{51}\text{Cr}$	1.6	ϵ	27.7 da	-	0.32	0.077
$^{52}\text{Cr}(\text{p},\text{n})^{52\text{m}}\text{Mn}$	6.0	β^+	21 min	2.63	1.434	42.
$^{56}\text{Fe}(\text{p},\text{n})^{56}\text{Co}$	5.5	ϵ, β^+	78 da	1.46	0.847	4.8×10^{-6}
$^{60}\text{Ni}(\text{p},\text{n})^{60}\text{Cu}$	7.0	β^+	23 min	3.77	1.76	8.0
$^{63}\text{Cu}(\text{p},\text{n})^{63}\text{Zn}$	4.2	β^+	38 min	2.34	0.51	39.
$^{65}\text{Cu}(\text{p},\text{n})^{65}\text{Zn}$	2.2	ϵ	244 da	-	1.115	0.008
$^{64}\text{Zn}(\text{p},\text{n})^{64}\text{Ga}$	8.0	β^+	2.6 min	6.05	0.51	37.
$^{66}\text{Zn}(\text{p},\text{n})^{66}\text{Ga}$	6.05	β^+, ϵ	9.5 hr	4.15	0.51	0.71
$^{68}\text{Zn}(\text{p},\text{n})^{68}\text{Ga}$	3.75	β^+	68 min	1.90	0.51	6.9

III. DEUTERON-INDUCED RADIOACTIVITIES

For deuteron induced reactions, radioactivities are produced primarily by (d,n), (d,p) and (d, α) reactions. The (d, α) yields are smaller than the (d,n) or (d,p) yields. Thick-target yields for the (d,n) and (d,p) reactions increase rapidly with incident deuteron energy and approach $\sim 5 \times 10^{-4}$ reactions/deuteron at 10 MeV. For a carbon target, the most prolific activity is ^{13}N from the $^{12}\text{C}(\text{d},\text{n})^{13}\text{N}$ reaction. The cross section and thick-target yield for this reaction are well known.⁴ For an aluminum target, the primary activity is ^{28}Al from the $^{27}\text{Al}(\text{d},\text{p})^{28}\text{Al}$ reaction. Large differences in measured cross sections for this reaction are reported, as indicated in Fig. 1. A fit to cross sections from Refs. 12, 13 and 14 is shown in this Figure. Two more recent cross section measurements^{15,16} are much larger than this best fit. The reason for the large differences at 3 MeV ($\times 160$) and at 6.8 MeV ($\times 4$) is not known. Results from Ref. 15 (0.6 to 3.2 MeV) are based on thick-target measurements. In a thick target, additional ^{28}Al activity may be produced by the $^{27}\text{Al}(\text{n},\gamma)^{28}\text{Al}$ reaction induced by neutrons from the $^{27}\text{Al}(\text{d},\text{n})$ reaction in the same target. This process may account for the large cross sections in Refs. 15 and 16. This process was shown to be negligible for the measurements in Ref. 14. Further measurements are needed to provide reliable cross sections for this reaction.

For the alloy targets, a specific radioactivity may be produced by several different deuteron induced reactions.

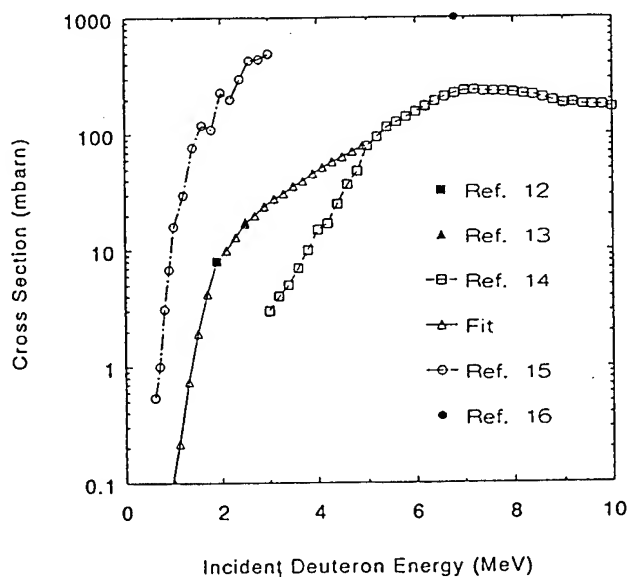


Fig. 1. Measured cross sections for $^{27}\text{Al}(\text{d},\text{p})^{28}\text{Al}$ reaction. The fit is for cross sections from Refs. 12, 13 and 14.

Therefore, it is difficult to associate a measured radioactivity with one nuclear reaction. Consequently, only a limited number of cross sections have been measured for these elements. Excitation functions, generated by piecing together cross sections from several different sources, were used to evaluate thick-target yields for deuteron induced activities in the alloy targets.⁴ Yields from 2 to 10 MeV were calculated for the following activities and targets: ^{52}Mn , and $^{52\text{m}}\text{Mn}$ for chromium; ^{54}Mn , ^{55}Co and ^{57}Co for iron; ^{56}Co , ^{58}Co , ^{59}Cu and ^{61}Cu for nickel; ^{64}Cu , ^{66}Cu , ^{63}Zn and ^{65}Zn for copper; and ^{64}Zn , ^{65}Zn , ^{69}Zn , $^{69\text{m}}\text{Zn}$, ^{67}Ga and ^{68}Ga for zinc. These yields for elemental targets may be proportioned appropriately for different alloy targets.

IV. LITHIUM-INDUCED RADIOACTIVITIES

The survey⁵ of ^7Li induced radioactivities includes only positive Q-value reactions. The ($^7\text{Li},\text{n}$), ($^7\text{Li},\text{p}$) and ($^7\text{Li},\alpha$) reactions have Q-values ranging from 5 to 17 MeV and are likely sources of residual activities. Cross sections or thick-target yields for these reactions leading to residual activities have been reported only for the $^{12}\text{C}(^7\text{Li},\text{n})^{18}\text{F}$ reaction.^{17,18} No measurements for reactions leading to residual activities were found for other targets in Table I. Measurements of other lithium induced reactions on low-atomic-number targets indicate that the yields of these reactions increase rapidly with incident energy until the energy becomes comparable with the Coulomb barrier. For carbon and aluminum, thick-target yields of up to 10^{-5} reactions/ ^7Li are estimated, and somewhat lower yields are estimated the higher-atomic-number targets.⁵

V. SUMMARY

Activities from these surveys are compared with measurements¹⁹ of radioactivities induced in various targets by 6- and 12-MeV protons, by 6-MeV deuterons, and by 10-, 15-, 20- and 30-MeV ^7Li ions. Composite half lives (min to hr) of activities in each target were determined to evaluate the radiological hazard from these intense pulsed beams. In addition, some long lived activities were identified using high resolution γ -ray spectroscopy. The composite half lives and activities from the proton and deuteron reactions are consistent with expectations from these surveys. For ^7Li ions, no activation of aluminum, stainless steel or brass was detectable for energies less than 20 MeV; however, these activities were observed to increase rapidly from 20 to 30 MeV, particularly for stainless steel and brass. These results are consistent with inhibition of the ^7Li induced reactions by Coulomb barrier penetration for ^7Li energies below 20 MeV.

It is difficult to diagnose intense pulsed ion beams.¹ However, measurements of residual nuclear activations have been used quite successfully for few MeV proton and deuteron beams.³ Appropriate nuclear reactions are chosen to provide high sensitivity and to avoid interfering reactions. As intense pulsed beams of higher energy and different species (e.g., lithium, boron) are developed, different nuclear reactions must be selected to diagnose such beams. Unfortunately, the present nuclear reaction data base is insufficient to guide the experimentalist in selecting appropriate reactions and targets for beams of higher energy and different species. For protons, (p,n) reactions are attractive because they are reasonably well characterized, and their yields are sensitive to the incident proton energy. For deuterons, the nuclear reaction data base is limited,⁴ and large discrepancies are reported for some reactions (see Fig. 1 and Ref. 20). For lithium beams, almost no activation measurements have been reported in the energy range of interest. Measurements of excitation functions and cross sections or thick-target yields for a variety of nuclear reactions will be required in order to extend the nuclear-activation technique as a diagnostic for higher-energy intense light-ion beams.

ACKNOWLEDGMENT

This work was supported by the U.S. Department of Energy through Sandia National Laboratories.

REFERENCES

1. S. Humphries, Jr., *Nuclear Fusion*, **20**, 1549 (1980).
2. J.P. VanDevender and D.L. Cook, *Science*, **232**, 831 (1986).
3. F.C. Young, J. Golden and C.A. Kapetanakis, *Rev. Sci. Instrum.*, **48**, 432 (1977).
4. F.C. Young and D.V. Rose, "Survey of Nuclear Activations for Intense Proton and Deuteron Beams," Naval Research Laboratory Report MR/6770-92-7155, December, 1992.
5. F.C. Young and D.V. Rose, "Survey of Radioactivities Induced by Lithium Ions," Naval Research Laboratory Report MR/4770-92-6974, June, 1992.
6. F.K. McGowan, W.T. Milner, H.J. Kim and Wanda Hyatt, *Nuclear Data Tables*, **A6**, 353 (1969); **A7**, 1 (1969); F.K. McGowan and W.T. Milner, *Nuclear Data Tables*, **A8**, 199 (1970); **9**, 469 (1971); **11**, 1 (1972); *Atomic Data and Nuclear Data Tables*, **12**, 499 (1973); **15**, 189 (1975); **18**, 1 (1976).
7. K.A. Keller, J. Lange, H. Münzel and G. Pfennig, "Excitation Functions for Charged-Particle Induced Nuclear Reactions", *Landolt-Bornstein Numerical Data and Functional Relationships in Science and Technology*, edited by H. Schopper, Vol. 5, Part b, Springer-Verlag, New York, 1973.
8. DIALOG Information Services, Inc., 3460 Hillview Ave., Palo Alto, CA 94304.
9. H.H. Andersen and J.F. Ziegler, *The Stopping and Ranges of Ions in Matter*, Vol. 3, Hydrogen, Pergamon Press, New York (1977).
10. *Chart of the Nuclides*, Knolls Atomic Power Laboratory, 11th Edition, April, 1972.
11. C.M. Lederer, J.M. Hollander and I. Perlman, *Table of Isotopes*, 6th Edition, John Wiley, New York (1967).
12. E. McMillan and E.O. Lawrence, *Phys. Rev.*, **47**, 343 (1935).
13. C.S. Lin and E.K. Lin, *Nuovo Cimento*, **66A**, 336 (1970).
14. J.M. Flores, *Phys. Rev.*, **127**, 1246 (1962).
15. E. Schuster and K. Wohleben, *J. Appl. Rad. Isotopes*, **19**, 471 (1968).
16. R.L. Wilson, D.J. Frantsvog, A.R. Kunselman, C. Détraz and C.S. Zaidins, *Phys. Rev.*, **C13**, 976 (1976).
17. E. Norbeck, Jr. and C.S. Littlejohn, *Phys. Rev.*, **108**, 754 (1957).
18. E. Norbeck, *Phys. Rev.*, **121**, 824 (1961).
19. S.K. Vosburg, C.L. Ruiz, G.W. Cooper and F.A. Schmidlapp, "An Experimental Investigation of Radioactivity Induced by Ions Associated with the Operation of Pulsed-Power Accelerators," Sandia National Laboratories Report SAND92-2075, March, 1993.
20. H. Okamura and S. Tamagawa, *Nucl. Phys.*, **A169**, 401 (1971).

Film deposition and surface modification using intense pulsed ion beams

C. A. Meli,^{a)} K. S. Grabowski,^{b)} D. D. Hinshelwood,^{c)} and S. J. Stephanakis
Naval Research Laboratory, Washington, DC 20375

(P)220

D. J. Rej^{d)} and W. J. Waganaar
Los Alamos National Laboratory, Los Alamos, New Mexico 87545

(Received 11 November 1994; accepted 14 March 1995)

High-power pulsed ion beams have been used to ablate material for ultrahigh-rate film deposition and to treat the surfaces of alloys. Pulsed ion beams were provided by the high-power-density Gamble II facility at the Naval Research Laboratory [high voltage (~ 900 keV), short pulse (60 ns)] and the lower-power-density Anaconda facility at Los Alamos National Laboratory [lower voltage (~ 300 keV), longer pulse (400 ns)]. Peak film deposition rates after target ablation reached 1 mm/s. Films of pure Al, pure Ta, YBCO, and Ni-Zn ferrite were deposited on glass and single-crystal substrates, in some cases heated. The film deposition process was studied with framing photography, a bolometer, and other diagnostics to gain an understanding of the ablation, transport, and deposition steps. Stoichiometric deposition of multicomponent targets has been demonstrated. Film morphology remains poor, but has steadily improved, and our present understanding points the way to further improvement. Lower fluences (~ 5 J/cm²) were used to investigate rapid thermal processing of metal surfaces for the enhancement of corrosion resistance. The results in this area have been negative, but here again the knowledge gained through these experiments allows us to propose directions for improvement. © 1995 American Vacuum Society.

I. INTRODUCTION

Over the past decade, interest has grown in the use of high-power, pulsed light-ion beams for intense heating of surfaces. High-power heating will vaporize and ablate material for physical deposition, while lower power heating can directly modify the surface properties of materials. Various factors make these applications of pulsed light-ion beams attractive for development.

Technology for ion-beam production continues to advance, with clean, intense, repetition-rated sources already in operation.¹ Ion-beam production is more energy efficient than laser-beam production, and the efficiency of ion-beam energy deposition in the target (which is 100%) can be orders of magnitude higher than that of laser-beam energy deposition; ions also penetrate both plasmas and metal targets. Hundreds of square centimeters can be irradiated per pulse, allowing for quick coating or modification of large areas.

High beam fluences (~ 100 J/cm²) from short pulses (~ 100 ns) combined with the relatively deep penetration of energetic ions (~ 10 μ m for 1 MeV H⁺) can lead to peak rates of ablation and associated deposition of a few centimeters per second. Many of the operational advantages of pulsed laser deposition² (PLD) apply (e.g., stoichiometric transfer of target material to the substrate; deposition in high-pressure, reactive ambients; energetic flux), and these are supplemented with a 10^4 -times increase in deposited thickness per beam pulse. This opens the possibility for quick deposition of thick multicomponent films over large areas. This technique has been demonstrated by production of

metal films and films of electronic and tribological interest.³⁻⁶

Lower beam fluences that do not vaporize the target can be used to directly modify the target's near-surface properties. Typical ion-beam energy distributions lead to relatively uniform energy deposition over a depth of a few microns. The short pulse duration allows rapid heating and cooling of the surface layer ($\sim 10^9$ K/s) with weak subsurface heating. The near-surface region can thus be selectively modified by a combination of annealing/quenching and thermal compression/shock, leading to dissolution of suspended particulates, and/or metastable alloy creation. (Although ion implantation also occurs, in the pulsed high-energy ion regime the implanted ion concentration is usually negligible.) As with film deposition, this can be accomplished quickly over a large target area. Previous experiments have shown that pulsed-ion-beam treatments can harden and polish steel and titanium alloy surfaces and extend the fatigue limit of turbine blade alloys.^{1,6,7}

We report here investigations of pulsed-ion-beam evaporation (PIBE), film deposition, and direct modification that were performed at two different ion-beam facilities: Gamble II at the Naval Research Laboratory, and Anaconda at Los Alamos National Laboratory. Single-component targets (Al, Ta) were used to characterize the effects of deposition parameters on film production, while Ni-Zn ferrite and YBCO were used as test targets for multicomponent deposition studies. Steel and coated Al samples were used to test the effects of direct irradiation.

II. PULSED-ION-BEAM SYSTEMS USED

The relevant operational parameters for the pulsed-ion-beam systems used in these experiments are shown in Table I. The bulk of this work utilized the Gamble II pulse power generation facility at the Naval Research Laboratory.⁸

^{a)}Electronic mail: meli@nrlfsl.nrl.navy.mil

^{b)}Electronic mail: grabowsk@nrlfsl.nrl.navy.mil

^{c)}Electronic mail: ddhesuzie.nrl.navy.mil

^{d)}Electronic mail: drej@lanl.gov

TABLE I. Operational parameters for pulsed-ion-beam systems used.

Parameter	Gamble II	Anaconda
Marx bank	72 stages	10 stages
Pulse forming line	Yes	No
Maximum output	267 kJ at 1.2 MV	300 kJ at 1.2 MV
Pulse rise time	30 ns	100 ns
Pulse full width at half maximum	60 ns	400 ns
Maximum power	5 TW	400 GW
Power into diode in these experiments	1 TW	9 GW
Diode voltage and current	~900 kV, 500 kA	200–400 kV, 30 kA
Beam composition	90% H ⁺ , 10% C ²⁺	20% H ⁺ , 42% C ⁺ /C ²⁺ , 38% O ⁺ /O ²⁺
PIBE		
Beam–target angle and beam area on target	45°, 22 cm ²	30°, 28 cm ²
Fluence at target, normal to beam	40–60 J/cm ²	30±15 J/cm ²
Current density at target, normal to beam	640–960 A/cm ²	250 A/cm ²
Power density at target, normal to beam	570–860 MW/cm ²	75±37 MW/cm ²
Direct modification		
Fluence at target, normal to beam	2–10 J/cm ²	...

A backless pinch-reflex ion diode was used in this system.⁹ The flat, circular anode was a 12 cm diameter, 13 μ m thick polyethylene sheet, which had to be replaced after each beam pulse. The target chamber pressure varied between 10^{-3} and 3 Torr of air or Ar before the beam pulse; pressure after the

beam pulse was not measured. Beam fluence on target decreased with both distance from the anode plane and distance from the anode centerline.

Additional film deposition experiments were carried out at the Anaconda intense ion beam accelerator at Los Alamos National Laboratory.^{10,11} An extraction-geometry, applied-*B* field, magnetically insulated ion diode was used on Anaconda.⁴ It employed an annular dielectric flashover anode (194 mm i.d., 292 mm o.d., 6.4 mm thick) made of Lucite. This diode was repetition-rated for 12 pulses/h, with cleaning necessary after approximately 20 beam pulses. A target chamber pressure of 10^{-5} Torr was required before the beam pulse, and this rose to 0.1 Torr immediately after each beam pulse.

III. FILM DEPOSITION

A. Gamble II experiments

A schematic of the setup for PIBE experiments is shown in Fig. 1. Only the central region of the ion beam was selected with a 2.2 cm diameter circular aperture. The diode–target distance was varied during initial experiments from 31 to 65 cm. At the low end of this range the ablation of the aperture plate was deemed deleterious, while at the high end fluence on the target was too low for significant film deposition. A diode–target distance of 41 cm was used in all experiments referenced here. The target and substrate were parallel, and the target–substrate distance was 10 cm. Substrates were mainly glass slides at room temperature, with a few experiments including single-crystal substrates (MgO, Si) at room temperature and elevated temperatures.

Four different materials were used as targets in this work. Al and Ta foils of various thicknesses (ranging from 2 to

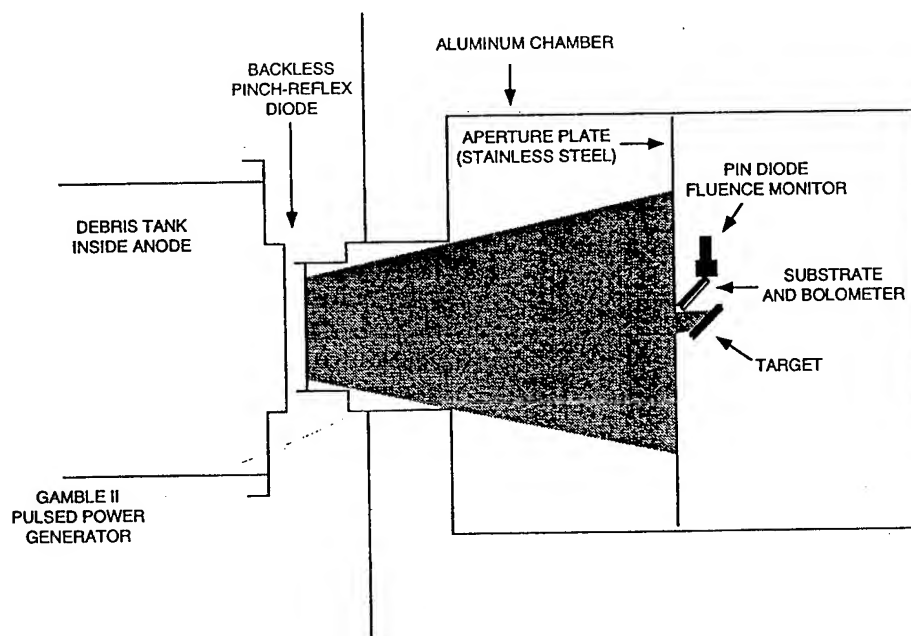


FIG. 1. Schematic arrangement for pulsed ion beam evaporation and film deposition using the Gamble II pulse power generator. (For a scale diagram of the similar arrangement using the Anaconda facility, see Ref. 4.)

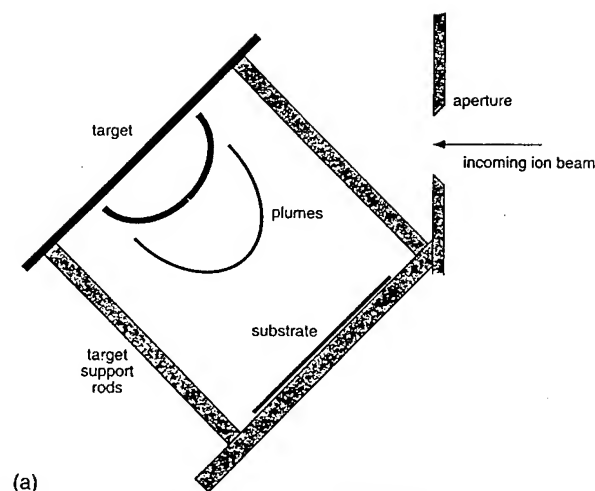
25 μm) were used as simple test materials to examine the effects of varying the beam conditions, deposition geometry, target thickness, and ambient conditions. The target thickness was important because ~ 1 MeV protons have a range of 15 μm in Al and 6 μm in Ta, so the ion range could exceed the target thickness in some cases. Energy deposition was roughly uniform throughout the thinner targets, while the effects of the finite proton range could be judged using the thicker targets. Thick YBCO ($\text{Y}_1\text{Ba}_2\text{Cu}_3\text{O}_{6.9}$) and Ni-Zn ferrite ($\text{Ni}_{0.75}\text{Zn}_{0.25}\text{Fe}_2\text{O}_4$) targets were used to evaluate the possibility of stoichiometric deposition, again with variation of deposition conditions.

The diode voltage and current were used to determine the ion energy distribution in the beam. For normal beam pulses this distribution consisted of a strong peak around 900 keV (proton energy) superimposed on a significant decaying distribution starting at the lowest ion energies. Fluence on target was determined either by measuring the postexposure activity of C targets mounted on the aperture plate, or with a *p-i-n* diode detector mounted near the substrate, which detected the intensity of ions backscattered from the target. (It should be noted that effective use of either of these techniques requires a knowledge of the energy distribution in the incoming beam.) Because the diode-target distance was fixed at 41 cm for these experiments, typical beam conditions led to fluences normal to the beam axis at the target position of 40–60 J/cm², or 28–42 J/cm² when corrected for the 45° tilt of the target with respect to the incoming beam.

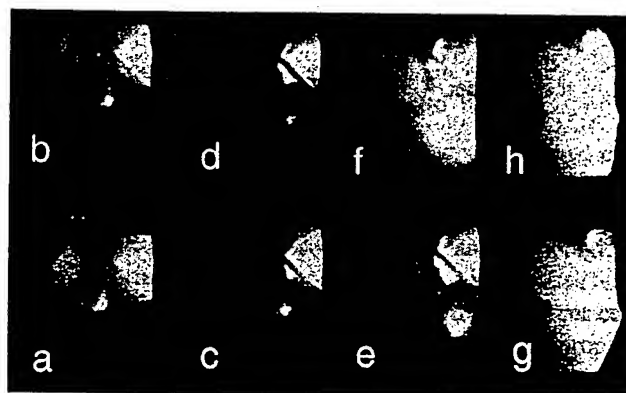
In some experiments using Al and Ni-Zn ferrite targets, the firing of the beam pulse activated a framing camera which was aimed at the target and substrate, perpendicular to the incoming beam (see Fig. 2). Eight frames were recorded in each photograph, with each frame separated by 1 μs . Luminous plumes traveling from the target to the substrate are clearly visible. A bright plume emanating from the beam aperture is also visible, and it is possible that the interaction of the target and aperture plumes had some effect on the deposition process. However, x-ray microanalysis of the films showed no measurable quantities of iron from the steel aperture plate.

In all framing photographs at least two luminous fronts are visible. The first, brighter, faster-moving front was observed to be turbulent for thin foil targets (1.8 and 6 μm Al) but smooth and symmetrical for thick targets (solid Al and ferrite). The speeds for these first fronts were found to be in the range $(5.6\text{--}10.2)\times 10^3$ m/s, with the particular speed apparently far more dependent on the beam pulse conditions than the target material. In some cases this leading front was photographed contacting the substrate, and in all cases this contact produced an extremely bright flash, possibly due to excitation of material adsorbed on the substrate as well as the substrate itself. The second dimmer and broader plume was in all cases smooth and symmetrical, with speeds of $(2.3\text{--}5.2)\times 10^3$ m/s, again uncorrelated with the target material.

An 8 μm thick W strip was positioned next to the substrate as a bolometric temperature sensor. Electronic noise obscured the output signal for approximately 10 μs after the beam pulse, but beyond this time the signal provided a re-



(a)



(b)

FIG. 2. (a) Target and substrate positions in framing photographs. (b) Representative series of framing photographs, separated by 1 μs intervals, beginning approximately 6 μs after the ion-beam impact on a thick Al plate 10 cm from a glass substrate. Two ablation plumes are clearly visible: a fast front ($v=8.8\times 10^3$ m/s) and a slower, dimmer extended cloud ($v=5.2\times 10^3$ m/s). (The bright plume on the right is from ablation of the admitting aperture.) Contact of the fast front to the substrate and its mounting produced an intense, sustained flash.

producible measure of bolometer heating by arriving material. Temperature equilibration through the bolometer after a heat pulse at the surface was calculated to occur in <1 μs .

The increase in bolometer temperature over time was qualitatively similar for different materials (see Fig. 3). The temperature rose rapidly over about 10 μs , then stabilized or cooled slightly for 5–10 μs , then rose again. In experiments utilizing thinner 1.8 μm thick Al targets, bolometer heating ceased approximately 30 μs after the beam pulse. When thick targets were used the bolometer temperature was still rising when the data collection limit was reached at 60 μs . The two heating regimes observed correspond to the fast and slow plumes seen in the framing photographs. The long-time heating seen with thick targets can be attributed to slow, relatively cool material ejected from the target surface by some secondary process related to the underlying substrate. (Perhaps ablation-generated shock waves splashed liquid droplets from the surface.) The target material also affected the bolometer response; thick Al targets led to stronger heating than thick ferrite targets. This could be due to hotter

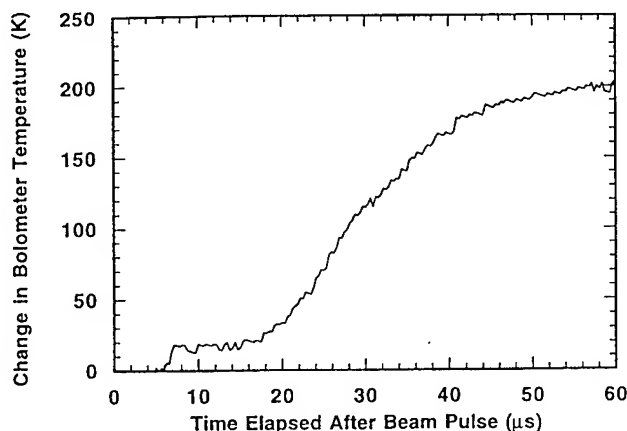


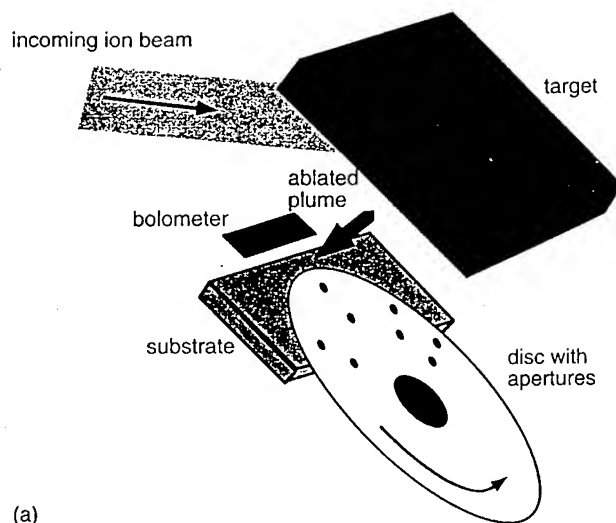
FIG. 3. Typical bolometer response to a plume arriving after a beam pulse: thick Ni-Zn ferrite target 10 cm from the substrate/bolometer mounting.

plumes, greater thermal mass arriving, better sticking of the Al to the bolometer, or a combination of these effects.

An estimate of the average temperature of incoming Al can be made by assuming that most of the material arrives within 60 μ s. For a particular deposition the change in bolometer temperature from room temperature was measured to be 605 K at 60 μ s. Subsequently the average film thickness was determined to be $\sim 1 \mu$ m with profilometry. Taking into account the thermal masses of the W bolometer and Al film, the average temperature of the incoming Al was calculated to be 1223 $^{\circ}$ C, within the liquid temperature range. It must be emphasized that this is merely an average; structure in the bolometer signal and other diagnostics indicate that small amounts of very hot vapor arrive at the beginning of the deposition process, followed by progressively cooler material as the process proceeds.

Both the framing photograph and bolometer results indicate that the deposition process involves two or more fronts of material arriving over relatively long (100 μ s) periods. To resolve the interaction of these different fronts with the substrate, a disk (11 cm diameter) with small apertures (1 mm diameter circles) located at various radii, rotating at 25 000 rpm, was introduced between the target and substrate. Arriving material was deposited in streaks, with a time resolution of $\sim 10 \mu$ s, so film properties as a function of arrival time could be judged (see Fig. 4).

Results using the spinning disk with different target materials were qualitatively similar, but the effect of target thickness was pronounced. The deposition from 1.8 μ m Al targets was confined to a $\sim 20 \mu$ s span. The bulk of the deposition from all thick targets took place over 40 μ s, but a thin tail stretched to $\sim 100 \mu$ s beyond the earliest arriving material. (The time from the beam pulse to earliest deposition of material was not conclusively determined, but inspection of the framing photographs suggests this occurred when the slower plume contacted the substrate, $\sim 20 \mu$ s after the beam pulse.) The earliest arriving material produced films that were rough on a 1 μ m scale. Later arriving material produced progressively rougher films, with films deposited beyond 40 μ s composed almost exclusively of $>10 \mu$ m droplets. Films due to the earliest arriving material were of-



(a)



(b)

FIG. 4. (a) Schematic arrangement for spinning aperture disk experiments. (b) Example of deposition through spinning aperture: thick Al target 10 cm from disk/substrate. Several overlapping fronts are visible. The first material arrives $\sim 20 \mu$ s after the beam pulse. Most material arrives over 21 μ s (time interval between crosses), but an increasingly rough, weak tail extends for $\sim 100 \mu$ s.

ten thin and cracked; these features suggest strong substrate heating and possible film evaporation.

All films deposited using PIBS were examined under optical or scanning electron microscopy [examples for Gamble II are shown in Figs. 5(a) and 5(b)]. Films ranged from smooth but grainy (1 μ m scale features) to extremely rough ($>100 \mu$ m scale features), depending mainly on target thickness and beam fluence. The smoothest films from Gamble II were produced using the thinnest targets (e.g., 1.8 μ m Al), with the structure in these films seemingly due to surface tension effects (perhaps from a liquid film not wetting the substrate). The roughest films were produced from high-fluence pulses incident on thick targets. The roughest films were also the thickest and were composed of very large droplets that apparently were splashed out of the target, remelting the film from earlier arriving material. Film morphologies varied over the large ($\sim 50 \text{ cm}^2$) deposition area, indicating inhomogeneity in the arriving plume.

Surface profilometry confirmed both the thickness and roughness of the deposited films. Films ranged from 0.5 to 1.5 μ m in average thickness, depending upon target and beam fluence conditions. Film roughness was typically $\pm 0.5 \mu$ m.

For one series of experiments a pulsed gas valve was installed in the sample chamber, to determine how high am-

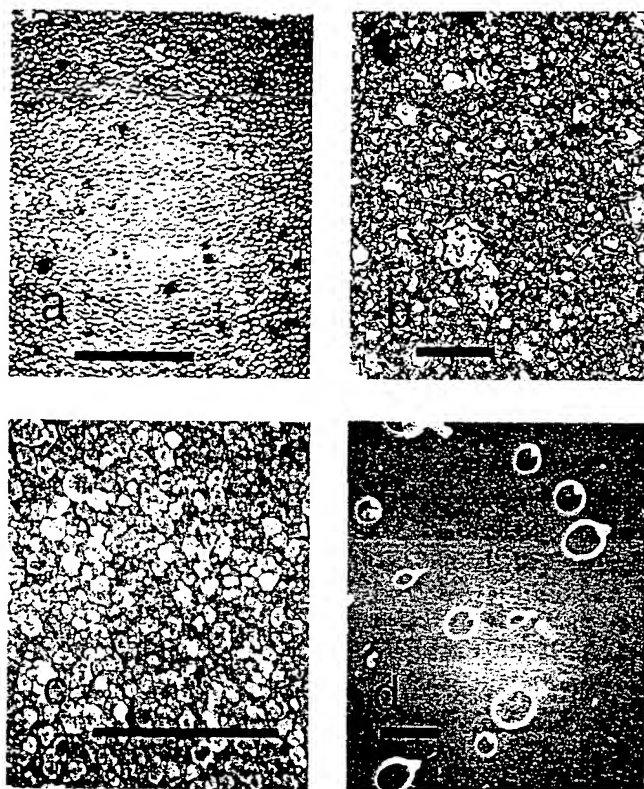


FIG. 5. Representative film morphologies; note the differences in magnification scales. (a) Gamble II, 1.8 μm thick Al target, glass slide substrate (bar=20 μm); (b) Gamble II, thick Al target, glass slide substrate (bar=20 μm); (c) Anaconda, thick Al target, Si substrate, ten pulses (bar=1 μm); (d) Anaconda, thick Ni-Zn ferrite target, Si substrate, single pulse (annular droplets on smooth film; bar=1 μm).

bient pressures affect the thermal and transport properties of the ablated plume. This valve was opened simultaneously with the beam pulse, and provided a maximum pressure of 500 Torr N_2 for 5 ms between the target and substrate.¹² This high gas pressure clearly blocked material transport, leaving film-free regions on the substrate surface nearest the gas valve. Similarly, framing photographs showed a large distortion of the ablated plume fronts. However, no systematic effects on film composition or morphology were observed. These results suggest that the interaction of the high-pressure ambient and high-density ablation plume are better treated as the interaction of two continuum fluids, rather than as the mixing of microscopic particles.

While film morphologies were generally poor, stoichiometric deposition of both YBCO and Ni-Zn ferrite was demonstrated. Films of both materials were examined using x-ray microanalysis and Rutherford backscattering. These measurements confirmed that the metal stoichiometric ratios were the same within measurement uncertainty as those of the target. X-ray diffraction measurements of YBCO films deposited on glass at room temperature showed no diffraction peaks, while similar measurements of Ni-Zn ferrite films led to weak peaks indicating a polycrystalline metastable phase. YBCO deposited on MgO at elevated substrate temperatures ($>500^\circ\text{C}$) was polycrystalline with some evidence for phase separation. Ni-Zn ferrite deposited on MgO at similar temperatures was found to be in the ferrite phase

and polycrystalline, with a weak preferred orientation in the [111] direction.

In general PIBE using Gamble II produced thick, stoichiometric films over a large area. The morphologies of these films were generally poor, but films produced using thin targets were much smoother than films produced with thick targets. Also, smoother films were observed as the result of early-arriving, hot material, while late-arriving material was predominantly in the form of liquid droplets. This late-arriving material is thought to be liquid on the surface of the target that was ejected by the ablation shock, rather than liquid condensed out of the ablation plume. These results suggest that film morphology could be improved by reducing the amount of low-temperature material in the plume. One approach to this problem would be to increase the fluence on target by a factor of two or more; this was precluded in the present experiments by the necessity of the aperture plate. Another approach would be to use heavier ions (e.g., Ne^+) at fluences similar to those in our experiments. The shallower penetration of these ions would heat less material, but the heated material would be vaporized rather than liquefied.

B. Anaconda experiments

The deposition arrangement using the Anaconda facility was similar to that using Gamble II. The annular beam from Anaconda was focused to a spot on the target, so no aperture was necessary. (A scale diagram of the diode-target-substrate geometry can be found in Ref. 4.) The target-substrate distance was 8 cm. Glass slides and single-crystal substrates (MgO , SrTiO_3 , Si, and Y-stabilized ZrO_2) at room temperature and at elevated temperatures were used as substrates, and thick Al and Ni-Zn ferrite plates were used as targets. The 30° inclination of the target with respect to the beam reduced the fluence on target to $15 \pm 8 \text{ J/cm}^2$. This lower fluence coupled with the lower beam energy of Anaconda led to much less target ablation per beam pulse than with Gamble II, so multiple pulses were necessary to produce films with thicknesses $>100 \text{ nm}$.

The investigations using Anaconda concentrated on analysis of deposited films. Films produced with single pulses were all much thinner than comparable films from Gamble II, as less material was ablated by the higher-mass, shallower-penetrating ion beam. Al films deposited onto glass at room temperature were much smoother than Al films produced with Gamble II; 100 nm grains could only be resolved using high-resolution scanning electron microscopy, and these were part of uniform and relatively thin (100 nm) film. Results with Ni-Zn ferrite targets were similar, with the addition of larger annular droplets on top of the very thin (few nm) uniform film. Multiple depositions on the same substrate led to increasing film roughness as droplet concentration increased.

Ni-Zn ferrite was deposited on single-crystal substrates held at room temperature, 500, 600, and 700°C , in an attempt to produce oriented crystalline films. However, x-ray diffraction revealed no crystalline material in any of these films. While elevated substrate temperature should have been beneficial for crystallization, it may also have depleted oxy-

gen from the films as they were held at temperature in vacuum.

These limited results from Anaconda are an interesting contrast to those with Gamble II, in that much smoother but much thinner films were produced. Heavier beam ions at lower energies, which provide higher specific energy deposition, clearly lead to smoother films under comparable fluence conditions, but at the expense of film thickness. This again suggests that beams with comparable fluence and energy, made up exclusively of heavier (e.g., Ne^+) ions, would be optimal for PIBE. Such a beam would suppress the weak, deep heating of the target, which apparently produces liquid droplets, while vaporizing the target surface.

IV. DIRECT MODIFICATION

Some initial tests of direct surface modification by pulsed ion beams were performed using Gamble II. Stainless steel (303 alloy) disks and aluminum (6061 alloy) disks coated with Cr on Zr (thickness 30 or 100 nm), all with faces polished to a 1 μm finish, were directly exposed to the beam. The targets were mounted on the front of the aperture plate used in the PIBE experiments, and this plate was moved back from the diode (95–160 cm) to reduce the fluence at the targets' surfaces. The sample chamber was also filled with 3 Torr Ar to eliminate C^{2+} ions and their associated high specific energy deposition.

The results of experiments with all target systems were qualitatively similar. Microscopic analysis of each sample surface combined with fluence measurements indicated a critical fluence existed for each of the systems (4.5 J/cm^2 for stainless steel, 3.4 J/cm^2 for Cr/Al, and <3.3 J/cm^2 for Zr/Al) below which the surface was not melted, and above which the surface was strongly roughened. No smoothing of small surface features was observed on the stainless steel samples exposed to subcritical fluences, indicating that no appreciable surface melting occurs below the roughening threshold. Below the critical fluence no mixing of the Cr or Zr into the Al was observed, and above the critical fluence the coatings were completely removed.

V. CONCLUSIONS

Pulsed-ion-beam evaporation and film deposition has been demonstrated with two different pulsed-ion-beam systems. The films produced have been thick, with the proper metal stoichiometries, but with relatively poor morphologies. These poor morphologies are attributed to slow-moving liquid droplets ejected from the target probably by the ablation shock. Complete vaporization of the heated surface region through greater energy deposition per unit volume should

minimize liquid production and increase film quality; this conclusion is born out in the successful results of experiments operating in this regime.^{5,6} Use of heavier ion beams of comparable energies and fluences as those used in these experiments could minimize liquid droplet production, and such beams should be available from gas ion diodes currently under development.

Initial tests of direct surface modification with pulsed ion beams from Gamble II have been disappointing. When beam fluences sufficient to melt target surfaces were used, both stainless steel and coated Al were strongly roughened, and Cr and Zr coatings on the Al targets were removed rather than intermixed. These results may come from the explosive removal of dissolved gases or from the large thermal and mechanical stresses that result from exposure. Possible remedies from these problems include use of heavier ions in the beam (to decrease penetration depth and decrease subsurface heating) and multiple beam pulses (for smoothing after dissolved gases are removed).

ACKNOWLEDGMENTS

The authors would like to thank B. Roberts for his technical assistance with experiments performed with Gamble II, and D. C. McIntyre and M. O. Thompson for preparation of the coated Al samples for the direct modification experiments. The portion of this work performed at Los Alamos is funded by the Laboratory Directed Research and Development Program at Los Alamos under the auspices of the U.S. Department of Energy.

¹R. W. Stinnett et al., in *Materials Synthesis and Processing Using Ion Beams*, edited by R. J. Culbertson (Materials Research Society, Pittsburgh, PA, 1994), Vol. 316, p. 521.

²*Pulsed Laser Deposition of Thin Films*, edited by D. B. Chrisey and G. K. Hubler (Wiley, New York, 1994).

³A. Kitamura, T. Asahina, Y. Furuyama, and T. Nakajima, in *Beams 92: Proceedings of the 9th International Conference on High-Power Particle Beams*, edited by D. Mosher and G. Cooperstein (NTIS, Springfield, VA, 1992), p. 976.

⁴G. P. Johnston et al., *J. Appl. Phys.* **76**, 5949 (1994).

⁵K. Yatsui et al., *Phys. Plasmas* **1**, 1730 (1994).

⁶G. E. Remnev and V. A. Shulov, *Laser Particle Beams* **11**, 707 (1993).

⁷V. A. Shulov et al., *Phys. Chem. Mater. Treat.* **26**, 647 (1992).

⁸J. R. Boller, J. K. Burton, and J. D. Shipman, Jr., in *Proceedings of the 2nd IEEE International Pulsed Power Conference*, edited by A. H. Guenther and M. Kristiansen (IEEE, Lubbock, TX, 1979), p. 205.

⁹S. J. Stephanakis et al., in *Beams 92: Proceedings of the 9th International Conference on High-Power Particle Beams*, edited by D. Mosher and G. Cooperstein (NTIS, Springfield, VA, 1992), p. 871.

¹⁰H. A. Davis, R. R. Bartsch, D. J. Rej, and W. J. Wagenaar, in *Beams 94: Proceedings of the 10th International Conference on High-Power Particle Beams*, edited by R. White and W. Rix (NTIS, Springfield, VA, 1995), p. 668.

¹¹D. J. Rej et al., *Rev. Sci. Instrum.* **64**, 2753 (1993).

¹²A. Fisher (private communication).

Numerical simulation of limiting currents for transport of intense relativistic electron beams in conducting waveguides

(P)219

D. V. Rose^{a)} and J. U. Guillory

Institute for Computational Sciences and Informatics, George Mason University, Fairfax, Virginia 22030

(Received 19 April 1995; accepted for publication 10 July 1995)

The space-charge limiting current for an intense, magnetized, relativistic electron beam injected into a grounded metallic pipe is investigated with a 2(1/2)-dimensional particle-in-cell code. Comparisons between the simulation results, the well known Bogdankevich-Rukhadze limiting current, and more recent theoretical estimates of the limiting current are presented. Transmitted currents >15% above those predicted by the Bogdankevich-Rukhadze and other limiting current estimates are observed. However, good agreement between the simulation results and the analytic estimates of Uhm [Phys. Fluids B 5, 1919 (1993)] and Fessenden [Lawrence Livermore Lab. Rep. No. UCID-16527 (1974)] is found. For an injected current above the limiting value, a virtual cathode is formed which alters the transmitted current density profile of the beam. A theoretical estimate of the magnitude of the transmitted current under this condition is compared with simulation results. The predicted transmitted current is found to be valid only for injected currents slightly above the limiting current. In addition, the transition between vacuum and ion-focused-regime transport, with and without an applied axial magnetic field is simulated. For ion-focus-regime densities ($n_p \sim n_b$), the effect of the virtual cathode in limiting the beam transmission is greatly diminished as expected. © 1995 American Institute of Physics.

I. INTRODUCTION

Intense relativistic electron beam transport has important application in a variety of areas, including collective ion acceleration,¹ x-ray production,² microwave generation,³ pasteurization of foods,⁴ and plasma heating for magnetically confined thermonuclear fusion.⁵ For many applications, it is desirable to transport the beam in vacuum, in a conducting, cylindrical tube. However, space charge and instabilities limit the amount of current that can be carried within the transport system. The amount of beam current that can be ideally transported is limited by the electrostatic potential "well" set up by the beam space charge, and is referred to as the limiting current. Relativistic beam energies can make the analytic determination of limiting currents difficult, and often approximate or numerical solutions are employed. One such limiting current for relativistic electron beams, the Bogdankevich-Rukhadze (BR) current,⁶ is investigated with the 2(1/2) dimensional, particle-in-cell (PIC) code MAGIC.⁷ Here, the BR limiting current is investigated for a single beam-to-wall radius ratio with a constant energy, constant current electron beam with a uniform density profile. Comparisons to more recent analytic estimates of the limiting current are also presented. It is found that all but one of published theories (that the authors are aware of) in the moderately relativistic energy range, $\gamma=1.5$ to 3.0, underestimate the limiting current value found in PIC codes. This overall result is consistent with other numerical simulations performed for $\gamma > 2.0$. The remaining theory provides a reasonably accurate estimate of the limiting current observed in the simulations. Possible mechanisms for the discrepancy between analytic estimates of the limiting current and the simu-

lations, such as induced axial electric fields and ponderomotive enhancements to the beam energy, are examined. The nonlinear behavior associated with the formation of virtual cathodes when these devices are operated near and above the limiting current values dictates the transmitted current. An analytic estimate of the transmitted current for a beam with injected current above the limiting value is compared with simulations.

In Section II, the BR limiting current is stated along with a discussion of the physical assumptions that are inherent in its derivation. Several more recent analytic estimates of the limiting current are also highlighted in this section. In Section III PIC simulations are presented under conditions similar to those under which the analytic limiting currents are derived. Also, this Section contains simulations to check the well known limiting current enhancements through the introduction of a low density background plasma. Conclusions are presented in Section IV.

II. LIMITING CURRENT THEORY

The problem of determining the maximum transportable current for a cylindrically symmetric electron beam propagating in an evacuated conducting tube was first solved for non-relativistic beams by Smith and Hartman.⁸ For an injected beam radius, r_b , and a guide tube radius, R , the limiting current was determined to be

$$I_l^{SH}(A) \approx 3 \times 10^{-5} \frac{V_b^{3/2}}{g}, \quad (1)$$

where

$$g = 1 + 2 \ln(R/r_b) \quad (2)$$

is a geometric inductance factor, and V_b is the accelerating potential at the beam source in volts. This result assumes a

^{a)}Permanent address: JAYCOR, Vienna, VA 22182; Electronic mail: rose@calvin.nrl.navy.mil

fully magnetized beam (via an infinite axial magnetic field) and it includes modeling of self-consistent radial variation in the axial velocity of the beam. It is also assumed that the length in the tube, L , is much greater than R . The g^{-1} factor in Eq. (1) is obtained from a fit to the limiting current values given in Ref. 8 and is valid over the range $g=1$ to 7.

For relativistic electron beams, the BR limiting current was derived for annular beams and extended, through an interpolation procedure, for solid beams⁶ to

$$I_l^{BR} = I_c \frac{(\gamma_o^{2/3} - 1)^{3/2}}{g}, \quad (3)$$

where

$$I_c = \frac{4\pi\epsilon_o m_o c^3}{e} = 17 \text{ kA}, \quad (4)$$

c is the speed of light, e is the electron charge, m_o is the electron mass, ϵ_o is the permittivity of free space, $\gamma_o = 1/\sqrt{1-\beta_o^2}$, $\beta_o = v/c$, and v is the beam speed. MKS units are used throughout, except where noted. This result [Eq. (3)] assumes an "infinite" axial magnetic field, but does not include the radial variation in γ . As noted by Olson,¹ this result is applicable in the limit that $\ln(R/r_b) > 1$. For $r_b = 0.8$ cm, and $R = 1.9$ cm, Eq. (2) gives $g = 2.73$. For $\gamma_o = 2$, and $g = 2.73$, Eq. (3) gives $I_l^{BR} = 2.8$ kA. The values of r_b , R , and γ_o chosen here are used in the PIC simulations discussed in Section III. Replacing γ_o in Eq. (3) by $1 + V_b/(0.511 \times 10^6)$, we find that $I_l^{BR}(A) \approx 2.53 \times 10^{-5} V_b^{3/2}/g$ to first order in V_b for $(V_b/0.511 \times 10^6) < 1$ for V_b in volts.

Next we note several more recent additions to the family of relativistic limiting current expressions for solid, magnetized, uniform current density beams, with constant injection energy. For the remainder of this section, we present the results of a considerable amount of pre-existing analysis. No attempt has been made to discuss the various methods and assumptions that were used to obtain these results. Reference 1 gives a short review of electron beam limiting current theory (through ~1977) relevant to collective ion acceleration. A rather substantial review of relativistic electron beam transport theory in vacuum and plasma through ~1974 can be found in Ref. 5.

Olson and Poukey⁹ have derived the limiting current expression

$$I_l^{OP} = I_c \frac{\beta_o(\gamma_o - 1)}{g}, \quad (5)$$

which does not include radial variation in γ , but is used as an upper current limit on the transport of electron beams in a gas-filled, conducting tube. Equation (5) expresses the limiting current in terms of vacuum propagation. For $\gamma_o = 2$, and $g = 2.73$, $I_l^{OP} = 5.39$ kA.

Thompson and Sloan¹⁰ have derived a limiting current estimate, I_l^{TS} , that is determined by maximizing the following expression for the current as a function of the equilibrium energy on axis, γ_c :

$$I(\gamma_c) = I_c (\gamma_c - \gamma_e)^2 \left\{ \gamma_c \beta_e - \gamma_e \beta_c \right.$$

$$\left. + \frac{\gamma_c}{g} \left[\ln \left(\frac{\gamma_c(\beta_e + 1)}{\gamma_e(\beta_c + 1)} \right) - \beta_c \ln \left(\frac{\gamma_c \gamma_e (\beta_c \beta_e + 1) - 1}{2(\gamma_c^2 - 1)} \right) \right] \right\}^{-1}, \quad (6)$$

where

$$\gamma_e = \frac{\gamma_o + \gamma_c(g-1)}{g}, \quad (7)$$

and Eq. (6) is second-order-accurate in γ_c . In Eq. (6), β_e and β_c are related to γ_c and γ_e in the conventional sense. For $\gamma_o = 2$ and $g = 2.73$, $I_l^{TS} = 3.20$ kA at $\gamma_c = 1.17$.

Genoni and Proctor have derived the following limiting current formula (see Ref. 11),

$$I_l^{GP} = I_l^{BR} \gamma_o^{2/3} \{ [(\gamma_o^{2/3} + g)^2 - \gamma_o^{2/3}]^{1/2} - g \}^{-1}. \quad (8)$$

For $\gamma_o = 2$, and $g = 2.73$, $I_l^{GP} = 3.18$ kA. The Genoni-Proctor and Thompson-Sloan limiting currents essentially overlay in the range $\gamma_o = 1.5$ –3.0 for $g = 2.73$.

Uhm¹² has derived an expression, similar to Fessenden,¹³ that gives the current flowing in the pipe as a function of the relativistic mass ratio at the center of the beam, γ_c . This equation must be maximized as a function of γ_c numerically in order to determine the limiting current, I_l^{UF} :

$$I(\gamma_c) = I_c \left[\sqrt{(\gamma_c + \nu)^2 - 1} - \sqrt{\gamma_c^2 - 1} - \tan^{-1} \sqrt{(\gamma_c + \nu)^2 - 1} + \tan^{-1} \sqrt{\gamma_c^2 - 1} \right], \quad (9)$$

where Budker's parameter, $\nu = I/(I_c \beta)$, is equated to

$$\nu = \frac{\gamma_o - \gamma_c}{g}. \quad (10)$$

For $\gamma_o = 2$, and $g = 2.73$, $I_l^{UF} = 3.36$ kA at $\gamma_c = 1.12$.

In addition to the above expressions, we note that an expression has been derived for the limiting current in a finite-length pipe¹⁴ (with a metallic foil across the downstream end). For a solid beam, the limiting current is given as

$$I_l^{AST} = I_l^{BR} \left(1 - \text{sech} \left(\frac{\lambda_1 L}{2R} \right) \right)^{-1}, \quad (11)$$

where $\lambda_1 \approx 2.4$, the root of the Bessel function J_o , and L is the guide tube length. For $L = 6$ cm, $\gamma_o = 2$, and $g = 2.73$, $I_l^{AST} = 2.93$ kA, a 5% correction to the BR limiting current. This estimate then indicates that the limiting current for these parameters is not "length-limited." A similar calculation has been performed by Genoni and Proctor,¹⁵ yielding an upper bound on the limiting current in a finite length guide tube. Though their result is expressed for arbitrary-thickness annular beams, the expression presented here is for solid beams:

$$I_l^{GP-UB} = \frac{I_c r_b^2}{4} \left(k^2 + \frac{\pi^2}{L^2} \right) (\gamma_o^{2/3} - 1)^{3/2}, \quad (12)$$

where k is determined by finding the root of

$$r_2 J_o(kr_b) + r_1 k r_b J_1(kr_b) = 0, \quad (13)$$

where the constants r_1 and r_2 are given by

Fl
So

In
Be
 J_n
cm
 r_1
Eq
 γ_o
mi
wit

tial
the
the
atic
eva
we
ete
lim
[ex
cun

$\left(\frac{r_b^2}{L^2} \right)$

and

$\left[\frac{r_b^2}{L^2} \right]$

J. A

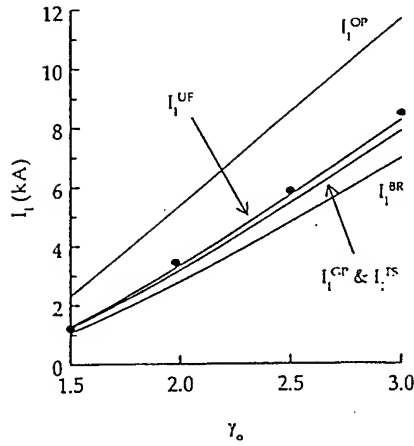


FIG. 1. Limiting current expressions as a function of γ_o for fixed $g=2.73$. Solid data points indicate simulation results.

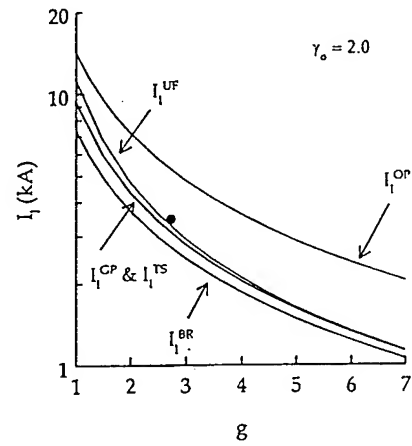


FIG. 2. Limiting current expressions as a function of g for fixed $\gamma_o=2.0$. Solid data point denotes simulation result.

$$r_1 = K_o \left(\frac{\pi R}{L} \right) I_o \left(\frac{\pi r_b}{L} \right) - I_o \left(\frac{\pi R}{L} \right) K_o \left(\frac{\pi r_b}{L} \right), \quad (14)$$

$$r_2 = \frac{\pi r_b}{L} \left[K_o \left(\frac{\pi R}{L} \right) I_1 \left(\frac{\pi r_b}{L} \right) + I_o \left(\frac{\pi R}{L} \right) K_1 \left(\frac{\pi r_b}{L} \right) \right]. \quad (15)$$

In Eqs. (13), (14), and (15), I_n and K_n are the modified Bessel functions of the first and second kind of order n , and J_n is the Bessel function of the first kind of order n . For $L=6$ cm, $R=1.9$ cm and $r_b=0.8$ cm, Eqs. (14) and (15) give $r_1=-0.914$ and $r_2=1.131$. Numerically finding the root of Eq. (13) gives $k=1.70$ cm $^{-1}$, and $I_l^{GP-UB}=3.88$ kA for $\gamma_o=2$. For these parameters, Eq. (12) is 13% greater than the minimum value ($L \gg 6$ cm). Therefore, I_l^{GP-UB} is nominally within the "length-limited" regime for these parameters.

The limiting currents presented in this section are essentially electrostatic limits, governed by the potential between the electron beam and the wall. It should be noted that due to the presence of an infinite axial magnetic field, no consideration of self magnetic field effects (pinching) should be relevant. The Alfvén magnetic limiting current, $I_A = I_c \beta_o \gamma_o$, is well above the limiting currents considered here for parameters used in Section III. However, in the ultra relativistic limit, all of the limiting currents presented in this section [except Eq. (1)] approach I_A/g . A comparison of the limiting currents I_l^{BR} , I_l^{GP} , I_l^{OP} , I_l^{TS} , and I_l^{UF} is given in Fig. 1 as a

function of γ_o for $g=2.73$ and in Fig. 2 as a function of g for $\gamma_o=2$. The beam completely fills the pipe for $g=1$, and $g=7$ corresponds to a sub-millimeter beam radius for values of R considered in this work ($R=1.9$ cm). Simulation results for I_l are also given in Figs. 1 and 2. A discussion of these results is given in Section III.

For injected currents that exceed the limiting value, γ approaches 1 at the center of the beam at a distance of roughly c/ω_{pb}^o beyond the injection plane (ω_{pb}^o is the beam plasma frequency). At this point, a virtual cathode (VC) is formed which has an axial oscillation with characteristic frequency of approximately $\omega_{pb}^{o-rel} = \sqrt{n_b^o e^2 / \epsilon_o m_o \gamma_o}$, where n_b^o is the injected beam density.^{3,16,17}

Even after the formation of the virtual cathode, an annular beam is transported outside of the VC. In addition, a small current is emitted from the VC in bursts with frequency approximately ω_{pb}^o . The dynamics of the VC in transmitting this "pulsed" current has been treated with one-dimensional impulse or "shock" models.¹⁸ An estimate of the current transmitted outside of the VC may be performed by calculating the axial position (z_*) and radial extent (r_*) of the VC. Assuming a transmitted current, I_t , between $r=r_*$ and r_b of I_o ($n_e=n_b^o$) and no net current between $r=0$ and r_* ($n_e=2n_b^o$), Al'terkep, Sokulin, and Tarakanov¹⁴ have found the following coupled set of transcendental equations for z_* and r_* (expressed here for an initially solid beam):

$$\left(\frac{r_b^2 - r_*^2}{r_b^2} g + \frac{r_*^2}{r_b^2} \ln \frac{r_*^2}{r_b^2} \right) \left(1 - \frac{\sinh(\lambda_1 z_*/R) + \sinh(\lambda_1 (L - z_*)/R)}{\sinh(\lambda_1 L/R)} \right) + \frac{2r_*^2}{r_b^2} \ln \frac{R^2}{r_*^2} \left(\frac{\sinh(\lambda_1 (L - z_*)/R) \cosh(\lambda_1 z_*/R) - \sinh(\lambda_1 (L - z_*)/R)}{\sinh(\lambda_1 L/R)} \right) = \frac{I_c}{I_o} (\gamma_o^{2/3} - 1)^{3/2} \quad (16)$$

and

$$\left[\frac{r_b^2 g + 1}{2} - r_*^2 \left(1 + \ln \frac{R^2}{r_*^2} \right) \right] \left[\cosh \left(\frac{\lambda_1 z_*}{R} \right) - \cosh \left(\frac{\lambda_1 (L - z_*)}{R} \right) \right] + 2r_*^2 \ln \frac{R^2}{r_*^2} \cosh \left(\frac{\lambda_1 (L - z_*)}{R} \right) \left[\cosh \left(\frac{\lambda_1 z_*}{R} \right) - 1 \right] = 0. \quad (17)$$

Numerically solving for z_* and r_* , and equating the injected and transmitted current densities, an estimate for the transmitted current, $I_t^{AST} = I_0(1 - r_*^2/r_b^2)$, is obtained. For $R=1.9$ cm, $r_b=0.8$ cm, $L=6$ cm, $I_0=6$ kA, and $\gamma_0=2$, we find $z_*=0.73$ cm and $r_*=0.42$ cm. This gives $I_t^{AST}=4.35$ kA. This model is only valid for injected currents greater than the limiting current for a solid beam and less than the limiting current for a hollow beam with an inner radius equal to r_* . For the parameters given above, I_t^{AST} is below the smallest limiting current value for a beam with inner and outer radii of r_* and r_b . A comparison between this result and our simulation results is given in Section III.

Other theoretical efforts have included the definition of a "useful" current value based on the degree of stratification in the transmitted beam¹⁹ [i.e., the magnitude of $\gamma(r_b) - \gamma(0)$]. We also note that analytic efforts have examined the impact of magnetically shielded vs. magnetically immersed beam sources on the limiting current value.^{20,21} These results are beyond the scope of this work.

Results presented in this section have thus far been applicable to solid, uniform current density electron beams. It is noted that the limiting currents for annular or hollow electron beams are generally higher. Substantial analytic,^{15,22,23} numerical,²⁴ and experimental²⁵⁻²⁷ efforts have been devoted specifically to the hollow beam geometry. While the present paper only considers limiting currents for solid beams, these calculations can be carried out for annular beams as well.

III. NUMERICAL SIMULATION

Numerical simulations of the BR relativistic electron beam limiting current have been carried out using the 2(1/2)-dimension code MAGIC.⁷ The code employs the particle-in-cell methodology, solving the full set of Maxwell's equations on a grid. Particles are advanced at each time step self-consistently via relativistically correct equations of motion.

In order to examine the BR limiting current, a computational region extending in radius from 0 to 2.0 cm and 0 to 6.0 cm in axial length was set up. The inner radius of the conducting tube is $R=1.9$ cm. A 0.8 cm radius beam, r_b , is injected at $z \approx 0$ into the waveguide. Other than the beam injection region, no other particle source was permitted. It has been shown elsewhere²⁸ that the perturbing effect of the electron beam source on the two-dimensional potential distribution has no effect on the limiting current. Also, the simulation length, L , satisfies the requirement²⁹ that

$$\frac{L}{R} \geq 2.58 \left(\frac{r_b}{R} \right)^{0.133}, \quad (18)$$

which evaluates to $L \geq 4.4$ cm. This inequality gives a somewhat different result than found in Eq. (12), both of which assume a conducting boundary at $z=L$. The possibility of "length-limited" results was tested in the simulations by performing specific cases at $L=6$ and 12 cm. No difference in the limiting or transmitted current values was found.

Preliminary calculations with a constant energy and current beam were carried out to examine the limit on transportable electron current. First, an electron beam of a constant

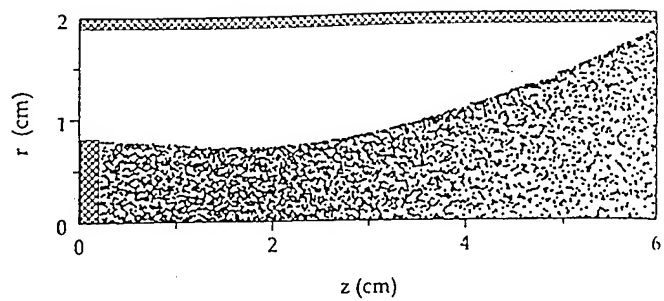


FIG. 3. Particle plots in r and z at 4.0 ns. These results are for an injected current of 2.7 kA, $\gamma_0=2$, and $B_0=0.0$.

$\gamma_0=2.0$ was injected with no externally applied magnetic field. The input current density was varied between runs. The beam current was programmed to rise linearly over 1 ns to I_0 . For an injected current of less than 2.0 kA, a steady and continuous beam was transported over the simulation axial distance with some beam expansion. However, when the current was raised to 2.7 kA, the beam expanded to the tube radius at $z \approx 6$ cm. This case is illustrated in Fig. 3 with the beam injected at $z \approx 0$ cm. Without a large applied axial magnetic field, this result has no bearing on the examination of the BR limiting current. However, such a simulation provides valuable information on energy conservation and boundary conditions. The limit on transportable current from this simulation is determined more from space charge limits than the potential between the beam and channel wall. The limiting current for a drifting beam spreading radially under its own self-fields is given approximately as

$$I_t^{RS} \approx I_c \frac{\beta_0^3 \gamma_0^3}{2(g-1)} \left(\frac{R}{L} \right)^2. \quad (19)$$

For $L=6$ cm, $R=1.9$ cm, $g=2.73$, and $\gamma_0=2$, $I_t^{RS}=2.6$ kA. This expression is not valid over all ranges of r_b , R , and L . As r_b approaches R , the logarithmic term in the denominator drives the limiting current in Eq. (19) to infinity. A more accurate envelope equation treatment gives essentially the same result for these parameters.³⁰

When a large (100 T), axial, magnetic field is applied uniformly throughout the simulation, laminar beam flow is observed, as expected. No attempt is made to resolve the gyro-orbit about the axial magnetic field. Electrons are injected into the simulation with no transverse temperature, and therefore they have a gyro-radius of zero. Numerical heating might introduce some radial acceleration, but if we assume a maximum transverse temperature due to numerical errors of $0.01\gamma_0$, the electron gyroradius is only 1.7×10^{-4} cm for parameters used in this report. Therefore, maximum displacement errors in the radial direction are on the order of 0.1% of the typical simulation cell size and are safely ignored.

Previous investigations with PIC codes¹¹ have determined a finite magnetic field strength of $\omega_c \geq 5\omega_{ph}$ (where $\omega_c = eB_0/m_0$, $\omega_{ph} = \sqrt{n_b e^2 / \epsilon_0 m_0}$), above which the observed limiting current is insensitive to B_0 . For parameters

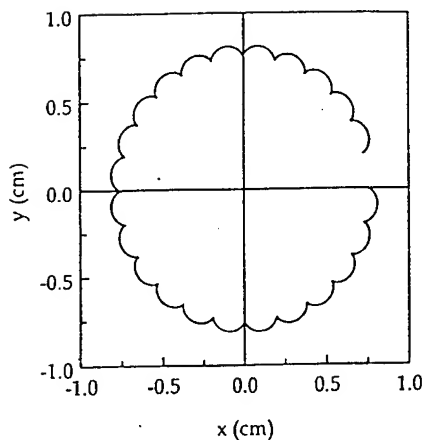


FIG. 4. Plot of cross-sectional trajectory of test electron in outer edge of beam. For this calculation, $\gamma_o=2$, $I_o=3.4$ kA, and $B_o=0.5$ T.

used in this work, this relation indicates that B_o should be greater than 1 T. This value for the applied magnetic field was checked in a set of runs in the problem geometry, and the inequality $\omega_c \geq 5\omega_{pb}^o$ was verified. As B_o is decreased below this minimum value, electrons at the outer edge of the beam begin to travel around the outside of the beam in helical orbits. These orbits were investigated by numerically solving the relativistic Lorentz equation in three-dimensions for a test electron traveling in the static electric and magnetic fields of the beam and the applied magnetic field. A typical orbit is shown in Fig. 4 for an electron at the outer edge of the beam for an applied magnetic field strength of 0.5 T and an injected current of 3.4 kA. A full electrodynamic orbit calculation, not performed here, would include the radial self-field dynamics of the beam envelope, distorting the trajectory plotted in Fig. 4.

Next, a set of simulations were performed to determine the limiting current, I_l , for this geometry with $\gamma_o=1.5, 2.0, 2.5$, and 3.0 . The total transmitted current, I_t , is measured near the downstream end of the simulation region. I_l was determined to be the point at which $I_o \neq I_t$ or when VC formation was observed in the simulation. The effect of radial variation in γ can be qualitatively seen in Figs. 5 and 6 for $\gamma_o=2.0$ and $I_o=6$ kA, well above the limiting current value.

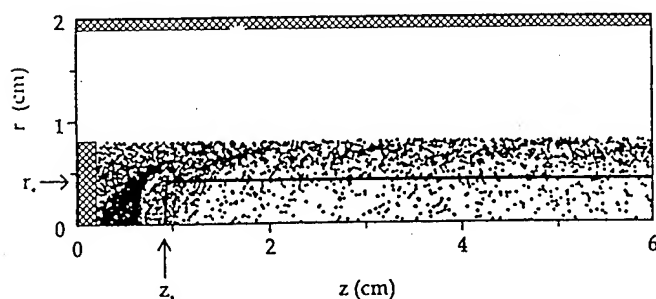


FIG. 5. Particle plots in r and z at 4.0 ns. These results are for an injected current of 6.0 kA, $\gamma_o=2$, and $B_o=100$ T. The analytic estimate of the transmitted beam inner radius and virtual cathode position are denoted by r_* and z_* .

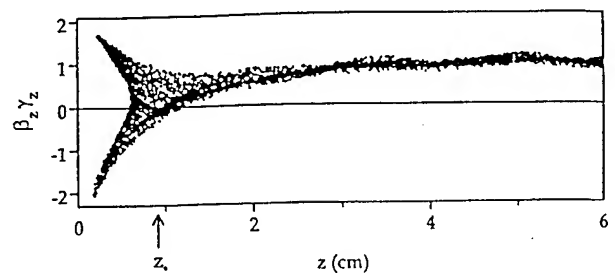


FIG. 6. Particle plots of P_z vs. z at 4.0 ns. These results are for an injected current of 6.0 kA, $\gamma_o=2$, and $B_o=100$ T. The analytic estimate of the virtual cathode position is denoted by z_* .

A virtual cathode is observed at approximately 0.7 cm into the pipe. This value is consistent with the electromagnetic interaction length, c/ω_{pb}^o .

The simulation results indicate that the limiting current for vacuum transport for these parameters is indeed $\sim 17\%$ higher than is predicted by the BR limiting current, as shown in Fig. 1. These results are roughly consistent with other recent PIC simulations^{11,31} for solid beams. We briefly investigate two possible mechanisms for this enhancement of the limiting current. One possibility is the coupling between an appropriate waveguide mode and the propagating beam.³² For a solid beam, this is the TE_{11} mode. For parameters used in the simulation, the enhancement of the limiting current due to the ponderomotive energy was found to be negligible. This is due primarily to the very large axial magnetic field used in the simulations. This does not preclude the use of such a technique in experimental configurations where axial magnetic fields smaller than those discussed in this work are often used.

In addition, the induced axial electric field at the cathode was examined as a possible source of the enhanced transported current values. It was found from code diagnostics that the fast rising current produced electric fields that were approximately two orders of magnitude smaller than the fields created by emitting charge from the cathode some discrete distance ($dz/2$) in the simulation region. These fields were found not to contribute substantially to the injected beam energy.

Further consideration of the results plotted in Fig. 1 indicated that the limiting current expressions obtained by Uhm¹² [Eq. (9)] and Fessenden¹³ give good agreement with the PIC simulation I_l over the parameter range considered in this work. A further comparison between the limiting current theory given in Refs. 12 and 13 and numerical simulations can be made by comparing the equilibrium radial γ variation

$$\gamma(r) = \gamma_o - \nu \left[g - \left(\frac{r}{r_b} \right)^2 \right], \quad (20)$$

where ν is given in Eq. (10). For $\gamma_o=2$ and $g=2.73$, $\gamma_c=1.12$ and $\nu=0.332$. Figure 7 plots Eq. (20) for these parameters as a function of r along with the simulation particle distribution for $I_o=3.36$ kA. Reasonable agreement is found over most of the beam profile.

As noted in Section II, for injected currents above the limiting value, a transmitted beam with an annular profile is

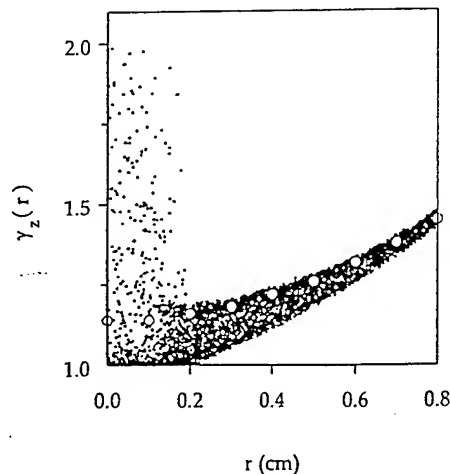


FIG. 7. Plots of equilibrium beam energy, γ , over the range $r=0$ to r_b , for the analytic approximation and the simulation results. The large hollow points are from Eq. (20) with $\nu=0.332$ and the smaller points are the simulation results with $g=2.73$, $\gamma_o=2.0$, and $I_o=3.4$ kA.

observed, both in simulations^{11,14} and experiments.³³ A simple, two-dimensional estimate of the charge density profile for beams above the limiting current¹⁴ yields the approximate position of the virtual cathode and transmitted beam inner radius, r_* and z_* , given by Eqs. (16) and (17). This result is plotted over the (r,z) plot in Fig. 5. The radial current density profile "snapshot" for the simulation given in Figs. 5 and 6 is shown in Fig. 8 at 4 ns. This simulation result is qualitatively similar to current density profiles observed in experiments.³³ Not accounted for in the model of Al'terko, Sokulin, and Tarakanov¹⁴ is the "pulsed" current at $r < r_*$ produced by the virtual cathode oscillations at frequency, ω_{pb}^{o-rel} .

In Fig. 9, the average transmitted current, collected at an axial distance many times c/ω_{pb} , is presented as a function of γ_o . From these results, the transmitted current continues to increase beyond the limiting value as I_o is increased. This current should peak at the limiting value for an annular beam. In Fig. 10, the results of Fig. 9 are plotted along with the results of Thode, Godfrey, and Shanahan.¹¹ It is important to note that the calculations of Ref. 11 were performed

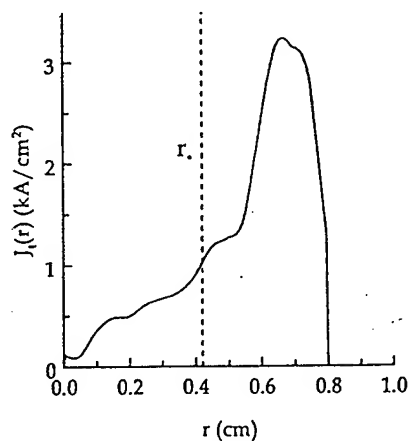


FIG. 8. Magnitude of the transmitted current density profile, $J_z(r)$, from a PIC simulation for $I_o=6$ kA, $\gamma_o=2$, and $B_o=100$ T. The analytic estimate of the transmitted beam inner radius is denoted by r_* .

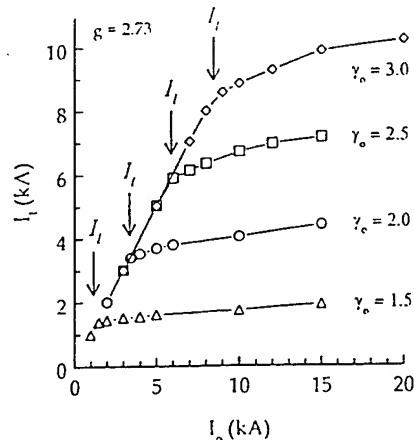


FIG. 9. Transmitted current, I_t , as a function of injected current, I_o , for several different injected beam energies. The limiting current value for each curve is marked by an arrow.

with constant ω_c/ω_{pb} (i.e., B_o was varied for different I_o), while the results presented in Fig. 8 are for B_o fixed at 100 T. In Fig. 10, the results of Thode, Godfrey, and Shanahan¹¹ do not clearly show the same continuous rise in I_t above I_l as found here for $\gamma_o=1.5-3.0$.

Inasmuch as the typical experimental conditions for "vacuum propagation" is a quite imperfect vacuum, with gas density often exceeding 10^{12} atoms/cm³ partially ionized by the beam, a set of simulations were performed with an electron beam injected into a low density plasma completely filling the conducting pipe. The background plasma density and the applied magnetic field magnitude were varied to examine the magnitude of the transmitted current. Previous PIC simulations³⁴ have examined this issue for hollow beams injected into partially plasma-filled waveguides at different applied magnetic field magnitudes. For our simulations, a uniform density, cold hydrogen plasma of density n_p was placed inside the conducting pipe from $r=0$ to R and $z=0$ to L . For injected beams with parameters $\gamma_o=2$ and $I_o=3$ kA, we found $I_t=3$ kA for a range of densities and magnetic field amplitudes ($n_p=0$ to 9.9×10^{11} cm⁻³ and $B_o=0$ to 100 T).

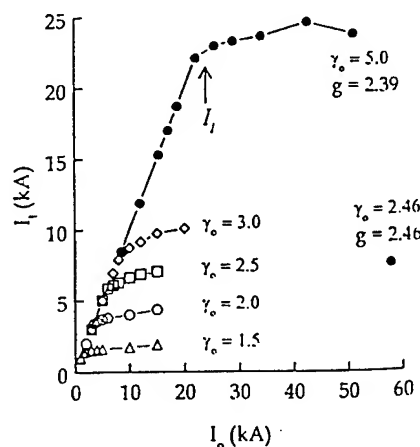


FIG. 10. Replot of Fig. 9 including results of Thode, Godfrey, and Shanahan, Ref. 11, as solid black circles. The limiting current value for the $\gamma_o=5.0$ curve is marked by an arrow.

However, the time required for the system to reach the equilibrium value of I_l varied as the logarithm of B_o (for $B_o \geq 0.1$ T and $n_p = 9.9 \times 10^{11}$ cm $^{-3}$). For $B_o = 100$ T, $\gamma_o = 2$, and $I_o = 6$ kA (well above the vacuum limiting current), we observed unimpeded beam transport, with $I_l \approx 6$ kA, above $n_p = 5 \times 10^{11}$ cm $^{-3}$ (up to 2×10^{12} cm $^{-3}$, the maximum value we considered). For these same beam and plasma parameters but with $B_o = 0$, we found $I_l \approx 5$ to 6 kA. For ion-focus-regime (IFR) transport,³⁵ $n_p \geq n_b$, as found here. IFR transport of electron beams in conducting tubes helps to center the beam and reduce beam sweep.³⁶ Note that in the simulations, the addition of the large applied magnetic field increases the ion channel formation time (because plasma electrons can not leave the IFR channel radially).

IV. CONCLUSIONS

The BR limiting current, Eq. (3), has been investigated with the 2(1/2) dimensional particle-in-cell code, MAGIC. Results confirm that the BR limiting current under-estimates the actual limiting current for solid, relativistic electron beams. These results are consistent with other published numerical simulations,^{11,31} performed for other values of γ_o and g . It is found that while the BR limit under-estimates the actual limiting current, the Olson-Poukey limiting current, Eq. (5), over-estimates the actual limiting current, at least for low γ beams. More recent analytic calculations of the limiting current provide better estimates of I_l as observed in PIC simulations, at least for parameters used in this work. A comparison between limiting current simulation and theory is given in Figs. 1 and 2. The results of Uhm¹² and Fessenden¹³ provide the most accurate prediction of I_l for parameters considered in the work. The simulations also qualitatively indicate radial γ variation for $I_o = I_l$, consistent with one-dimensional estimates^{12,13} (see Fig. 7). Figures 5 and 6 illustrate the dynamics of electron beam propagation above the limiting current.

For injected currents above the limiting current, an annular beam is transported outside the virtual cathode. Figures 9 and 10 plot transmitted currents above I_l from this work and previous simulations.¹¹ The results of an analytic model for the inner radius of the transmitted current and virtual cathode position are compared with the simulation results¹⁴ (Figs. 5, 6, 8). It is found that for parameters used in this work, the theory does not explain the relationship between I_l and I , as observed in the simulation results (see Figs. 8 and 9).

In addition to the perfect-vacuum transport simulations described above, several simulations were performed with a low-density plasma inside the waveguide. Connection was made to the known results of IFR transport for $n_b \leq n_p$ and B_o between 0 and 100 T. (This result corroborates that for IFR transport, large axial magnetic fields are not necessary for efficient transport, and that the presence of the background plasma minimizes VC formation and allows beam currents in excess of the vacuum limiting values to be transported.)

Most simulations reported in this work were performed with a constant current electron beam. Our results indicate that simply "turning on" the full current achieves roughly

the same results in vacuum as for a more realistic current ramp for the simulation setup described in Section III. In addition, several runs were performed with much longer guide tubes (up to 28 cm) in order to determine if the boundary conditions were allowing errors to propagate back into the system. No significant change in the results between short (6 cm) and long guide tubes was found.

The study of limiting currents extends well beyond the physics considerations highlighted in this report. Vacuum transport studies are extended in the regime of low density transport for collective ion acceleration, where it is desired to exceed vacuum limiting currents.³⁷ Other studies have examined the importance of beam bunching resulting from γ variation,³⁸ radiation produced at the virtual cathode,³⁹ and the impact of beam instabilities on limiting currents for small amounts of space-charge neutralization.⁴⁰ Additionally, investigations into finite temperature distributions⁴¹ and foil scattering^{11,33} at the beam source have yielded extensions to the BR limiting current theory, making it more applicable to warm-beam conditions.

Current research in relativistic, vacuum beam transport includes mechanisms to greatly increase the space-charge limiting current³² and control virtual cathode motion,⁴²⁻⁴⁴ primarily for microwave applications.

ACKNOWLEDGMENTS

The authors wish to thank John Grossmann and Steve Swanekamp for discussions of this problem and its numerical simulations. We also thank Matt Myers for providing us with an early draft of his manuscript. This work was completed in partial fulfillment of degree requirements at the Institute for Computational Science and Informatics, George Mason University. Simulation results were obtained using the Mission Research Corporation's MAGIC code under the AFOSR-sponsored MAGIC User's Group.

- ¹C.L. Olson, in *Collective Ion Acceleration* (Springer, New York, 1979).
- ²T.W.L. Sanford, J.A. Halbleib, and R.C. Mock, *IEEE Trans. Nucl. Sci.* NS-37, 1762 (1990).
- ³D.J. Sullivan, *IEEE Trans. Nucl. Sci.* NS-30, 3426 (1983).
- ⁴E.L. Patterson, R.J. Kaye, and E.L. Neau, 1994 IEEE International Conference on Plasma Science, Conference Record Abstracts, *IEEE Catalog No. 94CH3465-2*, 1994, p.143.
- ⁵B.N. Brejzman and D.D. Ryutov, *Nucl. Fusion* 14, 873 (1974).
- ⁶L.S. Bogdankevich and A. A. Rukhadze, *Sov. Phys. Usp.* 14, 163 (1971).
- ⁷B. Goplen, L. Ludeking, D. Smithe, and G. Warren, *Comp. Phys. Commun.* 87, 54 (1995).
- ⁸L.P. Smith and P.L. Hartman, *J. Appl. Phys.* 11, 220 (1940).
- ⁹C.L. Olson and J.W. Poukey, *Phys. Rev. A* 9, 2631 (1974).
- ¹⁰J.R. Thompson and M.L. Sloan, *Phys. Fluids* 21, 2032 (1978).
- ¹¹L.E. Thode, B.R. Godfrey, and W.R. Shanahan, *Phys. Fluids* 22, 747 (1979).
- ¹²H.S. Uhm, *Phys. Fluids B* 5, 1919 (1993).
- ¹³T.J. Fessenden, Lawrence Livermore Lab. Rep. No. UCID-16527, 1974 (unpublished).
- ¹⁴B.A. Al'terkop, A.Yu. Sokulin, and V.P. Tarakanov, in *Proceedings of the 7th International Conference on High-Power Particle Beams*, edited by W. Bauer and W. Schmidt (Kernforschungszentrum, Karlsruhe, Germany, 1987), p. 889; *Sov. J. Plasma Phys.* 15, 564 (1989).
- ¹⁵T.C. Genoni and W.A. Proctor, *J. Plasma Phys.* 23, 129 (1980).
- ¹⁶D.J. Sullivan, J.E. Walsh, and E. A. Coutias, in *High-Power Microwave Sources*, edited by V.L. Granatstein and I. Alexoff (Artech, Norwood, MA, 1987), p. 441.
- ¹⁷B.V. Alyokhin, A.E. Dubinov, V.D. Selemir, O.A. Shamro, K.V. Shibalko,

17. V. Stepanov, and V.E. Vatrutin, IEEE Trans. Plasma Sci. PS-22, 773 (1994); V.D. Selemir, B.V. Alekhin, V.E. Vatrutin, A.E. Dubinov, N.V. Stepanov, O.A. Shamro, and K.V. Shibalko, Plasma Phys. Rep. 20, 621 (1994).
18. A. Kadish, IEEE Trans. Plasma Sci. PS-13, 188 (1985); A. Kadish, R.J. Faehl, and C.M. Snell, Phys. Fluids 29, 4192 (1986).
19. V.E. Nechaev, Sov. J. Plasma Phys. 3, 64 (1977).
20. V.G. Leyman, Radio Eng. Electron. Phys. 25, No. 11 86 (1980).
21. M. Reiser, Phys. Fluids 20, 477 (1977).
22. J.W. Poukey and J.R. Freeman, Phys. Fluids 17, 1917 (1974).
23. A.T. Drobot and K. Kim, Int. J. Electronics 51, 351 (1981).
24. D.S. Filippichev and V.Yu. Shafer, Sov. J. Plasma Phys. 15, 103 (1989).
25. J.A. Nation and M. Read, Appl. Phys. Lett. 23, 426 (1973).
26. M.E. Read and J.A. Nation, J. Plasma Phys. 13, 127 (1975).
27. Y. Carmel and J.A. Nation, Phys. Rev. Lett. 31, 286 (1973).
28. V.I. Kuchero, P.B. Rutkevich, and V.V. Chernyi, J. Appl. Mech. Tech. Phys. 21, 440 (1980).
29. R.B. Miller and D.C. Straw, J. Appl. Phys. 48, 1061 (1977).
30. S. Humphries, Jr., *Charged Particle Beams* (Wiley, New York, 1990), Sec. 5.4.
31. D.J. Sullivan and N.F. Roderick, Phys. Fluids 22, 799 (1979).
32. C. Grebogi and H.S. Uhm, Phys. Fluids 31, 1277 (1988).
33. T.H. Gerdien, G.C.A.M. Janssen, and H.G. Hopman, Plasma Phys. Rep. 18, 1028 (1982).
34. A.A. Rukhadze, P.V. Rybak, and V.P. Tarakanov, Plasma Phys. Rep. 20, 369 (1994).
35. S.B. Swanekamp, J.P. Holloway, T. Kammash, and R.M. Gilgenbach, Phys. Fluids B 4, 1332 (1992), and references therein.
36. M.C. Myers, J.A. Antoniadis, R.A. Meger, D.P. Murphy, R.F. Fernster, and R.F. Hubbard, J. Appl. Phys. 78, 3580 (1995).
37. V.B. Krasovitskii, Sov. Phys. Tech. Phys. 33, 639 (1988).
38. Yu.K. Alekseev and A.I. Kostienko, Sov. Phys. Tech. Phys. 32, 1028 (1987).
39. V.K. Ablekov, V.P. Pugachev, and A.M. Frolov, Sov. Phys. Dokl. 25, 563 (1980).
40. S.I. Vybornov, A.V. Zharinov, and V.A. Malafae, Sov. J. Plasma Phys. 14, 51 (1988).
41. T. Antonsen Jr. and B. Levush, Int. J. Electronics 61, 871 (1986).
42. W. Peter, in *Proceedings of the 9th International Conference on High-Power Particle Beams*, Washington, DC, 1992, edited by G. Cooperstein and D. Mosher, p. 1819.
43. T.C. Genoni, J. Appl. Phys. 51, 3426 (1980).
44. A.M. Ignatov and V.P. Tarakanov, Phys. Plasmas 1, 741 (1994).